NUREG/CR-6153
SAND93-2588

A Simplified Model of Decontamination by BWR Steam Suppression Pools

Manuscript Completed: December 1996
Date Published: May 1997

Prepared by
D. A. Powers

Sandia National Laboratories
Albuquerque, NM 87185

J. H. Schaperow, NRC Project Manager

Prepared for
Division of Systems Technology
Office of Nuclear Regulatory Research
U.S. Nuclear Regulatory Commission
Washington, DC 20555-0001
NRC Job Code L2035

DISCLAIMER

Abstract

Phenomena that can decontaminate aerosol-laden gases sparging through steam suppression pools of boiling water reactors during reactor accidents are described. Uncertainties in aerosol properties, aerosol behavior within gas bubbles, and bubble behavior in plumes affect predictions of decontamination by steam suppression pools. Uncertainties in the boundary and initial conditions that are dictated by the progression of severe reactor accidents and that will affect predictions of decontamination by steam suppression pools are discussed.

Ten parameters that characterize boundary and initial condition uncertainties, nine parameters that characterize aerosol property and behavior uncertainties, and eleven parameters that characterize uncertainties in the behavior of bubbles in steam suppression pools are identified. Ranges for the values of these parameters and subjective probability distributions for parametric values within the ranges are defined. These uncertain parameters are used in Monte Carlo uncertainty analyses to develop uncertainty distributions for the decontamination that can be achieved by steam suppression pools and the size distribution of aerosols that do emerge from such pools.

A simplified model of decontamination by steam suppression pools is developed by correlating features of the uncertainty distributions for total decontamination factor, DF(total), mean size of emerging aerosol particles, d_p, and the standard deviation of the emerging aerosol size distribution, σ, with pool depth, H. Correlations of the median values of the uncertainty distributions are suggested as the best estimate of decontamination by suppression pools. Correlations of the 10 percentile and 90 percentile values of the uncertainty distributions characterize the uncertainty in the best estimates.

Table of Contents

Page

Abstract . . . iii
Table of Contents . . . v
List of Figures . . . ix
List of Tables . . . xv

I. Introduction . . . 1

II. Steam Suppression Pools . . . 5

A. Mark I Suppression Pools . . . 5
B. Mark II Suppression Pools . . . 5
C. Mark III Suppression Pools . . . 11
D. Conclusions . . . 16

III. Accident Analyses . . . 17

A. Overview . . . 17
B. Accidents in Mark I Reactors . . . 25
C. Accidents in Mark II Reactors . . . 34
D. Accidents in Mark III Reactors . . . 35
E. Conclusions . . . 37

IV. Physical Phenomena . . . 39

A. Bubble Formation . . . 39

1. Bubble Formation at Quencher Orifices . . . 41
2. Models of Bubble Formation . . . 52

a. The Davidson-Schuler Single-Stage Model . . . 52
b. Two-stage Bubble Formation Models . . . 53
c. Numerical Models . . . 59

3. Bubble Formation at Downcomers . . . 61
4. Bubble Formation at Horizontal Vents . . . 71

B. Collapse and Disintegration of Large Bubbles . . . 73
C. Bubble Size Distribution and the Coalescence of Bubbles . . . 85
D. Thermodynamics of Bubble Rise . . . 97
E. Bubble Plumes From Quenchers . . . 105
F. Overview of Bubble Behavior . . . 124
G. Slip Velocity of Bubbles . . . 131
H. Bubble Shapes . . . 134

Table of Contents (Continued)

Page

I. Heat and Mass Transport to and Within Bubbles 137

1. Heat Transport From Bubbles During Formation 140
2. Heat Transfer After Bubble Detachment 141
3. Heat and Mass Transfer During Bubble Rise 144

J. Thermophysical Properties 154

1. Properties of Liquid Water 154
2. Properties of Steam 158
3. Properties of Permanent Gases 161
4. Solubility of Gases in Water 173

K. Properties of Aerosol Particles 181

1. Shape Factors 183
2. Slip Correction Factors and Accommodation Coefficients 189
3. Hygroscopicity of Aerosols Produced in Reactor Accidents 200

L. Aerosol Behavior 203

1. Aerosol Trapping During Bubble Rise 204

a. Diffusion of Particles to the Bubble Walls 204
b. Sedimentation Within a Bubble 211
c. Inertial Deposition 212
d. Particle Deposition by Diffusiophoresis 215
e. Thermophoresis 221
f. Particle Growth by Water Condensation 229
g. Aerosol Capture by Bubble Oscillations 238

2. Aerosol Trapping During Bubble Collapse 242
3. Aerosol Capture During Bubble Formation 244

V. Uncertainty in Predictions of Aerosol Removal by Steam Suppression Pools 253

A. Mechanistic Model 253

1. Input 253
2. Generation of Random Numbers 255
3. Sampling Uncertain Inputs and Parametric Quantities 255
4. Properties of the Liquid 258
5. Discretization of the Aerosol Size Distribution 259
6. Formation of Bubbles and Decontamination During Bubble Formation 261

Table of Contents (Continued)

Page

7. Detachment and Equilibration of the Bubble 261
8. Plume Formation 261
9. Mass Transfer to the Bubble 265
10. Decontamination During Bubble Rise 265
11. Accumulation of Results 266

B. Uncertain Models, Inputs and Parametric Quantities 266

1. Input and Boundary Condition Uncertainties 268

a. Pool Depths 269
b. Orifice Sizes 269
c. Wetwell Pressures 269
d. Aerosol Particle Size 272
e. Aerosol Material Density 275
f. Uncertainty in Shape Factors 276
g. Gas Flow Rates 277

2. Phenomenological Uncertainties in Bubble Behavior 279

a. Uncertainty in Bubble Formation 279
b. Uncertainty in the Equilibration Distance 282
c. Initial Size of Bubbles in the Plume 282
d. Uncertainty in Bubble Shape 283
e. Bubble Slip Velocity 284
f. Uncertainty in Plume Parameters 286
g. Uncertainty in Bubble Growth 287
h. Radial Mixing in the Bubble Plume 288

3. Phenomenological Uncertainties in Aerosol Behavior 288

a. Uncertainty in Aerosol Trapping by Inertial Impaction 288
b. Uncertainty in Aerosol Trapping by Diffusion 295
c. Uncertainty in Slip Correction Factors 296
d. Uncertainty in Accommodation Coefficients 296
e. Uncertainty in Aerosol Capture by Bubble Oscillations 297
f. Uncertainty in the Summation of Aerosol Capture Processes 298
g. Uncertainty in Aerosol Capture During Bubble Formation 301

4. Summary of Uncertainties 302

Table of Contents (Concluded)

Page

VI. Results of the Uncertainty Analyses 303

A. Decontamination During Release Through 'T' Quenchers 304
B. Decontamination During Release Through 'X' Quenchers 328

VII. Simplified Model 341

VIII. Conclusions 345

IX. References 347

Appendix A Tabulations of Uncertainty Distributions 363

List of Figures

Figure		Page
1	Overall configurations of steam suppression pools in Mark I, Mark II, and Mark III boiling water reactors	2
2	Torus suppression pool of a Mark I containment	8
3	'T' Quencher for a Mark I suppression pool	9
4	Various types of vents from the drywells to the suppression pools in Mark I containments	10
5	Diagrams of the diaphragm floors of various Mark II containments	12
6	Positioning of quenchers in the Mark III suppression pool	13
7	Diagrams of X-quenchers in Mark III suppression pools	14
8	Horizontal vents in the Mark III suppression pool	15
9	Alternative core meltdown scenarios for boiling water reactors	22
10	Core debris expulsion from the reactor vessel into the drywell as predicted by the BWRSAR code	23
11	Molar gas flow ($\dot{M}$) through the reactor coolant system in a Mark I boiling water reactor during a TC3 accident sequence	26
12	Molar flows of gas to the suppression pool during core debris/concrete interactions in a TC3 accident sequence	27
13	Size distribution of aerosols in the reactor coolant system predicted with the Source Term Code Package	29
14	Mean size and material density of aerosols produced during core debris interactions with concrete in a TC3 accident in a Mark I boiling water reactor	30
15	Molar gas flow ($\dot{M}$) through the reactor coolant system in a Mark I boiling water reactor during a TB2 accident sequence	31
16	Molar flows of gas to the suppression pool during core debris/concrete interactions in a TB2 accident sequence	32
17	Mean size and material density of aerosols produced during core debris interactions with concrete in a TB2 accident in a Mark I boiling water reactor	33
18	Molar flow rates ($\dot{M}$) through the reactor coolant system in a Mark III boiling water reactor during a station blackout accident and an ATWS accident	36
19	Schematic representation of bubble behavior when released into a steam suppression pool from a quencher	40
20	Bubble injector apparatus used in tests of bubble hydraulics by Paul et al.	42
21	Comparison of bubble sizes predicted with correlation developed by Paul et al. to bubble sizes observed in various experiments	43
22	Comparison of observed volume equivalent spherical bubble diameter to predictions obtained with the Davidson-Schuler model with various coefficients	46
23	Comparison of Besset's bubble volume/data to the predictions of the modified Davidson-Schuler model	49
24	Fit of Schmidt's bubble volume data to a correlation in terms of the Weber number	51
25	Comparison of observed volume equivalent spherical bubble diameters to those predicted with the model of Kumar and Kaloor	55
26	Comparison of observed volume equivalent spherical bubble diameters to those predicted by Ruff's empirically modified model	57

List of Figures (Continued)

Figure		Page
27	Variation in the bubble diameter with orifice orientation predicted with the Kumar and Kaloor model	58
28	Comparison of the diameters of steam bubbles forming in subcooled water observed by Besset to predicted diameters obtained using Ruff's model corrected for the effects of condensation	60
29	Flow regime map developed from results of studies with a small-scale model of a suppression pool downcomer	62
30	Internal "chug" observed in tests by Lee and Chan	63
31	"Chugging" with bubble detachment observed in tests by Lee and Chan	65
32	"Chugging" without bubble detachment observed in tests by Lee and Chan	66
33	Comparison of various model predictions of the initial size of bubbles formed at a 60-cm-diameter downcomer	69
34	Comparison of various model predictions of the initial diameters of bubbles produced at a 72-cm-diameter horizontal vent	72
35	Isothermal, inertially-controlled collapse of a 2-cm bubble in water at 319 K according to Gilmore's model	76
36	Comparison of bubble collapse predictions to data from Levenspiel	78
37	Comparison of model predictions of bubble collapse to data from Wittke and Chao	79
38	Comparison of predictions of bubble collapse to data from Wittke and Chao	80
39	Rise velocities for very large bubbles	82
40	Bubble stability map for water at 298 K	83
41	Bubble stability map for water at 373 K	84
42	Effect of gas injection rate on bubble size distribution	86
43	Effect of orifice size on the bubble size distribution	87
44	Effect of orifice orientation on the bubble size distribution	88
45	Effect of the mole fraction of steam in air/steam mixtures on the mean bubble size	92
46	Effect of the mole fraction steam in air/steam mixtures on the geometric standard deviation of the bubble size distribution	93
47	Efficiency of bubble coalescence as a function of the ionic strength of the aqueous solution	95
48	Thermodynamic calculation of bubble rise in a water pool	103
49	Results of bubble rise calculation considering finite rates of heat and mass transport within the bubble	106
50	Schematic diagrams of bubble plumes: (a) simple plume, (b) plume with descending outer annulus and (c) plume with instability intrusions produced by unstable density stratification	108
51	Dependence of the entrainment coefficient on the bubble Froude number	114
52	Dependence of the momentum amplification factor on the phase distribution number	117
53	Comparison of plume model predictions to data obtained by Milgram in a pool ~ 5000 cm deep with Q = 19600 cm^3/s at the vent	121
54	Comparison of predictions of the plume model to data obtained by Milgram in a pool ~ 5000 cm deep with Q ≈ 97100 cm^3/s	122
55	Comparison of model predictions to centerline void fractions observed in experiments by Tacke et al.	123

List of Figures (Continued)

Figure		Page
56	Comparison of model predictions to bubble rise velocities observed in an experiment by Paul et al.	125
57	Comparison of model predictions to bubble rise velocities at various elevations observed in an experiment by Paul et al.	126
58	Effect of entrainment coefficient on predictions of bubble rise velocity	127
59	Variations in $\log_{10} M$ and E_o/D_B^2 with temperature in water	129
60	Comparison of predictions of bubble rise velocities by several models	133
61	Comparison of predicted bubble rise velocities to data for air bubbles in hot (322 K) tap water	135
62	Comparison of bubble eccentricity models to experimental data	138
63	General geometry of a spherical cap bubble	139
64	Heat transfer coefficients for bubbles rising in 373 K water as functions of bubble diameter	143
65	Comparison of predicted and observed mass transport coefficients for CO_2 from nearly spherical bubbles	146
66	Comparison of mass transport coefficients predicted for CO_2 in water from nonspherical bubbles to experimental data	150
67	External heat transfer coefficients for bubbles in water at 373 K derived from analogies to mass transport models	152
68	Correlation of the long-term Sherwood number in the gas phase for cases with a finite liquid phase Sherwood number	153
69	Comparison of predictions of the surface tension of water to experimental data	157
70	Comparison of the predicted thermal conductivity of water to critically assessed experimental data	159
71	Comparison of calculated steam viscosity to recommended values derived from experimental data	162
72	Comparison of calculated thermal conductivity of steam with experimental data	163
73	Comparison of calculated gas viscosities to recommended values derived from experimental data	166
74	Viscosity of hydrogen as a function of temperature	167
75	Predicted binary, gaseous diffusion coefficients for the H_2/H_2O, N_2/H_2O, and CO_2/H_2O systems	171
76	Comparison of the predicted thermal conductivity of CO_2 to experimental data	174
77	Comparison of the predicted thermal conductivity of O_2 to experimental data	175
78	Comparison of the predicted thermal conductivity of H_2 to experimental data	176
79	Comparison of the predicted thermal conductivity of CO to experimental data	177
80	Comparison of the predicted thermal conductivity of N_2 to experimental data	178
81	Comparison of the predicted thermal conductivity of H_2/N_2 mixtures at 300.5 K to experimental data	179
82	Comparison of the predicted thermal conductivities of N_2/CO mixtures at 300.5 K and N_2/CO_2 mixtures at 380.5 K to experimental data	180
83	Solubilities of gases in water at 1 atmosphere pressure as functions of temperature	182
84	Dynamic shape factor as a function of particle size for various particle material densities	187

List of Figures (Continued)

Figure		Page
85	Dynamic shape factors for doublets, triplets, and quadruplet agglomerates of spherical particles	188
86	Comparison of the predicted slip correction factor to values obtained in experiments with oil droplets and correlations of data for solid particles	192
87	Temperature accommodation coefficient of hydrogen on metal surfaces	194
88	Temperature accommodation coefficients of various gases on glass surfaces	195
89	Comparison of slip correction factors for a prolate distorted particle (E = 2.0) calculated using the adjusted sphere and the volume-equivalent sphere method	201
90	Diffusive deposition velocities according to several models for aerosol particles in a 0.5-cm bubble at 373 K	210
91	Patterns of particle deposition by sedimentation within ellipsoidal bubbles of various eccentricities	213
92	Sedimentation deposition velocity as a function of particle size	214
93	Patterns of particle deposition by inertial impaction in ellipsoidal bubbles of various eccentricities	216
94	Inertial impaction deposition velocities as functions of particle size	217
95	Relative variation in the water vapor pressure gradient at the surfaces of ellipsoidal bubbles of various eccentricities	222
96	Comparison of dimensionless thermophoretic velocity predicted by the Talbot et al. model to data for oil drops in hydrogen	226
97	Comparison of dimensionless thermophoretic velocity predicted by the Talbot et al. model to data for oil drops in carbon dioxide	227
98	Phase shift for motions of particles (ρ_p = 2 g/cm^3) of various sizes in bubbles undergoing sinusoidal oscillations	240
99	Amplitude magnification factors for motions of particles (ρ_p = 2 g/cm^3) of various sizes in bubbles undergoing sinusoidal oscillations	241
100	Natural vibration frequencies of bubbles in water at 373 K	243
101	Comparison of various models of aerosol deposition by impaction from the orifice stream	247
102	Particle capture by convective mass transport during bubble formation according to the mass transfer correlation developed by Skelland and Minhas	249
103	Essential elements of the mechanistic model of aerosol removal by steam suppression pools	254
104	Comparison of uniform, log-uniform, lognormal, and Student's t probability density functions	256
105	Variation of the normalized tangential velocities about a spherical bubble with various amounts of surface immobilization	292
106	Variation of the normalized, integrated particle deposition by inertial impaction as a function of the extent of surface immobilization	293
107	Variation of DF(FE) during gap release through a 'T' quencher with quencher submergence	310
108	Variation in DF(FE) during invessel release through a 'T' quencher with quencher submergence	311

List of Figures (Concluded)

Figure		Page
109	Variation in DF(rise) for gap release through a 'T' quencher with quencher submergence	315
110	Variation in DF(rise) for invessel release through a 'T' quencher with quencher submergence	316
111	Variation in DF(total) during gap release through a 'T' quencher with quencher submergence	319
112	Variation of DF(total) during invessel release through a 'T' quencher with quencher submergence	320
113	Variation of the mean size of aerosol particles that emerge from a suppression pool during gap release through a 'T' quencher with quencher submergence	324
114	Variation of the mean size of aerosol particles that emerge from a suppression pool during invessel release through a 'T' quencher with quencher submergence	325
115	Variation of the standard deviation of the size distribution of aerosol particles that emerge from a suppression pool during gap release through a 'T' quencher with quencher submergence	326
116	Variation of the standard deviation of the size distribution of aerosol particles that emerge from a suppression pool during invessel release through a 'T' quencher with quencher submergence	327
117	Variation of DF(FE) for invessel release through an 'X' quencher with quencher submergence.	334
118	Variation of DF(rise) for invessel release through an 'X' quencher with quencher submergence.	335
119	Variation of DF(total) for invessel release through an 'X' quencher with quencher submergence.	336
120	Variation of the mean size of aerosol particles emerging from a suppression pool for invessel release through an 'X' quencher with quencher submergence	337
121	Variation in the standard deviation of the size distribution of aerosols emerging from a suppression pool for invessel release through an 'X' quencher with quencher submergence	338

List of Tables

Table		Page
1	Containment types of existing boiling water reactors	6
2	Characteristics of downcomers in some Mark II containments	11
3	Proposed severe accident source term for boiling water reactors	18
4	Core inventories for a 3578 MW_{th} BWR-6	19
5	Sizes of bubbles formed at submerged orifices under constant flow conditions	44
6	Besset's data on steam bubble formation in subcooled water	48
7	Schmidt's data for steam bubble formation in water	50
8	Effect of orifice size on the bubble size distribution	89
9	Effect of orifice orientation on the bubble size distribution	89
10	Effect of steam concentration on the bubble size distribution	91
11	Coefficients in the term $\lambda_l(\overline{T,\rho})$ for thermal conductivity of liquid water	158
12	Coefficients in the term $\mu_l(\overline{T,\rho})$ for the viscosity of liquid water	160
13	Parameter values for calculation of gas properties	165
14	Parameter values for calculating the binary diffusion coefficients of gases	169
15	Comparison of predicted and observed binary diffusion coefficients in the H_2/H_2O system	170
16	Parametric values for correlations of gas thermal conductivities	173
17	Water solubilities of some materials expected to be present in aerosol produced during severe reactor accidents	202
18	Comparison of observed and predicted thermophoretic deposition velocities	228
19	Determinations of the sticking coefficient cited by Pruppacher and Klett	233
20	Dimensionless and example dimensional discretization of the particle size distributions	260
21	Example nodalizations of a plume	263
22	Input uncertainties	270
23	Uncertainties in the phenomena affecting bubbles	280
24	Uncertainties in the phenomena affecting aerosol behavior	289
25	Effects of coupling between diffusion and gravitational settling	300
26	Uncertainty distribution for the total decontamination of in-vessel release after passing through a 'T' quencher 500 cm deep	305
27	Uncertainty distribution for the mean particle size of in-vessel release after passing through a 'T' quencher 500 cm deep	306
28	Uncertainty distribution for the standard deviation of in-vessel release after passing through a 'T' quencher 500 cm deep	307
29	Summary of the uncertainty distributions for the decontamination factor associated with formation and equilibration of bubbles, DF(FE), during gap release and in-vessel release through 'T' quenchers	309
30	Summary of the uncertainty distributions for the decontamination factor associated with bubble rise through a suppression pool during gap release and in-vessel release through a 'T' quencher	313
31	Summary of the uncertainty distributions for the total decontamination factor for material released to a suppression pool during gap release and in-vessel release through a 'T' quencher	318

List of Tables (Continued)

Table		Page
32	Summary of the uncertainty distributions for the mean size of aerosol particles emerging from a suppression pool during gap release and in-vessel release through a 'T' quencher	322
33	Summary of the uncertainty distributions for the standard deviation of the size distribution of aerosol particles emerging from a suppression pool during gap release and in-vessel release through a 'T' quencher	323
34	Summary of uncertainty distributions for the decontamination factor associated with formation and equilibration of bubbles, DF(FE), during invessel release through an 'X' quencher	329
35	Summary of uncertainty distributions for the decontamination factor associated with bubble rise through a suppression pool, DF(rise), during invessel release through an 'X' quencher	330
36	Summary of the uncertainty distributions for the total decontamination factor, DF(total) for material released to a suppression pool during invessel release through an 'X' quencher	331
37	Summary of uncertainty distributions for the mean size of aerosol particles emerging from a suppression pool during invessel release through an 'X' quencher	332
38	Summary of the uncertainty distributions for the standard deviation of the size distributions of aerosol particles emerging from a suppression pool during invessel release through an 'X' quencher	333
A-1	Uncertainty distribution for decontamination during bubble formation and equilibration of gap release through a 'T' quencher 100 cm deep	364
A-2	Uncertainty distribution for decontamination of gap release during bubble rise from a 'T' quencher 100 cm deep	365
A-3	Uncertainty distribution for the total gap release decontamination after passing through a 'T' quencher 100 cm deep	366
A-4	Uncertainty distribution for the mean particle size of gap release after passing through a 'T' quencher 100 cm deep	367
A-5	Uncertainty distribution for the standard deviation of gap release after passing through a 'T' quencher 100 cm deep	368
A-6	Uncertainty distribution for decontamination during bubble formation and equilibration of gap release through a 'T' quencher 200 cm deep	369
A-7	Uncertainty distribution for decontamination of gap release during bubble rise from a 'T' quencher 200 cm deep	370
A-8	Uncertainty distribution for the total gap release decontamination after passing through a 'T' quencher 200 cm deep	371
A-9	Uncertainty distribution for mean particle size of gap release after flow through a 'T' quencher 200 cm deep	372
A-10	Uncertainty distribution for standard deviation of gap release after passing through a 'T' quencher 200 cm deep	373
A-11	Uncertainty distribution for the decontamination of gap release material during bubble formation and equilibration at a 'T' quencher 300 cm deep	374
A-12	Uncertainty distribution for the decontamination of gap release material during bubble rise from a 'T' quencher 300 cm deep	375

List of Tables (Continued)

Table		Page
A-13	Uncertainty distribution for the total decontamination of gap release material that has passed through a 'T' quencher 300 cm deep	376
A-14	Uncertainty distribution for the mean particle size of gap release material after passing through a 'T' quencher 300 cm deep	377
A-15	Uncertainty distribution for the standard deviation of gap release material after passing through a 'T' quencher 300 cm deep	378
A-16	Uncertainty distribution for decontamination during bubble formation and equilibration for gap release through a 'T' quencher 300 cm deep	379
A-17	Uncertainty distribution for decontamination of gap release during bubble rise from a 'T' quencher 500 cm deep	380
A-18	Uncertainty distribution for total gap release decontamination after passing through a 'T' quencher 500 cm deep	381
A-19	Uncertainty distribution for the mean particle size of gap release material after passing through a 'T' quencher 500 cm deep	382
A-20	Uncertainty distribution for the geometric standard deviation of release material after passing through a 'T' quencher 500 cm deep	383
A-21	Uncertainty distribution for decontamination of gap release by bubble formation and equilibration at a 'T' quencher 700 cm deep	384
A-22	Uncertainty distribution for decontamination of gap release during bubble rise from a 'T' quencher 700 cm deep	385
A-23	Uncertainty distribution for total decontamination of gap release after passing through a 'T' quencher 700 cm deep	386
A-24	Uncertainty distribution for the mean particle size of gap release after passing through a 'T' quencher 700 cm deep	387
A-25	Uncertainty distribution for the standard deviation of gap release after passing through a 'T' quencher 700 cm deep	388
A-26	Uncertainty distribution for decontamination of invessel release by bubble formation and equilibration at a 'T' quencher 100 cm deep	389
A-27	Uncertainty distribution for decontamination of invessel release during bubble rise from a 'T' quencher 100 cm deep	390
A-28	Uncertainty distribution for total decontamination of invessel release after passing through a 'T' quencher 100 cm deep	391
A-29	Uncertainty distribution for the mean particle size of invessel release after passing through a 'T' quencher 100 cm deep	392
A-30	Uncertainty distribution for the geometric standard deviation of invessel release after passing through a 'T' quencher 100 cm deep	393
A-31	Uncertainty distribution for decontamination during bubble formation and equilibration for invessel release through a 'T' quencher 200 cm deep	394
A-32	Uncertainty distribution for decontamination for invessel release during bubble rise from a 'T' quencher 200 cm deep	395
A-33	Uncertainty distribution for total invessel release decontamination after passing through a 'T' quencher 200 cm deep	396
A-34	Uncertainty distribution for mean particle size of invessel release after flow through a 'T' quencher 200 cm deep	397

List of Tables (Continued)

Table		Page
A-35	Uncertainty distribution for the geometric standard deviation of invessel release after passing through a 'T' quencher 200 cm deep	398
A-36	Uncertainty distribution for decontamination of invessel release material by bubble formation and equilibration at a 'T' quencher 300 cm deep	399
A-37	Uncertainty distribution for decontamination of invessel release during bubble rise from a 'T' quencher 300 cm deep	400
A-38	Uncertainty distribution for total decontamination of invessel release material after passing through a 'T' quencher 300 cm deep	401
A-39	Uncertainty distribution for the mean particle size of invessel release material after passing through a 'T' quencher 300 cm deep	402
A-40	Uncertainty distribution for the geometric standard deviation of invessel release material after passing through a 'T' quencher 300 cm deep	403
A-41	Uncertainty distribution for the decontamination of invessel release material during formation and equilibration of bubbles at a 'T' quencher 500 cm deep	404
A-42	Uncertainty distribution for the decontamination of invessel release during bubble rise from a 'T' quencher 500 cm deep	405
A-43	Uncertainty distribution for the total decontamination of invessel release material after passing through a 'T' quencher 500 cm deep	406
A-44	Uncertainty distribution for the mean particle size of invessel release after passing through a 'T' quencher 500 cm deep	407
A-45	Uncertainty distribution for the geometric standard deviation of invessel release after passing through a 'T' quencher 500 cm deep	408
A-46	Uncertainty distribution for decontamination of invessel release during bubble rise from a 'T' quencher 700 cm deep	409
A-47	Uncertainty distribution for decontamination of invessel release by bubble formation and decontamination at a 'T' quencher 700 cm deep	410
A-48	Uncertainty distribution for total decontamination of invessel release after passing through a 'T' quencher 700 cm deep	411
A-49	Uncertainty distribution for the mean particle size of invessel release after passing through a 'T' quencher 700 cm deep	412
A-50	Uncertainty distribution for the standard deviation of invessel release after passing through a 'T' quencher 700 cm deep	413
A-51	Uncertainty distribution for decontamination of invessel release material during bubble formation and equilibration at an 'X' quencher 100 cm deep	414
A-52	Uncertainty distribution for decontamination of invessel release material during bubble rise from an 'X' quencher 100 cm deep	415
A-53	Uncertainty distribution for the total decontamination of invessel release material after passing through an 'X' quencher 100 cm deep	416
A-54	Uncertainty distribution for the mean particle size of invessel release material after passing through an 'X' quencher 100 cm deep	417
A-55	Uncertainty distribution for the geometric standard deviation of invessel release material after passing through an 'X' quencher 100 cm deep	418
A-56	Uncertainty distribution for decontamination during bubble formation and equilibration of invessel release through an 'X' quencher 200 cm deep	419

List of Tables (Continued)

Table		Page
A-57	Uncertainty distribution for decontamination of invessel release during rise from an 'X' quencher 200 cm deep	420
A-58	Uncertainty distribution for the total invessel release decontamination after passing through an 'X' quencher 200 cm deep	421
A-59	Uncertainty distribution for the mean particle size after passing through an 'X' quencher 200 cm deep	422
A-60	Uncertainty distribution for the geometric standard deviation of invessel release after passing through an 'X' quencher 200 cm deep	423
A-61	Uncertainty distribution for the decontamination of invessel release by bubble formation and equilibration at an 'X' quencher 300 cm deep	424
A-62	Uncertainty distribution for decontamination of invessel release material during bubble rise from an 'X' quencher 300 cm deep	425
A-63	Uncertainty distribution for total decontamination of invessel release after passing through an 'X' quencher 300 cm deep	426
A-64	Uncertainty distribution for the mean particle size of invessel release after Passage through a 'X' quencher 300 cm deep	427
A-65	Uncertainty distribution for the geometric standard deviation of invessel release after passing through an 'X' quencher 300 cm deep	428
A-66	Uncertainty distribution for decontamination of invessel release by bubble formation and equilibration at an 'X' quencher 500 cm deep	429
A-67	Uncertainty distribution for decontamination of invessel release during bubble rise from an 'X' quencher 500 cm deep	430
A-68	Uncertainty distribution for total decontamination of invessel release after passing through an 'X' quencher 500 cm deep	431
A-69	Uncertainty distribution for the mean particle size of invessel release material after passing through an 'X' quencher 500 cm deep	432
A-70	Uncertainty distribution for the geometric standard deviation of invessel release material after passing through an 'X' quencher 500 cm deep	433
A-71	Uncertainty distribution for decontamination of invessel release by bubble formation and equilibration at an 'X' quencher 700 cm deep	434
A-72	Uncertainty distribution for decontamination of invessel release during bubble rise from an 'X' quencher 700 cm deep	435
A-73	Uncertainty distribution for total decontamination of invessel release after passing through an 'X' quencher 700 cm deep	436
A-74	Uncertainty distribution for the mean particle size of invessel release after passing through an 'X' quencher 700 cm deep	437
A-75	Uncertainty distribution for the standard deviation of invessel release after passing through an 'X' quencher 700 cm deep	438

I. Introduction

Formulation of a simplified model of aerosol removal by boiling water reactor steam suppression pools is described in this report. Development of this simplified model is one part of a program to define the attenuation of severe accident source terms by natural processes and by engineered safety features of nuclear power plants. Previous efforts in this program have led to the development of simplified models of source term attenuation by water pools overlying core debris interacting with concrete [1], aerosol removal by containment sprays [2], and aerosol removal by natural aerosol processes [256].

The simplified models are intended for use in conjunction with the revised severe accident source term proposed by the U.S. Nuclear Regulatory Commission [3]. The simplified models are not intended to replace detailed, mechanistic analyses of specific accidents hypothesized to occur at particular plants. Such detailed accident analyses of specific plants and accidents are best done with integrated accident analysis computer codes such as CONTAIN [4] or MELCOR [5]. Rather, a simplified model is intended to provide readily accessible indications of source term attenuation that can be achieved under generic circumstances. The simplified models are constructed so that selected levels of conservatism can be imposed on the predictions of source term attenuation.

In this document, attentions are directed toward the source term attenuation that can be produced by the steam suppression pools in boiling water reactors. These steam suppression pools were incorporated into the design of boiling water reactors to mitigate containment pressurization by steam in the event of a design-basis accident such as a large break in the reactor coolant system (a large break LOCA) or an anticipated reactor transient without scram (an ATWS accident). Steam vented from either the reactor coolant system or from the reactor drywell is condensed when injected into a steam suppression pool. It has long been recognized that venting steam and noncondensible gases through the suppression pools would also remove radioactive aerosols from the gases even during severe accidents that progressed beyond the design-basis conditions. Removal of radioactive aerosols by the steam suppression pools can significantly reduce risks posed by accidents at boiling water reactors.

Overall, the steam suppression pools in the three major types of boiling water reactor containments have qualitative similarities (see Figure 1). Pressure-relief lines from the reactor coolant system discharge gases and vapors into the suppression pools through quenchers. The drywell atmospheres of the containments vent to the suppression pools through large diameter downcomers or horizontal vents. Details of these venting arrangements are, however, quite different among the major types of boiling water reactor containments. These construction details can affect the efficiency of aerosol removal from gases discharged to the suppression pools and are discussed further in Chapter II of this report.

Flows to the suppression pools during design-basis accidents or during the deliberate depressurization of reactor coolant systems are intense, but of short duration. The flows to the suppression pools during events anticipated in the designs of boiling water reactors consist primarily of steam. Relative to the situation in severe reactor accidents, gases discharged to the suppression pools during design-basis events contain little radioactive material. Suppression pools are designed so that the pool temperature remains below saturation during design-basis events.

On the other hand, during severe reactor accidents when damage to the reactor fuel is taking place and radioactive materials are being released from the fuel, flows to the suppression pool are not especially vigorous. The gas discharged to the suppression pool can contain substantial amounts of noncondensible gas such as hydrogen or other gases produced in the reactor drywell. Substantial quantities of aerosol material; some of which is radioactive, will be present in gases discharged to the suppression pools.

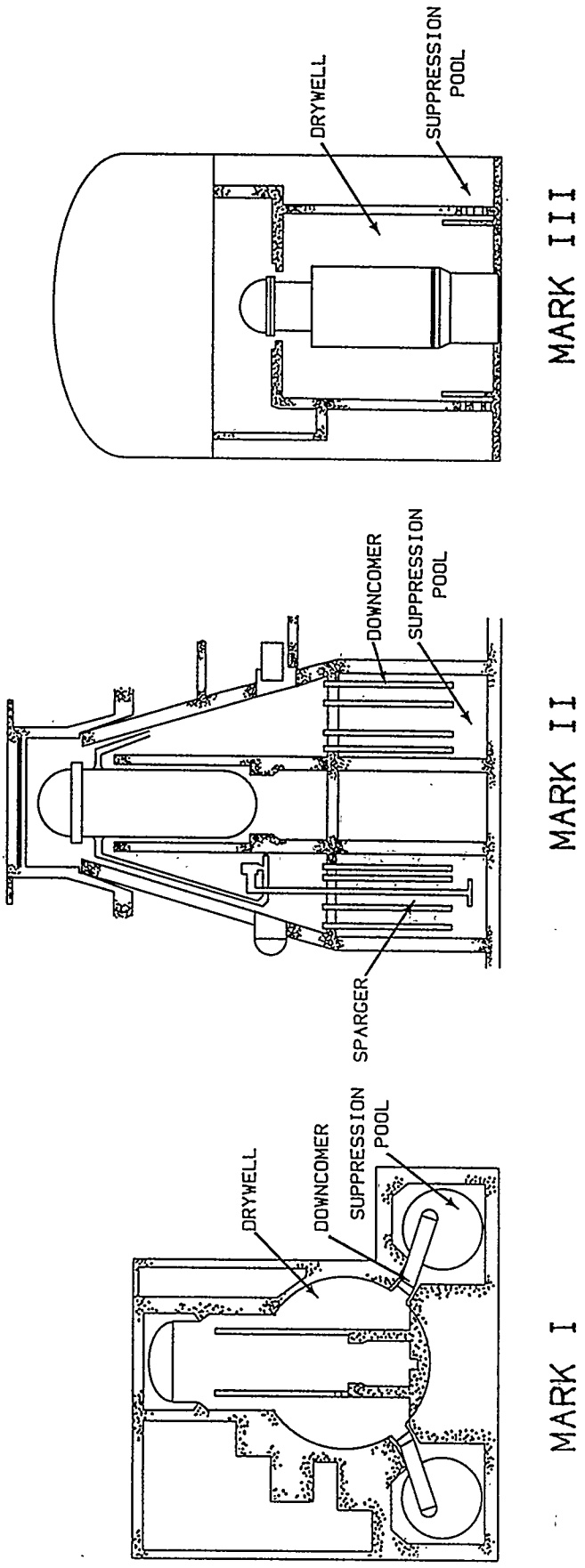

Figure 1. Overall configurations of steam suppression pools in Mark I, Mark II, and Mark III boiling water reactors

Sufficient energy can be imparted to the suppression pools that temperatures rise to near the boiling point. The gas discharge rate, gas composition, and the suppression pool temperature all affect the attenuation of the source term that can be produced by the pool. Further descriptions of the features of severe accidents that can affect the ability of suppression pools to remove radioactive aerosols from gas streams are provided in Chapter III of this report.

Steam suppression pools function by dispersing gases as relatively small bubbles into a water pool. Rapid heat and mass transfer from the bubbles to the liquid prevents overpressurization during accidents. Aerosols within the bubbles are captured in the water pool by a variety of mechanisms including inertial impaction, diffusion, gravitational settling, diffusiophoresis and thermophoresis. Detailed descriptions of the behavior of bubbles and the trapping of aerosols are provided in Chapter IV of this report.

The discussions of severe accident conditions in Chapter III and the physical phenomena affecting aerosol removal by suppression pools in Chapter IV identify a number of uncertainties that affect predictions of source term attenuation by suppression pools. These uncertainties include uncertainties in the boundary and initial conditions for suppression pool performance arising from the range of severe accidents thought possible in boiling water reactors as well as uncertainties in the predictions of accident progression. There are also uncertainties in bubble behavior and in the behavior of aerosols. A mechanistic model of aerosol removal by suppression pools is formulated in Chapter V of this report. The model is used to quantitatively characterize the magnitude of uncertainties in predictions of aerosol removal by suppression pools. This mechanistic model builds upon descriptions of aerosol removal by suppression pools found in some available computer codes such as SPARC [6], SUPRA [7,8], and BUSCA [9].

The analyses of uncertainties is done here in a manner similar to that employed in previous uncertainty analyses associated with the development of other simplified models [1,2]. Each of the important uncertainties identified in Chapters III and IV is characterized by a parameter that arises in the model used to predict source term attenuation. A plausible range of values for each of the parameters is found by examination of published analyses and experiments, bounding analyses based on physical limitations, or, when no other basis is available, engineering judgement. Parameters that describe the various uncertain aspects of the prediction of source term attenuation are selected so that the parameters are usually mutually independent. When independence of the parameters is thought not to be plausible, additional parameters are defined to describe the correlation among the parameters.

A subjective probability distribution is defined for values of each parameter within its plausible range. The subjective probability distribution is defined according to a set of rules described in Chapter V. The subjective probability distributions are used in a Monte Carlo uncertainty analysis of aerosol removal predicted by a mechanistic model. Parametric values are randomly selected according to the respective probability distribution of each parameter. A set of these parameter values is used to calculate aerosol removal by a suppression pool. The process is repeated until there is a 99 percent confidence that 95 percent of the range of values has been sampled. The accumulated predictions of aerosol removal are then used to construct uncertainty distributions at prescribed levels of confidence using nonparametric, order statistics (see Appendix A of Reference 1). Results of these uncertainty analyses are described in Chapter VI.

As mentioned above, aerosol-laden gases may be injected into steam suppression pools by way of quenchers or large diameter downcomers or horizontal vents. The method of gas injection does affect aerosol removal from the gas. Uncertainty analyses are reported here only for decontamination of gases injected through quenchers.

Results of the uncertainty analyses are used to formulate simplified expressions for aerosol removal by suppression pools. These simplified models are formulated by regression of results of the uncertainty analyses against suppression pool depth as described in Chapter VII. Application of the simplified models produced by this regression requires only minimal input. The user is required only to specify pool depth. Such models requiring minimal input are sought to render them readily useable. The simplified models are, of course, not replacements for mechanistic models or computer codes [6,7,8,9].

Regression analyses are done for the median, 90 percentile and 10 percentile values within the uncertainty distributions found for aerosol removal by suppression pools. For the purposes of this work, median values of the uncertainty distributions are considered "best estimates" of aerosol removal by suppression pools. The 90 percentile and the 10 percentile values are considered reasonable upper and lower bounds, respectively. From another point of view, the 90 percentile values may be used as conservative estimates of the radioactive material accumulated in a suppression pool. On the other hand, the 10 percentile values may be used as conservative estimates of the amount of radioactive material that escapes a suppression pool. The availability of simplified models for these various quantiles of the uncertainty distributions makes it convenient to estimate the uncertainty in predictions of aerosol removal by steam suppression pools.

II. Steam Suppression Pools

An overview of steam suppression pools in Mark I, Mark II and Mark III boiling water reactor containments is shown in Figure 1. Additional information on boiling water reactors is shown in Table 1. The qualitative similarity of the pools in these three designs lies in the modes of injection of aerosol-laden gases. Gases from an intact reactor coolant system are injected through the quenchers. These quenchers consist of large diameter pipes with many small holes in them. On the other hand, gases from the drywell are injected into the suppression pool through very large diameter vents. In the cases of Mark I and Mark II containments, these vents are downcomers. In the case of Mark III containments, there are horizontal vents from the drywell to the suppression pool.

The authors have not attempted a comprehensive survey of the design features of suppression pools in existing boiling water reactors. In fact, detailed information on these designs proves difficult to acquire from the open literature. It does appear that there can be important differences in the suppression pool designs even within a particular class of boiling water reactor containment types. Descriptions of the suppression pools presented below should, then, be taken as representative and not necessarily definitive for the containment types or even for particular reactors within a class of containments.

A. Mark I Suppression Pools

The suppression pool in a Mark I containment is a torus surrounding the distinctive "inverted light bulb" drywell as shown in Figure 2. The water volume in the torus is about 2.4×10^9 cm^3. The radius of the torus is about 1699 cm. The internal diameter of the torus is about 472 cm.

There are 12 discharge lines from safety relief valves on the reactor coolant system that go to 'T' quenchers in the suppression pool. A diagram of a 'T' quencher is shown in Figure 3. The 'T' quencher has two arms constructed from 30-cm-diameter schedule 80 piping. The inside diameter of such piping is 28.890 cm. The wall thickness is 1.748 cm. The flow area is 655.52 cm^2. At the end of each arm of the 'T' quenchers are 794 holes. The holes are typically 0.933 to 1.27 cm in diameter. Arms of the 'T' quenchers are typically submerged to a depth of 198 cm.

The venting arrangement from the Mark I drywell to the suppression pool is complicated and not well described in the readily accessible literature. There are eight vents symmetrically arrayed around the drywell. Some indication of the design variability of suppression pools in Mark I reactor containments is provided by the diagrams in Figure 4 of three classes of vents into the suppression pools. Typically, these vents are 206 cm in diameter.

Each vent from the drywell is supported in the suppression pool by two girders. The vents connect to a header about 145 cm in diameter within the pool. There are 96 downcomers from this header. Typically, the downcomers are 59.7 to 61 cm in diameter and are submerged to a depth of about 122 cm.

B. Mark II Suppression Pools

The suppression pool in a Mark II containment is a large body of water (2.3 to 4.4×10^9 cm^3) below the reactor vessel (see Figure 1). Vent lines from the reactor coolant system discharge to 'T' quenchers in this pool. The 'T' quenchers are rather similar to those used in Mark I suppression pools. They are, however, typically submerged to a depth of about 540 cm [11]. Each arm has only about 748 holes.

Table 1. Containment types of existing boiling water reactors

Reactor	Power (MW_{th})	BWR Type	Safety/relief valves		Water volume 10^9 cm^3	Wetwell design temp. (K)	Design pressure (atms)
			Number	Capacity (kg/s)			
Mark I Containment Reactors							
Brown's Ferry 1	3293	4	13	108 - 109	2.407	411	3.8
Brown's Ferry 2	3293	4	13	108 - 109	2.407	411	3.8
Brown's Ferry 3	3293	4	13	108 - 109	2.407	411	3.8
Brunswick 1	2436	4	11	105 - 114	2.481	377	4.2
Brunswick 2	2436	4	11	105 - 114	2.481	377	4.2
Cooper	2381	4	11	81 - 110	2.482	411	3.8
Dresden 1	2527	3	9	68 - 78	3.177	411	4.2
Dresden 2	2527	3	9	68 - 78	3.177	411	4.2
Duane Arnold	1658	4	8	81 - 105	1.742	411	3.8
Fermi 2	3293	4	15	111 - 114	3.429	411	3.8
Fitzpatrick	2436	4	11	101 - 108	2.973	377	4.2
Hatch 1	2436	4	11	110	2.482	411	3.8
Hatch 2	2436	4	11	110	2.482	411	3.8
Hope Creek 1	3293	4	14	111 - 114	3.429	427	4.2
Hope Creek 2	3293	4	14	111 - 114	3.429	427	4.2
Millstone 1	2011	3	6	101	2.365	411	4.2
Monticello	1670	3	6	106	2.208	411	3.8
Nine Mile Point 1	1850	2	16	80	2.520	369	2.4
Oyster Creek	1930	2	16	80	2.208	369	2.4
Peach Bottom 1	3293	4	13	103 - 117	3.483	411	3.8
Peach Bottom 2	3293	4	13	103 - 117	3.483	411	3.8
Pilgrim 1	1998	3	5	81 - 101	2.379	411	3.8
Quad Cities 1	2511	3	9	75 - 81	3.273	411	3.8
Quad Cities 2	2511	3	9	75 - 81	3.273	411	3.8
Vermont Yankee	1593	4	6	101 - 117	2.208	411	3.8

Table 1. Containment types of existing boiling water reactors (concluded)

Reactor	Power (MW_{th})	BWR Type	Safety/relief valves		Water volume 10^9 cm^3	Wetwell design temp. (K)	Design pressure (atms)
			Number	Capacity (kg/s)			
Mark II Containment Reactors							
La Salle 1	3293	5	17	108	3.511	408	3.1
La Salle 2	3293	5	17	108	3.511	408	3.1
Limerick 1	3293	4	14	114 - 116	3.811	411	3.8
Limerick 2	3293	4	14	114 - 116	3.811	411	3.8
Nine Mile Point 2	3323	5	18	114 - 117	4.383	373	3.6
Shoreham	2436	4	11	112	2.304	380	3.3
Susquehanna 1	3292	4	16	107	3.725	377	3.6
Susquehanna 2	3292	4	16	107	3.725	377	3.6
WNP2	3292	5	18	109 - 114	3.177	405	3.1
Mark III Containment Reactors							
Clinton 1	2894	6	16	107 - 115	3.843	358	1.0
Grand Gulf 1	3833	6	20	107 - 115	3.851	358	1.0
Grand Gulf 2	3833	6	20	107 - 115	3.851	358	1.0
Perry 1	3579	6	19	107 - 115	3.398	358	1.0
Perry 2	3579	6	19	107 - 115	3.398	358	1.0
River Bend 1	2894	6	16	115	3.623	358	1.0

Source: P. Lobner, C. Donahoe, and C. Cavallin, Overview and Comparison of U.S. Commercial Nuclear Power Plants, NUREG/CR-5640, SAIC-89/1541, Science Applications International Corp., San Diego, CA, September 1990.

Steam

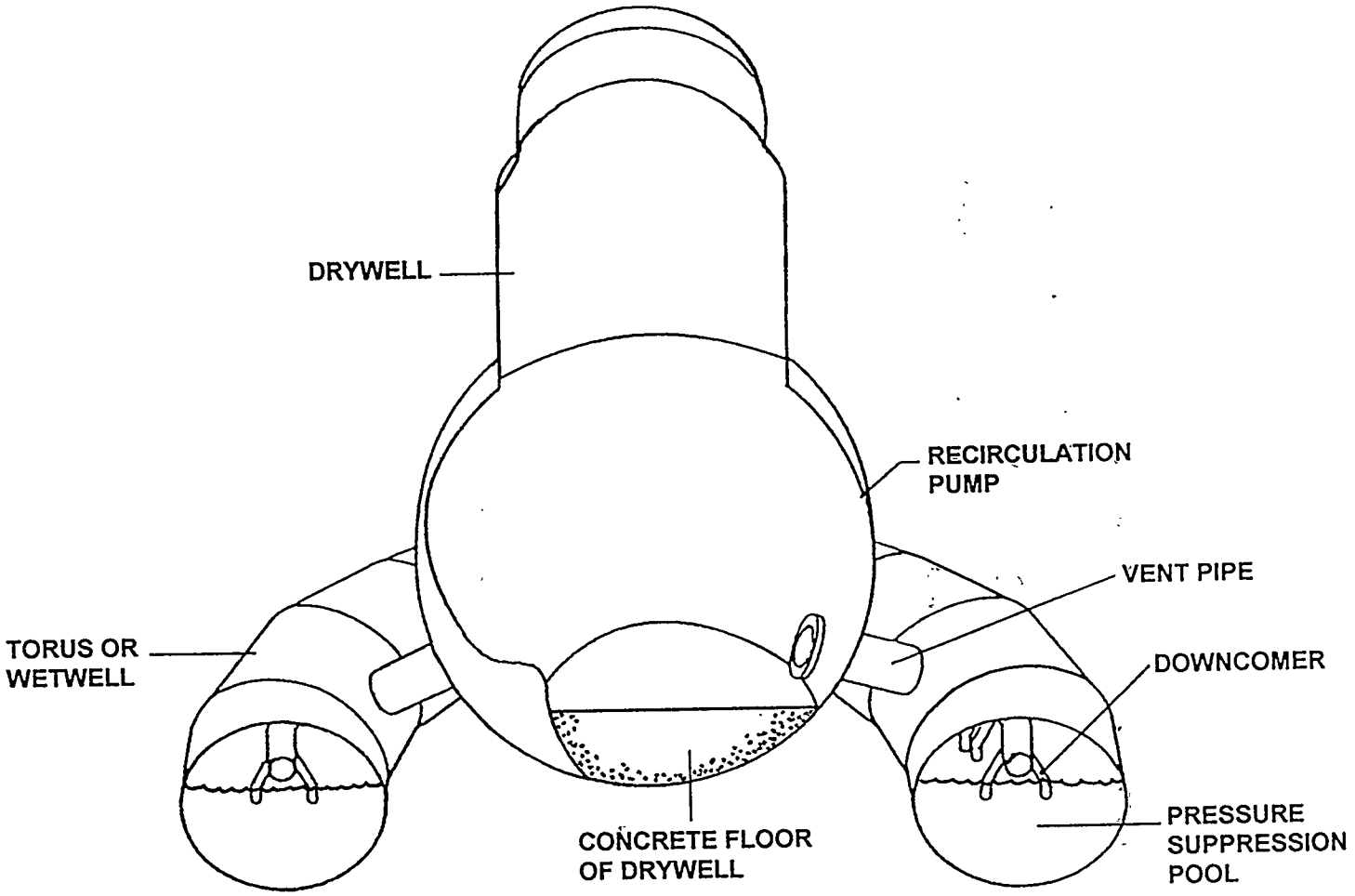

Figure 2. Torus suppression pool of a Mark I containment

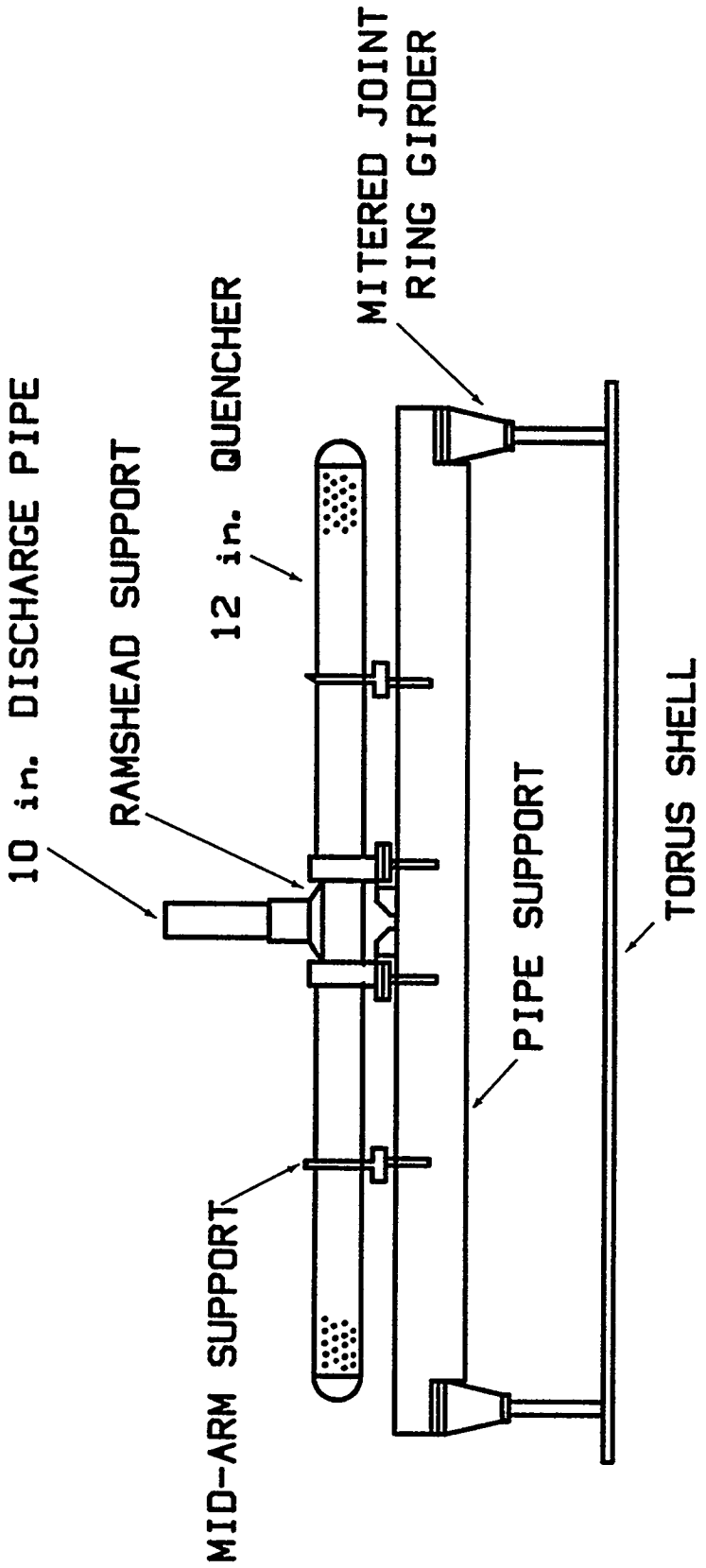

Figure 3. 'T' Quencher for a Mark I suppression pool

TYPE I

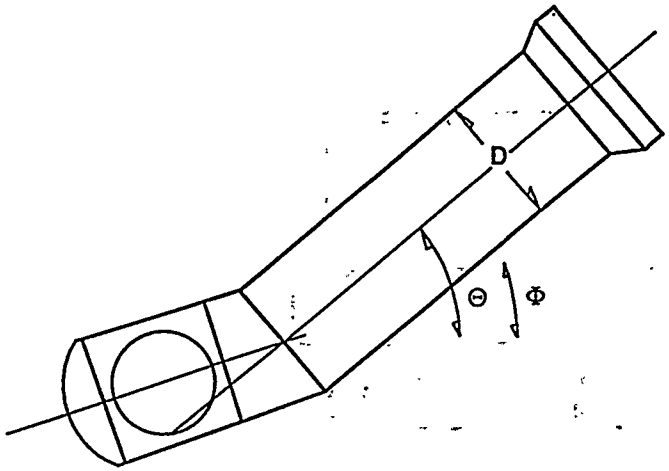

TYPICAL PLANT	D (cm)	Θ (°)	Φ (°)
OYSTER CREEK	198	38.21	17

TYPE II

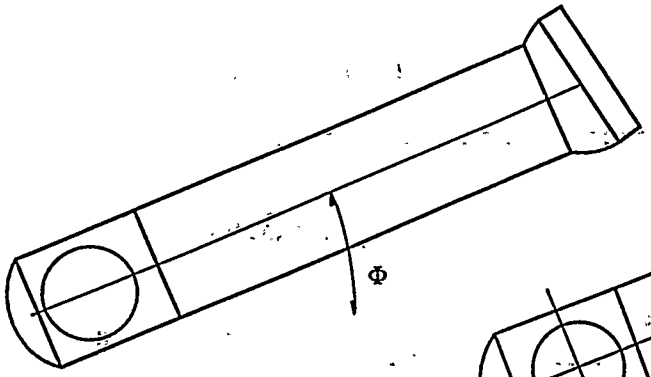

Plant	D (cm)	Φ (°)
Nine Mile Pt	206.4	22.002
Dresden 2 & 3	206.4	13.128
Quad Cities 1 & 2	206.4	12.104
Millstone	205.7	22.500
Monticello	205.7	20.100
Vermont Yankee	205.7	19.214
Pilgrim	205.7	22.177
Peach Bottom 2 & 3	205.7	22.343
Fitzpatrick	205.7	20.359
Cooper Station	210.8	24.288
Duane Arnold	144.8	23.806
Hatch 1	210.8	21.330
Hatch 2	190.5	21.330
Fermi 2	203.2	24.980
Brunswick 1 & 2	193.0	16.809

TYPE III

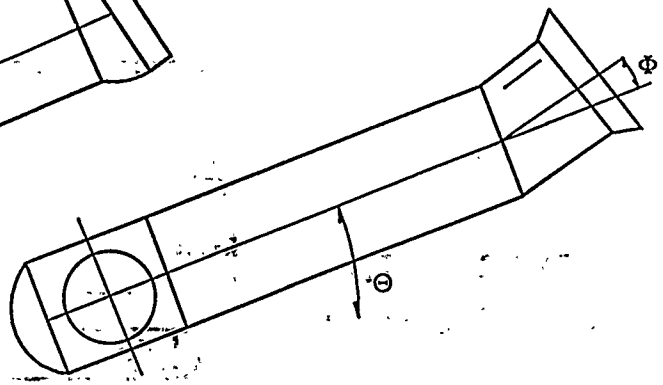

Plant	D (cm)	Θ (°)	Φ (°)
Brown's Ferry 1,2,3	205.7	20	16

Figure 4. Various types of vents from the drywells to the suppression pools in Mark I containments

Vertical downcomer pipes connect the Mark II drywell to the suppression pool. There are variations in the designs of these pipes. Some characteristics of the pipes are listed in Table 2. Kuhlman et al. [11] indicate that there may be as many as 136 of these downcomers. The variability in the details of the design can also be seen in the diagrams of the diaphragm floors of various Mark II containments shown in Figure 5.

C. Mark III Suppression Pools

The Mark III suppression pool is an annulus surrounding the base of the drywell (see Figure 1). There are eight quenchers fed by lines from 20 relief valves on the reactor coolant system as shown in Figure 6 [12]. The design outlet temperature and pressure for the relief valves are 533 K and 42.5 atmospheres.

The quenchers used in the Mark III suppression pools are called X-quenchers and are shown in Figure 7. Each arm of the X-quencher is 30-cm-diameter schedule 80 piping 148.6 cm long. Each arm has 374 holes 0.993 cm in diameter. The X-quenchers are submerged to depths of 427 to 579 cm.

The most unusual feature of the Mark III suppression pool is the venting from the drywell to the wetwell. There are 102 to 135 horizontal vents about 72 cm in diameter [13]. A diagram of the horizontal vents is shown in Figure 8. Vent submergence varies. The centerline of the uppermost vent is 213 cm below the low water level marked in Figure 8. The next layer of vents have centerlines 340 cm below the low water level. The bottom layer of vents have center lines at a depth of 465 cm.

A typical Mark III suppression pool volume is about 3.6×10^9 cm^3.

Table 2. Characteristics of downcomers in some Mark II containments [11]

	Downcomers		
Plant	Ex-pedestal	In-pedestal	Diameter (cm)
Limerick	87	0	61.0
LaSalle	98	0	59.7
Susquehanna	82	0	61.0
WNP-2	84	18	61*
Nine Mile Point Unit 2	115	8	59.0
Shoreham	78	4	59.0

*In-pedestal downcomers are 46 cm in diameter.

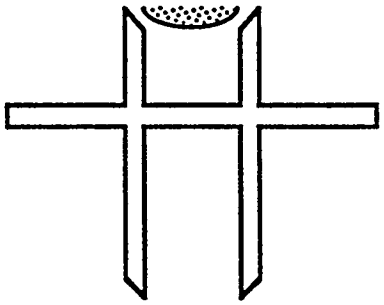

Limerick 1 & 2

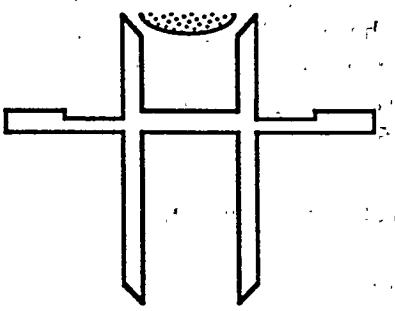

Susquehanna 1 & 2

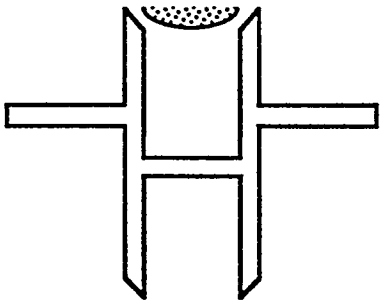

La Salle 1 & 2

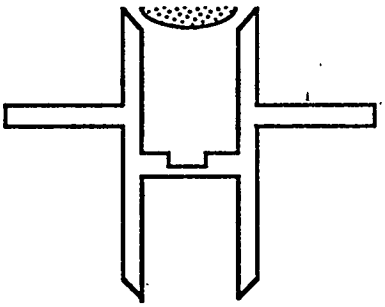

WNP-2

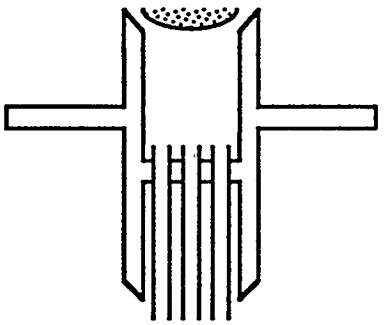

Nine Mile Point

Figure 5. Diagrams of the diaphragm floors of various Mark II containments [12]

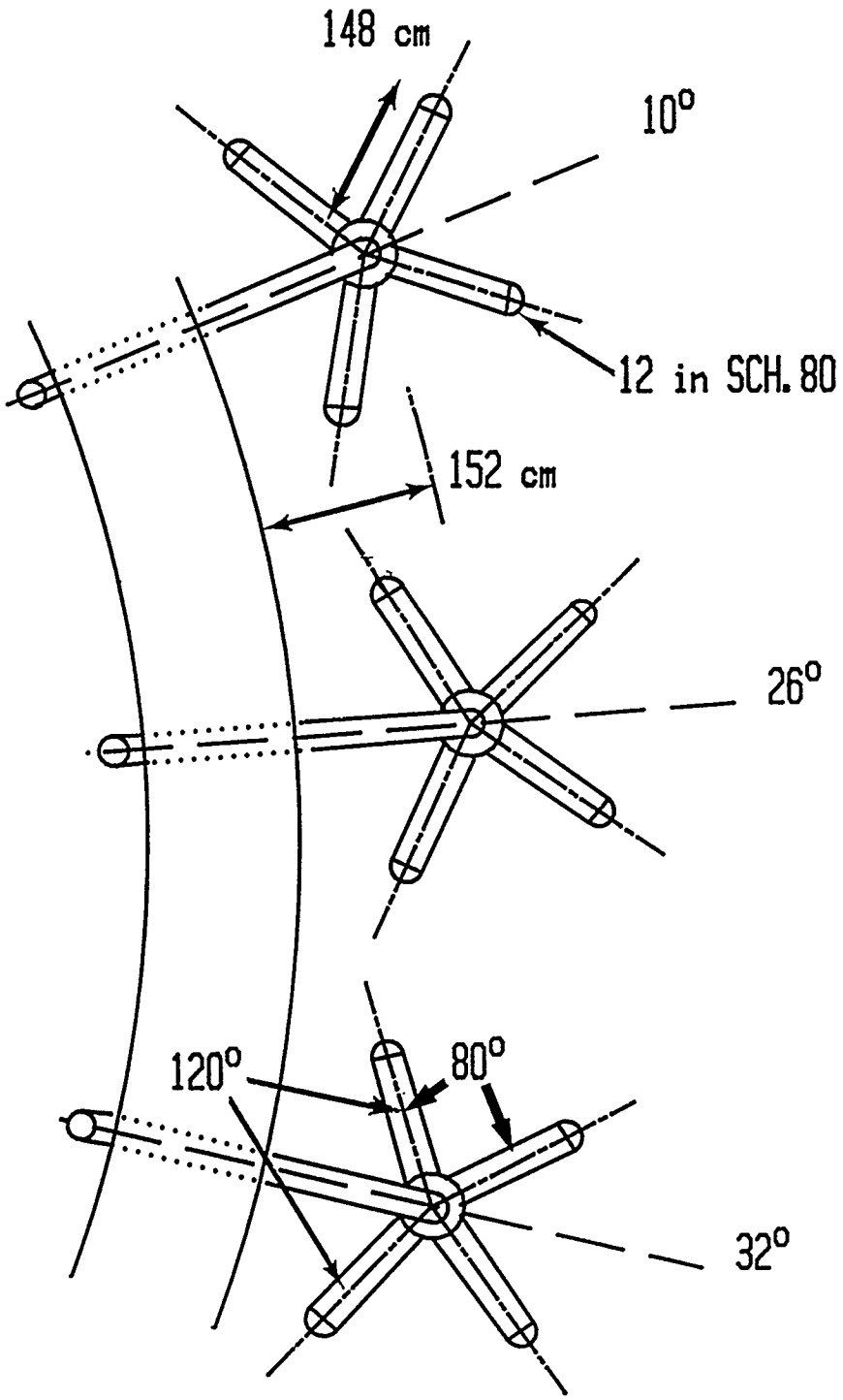

Figure 6. Positioning of quenchers in the Mark III suppression pool [13]

Steam

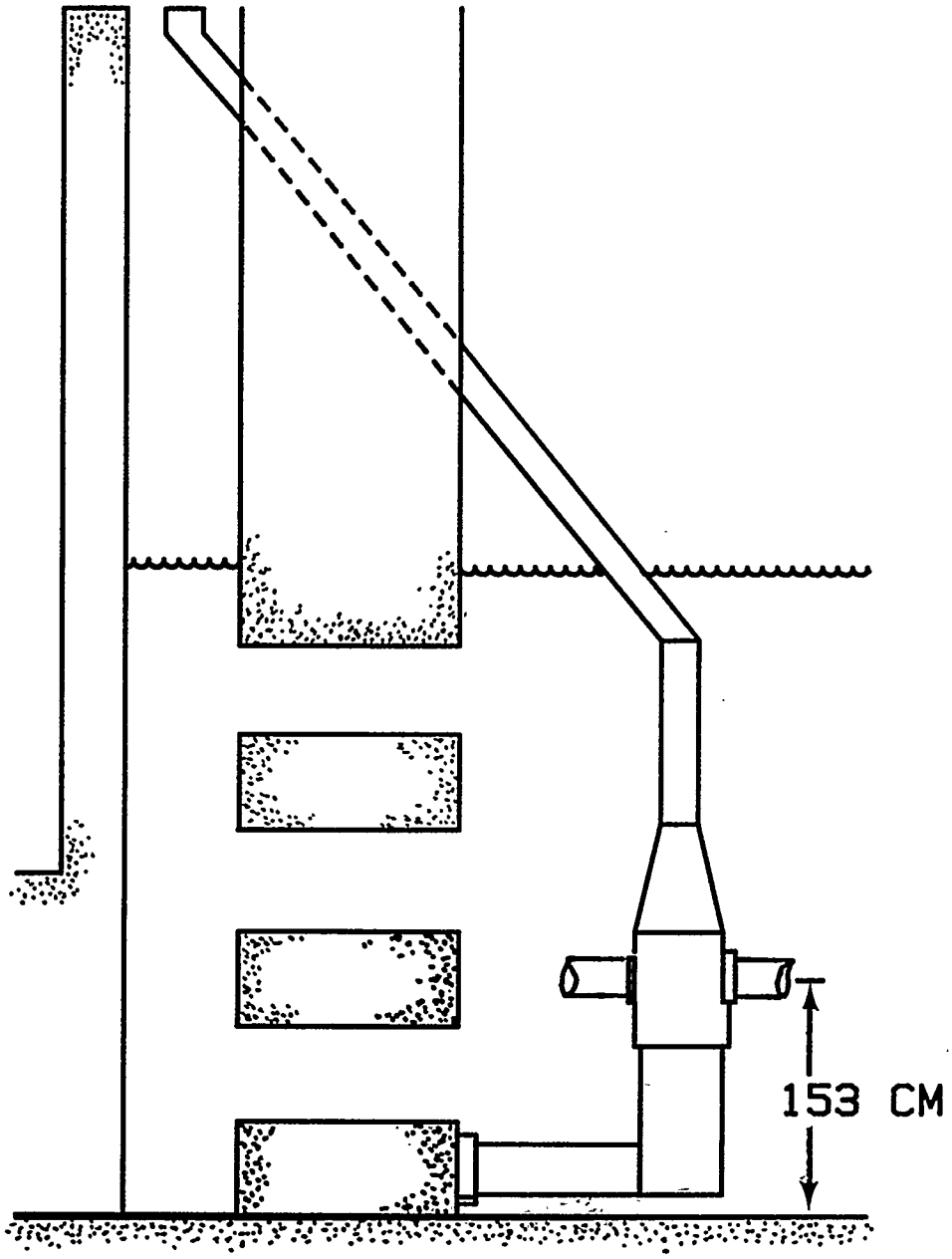

Figure 7. Diagrams of X-quenchers in Mark III suppression pools

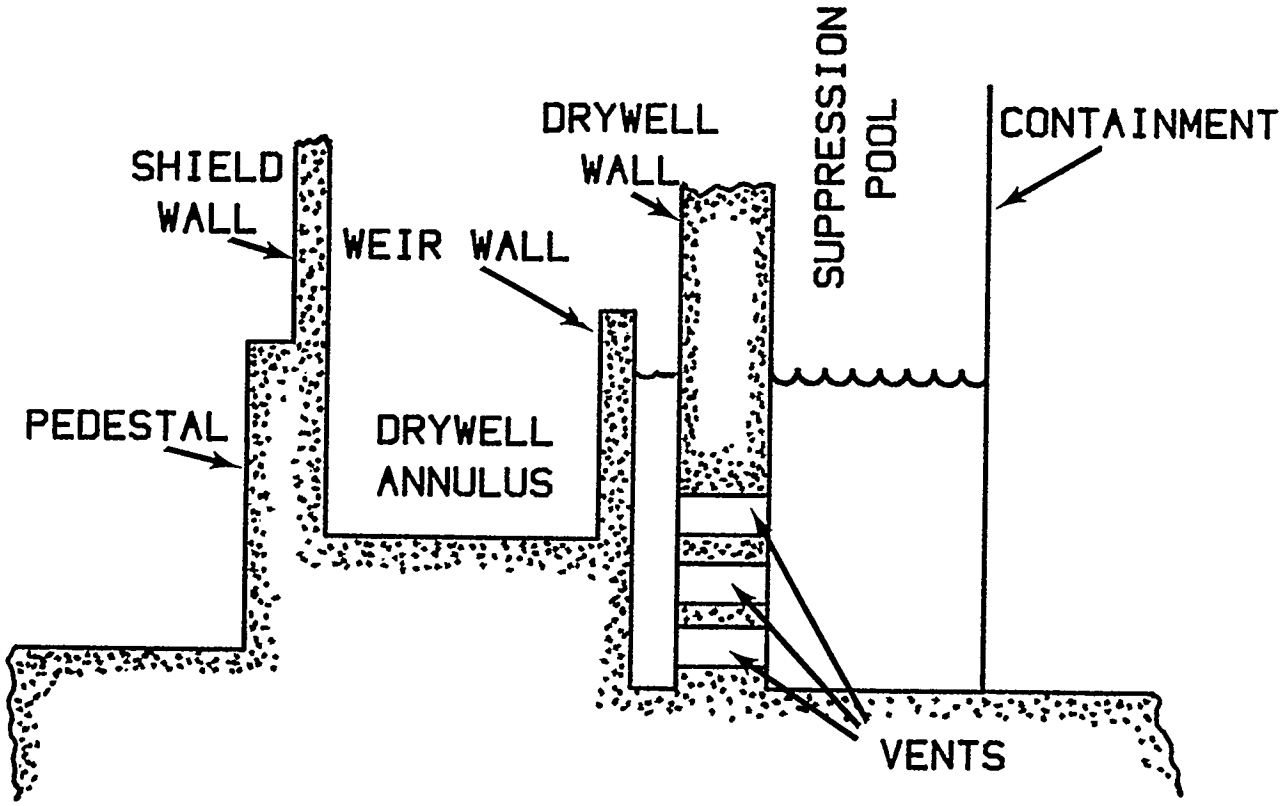

Figure 8. Horizontal vents in the Mark III suppression pool [13]

D. Conclusions

The details of suppression pool construction vary among classes of plants and even within each particular class of plant. But, similarities in the pool designs are noteworthy in connection with prediction of source term attenuation by steam suppression pools. Injection of aerosol-laden gases by way of quenchers are similar for all three major boiling water reactor containment types. That is, the injection is through small diameter holes clustered at the ends of quencher arms. Similarly, injection from the drywell is by large diameter vents. In the case of the Mark I and Mark II designs, the vents are downcomers. In the case of the Mark III containment, the vents are horizontal.

It appears that a single, simplified model of aerosol removal by steam suppression pools can be defined for gas injection through all types of quenchers. Only the depth of submergence is a significant difference among the various containment types.

A separate, simplified model has to be constructed to predict aerosol removal from gases injected into the suppression pool through large diameter vents. Injection through vents in Mark I and Mark II containment types can be treated with the same model. A different model may be needed for treating aerosol removal from gases injected through horizontal vents in the Mark III containment design. A difficulty in modeling the Mark III vent design will be prediction of the number of active vents and the initial sizes of bubbles emerging from these vents.

III. Accident Analyses

A. Overview

Steam suppression pools were designed to mitigate overpressurization threats posed to the integrity of boiling water reactor containments by design-basis accidents. The models discussed in this document are intended to predict the source term mitigation that suppression pools can achieve during severe reactor accidents that involve core degradation and fission product release well beyond what would be expected in design-basis accidents. The initial conditions and boundary conditions for suppression pool performance during severe reactor accidents are rather different than conditions considered in predicting suppression pool performance during design-basis accidents. The most intense challenges to suppression pools during design-basis accidents occur shortly after initiation of the accident and cease once other engineered safety systems return the nuclear plant to a safe condition. Severe accidents, on the other hand, can last for tens of hours if there is no intervention from outside the plant. During this protracted accident period, the boundary conditions on the suppression pool can change substantially. Prediction of the boundary conditions dictated by the accident progression is still far from an exact science. Uncertainties in the boundary conditions must create uncertainties in the predictions of suppression pool performance. It is necessary, then, to develop some sense of the range of initial and boundary conditions for suppression pool performance during severe accidents.

Among the varying factors affecting suppression pool performance during severe accidents is the nature of aerosols that must be scrubbed from gases sparging through the suppression pool. The severe accident source term for boiling water reactors proposed by the U.S. Nuclear Regulatory Commission [3] is shown in Table 3. The releases are listed in this table as fractions of the core inventory. Inventories for a particular plant are listed in Table 4. Note that the proposed releases include large amounts of nonradioactive materials. With the exception of the noble gases and a small fraction of the iodine, the released materials will be in the form of aerosols when they reach the suppression pool. Particle sizes for aerosols are not specified.

The first significant release of radioactivity occurs when the zircaloy cladding on the fuel ruptures. Volatile species accumulated in the gap between the fuel and the clad are then vented into the reactor vessel. The gap release takes place shortly after coolant has been boiled out of a substantial fraction of the core. The gap release is spread over time because fuel rods in the various regions of the core and even fuel rods within a particular subassembly do not heat at uniform rates. Temperatures necessary to cause the clad to rupture are reached at various times throughout the reactor core.

Gap inventories of volatile materials promptly released when the cladding on the fuel is ruptured are small. Precise values of the gap inventories have been controversial since the time of the Reactor Safety Study [29]. Values picked for NUREG-1465 and the proposed, revised Severe Accident Source Term appear to be conservatively large values. Release of these vapors will, typically, be into steam flowing at relatively high flow rates. Consequently, vapor concentrations will be small. If particles nucleate from the gas phase as the gas temperatures fall, these particles would be expected to remain quite small (<0.5 μm) because particle coagulation rates will be slow at the low particle concentrations. Vapors might, instead, condense on relatively coarse (~ 50 μm) fragments of fuel that escape into the flow when the clad ruptures [241]. Such coarse particles might not be carried as far as the suppression pool. If such large particles do reach the pool, they will be quantitatively trapped in the pool.

Table 3. Proposed severe accident source term for boiling water reactors [3]

Duration (hours)	Gap release 1.0	In-vessel release 1.5	Ex-vessel release 3.0	Late In-vessel release 10.0
Release (fraction of core inventory)				
Noble Gases	0.05	0.95	0	0
Iodine	0.05	0.22	0.37	0.07
Cesium	0.05	0.15	0.45	0.03
Tellurium	0	0.11	0.38	0.01
Strontium	0	0.03	0.24	0
Barium	0	0.03	0.21	0
Ruthenium	0	0.007	0.004	0
Cerium	0	0.009	0.01	0
Lanthanum	0	0.002	0.01	0
Nonradioactive materials (kg)		780	5600	

Table 4. Core inventories for a 3578 MW_{th} BWR-6

Radionuclide	Inventory** (g-atoms)	Representative Element*
Americium	30.54	La
Antimony	11.13	I
Barium	883.8	Ba
Berium	1711	Ce
Cesium	1741	Cs
Cobalt	142.1	Ru
Curium	8.62	Ce
Iodine	148.6	I
Lantharium	760.2	La
Molybdenum	2810	Ru
Niobium	38.99	Ru
Praeseodymium	671.1	La
Plutonium	3735	Ce
Phodium	339.5	Ru
Rubidium	372.1	Cs
Ruthenium	1768	Ru
Strontium	954.8	Sr
Technetium	710.6	Ru
Tellurium	289.7	Te
Yttrium	491.5	La
Zirconium	3341	Ce

*Representative element to use in estimating the release fraction according to the prescription shown in Table 3.

**Should scale with reactor power.

At the time fuel cladding ruptures, temperatures even in the hotter portions of the core will not be especially high. In the case of a depressurized reactor coolant system,* clad rupture may occur at temperatures in the vicinity of 1000 K [247]. If the reactor coolant system is pressurized at this early stage of the accident, clad rupture may occur at temperatures near the clad melting point, ~2125 K. Even if temperatures are this high in local regions, most of the reactor core is still relatively cool. At low temperatures, steam reactions with the cladding to form hydrogen will be limited by chemical kinetics [10]. Much of the gas that carries aerosol and vapors through the reactor coolant system will be steam.

Temperatures in the reactor core rise slowly early in the accident. Typical rates of temperature increase are less than 1 K/s. Steam production during this period is not expected to be large. Radiation heat transfer to residual coolant is limited by poor view factors from the hotter fuel rods to lower regions of the reactor vessel where cooling water remains.

Eventually, temperatures are reached by the fuel rods that are so high that the steam reaction with the clad becomes quite rapid. Heat transfer from the fuel rods to the fuel assembly channel boxes, which are made of a zirconium alloy, raises surface temperatures sufficiently that the channel boxes, too, react with steam to form hydrogen. It eventually becomes impossible to supply steam fast enough to meet the reactivity of the clad. Chemical heat produced by the reaction of steam with the clad greatly augments the heating of the fuel by radioactive decay. Fuel temperatures increase at rates of up to 20 K/s. Gas that emerges from the core is essentially hydrogen. This hydrogen is, however, diluted and cooled by steam that bypasses the core region. Nevertheless, the gas that carries aerosols through the reactor coolant system and into the suppression pool during this period contains much less steam than did the gas during the earlier, gap release stage of the accident.

As temperatures in the fuel rise, there is a corresponding increase in the rate of vaporization of both radionuclides and nonradioactive materials. Nonradioactive materials that can make significant contributions to the aerosol mass include tin from the zircaloy cladding and even UO_2 itself. Because the more rapid vaporization of more materials creates higher total aerosol concentrations, the rate of aerosol coagulation greatly increases. Thus, aerosol particles can grow to sizes greater than 1 μm.

Eventually, cladding on the fuel melts and drains down the fuel rods. Still later, fuel itself can melt or the fuel can collapse within the core into a rubble bed. Melting of cladding and melting or collapse of fuel can increase the rate of steam flow into the core. Relocation of molten cladding, channel boxes and the like bring hot material closer to residual water in the reactor coolant system.

Available accident-analysis models differ in their predictions of the extent to which steam production increases. Models in the Source Term Code Package [14] are based on the hypothesis that molten clad drains into lower, cooler portions of the core where it temporarily forms an impermeable crust. Fuel collapses onto this crust, heats and eventually melts. Once molten material penetrates the crust, it cascades into the lower plenum of the reactor vessel. The sudden interaction of large amounts of high temperature melt with water in the lower plenum produces large amounts of steam that will purge aerosols from the reactor coolant system into the steam suppression pool. Somewhat similar models are employed in the MELCOR code for severe reactor accident analysis [15].

---

*Boiling water reactors are equipped with automatic depressurization systems. Risk dominant accidents in boiling water reactors tend, however, to be those in which this automatic system fails to function.

Models in the BWRSAR code [16] are based on a different hypothesis concerning the behavior of molten material during core degradation (see Figure 9). It is hypothesized that molten material drains completely out of the core region. No crust is formed. Instead, molten material falls into residual water low in the reactor vessel. The continuous draining of small amounts of melt into the water, where it quenches, augments steam production. Decay heat eventually boils the water away, and the debris can heat to melting and cause rupture of the vessel head.

Available models differ in their predictions of the extent to which steam will be reduced to hydrogen. The MAAP code [18] indicates that blockages formed by freezing of molten material in lower, cooler regions of fuel subassemblies prevent steam from reaching and reacting with core debris. The bulk of the steam flow is diverted around the hottest region of the core. The gas that carries aerosol out of the core region to the suppression pool is then expected to be rich in steam. Other models assume local blockages do not completely prevent steam flow through fuel subassemblies so there are opportunities for vigorous reaction of the steam to form hydrogen. The condensible fraction of gases transporting aerosols from the reactor coolant system to the suppression pool is, then, smaller.

Eventually, core debris is expected to rupture the reactor pressure vessel, fall into the drywell and attack concrete. Accident progression models differ on the details of these events. Predictions of the models can be grouped into two classes. Most models predict that a molten pool forms in the lower plenum of the reactor and penetrates the vessel head. A substantial fraction ($\sim$50 percent) of the core material is suddenly released into the drywell. The remainder of the core slowly melts and drains into the drywell.

The BWRSAR code [16] predicts a different sequence of events. Core debris that falls from the core region is assumed to quench and form a debris bed in the lower plenum. As the debris bed drys and reheats, constituents of the debris bed melt according to their respective melting points. Melting points of metallic constituents are lowest so the metals form a molten pool that penetrates the vessel. Thus, the first core debris expelled into the drywell is a largely metallic melt. As shown in Figure 10, molten oxide materials drain into the drywell slowly over an extended period of time.

Interaction of core debris with concrete produces aerosols [19] and noncondensible gases such as hydrogen, carbon monoxide, and carbon dioxide [20]. Unless some modifications have been made to the plants to ensure water is in contact with the core debris in the drywell, there is little steam present in the gases generated during core debris interactions with concrete. If metallic zirconium is present in the core debris, water vapor evaporated from concrete exposed to core debris will be nearly completely reduced to hydrogen. (Equilibrium hydrogen-to-steam partial pressure ratios will be on the order of 10^5.) Once zirconium and chromium in the core debris have been oxidized, the hydrogen-to-steam partial pressure ratio in gases evolved during the attack on concrete will be determined by the reaction with iron:

$$Fe(l) + H_2O \rightleftarrows FeO(l) + H_2$$

and for most conditions the hydrogen-to-steam partial pressure ratio will be about 2.

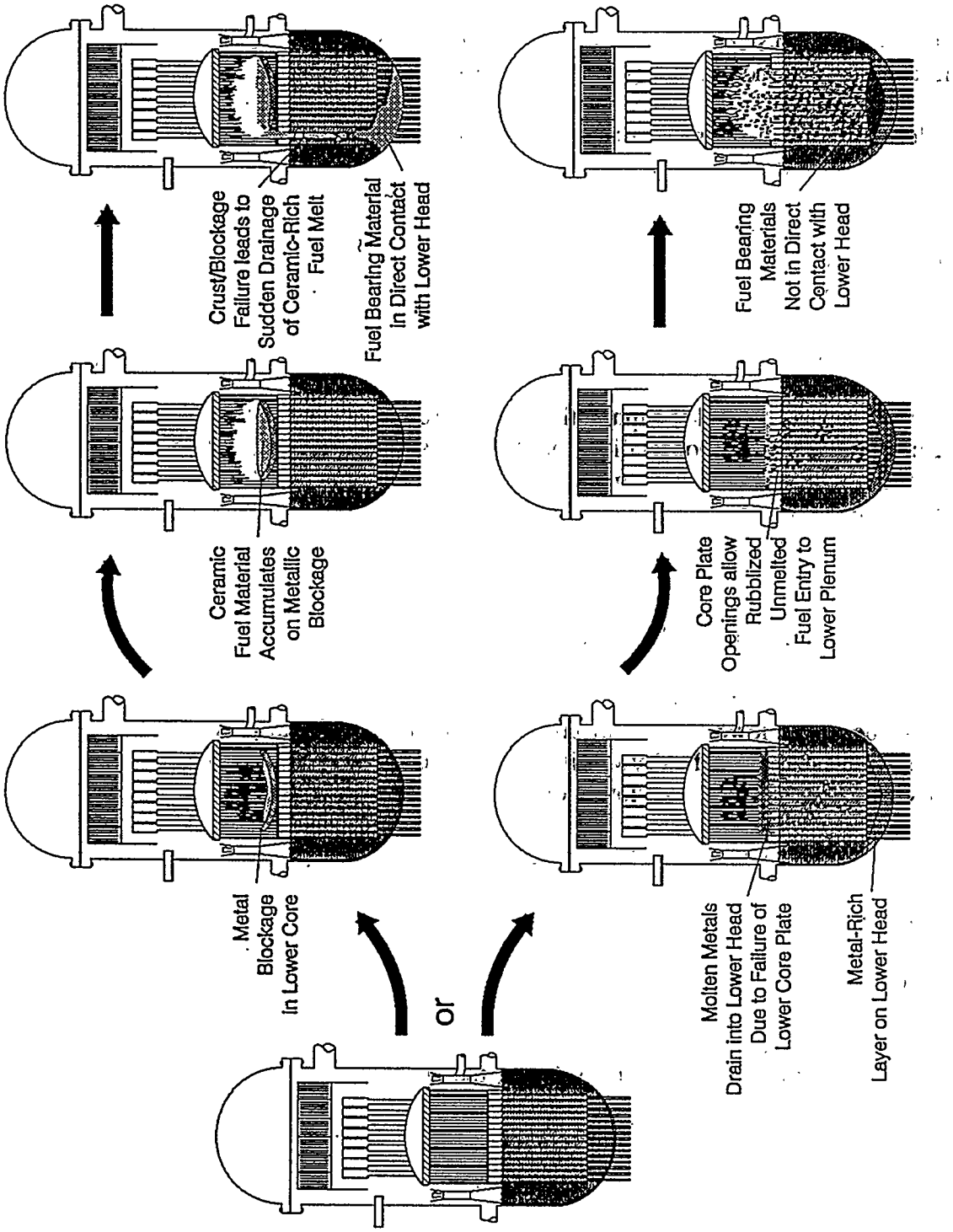

Figure 9. Alternative core meltdown scenarios for boiling water reactors

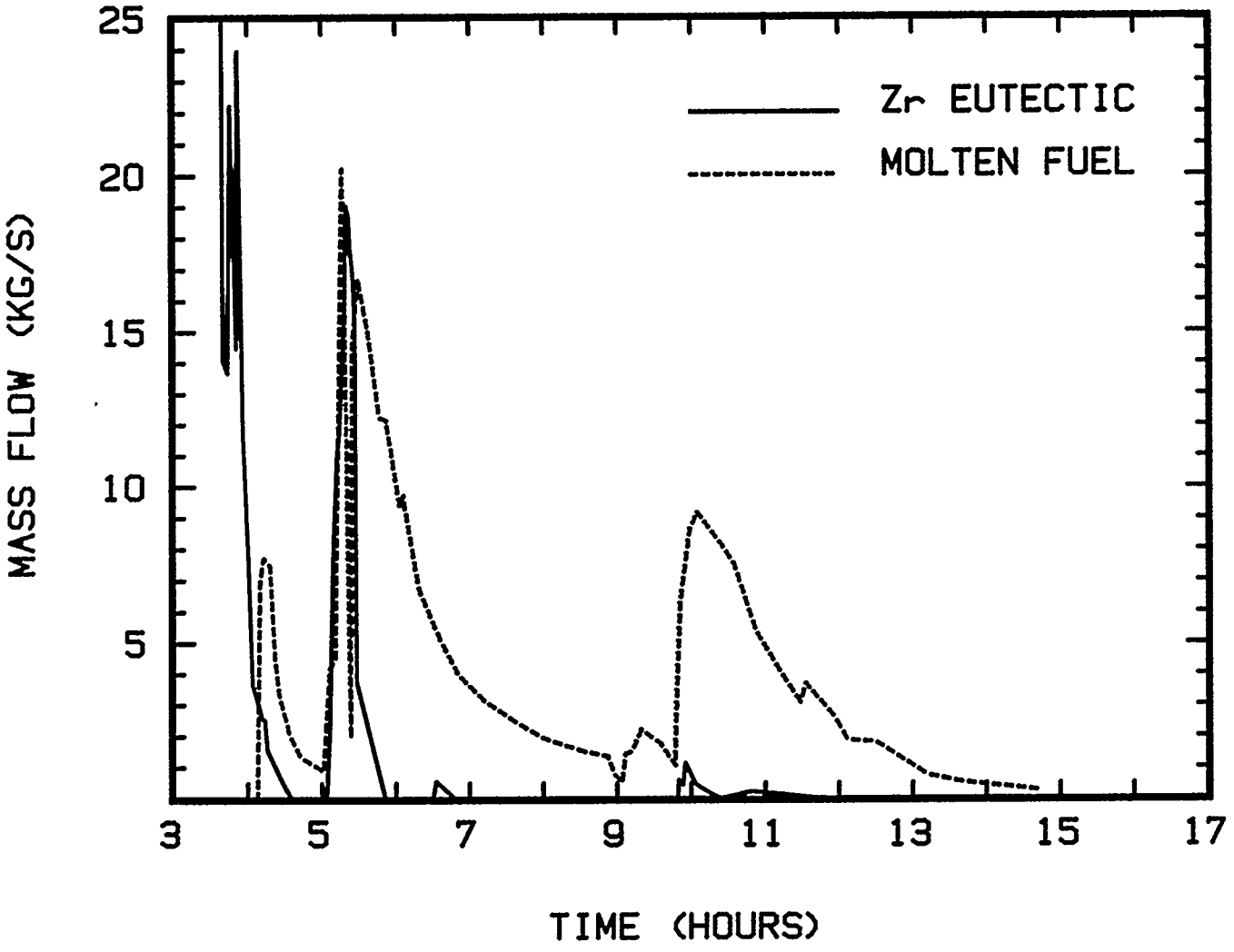

Figure 10. Core debris expulsion from the reactor vessel into the drywell as predicted by the BWRSAR code [16]

Aerosols and gases produced during core debris interactions with concrete in the reactor drywell will vent through downcomers into the suppression pool.

During the late stages of a reactor accident, volatile radionuclides previously deposited in the reactor coolant system may vaporize. The revaporization of these materials is driven by their continued decay heating. Some fraction of the revaporized materials will be transported out of the reactor coolant system into the drywell and then into the suppression pool. The revaporization release of deposited radionuclides can be a long term process. Analyses with the MAAP code of revaporization during hypothetical accidents at the Peach Bottom Mark I boiling water reactor indicate revaporization can persist for 50 hours after core meltdown started [21].

Quantitative details of the accident progression depend, of course, on the particular accident scenario. The NUREG-1150 study [22] identified the frequency-dominant accident scenarios caused by internal initiators for representative Mark I and Mark III boiling water reactors:

- Mark I:

  1. loss of offsite power (mean frequency = 2.2×10^{-6}/yr)

  2. anticipated transients without scram (mean frequency = 1.9×10^{-6}/yr)

  3. medium size breaks in the reactor coolant system (break areas of 3.7 to 93 cm^2) (mean frequency = 2.6×10^{-7}/yr)

- Mark III:

  1. loss of offsite power (mean frequency = 3.9×10^{-6}/yr)

  2. anticipated transients without scram (mean frequency = 1.1×10^{-7}/yr)

Payne [239] has described severe accident frequencies for the La Salle Mark II reactor. Over 70 percent of the risk from accidents caused by internal initiators is due to loss of off-site and on-site power.

For the loss-of-offsite-power accidents and the anticipated-transient-without-scram (ATWS) accidents, the reactor coolant system is intact throughout core degradation. Radionuclides released during core degradation vent to the suppression pool through the quenchers. Only after core debris has penetrated the reactor vessel do aerosol-laden gases pass into the suppression pool by way of the downcomers in the drywell.

Loss-of-coolant accidents are not exceptionally important contributors to the core meltdown accident frequency of boiling water reactors if only internal initiators are considered. Loss-of-coolant accidents are expected to make bigger contributions to the core meltdown frequency when external events such as earthquakes and fires are considered as initiators. In loss-of-coolant events, aerosol laden gases can vent from the reactor coolant system to the drywell and then from the drywell to the suppression pool by way of the drywell downcomers.

For the purposes of this development of a simplified model, scrubbing of aerosol-laden gases produced during the early stages of an accident is considered to occur only by injection into the suppression pool through the quenchers. That is, injection of aerosol-laden gases into the suppression pool through the drywell downcomers is considered to occur only after the core debris has penetrated the reactor vessel. Injection via the downcomers early in an accident, such as might occur during a loss of coolant accident, is neglected.

B. Accidents in Mark I Reactors

Detailed accident analyses were done for the NUREG-1150 study using the Source Term Code Package [14]. Results of these analyses provide some indication of the range of gas flows and gas compositions that will be discharged to the quenchers. Molar flows through the reactor coolant system for a TC3 sequence [23] are shown in Figure 11. The TC3 sequence is an anticipated transient without scram (ATWS) accident sequence. The reactor coolant system is assumed to remain pressurized during core degradation. The wetwell is assumed to be vented.

It is apparent from results shown in Figure 11 that gap release will take place under conditions of high flow. Molar flow rates during the period immediately following core uncovery vary from about 2500 to 400 moles per second. During this period, hydrogen makes up only about 2 to 3 percent of the gas flow through the core region. Early in-vessel releases will take place at flow rates of only 400 to 180 moles per second. Hydrogen will make up 10 to 95 percent of the gas flow. Core slumping and collapse prompt a huge increase in flow to about 2000 to 2500 moles/s. During this period of rapid flow, hydrogen will make up only 1 to 3 percent of the gas. The rapid flow associated with core slumping and core collapse will drive any aerosols suspended in the reactor coolant system into the suppression pool.

Had the BWRSAR code been used for these calculations instead of the Source Term Code Package, flows during core melting would have been somewhat higher—perhaps as high as 500 moles/s. The huge increase in flow at 86 minutes would not have occurred.

Flows to the suppression pool during the ex-vessel stages of the TC3 sequence are shown in Figure 12. Note that these calculations were done assuming that the concrete was fabricated with limestone aggregate. Limestone concrete produces more gas when it ablates than does siliceous aggregate concrete [24]. On the other hand, it takes more energy to ablate limestone concrete than it does to ablate siliceous concrete. Consequently, had siliceous rather than limestone concrete been assumed, molar flow rates would have been one-half to two-thirds those shown in Figure 12.

Early in the course of the core debris interactions with limestone or siliceous concrete essentially none of the gas is condensible. For the purposes of the analyses presented here, essentially all of the steam has been reduced to hydrogen. Other gases in the flow are noncondensible carbon monoxide and carbon dioxide. After 3 to 6 hours of core debris/concrete interactions [25] when iron is the strongest reducing agent in the core debris, about 12 percent of the gas evolved during interactions with limestone concrete is water vapor. During interactions with siliceous concrete, about 32 percent of the gas can be water vapor late in the interaction.

The Source Term Code Package uses an assumption that primary particles formed from vapors evolved from the core are 0.05 μm in diameter. It is also assumed the particle material has a

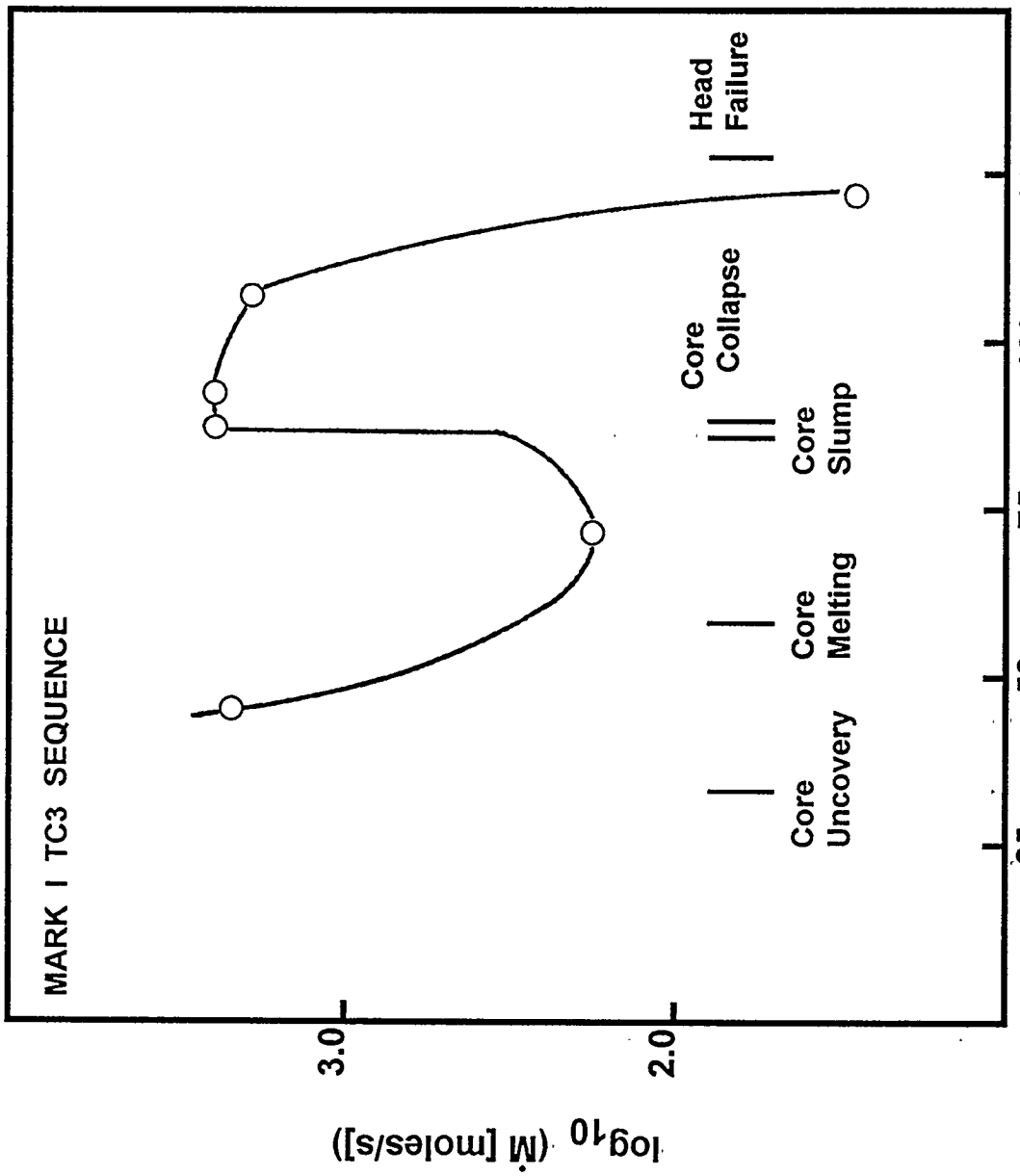

Figure 11. Molar gas flow ($\dot{M}$) through the reactor coolant system in a Mark I boiling water reactor during a TC3 accident sequence

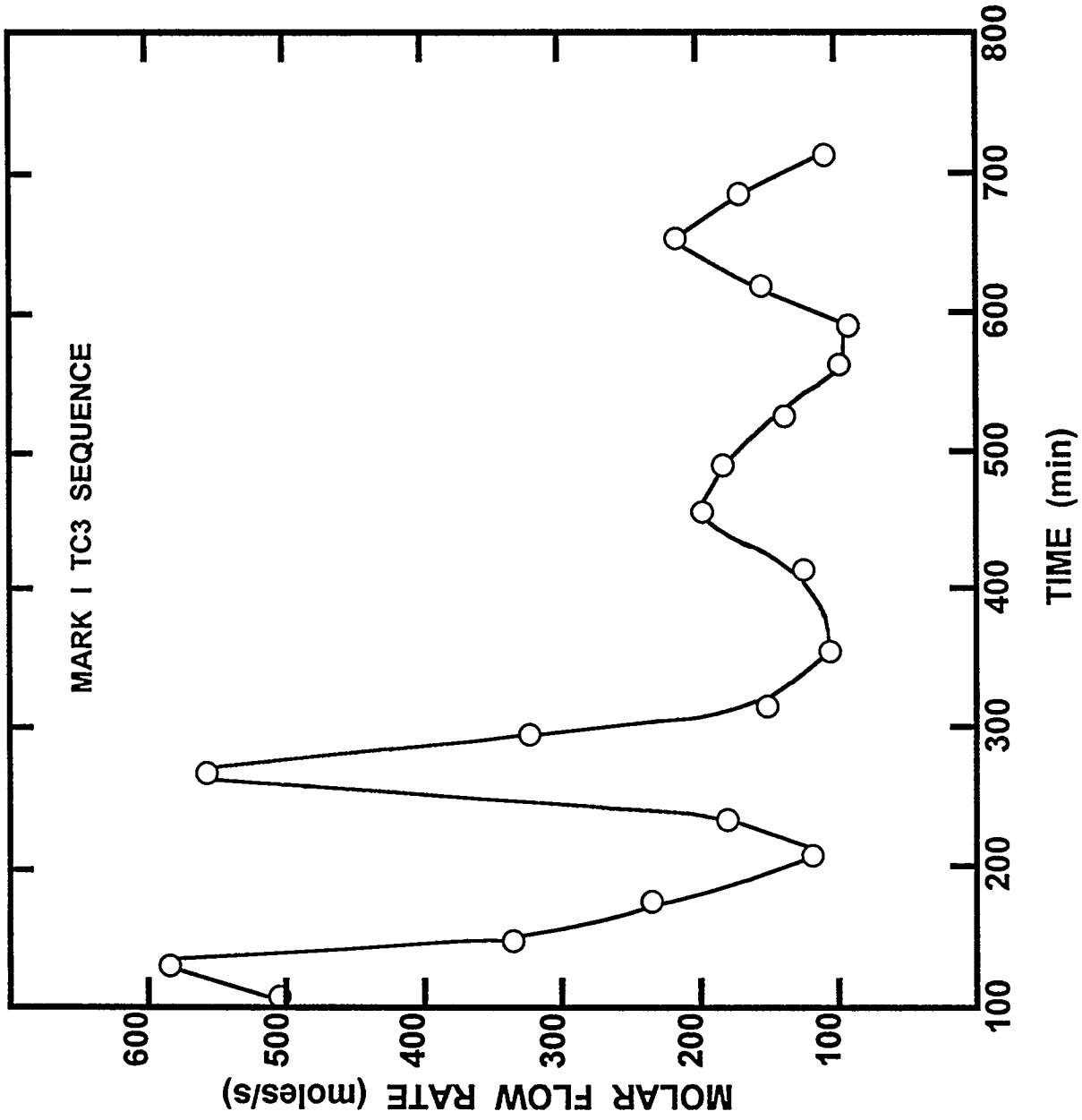

Figure 12. Molar flows of gas to the suppression pool during core debris/concrete interactions in a TC3 accident sequence

density of 3 g/cm^3. The code does a mechanistic calculation of aerosol growth by vapor condensation and coagulation of particles. Example predictions of aerosol particle size distribution for material venting through the safety relief valves are shown in Figure 13. The mean size of the aerosol particles is predicted to be about 3 μm. There must, however, be a great deal of uncertainty in this prediction. Despite the many tests of radionuclide release from degrading reactor fuel, there appears to be no suitable data base for comparison to the code predictions. Perhaps, the PHEBUS-FP tests now being planned [257] will provide the needed information on aerosol particle sizes being vented to the suppression pool from the reactor coolant system.

The mean sizes and densities of the aerosol particles predicted by the Source Term Code Package to be produced during core debris interactions with concrete are shown in Figure 14. These sizes are predicted based on fitting to experimental data and assuming that particles grow until the number concentration falls to about 10^9 particles per cm^3 [19]. The relatively large particle sizes predicted to be present during the early stages of vigorous attack on concrete are consistent with experimental data. The fall in aerosol mean size when aerosol generation rate falls is the product of the assumption concerning the particle growth and must be considered quite uncertain.

The proposed revision to the severe accident source term [3] indicates that the majority of the release of radionuclides during core debris/concrete interactions takes place during the first two hours of interaction. During this period the aerosol particle sizes are relatively coarse. Mean sizes of the particles are on the order of 1.2 μm. Aerosol material densities calculated with the Source Term Code Package during this stage of an accident in a Mark I boiling water reactor vary from 4.33 to 3.15 g/cm^3 [23].

The production of aerosol during longer term phases of core debris interactions with concrete does not contribute significantly to the radioactivity releases. These aerosols produced between 2 and 10 hours after the onset of core debris/concrete interactions are composed primarily of constituents of concrete—SiO_2, Na_2O, and K_2O. Particle sizes are predicted to be quite small. Mean sizes are on the order of 0.25 μm. These aerosol particles will mix with radioactive aerosols produced by the revaporization of radionuclides from the reactor coolant system. Material densities of aerosol produced by core debris/concrete interactions have been calculated with the Source Term Code Package [23] to be in the range of 3.15 to 2.65 g/cm^3.

Aerosols produced during core debris/concrete interactions are assumed here to have log-normal size distributions with a geometric standard deviation of 2.3. The geometric standard deviation of aerosols produced in experiments varies from 1.6 to 3.8 [26].

Molar flows through the reactor coolant system during a station blackout accident (the TB2 sequence) at a Mark I boiling water reactor as calculated with the Source Term Code Package are shown in Figure 15. Though the onset of core degradation is offset in time, molar flows following core uncovery exhibit qualitative similarities to molar flows calculated for the TC3 ATWS sequence. Molar flow rates to the suppression pool during the ex-vessel stages of the station blackout accident are shown in Figure 16. These flows exhibit qualitative similarities to those calculated for the ATWS sequence. Aerosol particle size and aerosol material density during the melt/concrete interactions in a station blackout accident are shown in Figure 17. Again, the similarities of these results to those calculated for the ATWS swquence are quite noticeable.

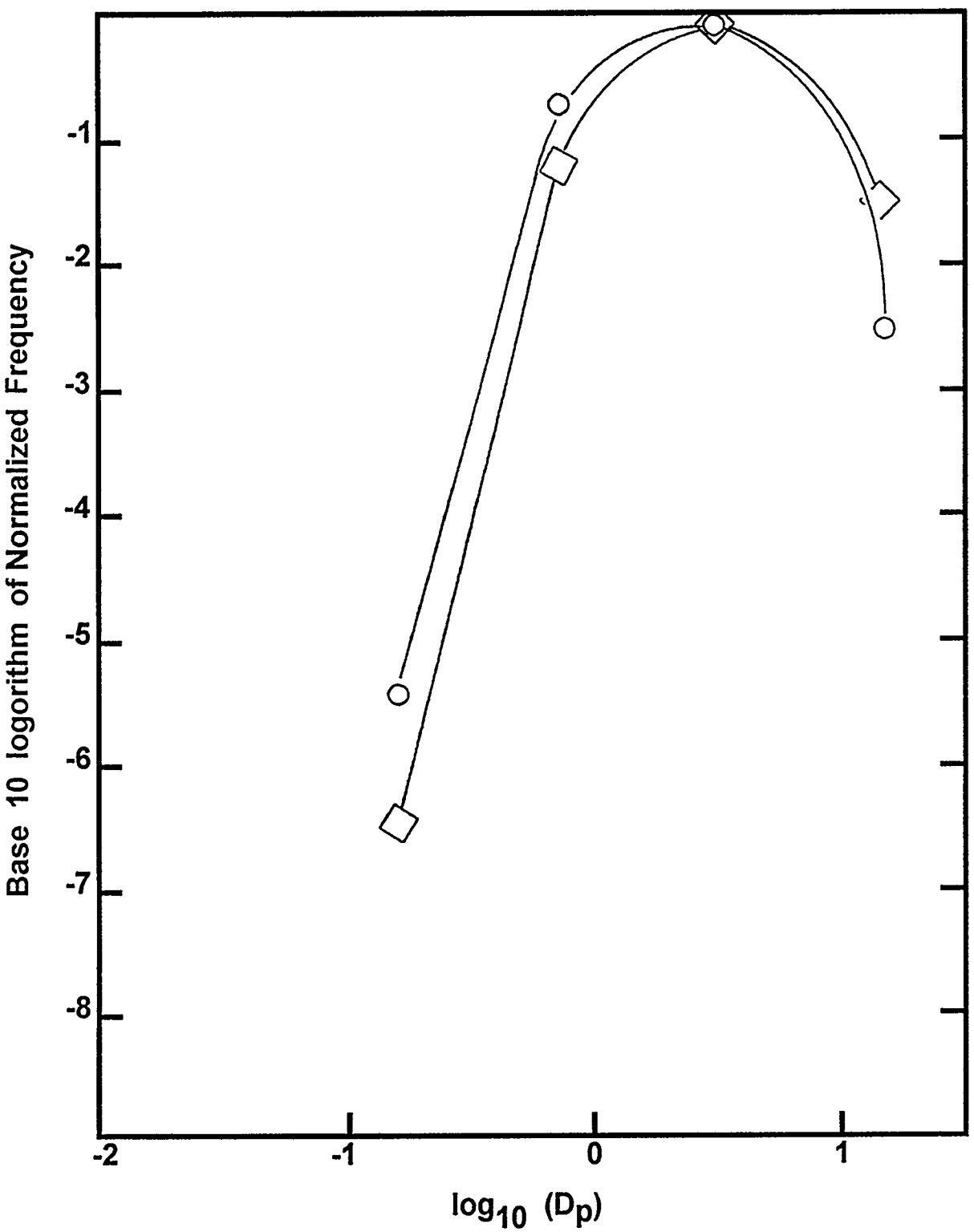

Figure 13. Size distribution of aerosols in the reactor coolant system predicted with the Source Term Code Package

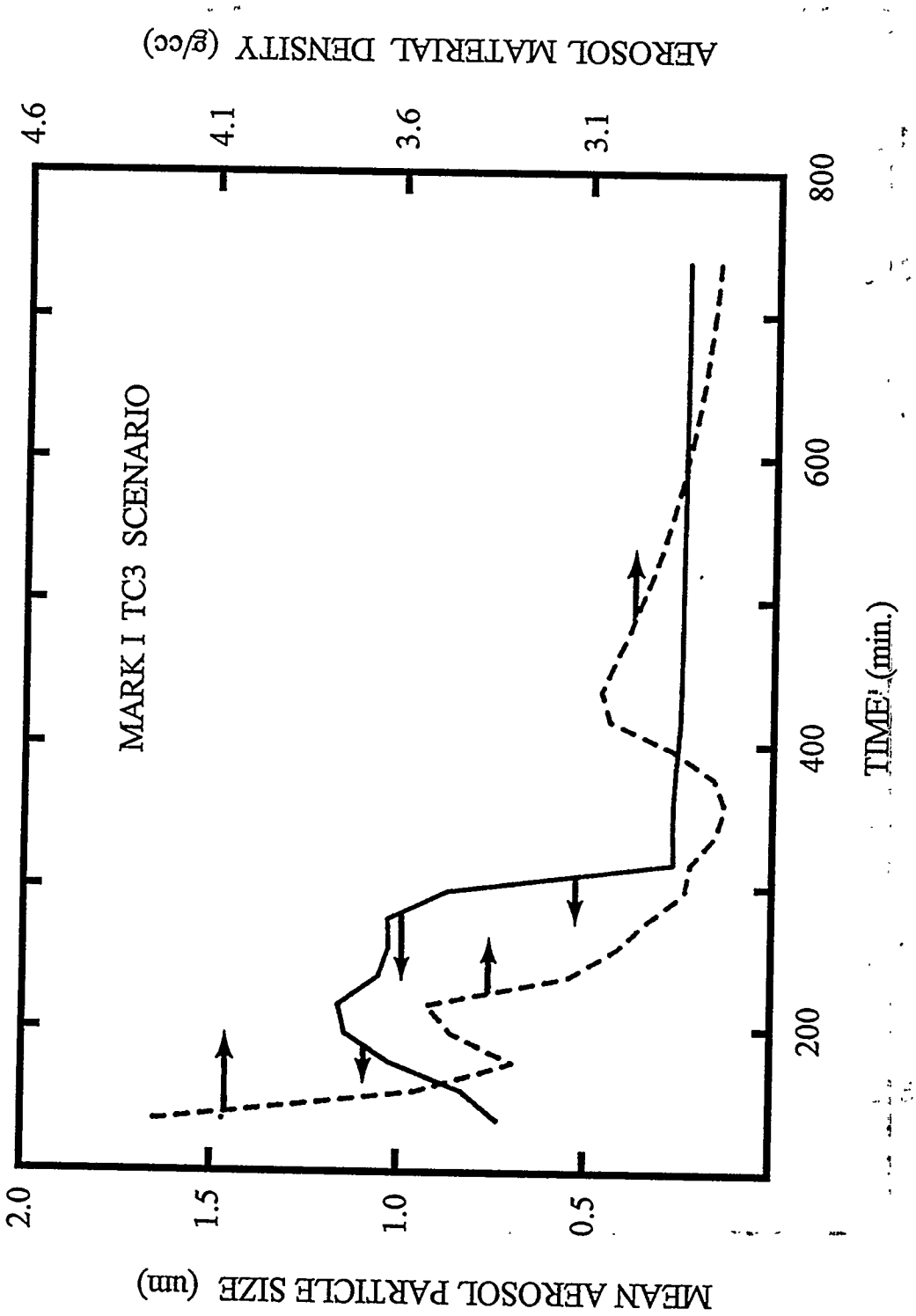

Figure 14. Mean size and material density of aerosols produced during core debris interactions with concrete in a TC3 accident in a Mark I boiling water reactor

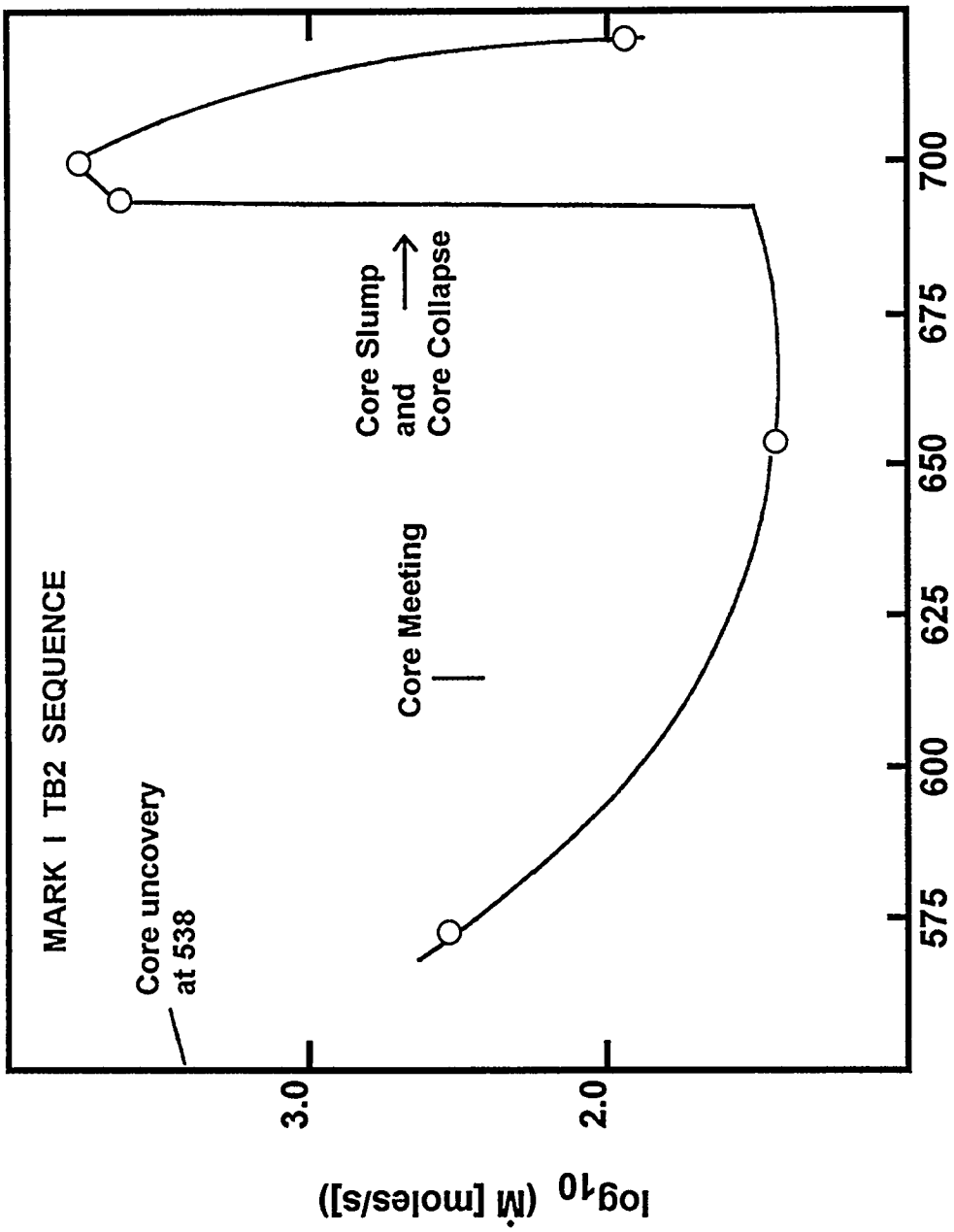

Figure 15. Molar gas flow ($\dot{M}$) through the reactor coolant system in a Mark I boiling water reactor during a TB2 accident sequence

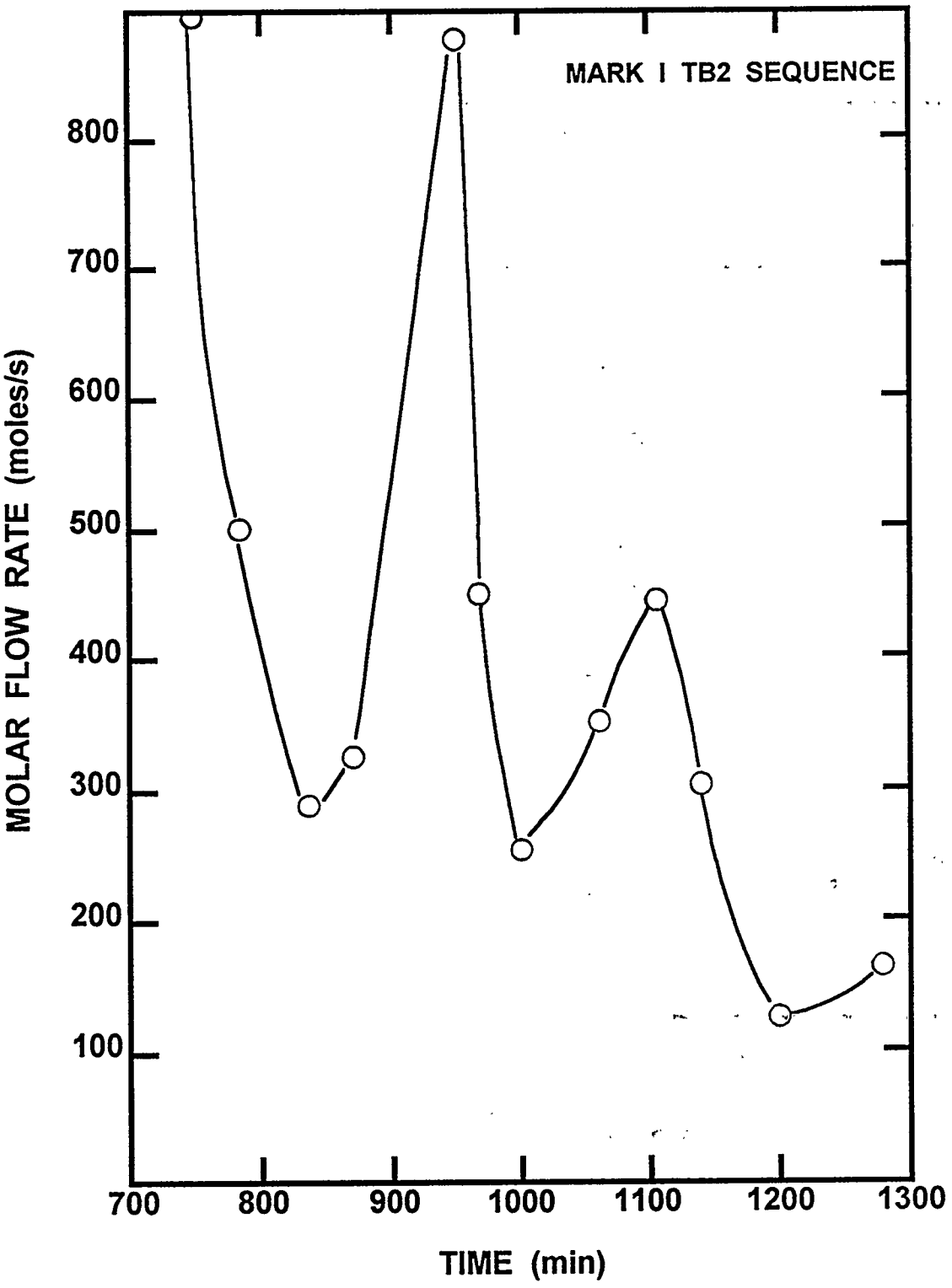

Figure 16. Molar flows of gas to the suppression pool during core debris/concrete interactions in a TB2 accident sequence

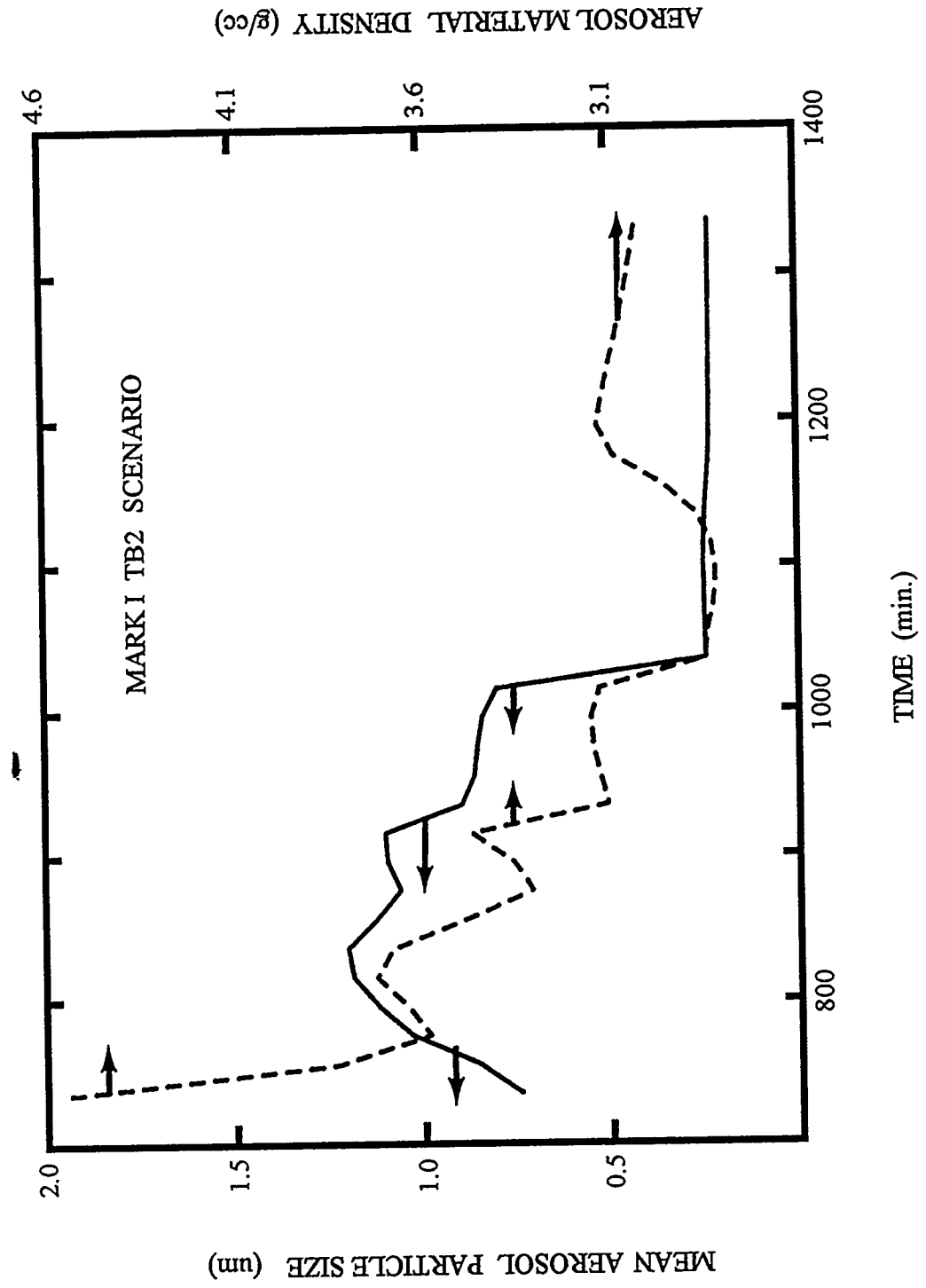

Figure 17. Mean size and material density of aerosols produced during core debris interactions with concrete in a TB2 accident in a Mark I boiling water reactor

C. Accidents in Mark II Reactors

There have been very few severe reactor accident analyses published for Mark II containment boiling water reactors. Dingman et al. [236] have used the MELCOR code to calculate the progression of a station blackout accident at the La Salle Mark II reactor. The progression of the accident is rather similar to the progression of station blackout accidents at other types of boiling water reactors. Gap release is predicted to occur over a 46 minute period beginning 73 minutes after accident initiation and 37 minutes after core uncovery. Vessel penetration by core debris occurs 281 minutes after accident initiation. During core degradation, hydrogen is produced at the rate of 94 moles per second.

The most remarkable results obtained by Dingman et al. in their analyses of the station blackout accident concerned the gas generation once core debris had been expelled from the reactor vessel. Their analyses indicate that degassing of concrete produces far more gas than do the direct interactions of core debris with structural concrete. Degassing of concrete is predicted to produce 29 moles/s of steam and between 7 and 25 moles/s of carbon dioxide. Hydrogen production during this period when core debris is interacting with concrete is reported to average about 1.4 moles/s. Carbon monoxide generation rates are not reported.

Steam production by concrete degassing is significant for the prediction of source term attenuation. This steam could be condensed in sufficiently sub-cooled steam suppression pools. Condensation of the steam could sweep aerosols from gas bubbles rising through the pool.

Shaffer et al. [235] have reported results of calculations with the MELCOR model for various types of station blackout accidents at the La Salle plant. For the "high pressure, short term, station blackout" scenario, hydrogen was calculated to be generated at the rate of about 60 moles/s during the period of gap release and the period of in-vessel release. Steam flow through the safety/relief valves fell from about 2400 moles/s prior to gap release to about 200 moles/s during the period of extensive core degradation. Sudden eruptions of steam were calculated to occur whenever core debris fell into the residual water in the reactor vessel.

Hydrogen generation rates calculated to occur during a "low pressure, short term, station blackout" scenario were about 21 moles/s during gap and in-vessel release. The hydrogen generation rate during a "long term, station blackout" scenario was about 20 moles/s. Steam flow through the relief valves during the core degradation process was small except for episodic eruptions of steam when core debris relocated.

Shaffer et al. also considered degassing of concrete as well as the interaction of core debris with concrete as sources of gas production during the ex-vessel phases of a severe reactor accident. Total gas production rates and gas compositions during the early stages of ex-vessel core debris interactions for various station blackout scenarios are compared below:

Scenario	Total Gas Production (moles/s)	Molar Gas Composition (%)			
		H_2	H_2O	CO	CO_2
Short term high pressure station blackout	200	26	24	30	20
Short term low pressure station blackout	159	19	20	45	16
Long term station blackout	134	14	31	38	17

Similar comparisons for longer term phases of the ex-vessel core debris interactions which will affect the attenuation of the late in-vessel release are:

Scenario	Total Gas Production (moles/s)	Molar Gas Composition (%)			
		H_2	H_2O	CO	CO_2
Short term high pressure station blackout	49	4.4	44	13	39
Short term low pressure station blackout	55	5.6	42	17	35
Long term station blackout	63	4.0	61	6.1	29

D. Accidents in Mark III Reactors

Molar flows to the suppression pool calculated with the Source Term Code Package [27] for a station blackout accident and an ATWS accident sequence in a Mark III reactor are shown in Figure 18. These flows are quite like those calculated for similar accidents in a Mark I reactor. Gas production and aerosol production during core debris interactions with concrete are also quite similar to results calculated for corresponding accidents in Mark I reactors.

Dingman et al. [236] have used the MELCOR code to predict the progression of a station blackout accident at the Grand Gulf Mark III boiling water reactor. Hydrogen production rates during the gap release phase of the accident and during much of the in-vessel release phase are predicted to be about 117 moles/s. This hydrogen production rate decreases to about 22 moles/s during the period fuel is relocating within the reactor vessel. Hydrogen production rates once fuel has been expelled from the reactor vessel and core debris/concrete interactions begin are about 14 moles/s.

Dingman et al. consider concrete degassing during the ex-vessel phase of the accident. They find steam release rates due to degassing to be about 20 moles/s. Their calculations indicate that the atmosphere of the drywell is 80 to 95 percent steam during most of the ex-vessel phase of the accident. The remainder of the gas is largely hydrogen. Carbon dioxide and carbon monoxide are found to make

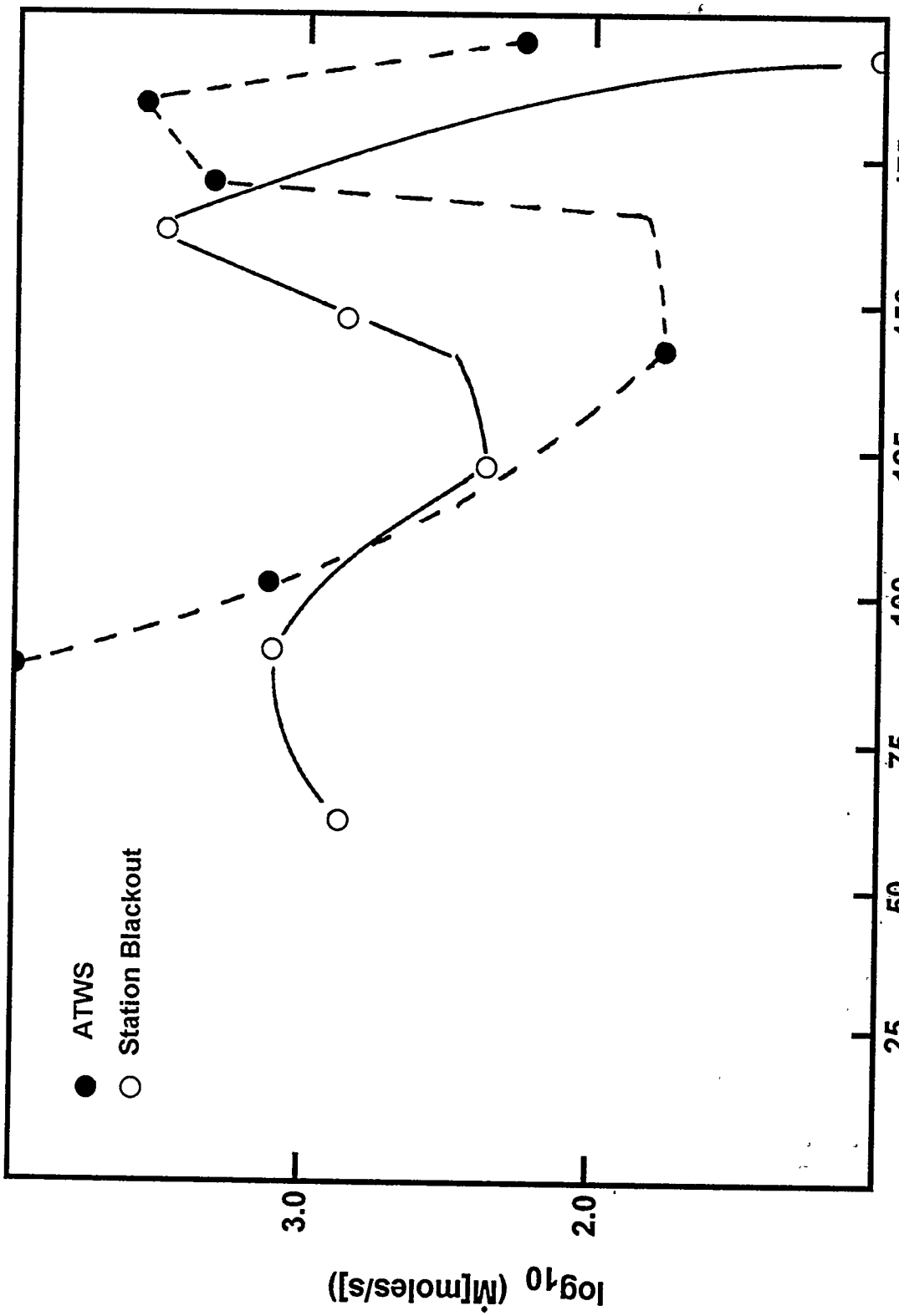

Figure 18. Molar flow rates (Ṁ) through the reactor coolant system in a Mark III boiling water reactor during a station blackout accident and an ATWS accident

negligible contributions to the drywell atmosphere composition throughout most of the ex-vessel phase of the accident. Only for a period of about 90 minutes, when gas production from core debris/concrete interactions is very high and presumably radionuclide releases are also high, carbon monoxide makes up 9 to 12 percent of the drywell gas.* During this period, hydrogen is about 3 percent of the drywell gas.

Calculations by Dingman et al. [236] show wildly varying flows through the suppression pool during the ex-vessel phase of the station blackout accident. Flows vary from about 160 moles/s to about 1055 moles/s. The time averaged flow rate to the steam suppression pool is about 470 moles/s. Much of this flow must come from steam formed from water that floods into the reactor cavity from the Mark III suppression pool.

Greene et al. [234] have used the MELCOR, BWRSAR, and BWR-LTAS codes to analyze station blackout accidents in the Grand Gulf Mark III boiling water reactor. They too find that the drywell atmosphere becomes rich in steam in the later phases of core debris/concrete interactions. The molar composition of the drywell atmosphere during the period of late, in-vessel release is found to vary between about 50 and 95 percent steam depending on the details of the accident scenario.

The QUEST study examined uncertainties in the aerosol produced by core debris interactions with concrete during a station blackout accident at a Mark III boiling water reactor [25]. Mean aerosol particle sizes during the periods of intense aerosol productions were found to vary between 0.9 and 1.1 μm. Aerosol material densities were calculated to vary from 2.9 to 3.5 g/cm^3 during this period. During later stages of the accident, mean aerosol particle diameters were calculated to be in the range of 0.4 to 0.6 μm. The aerosol material density was calculated to be 2.9 to 3.1 g/cm^3.

E. Conclusions

From the several accident analyses described above, it can be concluded that:

- gap release will involve production of rather fine aerosols. Steam production rates during this phase of the accident will vary from 2500 to 400 moles/s. Hydrogen generation rates will vary from about 120 to 20 moles per second.

- early in-vessel release will produce coarser aerosol particles in gas containing 10 to 90 percent hydrogen flowing at rates of 50 to 500 moles/s.

- the last portion of the early in-vessel release may be purged from the reactor coolant system by flows of 2000 to 6000 moles per second of steam containing 2 to 3 percent hydrogen.

- molar flows to the suppression pool during core debris/concrete interactions are 100 to 300 moles/s with occasional excursions to over 800 moles/s. Aerosols have uncertain sizes of 1.5 to 0.25 μm.

*The eruption of carbon monoxide release predicted in these calculations stems from the treatment of carbon dioxide reactions with molten, metallic zirconium in the core debris. This reaction is predicted to produce elemental carbon until the zirconium is completely oxidized. Then, carbon dioxide and steam from the concrete are predicted to react with the elemental carbon to form carbon monoxide. This type of behavior has not been observed in experiments done to date.

- Little of the gas produced during the early stages of core debris/concrete interaction in a Mark I boiling water reactor will be condensible. At later times during the so-called "late in-vessel release" stage of the accident, 10 to 35 percent of the gas being discharged to the steam suppression pool will be water vapor.

- Degassing of concrete during the ex-vessel stages of a severe reactor accident in Mark II and Mark III reactors can introduce substantial amounts of water vapor into the gases being discharged to the suppression pools.

There have not been detailed analyses of aerosol particle sizes for the late in-vessel release of radionuclides by revaporization. Some analyses for revaporization from the pressurized water reactor Sizewell B suggest these particles can be quite small (~ 0.1 μm) [28]. The aerosols produced by revaporization will be carried into the suppression pool by gases generated during core debris interactions with concrete.

IV. Physical Phenomena

The physical phenomena that affect aerosol removal from gases that sparge through steam suppression pools are described in this chapter. The important phenomena can be broadly categorized as those phenomena affecting bubble and gas behavior and those phenomena affecting aerosol behavior. In the discussions of these two categories of phenomena presented below, emphasis is placed on the identification of areas of uncertainty that will affect the accurate prediction of aerosol removal by steam suppression pools. These phenomenological uncertainties, together with uncertainties concerning severe reactor accidents, are summarized in Chapter V and used in an uncertainty analysis of scrubbing by steam suppression pools described in Chapter VI.

A. Bubble Formation

Gases are injected into steam suppression pools via both quenchers and downcomers. In both cases, the details of the bubble size, shape, rise velocity, and the like significantly affect the extent of aerosol removal. There have been two studies of the behavior of bubbles released from models of quenchers in simulated steam suppression pools [30,69]. Both studies showed the same qualitative behavior. A schematic depiction of the observed behavior is shown in Figure 19. Large bubbles form at an orifice, detach and begin to rise. These bubbles collapse and shatter into smaller bubbles because of steam condensation in a subcooled pool or because of simple physical instability. A swarm of small bubbles then rises through the pool as a plume. That is, the rising bubbles entrain water in the upward flow.

The various regimes in the bubble plume have been named. The region near the orifice and to a height of about 10 bubble diameters is called the "injection zone." The injection zone is the region of rapid heat transfer from the bubbles to the liquid. Completion of bubble collapse marks the end of the injection zone and the beginning of the "zone of established flow." The zone of established flow extends to within less than a meter of the surface. The "zone of surface influence" is the region of the plume where the vertical component of water velocity is converted entirely into radial flow.

In the discussions below, models of the injection zone and the zone of established flow will be presented. A detailed description of hydraulics in the zone of surface influence is not included here. Amos [70] has discussed the complexity of this regime and its relative unimportance in the prediction of aerosol scrubbing by steam suppression pools.

Though the scrubbing of aerosols from gases released to a steam suppression pool has some qualitative similarities to aerosol removal by water pools overlying core debris interacting with concrete, there are a number of quantitative differences and several additional phenomena to consider. Certainly, the way bubbles are formed in the water pool is different as is the plume behavior of rising bubbles. Furthermore, gases directed to the suppression pool through quenchers and downcomers can be very rich in condensible water vapor whereas water vapor produced during core debris interactions is largely reduced to hydrogen. These and other physical phenomena that affect bubble behavior are discussed further below.

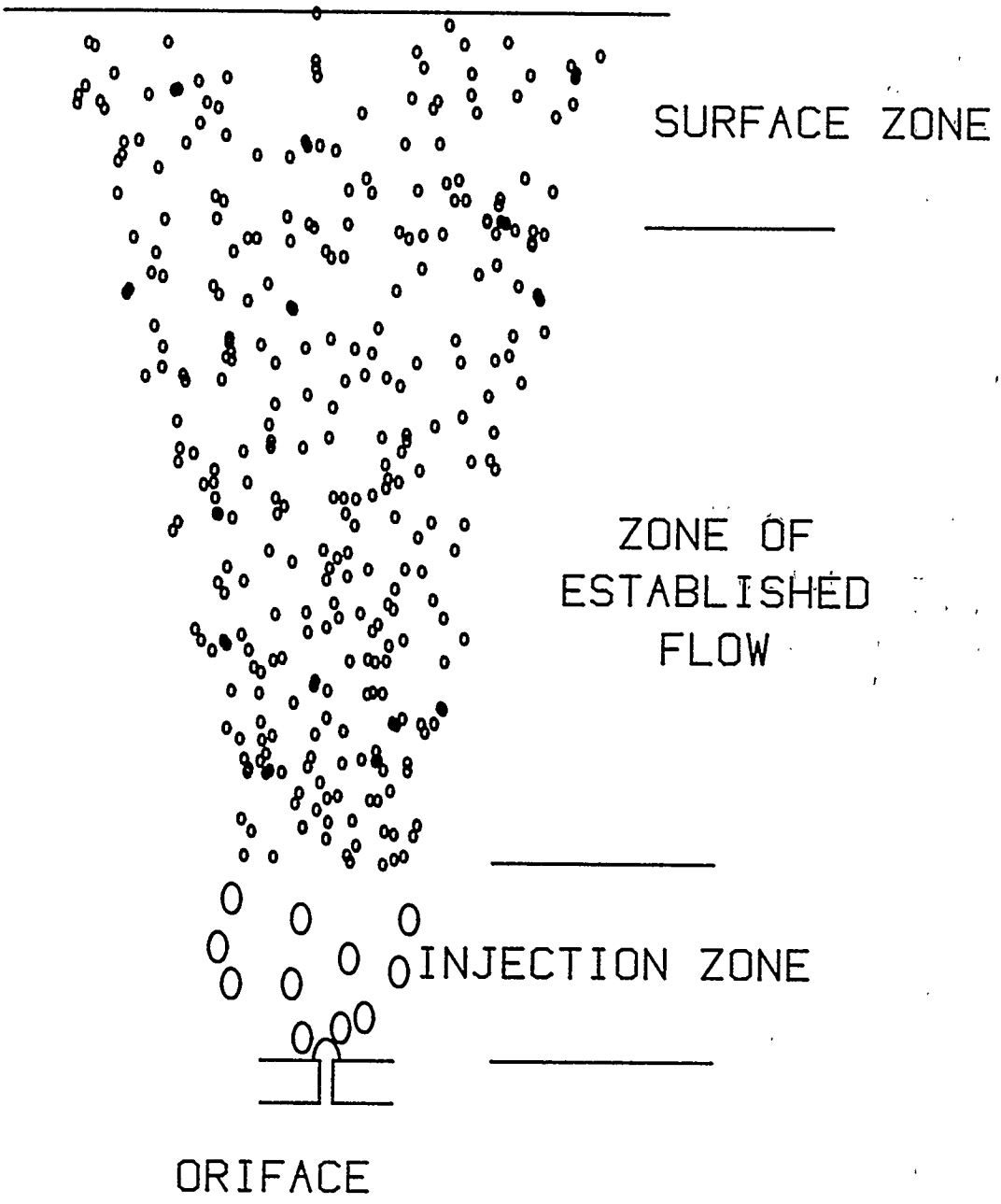

Figure 19. Schematic representation of bubble behavior when released into a steam suppression pool from a quencher

1. Bubble Formation at Quencher Orifices

Paul et al. [30] have examined bubble formation by noncondensible gases (He, H_2 and air) at orifices 0.9 to 2.02 cm in diameter.* A schematic diagram of the injection apparatus used in this work is shown in Figure 20. Paul et al. indicate the system capacitance to be 3.25. Tsuge and Hibino [207] indicate that bubble formation is sensitive to variations in system capacitance in this regime.

Volumes of the gas bubbles detaching from orifices were correlated by Paul et al. in terms of a Weber number:

$$V_N = 3.45\ We^{0.46}$$

where

$$V_N = \frac{\left(\pi D_B^3/6\right)}{\left(\pi D_o^2/4\right)} (\rho_l - \rho_g)^{1/2}\ g^{1/2} \sigma_l^{-1/2}$$

We = Weber number = $U_o^2 \rho_l D_o/\sigma_l > 40$,

D_B = diameter of the sphere with a volume equivalent to the bubble when it detaches from the orifice,

D_o = orifice diameter,

U_o = gas velocity in the orifice = $4\dot{m}/\rho_g(o)\ \pi D_o^2$,

$\dot{m}$ = mass input rate of gas to the pool,

$\rho_g(o)$ = density of the gas at the orifice,

ρ_l = liquid density,

g = gravitational constant, and

σ_l = liquid surface tension.

Predictions of this correlation are compared in Figure 21 to data obtained by Paul et al. [30] and data obtained by other investigators [32,36-39]. These data are listed in Table 5. Data are also consistent with the Davidson-Schuler model (see Figure 22) which will be discussed further below.

*The authors acknowledge the exemplary documentation provided by Paul et al. [30] for their work.

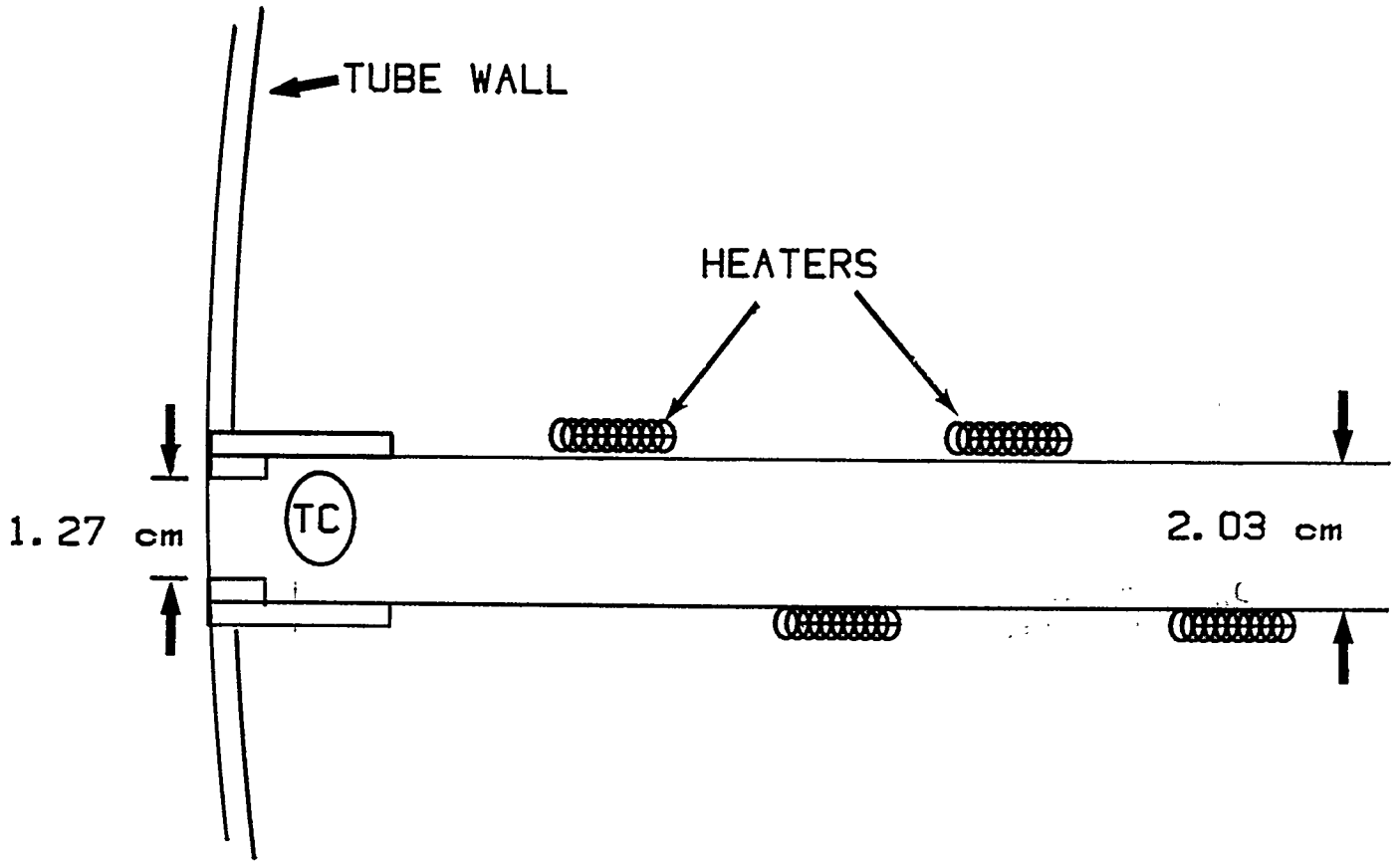

Figure 20. Bubble injector apparatus used in tests of bubble hydraulics by Paul et al. [30]

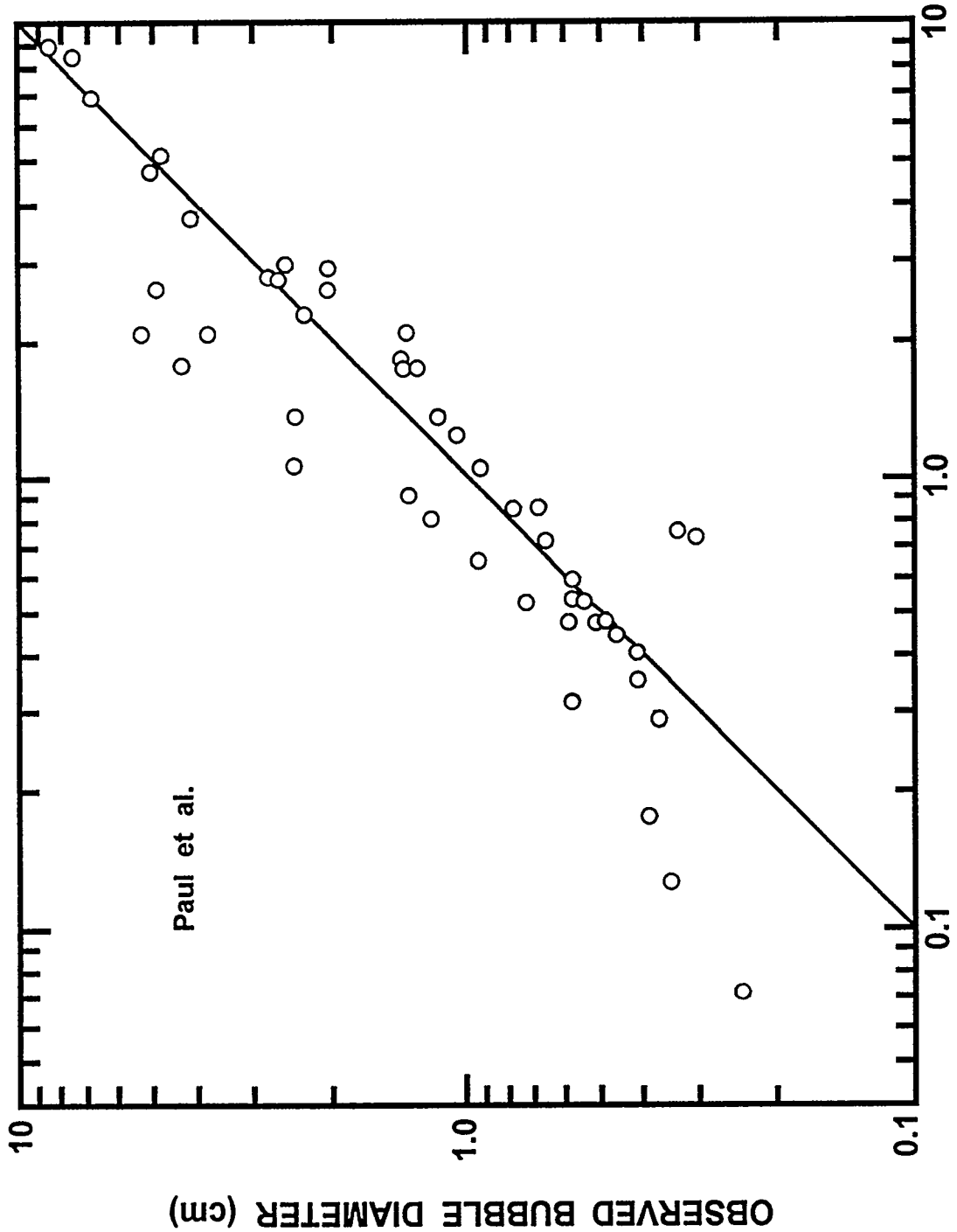

Figure 21. Comparison of bubble sizes predicted with correlation developed by Paul et al. [30] to bubble sizes observed in various experiments [30,32,36-39]

Table 5. Sizes of bubbles formed at submerged orifices under constant flow conditions

Liquid	Gas	Liquid viscosity (g/cm-s)	Surface tension (dyne/cm)	Flow rate (cm^3/s)	Orifice diameter (cm)	Bubble volume (cm^3)	Ref.
Water	Air	0.012	72.8	0.0081	0.036	0.0072	36
Water	Air	0.012	72.8	0.06083	0.141	0.0292	36
Water	Air	0.012	72.8	0.205	0.388	0.0984	36
Water	Air	0.01	72	0.025	0.102	0.0212	37
Water	Air	0.01	72.7	0.5	0.0668	0.026	32
Water	Air	0.01	72.7	1.0	0.0668	0.0365	32
Water	Air	0.01	72.7	1.5	0.0668	0.0365	32
Water	Air	0.01	72.7	2.0	0.0668	0.050	32
Water	Air	0.01	72.7	2.5	0.0668	0.068	32
Water	Air	0.01	72.7	5.0	0.04	0.2	32
Water	Air	0.01	72.7	10	0.04	0.42	32
Water	Air	0.01	72.7	20	0.04	0.90	32
Water	Air	0.01	72.7	30	0.04	1.3	32
Water	Air			59.5	1.27	6.33	30
				110	1.27	9.71	30
				140	1.27	8.62	30
				4070	1.27	225	30
				18000	1.27	1090	30
				579	2.02	57.9	30
				1590	2.02	164	30
				3510	2.02	328	30
				128	0.99	10.9	30
				349	0.99	35.9	30
				730	0.99	70.2	30

Table 5. Sizes of bubbles formed at submerged orifices under constant flow conditions (concluded)

Liquid	Gas	Liquid viscosity (g/cm-s)	Surface tension (dyne/cm)	Flow rate (cm^3/s)	Orifice diameter (cm)	Bubble volume (cm^3)	Ref.
Water	Helium			80.8	1.27	7.35	30
				309	1.27	28.1	30
				644	1.27	61.9	30
Water	Hydrogen			71.7	1.27	7.63	30
				360	1.27	42.8	30
				623	1.27	80.1	30
				1.5	0.43	0.1	39
				22	0.43	0.8	39
				1.5	0.27	0.1	39
				22	0.27	0.6	39
				1.5	0.15	0.06	39
				10	0.15	0.25	39
				1.5	0.107	0.05	39
				7	0.107	0.15	39
				1.249	0.32	0.0833	38
				160	0.96	4.445	38
				120	0.80	4.393	38
				60	0.79	1.335	38
				50	0.42	1.406	38
				60	0.40	1.443	38
				60	0.32	1.098	38
				18	0.164	0.418	38
				8	0.1	0.015	38
				9	0.1	0.019	38

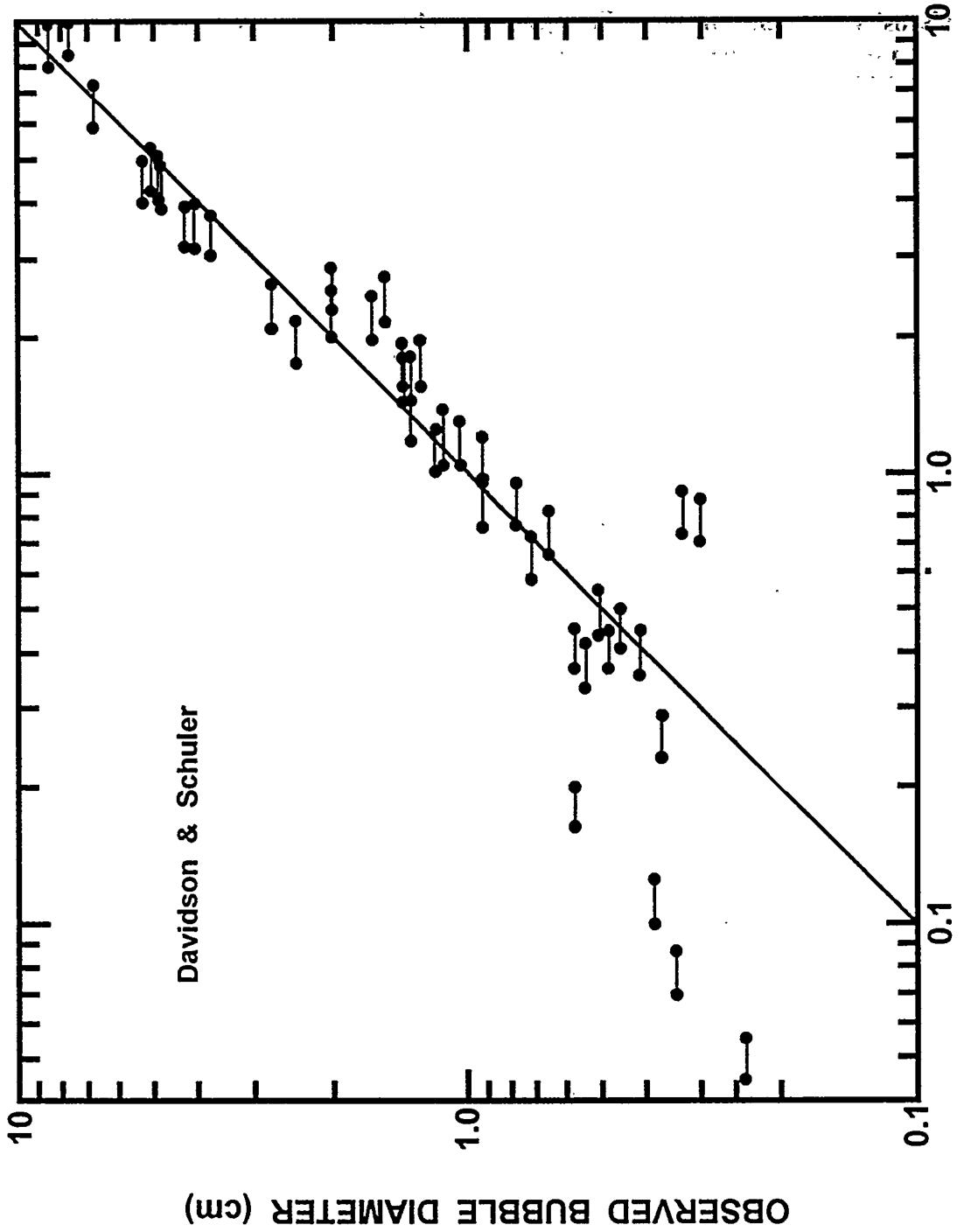

Figure 22. Comparison of observed volume equivalent spherical bubble diameter to predictions obtained with the Davidson-Schuler model with various coefficients

Though Paul et al. did experiments with bubbles supersaturated with steam (relative to the pool), they did not indicate that the above correlation was applicable to condensible gases. Besset [208] has investigated bubble formation with 373 K steam in subcooled water pools. This work was done with a 0.2-cm orifice. Some of the data she obtained are listed in Table 6. Besset found her data somewhat similar to predictions of the Davidson-Schuler model. Besset proposed a modification of this model to account for the effects of steam condensation during bubble formation:

$$V_B = \frac{1.138\ Q^{6/5}}{g^{3/5}} - \frac{2.5 \times 10^{-4}}{g\ D_o^{\,2}}\ QJa - 3D_o^{\,3}$$

where

Q = volumetric flow rate

Ja = Jakob number = $\rho_l\ C_p\ \Delta T/\rho_g\ L$,

C_p = heat capacity of water,

ΔT = $T_o - T_p$,

T_o = temperature of the vapor in the orifice,

T_p = water pool temperature, and

L = latent heat of vaporization of water.

Her data are compared to this correlation in Figure 23. Deviations from the correlation become significant when ΔT is greater than about 30 degrees Kelvin. The modified model tends to underpredict bubble sizes when the driving force for condensation is large. This may be complicated by the presence of small amounts of noncondensible gas dissolved in the water or in the steam.

Schmidt [293] has reported data on the formation of steam bubbles in subcooled water with very large driving forces for steam condensation. Some of his data is listed in Table 7. These data are not well predicted by the modified Davidson-Schuler correlation suggested by Besset. The data can be fit to a Weber number correlation similar to that suggested by Paul et al. [30], but the coefficients derived from such a fit are quite different than those found by Paul et al.:

$$V_N = 0.306\ We^{0.303}$$

The fit of the data to this correlation is shown in Figure 24. Schmidt suggested a rather different correlation for the data:

Table 6. Besset's data on steam bubble formation in subcooled water [208]

T(water) (K)	$\dot{m}$ (g/s)	$\dot{Q}$ (cm^3/s)	V(bubble) (cm^3)	f = frequency (bubbles/s)	f V (bubble) (cm^3/s)
296	0.0013	2.18	0.017 ± 0.0060	130 ± 23	2.21
296	0.0016	2.68	0.008 ± 0.0034	340 ± 167	2.72
296	0.0016	2.68	0.014 ± 0.0059	200 ± 64	2.80
296	0.00178	2.98	0.015 ± 0.0054	200 ± 64	3.00
325	0.0033	5.52	0.050 ± 0.0085	110 ± 13	5.50
325	0.0040	6.69	0.050 ± 0.014	140 ± 15	7.00
325	0.0043	7.19	0.033 ± 0.012	220 ± 31	7.26
325	0.0052	8.70	0.018 ± 0.0063	450 ± 99	8.10
339	0.0035	5.86	0.083 ± 0.008	75 ± 5	6.22
339	0.0047	7.86	0.100 ± 0.013	80 ± 7	8.00
339	0.0093	15.56	0.130 ± 0.025	120 ± 13	15.60
339	0.0098	16.40	0.096 ± 0.021	176 ± 21	16.90
347	0.0040	6.69	0.120 ± 0.011	55 ± 3	6.60
347	0.0058	9.70	0.170 ± 0.019	59 ± 6	10.03
347	0.013	21.75	0.250 ± 0.028	86 ± 9	21.50
347	0.0195	32.62	0.290 ± 0.041	115 ± 14	33.35
354	0.00058	0.97	0.040 ± 0.016	25 ± 4	1.00
354	0.0095	15.89	0.320 ± 0.045	51 ± 6	16.32
359	0.0013	2.18	0.056 ± 0.005	41 ± 2	2.30
359	0.0076	12.72	0.340 ± 0.119	39 ± 7	13.26
359	0.0092	15.39	0.410 ± 0.057	38 ± 4	15.58
359	0.0108	18.07	0.460 ± 0.138	41 ± 9	18.86
359	0.0155	25.93	0.700 ± 0.119	38 ± 10	26.60
359	0.0293	49.02	1.100 ± 0.297	46 ± 12	50.60
363	0.0022	3.68	0.098 ± 0.021	37 ± 7	3.63
363	0.0045	7.53	0.210 ± 0.010	36 ± 1	7.56
366	0.0016	2.68	0.093 ± 0.010	29 ± 3	2.70
366	0.0108	18.07	0.450 ± 0.018	41 ± 8	18.45

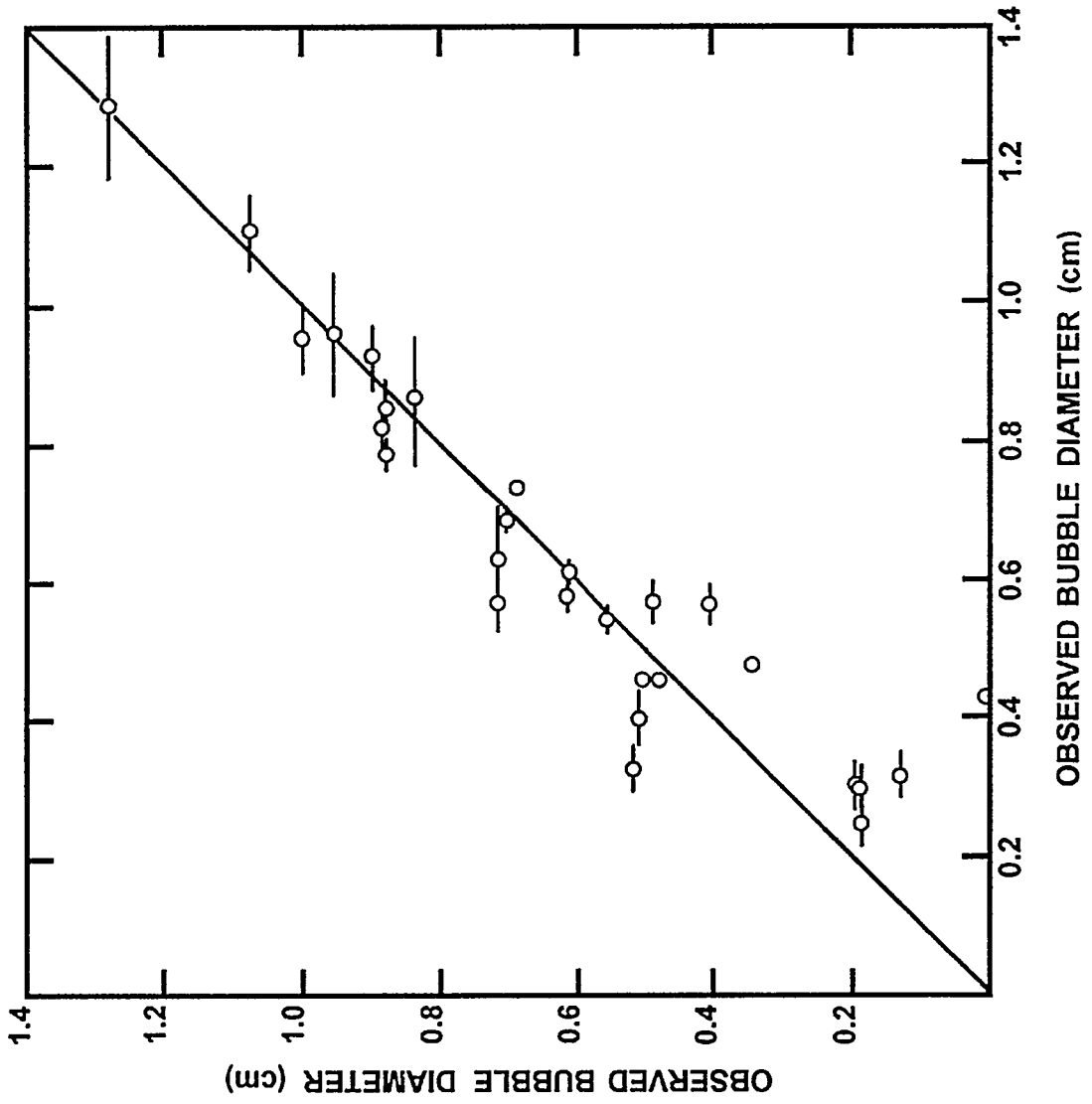

Figure 23. Comparison of Besset's bubble volume/data to the predictions of the modified Davidson-Schuler model

Table 7. Schmidt's data [293] for steam bubble formation in water

P_a (atms)	D_o (cm)	T_o-T_p (K)	$\dot{m}$ (g/s)	V_{B_3} (cm^3)	Q_3 (cm^3/s)	A_{B_2} (cm^2)
40	0.3	150	2.63	0.140	190.6	1.304
			2.74	0.151	198.5	1.371
			2.74	0.169	198.5	1.478
			4.25	0.159	308	1.419
			4.93	0.174	357	1.507
			11.5	0.248	833	1.909
			11.5	0.276	833	2.050
			16.1	0.259	1167	1.965
			16.8	0.374	1217	2.510
			19.1	0.326	1384	2.291
40	0.3	100	2.54	0.127	167	1.222
			5.00	0.149	328	1.359
			6.03	0.192	395	1.610
			8.24	0.205	540	1.681
			8.24	0.220	540	1.762
			9.56	0.262	627	1.989
			11.5	0.286	754	2.099
			13.1	0.325	859	2.286
			16.8	0.290	1102	2.119
			16.8	0.281	1102	2.075
40	0.3	200	2.63	0.154	208	1.389
			3.40	0.180	269	1.542
			6.14	0.220	485	1.762
			8.24	0.311	651	2.220
			8.24	0.294	651	2.138
			11.55	0.325	913	2.286
			11.55	0.364	913	2.465
			16.11	0.402	1273	2.634
			16.8	0.465	1329	2.903
			19.1	0.414	1510	2.686
			19.1	0.339	1518	2.351
			8.24	0.280	651	2.070
			6.14	0.205	485	1.681
80	0.3	100	3.11	0.0542	104	0.693
			5.09	0.0752	170	0.862
			8.40	0.118	283	1.163
			9.38	0.0918	313	0.984
			9.54	0.131	318	1.247
80	0.3	150	1.93	0.0612	71.9	0.751
			2.59	0.0656	96.5	0.787
			2.76	0.0682	103	0.807
			3.16	0.0656	118	0.787
			5.00	0.0856	186	0.939
			5.31	0.115	198	1.144
			6.10	0.109	227	1.104
			6.64	0.122	247	1.190
			9.36	0.129	348	1.235
			9.52	0.163	355	1.443

[a]At 40 atms, the water temperature is 524 K. Liquid surface tension is 26 dynes/cm and the liquid density is 0.7977 g/cm^3.
At 80 atms, the water temperature is 569 K. The liquid surface tension is 15.2 dynes/cm and the liquid density is 0.7206 g/cm^3.

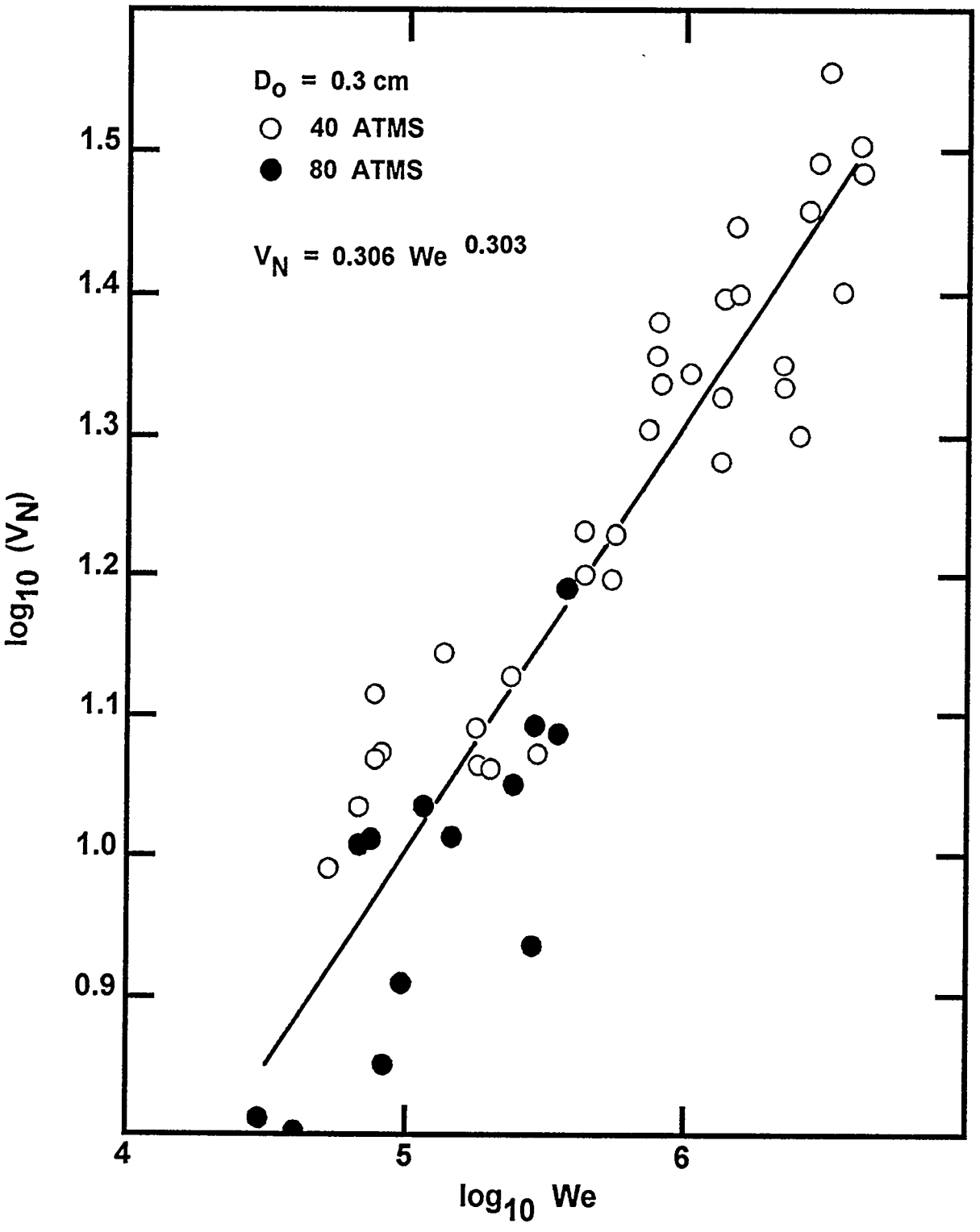

Figure 24. Fit of Schmidt's bubble volume data to a correlation in terms of the Weber number

$$A_B = 1.913 \times 10^{-3} D_o^2 f^{1/3}$$

where

A_B = bubble surface area, and

$$f = (\dot{m})^{1.35} [C_p(T_o-T_p)/P]^{2.675} \sigma_l^2 D_o^{-2.35} g \mu_l^{3.35}$$

Note that f is dimensionless so some care must be taken in the selection of units for the heat capacity and the pressure.

2. Models of Bubble Formation

The modeling of bubble formation at an orifice has received a great deal of attention. Available models can be categorized as:

a. Single-stage models

b. Two-stage models

c. Numerical models

Some of the many examples of these various models are discussed below.

a. The Davidson-Schuler Single-Stage Model

The quintessential example of a single-stage model is that developed by Davidson and Schuler [32]. The volume of the bubble at the time it detaches from the orifice is given in this model by:

$$V_B = \frac{\pi D_B^3}{6} = \frac{C\,Q^{6/5}}{g^{3/5}}$$

where C is a constant and Q is the volumetric flow rate into the bubble. The original model, developed for constant flow conditions, used C = 1.378. Empirical correlation of data yields C = 1.722 [33]. Kumar and Kaloor [31] have shown that a simplification of a two-stage model yields C = 0.976. An alternative derivation by Davidson and Harrison [34] yields C = 1.138. A critical step in the derivation of the model is the specification of the volume of water that is "attached" to the bubble. It is assumed that this water volume is proportional to the volume of the bubble. The proportionality constant is often taken to be 11/16. But, values as low as 1/2 have been used. The selection of the proportionality constant will affect the value of C in the Davidson-Schuler model.

The Davidson-Schuler model has been compared to data for noncondensible gases above (see Figure 22). The derivation of the model does not include treatment of condensation of the gas within the forming bubble. As noted above, when the driving force for steam condensation is not too large,

observed bubble volumes agree rather well with the Davidson-Schuler model predictions especially if the uncertainty in the multiplicative coefficient C is recognized.

b. Two-stage Bubble Formation Models

Two-stage bubble formation models make a distinction between the initial growth of a bubble, which is assumed spherical, and growth once the zone of attachment between the bubble and the orifice begins to "neck down." The model suggested by Kumar and Kaloor for constant flow conditions is [31]:

$$V_1^{5/3} = \frac{0.04739\ Q^2}{g} + \frac{2.418\ \mu_l Q V_1^{1/3}}{\rho_l g} + \frac{\pi D_o \sigma_l\ V_1^{2/3} \cos\theta}{\rho_l\ g}$$

$$r_1 \cos\theta + 0.5 D_o \sin\theta = \frac{B\left(V_B^{\ 2} - V_1^{\ 2}\right)}{2Q(A+1)} - \frac{C(V_B - V_1)}{AQ} - \frac{3D\left(V_B^{\ 2/3} - V_1^{\ 2/3}\right)}{2Q(A-1/3)}$$

where:

V_B = final bubble volume

V_1 = bubble volume at the end of the first growth stage

$r_1 = (3V_1/4\pi)^{1/3}$

$A = 1 + 14.6167\ V_1^{1/3}\ \mu_l\ /\ Q(\rho_g + 11\rho_l/16)$

$B = (\rho_l - \rho_g)\ g\ /\ Q\ (\rho_g + 11\rho_l/16)$

$C = \pi D_o\ \sigma_l \cos\theta\ /\ Q\ (\rho_g + 11\rho_l/16)$

$D = 2.418\ \mu_l\ /\ (\rho_g + 11\rho_l/16)$

and θ is the angle describing the orientation of the orifice. When $\theta = 0$, the orifice is horizontal with its axis pointing upward. When $\theta = 90°$, the orifice is vertical with its axis horizontal. The physical descriptions of bubble behavior that are the basis of the Kumar and Kaloor model are questionable for $\theta > 60°$ and inappropriate for $\theta > 90°$.

As the volume behind the orifice becomes very large, it becomes better to consider bubble formation to occur at constant pressure rather than at constant flow. Kumar and Kaloor's model for bubble formation at constant pressure is [31]:

$$V_1(\rho_l - \rho_g)g = \left\{\frac{0.2068\ K^2\ (\rho_g + 11\rho_l/16)}{V_1^{2/3}}\right\}\left\{P + 0.6204\rho_l g V_1^{1/3} - \frac{3.224\sigma_l}{V_1^{2/3}}\right\}$$

$$- \left\{\frac{0.055556\ K^2\ (\rho_g + 11\rho_l/16)}{V_1}\right\}\left\{2.4814\ PV_1^{1/3} - 1.1545\rho_l g V_1^{2/3} - 10\sigma_l\right\}$$

$$+ \frac{2.418\ K\mu_l}{V_1^{2/3}}\left[P + 0.6204\rho_l g\ V_1^{1/3} - \frac{3.224\sigma_l}{V_1^{1/3}}\right]^{1/2} + \pi D_o \sigma_l \cos(\theta)$$

and

$$r_1 \cos\theta + 0.5 D_o \sin\theta = \frac{B(V_B^2 - V_1^2)}{2Q(A+1)} - \frac{C(V_B - V_1)}{AQ} - \frac{3D\ (V_B^{2/3} - V_1^{2/3}}{2Q\ (A - 1/3)}$$

where K is a constant peculiar to the system. When multiple orifices are connected to the chamber volume, it is not immediately obvious whether the constant pressure or the constant flow models should be applied. Typically, analysts seem to have divided the chamber volume by the number of orifices and have used the resulting quotient to adjudicate the appropriate model to use. Such an analysis suggests that quenchers would be properly treated as they yielded bubbles formed under constant flow conditions.

The predictions of bubble diameter for noncondensible gases discharged into water obtained from the Kumar and Kaloor model are compared to data (Table 5) in Figure 25. It is clear from the comparison in this figure that the Kumar and Kaloor model is a much better predictor of the data than either the Davidson and Schuler model (see Figure 22) or the correlation developed by Paul et al. (see Figure 21). The Kumar and Kaloor model predicts well data obtained for small orifices at low flow rates which are not predicted well by the other model and correlation.

Ruff [35] has made empirical modifications to the Kumar and Kaloor model. His modified model is:

$$V_B = V_B^*\ Q^{6/5}\ g^{-3/5}$$

$$V_B^* = V^* + \Delta V^*$$

$$V^* = \frac{0.0578}{(V^*)^{2/3}} + \frac{2.417\ \mu^*}{(V^*)^{1/3}} + 0.204\sqrt{\frac{\mu^*}{V^*}} + \pi(D_o\sigma_l)^*$$

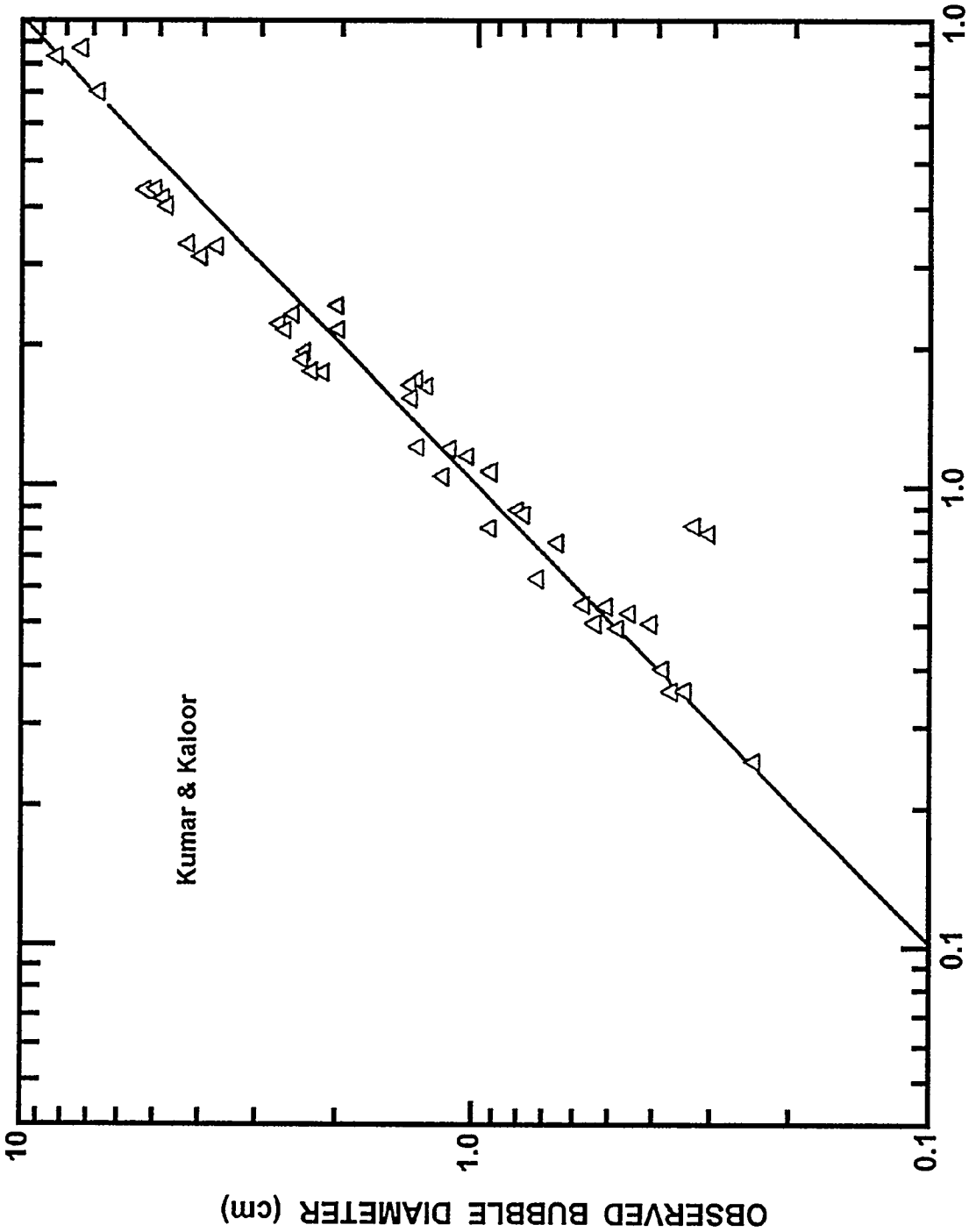

Figure 25. Comparison of observed volume equivalent spherical bubble diameters to those predicted with the model of Kumar and Kaloor

$$\Delta V^* = 1 + 4(\mu^*)^{3/4}$$

where

$$\mu^* = \mu_1/\rho_1 \, g^{1/5} \, Q^{3/5}$$

$$(D_o \, \sigma_1)^* = D_o \, \sigma_1/g^{2/5} \, Q^{6/5} \, \rho_1$$

Ruff's empirical corrections modestly improve the prediction of data as is shown in Figure 26.

The variation in the bubble diameter with orifice orientation predicted with the Kumar and Kaloor model is shown in Figure 27 for air injected into water through a 1.27-cm orifice. Also shown in Figure 27 is the bubble diameter that would be predicted with Ruff's empirically modified model for a horizontal orifice ($\theta = 0$) and the range of bubble diameters that would be predicted with the Davidson-Schuler model. The prediction obtained with the correlation developed by Paul et al. [30] is off the scale of this figure. The Kumar and Kaloor model predicts that bubble diameter increases with increasing orifice angle to a broad maximum centered at about 37°. The bubble diameter decreases noticeably with increasing orifice angle for angles greater than about 45°. The range of variation is, however, not large in comparison to the scatter in data about the model predictions for horizontal orifices (see Figure 25).

The two-stage models of bubble formation seem to be superior to the single-stage model or the empirical correlation by Paul et al. The superiority is revealed, however, by comparisons to data for orifices much smaller than those encountered in steam suppression pools. It might, then, be argued that the superiority is irrelevant. All of the models and the correlation do equivalently well predicting data for orifices that are about 1 cm in diameter. The problem is, however, that the available data do not really span the entire regime of interest for the analysis of aerosol removal by suppression pools during severe reactor accidents. Since extrapolations will be necessary, the physically-based model developed by Kumar and Kaloor is quite attractive. Extrapolations can be done with more confidence since the model does account for so much data.

Attractive as they are, the Kumar and Kaloor model or the empirical modification by Ruff do not account for condensation of water vapor during bubble formation. Perhaps the simplest modification to account for condensation is to correct the volume flow of gas through the orifice for steam condensation. The rate limitation for steam condensation is the convective removal of heat from the bubble by the suppression pool water. Detailed calculation of the rate of heat removal by water during the growth of a bubble would be a challenging undertaking. This also might be substantially more detailed than the available data on bubble formation. A simpler approach is to estimate an average heat transfer over the period of bubble formation. Then, the corrected volume flow of gas to form the bubble is given by:

$$Q' = Q - \frac{\overline{Ah}}{L} (T_B - T_W) \frac{RT_B}{P}$$

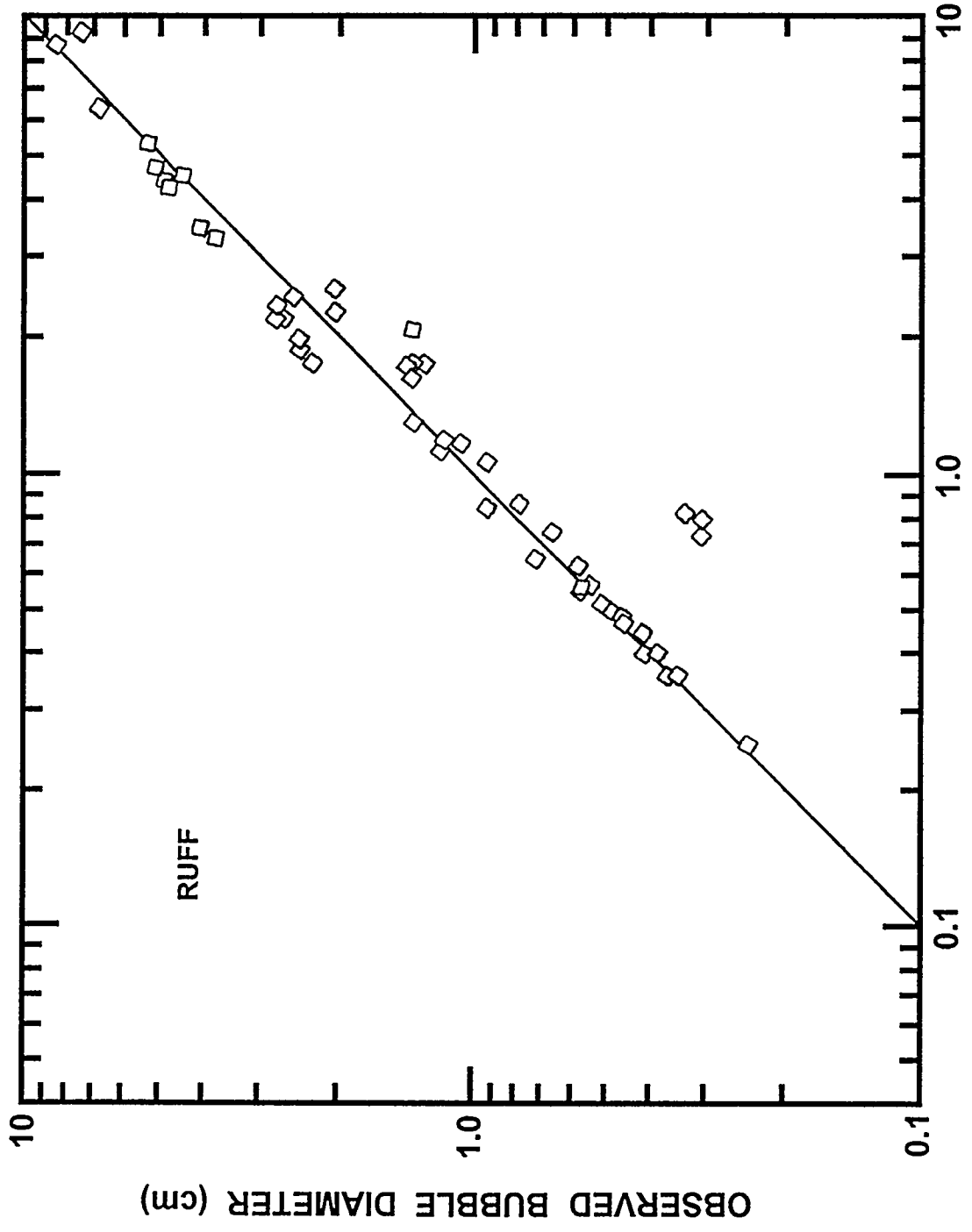

Figure 26. Comparison of observed volume equivalent spherical bubble diameters to those predicted by Ruff's empirically modified model

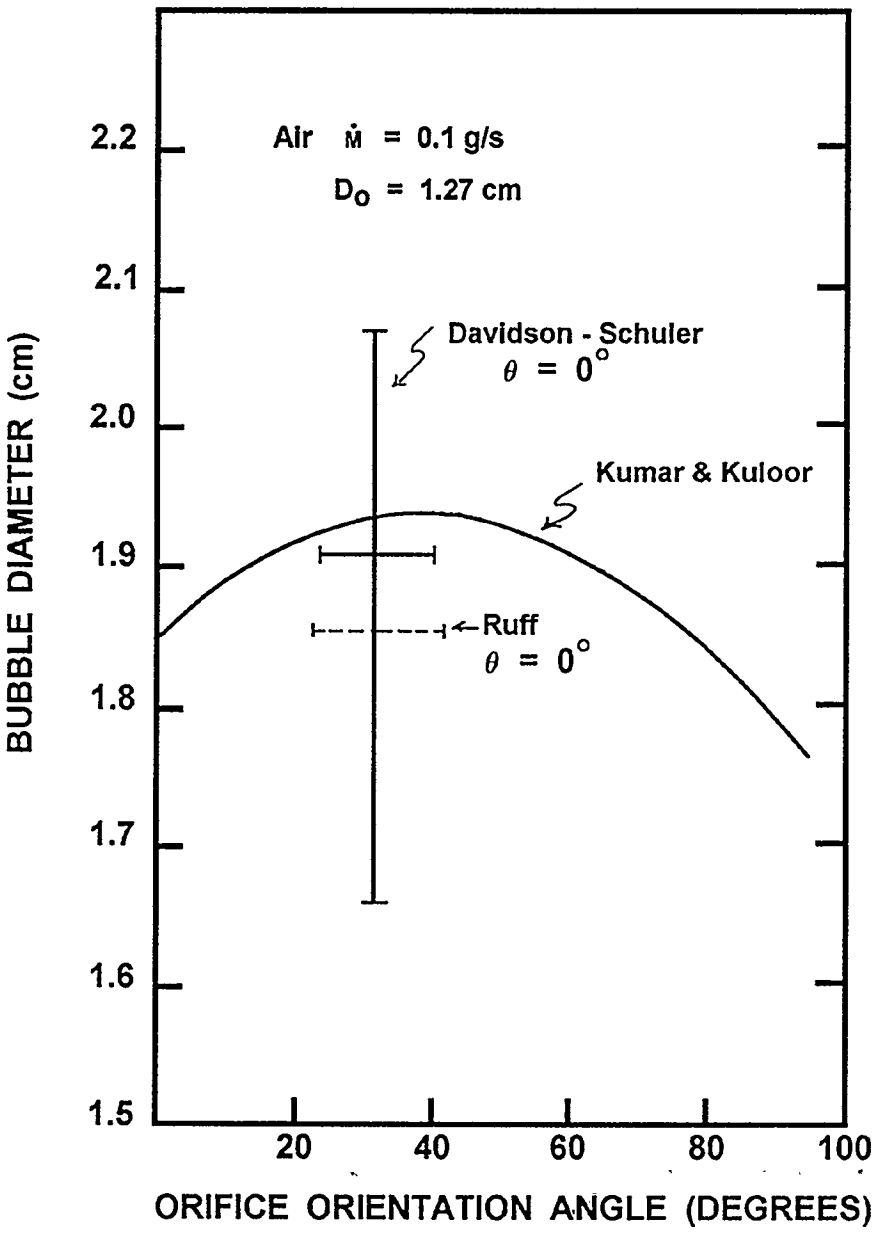

Figure 27. Variation in the bubble diameter with orifice orientation predicted with the Kumar and Kaloor model

where

Q' = volume flow corrected for the effect of condensation,

Q = measured volume flow

$\overline{Ah}$ = average product of bubble area and the heat transfer coefficient,

T_B = saturation temperature in the bubble gas,

T_W = bulk water temperature, and

P = pressure in the bubble.

Similar averaging formulations have been found useful for the estimation of mass transport during bubble formation [82].

Under most conditions hypothesized to develop in steam suppression pools during reactor accidents, the driving force for steam condensation, $T_B - T_W$, is not expected to be large. Certainly, it is not expected to be as large as the driving force for steam condensation in Schmidt's experiments [72]. Data obtained by Besset [208] involve conditions more nearly like those expected to exist during bubble formation in a steam suppression pool. Consequently, the Ruff model with the simple average correction for the effects of steam condensation was fit to Besset's data. It was found that a decidedly better fit could be obtained by allowing the heat transfer coefficient to be proportional to the steam flow rate:

$$\overline{Ah} = \xi Q$$

The value of the proportionality constant derived from the fit is:

$$\xi = 4.24 \times 10^{-3} \text{ cal/cm}^3\text{-K}$$

Predicted and observed bubble diameters are compared in Figure 28. The simple correction for the effects of condensation tends to overpredict bubble sizes for $T_B - T_W < 50$ K. For larger condensation driving forces, the simple model under-predicts bubble size. The differences between predictions and observations are, however, not large.

c. Numerical Models

In recent years, detailed numerical models of bubble formation at submerged orifices have become more popular than derivation of approximate analytic expressions. The numerical models are able to account for the nonspherical nature of bubbles and other complexities such as flows in the liquid phase. The numerical modeling of bubble formation was, apparently, pioneered by Kupferberg [258]. Since this original work, the method has been developed substantially [207, 259-264]. Recent models are able to show the "necking" of bubbles (that leads to detachment) is a natural consequence of the governing equations [262].

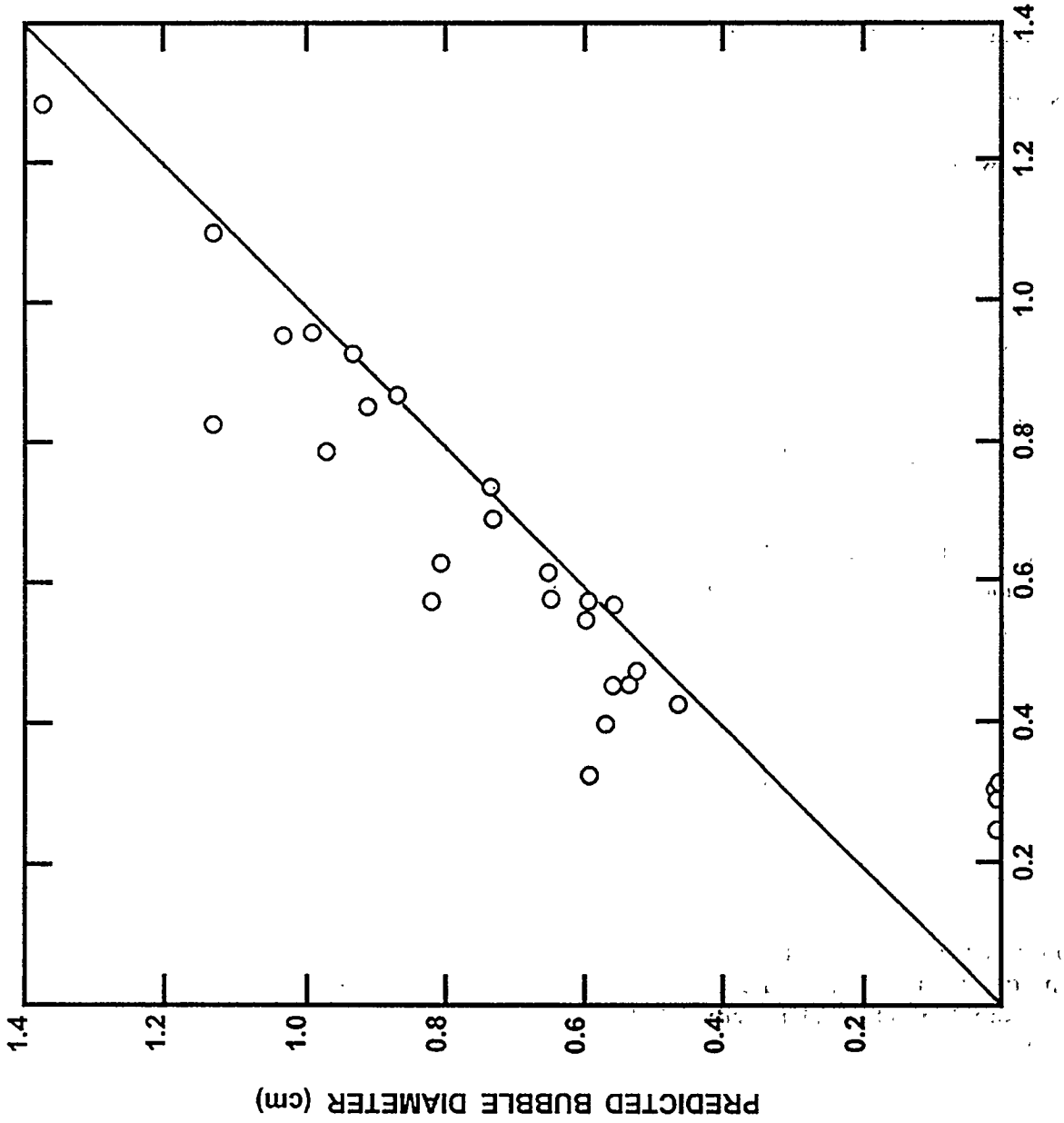

Figure 28. Comparison of the diameters of steam bubbles forming in subcooled water observed by Besset [208] to predicted diameters obtained using Ruff's model corrected for the effects of condensation

Most of the very detailed, numerical simulations of bubble growth have not considered condensation. In any event, the models are far more detailed than can be used or is needed for this work. Though this topic will be pursued further in connection with aerosol trapping, it is not discussed further here.

3. Bubble Formation at Downcomers

The regimes of bubble formation at downcomers have been studied primarily in connection with investigations of steam suppression pool behavior during design-basis accidents. Lee and Chan [40] have reviewed some of this literature. Based on small-scale experiments with a 5.08-cm-diameter downcomer, they produced the flow regime map shown in Figure 29. This work was done for higher mass flows than would be expected for the ex-vessel phases of severe accidents. Also, the vapor of interest in design basis studies is nearly all steam and does not contain the substantial fraction of noncondensible gases (nitrogen, hydrogen, carbon dioxide and carbon monoxide) that would be expected to be present in gases passing through downcomers in a severe accident. The disparities between flow rates and gas compositions in severe accidents versus flow rates and gas compositions in design basis accidents, make it difficult to believe the precise boundaries between regimes found by Lee and Chan are applicable to severe accident source term attenuation that is of interest here. Further doubt on the absolute applicability of the Lee and Chan results is raised by the issues of scaling the findings from tests with a 5-cm diameter vent to full-size vents and downcomers that have diameters of about 60 cm. Certainly, the regime that Lee and Chan indicate will allow steam to escape their small scale pool cannot be extrapolated to actual suppression pools in which the downcomer is more deeply submerged. The qualitative features of flow through a downcomer observed by Lee and Chan may be applicable to issues of severe accidents if allowances are made for the presence of noncondensible gases.

At very low flows, Lee and Chan observed no bubble formation. Steam simply condensed within the piping system. An interface with the liquid in the pipe was maintained. Were substantial amounts of noncondensible gas present, bubbles would form in the downcomer at least episodically. Nevertheless, the important observation that at low flows substantial condensation can take place within the downcomer has a bearing on aerosol removal. Condensation of vapor would sweep out aerosol particles (diffusiophoretic deposition). Temperature gradients within the gas phase could also cause some decontamination (thermophoretic deposition).

Lee and Chan [40] clearly felt most of the vapor condensation took place on the submerged walls of the downcomer. The interface between the liquid and the gas phase within the downcomer was assumed to be quickly steam-saturated. Other theoretical analyses of downcomer performance have considered mechanisms by which condensation at the interface could be important [41].

The focus of studies by Lee and Chan was on "chugging" in the downcomer. Chugging occurs when condensation of steam proceeds more rapidly than supply. A partial vacuum is created and water is pulled up into the downcomer until the rate of condensation falls below the rate of supply of steam. At low flow rates of steam, the chugging phenomenon occurs entirely within the downcomer. A schematic illustration of liquid behavior in such an internal chugging event observed by Lee and Chan is shown in Figure 30. Of course, with substantial amounts of noncondensible gas present, chugging could not be confined entirely to within the downcomer even at very low flows.

With increases in mass flow and decreases in the water pool subcooling, Lee and Chan observed chugging phenomena outside the downcomer. Schematic illustrations of gas behavior in chugging with

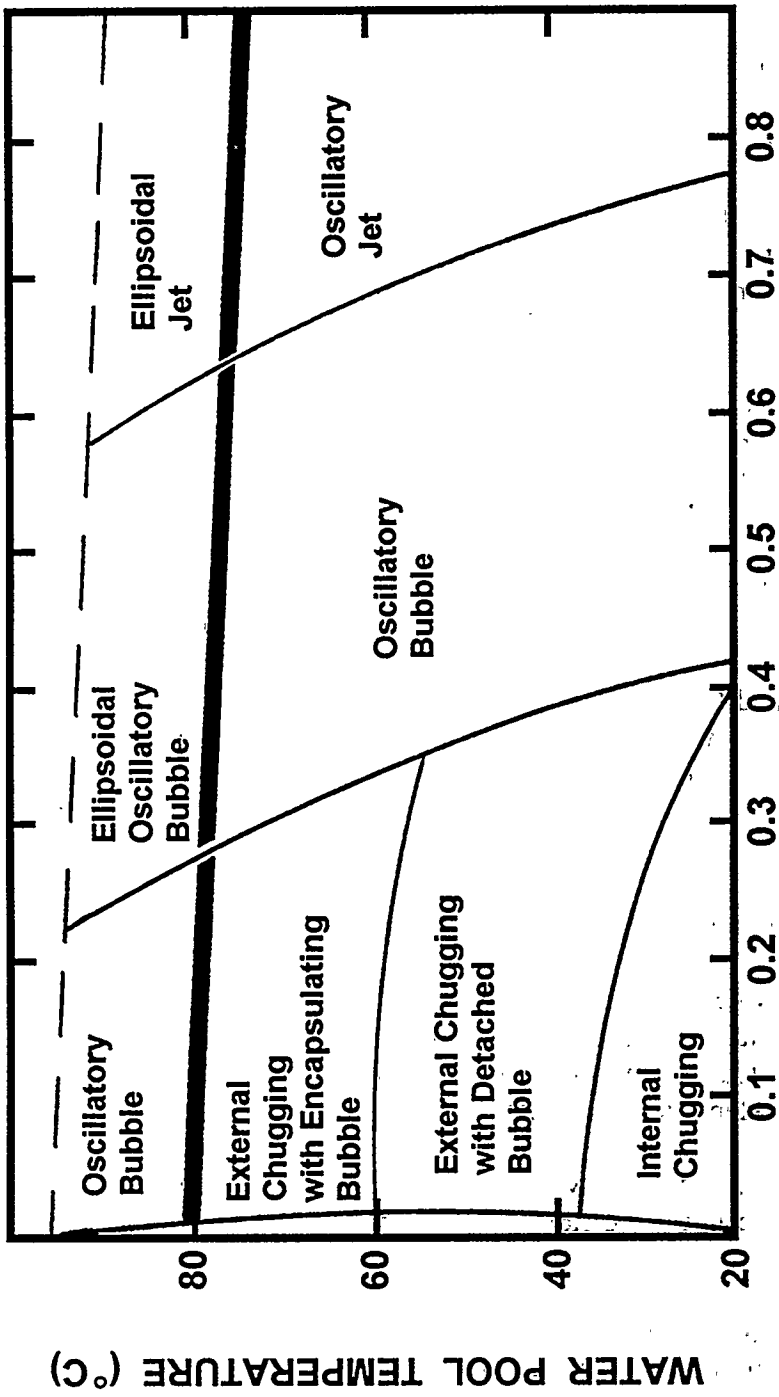

Figure 29. Flow regime map developed from results of studies with a small-scale model of a suppression pool downcomer

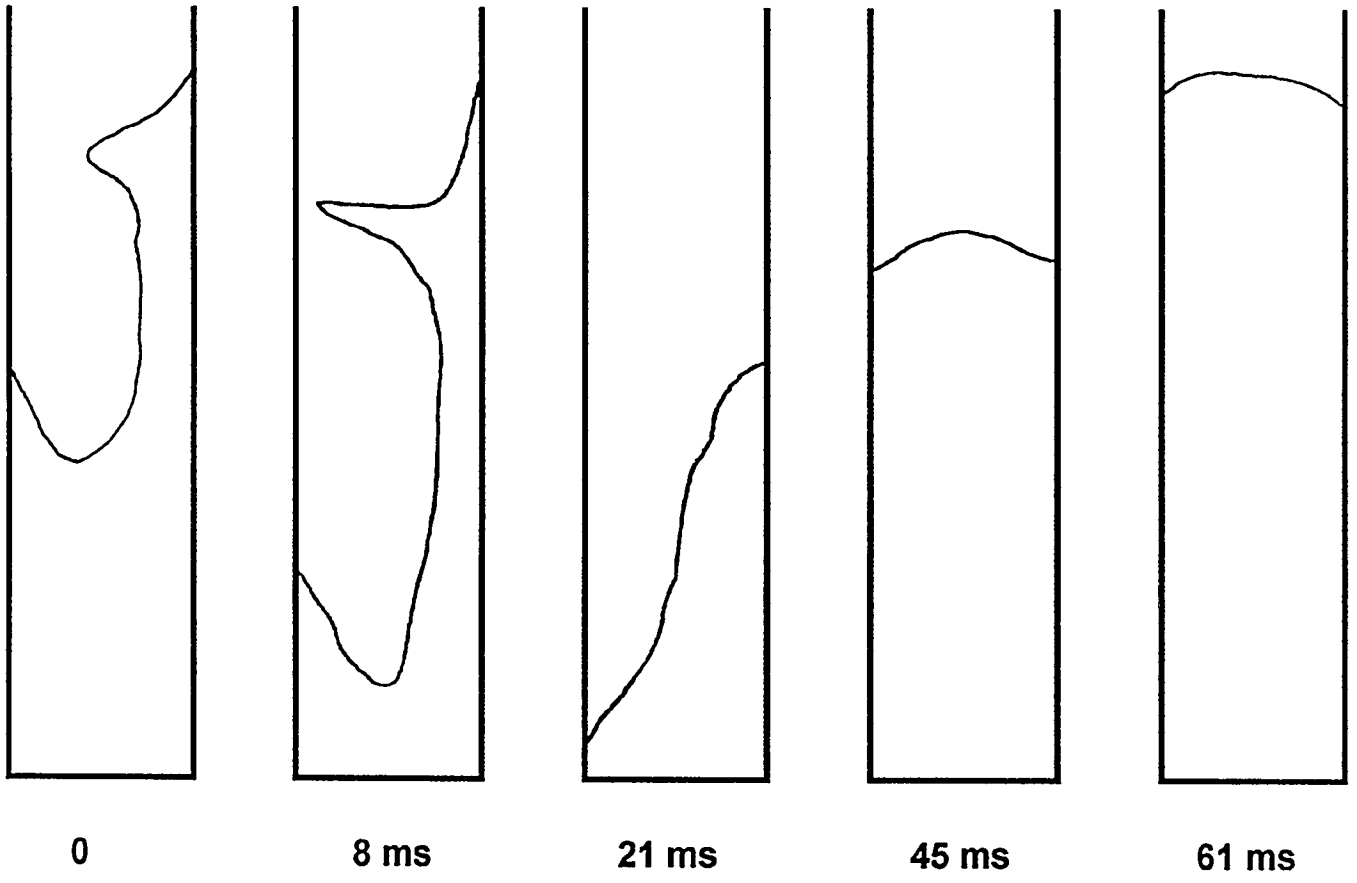

Figure 30. Internal "chug" observed in tests by Lee and Chan [40]

bubble detachment and without bubble detachment are shown in Figures 31 and 32. In the case of chugging without bubble detachment, a vapor volume rose up around the downcomer.
Finally, Lee and Chan did not observe chugging at low levels of subcooling. Instead, vapor permanently extended to the end of the downcomer. Bubbles would detach and rise up around the downcomer.

Detached bubbles were observed to collapse and disintegrate as they rose through the subcooled water pool. Lee and Chan describe the collapse as beginning in a smooth fashion. As collapse progressed, indentations and evidence of instability appeared on the surface of the bubble. The appearance of irregularity in the bubble surface marked the beginning of bubble disintegration.

The qualitative observations made by Lee and Chan indicate that there are two classes of bubble behavior in the case of downcomers. In some cases, bubbles detach from the orifice and disintegrate. This case is not greatly different than the situation considered for bubbles forming at orifices on quenchers. The second class of bubble behavior does not involve detachment of the bubble. Instead, the bubble envelops the downcomer and rises up around it before disintegrating. This is called the "encapsulating bubble" case.

One would expect that there is some effect of the downcomer on the bubble swarm produced by bubble disintegration. It may be that bubbles rising near the downcomer behave differently than bubbles rising in the bulk suppression pool. Entrainment of liquid by the rising swarm to form a plume (see below) must be affected. This issue is not pursued further here aside from acknowledging it as an uncertainty that might affect predictions of aerosol behavior in the bubbles.

Lee and Chan do not provide much detail concerning bubbles expelled from the downcomer. They consider the bubble volume to be approximately:

$$V_B = \frac{\pi}{6} D^3$$

where D is the diameter of the downcomer.

The SPARC model [6] uses a Weber number correlation developed from data obtained at the Battelle Columbus Laboratory [42] to describe the bubbles formed by a downcomer:

$$\left[\frac{V_B}{\pi D^2/4}\right] \frac{(\rho_l - \rho_g)^{1/2} g^{1/2}}{\sigma_l^{1/2}} = 0.0891\ We^{0.616}$$

where

$$We = U_o^2\, \rho_l\, D_p / \sigma_l$$

D_p = downcomer diameter

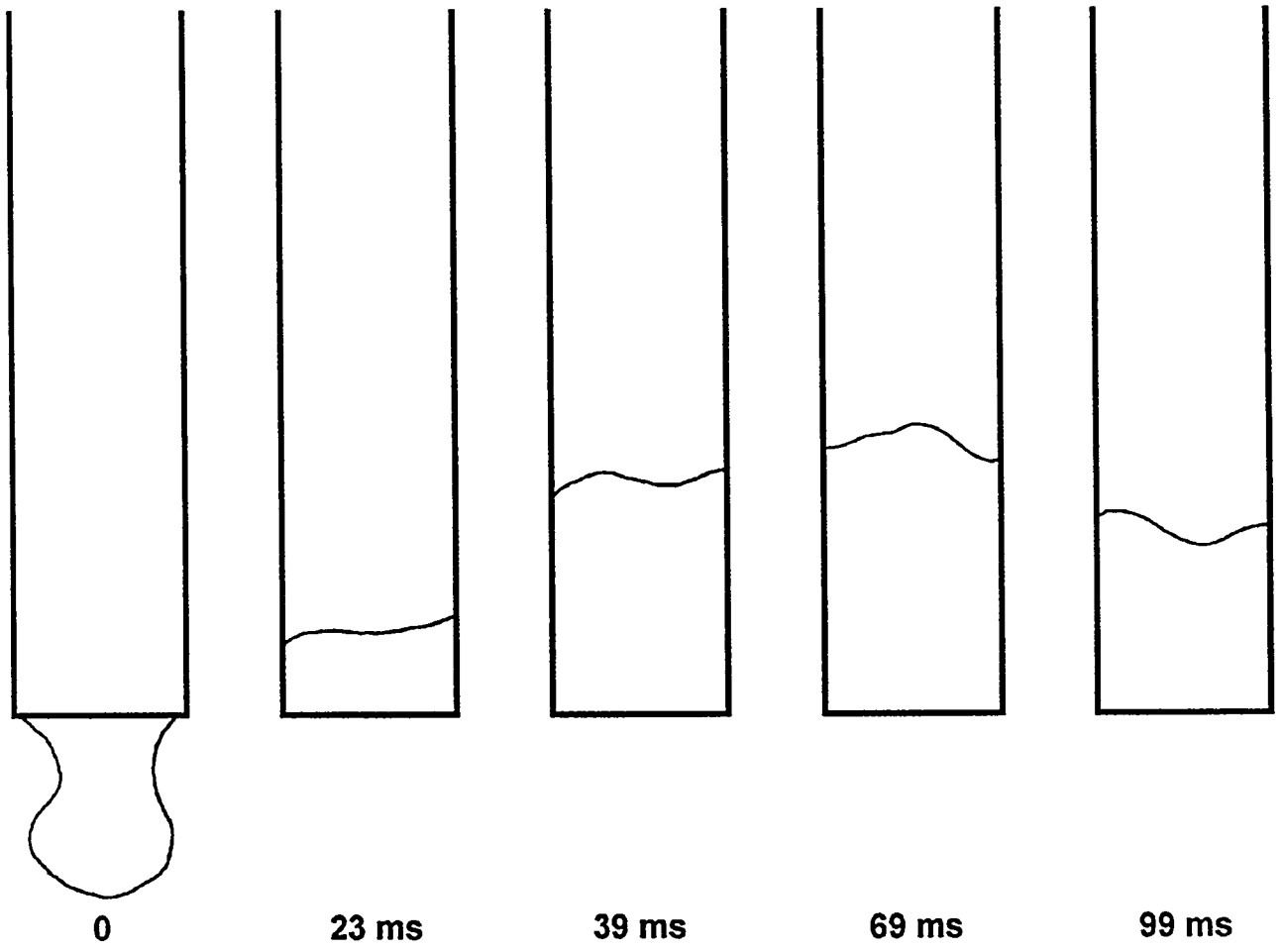

Figure 31. "Chugging" with bubble detachment observed in tests by Lee and Chan [40]

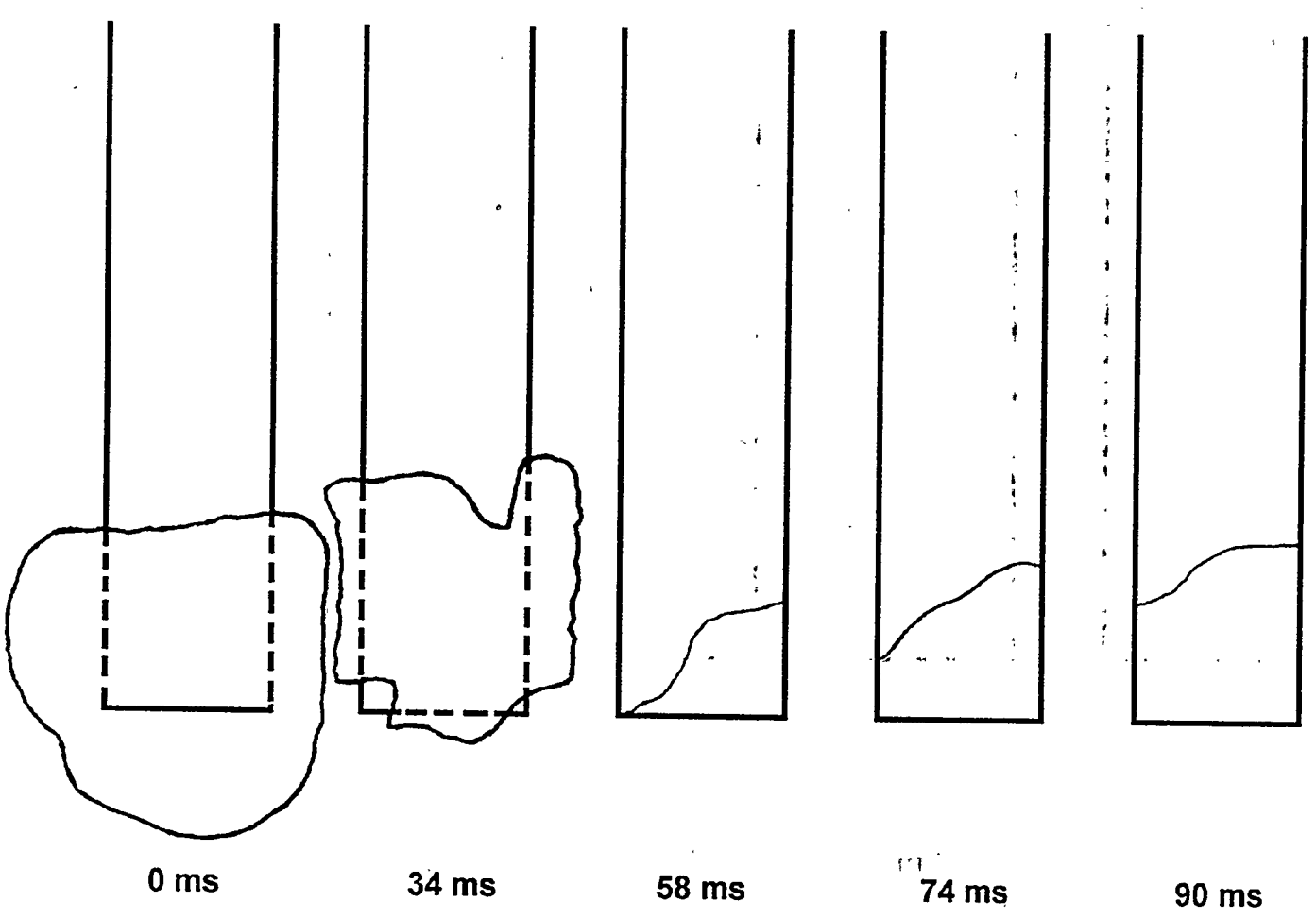

Figure 32. "Chugging" without bubble detachment observed in tests by Lee and Chan [40]

The BUSCA model [9] uses a correlation of data [38] suggested by Paul et al. [30]:

$$V_B(mm^3) = 0.0505[U_o(mm/s)]^{0.95}\ [D_p(mm)]^{2.38}$$

Wraith [214] has developed a description of bubble formation at downward facing nozzles at the same level of approximation as the Davidson-Schuler model of bubble formation at upward facing nozzles. This description yields:

$$D_B(cm) = 0.327\ Q(cm^3/s)^{0.4}$$

Tsuge et al. [215] have described a two-stage model of bubble formation at a downward facing nozzle. They provide differential equations for the "expansion phase" and the detachment" phase of bubble formation. For constant flow the bubble volume change with time is given by:

$$\frac{d\ V_B(1)}{dt} = \frac{d\ (4/3)\pi r^3}{dt} = Q$$

where Q is the volumetric flow rate of gas. The expansion phase ends when

$$\rho_l g\left[(4/3)\pi r^3 - \pi D^2(o)r/2\right] = 0.5C_D\ \rho_l\ \pi r^2\ \left[\frac{dr}{dt}\right]^2 + \frac{d}{dt}\left[(2/3)\pi r^3 \rho_l\ \frac{dr}{dt}\right] + 4\rho_g\ Q^2/\pi D(i)^2 + \pi D(i)\sigma_l$$

where

D(o) = outer diameter of the downcomer,

C_D = drag coefficient, and

D(i) = inner diameter of the downcomer.

The expansion phase is characterized by:

$$Q = \frac{d}{dt}\left[4\pi r^3/3 - \pi D^2(o)\ (r + x)/4\right] = \frac{d\ V_B(3)}{dt}$$

and

$$\frac{d\ 0.5\ V_B(3)\rho_l}{dt} = \rho_l\ V_B(3)g - 0.5C_D\rho_l\pi r^2\left[\frac{dx}{dt}\right]^2 - 4\rho_g\ Q^2/\pi D^2(i) - \pi D(i)\sigma_l$$

where x is the location of the bubble center relative to the opening of the downcomer. The bubble is taken to detach from the downcomer when x = r. The detached bubble volume is:

$$4\pi r^3/3 - \pi D(o)^2 r/2 = V_B$$

and

$$D_B = \left[\frac{6\ V_B}{\pi}\right]^{1/3}$$

Tsuge et al. show good agreement between model predictions and bubble diameters for high gas flow through downcomers with inner diameters of 1 cm and less. At lower gas flows, the model somewhat overpredicts bubble size.

The model developed by Tsug et al. has been used here to calculate bubble volumes for flow Weber numbers of 1×10^{-5} to 3.6×10^{4} for a 60 cm diameter downcomer submerged to a depth of 400 cm. The predicted volume-equivalent spherical bubble diameters varied from 73.5 to 75 cm over this flow range! The essentially constant bubble diameter predicted with the model is not sensitive to any significant extent to the submergence of the downcomer.

Predictions of the various models are compared in Figure 33. Predictions derived from the correlations of small bubble sizes at low flow rates are certainly at odds with predictions of the two-stage model developed by Tsuge et al. [215] and do not seem physically reasonable.

Another qualitative observation made by Lee and Chan [40] is that substantial heat transfer from the gas phase takes place within the downcomer itself. Thermal gradients as well as steam condensation taking place within the downcomer could be important mechanisms for the removal of aerosols from the gas phase. Lee and Chan seem to feel that most of the heat transfer is to the submerged walls of the downcomer. They argue that the water interface with gas in the downcomer quickly becomes steam saturated and does not provide an important heat sink until the bubble forms. Lee and Chan take the heat transfer coefficient to be:

$$h = 15.8 \left[\frac{g\rho_w^2\ \Delta H_{fg}\ H^3}{\mu_l\ k_l\ (T_s - T_p)}\right]^{1/4} \frac{k_g}{D_p\ \mu_g\ \rho_g}$$

where

h = heat transfer coefficient,

T_s = saturation temperature of the gas,

T_p = bulk water temperature,

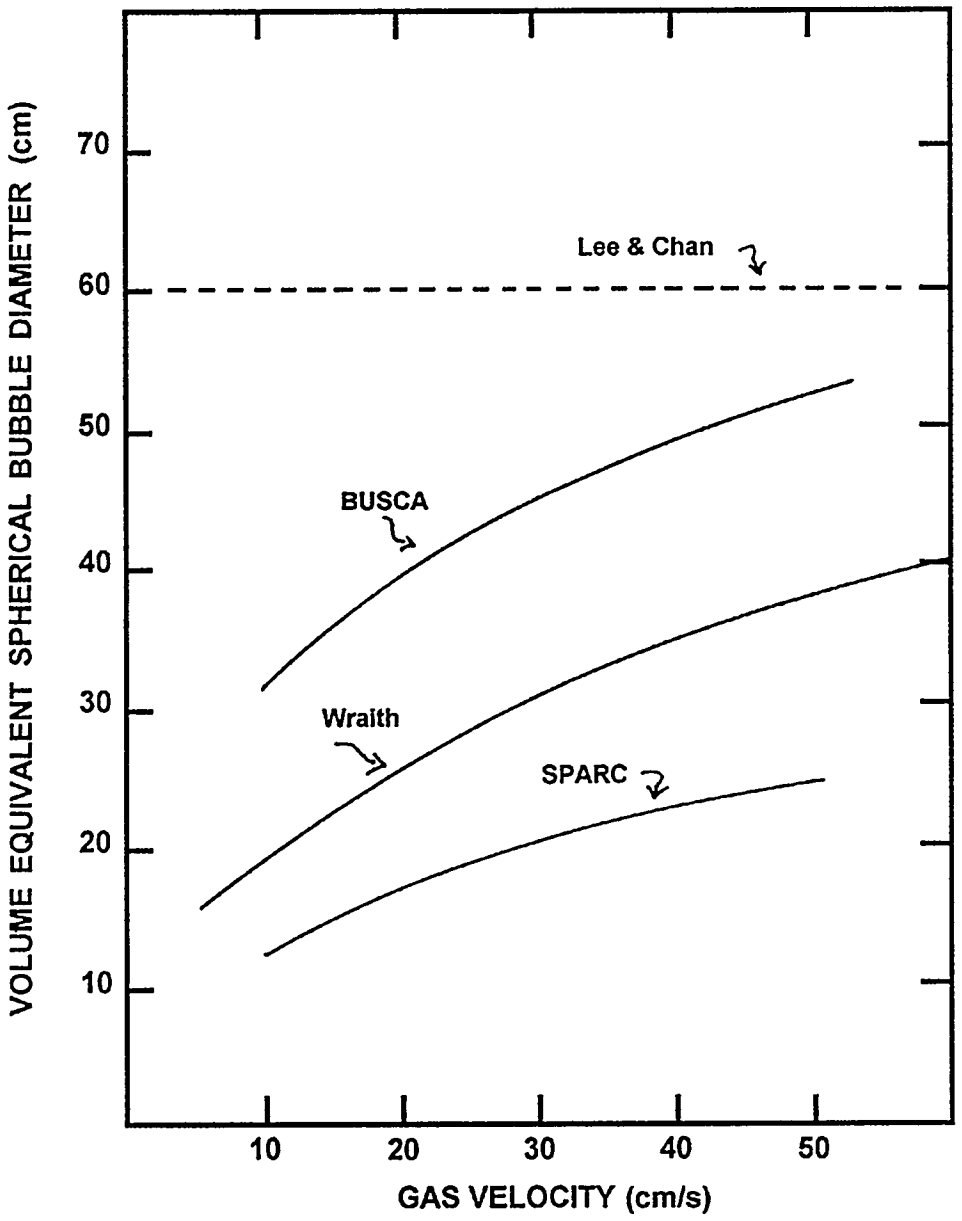

Figure 33. Comparison of various model predictions of the initial size of bubbles formed at a 60-cm-diameter downcomer

ρ_w = density of water,

ρ_g = gas density,

ΔH_{fg} = latent heat of condensation per unit mass of steam,

k_l = thermal conductivity of the liquid,

k_g = thermal conductivity of the gas,

μ_l = viscosity of the liquid,

μ_g = viscosity of the gas, and

H = submergence length of the downcomer.

This expression, of course, defines a laminar, liquid film, heat transfer coefficient. Lee and Chan acknowledge that this is, at best, a very approximate model of the actual heat transfer taking place in the downcomer. Interestingly, the CHUG1 computer code [43] sets this wall heat transfer coefficient to zero.

Kowalchuk and Sonin [41], on the other hand, focused on heat transfer from the gas to the liquid interface in the downcomers. They considered that the rate of vapor condensation could be limited by:

- the supply of vapor, or
- turbulent thermal diffusion in the water

The mass rate of steam condensation was estimated to be:

$$\dot{m}_c = \frac{St\rho_w C_w \overline{V} (T_s - T_p)}{\Delta H_{fg} \left[1 + \frac{\pi St^2}{\beta} \frac{\overline{V}t}{D_p}\right]^{1/2}}$$

where

C_w = heat capacity of water,

$\overline{V}$ = average speed at which water, rises and falls within the downcomer,

St = Stanton number taken to be about 0.1, and

β = uncertain turbulence parameter taken to have values between 0.01 and 0.015.

The conclusion that can be derived from this expression is that heat transfer and condensation will occur in the downcomers. Quantitative details about the heat transfer are not at all certain. Condensation and heat transfer within the downcomers could be responsible for significant aerosol removal from the gas phase. But, the topic of aerosol removal within the piping system is outside the scope of this work and will be neglected here. The risk in neglecting the mass removal from the gas phase during passage through the downcomers is that the size distribution of aerosols that reach the pool might be altered. As will be discussed at length below, aerosol trapping from bubbles in a suppression pool is very dependent on the aerosol particle size.

4. Bubble Formation at Horizontal Vents

The SPARC code [6] incorporates a Weber number correlation derived from experimental data [42] to predict the initial volumes of bubbles formed at horizontal vents:

$$\frac{4V_B}{\pi D_p^2} \frac{(\rho_l-\rho_g)^{1/2}\, g^{1/2}}{\sigma_l^{1/2}} = 0.857\ We^{0.73}$$

where D_p is the diameter of the vent. The BUSCA code [9] employs the dimensional correlation suggested by Paul et al. [30] for bubble volumes from horizontal vents:

$$V_B(mm^3) = 0.0429\ [U_o(mm/s)]^{0.92}\ [D_p(mm)]^{2.46}$$

Presumably, the angle-dependent orifice model developed by Kumar and Kaloor (see Section IV-A2, above) could also be used. Horizontal vent diameters of interest here (~72 cm) are, of course, very much larger than what was in mind when this model was developed.

Comparison of the predictions of these models are shown in Figure 34. Predictions of the various models diverge with increasing gas velocity. Interestingly, the Davidson-Schuler model predicts results within the range of predictions by the other models.

The essential difficulty with large diameter horizontal vents to the suppression pool is that at lower gas generation rates, water is not expelled completely from the vent during bubble formation. Consequently, for most accident situation, the orifice is not circular and the "effective diameter" of the orifice is not equal to the geometric diameter of the vent. Fischer and Hafner [292] cite data for bubble formation at a 68.6 cm horizontal orifice obtained by Battelle Columbus Laboratory and unavailable to the authors of this document that can be correlated in terms of the nondimensional bubble size and the bubble Weber number

$$V_N = 0.594\ \ We^{0.8399}$$

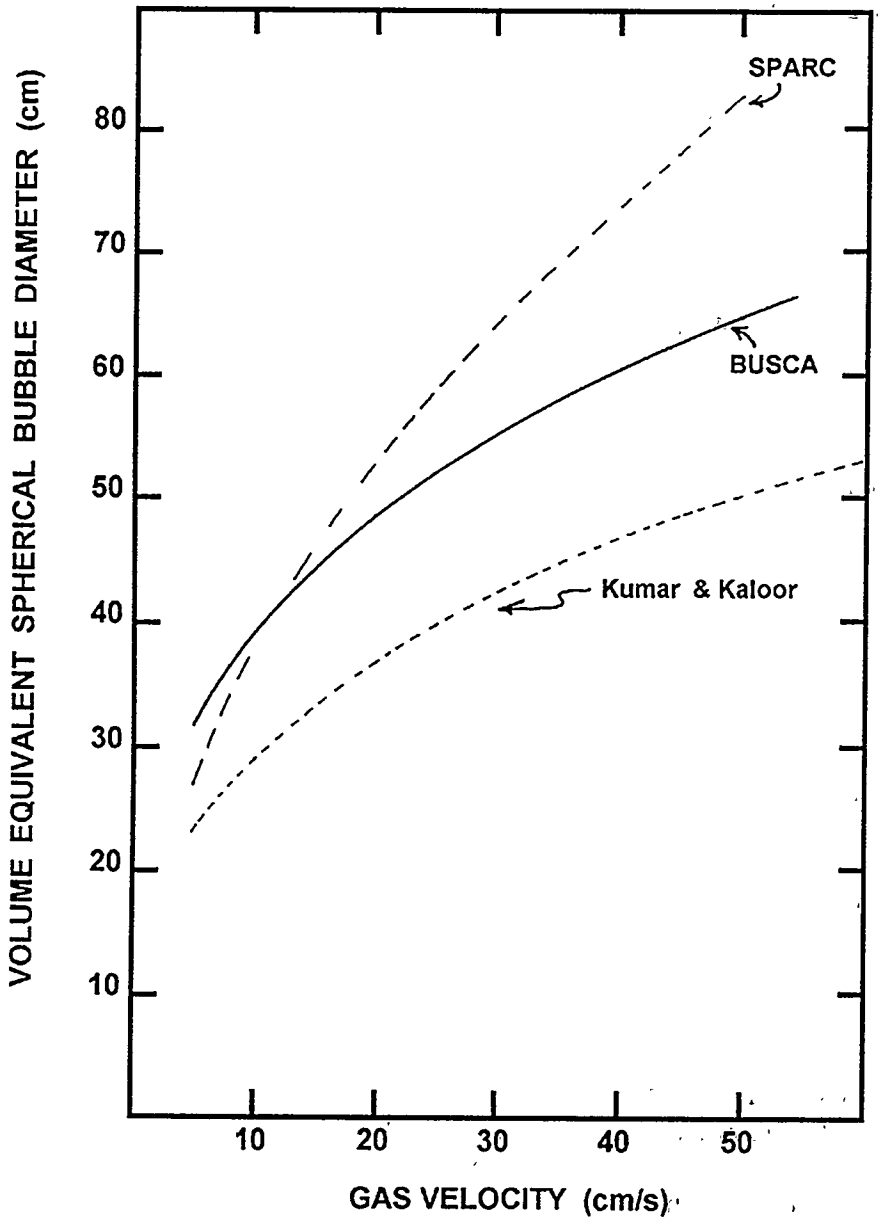

Figure 34. Comparison of various model predictions of the initial diameters of bubbles produced at a 72-cm-diameter horizontal vent

where, as above:

$$V_N = (\pi D_B^3/6)(\rho_l-\rho_g)^{1/2}\, g^{1/2} / \frac{\pi D_o^2}{4}\, \sqrt{\sigma_l}$$

$$We = U_o^2\, \rho_l D_o/\sigma_l$$

Note that the geometric vent diameter, D_o, is used in the correlation. Fischer and Hafner considered this to be very questionable.

B. Collapse and Disintegration of Large Bubbles

Bubbles released from orifices and vents in the steam suppression pool may not be stable. The gases that make up the initial bubbles may be supersaturated in steam relative to the bulk water pool temperature. Formation of the bubble is possible only because heat liberated by condensation of steam raises the interface temperature to saturation. Once the bubble detaches from the orifice or vent and begins to rise in the pool, colder water is encountered and heat transfer from the interface becomes more efficient.

The collapse of vapor bubbles has received a lot of attention. Pressure pulses produced by bubble collapse are thought to be responsible for equipment damage during cavitation [90] and during "chugging" in steam suppression pools [40]. The rate of bubble collapse may be limited by inertia or by the rate of heat transfer. Bubble collapse limited by inertial effects alone has received the most attention and models of varying sophistication have been proposed [91]:

- Rayleigh model [92]
  - water is treated as incompressible; $C = \infty$

$$R(t)\,\frac{\partial^2 R(t)}{\partial t^2} + \frac{3}{2}\left[\frac{\partial R(t)}{\partial t}\right]^2 = \frac{1}{\rho(\infty)}\,(P(t) - P(\infty))$$

- Herring's model [91]
  - speed of sound independent of pressure

$$\frac{R(t)\,\partial^2 R(t)}{\partial t^2} + \frac{3}{2}\left[1 - \frac{4}{3}\,\frac{1}{C(\infty)}\,\frac{\partial R(t)}{\partial t}\right]\left[\frac{\partial R(t)}{\partial t}\right]^2$$

$$= \frac{1}{\rho(\infty)}\left[P(t) - P(\infty) + \frac{R(t)}{C(\infty)}\,\frac{2P(t)}{2t}\left[1 - \frac{1}{C(\infty)}\,\frac{\partial R(t)}{\partial t}\right]\right]$$

- Gilmore's model [91]

  - pressure-dependent speed of sound in water

$$C(P) = C(\infty)\left[(P + B)/(P(\infty) + B)\right]^{3/7}$$

$$R(t)\frac{\partial^2 R(t)}{\partial t^2}\left[1 - \frac{1}{C(R)}\frac{\partial R(t)}{\partial t}\right] + \frac{3}{2}\left[\frac{\partial R(t)}{\partial t}\right]^2\left[1 - \frac{1}{3C(R)}\frac{\partial R(t)}{\partial t}\right] = H(P)\left[1 + \frac{1}{C(R)}\frac{\partial R(t)}{\partial t}\right] + \frac{R(t)}{C(R)}\frac{\partial H}{\partial t}\left[1 - \frac{1}{C(R)}\frac{\partial R(t)}{\partial t}\right]$$

$$H(P) = \frac{1}{\rho(\infty)}\frac{7}{6}(P(\infty) + B)\left[((P + B)/(P(\infty) + B))^{6/7} - 1\right]$$

where

R(t) = bubble radius at time t,

P(t) = pressure at the bubble walls at time t,

C = speed of sound in water, and

B = 2961 atms.

If the collapse is adiabatic, then

$$P(t) = P(o)\left[\frac{R(o)}{R(t)}\right]^{3\gamma}$$

$$\gamma = C_p(\text{gas})/C_v(\text{gas})$$

In the case where heat transfer from the bubble is rapid relative to collapse:

$$P(t) = P_{eq}(H_2O) + \frac{n(NC)RT}{\frac{4}{3}\pi R(t)^3}$$

where $P_{eq}(H_2O)$ is the equilibrium partial pressure of water at the bulk pool temperature T, R is the gas constant and n(NC) is the moles of noncondensible gas in the bubble.

For the bubbles of interest in the analyses of suppression pool scrubbing, introduction of the compressibility of water hardly affects the predicted results. An example calculation of the timing of bubble collapse under inertial control using Gilmore's model is shown in Figure 35. Note that spherical collapse becomes unstable to nonspherical perturbations once R(t) / R(o) falls below 0.2 [93].

Inertially limited bubble collapse is quite rapid. The example shown in Figure 35 would require Nusselt numbers for heat transfer from the bubble on the order of 3×10^4 which, as will be seen in the discussion in a later section, would be difficult to achieve in most situations. It seems likely, then, that heat transfer will be an important if not dominant factor in the collapse of supersaturated bubbles discharged into the suppression pool.

Florschuetz and Chao [94] introduced the parameter B to distinguish regimes of bubble collapse:

$$B = \left[\frac{\rho_l C_l \Delta T}{\rho_g L}\right]^2 \frac{k_l}{\rho_l C_l} \frac{1}{R(o)} \left[\frac{\rho_l}{\Delta P}\right]^{1/2}$$

where

$$\Delta T = T_s - T_p$$

$$\Delta P = P_{pool} - P_{eq}(T_p)$$

For B values greater than 10, inertial processes control. For B values less than 0.05, heat transfer processes control bubble collapse. For values of ΔT up to about 50 K, collapse is well within the heat transfer control regime.

Much of the analysis of bubble collapse under heat transfer control has been for stationary bubbles [94,95]. Wittke and Chao [96] have demonstrated there to be a substantial effect of motion on the collapse of bubbles. Moalem and Sideman [97] have developed a simple description of bubble collapse which treats the effects of both motion and the presence of noncondensible gas:

$$\frac{d\beta}{d\tau} = -\frac{1}{\sqrt{\pi}} \frac{\beta^3 - \beta_f^3}{\beta^{13/4}}$$

where

$$\beta = R(t) / R(o)$$

$$\tau = Ja\, Pe_o^{1/2}\, Fo$$

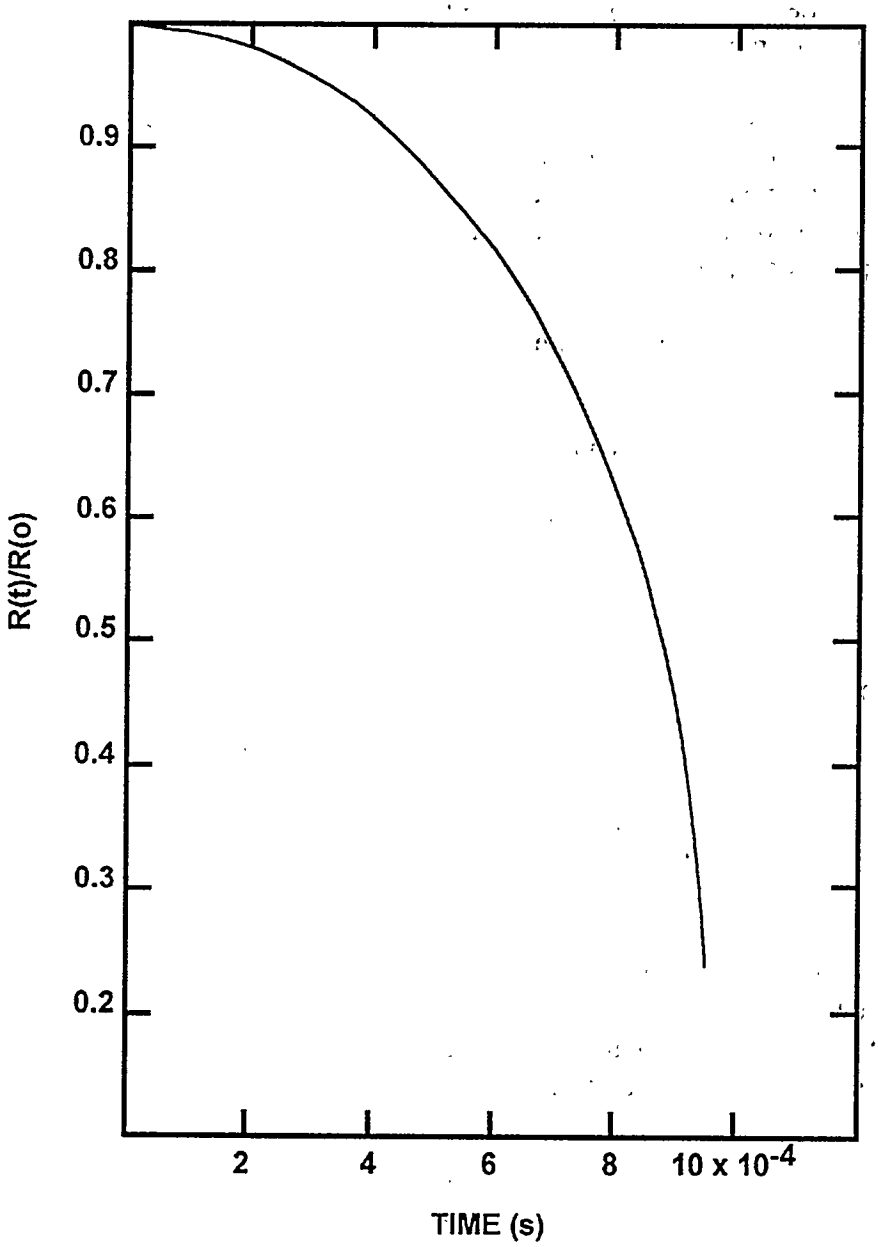

Figure 35. Isothermal, inertially-controlled collapse of a 2-cm bubble in water at 319 K according to Gilmore's model

$$Ja = \rho_l C_l (T_{sat} - T(\infty)) / L\rho_g$$

$$Pe_o = 2R(o)U_o / k_l / \rho_l C_l$$

$$F_o = k_l t / R(o)^2 \rho_l C_l$$

U_o = rise velocity of bubble

They derived this model for potential flow conditions and assumed the Nusselt number to be:

$$Nu = \frac{hD_B}{k_l} = 1.13\ Pe^{1/2}$$

where h is the heat transfer coefficient. The final dimensionless bubble volume, β_f, is given by:

$$\beta_f = \left[\frac{RT_{sat}^{\ 2}\ y_o}{L(T_{sat} - T(\infty))}\right]^{1/3}$$

where

T_{sat} = saturation temperature corresponding to the initial partial pressure of steam in the bubble

$T(\infty)$ = pool temperature

L = heat of vaporization of water

y_o = initial mole fraction of noncondensible gases in the bubble.

Predictions of this model are compared in Figure 36 to data obtained by Levenspiel [98] and in Figures 37 and 38 to data obtained by Wittke and Chao [96]. The agreement between data and model predictions is about the same as that obtained by Wittke and Chao with a more detailed, finite-difference, model. Agreement between the model and the data could probably be improved by using a size dependent model of the bubble rise velocity and a more detailed heat transfer model.

Note that the data for bubble collapse are for bubbles that are much smaller than those expected to form at vents and orifices in steam suppression pools. Bubbles formed initially in the suppression pool can be so large that they are hydrodynamically unstable even if they are not supersaturated in steam. The classic limiting size for a stable bubble is given by Levich [99] to be:

$$D_{limit} = 1.0\sigma_l / U_T^{\ 2}\ (\rho_g \rho_l^{\ 2})^{1/3}$$

Loertschuer et al. [100] have found for large bubbles that the rise velocity in water is given by:

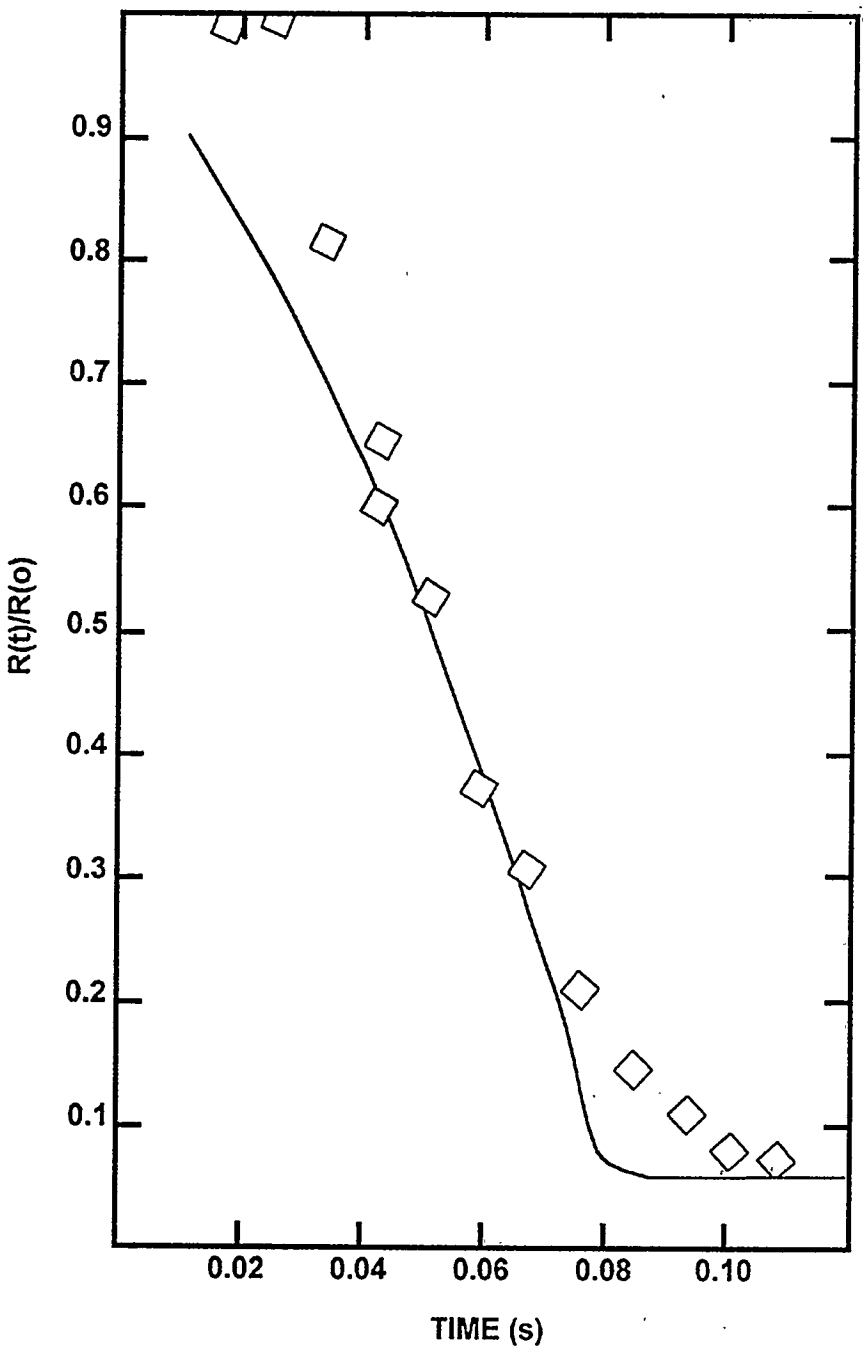

Figure 36. Comparison of bubble collapse predictions to data from Levenspiel [98]

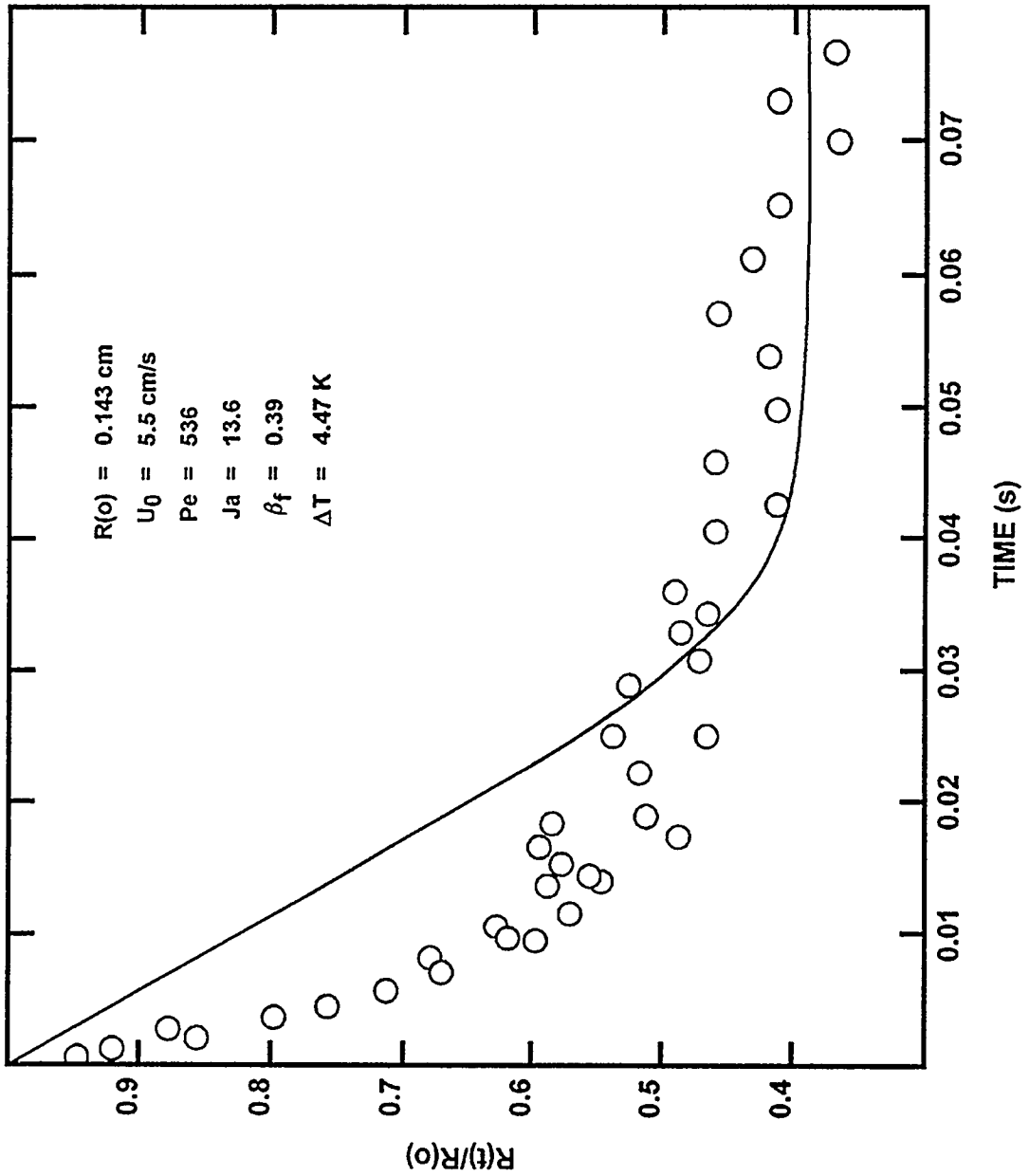

Figure 37. Comparison of model predictions of bubble collapse to data from Wittke and Chao [96]

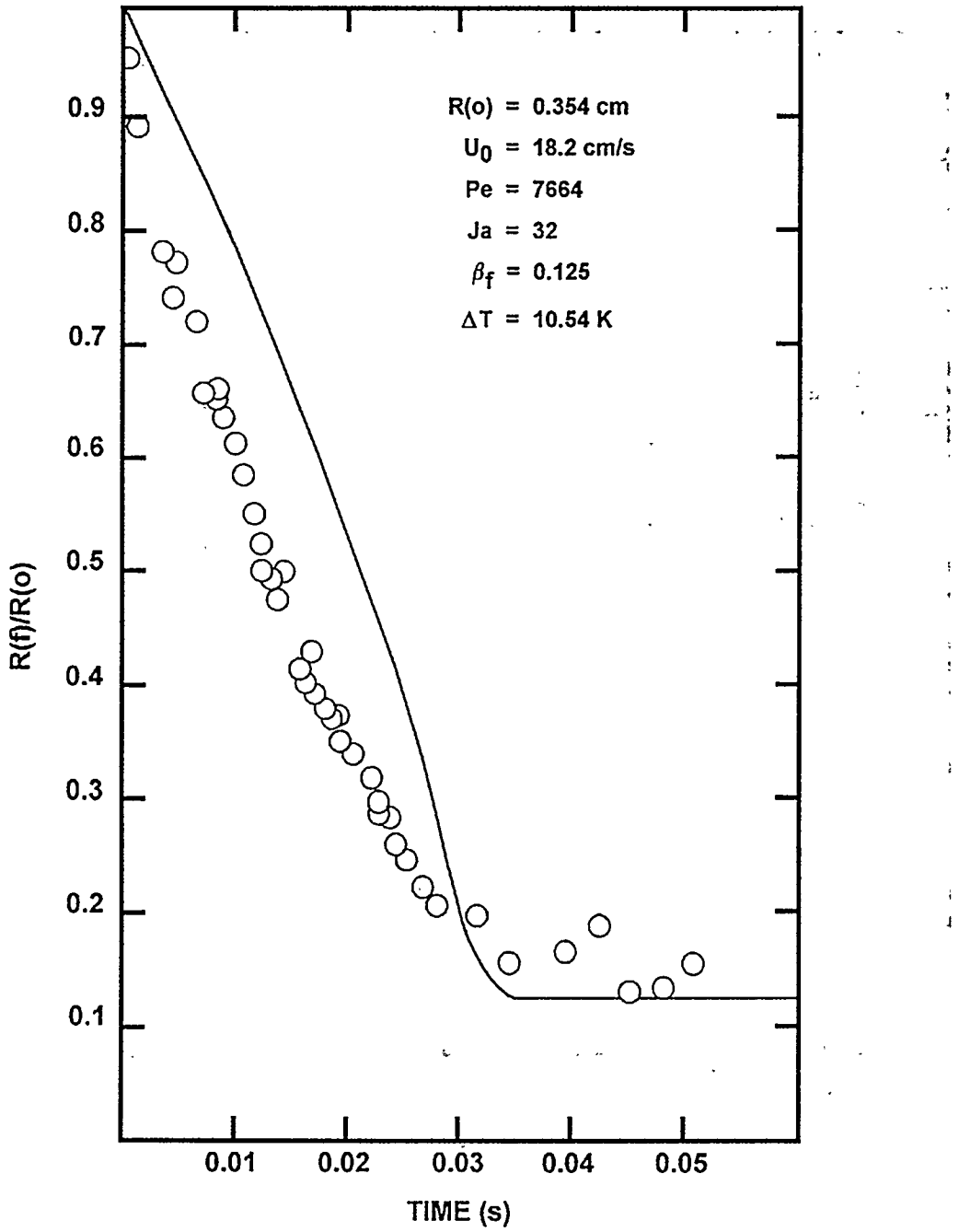

Figure 38. Comparison of predictions of bubble collapse to data from Wittke and Chao [96]

$$U_T \text{ (cm/s)} = 0.7354 \sqrt{gD_B}$$

These data are shown in Figure 39. This, then, yields for the maximum stable bubble size in water about 2 cm.

Grace et al. [101] have conducted a two dimensional Rayleigh-Taylor instability analysis of rising bubbles. They consider the growth of sinusoidal disturbances at the interface of the bubble. Surface tension will prevent the growth of disturbances smaller than a critical wavelength given by:

$$\lambda_c = 2\pi/\sqrt{\rho_l g/\sigma_l}$$

Disturbances with larger wavelengths can grow. But, disturbances larger than about $\lambda_u = \pi D_B/2$ amount to gross translations of the bubble as a whole and need not be considered responsible for breakup of oversized bubbles.

Disturbances with wavelengths between λ_c and λ_u will grow as they are swept along the interface during bubble rise. The time available for disturbances to grow is given by:

$$t(a) = \frac{2D_B}{U_T} \ln\{\cot(\lambda/4D_B)\}$$

where

$t(a)$ = time available for disturbance growth,

D_B = bubble diameter,

U_T = rise velocity, and

λ = wavelength of a disturbance.

Disturbances grow as does $\exp(\alpha t)$ where α is given by:

$$\left[\left[\frac{2\pi}{\lambda}\right]^2 + \frac{\alpha\rho_l}{\mu_l}\right]^2 + 2\left[\left[\frac{2\pi}{\lambda}\right]^2 + \frac{\alpha\rho_l}{\mu_l}\right] - 4\left[\left[\frac{2\pi}{\lambda}\right]^2 + \frac{\alpha\rho_l}{\mu_l}\right]^{1/2}$$

$$+ 1 + \frac{\lambda}{2\pi}\frac{\rho_l}{\mu_l^2}(\sigma_l - \lambda^2 g\rho_l/4\pi^2) = 0$$

Experience indicates that when the product $t(a)\alpha$ exceeds 3.8 for disturbances with wavelengths between λ_c and λ_μ, the bubble will break up. Bubble stability maps for water based on this criterion are shown in Figures 40 and 41. Other discussions of bubble stability are to be found in References 216 and 217.

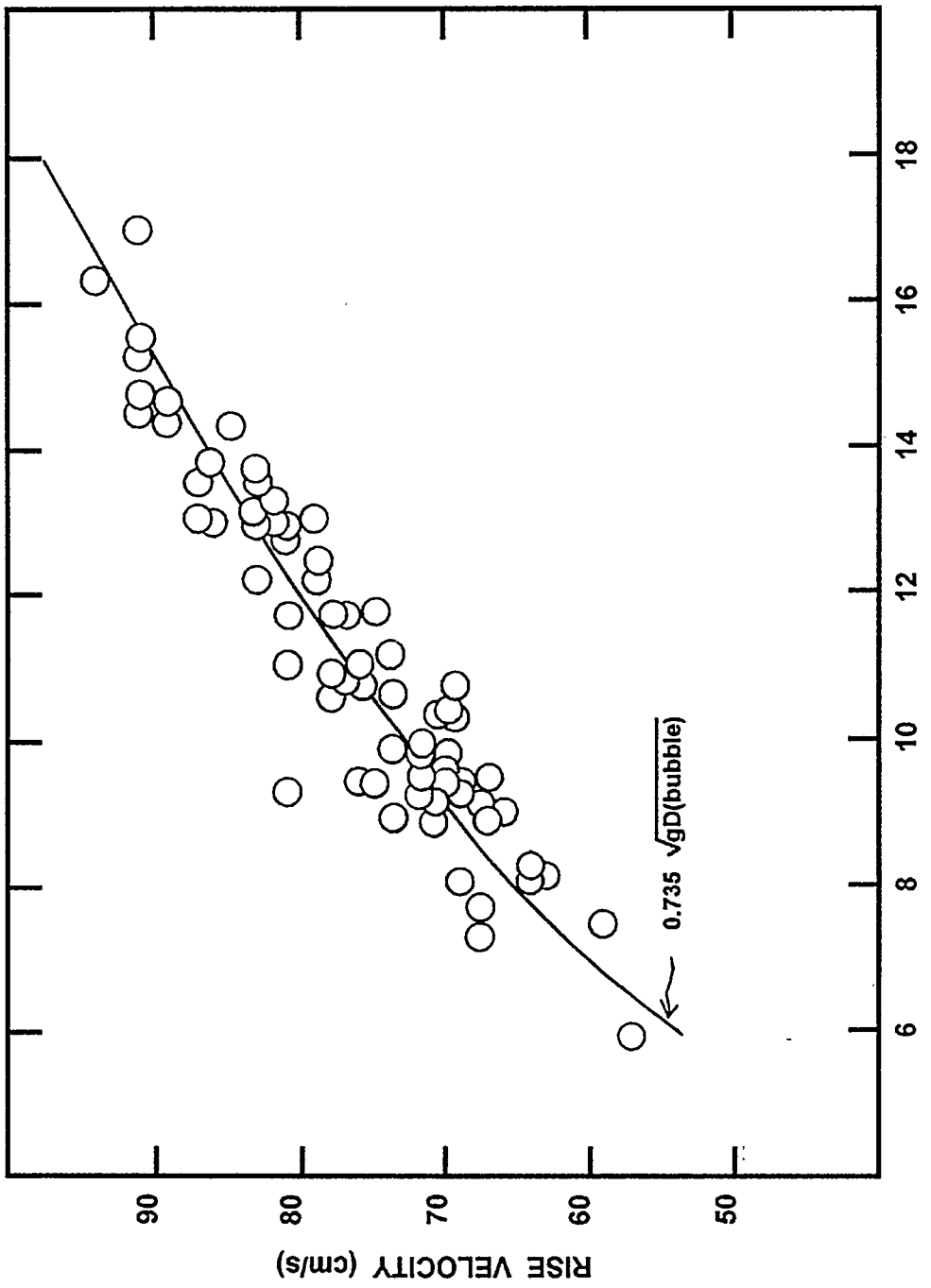

Figure 39. Rise velocities for very large bubbles

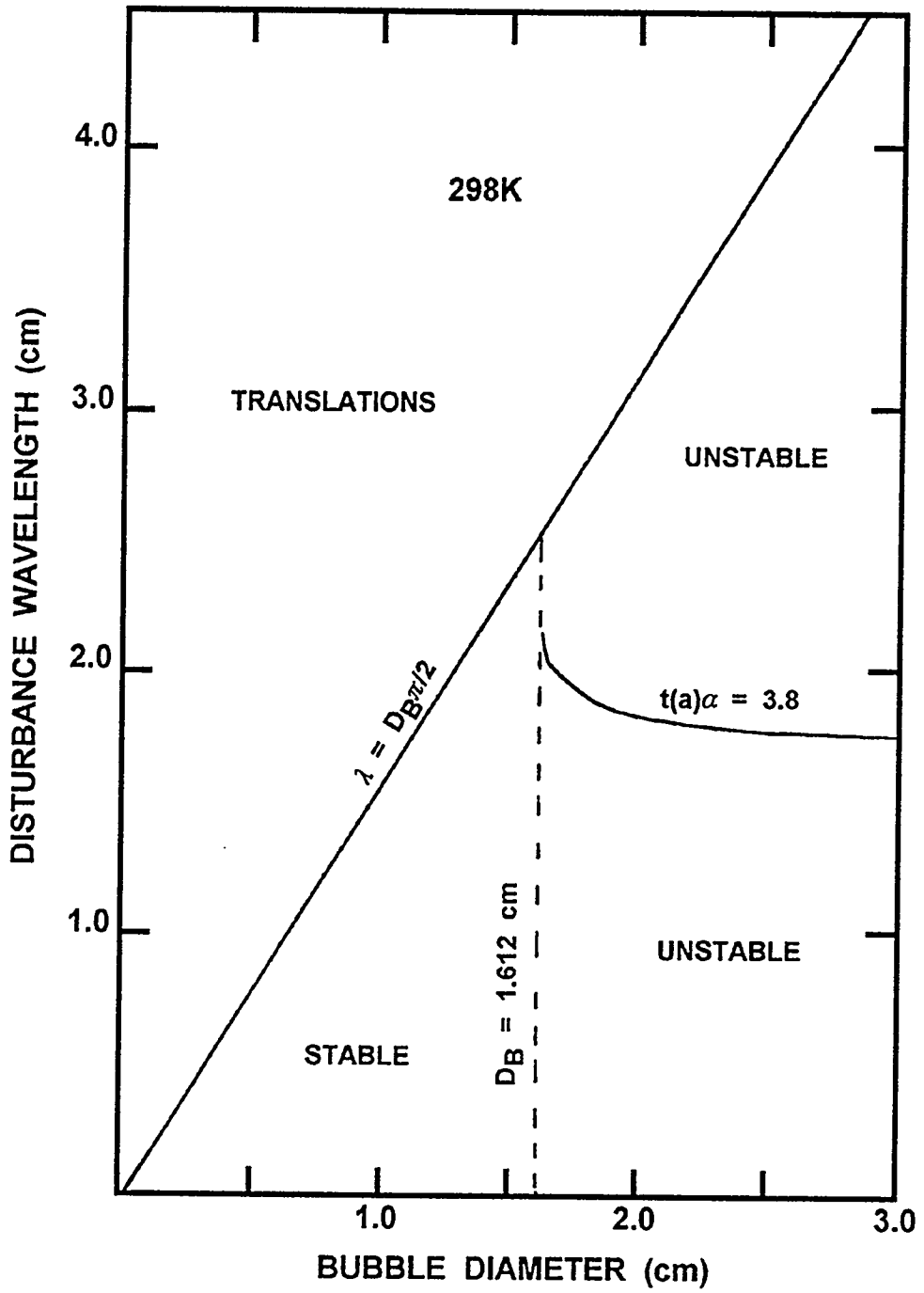

Figure 40. Bubble stability map for water at 298 K

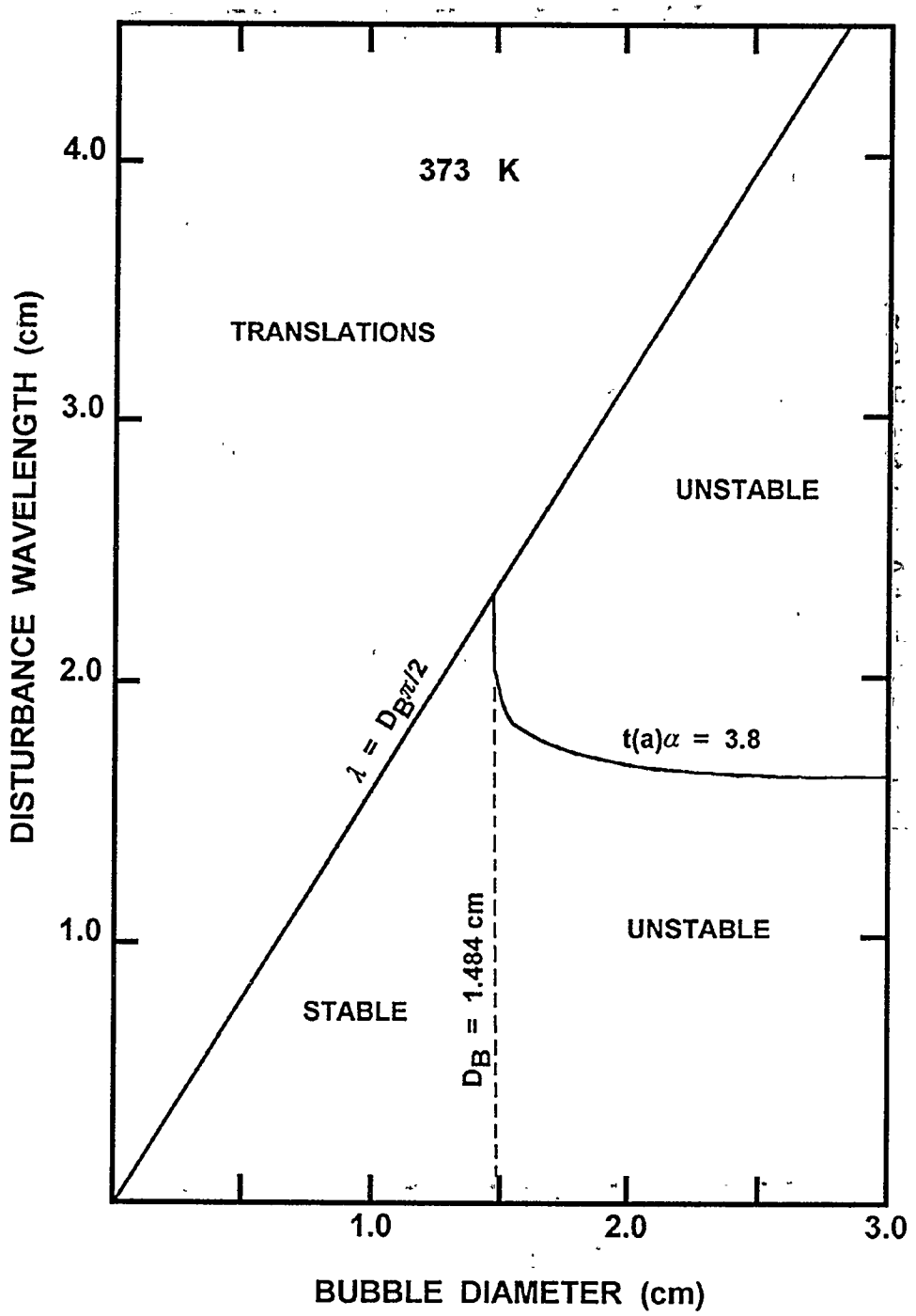

Figure 41. Bubble stability map for water at 373 K

The stability analysis indicates that overly large bubbles will break up. The analysis does not indicate the sizes of the bubbles left after the breakup. Empirical evidence suggest that the bubble will "calve" off fragments of fairly random size. Fragments that are small enough to be stable may coalesce to form larger bubbles.

C. Bubble Size Distribution and the Coalescence of Bubbles

At the conclusion of the bubble formation and breakup process there will be a swarm of bubbles rising through the suppression pool. Presumably bubbles in the swarm will have a distribution of sizes. As will be discussed further, below, bubble size has an important bearing on the efficiency of aerosol removal. It is, then, necessary to have a good estimate of the bubble size distribution.

Empirical evidence on the size distribution of bubbles rising through suppression pools has been obtained by Paul et al. [30] and by Hakii et al. [69]. Both teams of investigators examined bubble size distributions produced by orifices found on quenchers. Both groups obtained about the same results. The experiments conducted by Paul et al. are especially well documented.

Paul et al. examined bubble size distributions at several elevations above a quencher orifice. They examined the effects on the size distribution of gas injection rate (see Figure 42), orifice orientation (see Figure 43) and orifice size (see Figure 44). Bubble size distributions were found to be approximately lognormal and could be characterized adequately by a mean and a geometric standard deviation.

Mean bubble diameters and geometric standard deviations as functions of gas injection rates are shown in Figure 42. It appears that there may be a dependence of bubble size on gas injection rates for injection rates less than 0.1 moles/s. A dependence on gas injection rates would be expected if very small bubbles were coalescing to form bubbles of a stable size. There is no obvious dependence of the geometric standard deviation on gas injection rates. The logarithmic mean geometric standard deviation is 1.44 to 1.63. The geometric standard deviation does not appear to be strongly correlated with the mean bubble size.

Bubble size distribution data listed in Table 8 are plotted against orifice size in Figure 43. Though system parameters other than orifice size vary within this data set, it is not obvious that parameters characterizing the bubble size distribution depend on orifice size. Whether this conclusion can be extrapolated to orifices the size of downcomers and horizontal vents is problematic.

Data listed in Table 9 are plotted in Figure 44 against the orientation angle of the orifice (a 90° orientation corresponds to an orifice opening horizontally). Data for all orientations other than 90° were obtained at lower gas injection rates than data obtained for the 90° orientation. The mean diameters of the bubble size distribution are sensitive to gas injection rates in this range. Consequently, data shown in Figure 42 were extrapolated to 0.027 moles/s to obtain data points for the 90° orientation shown in Figure 44. There is some indication that bubbles formed after injection at angles greater than 90° have somewhat larger mean diameters than bubble size distribution produced by gas injection at orientations of 0 to 90°. The effect is, however, not much greater than the expected uncertainty in the measurements.

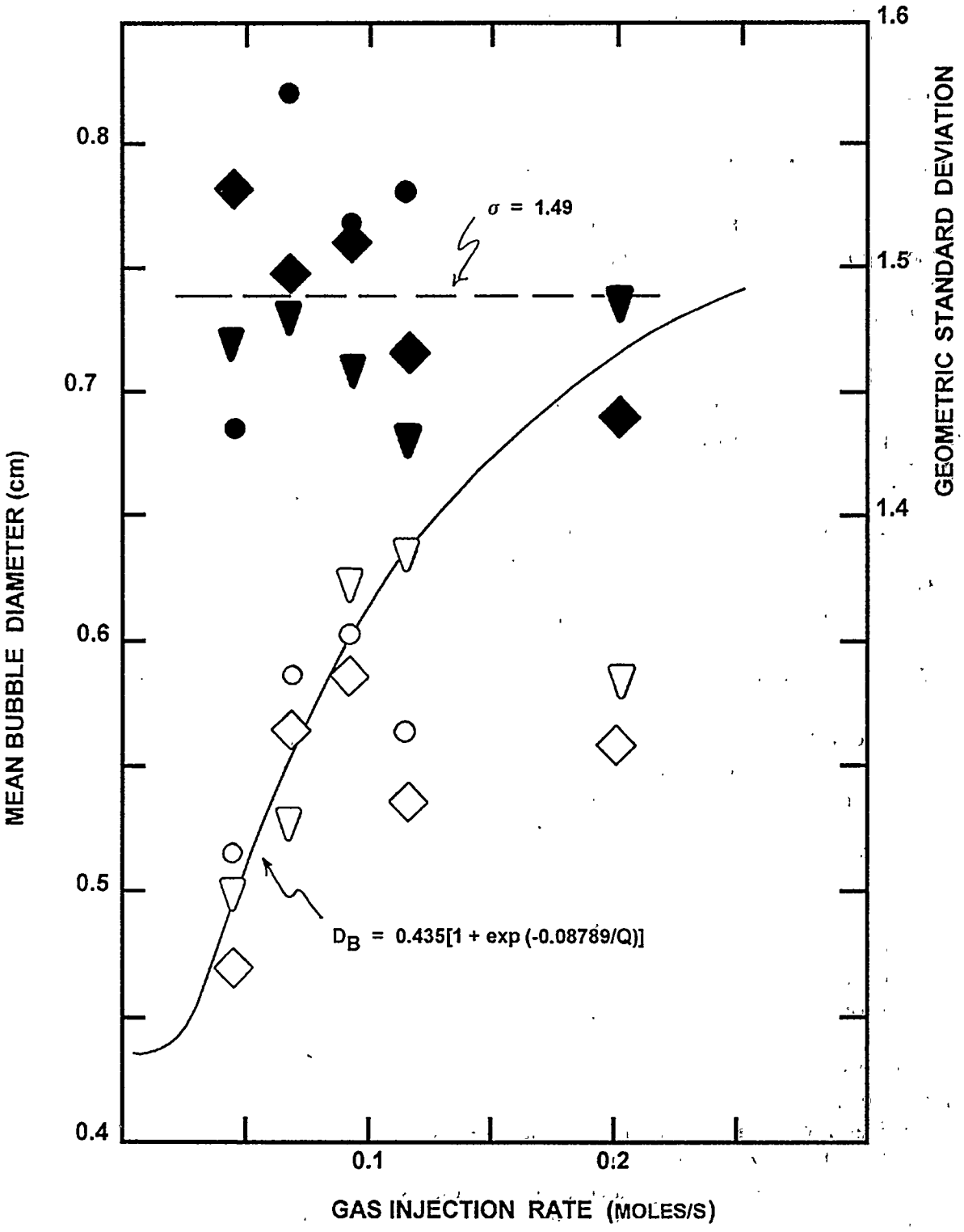

Figure 42. Effect of gas injection rate on bubble size distribution. Distributions were measured at elevations above the orifice of 122 cm (circles), 198 cm (diamonds) and 305 cm (triangle). Open symbols are for mean sizes (left scale) and filed symbols are for the geometric standard deviation (right scale). Air and a 0.99-cm orifice with an orientation of 0° were used for these tests.

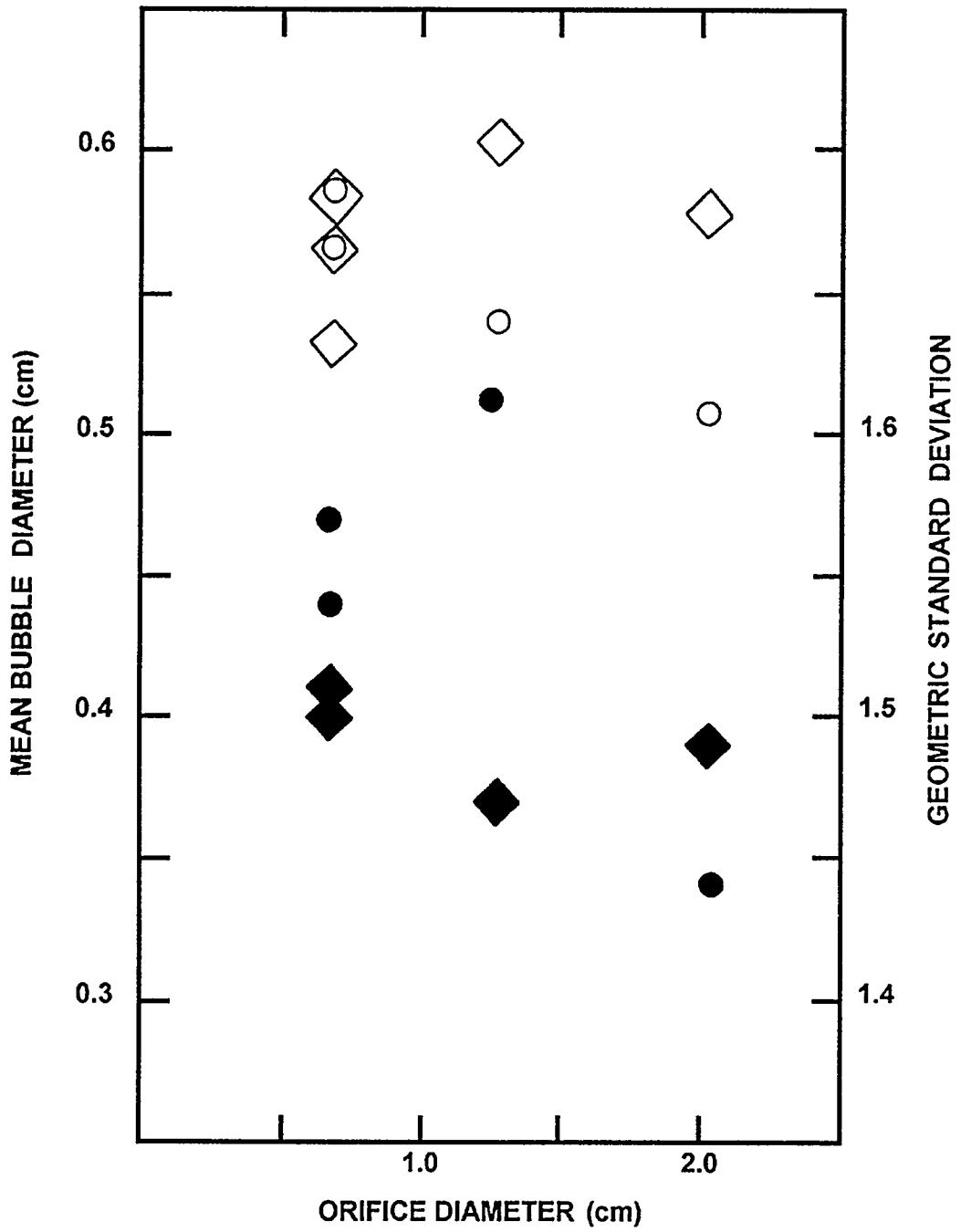

Figure 43. Effect of orifice size on the bubble size distribution. Measurements were taken at 122 cm (circles) and 198 cm (diamonds) above the orifice. Open symbols refer to the mean bubble size (left scale). Filled symbols refer to the geometric standard deviation (right scale).

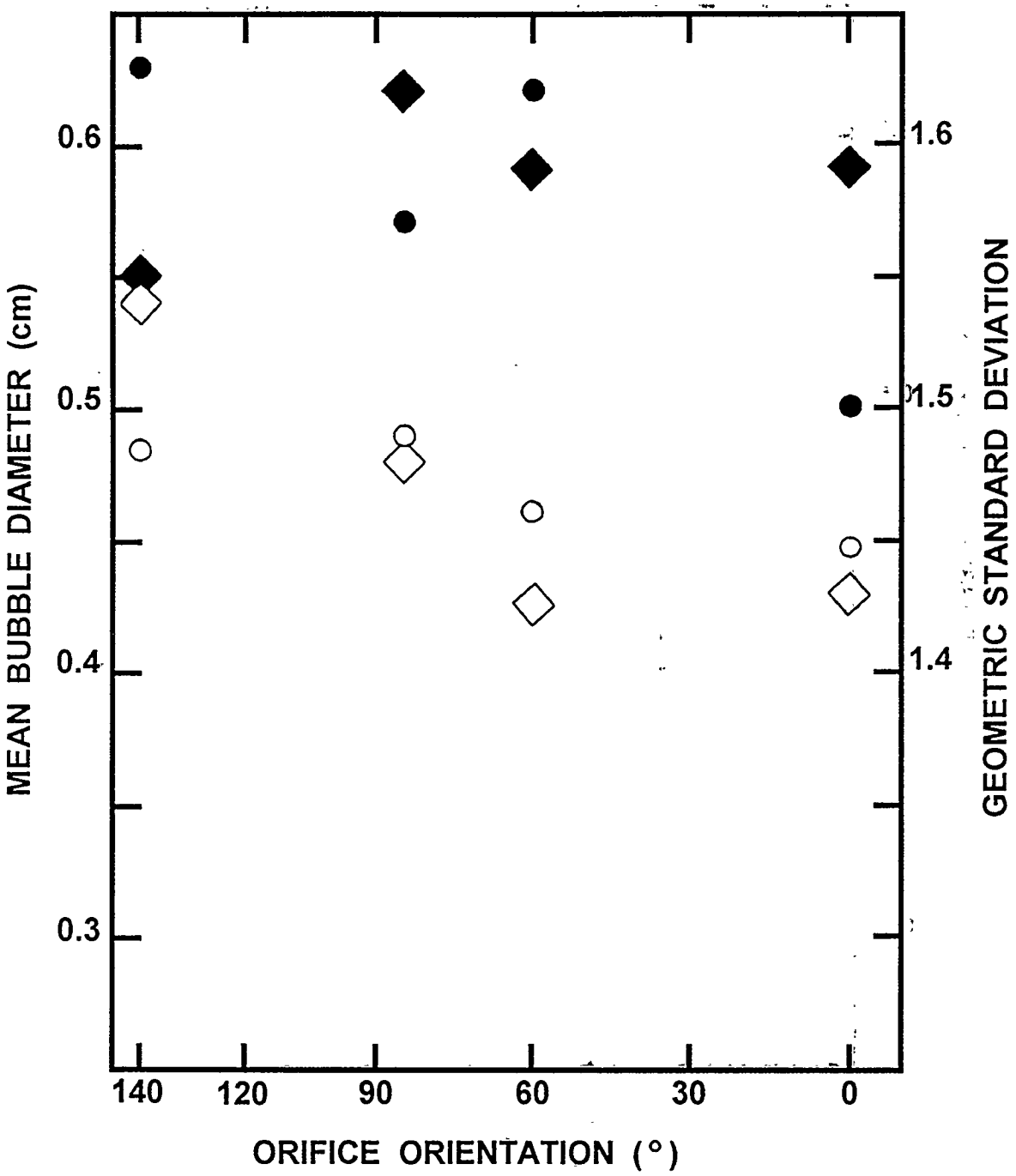

Figure 44. Effect of orifice orientation on the bubble size distribution. Data for air bubbles were measured 122 cm (circles) and 198 cm (diamonds) above a 1.27-cm orifice. Open symbols refer to the mean bubble diameter (left scale) and filled symbols refer to the geometric standard deviation (right scale).

Table 8. Effect of orifice size on the bubble size distribution

Orifice diameter (cm)	Gas injection rate (mole/s)	Elevation above orifice (cm)	Mean bubble size (cm)	Geometric standard deviation (-)
0.99	0.068	122	0.586	1.57
0.99	0.114	122	0.566	1.54
1.27	0.070	122	0.540	1.63
2.02	0.108	122	0.509	1.44
0.99	0.068	198	0.564	1.50
0.99	0.090	198	0.583	1.51
0.99	0.114	198	0.533	1.47
1.27	0.070	198	0.603	1.55
2.02	0.104	198	0.578	1.49

Table 9. Effect of orifice orientation on the bubble size distribution

Orifice diameter (cm)	Gas injection rate (moles/s)	Orifice orientation (°)	Elevation above orifice (cm)	Mean bubble size (cm)	Geometric standard deviation (-)
1.27	0.027	0	122	0.446	1.50
1.27	0.027	60	122	0.461	1.62
1.27	0.027	140	122	0.485	1.57
1.27	0.070	90	122	0.540	1.63
(1.27)*	(0.027)	(90)	(122)	(0.49)	-
1.27	0.027	0	198	0.430	1.59
1.27	0.027	60	198	0.424	1.59
1.27	0.027	140	198	0.540	1.62
1.27	0.070	90	198	0.603	1.55
(1.27)*	(0.027)	(90)	(198)	(0.48)	-

*Extrapolated based on gas injection rate dependence of bubble size.

The mean of the final bubble size distribution is strongly affected by the mole fraction of steam in the gas initially discharged to the suppression pool. Data for air-steam mixtures are listed in Table 10 and are plotted in Figures 45 and 46. The mean bubble size data were fit by linear least-squares methods to:

$$\ln D_B = -0.4837 - 0.5972 y^2$$

where y is the mole fraction of steam in the initial gas discharged to the pool. (The pool in these tests was cool enough that essentially all of the steam would condense, eventually). The 100 (1 - α) percent confidence bands for predictions derived from this correlation can be obtained from

$$\ln D_B = \ln D_B|_{reg} \pm 0.0634\ t_{(1-\alpha/2)(10)} \left[\frac{1}{12} + \frac{(y^2 - 0.4434)^2}{1.1847} \right]^{1/2}$$

where

$\ln D_B|_{reg}$ = value of ln D_B calculated from the regression equation, and

$t_{(1-\alpha/2)(10)}$ = critical Student's t statistic for 10 degrees of freedom and a confidence level of 100 (1 - α/2) percent.

According to the data shown in Figure 42 there is some small dependence of the mean bubble size on gas injection rate. A multiplicative coefficient can then be derived to yield an overall regression equation for the mean bubble size:

$$D_B = 0.435\ \{1 + \exp[-0.08789/Q]\}\ \exp[-0.5972 y^2]$$

Results obtained by Paul et al. [30] and the rather similar results obtained by Hakii et al. [69] are not readily interpreted in terms of mechanism. It appears that oversized bubbles form, break up, and rapidly coalesce to form bubble swarms with mean bubble diameters very near 0.5 cm. A coalescence step is hypothesized because there is nothing in the bubble breakup process that would seem to produce such narrow distributions of bubble sizes as are observed in the experiments.

Coalescence of gas bubbles is known to be a major factor in gas-liquid interactions [72]. Coalescence of bubbles is observed to occur easily in very pure systems if the relative velocities of the interacting bubbles are not too different [73]. Contamination of the liquid with ionic or organic solutes is found to inhibit bubble coalescence.

Table 10. Effect of steam concentration on the bubble size distribution

Orifice diameter (cm)	Steam injection rate (moles/s)	Noncondensible injection rate (moles/s)	Elevation above orifice (cm)	Mean bubble size (cm)	Geometric standard deviation (-)
0.99	0.0264	0.0680	122	0.556	1.54
0.99	0.0440	0.0452	122	0.544	1.52
0.99	0.0677	0.0225	122	0.447	1.53
0.99	0.0827	0.0045	122	0.374	1.36
0.99	0.0260	0.0687	198	0.578	1.52
0.99	0.0432	0.0459	198	0.524	1.44
0.99	0.0638	0.0229	198	0.498	1.61
0.99	0.0833	0.0046	198	0.313	1.48
0.99	0.0276	0.0691	305	0.566	1.51
0.99	0.0445	0.0456	305	0.566	1.46
0.99	0.0677	0.0227	305	0.455	1.50
0.99	0.0855	0.0046	305	0.361	1.46

Oolman and Blanch [71] consider bubble coalescence to be a three step process:

- hydrodynamic processes bring bubbles into close proximity so that a liquid layer 10^{-3} to 10^{-4} cm thick separates the bubbles,
- processes driven by surface tension thin the separation layer to a thickness of about 10^{-6} cm, and
- the separation layer ruptures so the bubbles unite.

It has been argued [74] that an electric double layer produced by dissolved ions resists the thinning of the liquid layer between bubbles brought into close proximity by hydrodynamic processes. Oolman and Blanch [71] reject this argument because they believe the electric double layer has too small an effect. They argue, instead, that the resistance to coalescence observed for contaminated liquids is the result of surface tension effects.

Consider two bubbles brought together so that there is a liquid film of thickness $h_o \cong 1 \times 10^{-3}$ cm between them. At the center, the film is flat and the pressure is the bubble pressure. At the perimeter of the film, there are curvature effects. As a result, there is a pressure variation along the film given by:

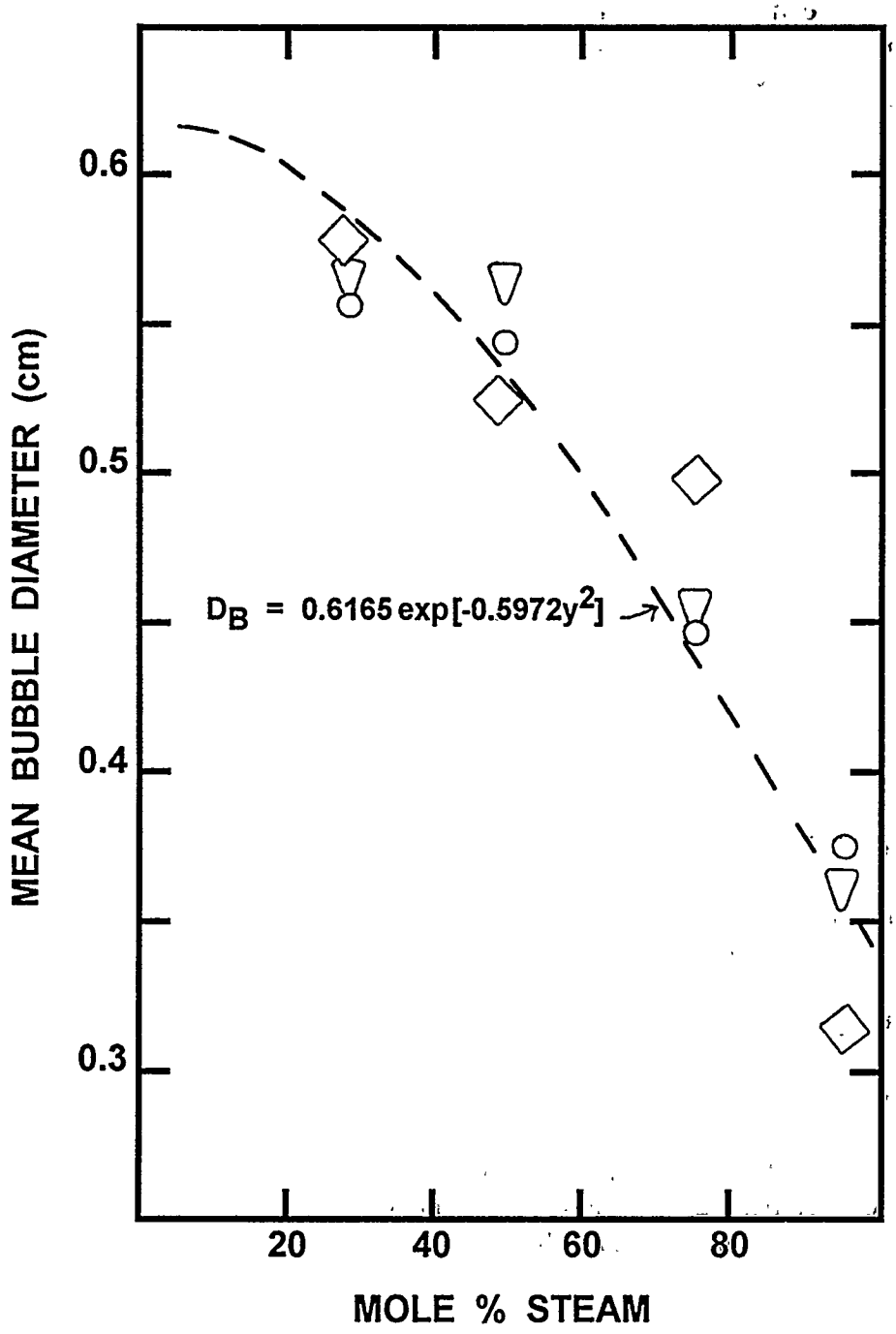

Figure 45. Effect of the mole fraction of steam in air/steam mixtures on the mean bubble size

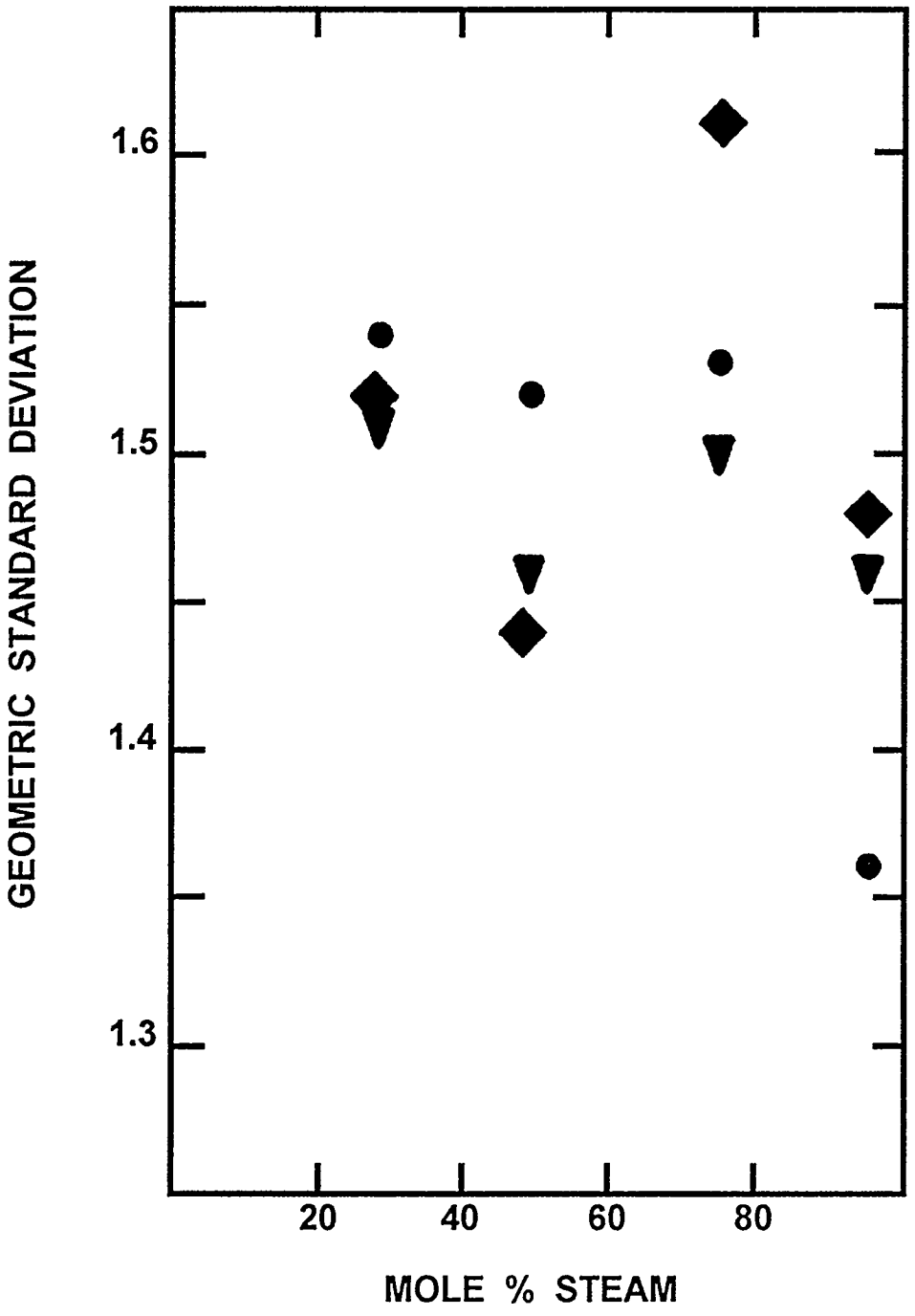

Figure 46. Effect of the mole fraction steam in air/steam mixtures on the geometric standard deviation of the bubble size distribution

$$\Delta P = 4\sigma_l/D_B + A/6\pi h^3$$

where A is the Hanamaker constant taken to be 10^{-12} ergs. If a solute is present, it will impart an opposing force given by [75]:

$$\Delta\sigma_l = \frac{1}{h}\frac{2c}{RT}\left[\frac{\partial\sigma_l}{\partial c}\right]^2$$

where c is the concentration of the solute in moles per liter. Then, from the Navier-Stokes equation:

$$\frac{1}{h_o}\frac{\partial^2 h}{\partial\tau^2} = \frac{1.5h_o}{h}\left[\frac{\partial h}{\partial\tau}\right]^2 - \frac{h}{h_o}A_1 - \left[\frac{h}{h_o}\right]^2 A_2 + \frac{h_o A_3}{h}$$

where

$$\tau = \left[\frac{\sigma_l}{\rho_l h_o^3}\right]^{1/2} t\,,$$

$$A_1 = 16\,h_o^3 / D_B\,r^2\,,$$

$$A_2 = 2\,A / 3\pi\,\sigma_l\,r^2\,,$$

$$A_3 = \frac{16c}{h_o}\left[\frac{\partial\sigma_l}{\partial c}\right]^2 (1/\sigma_l\,RT\,r^2),\ \text{and}$$

r = radius of film disk separating the bubbles.

Solution of this equation for various values of A_3 shows there to be a critical solution concentration that marks a transition from rapid bubble coalescence to slow bubble coalescence. Such behavior is observed in the coalescence of bubble pairs rising through aqueous salt solutions [75,76]. Data correlate best when plotted against ionic strength, I, rather than concentration. Data on coalescence efficiency (percent of bubble pairs observed to coalescence for solutions of KCl, $AlCl_3$, Mg_2SO_4, $MgCl_2$, $CaCl_2$, Na_2SO_4, LiCl, NaCl, and NaBr are shown in Figure 47. There appears to be a sharp increase in the efficiency of bubble coalescence once the ionic strength drops below about 0.18. Prince and Blanch [209] indicate that the critical concentration for ionic solutes is given by:

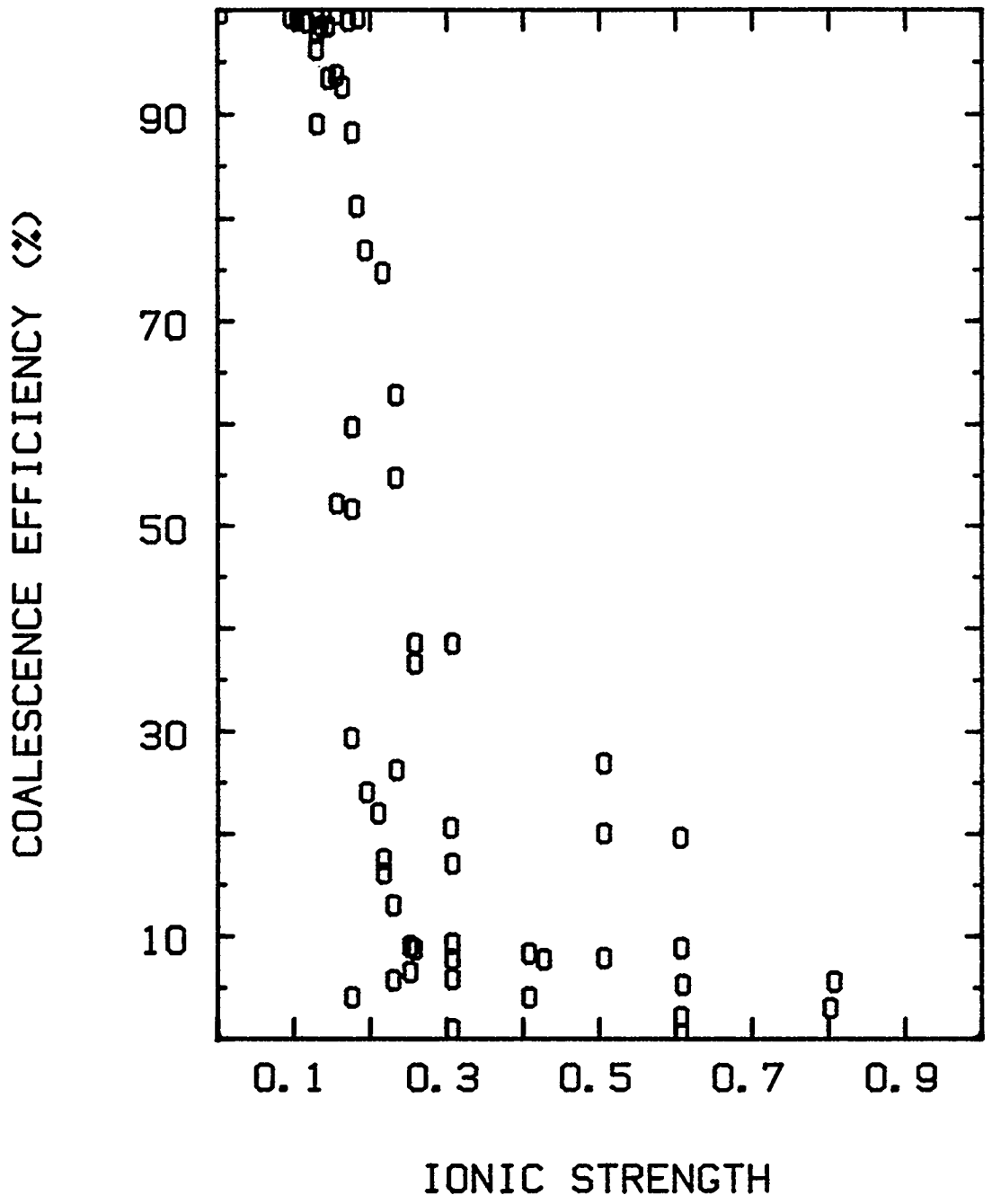

Figure 47. Efficiency of bubble coalescence as a function of the ionic strength of the aqueous solution

$$C = 1.18\ n(\pm) \left[\frac{2B\sigma_l}{D_B}\right]^{1/2} \frac{RT}{\left[\frac{\partial\sigma_l}{\partial c}\right]^2}$$

where

C = concentration of the dissolved salt,

$n(\pm)$ = number of ions produced when a "molecule" of salt dissolves,

B = 1.5×10^{-19} erg cm, and

$\frac{\partial\sigma_l}{\partial c}$ = derivative of the liquid surface tension with respect to salt concentration.

Work done by Paul et al. [30] and by Hakii et al. [69] involved essentially uncontaminated water. In such systems, efficient coalescence of bubbles to produce the observed bubble size distribution could occur. This may not be the situation in reactor accidents. As the accident progresses, the water in the steam suppression pool becomes contaminated. Especially in the late phases of a reactor accident, contamination of the steam suppression pool may be sufficient to interfere in the coalescence of gas bubbles. Bubble size distributions different (presumably smaller) than those observed by Paul et al. [30] or Hakii et al. [69] may form.

The inhibition to coalescence by organic, volatile materials is even more striking than the effect of ionic solutes. Transitions from rapid coalescence to slow coalescence occur at organic volume fractions of 10^{-5} to 10^{-3}. Later in the discussion of phenomena, it will be shown that organic contaminants affect rise velocities of bubbles and the inertial impaction of aerosol particles.

Lee et al. [220] have developed a probabilistic description of bubble coalescence. They describe the rate of coalescence of bubbles of diameter d(1) and d(2) at number concentrations of n(1) and n(2), respectively, as:

$$\text{Rate} = C \exp\left\{\frac{-\alpha\epsilon^{1/3}t_c}{d^{2/3}}\right\} \epsilon^{1/3}\, d^2 \left(d(1)^{2/3} + d(2)^{2/3}\right)^{1/2} n(1)n(2)$$

where

$d = d(1) + d(2)$,

ϵ = turbulent energy dissipation rate per unit mass,

t_c = coalescence time = t(a) + t(b),

$$t(a) = 24\pi^2 \sigma_l \mu_l h_f^5 z / A_h^2,$$

$$t(b) = \frac{R'}{4}(\rho_l d/2\sigma_l)^{1/2} \ln[h(i)/h(f)] \quad ,$$

A_h = Hanamaker's constant, and

other symbols denote empirical constants. When plotted against bubble size, this rate of coalescence for aqueous systems passes through a minimum at bubble diameters of about 0.25 cm. Coalescence rates decrease with the intensity of turbulent energy dissipation. The coalescence rate, combined with similar expressions developed by Lee et al. on the rates of bubble breakup in turbulent environments, might form the basis for rationalizing the invariance in the final bubble size distribution observed by Paul et al. [30]. The matter is not pursued further here. Moreover, the dependence of coalescence on the turbulent energy dissipation makes it unclear that size distributions for bubbles observed by Paul et al. in tests with one or a few orifices can be unequivocally applied to quenchers with hundreds of orifices at conditions substantially different than those of the tests.

In the simplified model of suppression pool scrubbing developed below, keeping track of ionic strength in the water pool is really impracticable. Water in the suppression pools of boiling water reactors will usually be quite pure at the start of an accident, and bubble coalescence as observed by Paul et al. [30] should be possible. As the accident progresses, the suppression pool will become progressively more contaminated with both soluble and insoluble materials. Surely during the ex-vessel phases of an accident, the contamination will become sufficient to meet the concentration criterion that bubble coalescence is inhibited.

D. Thermodynamics of Bubble Rise

Bubbles detach from vents and orifices and begin to equilibrate with the bulk pool. Achieving equilibrium is quite dynamic and can involve disintegration or collapse of the initial bubble and subsequent coalescence of the bubbles. All these dynamic processes take place rather quickly—within 2 to 10 initial bubble diameters of the vents in the suppression pool [30]. A swarm of bubbles then rises through the pool. As bubbles rise, there is a loss of pressure head so the bubbles expand. In order to maintain equilibrium with the water pool, water will have to vaporize into the bubble. There is, then, a flux of water vapor coming off the walls of the bubble. This flux of water vapor will oppose the motion of particles toward the walls. At the same time, expansion of the bubble will cool the gas within the bubble. This will create a temperature difference between the bulk gas and the bubble surface. As a result, there will be a thermophoretic driving force pushing particles away from the bubble surface.

Analysis of the vaporization of water into the bubble must be done in terms of the internal energy of an open system since neither the pressure nor the volume is constant. The analysis below follows in outline the general features of an analysis by Owczarski and Burk [6]. The gas in the bubble is taken to be ideal. Here, aerosols within the bubble are neglected. Aerosols in the bubbles could be heat sinks

and sources of decay heat. Concentrations of the aerosols are, however, thought to be sufficiently low so that the aerosols will not significantly perturb the thermodynamic properties of the gas. That is, at an aerosol concentration of 0.1 g/m^3, the aerosol would, typically, only increase the heat capacity of the gas by about 0.01 percent. It is possible that water could condense on aerosol particles within a bubble. Whether or not this happens is dependent on the properties of the aerosol material. This topic is discussed further below. Aerosols could be a source of decay heat. At typical decay heating rates of 0.3 W/g and a bubble rise time of 20 seconds, decay heating by aerosols at a concentration of 0.1 g/m^3 would only increase the energy in the gas phase by the equivalent of 5×10^{-4} K. Thus, decay heating is neglected here.

Consider a bubble of initial volume V(i), pressure P(i), and temperature T(i). A differential upward displacement of the bubble, dx, is imagined to change the volume, pressure, and temperature to V(f), P(f) and T(f), respectively. A molar amount of water, $dn(H_2O)$ is also imagined to vaporize into the bubble during the displacement.

Changes in the internal energy of the bubble during the displacement are defined by:

$$\Delta U = \Delta Q - \Delta W$$

where

ΔU = change in the internal energy,

ΔQ = change in the heat content, and

ΔW = work done by the bubble.

For the situation of interest here, work is taken to be pressure-volume work:

$$\Delta W = \int_{V(i)}^{V(f)} P dV$$

The thermodynamic cycle that can be used to define the change in state associated with the differential displacement of the bubble involves the following steps:

- an isothermal vaporization of $dn(H_2O)$ moles of water into the bubble which causes the bubble to expand from V(i) to V′,
- an isothermal expansion from P(i), V′, T(i) to P(f), V*, T(i), and
- a constant pressure expansion from P(f), V*, T(i) to P(f), V(f), T(f).

These steps can be compared to the internal energy change of an isothermal vaporization and a change from T(i) to T(f).

For the first step in the cycle, a constant temperature, constant pressure vaporization of $dn(H_2O)$ moles of water, the work done is:

$$\Delta W_1 = \int_{V(i)}^{V'} P(i)\,dV = \int_{n(H_2O)}^{n(H_2O)+dn(H_2O)} P(i)\,dn(H_2O)\,RT/P(i) = P(i)\,(V' - V(i))$$

and, thus,

$$V' = V(i) + \frac{RT(i)\,dn(H_2O)}{P(i)}$$

The work done in the second step, the isothermal expansion from P(i), V′, T(i) to P(f), V*, T(i) is:

$$\Delta W_2 = \int_{V'}^{V^*} P\,dV = \int_{V'}^{V^*} \frac{nRT(i)}{V}\,dV = nRT(i)\,\ln(V^*/V')$$
$$= [n_0(H_2O) + dn(H_2O) + n(NC)]\,RT(i)\ln(V^*/V')$$

where

R = gas constant,

$n_0(H_2O)$ = moles of water vapor present in the bubble prior to the displacement, and

n(NC) = moles of noncondensible gas in the bubble.

Since, by assumption, the gas is ideal:

$$V^* = \frac{nRT(i)}{P(f)} \text{ and } V' = \frac{nRT(i)}{P(i)}$$

Then,

$$\Delta W_2 = [n_o(H_2O) + dn(H_2O) + n(NC)]\ RT(i)\ \ln[P(i)/P(f)]$$

The total work done in going from the initial to the final state is:

$$\Delta W = \Delta W_1 + \Delta W_2 + \Delta W_3 = dn(H_2O)\ RT(i) + [n_o(H_2O) + n(NC) + dn(H_2O)]\ RT(i)\ \ln\frac{P(i)}{P(f)}$$
$$+ [n_o(H_2O) + n(NC) + dn(H_2O)]\ R(T(f) - T(i))$$

In the limit of small dx:

$$\frac{dW}{dx} = RT\ \frac{dn(H_2O)}{dx} - [n(H_2O) + n(NC)]RT\ \frac{d\ln P}{dx} + [n(H_2O) + n(NC)]R\ \frac{dT}{dx}$$

The change in the internal energy of an ideal gas is just a function of temperature. Therefore, the internal energy change in going from the initial to the final state is:

$$\frac{dU}{dx} = n(H_2O)\ C_v(H_2O)\frac{dT}{dx} + n(NC)C_v(NC)\frac{dT}{dx} + \left[L + \int_{T(ref)}^{T} C_v(H_2O)dT\right]\frac{dn(H_2O)}{dx}$$

where

$C_v(i)$ = constant volume heat capacity of species i, and

T(ref) = reference temperature for the internal energy

The heat input to the bubble during a differential displacement is given by:

$$\frac{dQ}{dx} = \frac{dU}{dx} + \frac{dW}{dx} = [n(H_2O)C_p(H_2O) + n(NC)C_p(NC)]\ \frac{dT}{dx}$$
$$- [n(H_2O) + n(NC)]\ RT\ \frac{d\ln P}{dx} + \left[L + \int_{T(ref)}^{T} C_v(H_2O)\ dT + RT\right]\frac{dn(H_2O)}{dx}$$

where use has been made in deriving the above result of the relationship between the constant pressure heat capacity, $C_p(i)$, and the constant volume heat capacity, $C_v(i)$:

$$C_p(i) = C_v(i) + R$$

The differential equation above, along with the assumption that noncondensible gases neither dissolve in the water or vaporize from water into the bubble:

$$\frac{dn(NC)}{dx} = 0$$

define constraints on variations of the thermodynamic variables of the system. Phenomenological descriptions of any three of the derivatives of the thermodynamic variables allows the fourth to be determined.

As the ambient conditions change, the system will respond in a way that minimizes changes to the system. Thus, a reduction in pressure will cause the bubble to expand. To minimize this expansion, the gas will attempt to cool. If heat is supplied, this cooling will be limited and water vapor will evaporate into the bubble.

The flux of water vapor into the bubble is, of course, of interest because it will constitute a flow that opposes particle deposition. On the other hand, if water vapor condenses on the bubble wall, it provides a flow that will enhance particle deposition. The magnitude and direction of the flow can be found by evaluating the above differential expression. The change in pressure associated with bubble rise is found from:

$$\frac{1}{P}\frac{dP}{dx} = -\rho_l g\, \xi / P = \frac{d\ln P}{dx}$$

where ξ is a constant to correct units (1013250 g/cm-s^2 = 1 atmosphere). If transfer processes within the bubble are very fast, then the heat supplied to the bubble is:

$$\frac{dQ}{dx} = h(x)\pi D^2(\text{bubble})[T(\infty) - T]$$

where h(x) is an external heat transfer coefficient discussed below (see Section IV-I).

The rate of vaporization of water into the bubble must be sufficient to keep the bubble atmosphere at saturation. From the ideal gas equation of state:

$$\frac{P n(H_2O)}{n(NC) + n(H_2O)} = P(sat)$$

where the saturation partial pressure of water vapor, P(sat), is strictly a function of temperature. Near 373 K, the functional dependence of P(sat) on temperature is approximately,

$$\ln P(sat) = 13.3349 - 4976.65/T(K)$$

when P(sat) is in units of atmospheres.*

Then,

$$\frac{dn(H_2O)}{dx} = \frac{4976.65\ nP(sat)}{T^2\ (P - P(sat))}\ \frac{dT}{dx} - \frac{n(H_2O)}{P - P(sat)}\ \frac{dP}{dx}$$

and

$$\frac{dQ}{dx} + \frac{dP}{dx}\left[\frac{nRT}{P} + \frac{n(H_2O)L}{P - P(sat)}\right] = \left[n(H_2O)C_p(H_2O) + n(NC)C_p(NC) + \frac{4976.65\,nP(sat)L}{T^2(P - P(sat))}\right]\frac{dT}{dx}$$

where $n = n(H_2O) + n(NC)$.

Inspection of these equations shows that if heat is not supplied to the bubble, the bubble cools as it rises through the pool. If the cooling rate is rapid enough, water vapor will condense on the bubble surface. Convective heating of the bubble can slow the cooling and cause water vapor to evaporate into the bubble.

Results of an example calculation for a steam-hydrogen bubble in a 400-cm-deep pool of water at 373 K are shown in Figure 48. The initial bubble size was taken to be 0.5 cm. Growth of the bubble as it rises is quite small initially. Only in the last 100 cm or so is there an easily measured increase in the bubble diameter. For this example calculation, the convective heat transfer coefficient was taken to be given by:

*More accurate expressions for the saturation vapor pressure of water are described later in the chapter.

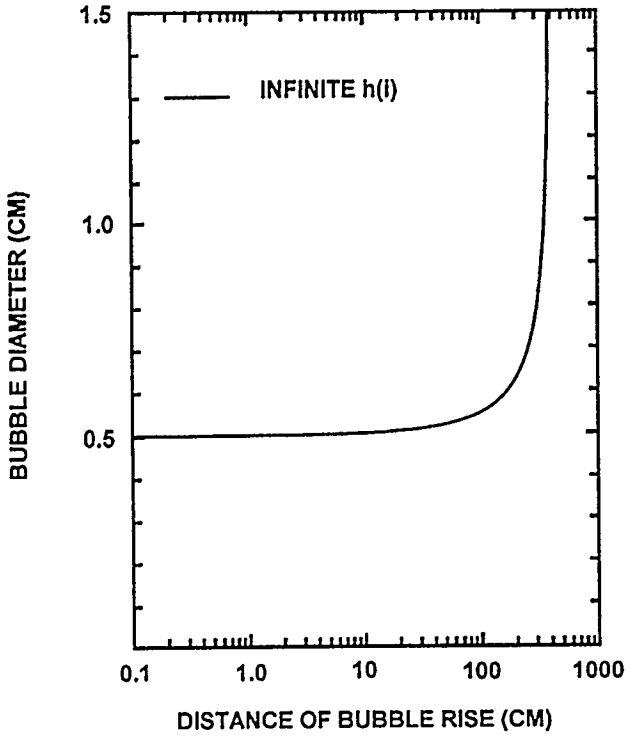

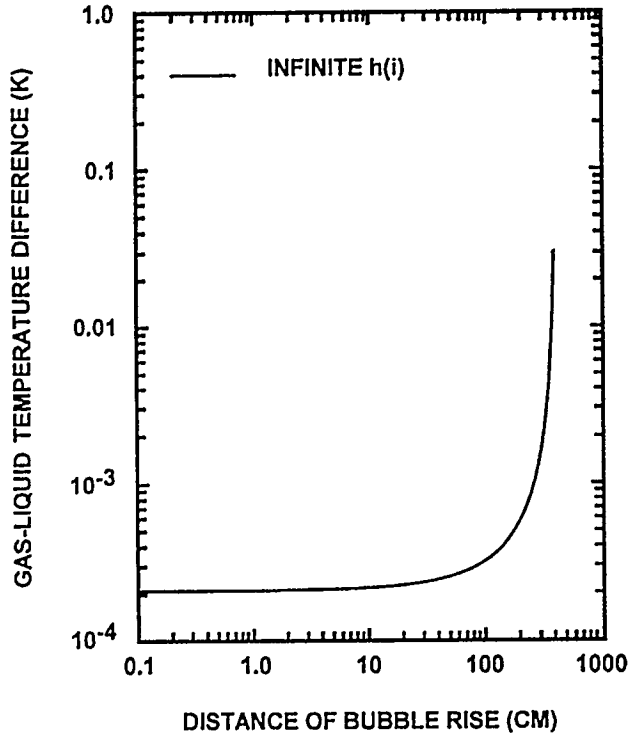

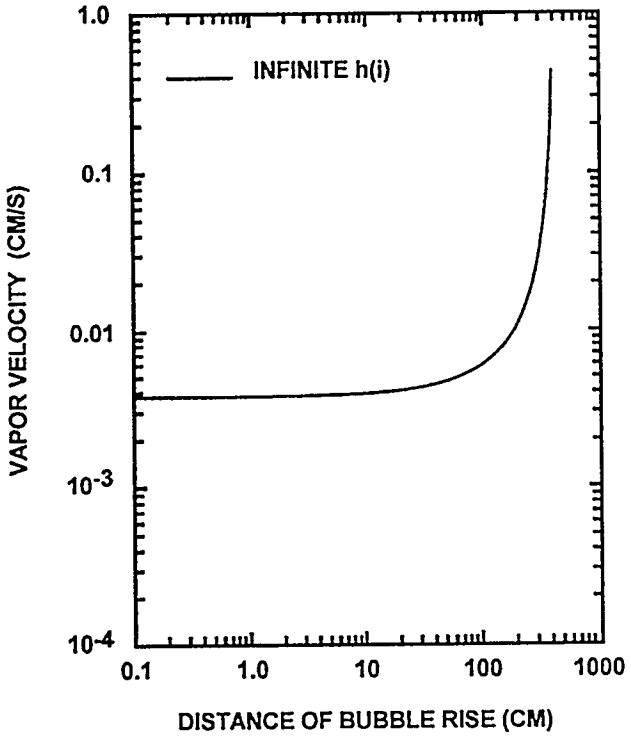

Figure 48. Thermodynamic calculation of bubble rise in a water pool. For this calculation T_{pool} = 373.15 K, H = 400 cm and the heat transfer within the bubble is assumed to be infinitely fast.

$$Nu = h(x)D_B/k_{th}(l) = 1.13\sqrt{Pe}$$

where

Nu = Nusselt number,

h(x) = external heat transfer coefficient,

$k_{th}(l)$ = thermal conductivity of water,

$$Pe = \text{Peclet number} = \frac{U(\text{bubble})\ D_B\ \rho_l C_p(l)}{k_{th}(l)}$$

U(bubble) = rise velocity of the bubble, and

$C_p(l)$ = heat capacity of water.

Heat transfer to rising bubbles is discussed further below (see Section IV-I).

The velocity of water vapor coming off the bubble walls varies between 10^{-3} and 0.1 cm/s. This vapor velocity is comparable to aerosol deposition velocities discussed below and should retard deposition processes.

The temperature differences between the bulk pool and the bubble surface are always quite small. For this example calculation, heat transfer within the bubble has been assumed to be infinitely rapid. There is, then, no thermophoretic force on particles that might be present.

Incorporation of finite rates of mass and heat transfer within the bubble requires that a distinction be made between the surface temperature of the bubble, T(s), and the temperature of the bulk gas in the bubble, T. The surface temperature of the bubble is found by assuming a quasi-steady state exists. Then,

$$h(x)[T_p - T(s)] = \frac{k_m L}{R}\left[\frac{P(sat)}{T(s)} - \frac{Pn(H_2O)}{nT}\right] + h(i)\ [T(s) - T]$$

where

k_m = mass transfer coefficient for steam in the bubble,

L = molar latent heat of water vaporization,

P = pressure including the hydrostatic pressure, and

h(i) = internal heat transfer coefficient.

Results of an example calculation similar to that discussed above are shown as solid lines in Figure 49. Also shown in Figure 49, as dashed lines, are results for the calculation with infinitely fast transfer processes within the bubble. Mass and heat transfer coefficients for the example calculation were obtained from the Kronig-Brink equation which is discussed further below. This model assumes that the gases in the bubble are well mixed.

In comparison to the results for infinitely fast internal processes, the vapor velocities from the bubble walls are somewhat lower and thus a lower diffusiophoretic resistance to aerosol deposition. On the other hand, there is a difference between the surface temperature of the bubble and the bulk gas in the bubble so there is a predicted potential for thermophoretic resistance to aerosol deposition on the bubble walls. This thermophoretic force is, however, not very large.

E. Bubble Plumes From Quenchers

Most of the detailed information on bubble behavior has been derived from experiments in which there were elaborate efforts to generate single, well-isolated bubbles. Quenchers and vents in suppression pools will, instead, generate swarms of bubbles. Wakes created by bubbles will affect the behaviors of succeeding bubbles. Perhaps the most important effect of bubble swarms is that they entrain liquid. Because the points of bubble generation are localized within the pool, the entrainment of liquid can have a profound effect on bubble behavior. (Note that this entrainment effect does not arise in such a dramatic fashion in the case of water pools overlying core debris where bubble generation takes place over the entire base of the pool.) Coupling of bubble and liquid motion creates an expanding plume. Bubbles within the plume rise faster than do isolated bubbles because their velocities are augmented by the velocity of the entrained water. Because the bubbles rise more rapidly to the pool surface, there is less opportunity to remove aerosols from the bubble than there is for aerosol removal from isolated bubbles. As discussed at length below, there is a distribution of bubble concentrations and velocities across a plume so that aerosol removal will not be the same for every bubble.

Bubble plumes present some interesting complexities. Significant approximations will be made in the description of bubble plumes adopted here. Plumes will be represented as coming from a point source. In the case of quenchers, the entire arm of a quencher, which may have several hundred orifices, will be treated as a single source. The effect of the submerged pipe will be neglected for bubble plumes created by downcomers. The effects of the weir wall will be neglected in the treatment of bubble plumes from horizontal vents. In all of the analyses, the water pool will be considered infinite in extent. That is, the boundaries of the pool and the presence of other plumes will be assumed to have negligible effects on the quantities of interest.

The description of bubble plumes will follow the integral representations developed by Milgram [44], Tacke et al. [45], Chester et al. [265] and by Sahai and Guthrie [266]. These developments do not treat the condensation and evaporation of water. Analyses of the thermodynamics of bubble rise (Section IV-D, above) suggest that condensation and evaporation ought not affect bubble behavior too much except near the surface. Except for the effect of evaporation of water vapor into the bubble on the momentum equation and the gas continuity equation, condensation and evaporation effects on plume

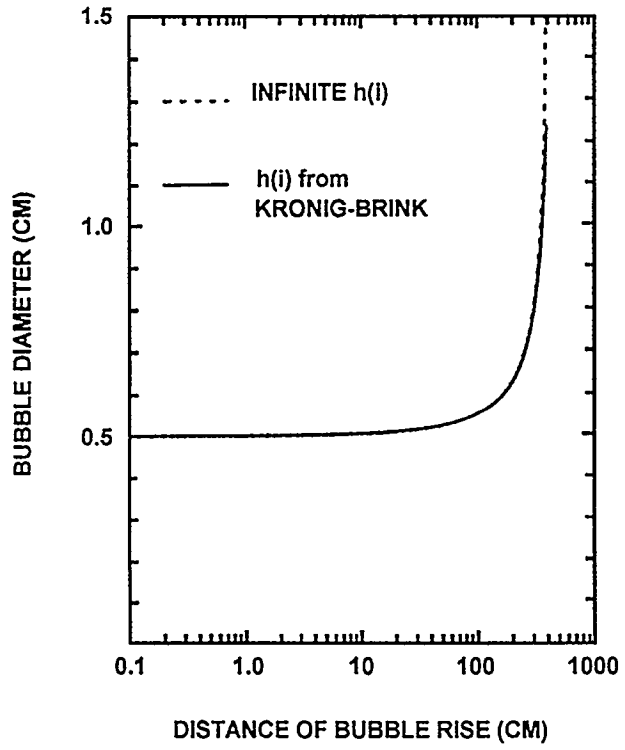

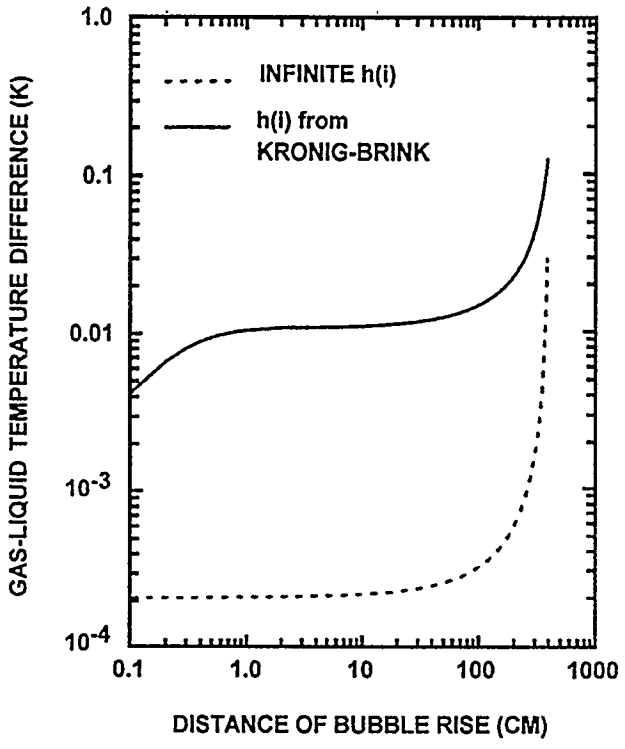

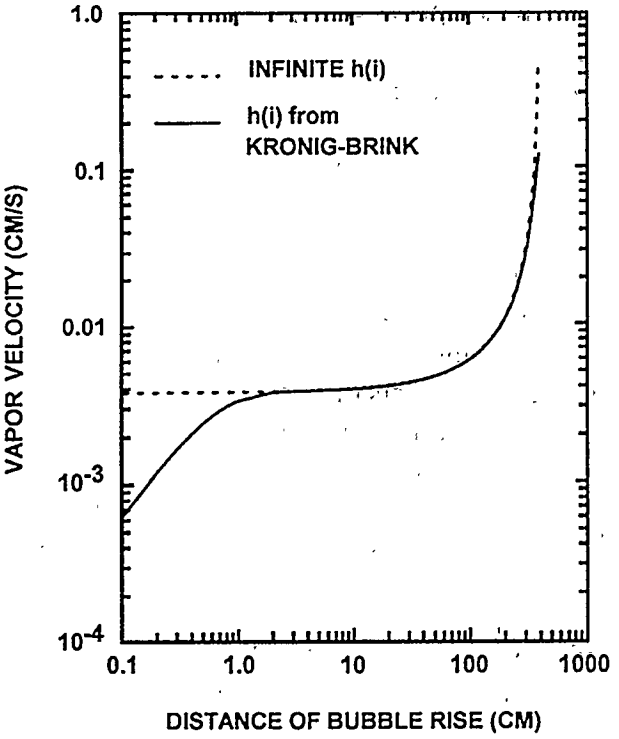

Figure 49. Results of bubble rise calculation considering finite rates of heat and mass transport within the bubble (solid lines). Dashed lines are results obtained assuming infinitely fast transport processes within the bubble.

behavior will be ignored here. More detailed, differential descriptions of bubble plumes to be found in References 46 to 50 would more easily accommodate detailed treatments of condensation and evaporation than the integral approach used here.

A suppression pool can develop unstable density stratification. Heat is imparted to the pool at a water depth which produces a significant pressure head. The pool surface temperature is limited by the boiling point at the ambient atmospheric pressure. It is possible, then, for a temperature gradient and, consequently, a water density gradient to develop. The stratification of the pool with more dense water on top is unstable. Flow that can develop to relieve this instability can greatly complicate the behavior of plumes [51,52] (see Figure 50). No attempt is made here to account for such effects.

The objective of the analysis of bubble plumes here is to determine the velocities of water and bubbles across the plume and the concentration of bubbles across the plume. A variety of experimental studies including experiments by Paul et al. [30], Tacke et al. [45] as well as studies cited by Milgram [44] suggest that the water at a specified elevation in the plume, z, will have a Gaussian velocity distribution:

$$U_l(r,z) = U_l(z)\ \exp[-(r/b(z))^2]$$

where

r = radial coordinate

z = axial coordinate

$U_l(r,z)$ = upward water velocity at point r, z,

$U_l(z)$ = upward velocity along the plume centerline, and

$b(z)$ = distribution parameter that varies with z.

Bubble velocities are then given by:

$$U_g(r,z) = U_l(r,z) + U(slip)$$

where U(slip) is the slip velocity which is related to the rise velocity of isolated bubbles, U_B (see below and Section IV-G).

It is, then, assumed that the gas fraction in the liquid at a given elevation also has a Gaussian distribution:

$$\epsilon(r,z) = \epsilon(z)\ \exp[-(r/b_\epsilon(z))^2]$$

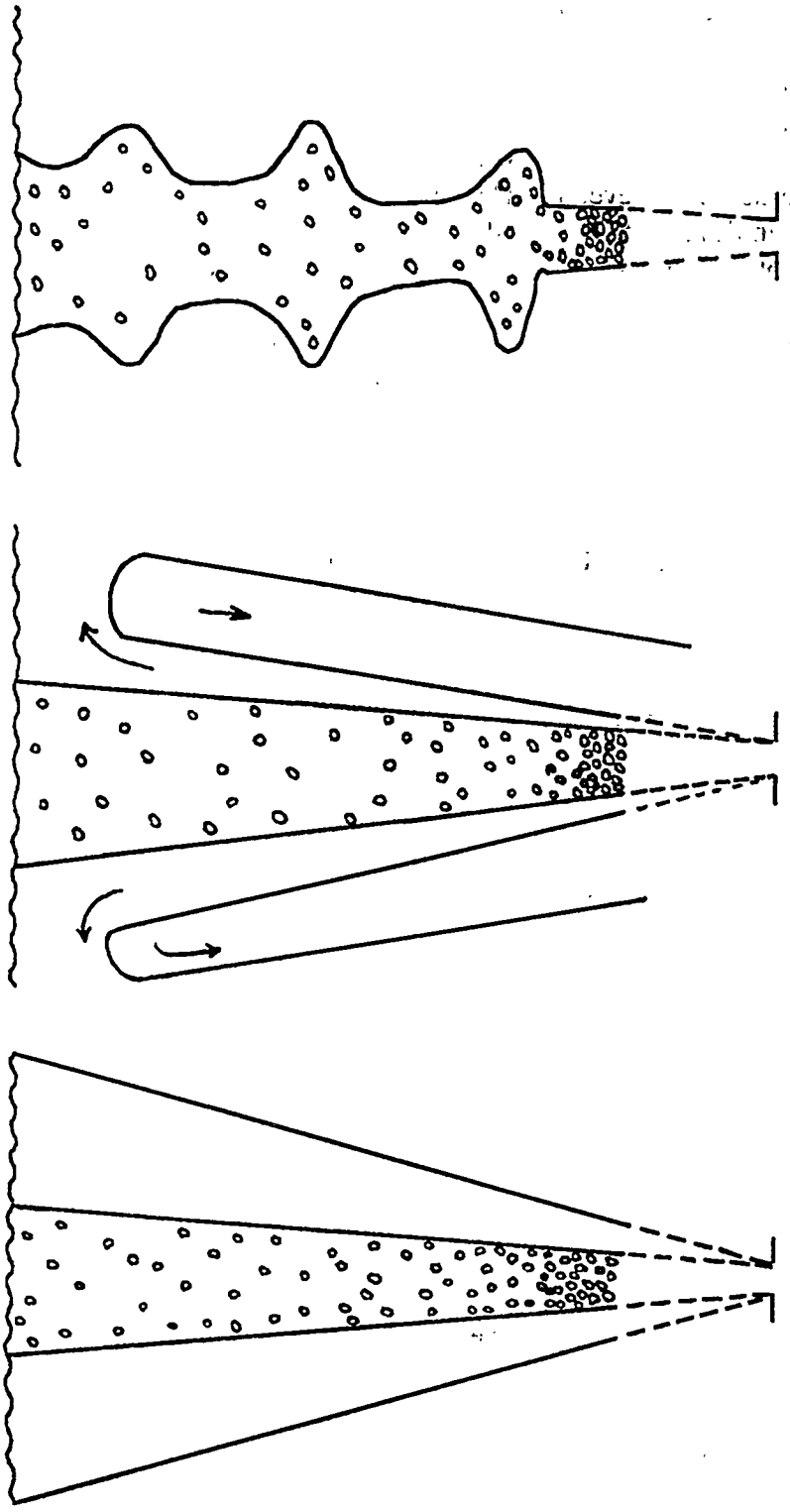

Figure 50. Schematic diagrams of bubble plumes: (a) simple plume, (b) plume with descending outer annulus and (c) plume with instability intrusions produced by unstable density stratification

where $\epsilon(r,z)$ is the gas fraction at point r, z. The distribution parameter $b_\epsilon(z)$ is not necessarily the same as the distribution parameter for water velocity. But, an additional assumption is made that the two parameters are related by

$$b_\epsilon(z)/b(z) = \lambda$$

where λ is independent of elevation. Milgram [44] takes λ to be 0.8, Tacke et al. [45] assume λ = 0.7. Sun and Faeth [47] present results of numerical calculations that indicate λ may be as high as 0.96.

The unknown quantities, centerline velocity, u(z), centerline gas fraction, $\epsilon(z)$, and the water velocity distribution parameter, b(z), are found by integrating the gas continuity equation, the water continuity equation and the momentum equation.

The gas continuity equation is:

$$Q(z) = 2\pi \int_0^\infty U_g(r,z)\ \epsilon(r,z) r\, dr$$

where Q(z) is the volumetric gas flow. If evaporation is negligible, Q(z) varies with elevation:

$$Q(z) = \frac{Q_T\ (P_a + \xi\rho_l H)}{P_a + \xi\rho_l (H - z)}$$

where

P_a = ambient pressure (atms),

H = pool depth (cm)

ρ_l = water density (g/cm^3),

ξ = parameter to correct units = 1/1033.23, and

Q_T = input volumetric flow to the plume.

Here, the input volumetric flow to the plume is not the flow from the gas source. For the calculations of interest here, Q_T is the gas left after the dynamic events of bubble formation, collapse and coalescence.

To account for evaporation of water vapor into the bubbles as they rise through the pool, it is assumed that the bubble is always in local equilibrium. Then,

$$Q(z) = Q_T \left\{ \frac{P_a + \rho_l H \xi - P(sat)}{P_a + \rho_l (H - z) \xi - P(sat)} \right\}$$

where P(sat) is the saturation partial pressure at the bulk pool temperature which is taken to be invariant throughout the plume. This simplified description is used here to make derivations more transparent. In the model described in Chapter V, the gas flux is calculated from the thermodynamic description presented in the previous subsection.

Integration of the gas continuity equation yields:

$$Q(z) = \pi \lambda^2 b^2(z) \epsilon(z) \left[\frac{U_l(z)}{1 + \lambda^2} + U_B f \right]$$

where

$$f = \begin{cases} 1 & \text{for } U(slip) = U_B \\ 1 - \epsilon(z)/2 & \text{for } U(slip) = U_B(1 - \epsilon(r,z)) \\ 1 - \epsilon(z) + \epsilon(z)^2/3 & \text{for } U(slip) = U_B(1 - \epsilon(r,z))^2 \end{cases}$$

U_B = rise velocity of an isolated bubble of the same size, and

U(slip) = slip velocity of bubbles in the plume.

Note that three, relatively simple, descriptions of two phase flow have been considered here in the definition of f. These are the descriptions considered by Tacke et al. [45]. Other descriptions exist [51].

The liquid continuity equation is formulated assuming that liquid is entrained by rising bubbles:

$$\frac{d}{dz} \int_0^\infty [1 - \epsilon(r,z)] \, U_l(r,z) r dr = 2\pi b(z) \alpha U_l(z) k(z)$$

where

α = entrainment coefficient, and

k(z) = factor to correct for gas concentration in the entraining liquid.

Milgram [44] takes:

$$k(z) = 1$$

Tacke et al. [45] take:

$$k(z) = 1 - \epsilon(z) \exp(-1/\lambda^2)$$

The authors of this document prefer:

$$k(z) = 1 - \lambda^2 \epsilon(z)[1 - \exp(-1/\lambda^2)]$$

Then,

$$\frac{d}{dz} U(z) b^2(z) \left[1 - \frac{\epsilon(z)\lambda^2}{1 + \lambda^2} \right] = 2b(z)\alpha U(z) k(z) \quad .$$

Milgram [44] develops the momentum equation considering the momentum of the gas as well as the liquid momentum. Tacke et al. [45] neglect the small contribution of gas momentum. Milgram also introduces the momentum amplification factor, γ. Neglect of this momentum amplification factor amounts to treating the plume as though it were a single phase. (Milgram notes that measurements by George et al. [53] indicate that γ may be as large as 1.07 even in single phase plumes.) Momentum amplification is considered here and the momentum equation is taken to be:

$$\frac{d}{dz} 2\pi\gamma \int_0^\infty \left\{ U_l^{\,2}(r,z)\rho_W [1 - \epsilon(r,z)] + U_g^{\,2}(r,z)\rho_g(z)\epsilon(r,z) \right\} rdr =$$

$$= 2\pi g \int_0^\infty [\rho_W - \rho_g(z)] \epsilon(r,z)\, rdr$$

Then, substituting in expressions for liquid and gas velocities yields:

$$\frac{d}{dz}\gamma\left\{ b^2(z)U_l{}^2(z)\left[\frac{\rho_w}{2} - \frac{\lambda^2\epsilon(z)(\rho_w-\rho_g(z))}{2\lambda^2+1}\right] + U_B\lambda^2 b(z)^2\rho_g(z)\epsilon(z)[U_l(z)h(z)+U_B l(z)]\right\} =$$

$$= g[\rho_w-\rho_g(z)]\epsilon(z)\lambda^2 b^2(z)$$

where

$$h(z) = \begin{cases} \dfrac{2}{1+\lambda^2} & \text{for U(slip)} = U_B \\ \dfrac{2}{\lambda^2+1} - \dfrac{2\epsilon(z)}{\lambda^2+2} & \text{for U(slip)} = U_B(1-\epsilon(r,z)) \\ \dfrac{2}{\lambda^2+1} - \dfrac{4\epsilon(z)}{\lambda^2+2} + \dfrac{2\epsilon^2(z)}{\lambda^2+3} & \text{for U(slip)} = U_B(1-\epsilon(r,z))^2 \end{cases}$$

and

$$l(z) = \begin{cases} 1 & \text{for U(slip)} = U_B \\ 1 - \epsilon(z) + \epsilon^2(z)/3 & \text{for U(slip)} = U_B(1-\epsilon(r,z)) \\ 1 - 2\epsilon(z) + 2\epsilon^2(z) - \epsilon^3(z) + \epsilon^4(z)/5 & \text{for U(slip)} = U_B(1-\epsilon(r,z))^2 \end{cases}$$

Milgram [44] correlated the entrainment coefficient, α, with a bubble Froude number, F_B:

$$\alpha = kF_B/(A + F_B)$$

where

$$F_B = \epsilon(z)^{1/3}\, Q(z)^{2/5}\, g^{3/10}\, (\rho_w - \rho_g(z))^{1/2} / \sigma_l{}^{1/2}$$

$k = 0.165$, and

$A = 7.598$

Milgram apparently found the parametric values in the correlation by linear least squares analysis after recasting the correlation in a form that is linear in $1/\alpha$:

$$1/\alpha = \frac{A}{k}\frac{1}{F_B} + 1/k$$

Refitting data digitized from a small plot provided by Milgram yielded the coefficients:

$$\frac{A}{k} = 23.0688 \pm 3.0299$$

$$1/k = 9.379 \pm 0.815$$

or

$$k = 0.1066 \pm 0.0093$$

$$A = 2.460 \pm 0.387$$

These are the parametric values adopted here. (It should be noted that if both the Froude number and the entrainment coefficient are considered uncertain, the existence of a correlation between the two become dubious.)

This linear form of the correlation is shown in comparison to the data used by Milgram in Figure 51.

There is, obviously, some substantial scatter in values of $1/\alpha$ about the regression line. Because the regression line has been determined by linear least-squares methods, the uncertainty in a predicted value of $1/\alpha$ is distributed according to a Student's t distribution. The uncertainty range for a prediction at a confidence level of $100(1 - \beta)$ percent is given by:

$$1/\alpha = 1/\alpha|_{reg} \pm st_{(1-\beta/2)(n-2)} \left\{ \frac{1}{n} + \frac{(x-\bar{x})^2}{\sum_{i=1}^{n} (x(i)-\bar{x})^2} \right\}^{1/2}$$

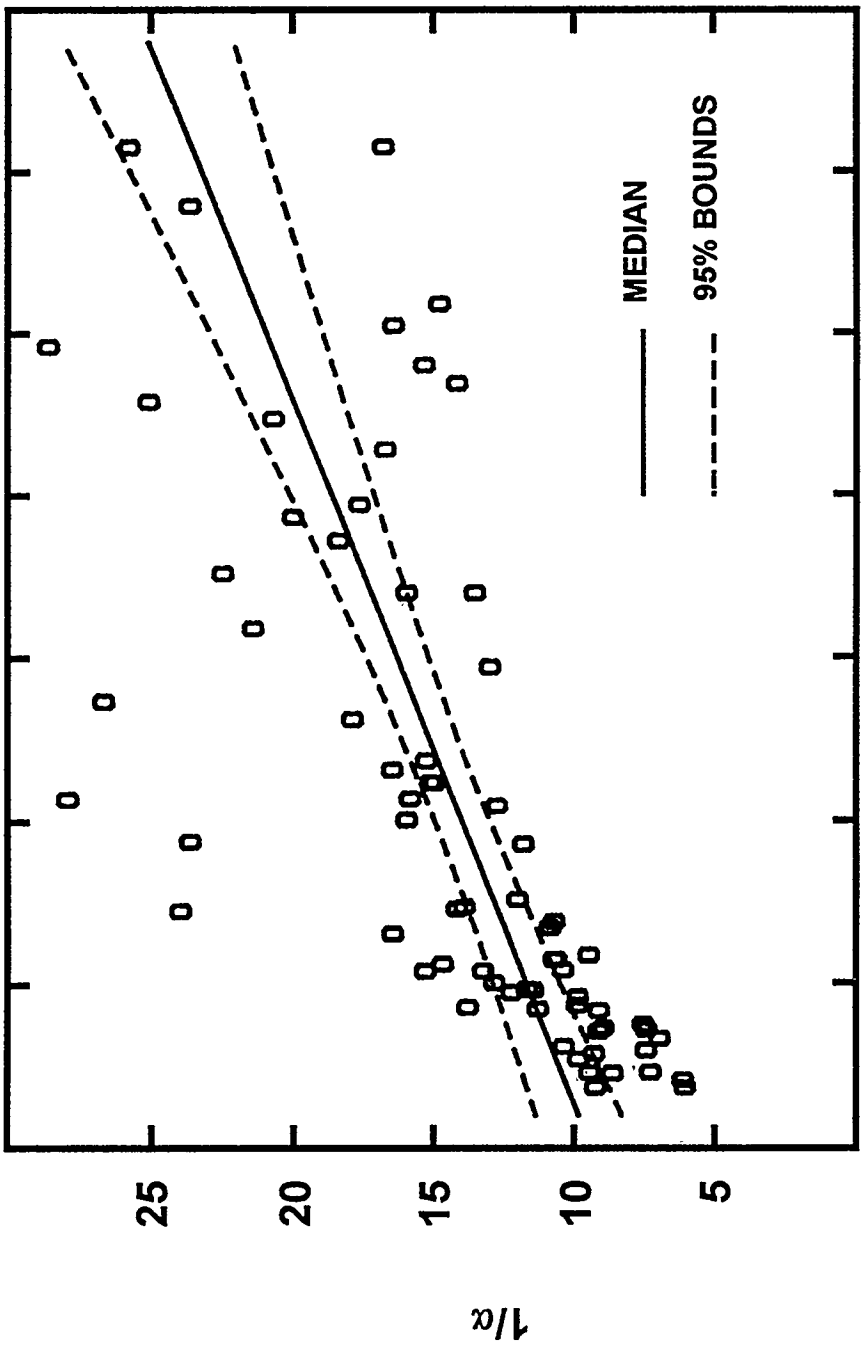

Figure 51. Dependence of the entrainment coefficient on the bubble Froude number

where

$1/\alpha|_{reg}$ = value of $1/\alpha$ calculated from the correlation,

s = standard error in the regression = 4.185

$t_{(1-\beta/2)(n-2)}$ = critical value of the Student's t statistic for n - 2 degrees of freedom at a confidence level of $100(1 - \beta/2)$ percent

n = number of data points used in the regression = 69

x = $1/F_B$ for which the estimate of $1/\alpha$ is sought,

$\overline{x}$ = mean value of $1/F_B$ in the data set, and

x(i) = value of $1/F_B$ for the ith data point.

From data provided by Milgram:

$$\overline{x} = 0.2145$$

$$\sum_{i=1}^{n} [x(i) - \overline{x}]^2 = 1.8474$$

The 95 percent confidence bounds on predictions of $1/\alpha$ from Milgram's correlation are plotted as dashed lines in Figure 51.

Milgram [44] presented correlations of the momentum amplification factor, γ, in terms of the so-called phase distribution number, N_p:

$$\gamma = 1 + C/N_p^{\,a}$$

or

$$\gamma = 1.07 + C'/N_p^{\,a'}$$

where

$$N_p = \frac{U(z)^2 \, (\rho_w - \rho_g)^{1/2}}{\epsilon(z)^{2/3} \sqrt{g \sigma_l}} \quad , \text{ and}$$

a, c, c′, a′ = parameters.

Milgram contends that the lower bound on the momentum amplification factor is 1.0 or perhaps 1.07. He shows, however, values derived by modeling experiments that are less than 1.0. Ignoring these values, the correlation can be parameterized by linear, least-squares methods when recast in the form:

$$\ln (\gamma - 1) = \ln C - D \ln Np$$

where

$$\ln C = 5.216 \pm 0.835, \text{ and}$$

$$D = -1.0895 \pm 0.1402.$$

Uncertainties in ln (γ - 1) predicted with this correlation can be found at the 100(1 - β) percent confidence level from:

$$\ln(\gamma-1) = \ln(\gamma-1)\,|_{reg} \pm 0.837 t_{(1-\beta/2)(45)} \left\{ \frac{1}{47} + \frac{(x-5.891)^2}{35.615} \right\}^{1/2}$$

where

$\ln (\gamma-1)|_{reg}$ = value of ln (γ-1) found from the correlation,

$t_{1-\beta/2(45)}$ = critical Student's t statistic for 45 degrees of freedom at the 100(1 - β/2) percent confidence level, and

$x = \ln N_p$.

The predicted values of γ derived from the correlation, the 95 percent confidence bounds on these predictions, and data presented by Milgram are plotted against the phase distribution number in Figure 52.

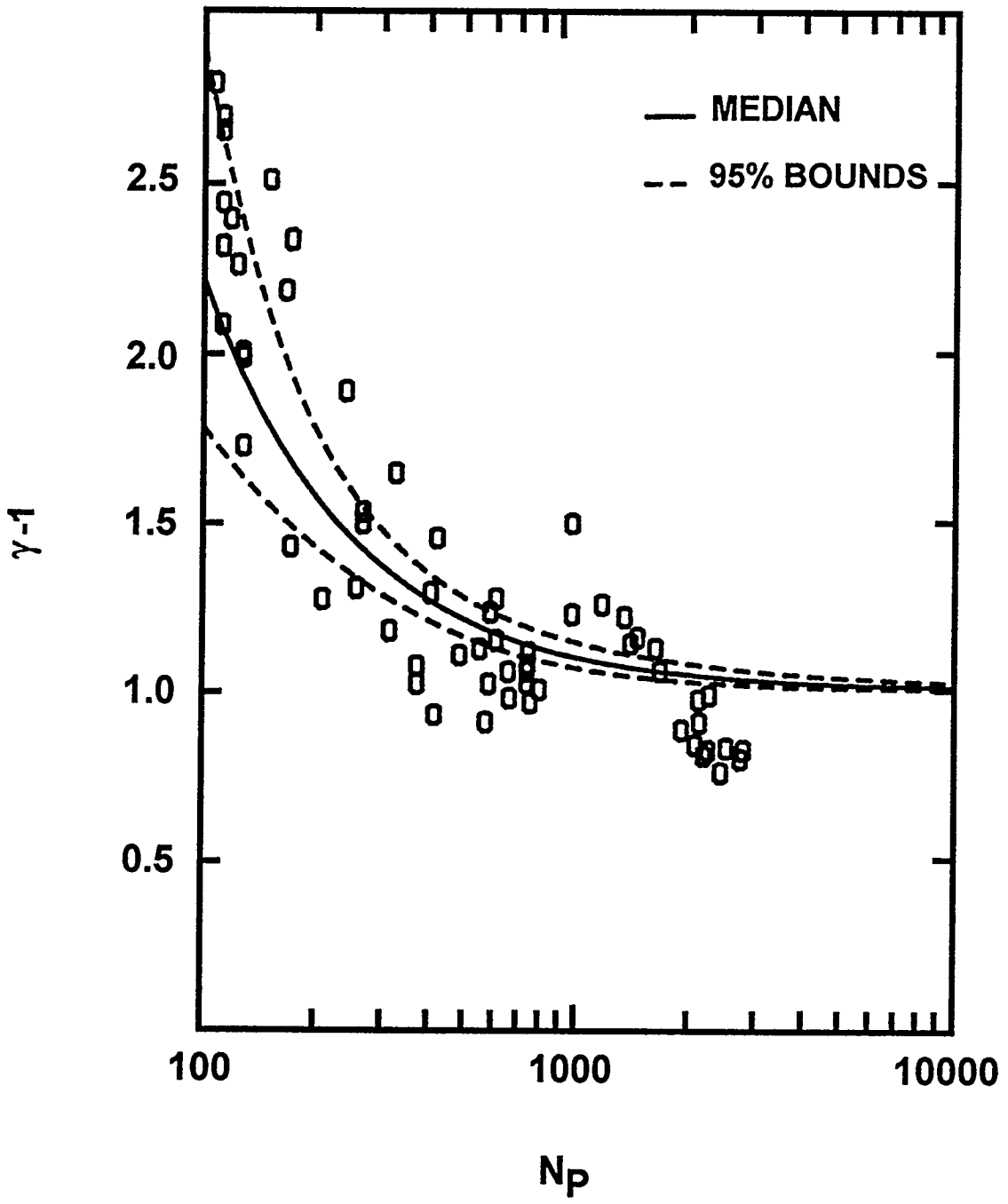

Figure 52. Dependence of the momentum amplification factor on the phase distribution number

A final issue to confront is the definition of initial conditions for the two differential equations described above. It is clear that the Gaussion profiles for liquid velocity and for gas fraction used in the development above do not apply in the immediate vicinity of the gas source. In the situations of interest here, a lot of dynamic activity takes place before the plume develops. Milgram [44] recommends that initial conditions be defined at an elevation Z(E) given by:

$$Z(E) = \min \begin{cases} 5\ D_o \\ 10\ U_o \left[\frac{D_o}{g}\right]^{1/2} \left[\frac{\rho_g(o)}{\rho_w}\right]^{0.75} \end{cases}$$

where

D_o = orifice diameter,

U_o = gas velocity through the orifice, and

$\rho_g(o)$ = gas density at the orifice.

For the analysis here, the values of U_o and $\rho_g(o)$ should be taken as the hypothetical values that would exist if no condensation of water vapor took place during the formation and initial rise of gas bubbles. The distance 5 D_o suggested by Milgram is, of course, reminiscent of observations made by Paul et al. [30]. They observed that bubble breakup was complete in a few initial bubble diameters. Following Milgram's suggestion, the plume model equation would apply to within about 10 cm of the orifices in quenchers. The equations would apply very close to downcomers and vents according to Milgram. But, observations by Paul et al. [30] and by Lee and Chan [40] suggest plume equations might not be appropriate for several tens of centimeters from the large vents.

The initial conditions specified by Milgram are:

$$\epsilon(z(E)) = 0.5\rho_w / [\rho_w - \rho_g(z(E))]$$

$$\text{Momentum} = Q\rho_g(H)U_o + \frac{2Q}{U_o}\,[\rho_w - \rho_g(z(E/2))]\,g\,z(E)$$

Milgram notes that initial conditions do not strongly affect calculated results.

Tacke et al. [45] recommend that the initial state be taken as $\epsilon(z) = 0.5$. They then define

$$\frac{z(E)}{D_o} = 5.0 \left[\frac{Q_T^2 \rho_g(o)}{g D_o^5 \rho_w} \right]^{0.5}$$

$$\lambda b(z(E)) = 0.5045 \left[\frac{Q_T^2}{D_o^5 g} \right]^{1/5}$$

$$\epsilon(z) = 50 \left[0.2 \frac{z(E)}{D_o} \left[g \frac{D_o^5 \rho_w}{Q_T^2 \rho_g(o)} \right] \right]^{\psi}$$

where ψ depends on the ratio ρ_g/ρ_w:

$$\psi = \begin{cases} 0.866 & \text{for He in water} \\ 1.22 & \text{for } N_2 \text{ or air in water} \end{cases}$$

This suggests:

$$\psi = 0.807 + 360\ \rho_g/\rho_w$$

McDougall [54] recommends:

$$z(E) = 0.025\ H'$$

$$\frac{U_l(z(E))}{U_B\ M^{1/3}} = x^{-1/3} \left[1.609 - \frac{0.3195}{M^{1/3}} x^{1/3} + 0.06693\ (x/M)^{2/3} + x(0.4536 - 0.0105/M) \right]$$

$$\frac{b(z(E))}{2\alpha H'} = x\left[0.6 + 0.01719(x/M)^{1/3} - 0.002527\,(x/M)^{2/3} + x\left[\frac{0.000031}{M} - 0.04609\right]\right]$$

where

$$X = z/H'$$

$$M = \frac{Q_T P_a(\lambda^2 + 1)\xi}{4\pi\alpha^2\rho_w H^2 U_B^3}$$

$$H' = H + P/\rho_l g$$

None of the initial conditions models is particularly satisfactory. Here Milgram's suggestions are adopted for the example calculations. These suggestions are not, however, applicable to cases involving substantial vapor condensation which can occur in steam suppression pools. Alternate initial conditions for such cases are discussed in Chapter V.

Predictions of the plume model compared with data obtained by Milgram [44] for large and small flows through a 5-cm vent in a natural pool 5000 cm deep are shown in Figures 53 and 54. Predictions shown in these figures were based on the assumption that the gas bubbles were, initially, 0.5 cm in diameter. Bubble slip velocities were taken to be equal to the rise velocity of an isolated bubble which was calculated from the correlation described above (see Section IV-G). The parameter λ was taken to be 0.8. Milgram has shown that model predictions are not very sensitive to this parameter. Calculated results shown in the figures as solid lines were obtained using Milgram's correlations to calculate the entrainment coefficient, α, and the momentum amplification factor, γ, at local conditions. Agreement between calculated and observed quantities is good on an overall basis. Agreement can be improved by using selected average values of α and γ that are independent of elevation of the plume. Such calculated results are shown as dashed lines in Figure 53.

Model predictions of the void fraction along the centerline of a small-scale plume are compared in Figure 55 to data obtained by Tacke et al [45]. These data were obtained using air flow through a 0.05-cm vent in a 60-cm- deep pool. Calculations using Milgram's correlation for the entrainment coefficient α agree only qualitatively with the test data regardless of the value of λ in the range from $\lambda = 0.7$ (recommended by Tacke et al.) to $\lambda = 0.9$ (recommended by Milgram). Increasing the entrainment coefficient to $\alpha = 0.1$ independent of elevation in the plume yields quantitatively accurate predictions of the centerline void fraction. Tacke et al. note that there is a great deal of uncertainty in the entrainment coefficient and recommend overall average values in preference to Milgram's correlation.

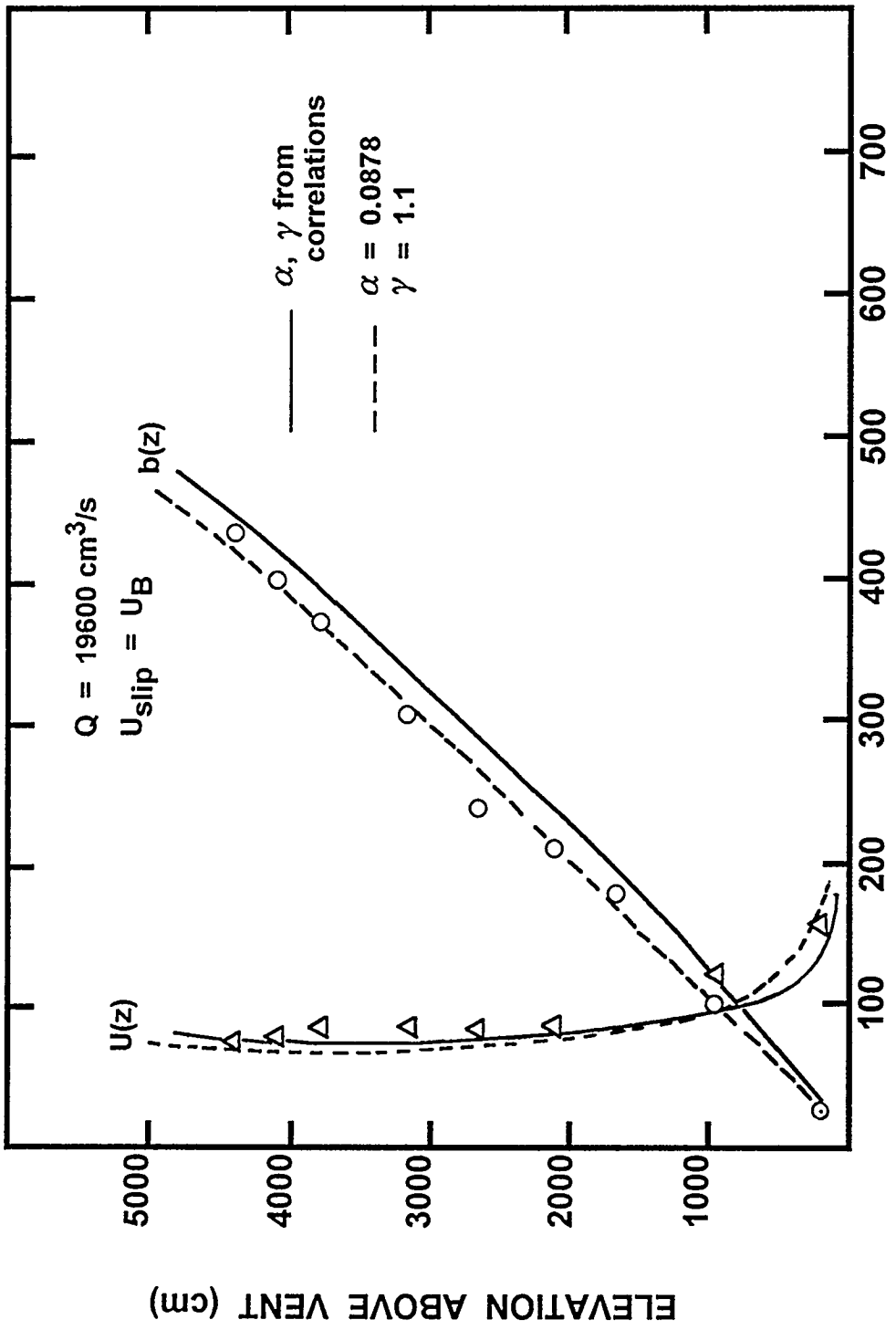

Figure 53. Comparison of plume model predictions to data obtained by Milgram [44] in a pool ~ 5000 cm deep with Q = 19600 cm^3/s at the vent. Calculated results are shown for two ways of calculating the entrainment coefficient as described in the text.

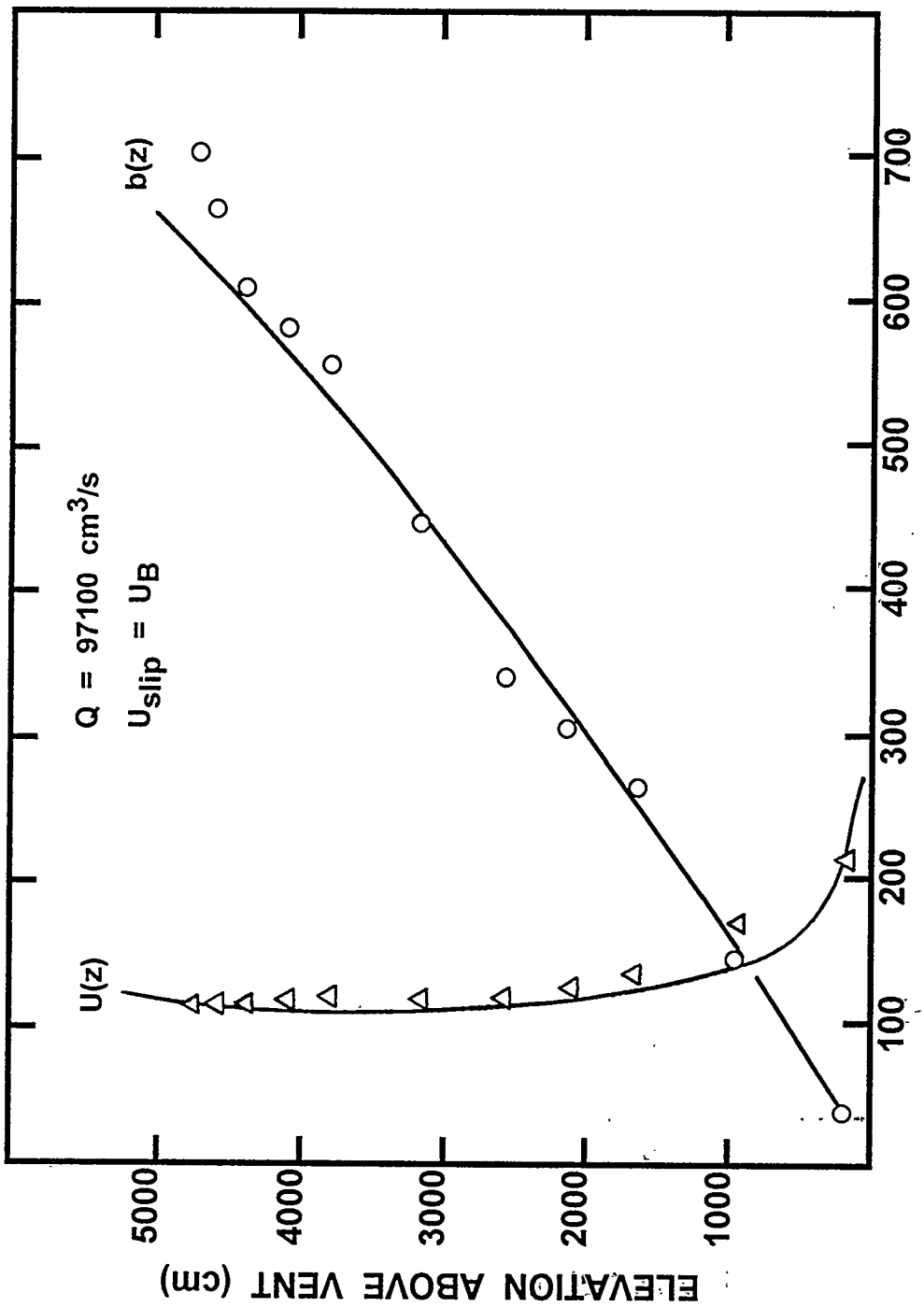

Figure 54. Comparison of predictions of the plume model to data obtained by Milgram [44] in a pool ~ 5000 cm deep with $Q \approx 97100$ cm^3/s. Calculations are shown for two values of the entrainment coefficient as described in the text.

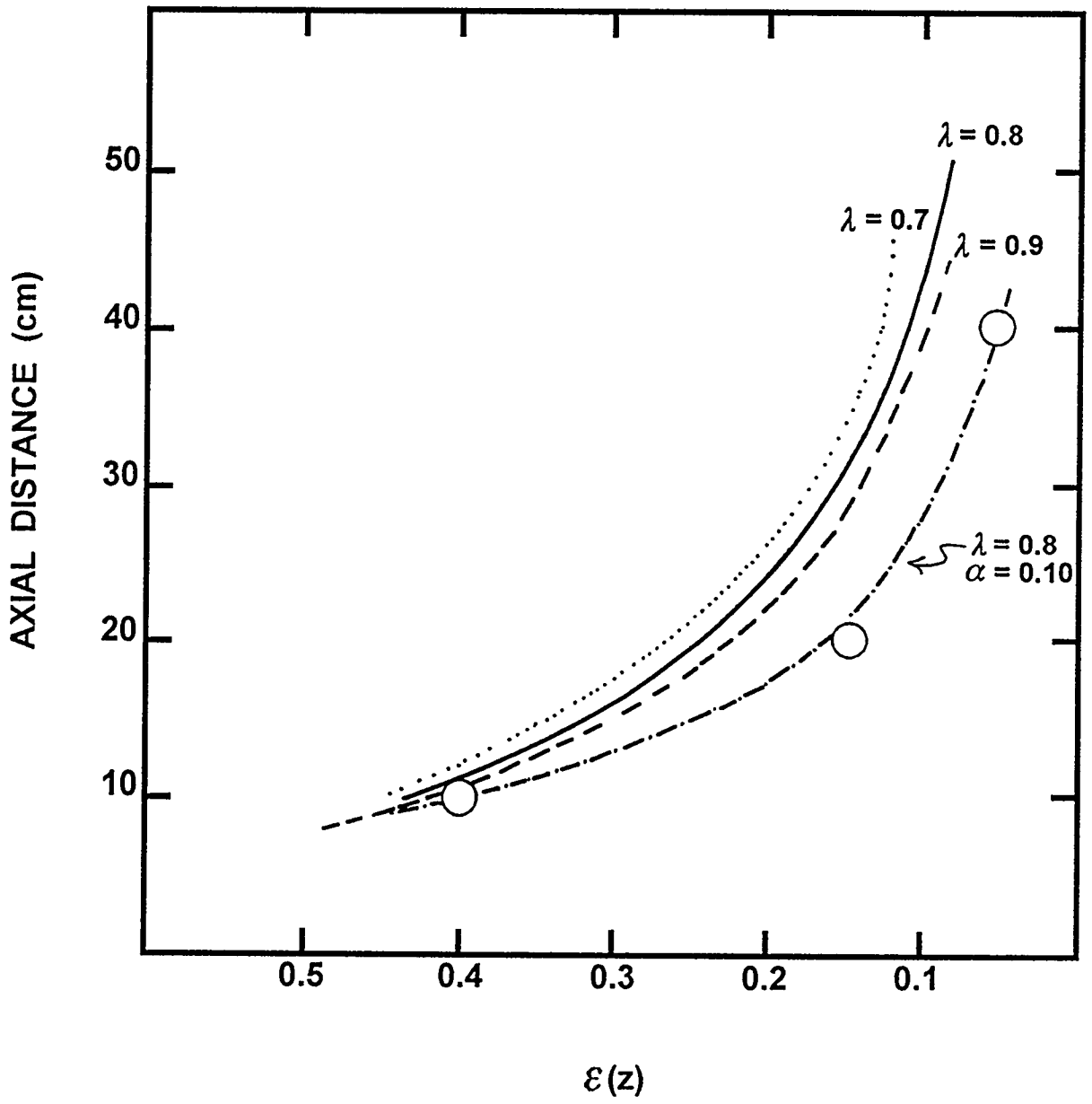

Figure 55. Comparison of model predictions to centerline void fractions observed in experiments by Tacke et al. [45]. Results calculated with various values of λ and the entrainment coefficient calculated from Milgram's correlation are shown. Also shown are results calculated with entrainment coefficient fixed at 0.1.

Predicted bubble rise velocities as functions of radial distance at various elevations in plumes produced by large and small flows in tests by Paul et al. [30] are shown in Figures 56 and 57. These predictions were obtained using various values of the momentum amplification factor that were independent of elevation. The entrainment coefficient was calculated using local conditions in the plume and Milgram's correlation.

Tacke et al. [45] and other investigators have obtained data that suggest that bubble plumes conform quite closely to the exponential structure assumed above in the development of the plume model. The experimental results for bubble rise velocities obtained by Paul et al. [30] suggest this exponential model of the plume structure is only an approximation. These data suggest the plume might be more accurately portrayed as consisting of a central core with nearly constant properties surrounded by a peripheral region with exponentially distributed properties. Nevertheless, it is evident that reasonably good comparisons to data can be obtained by suitable variations in the momentum amplification factor. Comparisons in Figure 58 show that using elevation independent values of the entrainment coefficient rather than local entrainment coefficients provides additional flexibility in matching predicted and observed values of the bubble rise velocity.

Some caution should be exercised in drawing conclusions from the comparison of predicted and observed bubble rise velocities shown in Figures 56 through 58. The predictions were prepared assuming that bubbles were uniformly 0.5 cm in diameter. Paul et al. have shown that bubble sizes are approximately lognormally distributed in size. Some of the variability between predicted and observed rise velocities may come from distributions of the bubble sizes in experiments.

It is evident that bubbles in a plume rise much more rapidly than isolated bubbles (rise velocities of isolated bubbles considered in preparing predictions shown in Figures 56 through 58 would be about 24 cm/s). The more rapid rise velocities shorten the time available for scrubbing aerosols from the bubbles. Because there is a distribution of rise velocities across a plume, there will, presumably, be a distribution of aerosol removal efficiencies across the plume.

Three essential parameters arise in the characterization of the bubble rise velocities in the plume, λ, γ, and α. The parameter λ is not especially influential. It can be directly determined in experiments and apparently is widely accepted as being in the range of 0.7 to 1.0. The parameters γ and α are influential and cannot be directly measured. These parameters are found from experimental data by calculation, but such calculation yield results depend on other assumptions in the plume model. They do seem to vary with flow and pool depth, but there are not sufficient data to produce reliable correlations of these parameters. The momentum amplification factor is particularly mysterious. Many investigators of plume behavior seem to neglect it. It does, however, have a theoretical basis and provides the flexibility in models to match experimental data.

F. Overview of Bubble Behavior

The behaviors of individual bubbles enter into the descriptions of bubble swarms and plumes. The features of bubble behavior of interest include rise velocity, which is affected by both bubble size and shape, as well as heat and mass transport coefficients that can be ascribed to bubbles. It is convenient to categorize bubble behavior into regimes based on the dimensionless Eotvos and Morton numbers:

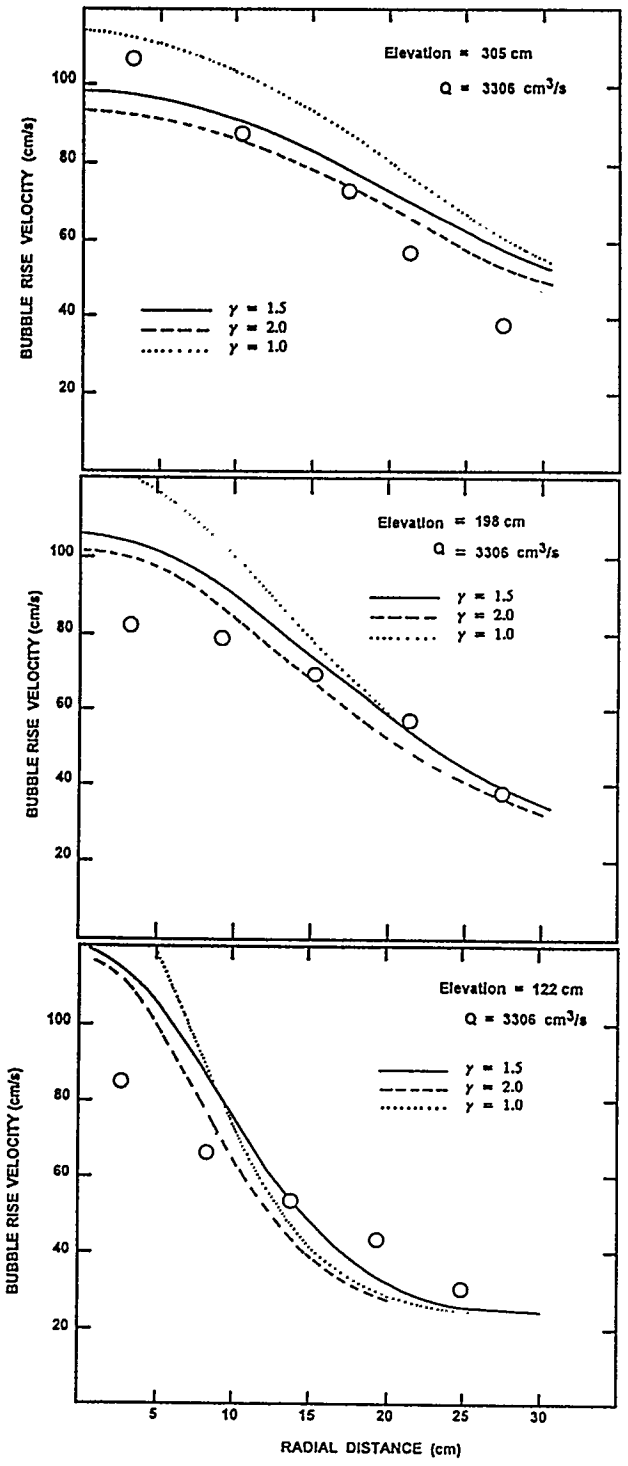

Figure 56. Comparison of model predictions to bubble rise velocities observed in an experiment by Paul et al.

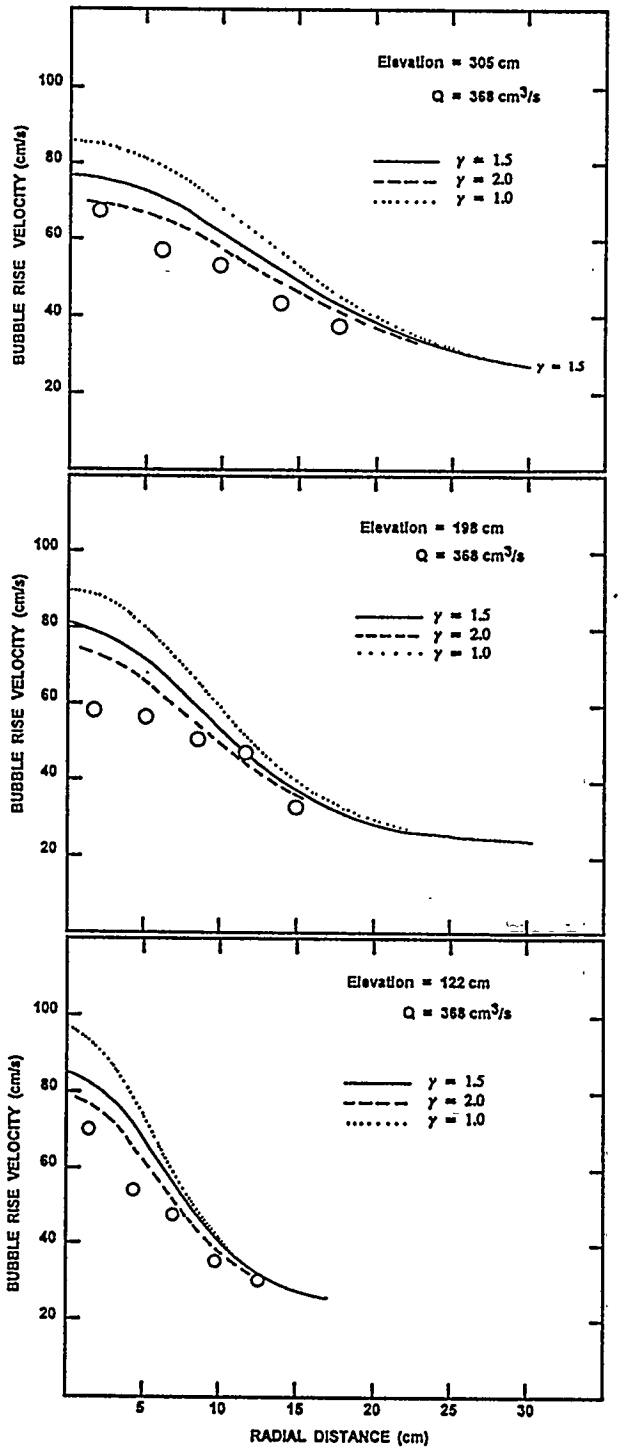

Figure 57. Comparison of model predictions to bubble rise velocities at various elevations observed in an experiment by Paul et al.

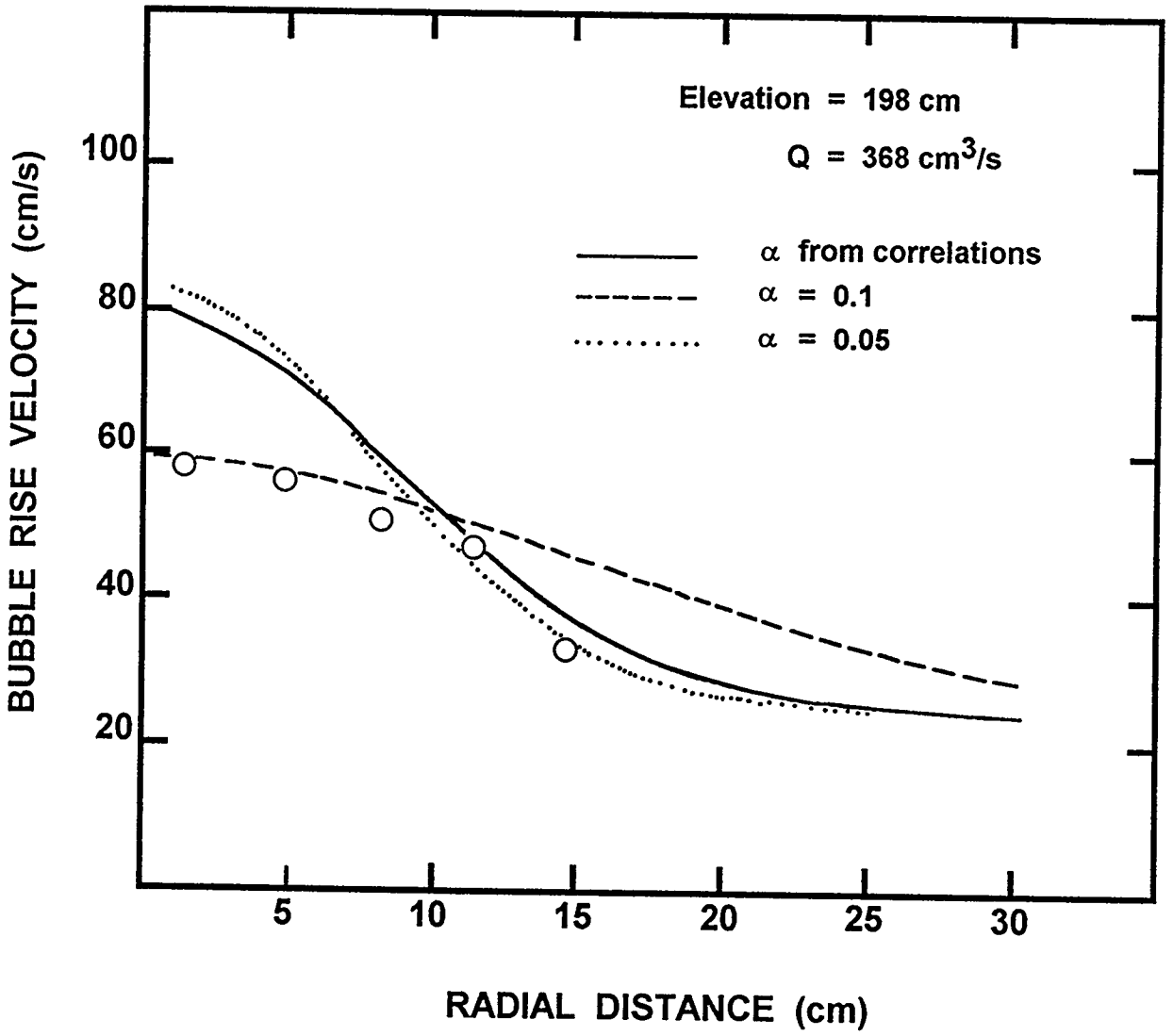

Figure 58. Effect of entrainment coefficient on predictions of bubble rise velocity

$$E_o = \text{Eotvos number} = g(\rho_l - \rho_g)D_B^2/\sigma_l$$

$$M = \text{Morton number} = g\mu_l^4(\rho_l - \rho_g)/\rho_l^2\sigma_l^3$$

The Morton number is a property of the fluid phase. As shown in Figure 59, the Morton number of water varies from 2.6×10^{-11} at 298 K to 7.5×10^{-14} in saturated water at 453 K where the vapor pressure is about 10 atmospheres. The Eotvos number is a property of the bubble and the fluid. At 293 K, a 0.1-cm-diameter bubble in water has an Eotvos number of about 0.13 whereas the Eotvos number of a 1-cm-bubble is 13.4. The Eotvos number of a 1-cm-diameter bubble in water at 453 K is 20.6.

At a fixed Morton number, the behavior of bubbles varies with bubble size. Very small bubbles are essentially spherical and rise through water as though they were rigid spheres [77,78,79,80]. Somewhat larger bubbles develop internal circulation of gas. They are still spherical but rise through the liquid about 50 percent faster. Still larger bubbles distort into oblate ellipsoid shapes. With further increases in size, the shape becomes unstable, and the bubble can undergo oblate-to-spherical or even oblate-to-prolate shape oscillations. The onset of shape oscillations is accompanied by a sharp increase in the drag coefficient of the bubble. With further increases in bubble size, the bubble distorts into a spherical cap shape. As discussed above, bubbles that become too large are unstable and will break up into smaller bubbles.

The onset of internal circulation of gases within a bubble has important ramifications on aerosol trapping. The circulation of gases makes possible aerosol deposition by inertial impaction. On the other hand, the increase in the rise velocity decreases the time aerosols within the bubble are exposed to water. Why gases do not circulate within bubbles of all sizes has been much debated [81,82]. It is generally believed that the accumulation of surface active agents at the interface between the gas and the water is responsible. Because the agents accumulate preferentially at the rear of the rising bubble, a surface tension gradient is created which tends to oppose liquid motion. The effect is often considered small except in very small bubbles. This may well be the case in laboratory situations in which there are efforts to keep water pure. In suppression pools under accident conditions, the water will become very contaminated with a variety of chemical species. Some fraction of these contaminants may be surface active and may affect the mobility of the gas/water interface and consequently the circulation of gases within the bubble.

The usual criterion for the onset of internal circulation is the Bond criterion that $E_o > 4$. This criterion is applicable only for bubble Reynolds numbers, Re_B, less than 1 where:

$$Re_B = U_{rise}\rho_l D_B/\mu_l$$

and U_{rise} is the rise velocity of the bubble. Clift, Grace, and Weber [81] suggest a rise velocity relationship in terms of the modified Eotvos number:

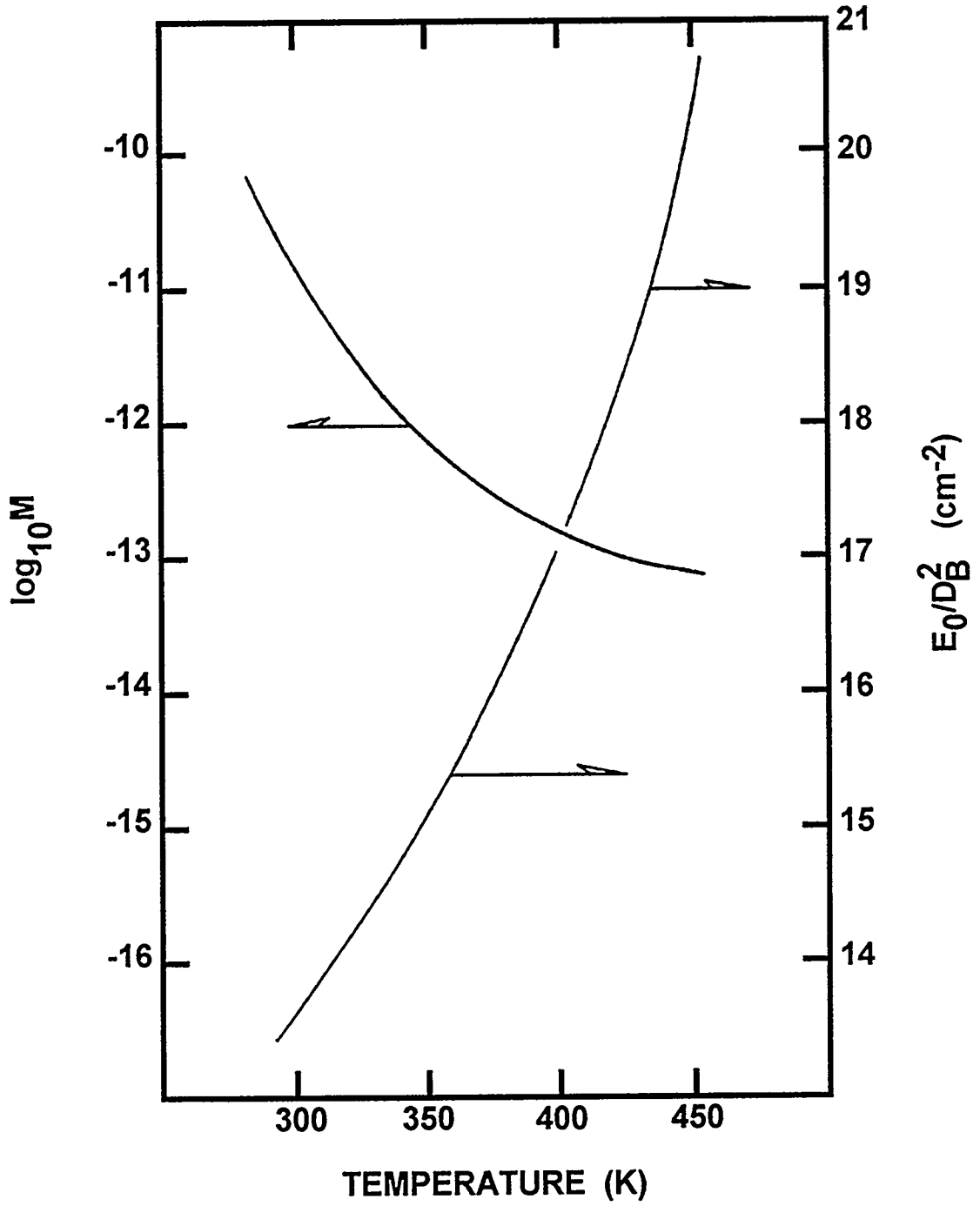

Figure 59. Variations in $\log_{10}$ M and $E_o/D_B{}^2$ with temperature in water

$$\frac{U}{U(\text{rigid})} = 1 + Z/2$$

$$Z = \left[\frac{2}{2+3\mu_g/\mu_l}\right] (2(y-1))$$

$$y = 1 + 0.5\tanh(1.9646\ E_o^{'} - 2.63415)$$

$$E_o^{'} = g(\rho_l - \rho_g)D_B^2/\Delta\sigma_l$$

where $\Delta\sigma_l$ is the difference between the surface tension of the pure liquid and the surface tension with a surface active agent present. Sadhal and Johnson [238] suggest a refinement to this factor used by Clift, Grace, and Weber. They suggest:

$$\frac{U}{U(\text{rigid})} = \frac{1}{1 - Z/3}$$

where

$$Z = [1 - m(\phi)]/(1 + \mu/\mu_l),$$

$$m(\phi) = \frac{1}{2\pi}[2\phi + \sin\phi - \sin 2\phi - 1/3\sin 3\phi], \text{ and}$$

ϕ = polar angle marking the region of the bubble surface immobilized by accumulated surface active agents.

Various quantitative criteria have been suggested for the onset of shape oscillations. Peebles and Garber [58] found shape oscillations of air bubbles in water when:

$$\left[\frac{\rho_l}{\sigma_l} U_T^3 D_B\right] > 3.65$$

Coester [59] observed shape oscillations for air bubbles in water when:

$$\left[\frac{\rho_l}{\sigma_l} U_T^3 D_B\right] > 2.96$$

In glycerine-water solutions, oscillations occurred when:

$$\left[\frac{\rho_l}{\sigma_l} U_T^3 D_B\right] > 3.44 \text{ to } 4.24$$

The strong dependencies of these criteria on rise velocity suggest that the onset of shape oscillations is delayed by impurities in the water.

Quantitative criteria for the distortion of bubbles from spherical to ellipsoidal and from ellipsoidal to spherical cap are discussed in the subsection below on bubble shape.

G. Slip Velocity of Bubbles

The slip velocities of bubbles in plumes are related to the rise velocities of isolated bubbles. The rise velocities of bubbles in water have been studied numerous times (see as examples References 78 to 80). Rise velocities do depend on the purity of the water. Even the very low levels of impurities found in distilled water are suspected to influence bubble behavior. Certainly, the water in a steam suppression pool must be considered contaminated—if not initially, it will certainly become contaminated as a reactor accident progresses.

Here a correlation of the rise velocity of gas bubbles in "contaminated" water is adopted [66]:

$$U_T = \frac{\mu_l}{\rho_l D_B} M^{-0.149} (J - 0.857)$$

where

D_B = diameter of the sphere with an equivalent volume of the bubble

M = Morton number

$$J = \begin{cases} 0.94\ H^{0.757} & \text{for } 2 \le H \le 59.3 \\ 3.42\ H^{0.441} & \text{for } H > 59.3 \end{cases}$$

$$H = 4/3\ E_o\ M^{-0.149}\ (\mu_l/0.009)^{-0.14}$$

E_o = Eotvos number

μ_l = liquid phase viscosity in poises.

For $H > 1000$, the large bubble correlation discussed above (see Figure 39) is used to calculate bubble rise velocity:

$$U_T = 0.735\sqrt{gD_B(cm)} \quad cm/s$$

For bubbles with H < 2, the following correlations in terms of the Reynolds number are used [67]:

a. for 4 < Re < 100:

$$U_T^2 = \frac{4}{3}\frac{(\rho_l-\rho_g)g\ D_B}{\rho_l}\frac{\left[60+\frac{29\mu_g}{\mu_l}\right]\left[\frac{4+3\mu_g}{\mu_l}\right]Re^{0.74}}{3.05\left[783\left[\frac{\mu_g}{\mu_l}\right]^2+2142\frac{\mu_g}{\mu_l}+1080\right]}$$

b. for 0.01 < Re ≤ 4

$$U_T^2 = \frac{4}{3}\frac{(\rho_l-\rho_g)g\ D_B}{\rho_l}\frac{1}{C_D}$$

$$\log_{10}\left[\frac{C_D Re}{24}-1\right] = -0.881 + 0.82\log_{10} Re - 0.05(\log_{10} Re)^2$$

c. for Re < 0.01

$$U_T^2 = \frac{4}{3}\frac{(\rho_l-\rho_g)g\ D_B}{\rho_l}\left[\frac{1}{3/16+24/Re}\right]$$

These correlations are compared to experimental data in Figure 60.

The SUPRA [7,8] and BUSCA [9] computer codes use a model for bubble rise velocities due to Wallis [85]. Five regimes are considered:

1. If $D_B > 4.66\ (\sigma_l/\rho_l g)^{1/2}$,

$$U_T = 0.709\sqrt{gD_B}$$

2. If Re ≤ 2 ,

$$U_T = D_B^2\rho_l g/18\mu_l$$

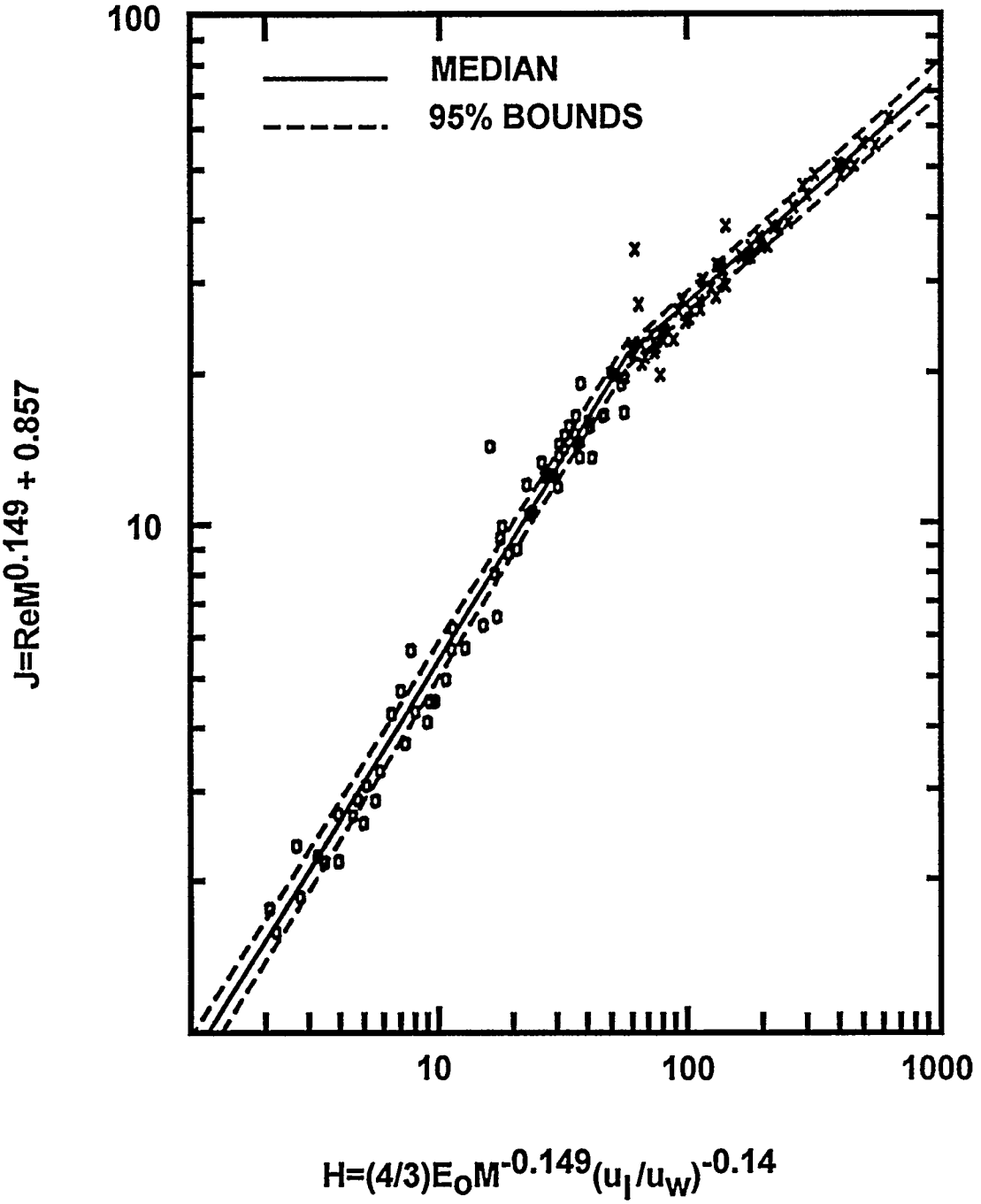

Figure 60. Comparison of predictions of bubble rise velocities by several models

3. If $2 < Re \leq 4.02\ M^{-0.214}$,

$$U_T = 0.33\ g^{0.76} \left[\frac{\rho_l}{\mu_l}\right]^{0.52} \left[\frac{D_B}{2}\right]^{1.28}$$

4. If $4.02\ M^{-0.214} < Re \leq 3.1\ M^{-0.25}$,

$$U_T = 1.35(2\sigma_l/\rho_l D_B)^{1/2}$$

5. If $Re > 3.1\ M^{-0.25}$

$$U_T = 1.53(g\sigma_l/\rho_l)^{1/4}$$

where Re is the Reynold's number.

The SPARC code uses a rather simple model [6]:

$$U_T = \begin{cases} 7.876(\sigma_l/\rho_l)^{1/4} & \text{for } D_B \leq 0.5 \text{ cm} \\ 11.0826(\sigma_l/\rho_l)^{1/4} D_B^{0.49275} & \text{for } D_B > 0.5 \text{ cm} \end{cases}$$

These various descriptions of the rise velocities are compared in Figure 61 for bubbles of various sizes rising through water. The sharp peak in the rise velocity for $D_B = 0.2$ cm exhibited by the model used in the SUPRA and BUSCA computer codes is appropriate for gas bubbles rising in very pure water. Such a peak would not be expected in even modestly contaminated water such as tap water [79]. Certainly, during the progression of a severe reactor accident, water in the suppression pool will become sufficiently contaminated that rise velocities of bubbles will be affected.

H. Bubble Shapes

The distortion of bubbles from spherical to oblate ellipsoidal is conveniently described in terms of the eccentricity, E, which is the length of the semi-major axis, a, divided by the length of the semi-minor axis, b:

$$E = a/b$$

The volume and surface area of an oblate ellipsoid of eccentricity E are:

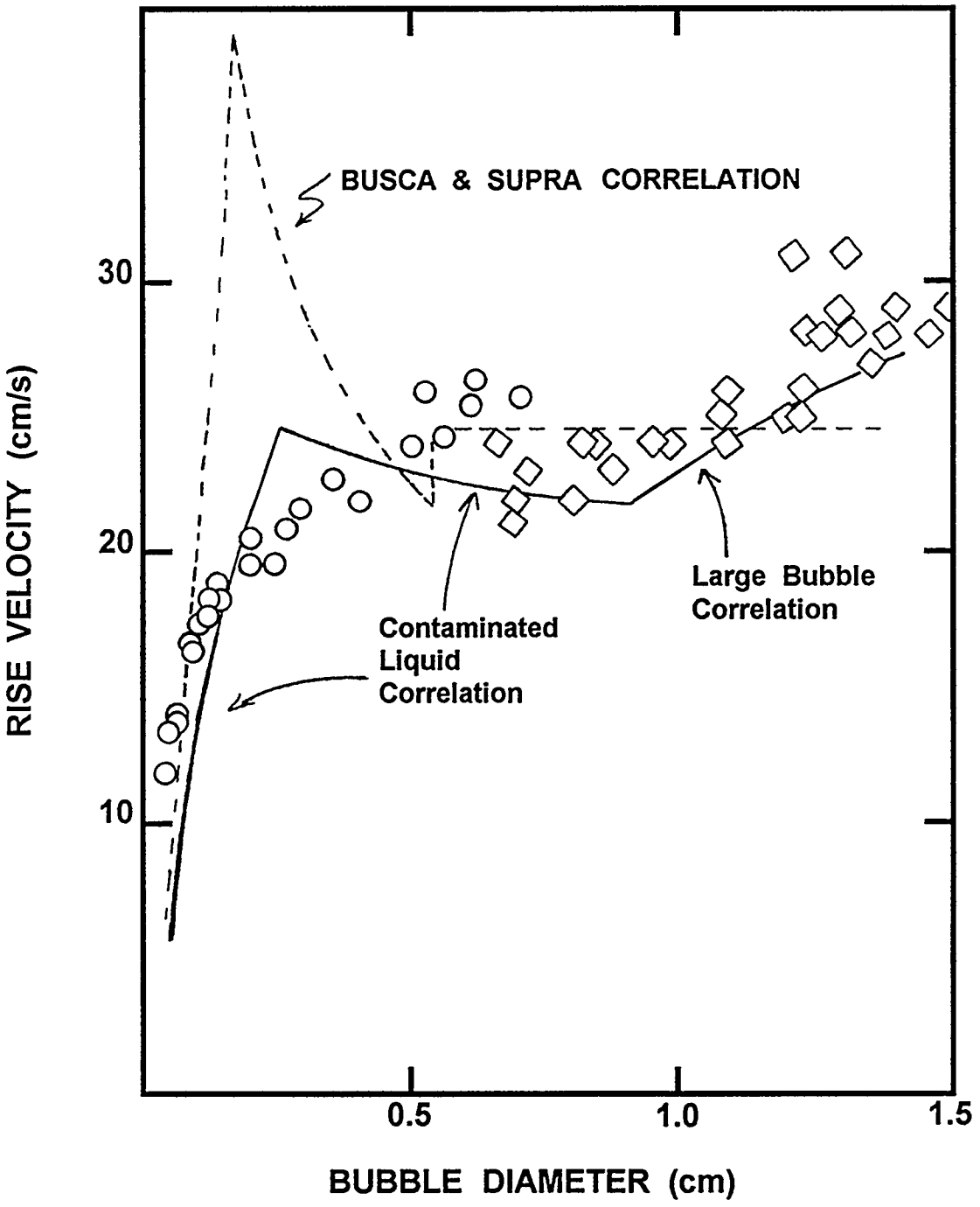

Figure 61. Comparison of predicted bubble rise velocities to data for air bubbles in hot (322 K) tap water [79]

$$V = \frac{4}{3}\pi a^2 b = \frac{4}{3}\pi a^3/E = \frac{\pi}{6} D_B^3(e)$$

$$A = \frac{\pi}{2} D_B(e)^2 E^{2/3} \left\{ 1 + \frac{1}{2E(E^2-1)^{1/2}} \ln \left[\frac{E + (E^2-1)^{1/2}}{E - (E^2-1)^{1/2}} \right] \right\}$$

where $D_B(e) = 2a/E^{1/3}$ is the diameter of the sphere with an equivalent volume.

A compact correlation for eccentricities of bubbles is [82]:

$$\frac{1}{E} = \begin{cases} 1 & \text{for } Ta \le 1 \\ [0.81 + 0.206 \tanh \{2(0.8 - \log_{10} Ta)\}]^3 & \text{for } 1 \le Ta \le 39.8 \\ 0.24 & \text{for } Ta > 39.8 \end{cases}$$

where $Ta = ReM^{0.23}$. In cases where Ta exceeds 39.8, the bubble has a spherical cap shape which will be discussed further below.

The BUSCA code [9] uses a correlation of eccentricity with the Eotvos number, E_o:

$$E = \begin{cases} 0.8526 + 0.22498 E_o - 5.6918 \times 10^{-3} E_o^2 + 4.86 \times 10^{-5} E_o^3 & \text{for } E_o < 38.5 \\ 3.85 + 7.6472 \times 10^{-5} (E_o - 38.5) & \text{for } 38.5 \le E_o \le 2000 \\ 4 & \text{for } E_o > 2000 \end{cases}$$

Okhotskii [224] has proposed a theory of bubble eccentricity that yields the implicit expression:

$$E = 1 + \left[\frac{2}{3}\right] \left[\frac{1}{E^{1/3}}\right] \left[\frac{E_o}{1 + E_o/4}\right]^{1/2}$$

Paul et al. [30] examined the shapes of bubbles produced in their experiments with quenchers. They developed a regression equation for their data:

$$\frac{1}{E} = \begin{cases} 1 & \text{for } D_B(e) \le 0.15 \text{ cm} \\ 0.68 + 0.57 \exp [-D_B(e)/0.26] & \text{for } D_B(e) > 0.15 \text{ cm} \end{cases}$$

Their data for bubbles in swarms as well as data for isolated bubbles [39,79,80] are compared to the correlations in Figure 62. It is apparent from this comparison that there is significant scatter, even in the data for isolated bubbles, about the correlation. There appears also to be some indication that bubble distortion is suppressed in swarms.

Bhaga and Weber [84] conducted studies of bubble shapes in liquids with large Morton numbers ($M = 10^{-3}$ to 10^{3} versus $M = 10^{-10}$ to 10^{-14} of interest here). They found eccentricity to be a function of the Reynolds number and independent of the Morton number. They draw attention in their writings to differences between liquids characterized by large Morton numbers and liquids characterized by small Morton numbers. It appears then that results reported by Bhaga and Weber are not applicable to the topics of interest here.

Bubbles predicted to have eccentricitities greater than about 4 are spherical caps. The general geometry of a spherical cap bubble is shown in Figure 63. The spherical portion has a radius, R, given by [82]:

$$R = D_B(e)/[2g(\theta_w)]^{1/3}$$

where

$$g(\theta_w) = 2 - 3\cos(\theta_w) + \cos^3\theta_w$$

$$\theta_w = 50 + 190\exp[-0.62\,Re^{0.4}] \text{ degrees}$$

In water, all real spherical cap bubbles have wake angles near 50° according to this description.

The BUSCA model [9] uses a rather different method to describe the geometrical features of a spherical cap bubble. Eccentricities are calculated from the correlations in terms of the Eotvos number described above. The radius of the spherical portion and the wake angle are then found from:

$$R = \frac{D_b(e)(E^2 + 1)}{2(3E^2 + 1)^{1/3}}$$

$$\theta = 2\tan^{-1}(1/E)$$

The authors of this document do not understand this model.

I. Heat and Mass Transport to and Within Bubbles

Heat transport and mass transport within bubbles and from the water pool to the bubbles are of interest in three regimes of bubble behavior within a suppression pool:

- during bubble formation at orifices and at vents to the pool,
- immediately after bubbles detach and begin to equilibrate with the pool, and

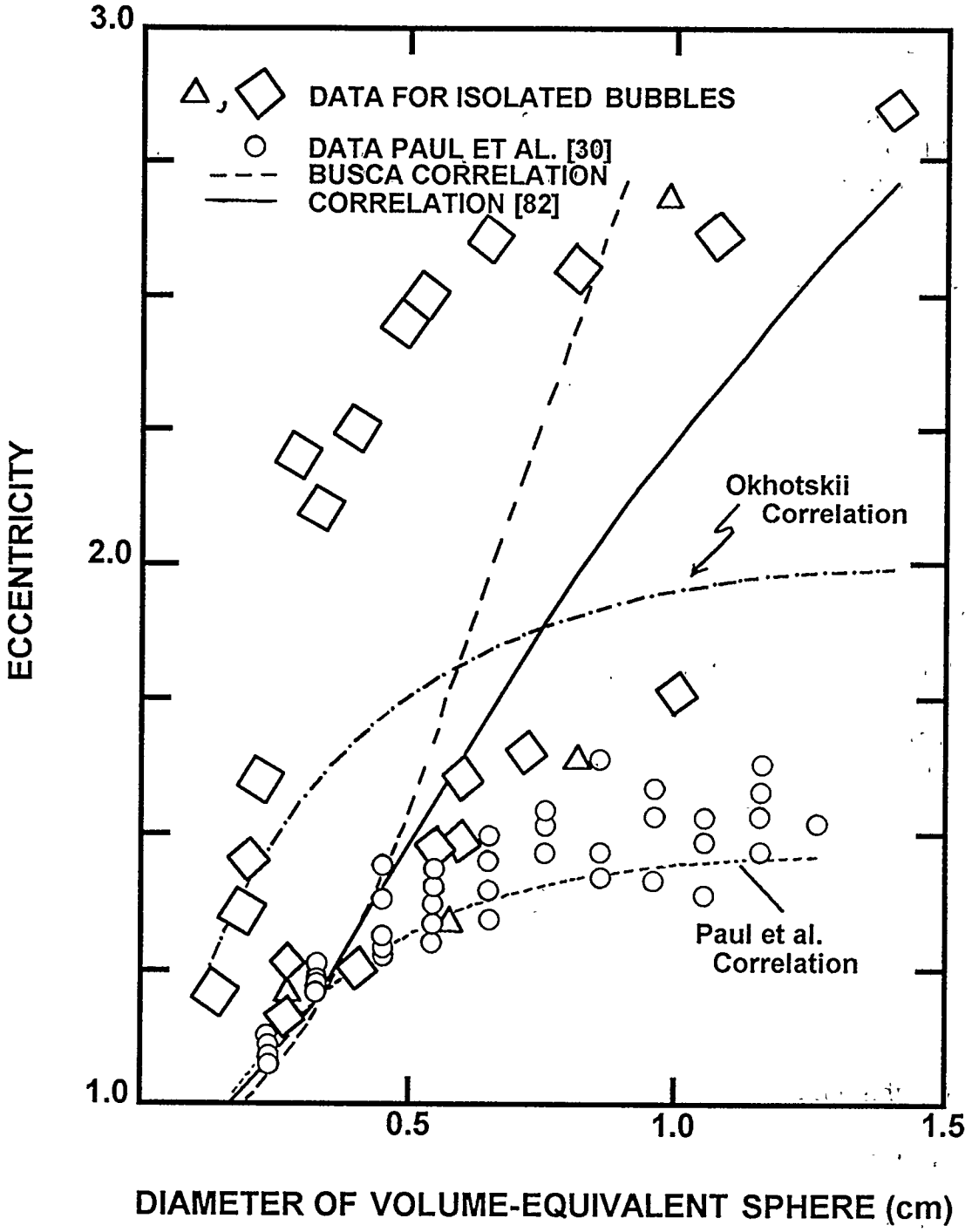

Figure 62. Comparison of bubble eccentricity models to experimental data

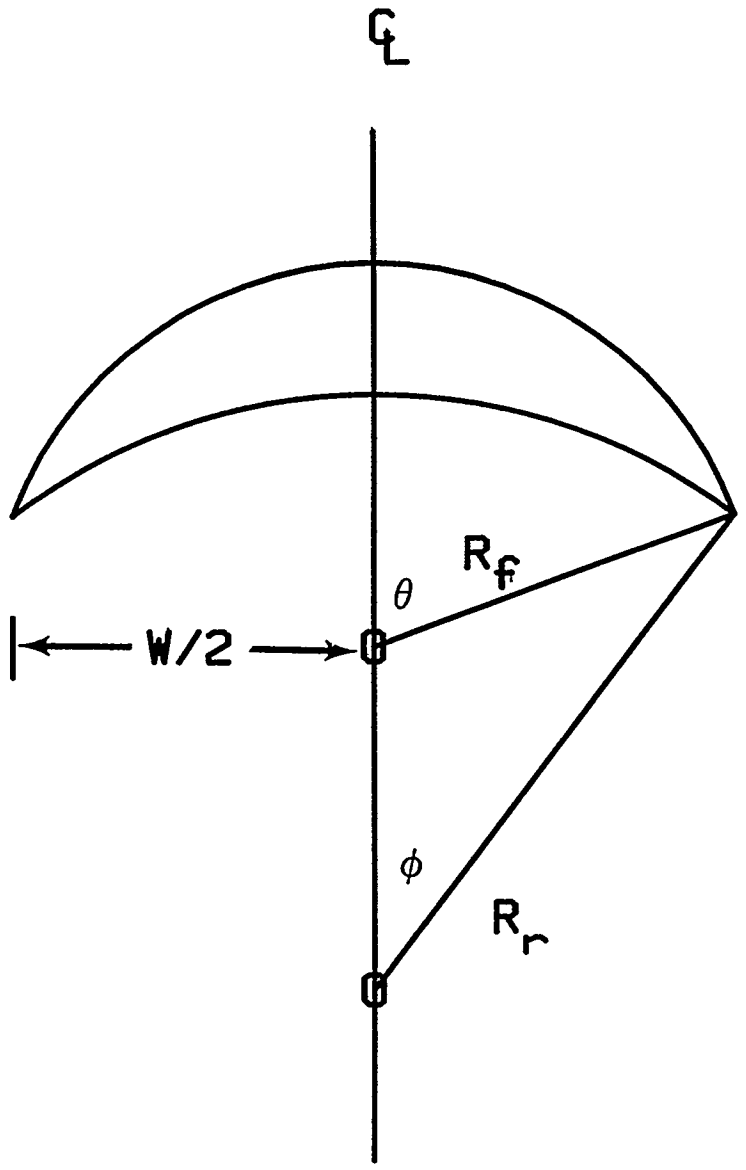

Figure 63. General geometry of a spherical cap bubble

- during the quasi-steady state as bubbles rise through the pool.

The interest in heat and mass transport does not stem from a need to understand the detailed timing of bubble behavior. Rather, heat transport and mass transport within the bubble are expected to affect aerosol behavior. It is, then, necessary to have some estimate of the heat transport and mass transport coefficients to predict aerosol removal during the three regimes of bubble behavior.

1. Heat Transport From Bubbles During Formation

Some aspects of heat transport during bubble formation have been discussed above in Section IV-A-1. It is quite difficult to obtain detailed data on the condensation heat transfer during bubble formation at orifices. Mayinger and Chen [190] have employed a novel, optical-interference pattern method to measure heat transfer from vapor bubbles. They recommend:

$$Nu = \frac{\bar{h} D_B^*}{k_{th}(l)} = 0.185\ Re^{0.7}\ Pr^{1/2}$$

where

$\bar{h}$ = average heat transfer coefficient during bubble formation,

R_e = $U_B D_B^*\ \rho_l / \mu_l$

Pr = $\mu_l\ C_p(l) / k_{th}(l)$, and

D_B^* = bubble diameter at the time the bubble detaches from the orifice.

Unfortunately, Chen and Mayinger do not indicate clearly what velocity is to be used to calculate the Reynolds number. They mention both the rise velocity of the bubble when it detaches and the relative motion of the bubble and liquid as the bubble grows. An example they provide for:

$$Ja = \frac{\rho_l\ (T_s - T_p)}{L\ \rho_g} = 10$$

yields a heat transfer coefficient of 0.13 cal/cm^2-s-K. The correlation they recommend yields a value about twice that which is measured.

Chen and Mayinger's studies involved bubbles formed at a 0.16-cm upward facing nozzle. These data can be used only with considerable extrapolation to estimate heat transfer from bubbles formed at orifices in quenchers. Jeje et al. [213] observed a sharp decrease in the heat transfer coefficient as bubbles formed at a nozzle 0.5 cm in diameter. Initial values were as high as 60 cal/cm^2-s-K. Heat transfer coefficients at the time of bubble detachment were about 1/10 of this.

Pitts [210] cites work by Engeldiner, unavailable to the authors, for heat transfer from bubbles formed at the end of downcomers. This work was, apparently, done specifically for the study of steam suppression pools. Pitts utilized for the heat transfer coefficient:

$$h = 8.4 + 3.6 \times 10^{-4} A_B(cm^2) \quad cal/cm^2\text{-}s\text{-}K$$

where A_B is the surface area of the bubble at the end of the downcomer. He took the maximum heat transfer coefficient to be 24 cal/cm^2-s-K based on experimental studies. This value is quite similar to the value found by Kerney et al. [291] for submerged jets of steam into water, 23 cal/cm^2-s-K. This value correlated well data for jets from orifices 0.04 to 0.95 cm in diameter and Kerney et al. suggest a simple correlation for a variety of data:

$$h = 1.932\ C_p(\text{steam})\ \dot{Q}(m)/\pi D_o^2$$

where

C_p(steam) = heat capacity of steam

$\dot{Q}$(m) = mass flow rate of steam through an orifice,

D_o = diameter of the orifice.

The also suggest are more complicated but better correlation:

$$\frac{\pi h D_o^2}{C_p \dot{Q}(m)} = 1.395 \left[\frac{\Delta H_{fg}}{C_p(T_g - T_p)}\right]^{0.1689} \left[\frac{z\pi D_o^2}{\dot{Q}(m)}\right]^{0.1446}$$

where

ΔH_{fg} = latent heat of vaporization of water, and

z = 27.5 g steam/cm^2-s.

2. Heat Transfer After Bubble Detachment

As discussed above (Section IV-B), the collapse of bubbles has been the subject of much study. Collapse may be limited by inertial effects or by heat transfer effects. Heat transfer effects dominate when the driving force for condensation is not too large. Mayinger and Chen [190] seem* to recommend:

*Mayinger and Chen list the leading coefficient in the correlation as 0.6. But, the text indicates the coefficient is 0.185 and this value yields results in better agreement with plotted data.

$$Nu = 0.185\ Re^{0.6}\ Pr^{1/2}$$

Values they obtained for the Nusselt number for steam bubbles varied by about ±25 percent.

Experimental studies by Brucker and Sparrow [211] with 0.3-cm-diameter, well-isolated, steam bubbles yielded a heat transfer coefficient of 0.24 cal/cm^2-s-K. These authors recommended as a correlation for the heat transfer coefficient:

$$Nu = 0.37\ Re^{0.6}$$

They indicated an uncertainty of ±50 percent. In light of this uncertainty, the correlation is consistent with that found by Mayinger and Chen.

Theoretical consideration of bubble collapse in the heat-transfer limited regime [212] yields:

$$h = \phi \left[\frac{U_B\ C_p(l)\ \rho_l\ k_{th}(l)}{D_B^*} \right]^{1/2}$$

where ϕ can be 0.42 to 0.35.

These various correlations of the heat transfer coefficient from bubbles rising in water at 373 K are shown in Figure 64 as functions of bubble diameter.

The correlations give fairly consistent values in light of the uncertainties ascribed to them. It is apparent that the correlation recommended by Bruckner and Sparrow and the theoretical analysis by Moalem and Sideman [212] describe the uncertainty range for the heat transfer coefficients.

Lee [71] recommends an average heat transfer for bubbles that detach from downcomers:

$$\overline{hA} = 2/3\ A(i)\ h_o$$

$$\frac{h_o\ D_p}{k_{th}(l)} = 0.04\ Re^{7/8}\ Pr^{1/2}$$

where

D_p = diameter of the downcomer,

$\overline{hA}$ = average of the product of the heat transfer coefficient and the bubble surface area, and

$A(i)$ = initial surface area of the bubbles.

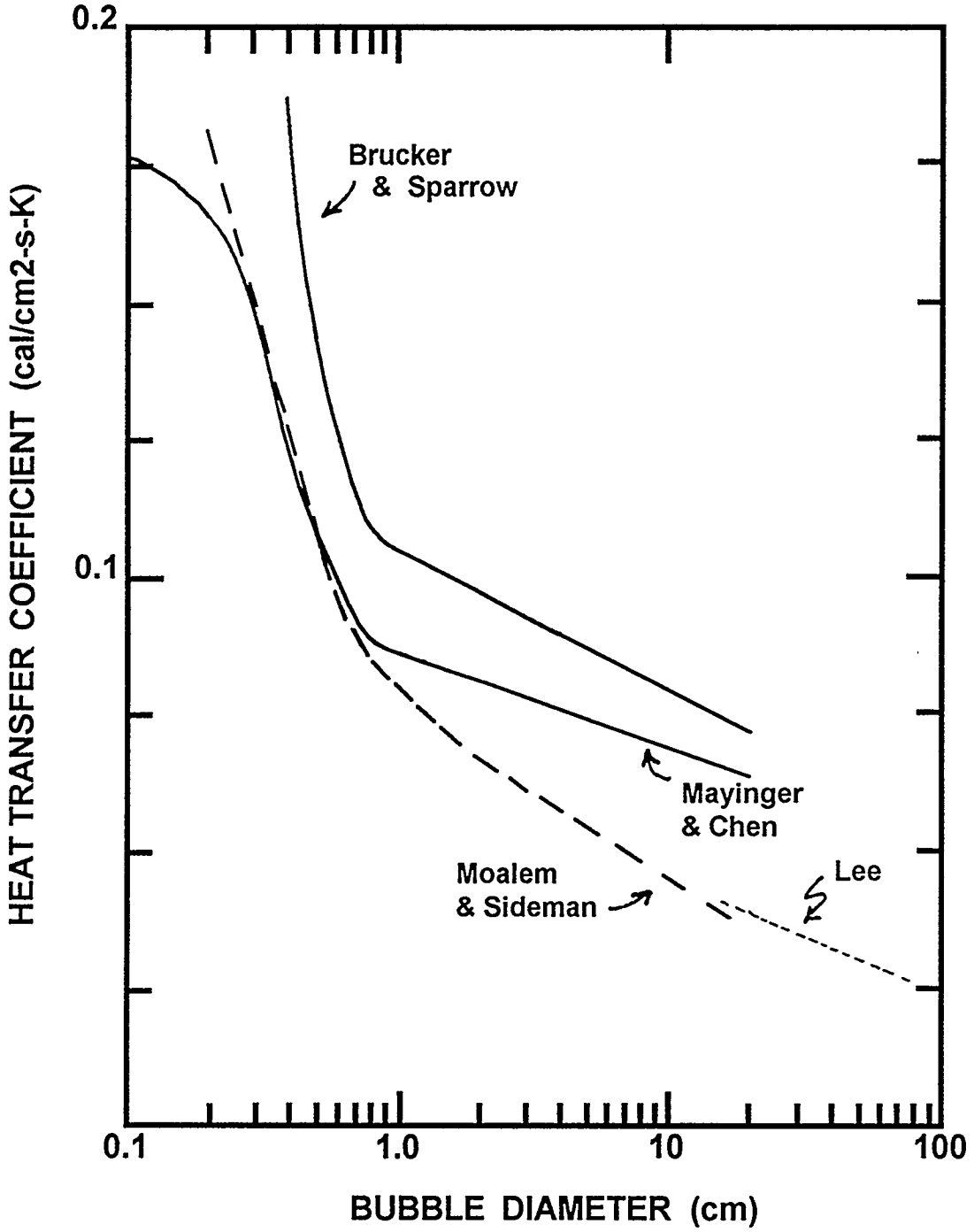

Figure 64. Heat transfer coefficients for bubbles rising in 373 K water as functions of bubble diameter

Values of h_o for large bubbles expected to form at downcomers are also shown in Figure 64.

For bubbles that encapsulate the downcomer as they rise, Lee [71] found the heat transfer coefficient to be 3.6 cal/cm^2-s-K independent of the bubble Reynolds number.

3. Heat and Mass Transfer During Bubble Rise

Once the bubbles have equilibrated with the pool and have begun a quasi-steady state rise through the suppression pool, both external heat transfer and mass transport within the bubble are of interest as discussed in connection with the thermodynamics of bubbles (see Section IV-D). It is certainly not evident that the external heat transfer coefficients for steam-rich large bubbles are applicable to the quasi-steady state bubble rise.

The vast bulk of information on external transport to bubbles comes from mass transport studies. An analogy between mass transport and heat transport must, then, be used to get the heat transport coefficient.

Spherical bubbles have received by far the most attention. For Reynolds numbers up to about 1 and for all Peclet numbers, Pe, the Sherwood number for external mass transport is given by [82]:

$$Sh_A = 1 + (1 + Pe)^{1/3}$$

where

$Sh = k_m D_B/Đ$

$Pe = D_B U_{slip}/Đ$

k_m = mass transport coefficient

$Đ$ = diffusion coefficient

By analogy, the Nusselt number for heat transport is given by:

$$Nu = hD_B/k_{th} = 1 + \left[1 + \frac{D_B U_{slip} \rho_l C_l}{k_{th}(l)}\right]^{1/3}$$

where

Nu = Nusselt number

$k_{th}(l)$ = thermal conductivity of the liquid

For Reynolds numbers greater than about 70,

$$Sh_B = 1 + \frac{2}{\sqrt{\pi}} \left[1 - \frac{\frac{2+3\xi}{3(1+\xi)}}{\left\{ 1 + \left[\frac{(2+3\xi)Re^{1/2}}{(1+\xi)(8.67+6.45\xi^{0.64})} \right]^n \right\}^{1/n}} \right]^{1/2} Pe^{1/2}$$

where

$$n = 4/3 + 3\xi$$

$$\xi = \mu_g/\mu_l$$

A somewhat *ad hoc* transition between the model for Re $\leq$ 1 and Re > 70 is provided by:

$$Sh = \frac{Sh_A + ReSh_B/50}{1 + Re/50}$$

Predictions of the mass transport coefficient obtained with this model for CO_2 transport in water at room temperature are compared to data (86,87) in Figure 65. For this comparison the aqueous phase diffusion coefficient of CO_2 was taken to be 1.95 x 10^{-5} cm^2/s. The data show a substantial scatter. The theoretical model seems to provide an upper bound on the data for bubbles larger than about 0.25 cm. For smaller bubbles, predictions and data diverge.

For ellipsoidal bubbles without shape oscillations, Clift, Grace and Weber [82] recommend for contaminated systems:

$$\frac{\overline{k_m A}}{A_e Đ^{1/2}} = 6.5 \qquad s^{-1/2}$$

or

$$\frac{\overline{hA}}{A_e(k_{th}/\rho_l C_l)^{1/2}} = 6.5 \qquad s^{-1/2}$$

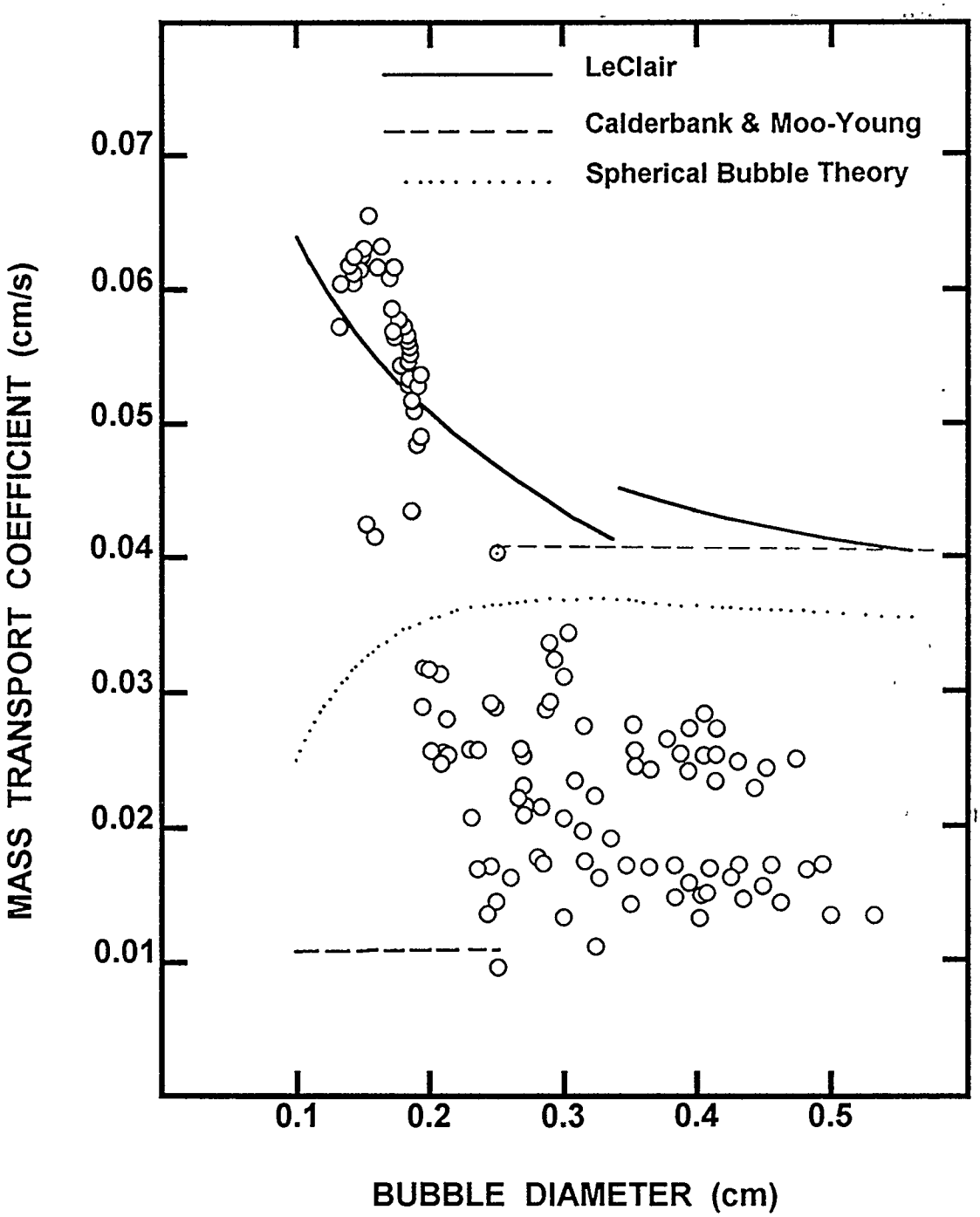

Figure 65. Comparison of predicted and observed mass transport coefficients for CO_2 from nearly spherical bubbles. The spherical bubble theory is for isolated bubbles. Other models are for bubble swarms.

where

$\overline{k_m A}$ = average product of the surface area of the bubble and the mass transport coefficient, and

A_e = surface area of the sphere with the equivalent volume = $\pi D_B^2(e)$

For pure systems, they recommend

$$\frac{\overline{k_m A}}{A_e Đ^{1/2}} = \frac{0.14}{D_B(e)} + \frac{6.94}{D_B(e)^{1/2}} \qquad s^{-1/2}$$

They prefer these empirical correlations over the theoretical expression for potential flow conditions [267]:

$$Sh = \frac{\frac{2}{\sqrt{\pi}} Pe^{1/2} \left\{ \frac{8(E^2-1)^{3/2}}{3E^{10/3} \sin^{-1}\left[(E^2-1)^{3/2}/E^2(E+1)\right]} \right\}^{1/2}}{1 + \frac{1}{2E(E^2-1)^{1/2}} \ln\left[\frac{E + (E^2-1)^{1/2}}{E - (E^2-1)^{1/2}}\right]} + 1$$

or

$$\frac{\overline{k_m A}}{A_e Đ^{1/2}} = 2\sqrt{\frac{2}{3\pi}} \frac{U_{slip}^{1/2}}{D_B^{1/2} E} \left\{ \frac{(E^2-1)^{3/2}}{3 \sin^{-1}\left[(E^2-1)^{3/2}/E^2 (E+1)\right]} \right\}^{1/2}$$

Johnson et al. [86] found they could account for mass transport of CO_2 and other gases from bubbles with equivalent diameters of 0.6 to 4.0 cm rising in water with the expression:

$$Sh = 2 + 1.13\ Pe^{1/2} \left[\frac{D_B(e)}{0.45 + 0.2\ D_B(e)} \right]^{1/2}$$

They found, in fact, fairly good agreement between experimental results and predictions with this correlation for Reynolds numbers from 500 to 8000.

For ellipsoidal bubbles with shape oscillations, Clift, Grace, and Weber [82] consider the surface stretch model:

$$\frac{\overline{k_m A}}{A_e} = \frac{Đ}{D_B(e)} \frac{2}{\sqrt{\pi}} \sqrt{\frac{D_B^2 f}{Đ}} \left[1 + \delta + \frac{3\delta^2}{8}\right]^{1/2}$$

and the fresh surface model:

$$\frac{\overline{k_m A}}{A_e} = \frac{Đ}{D_B(e)} \frac{2}{\sqrt{\pi}} \sqrt{D_B^2 f/Đ}$$

where

$1 + \delta =$ ratio of the maximum surface area to the minimum surface area over an oscillation cycle, and

$f =$ frequency of oscillation

For oblate-to-spherical oscillations,

$$1 + \delta = \frac{1}{2} E^{2/3} \left\{1 + \frac{1}{2E(E^2-1)^{1/2}} \ln \left[\frac{E + (E^2-1)^{1/2}}{E - (E^2-1)^{1/2}}\right]\right\}$$

The frequency of oscillations is difficult to predict. The natural frequencies for a spherical bubble in a viscous medium are given by [61]:

$$(2\pi f)^2 = \frac{8n(n+1)(n-1)(n+2)\ \sigma_l}{[(n+1)\rho_l + n\rho_g]\ D_B^3}$$

where n is a small integer. The first meaningful frequency is at n = 2, but Schmidt [293] finds n = 3 to be a more important oscillation frequency.

At Reynolds numbers less than 110, mass transfer to spherical cap bubbles is given approximately by [82]:

$$\frac{\overline{k_m A}}{Ae} = 2.83 \left[\frac{Pe}{\pi}\right]^{1/2} \frac{Đ}{D_B(e)}$$

At higher Reynolds numbers, assuming that mass transfer to the spherical portion and the base of the bubble are independent, the average mass transport is given by [82]:

$$\frac{\overline{k_m A}}{A_e} = \frac{2Đ}{D_B(e)} \left[\frac{Pe}{\pi}\right]^{1/2} + \frac{Sr \sin^3 \theta_w}{4\pi} \left[\frac{2a}{D_B(e)}\right]^{3/2} \left[\frac{U_{slip} Đ}{D_B(e)}\right]^{1/2}$$

where

$$Sr = 2f_w \, a \sin \theta_w / U_{slip}$$

$$\theta_w = 50 + 190 \exp(-0.62 \, Re^{0.4})$$

f_w = wake shedding frequency

At Reynolds numbers greater than about 150, Sr has values of 0.2 to 0.5.

The various models of mass transport coefficients are compared in Figure 66 to data on the mass transport of CO_2 in water at room temperature (86,87,218). All of the models predict similar results to within about a factor of 3. These predictions are in accord with the scattered data.

The discussions to this point have focused on external transfer processes to isolated bubbles. Convective transport processes to bubbles in swarms might be expected to be different. Calderbank and Moo-Young [64] have correlated data for bubbles in swarms by

$$k_m = \begin{cases} 0.31(\mu_l g/\rho_l)^{1/3} Sc^{-2/3} & \text{for } D_B(e) < 0.25\,\text{cm} \\ 0.42(\mu_l g/\rho_l)^{1/3} Sc^{-1/2} & \text{for } D_B(e) > 0.25\,\text{cm} \end{cases}$$

where

$$Sc = \mu_l / \rho_l Đ$$

LeClair and Hamielec [65] have developed a theoretical expression for mass transfer to bubbles in swarms:

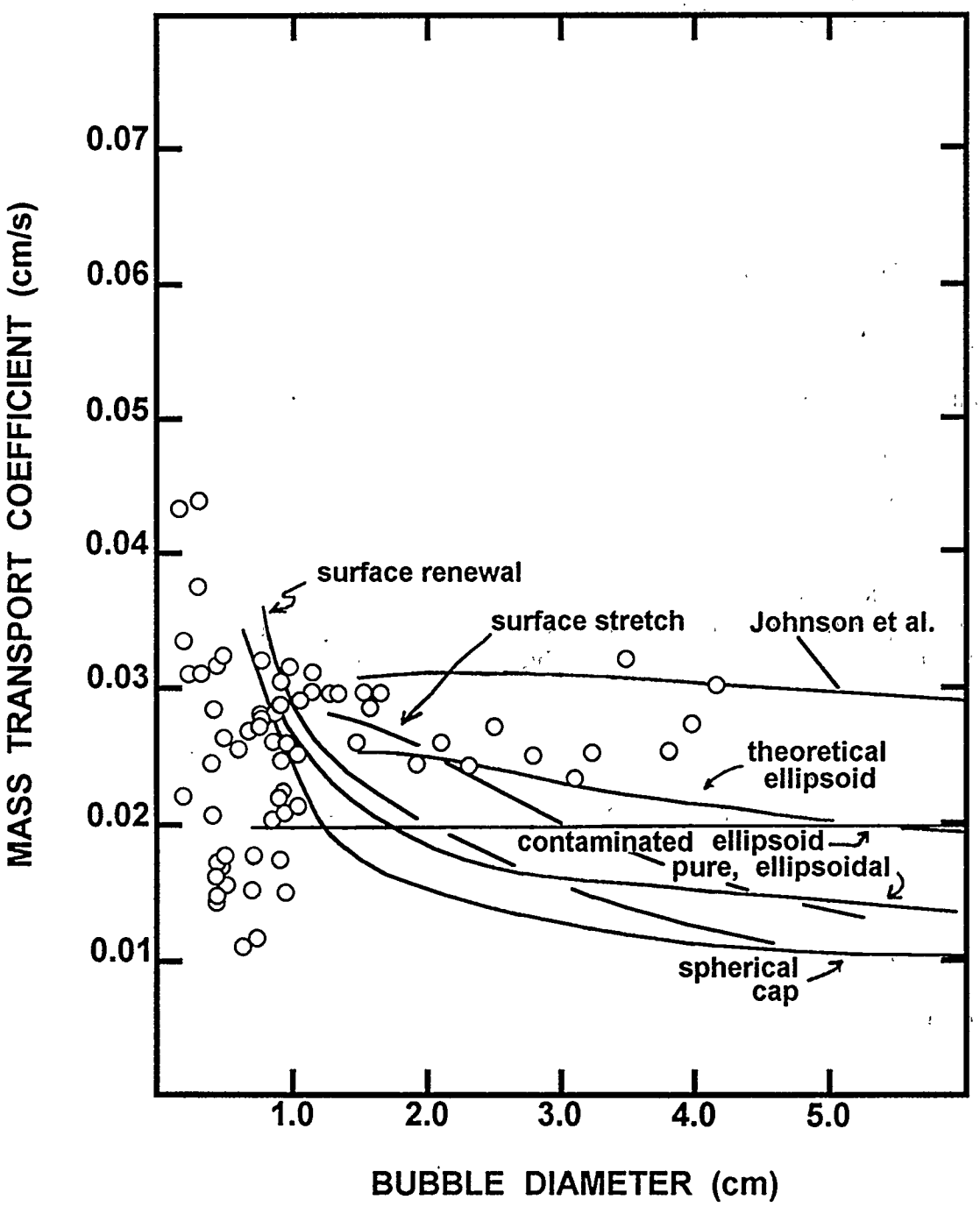

Figure 66. Comparison of mass transport coefficients predicted for CO_2 in water from nonspherical bubbles to experimental data. Bubble diameter in this figure refers to the spherical bubble with an equivalent volume.

$$Sh = \begin{cases} 1.13\,Pe^{1/2}/\sqrt{1-\epsilon} & \text{for } Re \to \infty \\ 2.213\,Pe^{1/2}/Re^{0.108\sqrt{1-\epsilon}} & \text{for } 10 \le Re \le 1000 \\ \dfrac{(0.65+0.06Re^{1/2})Pe^{1/2}}{\left[\dfrac{5-6(\epsilon)^{1/3}+(\epsilon)^2}{5(1-\epsilon)}\right]^{1/2}} & \text{for } Re < 10 \end{cases}$$

where ϵ is the volume fraction gas.

Predictions of the Calderbank and Moo-Young correlations and the LeClair and Hamielec theoretical models are compared to experimental data in Figures 65 and 66. The Calderbank-Moo-Young correlation provides an upperbound on data for bubbles larger than 0.25 cm. The predictions for these bubbles are consistent with theoretical predictions for isolated spherical bubbles. The discontinuous shift in the correlation prediction for bubbles smaller than 0.25 cm seems to be opposite the trend in the data.

The predictions of LeClair-Hamielec model are shown in Figures 65 and 66 in the limit of zero gas fraction. The model seems to predict well data for very small bubbles. Like the Calderbank-Moo-Young correlation and the theoretical model for isolated spherical bubbles, the LeClair-Hamielec theoretical model bounds from above the experimental data.

The heat transfer coefficients that can be derived by analogy to the mass transport models and correlations are shown as functions of bubble diameter in Figure 67. The heat transfer coefficients shown in this figure are for water at 373 K. The analogy drawn from the Calderbank-Moo-Young correlation appears to be at odds with predictions derived from analogies to other models. The predicted heat transfer coefficients are about a factor of 2 higher than heat transfer coefficients derived above for steam bubbles.

Internal transfer processes in small bubbles are expected to be quite rapid. Only theoretical expressions for transfer rate coefficients are available. The case in which there is circulation within the bubble yields the Kronig-Brink solution [88] for $4Đt/D_B^2(e) \to \infty$:

$$Sh = 17.66$$

The long term limit without internal circulation [89] is:

$$Sh = 6.58$$

The Kronig-Brink model was derived for conditions in which mass transport in the liquid phase is infinitely fast. The long-time, internal Sherwood number when the external mass transport rate is finite is shown as a function of the external Sherwood number [102] in Figure 68. The correlation line in this figure is given by:

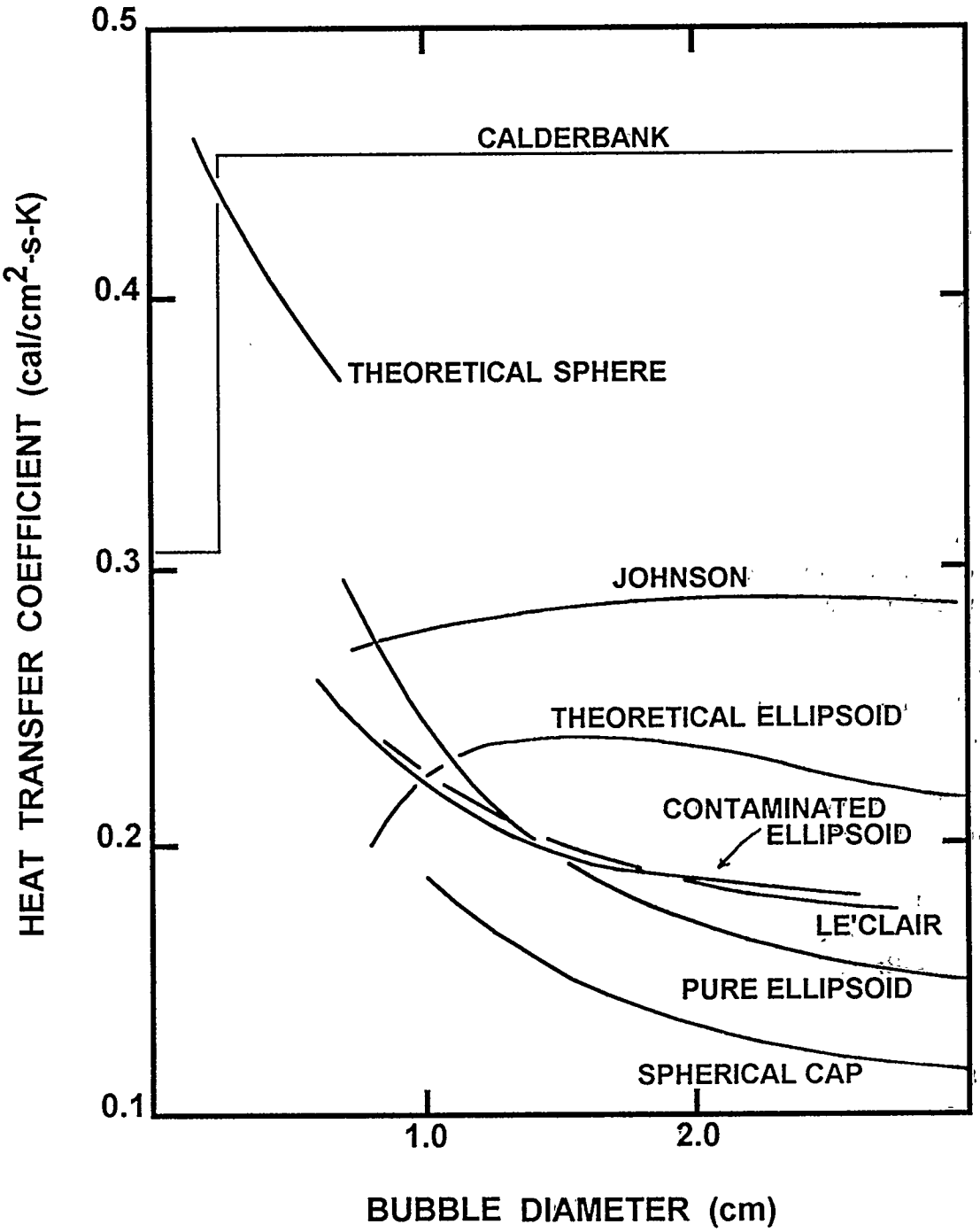

Figure 67. External heat transfer coefficients for bubbles in water at 373 K derived from analogies to mass transport models

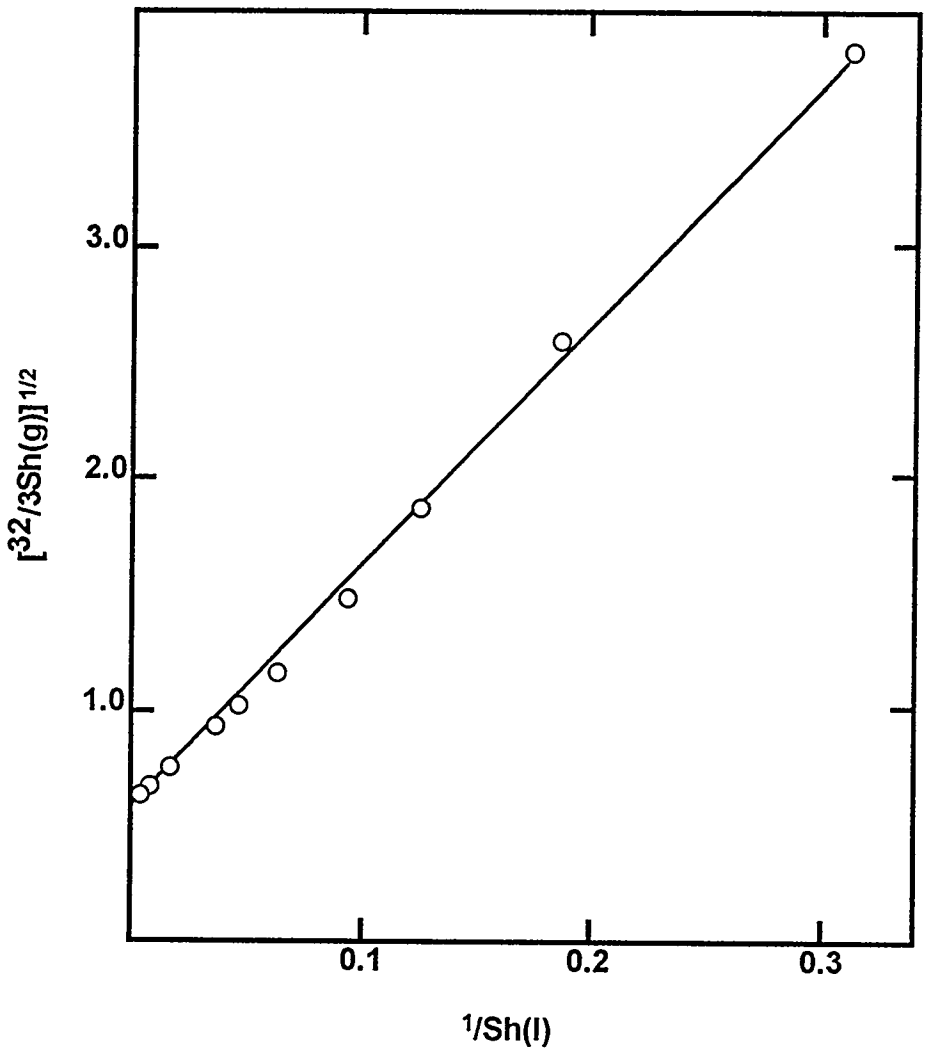

Figure 68. Correlation of the long-term Sherwood number in the gas phase for cases with a finite liquid phase Sherwood number

$$\left[\frac{32}{3\,Sh(g)}\right]^{1/2} = \frac{1}{1.656} + 10.20874/Sh(l)$$

where

Sh(g) = Sherwood number in the gas phase, and

Sh(l) = Sherwood number in the liquid phase.

J. Thermophysical Properties

The thermophysical properties of water, steam and permanent gases used in this study are described in the subsections below.

1. Properties of Liquid Water

Properties of suppression pool water were calculated assuming that the liquid was pure water. Powers and Sprung [1] have discussed the effects dissolved and suspended impurities can have on the properties of water. If the impurities are not strongly surface active, concentrations are expected to be so low in the suppression pool that any error arising from neglect of the impurity effects on water properties is likely to be negligible in comparison to other uncertainties.

The thermodynamic quantities enthalpy, vapor pressure, and density were calculated using correlations recently recommended by the Association for the Properties of Water and Steam [83]:

- Enthalpy (cal/gm)

$$h = \alpha + \frac{T}{\rho}\frac{dP}{dT}$$

$$\alpha = 0.23900\left[d_\alpha + d_1\theta^{-19} + d_2\theta + d_3\theta^{4.5} + d_4\theta^{5} + d_5\theta^{54.5}\right]$$

- Vapor pressure (atmospheres)

$$\ln\frac{P}{P_c} = \frac{T_c}{T}\left[a_1\tau + a_2\tau^{1.5} + a_3\tau^{3} + a_4\tau^{3.5} + a_5\tau^{4} + a_6\tau^{7.5}\right]$$

- Density (g/cm^3) of the saturated liquid

$$\frac{\rho}{\rho_c} = 1 + b_1\tau^{1/3} + b_2\tau^{2/3} + b_3\tau^{5/3} + b_4\tau^{16/3} + b_5\tau^{43/3} + b_6\tau^{110/3}$$

where

$\theta = T/T_c$

$\tau = 1 - T/T_c$

$y = \tau^{1/3}$

$T_c = 647.096$ K

$P_c = 217.755$ atms

$\rho_c = 0.322$ g/cm^3

$d_\alpha = -1135.905627715$

$d_1 = -5.65134998 \times 10^{-8}$

$d_2 = 2690.66631$

$d_3 = 127.287297$

$d_4 = -135.003439$

$d_5 = 0.981825814$

$a_1 = -7.85951783$

$a_2 = 1.84408259$

$a_3 = -11.7866497$

$a_4 = 22.6807411$

$a_5 = -15.9618719$

$a_6 = 1.80122502$

$b_1 = 1.99274064$

$b_2 = 1.09965342$

$b_3 = -0.510839303$

$b_4 = -1.75493479$

$b_5 = -45.5170352$

$b_6 = -6.74694450 \times 10^5$

Internal energy was derived from the expression:

$$h - P/\rho = U$$

Heat capacities at constant pressure, C_p, and at constant volume, C_v, were found by numerically differentiating with respect to temperature expressions for enthalpy and internal energy, respectively.

Surface tension was calculated from the expression [56]:

$$\sigma(\text{dynes/cm}) = 235.8\left[\frac{0.999686 - \overline{T}}{0.999686}\right]^{1.256}\left(1 - 0.625\left[\frac{0.999686 - \overline{T}}{0.999686}\right]\right)$$

where $\overline{T} = T/647.27$. Predictions of this correlation are compared to experimental data [103] in Figure 69.

The thermal conductivity of saturated liquid water was calculated from [55]:

$$\frac{\lambda}{\lambda^*} = \lambda_o(\overline{T})\ \lambda_1\ (\overline{T},\overline{\rho})$$

where

$$\lambda^* = 0.4945 \quad \text{W/m-K} = 1.1819 \times 10^{-3} \text{ cal/cm-s-K}$$

$$\lambda_o(\overline{T}) = \sqrt{\overline{T}}/\{1 + 6.978267/\overline{T} + 2.599096/\overline{T}^2 - 0.998254/\overline{T}^3\}$$

$$\lambda_1(\overline{T},\overline{\rho}) = \exp\left[\overline{\rho}\sum_{i=1}^{5}\sum_{j=1}^{6} L(i,j)\left(\frac{1}{\overline{T}} - 1\right)^{(i-1)}(\overline{\rho} - 1)^{(j-1)}\right]$$

$$\overline{\rho} = \rho/0.317763$$

ρ = density (g/cm^3)

The nonzero coefficients L(i,j) are listed in Table 11. Predictions of the correlation are compared to data in Figure 70.

The viscosity of saturated liquid water was calculated from [55]:

$$\mu(\text{g/cm-s}) = 5.5 \times 10^{-4}\mu_o(\overline{T})\mu_1\ (\overline{T},\overline{\rho})$$

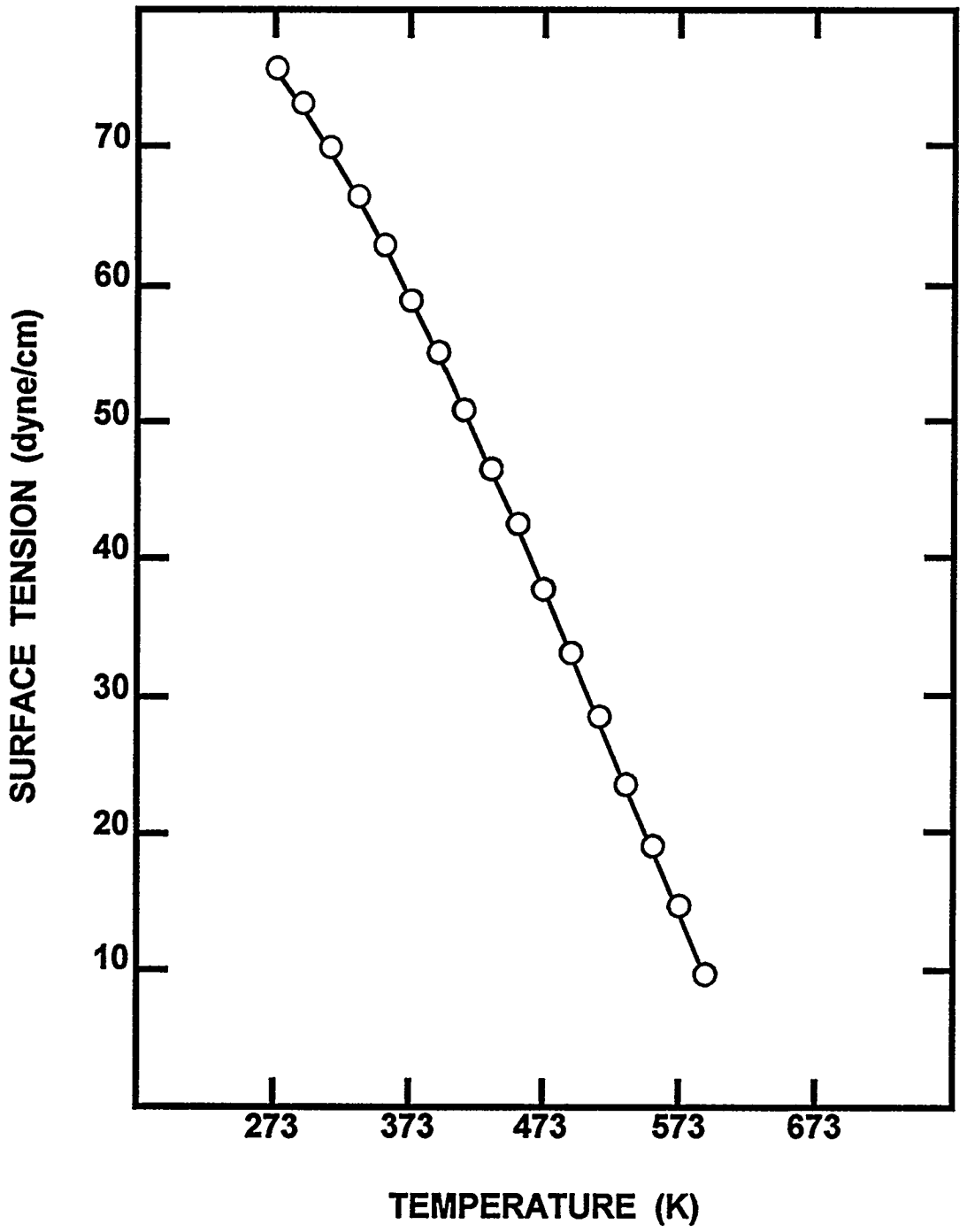

Figure 69. Comparison of predictions of the surface tension of water to experimental data [103]

Table 11. Coefficients in the term $\lambda_1(\overline{T},\overline{\rho})$ for thermal conductivity of liquid water

	j=1	2	3	4	5
L(1,j)	1.3293046	1.7018363	5.2246158	-8.7127675	-1.8525999
L(2,j)	-0.40452437	-2.2156845	-10.124111	-9.5000611	0.93404690
L(3,j)	0.24409490	1.6511057	4.9874687	4.3786606	0
L(4,j)	0.018660751	-0.76736002	-0.27297694	-0.91783782	0
L(5,j)	-0.12961068	0.37283344	-0.4308393	0	0
L(6,j)	0.044809953	-0.11203160	0.13333849	0	0

where:

$$\overline{T} = T(K) / 647.27$$

$$\mu_o(\overline{T}) = \sqrt{\overline{T}} \Big/ \left\{ 1 + \frac{0.978197}{\overline{T}} + \frac{0.579829}{\overline{T}^2} - \frac{0.202354}{\overline{T}^3} \right\}$$

$$\mu_1(\overline{T},\overline{\rho}) = \exp\left[\overline{\rho} \sum_{i=1}^{6} \sum_{j=1}^{7} H(i,j) \left(\frac{1}{\overline{T}} - 1 \right)^{(i-1)} (\overline{\rho} - 1)^{(j-1)} \right]$$

$$\overline{\rho} = \rho(g/cm^3) / 0.317763$$

The coefficients H(i,j) are listed in Table 12.

2. Properties of Steam

The thermodynamic properties of steam (enthalpy, internal energy, and heat capacities) were calculated from the expressions described for liquid water, above, using the density of steam in place of the density of liquid water. The density of saturated steam is given by [83]:

$$\left[\frac{\rho(g/cm^3)}{0.322} \right] = \exp(C_1\tau^{1/3} + C_2\tau^{2/3} + C_3\tau^{4/3} + C_4\tau^3 + C_5\tau^{37/6} + C_6\tau^{71/6})$$

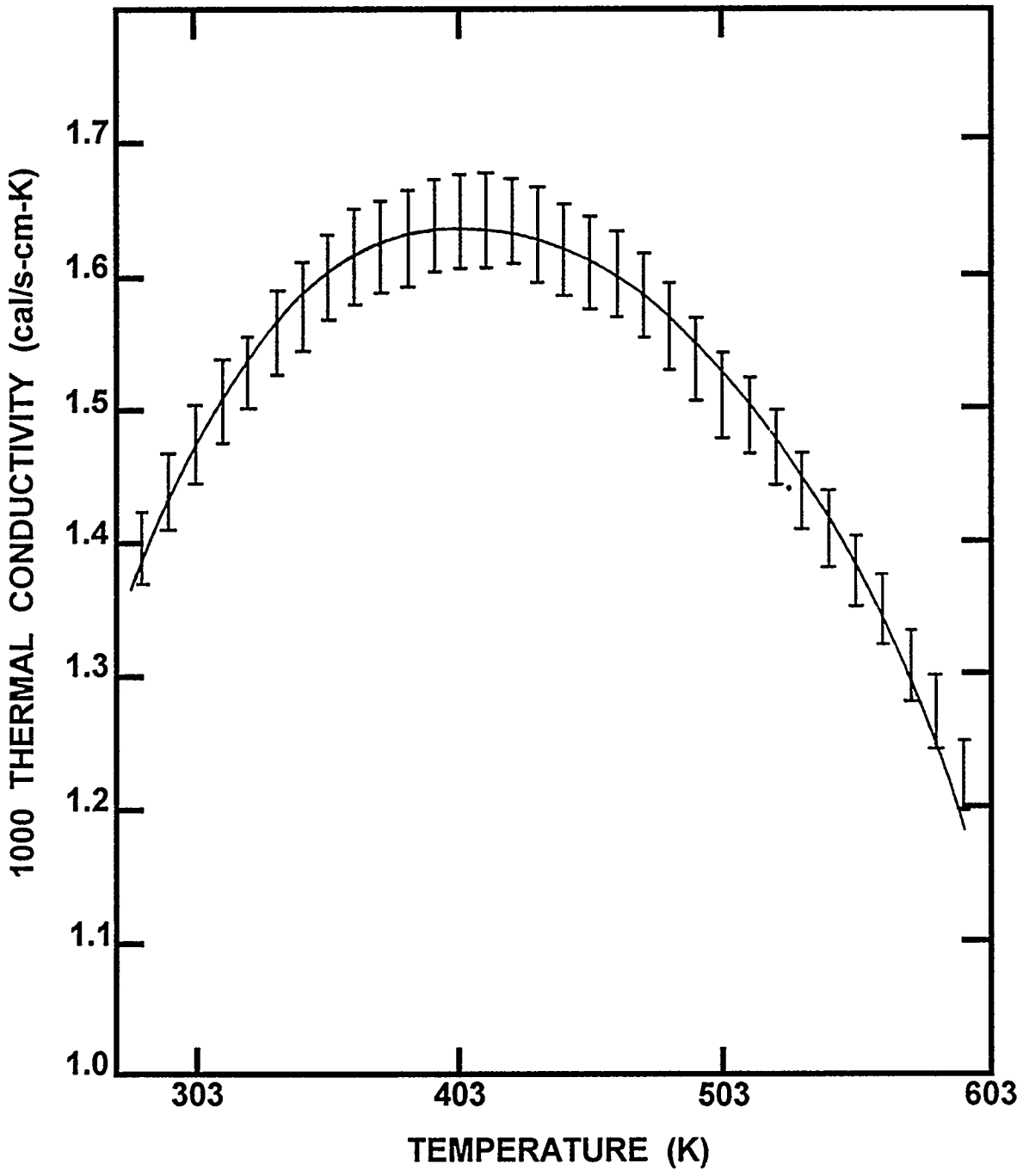

Figure 70. Comparison of the predicted thermal conductivity of water to critically assessed experimental data [223]

Table 12. Coefficients in the term $\mu_1(\overline{T},\overline{\rho})$ for the viscosity of liquid water

	j=1	2	3	4
H[1,j]	0.5132047	0.2151778	-0.2818107	0.1778064
H[2,j]	0.3205656	0.7317883	-1.070786	0.4605040
H[3,j]	0	1.241044	-1.263184	0.2340379
H[4,j]	0	1.476783	0	-0.4924179
H[5,j]	-0.7782567	0	0	0
H[6,j]	0.1885447	0	0	0

	j=5	j=6	j=7
H[1,j]	-0.0417661	0	0
H[2,j]	0	-0.01578386	0
H[3,j]	0	0	0
H[4,j]	0.1600435	0	-0.003629481
H[5,j]	0	0	0
H[6,j]	0	0	0

where

$$\tau = 1 - T/647.096$$

$$C_1 = -2.0315024$$

$$C_2 = -2.6830294$$

$$C_3 = -5.38626492$$

$$C_4 = -17.2991605$$

$$C_5 = -44.7586581$$

$$C_6 = -63.9201063$$

Similarly, the viscosity and thermal conductivity of steam were calculated from correlations used for liquid water substituting the density of steam for the density of water in the formulae described above.

The calculated viscosities and thermal conductivities are compared to critically evaluated data in Figures 71 and 72, respectively.

3. Properties of Permanent Gases

The gas phase injected into the suppression pool during the in-vessel phases of an accident is assumed to be a mixture of hydrogen and steam. During the ex-vessel stages of an accident, air (assumed here to be a mixture of nitrogen and oxygen) nitrogen, as well as the gaseous products of concrete decomposition, carbon dioxide and carbon monoxide, can contribute to gases injected into the steam suppression pool. Properties of the permanent gases that are of interest, density, viscosity, and thermal conductivity, are calculated from conventional gas kinetic theory as described in the subsections below.

Viscosity

The viscosities of N_2, CO, CO_2 and O_2 can be calculated using [294]:

$$\mu(T) = \frac{5}{16}\left[\frac{MRT}{\pi}\right]^{1/2}\frac{f(\eta)}{N_A\sigma^2\Omega^{(2,2)}}$$

where

M = molecular weight of the gaseous species

R = gas constant = 8.31451×10^7 ergs/mole-K

N_A = Avogadro's number = 6.0221367×10^{23}

σ = collision cross section

$$f(\eta) = 1 + \frac{3}{196}(8E^* - 7)^2$$

$\Omega^{(2,2)}$ = collision integral

$$E^* = 1 + 0.25T^* \, d \ln \Omega^{(2,2)}/dT^*$$

The collision integral is found from:

$$\Omega^{(2,2)} = \exp[0.46641 - 0.56991z + 0.19591z^2 - 0.03879z^3 + 0.00259z^4] \quad \text{for } 1 \le T^* \le 10$$

$$z = \ln T^*$$

$$T^* = kT/\epsilon$$

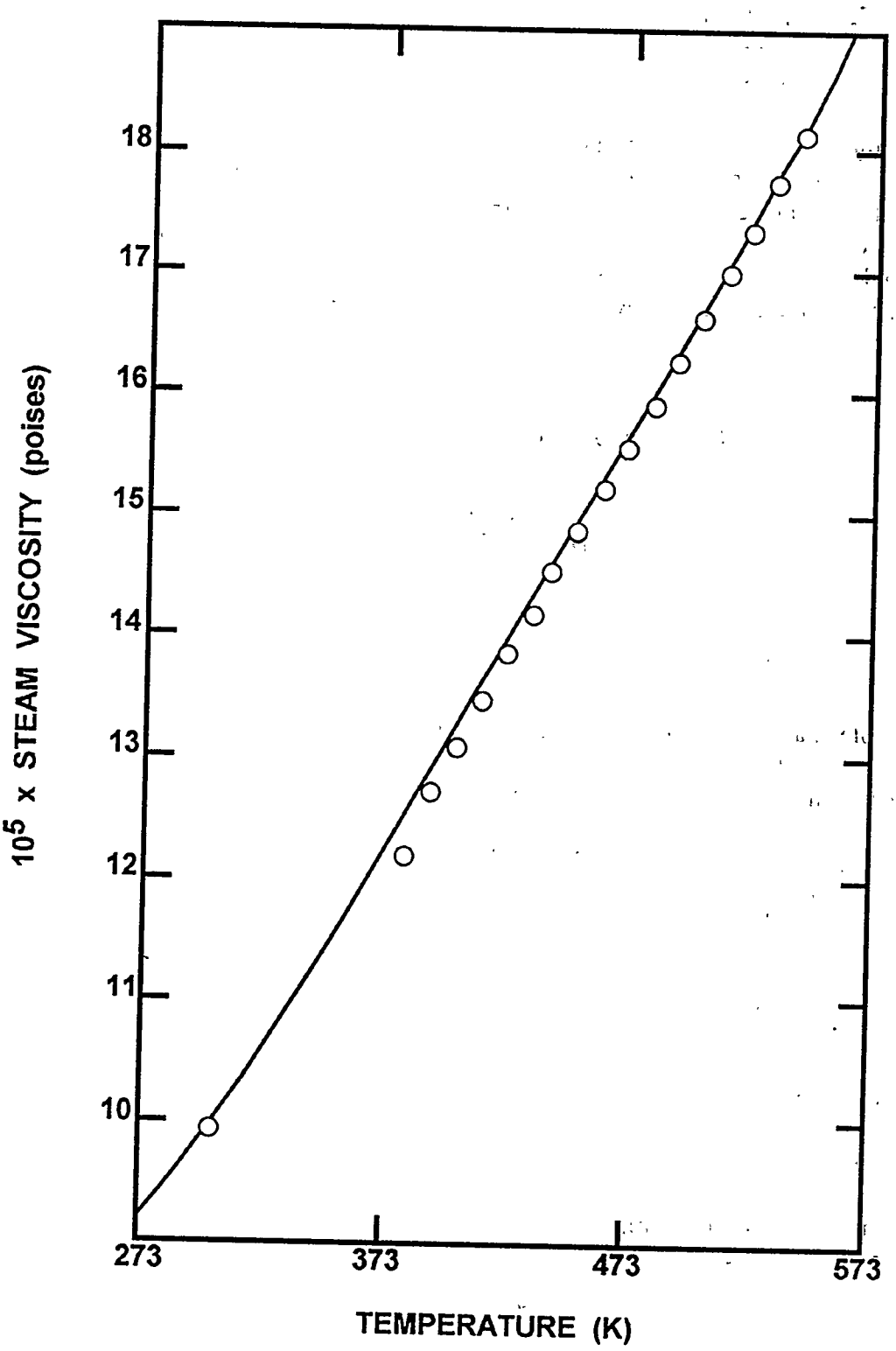

Figure 71. Comparison of calculated steam viscosity to recommended values derived from experimental data [106]

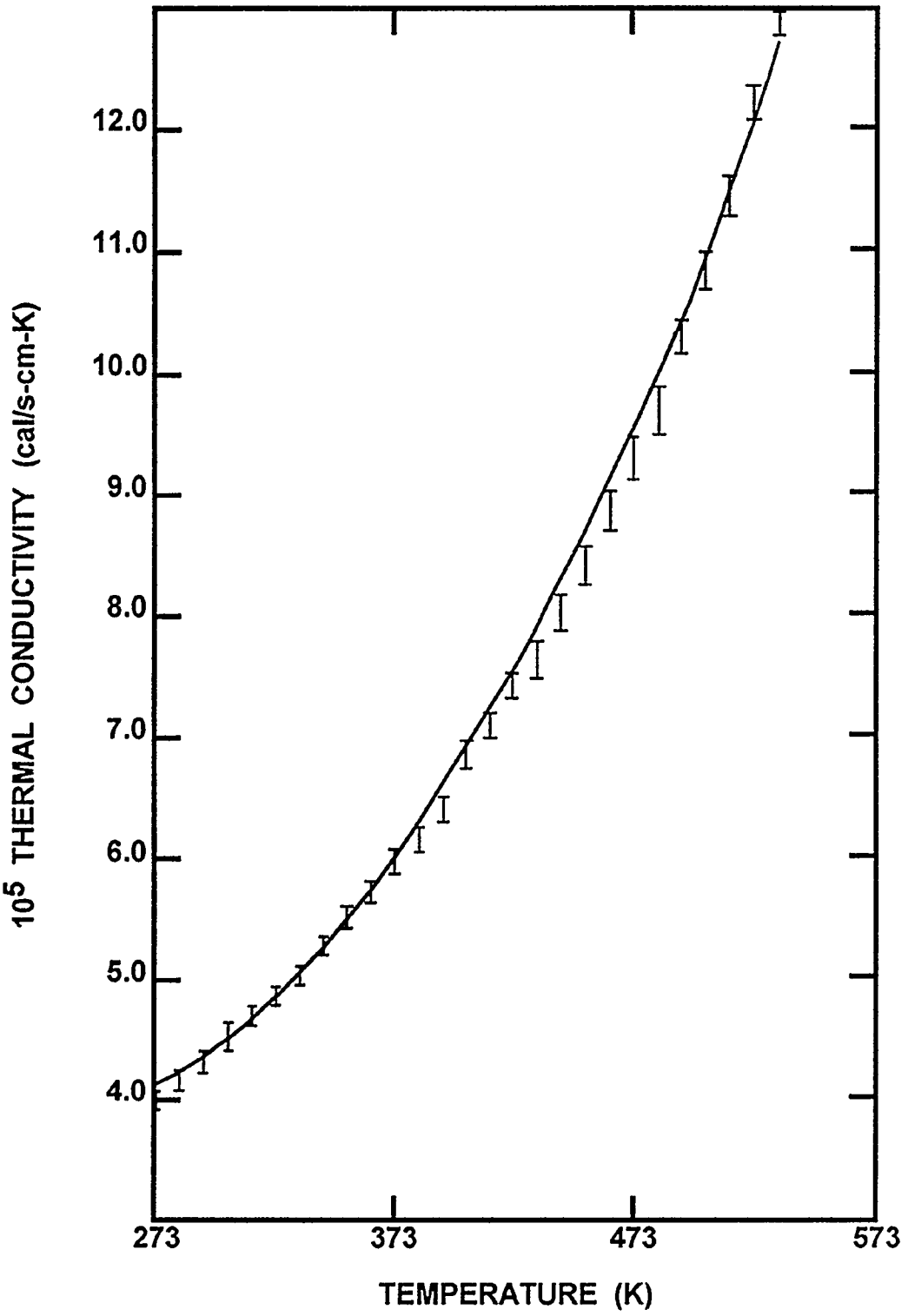

Figure 72. Comparison of calculated thermal conductivity of steam with experimental data [55]

k = Boltzmann's constant = 1.380658×10^{-16} ergs/K

ϵ = energy scaling parameter

At higher temperatures,

$$\Omega^{(2,2)} = (\rho^*)^2 \alpha \left[1.04 + a_1/z + a_2/z^2 + a_3/z^3 + a_4/z^4\right] \quad \text{for } T^* \geq 10$$

where

$$a_2 = -33.0383 + (\alpha_{10}\rho^*)^{-2} \left[20.0862 + 72.1059/\alpha_{10} + (8.27648/\alpha_{10})^2\right]$$

$$a_3 = 101.571 - (\alpha_{10}\rho^*)^{-2} \left[56.4472 + 286.393/\alpha_{10} + (17.7610/\alpha_{10})^2\right]$$

$$a_4 = -87.7036 + (\alpha_{10}\rho^*)^{-2} \left[46.3130 + 277.146/\alpha_{10} + (19.0573/\alpha_{10})^2\right]$$

$$\alpha_{10} = \ln (V_o^*/10)$$

$$\rho^* = \rho/\sigma$$

$$V_o^* = V_o/\epsilon$$

The various parameter values used in the theoretical expressions are listed in Table 13. The calculated viscosities are compared to experimental data in Figure 73.

The viscosity of hydrogen was correlated using recommended values [103,106] to the expression

$$\mu(\text{g/cm-s}) = 10^{-6}\{20.9161 + 248.797\xi - 83.6226\xi^2 + 19.551\xi^3\}$$

where ξ = T(K)/1000. The recommended values of the viscosity of hydrogen and predictions from the regression equation are shown in Figure 74.

Viscosities of Gaseous Mixtures

The viscosities of gaseous mixtures can be estimated from the Herning-Zipperer equation [289]:

$$\mu(\text{mix}) = \sum_{i=1}^{N} \mu(i)\, x(i)\, M(i)^{1/2} \Big/ \sum_{i=1}^{N} x(i)\, M(i)^{1/2}$$

where

$\mu(i)$ = viscosity of the pure, i^{th} constituent

Table 13. Parameter values for calculation of gas properties

	N_2	O_2	CO	CO_2	H_2
M(g/mole)	28.0135	31.9988	28.010	44.010	
σ(cm)	3.652×10^{-8}	3.407×10^{-8}	3.652×10^{-8}	3.769×10^{-8}	
ϵ/k(K)	98.4	121.1	98.4	245.3	
ρ*	0.1080	0.0745	0.1080	0.0720	
V_o*	5.308×10^{4}	1.322×10^{6}	5.308×10^{4}	2.800×10^{6}	
C_6*	2.18	2.27	2.63	1.86	
a(cal/mole-K)	6.37936	7.27376	6.54038	10.6120	6.12942
b(cal/mole-K^2)	1.66422×10^{-3}	1.17309×10^{-3}	1.61207×10^{-3}	2.96216×10^{-3}	1.22008×10^{-3}
c(cal/mole-K^3)	-2.76494×10^{-7}	-1.38817×10^{-7}	-2.7182×10^{-7}	-5.03906×10^{-7}	-1.0301×10^{-7}
d(cal-K/mole)	0.0614977	-0.589293	-0.0766475	-2.43100	0.410398

x(i) = mole fraction of the i^{th} constituent

M(i) = molecular weight of the i^{th} constituent

N = number of constituents.

Heat Capacities

Heat capacities of the gases H_2, N_2, O_2, CO, and CO_2 were evaluated at the ideal gas limit. Data from the JANAF Tables [104,105] were correlated with temperature using the expression

$$C_p = a + bT + cT^2 + dx10^5/T^2$$

using nonlinear least-squares methods. Derived parameter values are listed in Table 13. In the ideal gas limit, the constant volume heat capacity is related to the constant pressure heat capacity by:

$$C_p = C_v + R$$

where R is the gas constant.

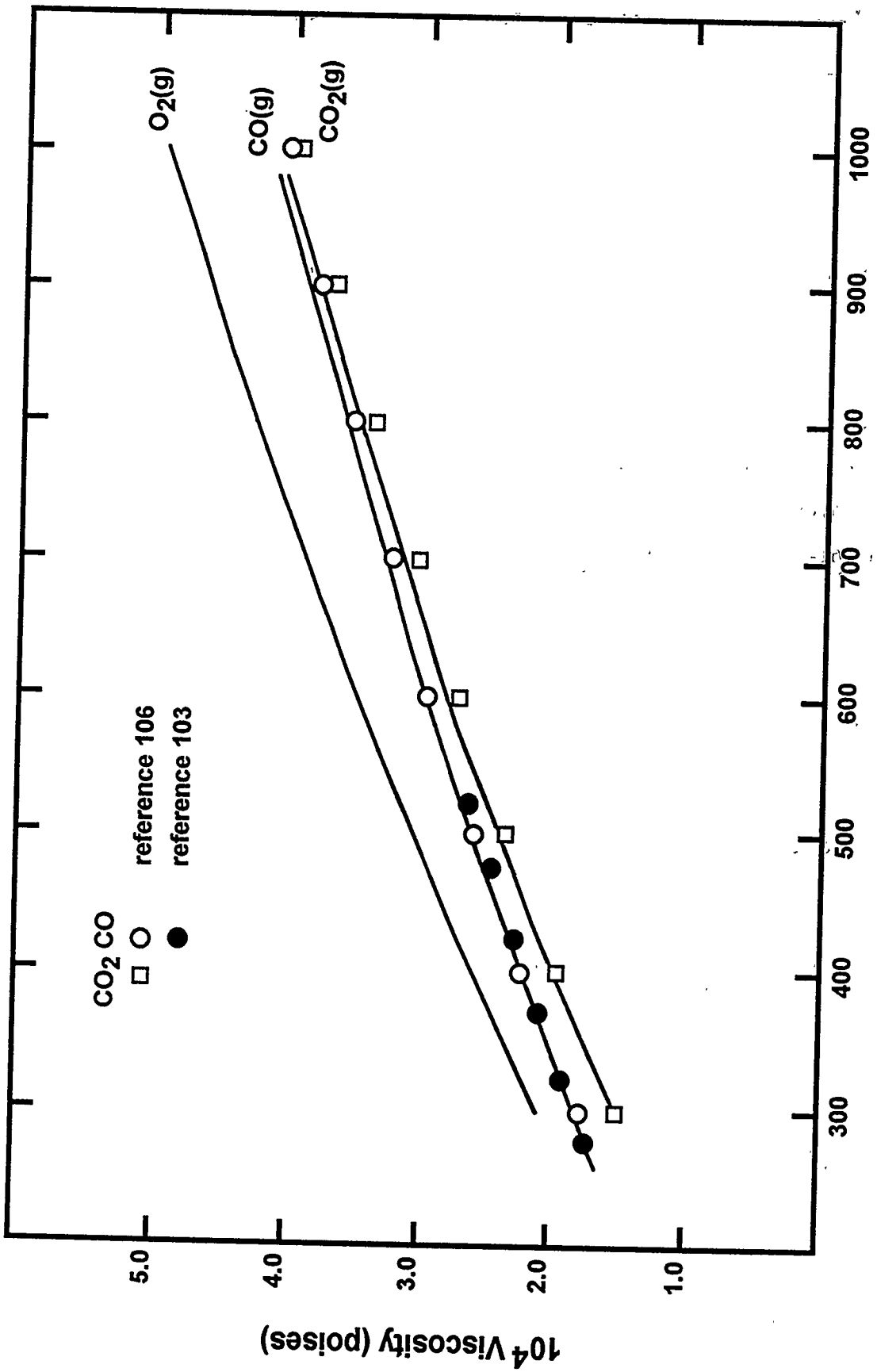

Figure 73. Comparison of calculated gas viscosities to recommended values derived from experimental data [103,106]

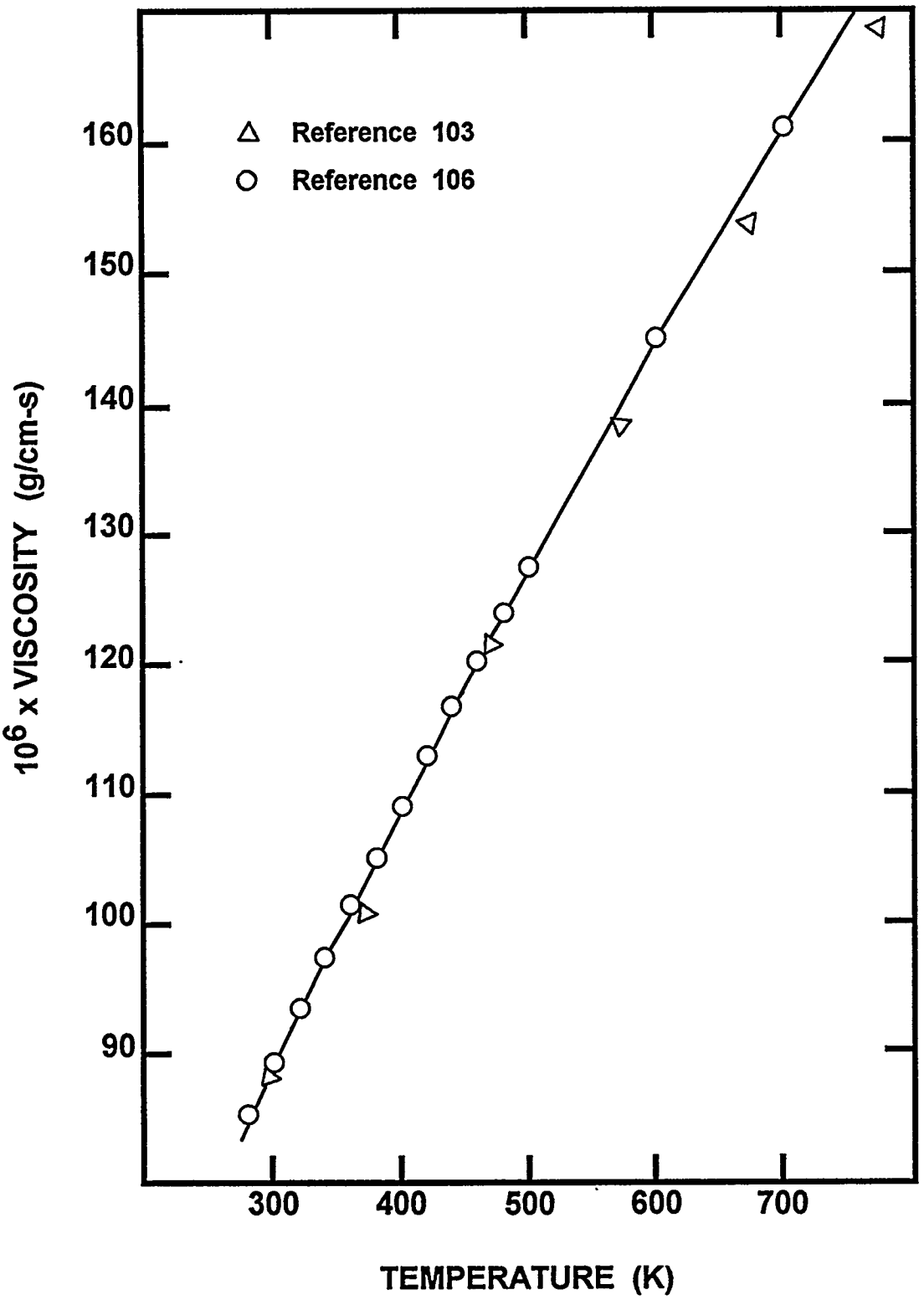

Figure 74. Viscosity of hydrogen as a function of temperature. Solid line calculated from the regression equation described is in the text.

Gaseous Diffusion Coefficients

Molecular mechanics and gas kinetic theory give rise to elaborate theoretical expressions for binary diffusion coefficients. Theory is best developed for gases that are not polar and do not have internal structure. Unfortunately, the polarity of H_2O poses a challenge to completely theoretical expressions for binary diffusion coefficients. Reid, Prausnitz and Poling [127] find the accuracy of theoretical models to be erratic. These authors recommend an empirical formulation by Fuller et al. [128,129]:

$$Đ_{AB} = \frac{0.00143\ T^{1.75}}{P\ M_{AB}^{1/2} \left[V_D(A)^{1/3} + V_D(B)^{1/3}\right]^2} \quad cm^2/s$$

where

M_{AB} = 2 / [1/M(A) + 1/M(B)], and

$V_D(i)$ = diffusion volume (listed in Table 14)

Other studies [131-135] have supported use of this formulation or one by Wilke and Lee [130]:

$$Đ_{AB} = \frac{0.001 \left[3.03 - \left(0.98/M_{AB}^{1/2}\right)\right] T^{3/2}}{P\ M_{AB}^{1/2}\ \sigma_{AB}^{2}\ \Omega_D}$$

where

σ_{AB} = 1/2 ($\sigma_A + \sigma_B$)

Ω_D = collision integral

The collision integral, Ω_D, is given by [136]:

$$\Omega_D = \frac{A}{(T^*)^B} + \frac{C}{\exp(DT^*)} + \frac{E}{\exp(FT^*)} + \frac{G}{\exp(HT^*)}$$

where

A = 1.06036

B = 0.15610

C = 0.193

D = 0.47635

Table 14. Parameter values for calculating the binary diffusion coefficients of gases

Gas	M(i) (g/mole)	$V_D(i)$ (cm^3/mole)*	$\sigma(i)$ (A°)*	$\epsilon(i)/k$ (K)*	$V_A(i)$ (cm^3/mole)**
H_2	2.01594	6.12	2.827	59.7	28.5
H_2O	18.01534	13.1	2.641	809.1	18.7
N_2	28.0134	18.5	3.798	71.4	34.7
O_2	31.9988	16.3	3.467	106.7	27.9
CO	28.01050	18.0	3.690	91.7	
CO_2	44.0099	26.9	3.941	195.2	37.3

*Reference 127
**Reference 137

E = 1.03587

F = 1.52996

G = 1.76474

H = 3.89411

Perhaps the most important binary, gaseous diffusion couple of interest here is the H_2/H_2O mixture. Predictions of the binary diffusion coefficient in this system obtained from the two empirical correlations are compared to data [223] in Table 15. The correlation by Fuller et al. usually yields values somewhat higher than those observed whereas the correlation by Wilke and Lee yields values that are consistently low in comparison to the data. Modifications of the correlations to account for the dipole moment of H_2O and the polarizability of H_2 do not greatly improve the agreement between predictions and the observations.

The predicted diffusion coefficients of steam in H_2, N_2, and CO_2 at 1 atms predicted with the correlations are shown in Figure 75 as functions of temperature.

Table 15. Comparison of predicted and observed binary diffusion coefficients in the H_2/H_2O system

T (K)	P (atms)	Diffusion coefficient (cm^2/s)		
		Observed [223]	Fuller et al. [128,129]	Wilke-Lee [130]
307.1	1	1.020	0.965	0.770
328.4	1	1.121	1.085	0.876
352.2	1	1.200	1.227	1.000
322.5	1	1.000	1.052	0.846
365.4	1	1.179	1.308	1.072
307.0	1	0.915	0.965	0.769
328.5	1	0.961	1.086	0.876
297.93	1	0.802	0.915	0.726
312.79	1	0.937	0.997	0.798
327.95	1	0.998	1.094	0.883
292.95	1	0.850	0.889	0.703
324.5	1	1.012	1.063	0.856
365.4	1	1.25	1.308	1.072
372.3	1	1.28	1.352	1.111
321.15	25.2	0.0316	0.0414	0.0333
321.15	49.4	0.0135	0.0211	0.0170
321.15	98.8	0.0065	0.0106	0.0085
321.15	194.6	0.0026	0.0054	0.0043
321.15	291.4	0.0021	0.0036	0.0029
341.15	25.2	0.0650	0.0460	0.0374
341.15	49.4	0.0338	0.0235	0.0190
341.15	98.8	0.0176	0.0117	0.0095
341.15	194.6	0.0101	0.0060	0.0048
341.15	291.4	0.0065	0.0040	0.0032

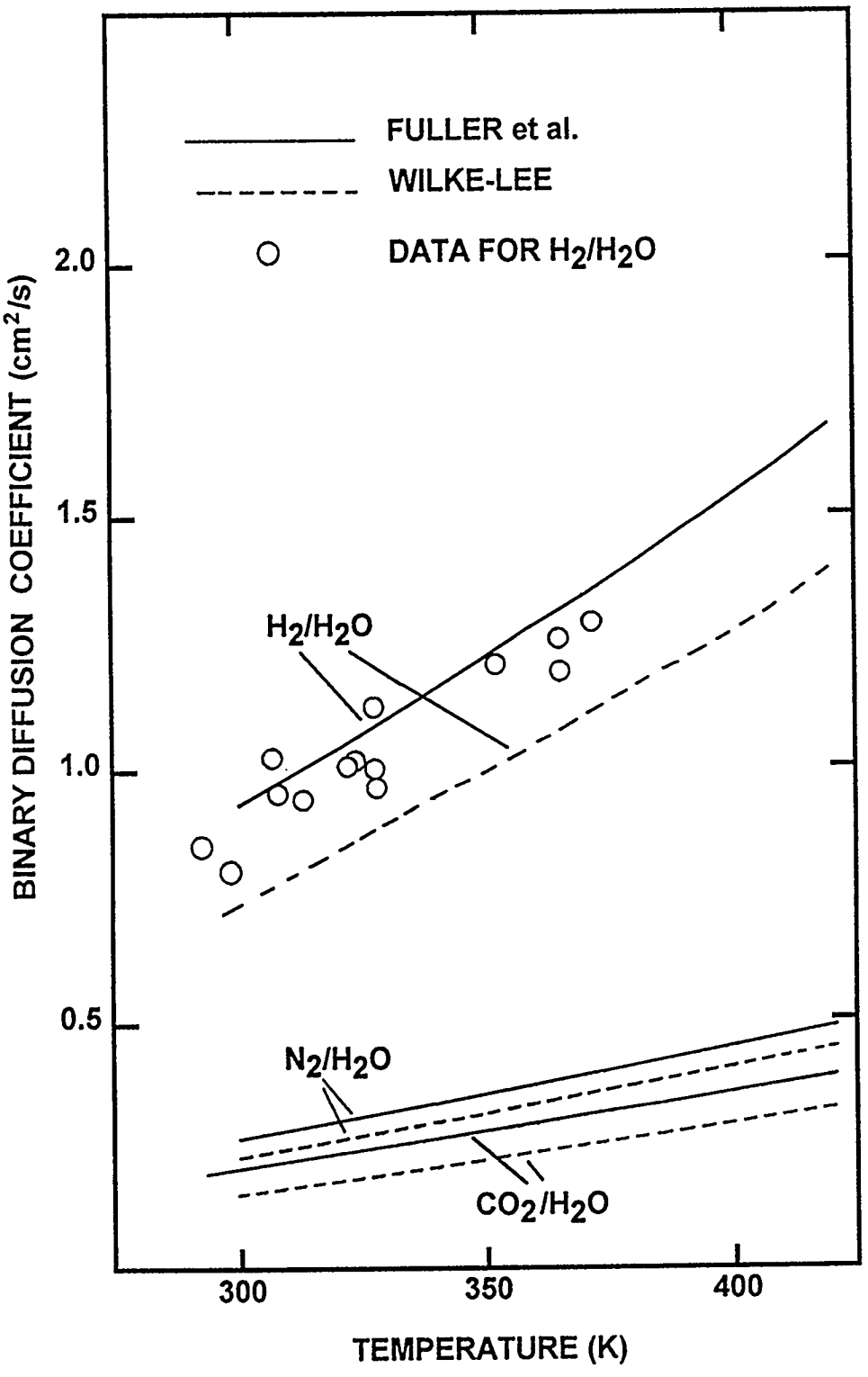

Figure 75. **Predicted binary, gaseous diffusion coefficients for the H_2/H_2O, N_2/H_2O, and CO_2/H_2O systems**

Thermal Conductivity

Uribe et al. [107] have developed elaborate theoretical expressions for the thermal conductivities of the gases N_2, O_2, CO, and CO_2 in the limit of zero density. These theoretical models allow contributions from the molecular translations, rotations, and vibrations as well as electronic states to be separately determined. Such models appear overly sophisticated for the purposes of this work. Consequently, results obtained by Uribe et al. were simply used to fit a simple polynomial expression:

$$k_{th}\left(\frac{cal}{cm-s-K}\right) = \frac{10^{-2}}{4.184}\left[L_o + L_1 T + L_2 T^2/1000 + L_3 T^3/10^6\right]$$

using nonlinear least-squares methods. Parameters determined in this way are shown in Table 16. Predictions obtained with the regression equations are compared to experimental data in Figures 76 through 80. A similar expression for the temperature-dependence of the thermal conductivity of hydrogen was found by fitting the above expression to recommended values of the thermal conductivity [103].

The thermal conductivity of mixtures can be estimated from the thermal conductivities of individual gases using an expression recommended by Mason and Saxena [120]:

$$k_{th}(mix) = \sum_{i=1}^{n}\left\{k_{th}(i) \Big/ \left[1 + \sum_{j\neq i}^{n} \phi(i,j)\ x(j)/x(i)\right]\right\}$$

$$\phi(i,j) = \frac{C}{2\sqrt{2}} \frac{\left[1 + \left(\frac{k_{th}(i)}{k_{th}(j)}\right)^{1/2}\left(\frac{M(i)}{M(j)}\right)^{1/4}\right]^2}{\left[1 + \frac{M(i)}{M(j)}\right]^{1/2}}$$

where

$k_{th}(mix)$ = thermal conductivity of the mixture,

$k_{th}(i,j)$ = thermal conductivity of the i^{th} constituent of the mixture,

$x(i)$ = mole fraction of the i^{th} constituent in the mixture,

$M(i)$ = molecular weight of the i^{th} constituent in the mixture,

C = constant.

Table 16. Parametric values for correlations of gas thermal conductivities

Gas	L_0	L_1	L_2	L_3
H_2	1.87×10^{-2}	0.5886×10^{-3}	-0.226342×10^{-3}	7.50673×10^{-6}
N_2	2.78051×10^{-3}	7.89354×10^{-5}	-1.22826×10^{-5}	1.53154×10^{-6}
O_2	1.52688×10^{-4}	9.38983×10^{-5}	-1.87753×10^{-5}	2.74421×10^{-6}
CO	1.60784×10^{-3}	8.04387×10^{-5}	-1.22788×10^{-5}	1.43727×10^{-6}
CO_2	-1.10485×10^{-2}	9.74176×10^{-5}	-1.72780×10^{-5}	1.77916×10^{-6}

Mason and Saxena recommend C = 1.065. Tondon and Saxena [121] recommend C = 0.85 for mixtures of polar and nonpolar gases.

The predictions obtained from the Saxena and Mason formula for the thermal conductivities of mixtures are compared to data for H_2/N_2 [118], N_2/CO [113] and N_2/CO_2 [116] mixtures in Figures 81 and 82.

4. Solubility of Gases in Water

The solubilities of gases in water are conveniently expressed by Henry's law:

$$P(i) = H(i)\ x(i)$$

where

P(i) = partial pressure (atms) of species i in equilibrium with water,

x(i) = mole fraction of species i in the mixture with water, and

H(i) = Henry's Law coefficient for species i and water.

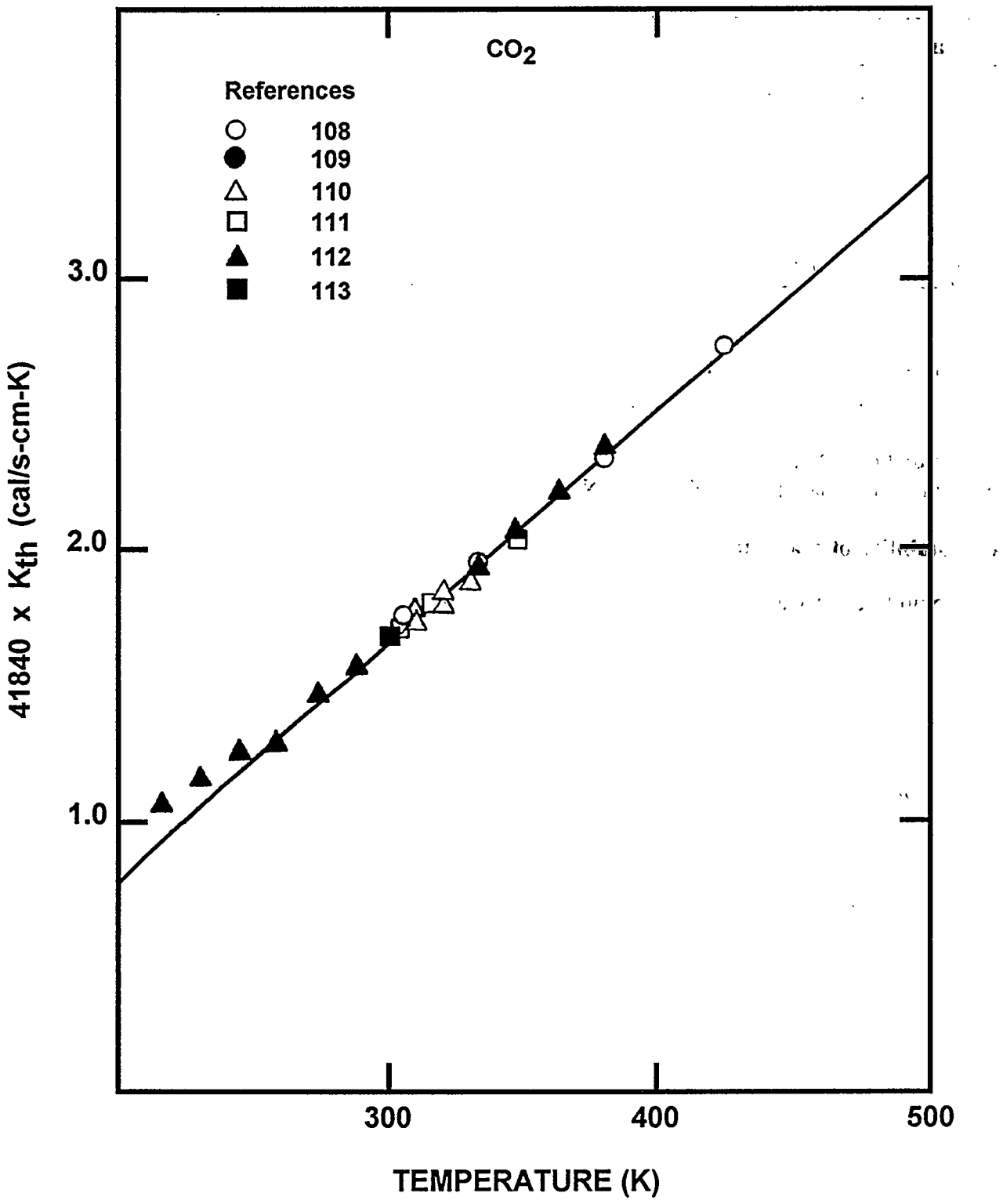

Figure 76. Comparison of the predicted thermal conductivity of CO_2 to experimental data [108-113]

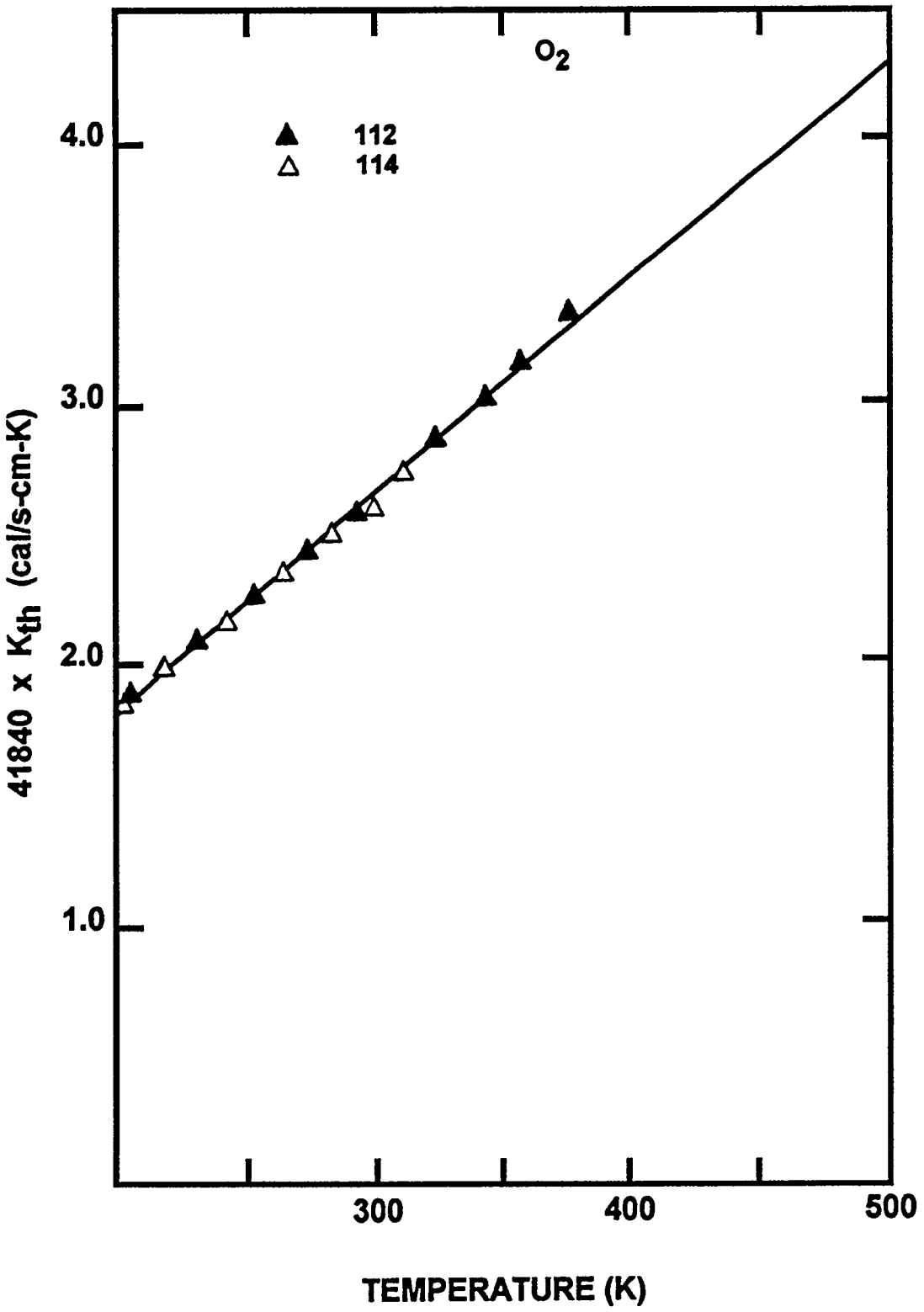

Figure 77. Comparison of the predicted thermal conductivity of O_2 to experimental data

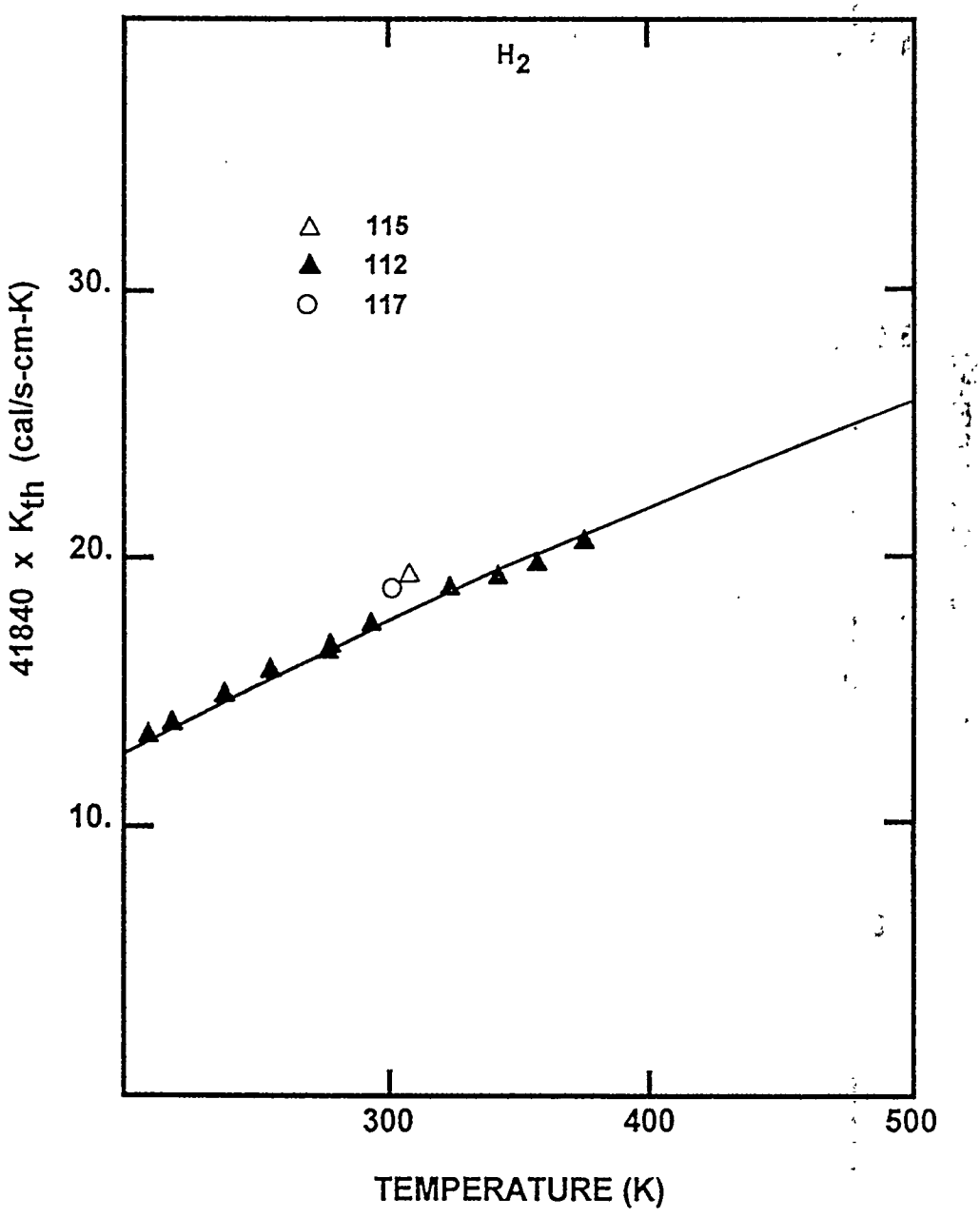

Figure 78. Comparison of the predicted thermal conductivity of H_2 to experimental data

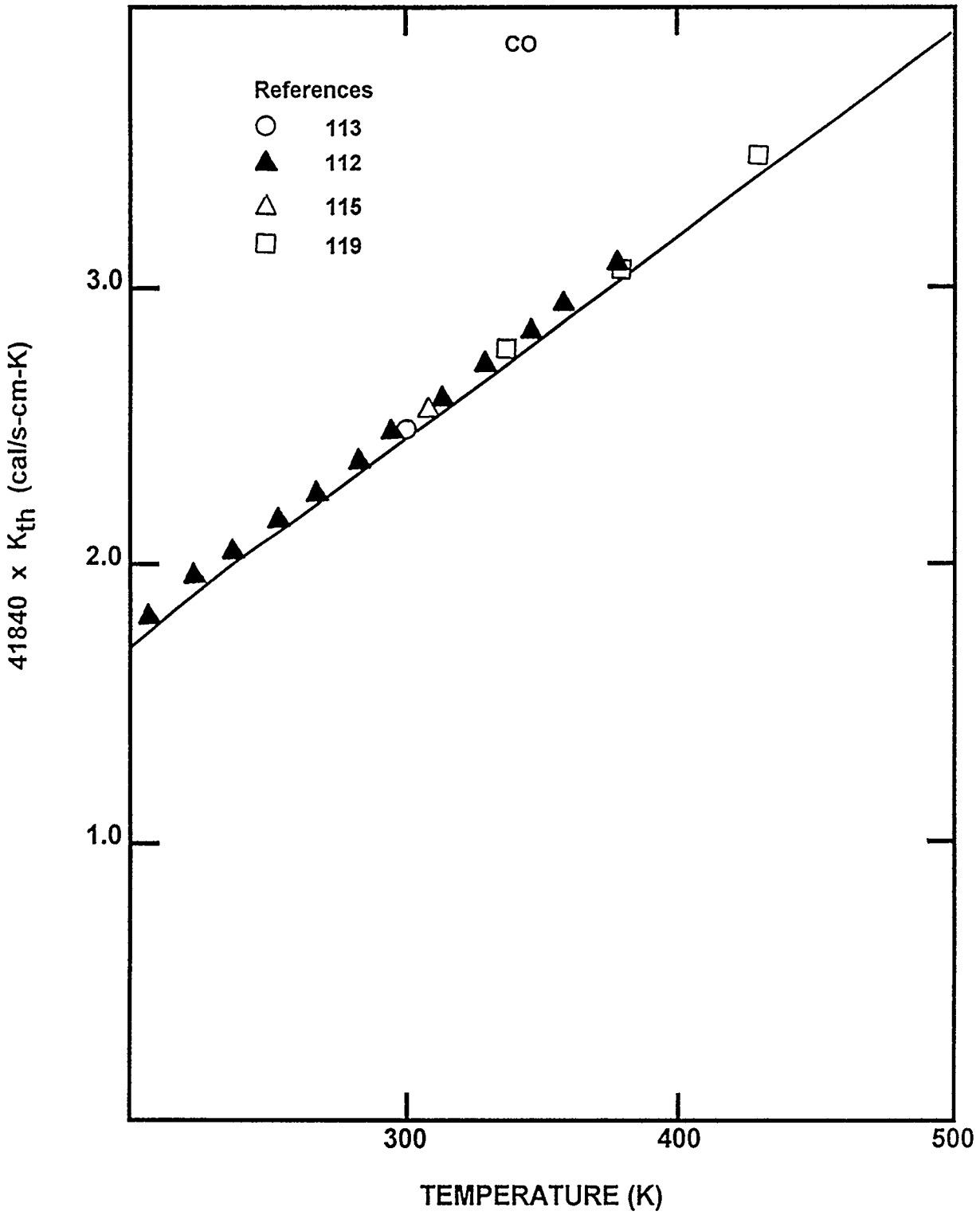

Figure 79. Comparison of the predicted thermal conductivity of CO to experimental data

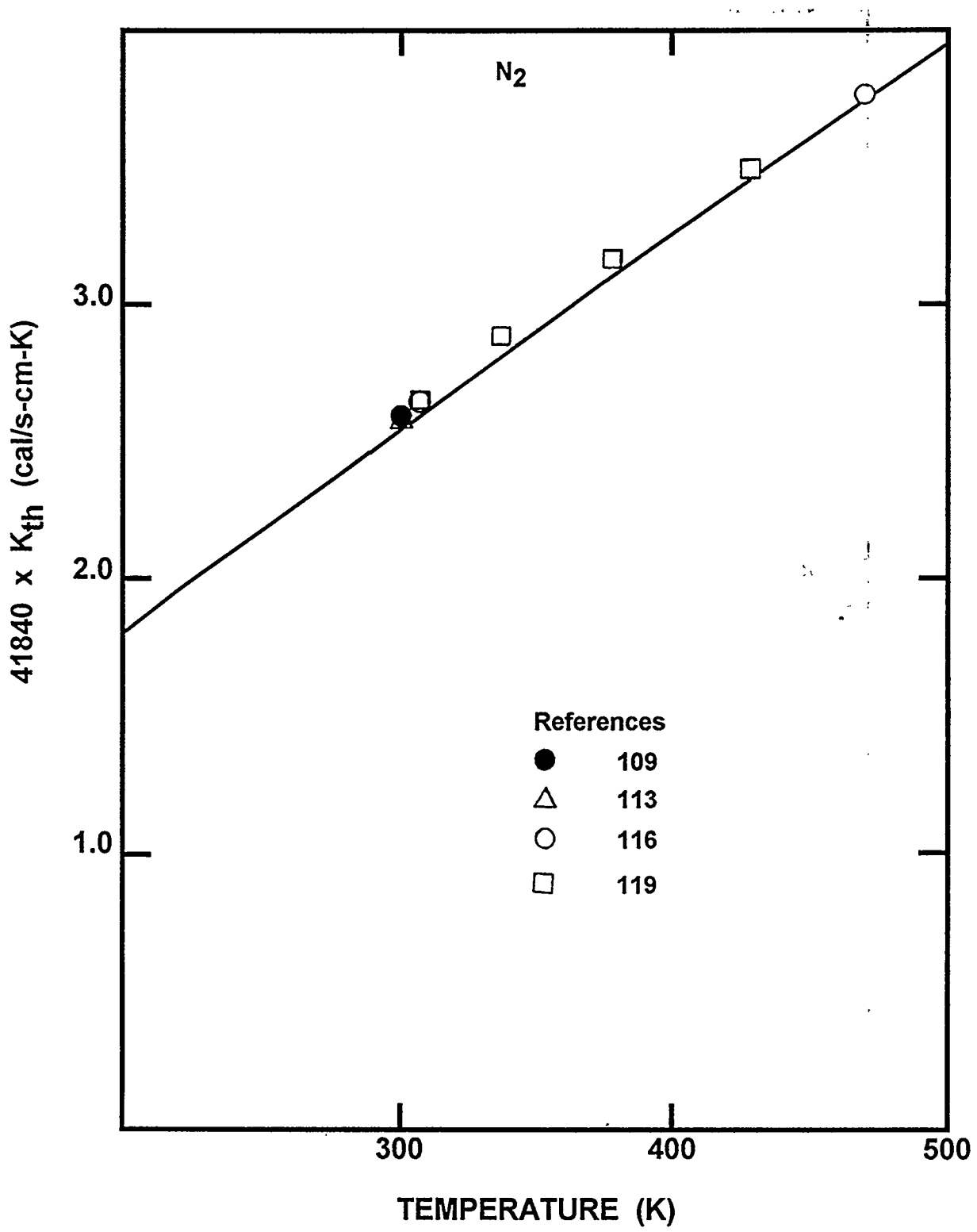

Figure 80. Comparison of the predicted thermal conductivity of N_2 to experimental data

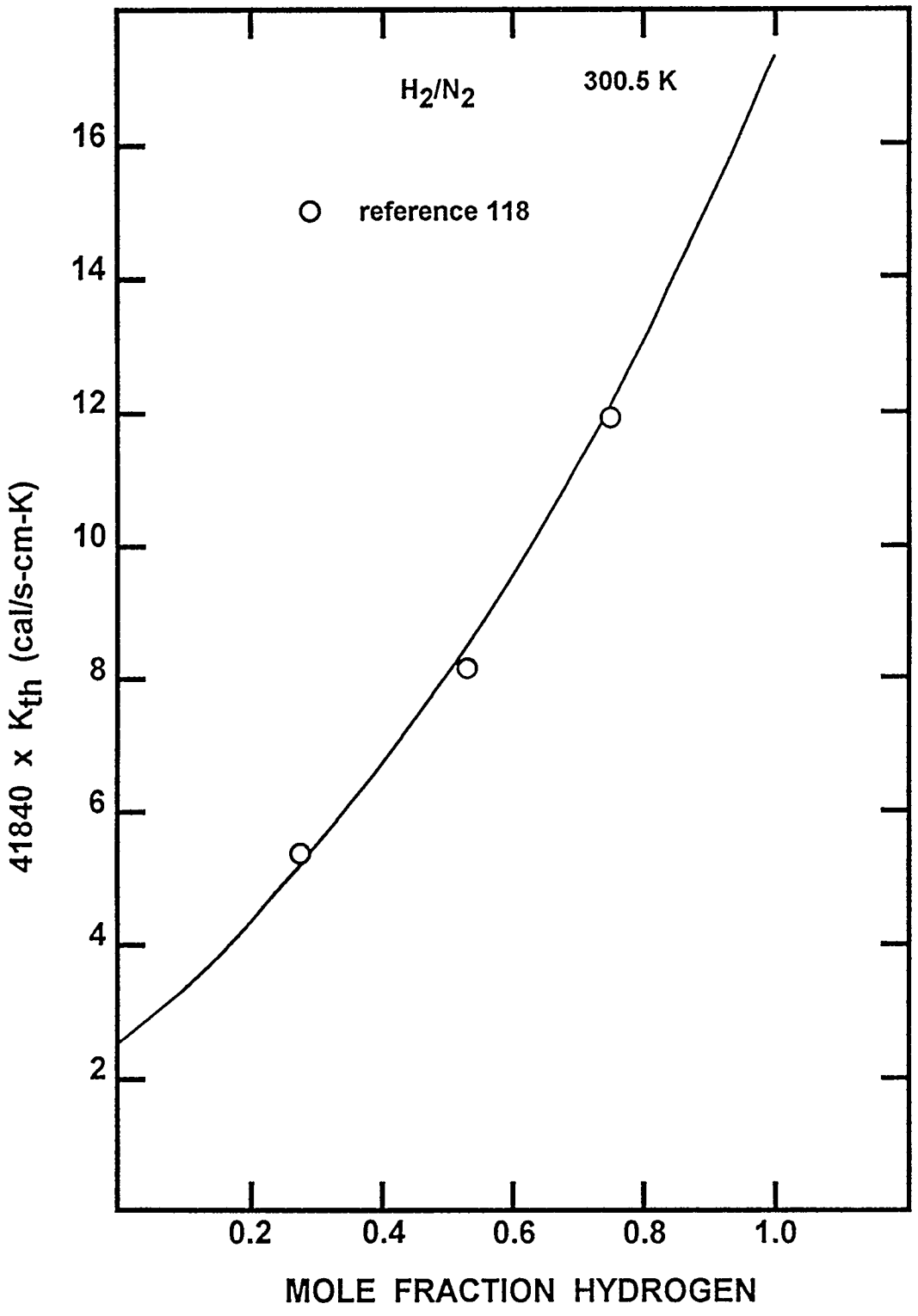

Figure 81. **Comparison of the predicted thermal conductivity of H_2/N_2 mixtures at 300.5 K to experimental data**

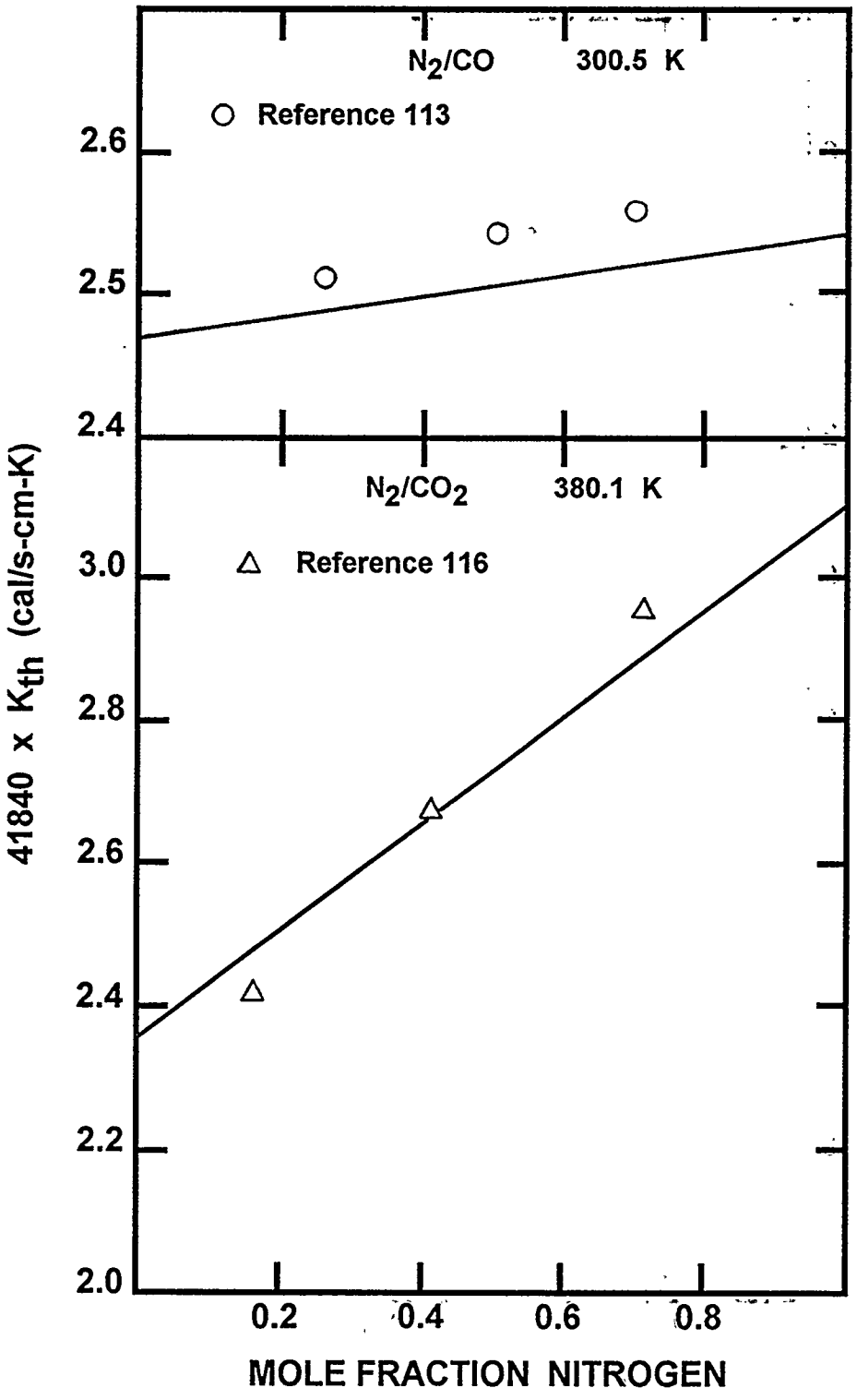

Figure 82. Comparison of the predicted thermal conductivities of N_2/CO mixtures at 300.5 K and N_2/CO_2 mixtures at 380.5 K to experimental data

Henry's Law coefficients are functions of temperature. Correlations of these coefficients used here are:

- CO [122]

$$\ln H(CO) = 115.22767 - 152.599953/\xi - 67.8429542 \ln \xi + 7.04595359\ \xi$$

- CO_2 [123]

$$\ln H(CO_2) = -4.54518 + 128.17/\xi - 376.68/\xi^2 + 299.7/\xi^3$$

- H_2 [124]

$$\ln H(H_2) = 48.1611 - 55.2845/\xi - 16.8893 \ln \xi$$

- O_2 [125]

$$\ln H(O_2) = 66.73538 - 87.47547/\xi - 24.45264 \ln \xi$$

- N_2 [126]

$$\ln H(N_2) = 67.38765 - 86.32129/\xi + 24.79808 \ln \xi$$

where ξ = T(K)/100 and pressure is in atmospheres. Solubilities of gases predicted with these correlations for gas partial pressures of 1 atmosphere are shown in Figure 83. Reliable data only extend up to about the boiling point of water for the gases except CO_2. The correlation for the Henry's law coefficient of CO_2 listed above can be used for temperature up to about 430 K. Over the temperature range for which there are suitable data, the gas solubility decreases with increasing temperature. This trend must eventually reverse since at the critical point of water the gases become completely miscible with water.

It is evident from the curves shown in Figure 83 that, until the water pool is saturated, diffusiophoresis by soluble gases can contribute to aerosol removal from bubbles in cold water. The effect might be especially important in the late stages of an accident in which CO_2 from concrete is an important constituent of gases entering suppression pools. Unlike the case of a water pool overlying core debris interacting with concrete, there are no alternate mechanisms to gas sparging to saturate the pool with CO_2. Of course, late in the accident, pool temperatures can be quite high and CO_2 solubility low.

K. Properties of Aerosol Particles

Discussions in the next section of this report will show how the rate of aerosol trapping depends on the properties of aerosol particles. Certainly, the size of aerosol particles will indeed affect rates of trapping. The discussions of aerosol size distributions are included in Chapter V as part of the

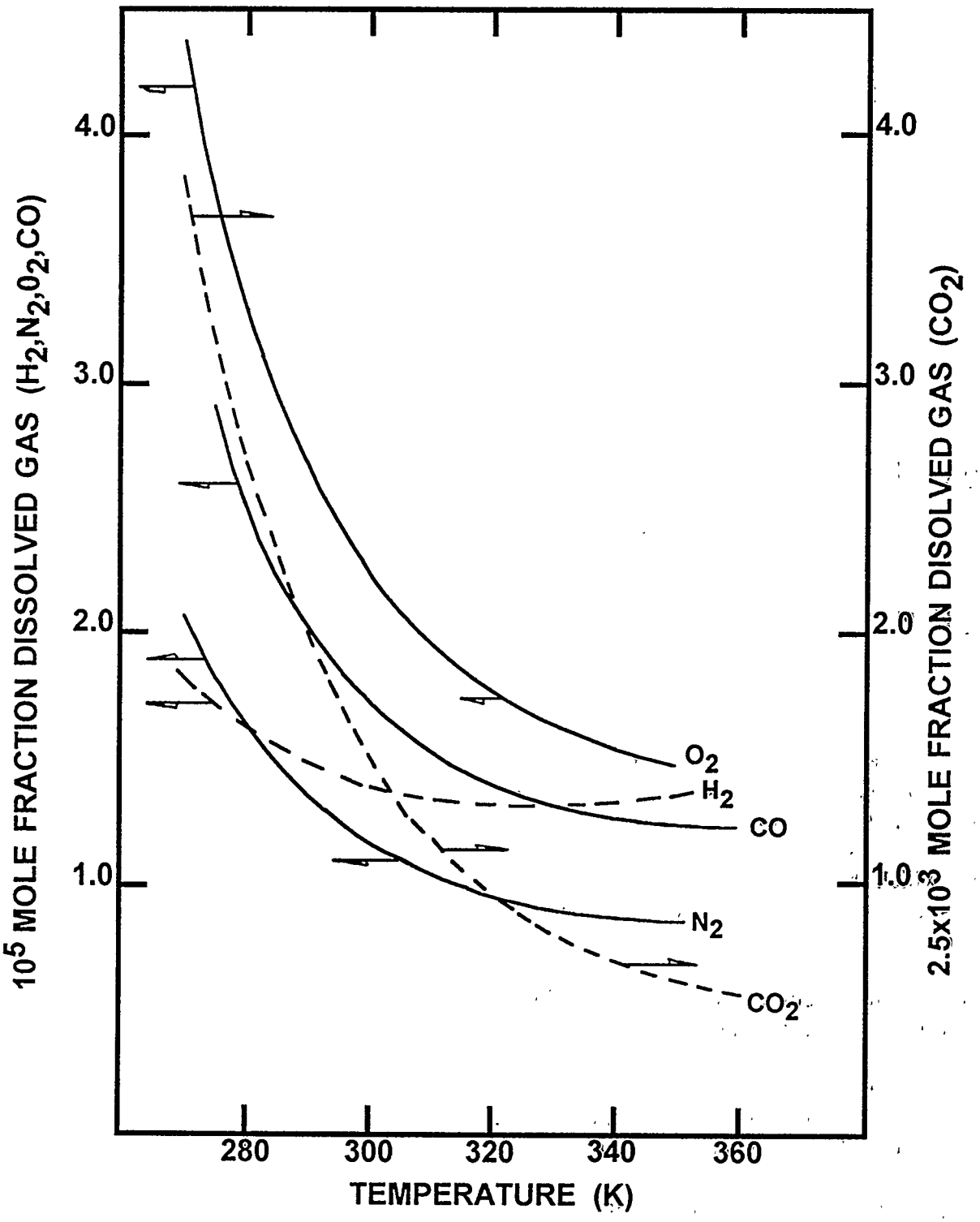

Figure 83. Solubilities of gases in water at 1 atmosphere pressure as functions of temperature. Note that the scale for CO, N_2, H_2, and O_2 solubilities is different than the scale for CO_2 solubility.

discussion of uncertainties that arise from details of severe accident progression. Similarly, the density of materials that make up the aerosol particles will be discussed in connection with accident progression uncertainties.

In this section, discussions focus on three properties of aerosol particles:

- shape factors,
- slip correction factors, and
- hygroscopicity of aerosols.

1. Shape Factors

The equations of aerosol physics are written for spherical aerosol particles. Of course, real aerosol particles are not spheres. To approximately account for nonspherical shapes, shape factors are introduced into the equations. Of most interest here is the dynamic shape factor, χ. Of somewhat less interest is the collision shape factor, γ. The dynamic shape factor accounts for the increase in the drag on a nonspherical particle. The collision shape factor accounts for the increase in the collisional cross section of a nonspherical particle.

In principle, the deviation of aerosols from spherical shape can be dramatic, especially when primary particles agglomerate to form chains of adhering particles [164]. Very large values of the shape factors occur only when the aerosol is kept dry. For the application of interest here, water will be present in abundance. Adsorption of water onto particle agglomerates will draw particle chains into nearly spherical compacts. Brockmann [164] has suggested that under these conditions, the dynamic shape factor and the collision shape factor are equal and that they are determined by the packing density of the aerosol:

$$\chi = \gamma = 1/\alpha^{1/3}$$

where α is the effective density of the aerosol particle divided by the density of the material making up the primary particles.

It is likely that voids in compacted particles will be filled with condensed water in the situation of interest here. These voids within the particle can be likened to "ink bottle" pores in solids [174]. That is, the pores have entrances that are narrower than the body of the pore. The prototype pore is one formed by the close packing of four spheres to form a tetrahedron. The approximate diameter of the pore body is:

$$(\sqrt{3}-1)d_p \cong 0.73d_p$$

where d_p is the diameter of a sphere. The entrance to the pore, however, has a diameter of only:

$$d_p(2-\sqrt{3})/\sqrt{3} = 0.15 d_p$$

The pore will fill with condensed water when the ambient partial pressure of steam is:

$$P_{fill} = P_{eq} \exp\left[-\sigma_l \bar{v}/0.366\ d_p\ RT\right]$$

where P_{eq} is the equilibrium partial pressure of water at the prevailing temperature. The pore will empty when the steam partial pressure is:

$$P_{empty} = P_{eq} \exp[-2\sigma_l \bar{v}/0.0774\ d_p\ RT]$$

At 373 K and for primary particles 0.1 μm in diameter,

$$P_{fill} = 0.991 \text{ atms}$$

$$P_{empty} = 0.915 \text{ atms}$$

There is, then, hysteresis in the isotherm for water adsorption by the pore. It might be anticipated, because the primary particles in aerosols have variable sizes so that pores have variable geometry, that the hysteresis will be of Barrer's Type C [175]. The essential points are that water can condense in the pores of particle agglomerates at partial pressures less than saturation and that the presence of the condensed water is stable to small fluctuations in the ambient partial pressure of steam.

Condensation of water in the internal voids of particle agglomerates is even more likely if the aerosol material is soluble in water. Dissolution of aerosol material will reduce the chemical activity and consequently the vapor pressure of the condensed water.

If water condensed in the pores of the particle aggregates is considered, then

$$\alpha = (\epsilon\rho_p + (1 - \epsilon)\rho_w) / \rho_p$$

where ϵ is the packing fraction and ρ_w is the density of water. (Of course, if water does not condense in the internal voids of the particle agglomerates, then $\alpha \cong \epsilon$.) Random packing of equal sized spheres produces $\epsilon = 0.63$. Experimental studies of the packing fraction cited by Brockman [164] typically yielded values of $\epsilon = 0.18$ to 0.5. An exceptional case produced $\epsilon = 3 \times 10^{-4}$.

Neglecting the exceptional case, the dynamic shape factors for aerosol particles discharged to the suppression pool ought to be between 1.0 and 1.6 with values in the vicinity of 1.15 likely. Over the last several years, there have been many studies of aerosol particle growth in terms of fractal geometry. That is, the aggregation of primary particles to form a composite particle is such that the geometric size of the composite is related to the volume of aerosol material by a fractal dimension:

$$d_p = k n^{1/d_f}$$

where

n = number of primary (fully dense) aerosol particles that make up the composite,

d_p = geometric diameter of the composite,

k = proportionality constant, and

d_f = fractal dimension of the composite.

Were the composite particle fully dense, then the fractal dimension, d_f, would be 3. A large number of experimental and analytic studies suggest that the fractal dimension is less than 3:

- Forrest and Witten [275] found fractal dimensions of inorganic "smoke" particles including iron and zinc particles to be 1.5 to 1.7,
- Meakin [276] calculated fractal dimensions for aerosol particles growing by Brownian processes to be between 1.40 and 1.45,
- Richter et al. [277] calculated fractal dimensions as high as 2.4,
- Feder et al. [278] reported fractal dimensions for carbon black as high as 2.3, but dimensions may actually have been lower,
- Martin et al. [279] measured fractal dimensions of particles by x-ray and light scattering to be 1.84 ± 0.08,
- Mountain et al. [280] calculated fractal dimensions in the free molecular and the continuum flow regimes to be 1.7 to 1.9,
- experimental studies by Samson et al. [281] yielded fractal dimensions of 1.5 to 1.6,
- data obtained by Hurd and Fowler [282] for flame generated SiO_2 particles indicated fractal dimensions of 1.49 ± 0.15,
- Zhang et al. [283] measured fractal dimensions for aerosol particles of 1.62 ± 0.06 by light scattering and 1.72 ± 0.10 by transmission electron microscopy,
- Mulholland et al. [284] calculated fractal dimensions in the free molecular regime of 2.07 ± 0.08 to 1.89 ± 0.08,
- Lesaffre [285] found the fractal dimensions of aerosol particles formed from $TiCl_4$ in moist air to increase from 1.52 - 1.57 to 1.71 - 1.83 as the relative humidity increased from 13.3 percent to 87.4 percent,
- Meakin et al. [286] found calculated fractal dimensions of 1.8 to 2.12 depending on the detail collision and trajectory models used in the calculation,

- Megaridis and Dobbins [287] measured fractal dimensions of particles of 1.62 to 1.74, and
- Charalampopoulos and Chang [288] reported measured fractal dimensions of 1.7 $\pm$ 0.08.

If, as is suggested by these many studies, aerosol particles do have fractal dimensionality, then the packing fraction and, consequently, the shape factors depend on particle size. If the primary particle size is d(pr) and the packing fraction, ϵ, goes to one as the particle size d_p approaches the primary particle size, then

$$\epsilon = \left[\frac{d(pr)}{d_p}\right]^{3-d_f}$$

or, to avoid physical impossibilities for continuous size distributions

$$\epsilon = \min\left[\left[1, \frac{d(pr)}{d_p}\right]^{3-d_f}\right]$$

Both the fractal dimension, d_f, and the primary particle size in this expression are uncertain.

Calculated shape factors for particles of various material densities are shown as functions of particle size in Figure 84. For these calculations the fractal dimension was taken to be 1.786 and the primary particle size was taken to be 0.05 μm. Water was assumed to fill the voids in the agglomerated particles. Shape factors are calculated to increase rapidly with particle size for sizes in the vicinity of the primary particle size. The shape factors become nearly size-independent and different than one for large particles.

The model can be refined somewhat by recognizing that agglomerates containing 2, 3, and perhaps 4 primary particles will not have concave voids that can fill with water unless the material is quite hygroscopic (see below). The agglomerates of small numbers of spherical particles will be quite distorted from spherical and, consequently, shape factors for these agglomerates need to be defined. Hansen and Ahlberg [168] have reviewed experimental data on the dynamic shape factors of agglomerates composed of 2 to 5 spheres. They argue that there is a dependence of the dynamic shape factor on the Knudsen number. Certainly, the scatter and uncertainty in data for doublets are large enough that it is difficult to confidently identify a dependence on Knudsen number (see Figure 85). The average dynamic shape factor for doublets is χ (doublet) = 1.32 with a standard error of $\pm$0.043. Data for triplets and quadruplets might arguably be weakly dependent on the Knudsen number. The hypothesis that the slope of a linear correlation of the shape factor with Knudsen number is different than zero can be rejected at fairly high confidence. Shape factors are taken here to be independent of the Knudsen number:

$$\chi \text{ (triplet)} = 1.554 \pm 0.026$$

$$\chi \text{ (quadruplet)} = 1.765 \pm 0.038$$

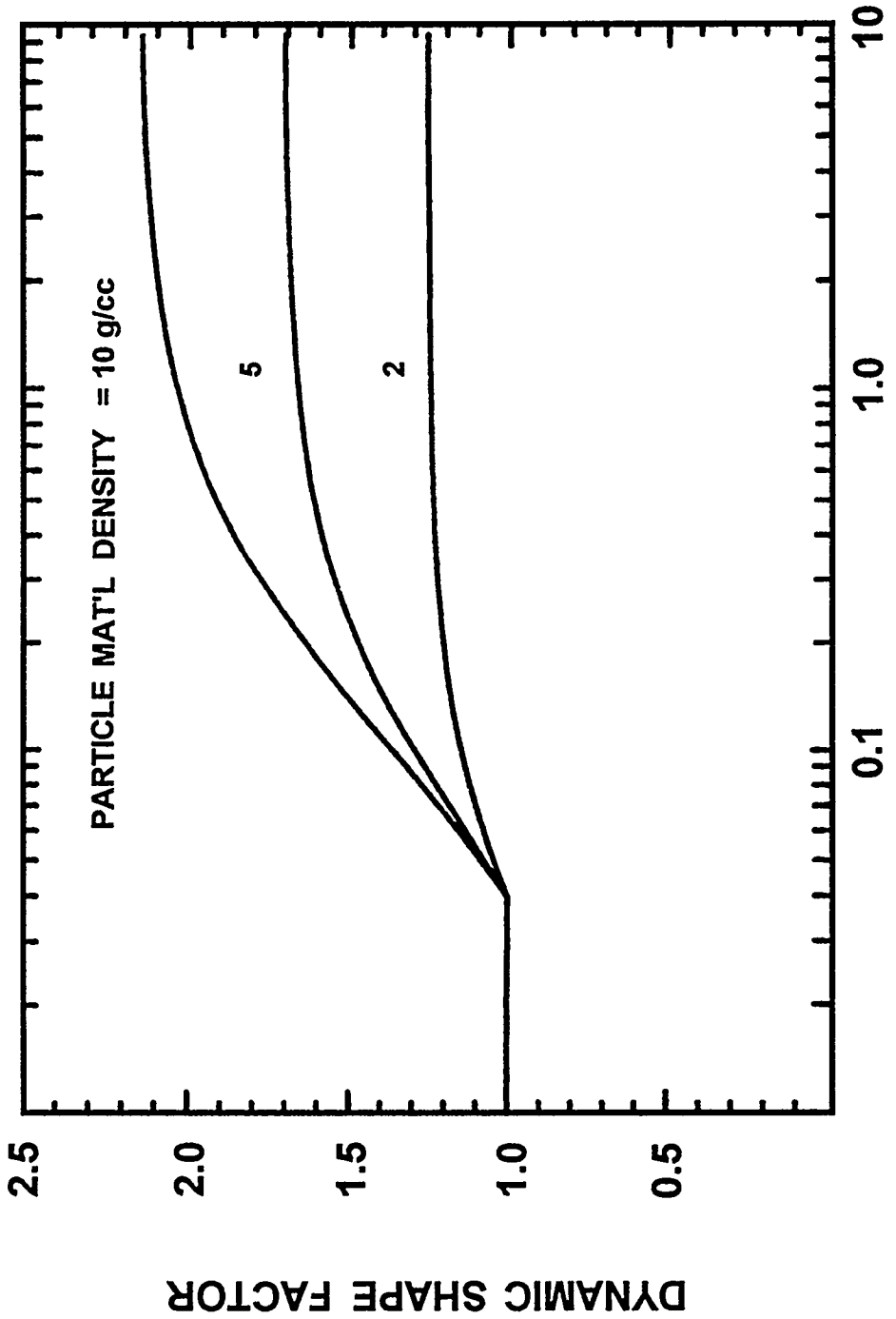

Figure 84. Dynamic shape factor as a function of particle size for various particle material densities. Particles are assumed to have interstices filled with water.

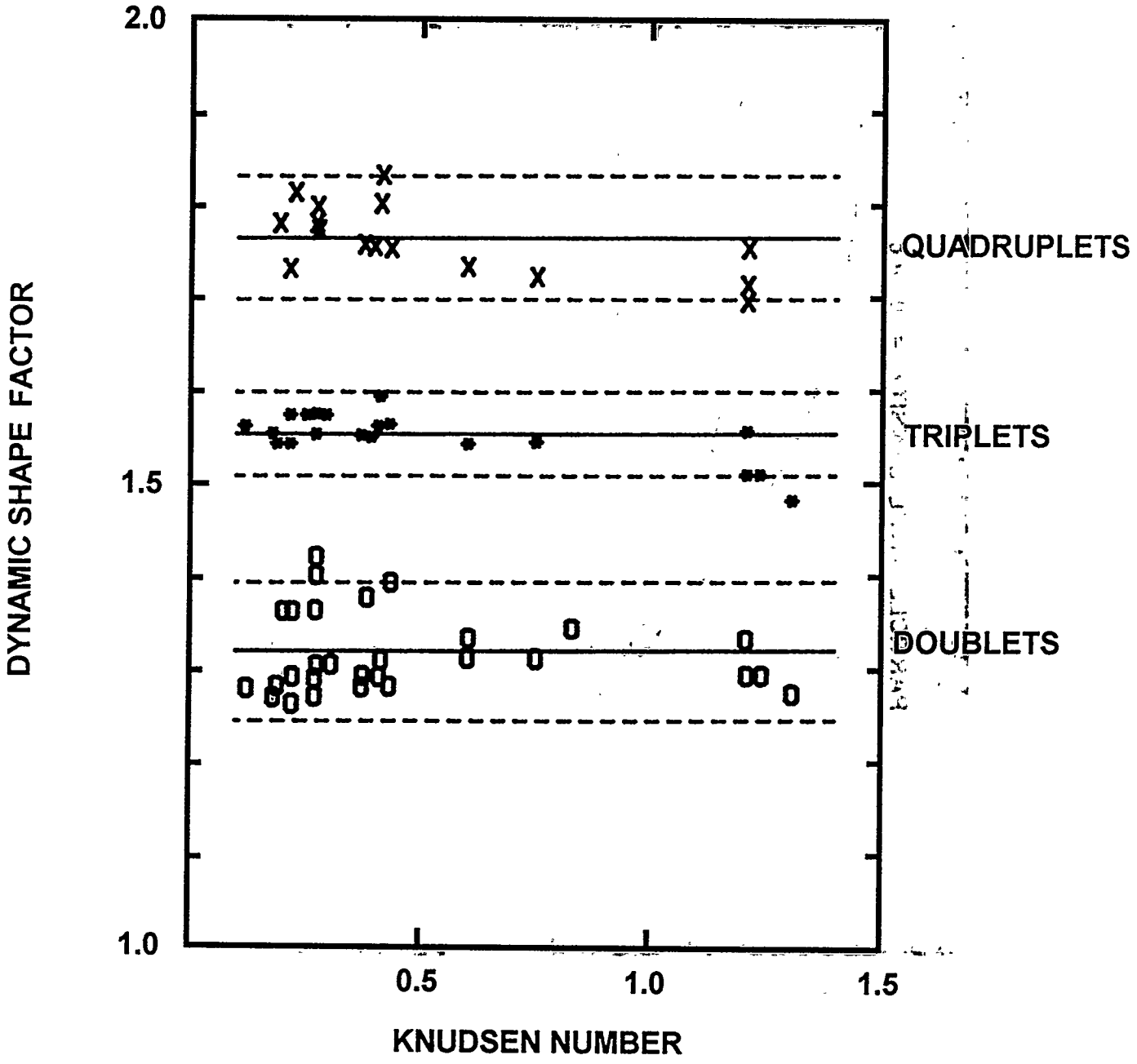

Figure 85. Dynamic shape factors for doublets, triplets, and quadruplet agglomerates of spherical particles. Solid lines indicate mean values. Dashed lines define 95 percent confidence bounds.

2. Slip Correction Factors and Accommodation Coefficients

The friction drag on a spherical particle is taken to be

$$F_D = 3\pi \mu_g d_p \chi / C$$

where

F_D = drag force,

μ_g = viscosity of the gas phase,

χ = dynamic shape factor, and

C = slip correction factor.

The slip correction factor is included so that the expression can apply to particles smaller than the mean free path of gas molecules as well as to particles so large that the gas phase can be treated as a continuum. The Knudsen number,

$$Kn = 2 \lambda / d_p$$

where λ is the mean free path of gas molecules, characterizes the range of application. The mean free path of gas phase molecules is the average distance of travel of gas molecules before they collide with other gas molecules. It is a concept that only makes sense if gas molecules are approximated as rigid, noninteracting particles. Indeed, this is the approximation adopted in nearly all of the analysis of aerosol behavior. Within this approximation, the mean free path is given by:

$$\lambda = kT/\sqrt{2}\ P\pi\sigma^2$$

where

σ = collision cross section of the gas molecules (see Table 14),

k = Boltzmann's constant, and

P = pressure in rational units.

In conventional units,

$$\lambda \text{ (cm)} = 3.065 \times 10^{-7}\ T(K) / P(\text{atms})\ \sigma^2\ (A°)$$

More empirical expressions for λ are often used:

$$\lambda = 2\left[\frac{m}{2kT}\right]^{1/2} \mu_g/\rho_g = \left[\frac{2M}{RT}\right]^{1/2} \frac{\mu_g}{\rho_g}$$

or

$$\lambda \text{ (cm)} = 0.0127\ \mu_g\,(T/M)^{1/2}$$

where

m = mass of a gas molecule and

M = molecular weight of the gas

These expressions make it somewhat easier to define a parameter that can be called the mean free path for gas mixtures.

Empirical expressions for the slip correction factors for spheres (also called Cunningham slip correction factors) have been made famous by Milliken as part of his work with oil droplets (see Reference 143 for some interesting comments on this work.) Milliken found for oil droplets:

$$C = 1 + Kn\,[1.23 + 0.414 \exp(-0.876/Kn)]$$

Since then, other expressions have been determined:

- Allen and Raabe [143] for solid particles

$$C = 1 + Kn\,[1.142 + 0.588 \exp(-0.999/Kn)]$$

- Davies [144]

$$C = 1 + Kn[1.257 + 0.400 \exp(-1.10/Kn)]$$

- Annis [295]

$$C = 1 + Kn\,[1.558 + 0.173 \exp(-0.769/Kn)]$$

- Jennings [185]

$$C = 1 + Kn\,[1.255 + 0.399 \exp(-1.10/Kn)]$$

There is no significant difference among these expressions. They exhibit a classic "compensation" effect among parameters determined by least squares fitting.

All of the empirical expressions treat the slip correction as strictly a function of geometry. Phillips [145], however, finds theoretically:

$$C = \frac{15 + 12C_1Kn + 9(C_1^2+1)Kn^2 + 18C_2(C_1^2+2)Kn^3}{15 - 3C_1Kn + C_2(8+\pi\alpha_t)(C_1^2+2)Kn^2}$$

where

α_m = momentum accommodation coefficient,

α_t = energy accommodation coefficient,

C_1 = $(2 - \alpha_m) / \alpha_m$, and

C_2 = $1 / (2-\alpha_m)$.

Phillips' analysis suggests that the slip correction is dependent on the gas and the particle properties by means of the momentum accommodation coefficient. Comparison of the slip correction factors predicted with Phillips' model to data for oil droplets [146,147] using $\alpha_m = 0.895$ [145] and to predictions obtained from the empirical correction by Allen and Raabe [143] are shown in Figure 86.

Accommodation coefficients arise frequently in the discussion of gas interactions with aerosol particles. There are four so-called Knudsen accommodation coefficients:

- accommodation of normal momentum
- accommodation of tangential momentum
- accommodation of energy, and
- the radiometric accommodation coefficient.

Here, interests are confined to the accommodation of normal momentum and energy. Because the energy of an ideal monatomic gas is a function of temperature and because the concept of accommodation arose in the study of heat transfer at low pressures, the energy accommodation coefficient is often called the temperature accommodation coefficient. Accommodation is most intuitively defined in terms of temperature. Consider a gas of temperature T(g) and a surface of temperature T(s). Gas species that collide with the surface reflect back into the gas phase with properties indicative of a temperature T(r). Then, the temperature accommodation coefficient, α_t, is defined by:

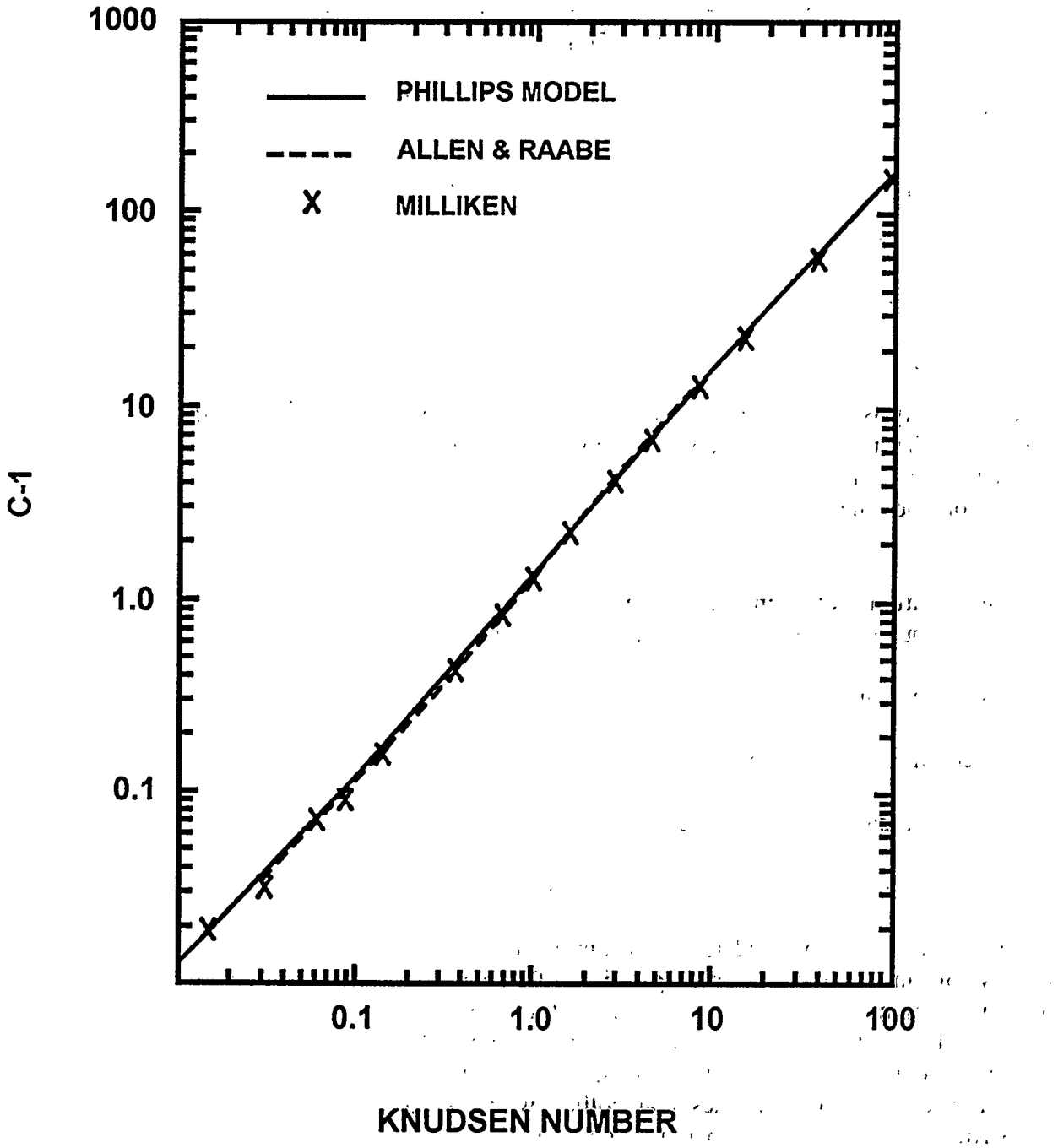

Figure 86. Comparison of the predicted slip correction factor to values obtained in experiments with oil droplets [146,147] and correlations of data for solid particles [143].

$$\alpha_t \doteq \lim_{T(g) \to T(s)} \frac{T(r) - T(g)}{T(s) - T(g)}$$

The definition is more rigorously correct if energy rather than temperature is used in the equation. Similar definitions can be constructed for the other accommodation coefficients. From these definitions, it appears that accommodation coefficients can assume values between 0 and 1. Closer examination of the gas-solid interaction process shows the conceivable range for the accommodation coefficients is not so narrowly restricted. But, in reality, measurements of these coefficients are nearly always in this range.

Measurements of accommodation coefficients for aerosol particles of interest here are, of course, non-existent. Momentum accommodation coefficients have been derived from the data used to define slip correction factors. Rader [160] seems to consider the momentum accommodation coefficient a function of the gas and provides:

Gas	α_m
air	0.8972
Ar	0.8891
He	0.8694
H_2	0.9251
CH_4	0.9195
C_2H_6	0.8784
N_2O	0.8972
CO_2	0.8968

There are few surface materials for which momentum accommodation has been measured. Nearly all the data examined by Rader were for oil droplets. Indeed, the only systemmatics in the results he cites is a rough correlation of momentum accommodation with the molecular weight of the gas and the solubility of the gas in oil. One would also expect that surface roughness on a molecular level would lead to higher accommodation coefficients. Such roughness would seem to make it more likely that a colliding gas species would be trapped or adsorbed on the surface at least temporarily and there would be an opportunity for the gas species to equilibrate with the surface.

Data available for review by Rader were obtained at temperatures not too different than room temperature. If the view that transient adsorption of gases on surfaces leads to higher accommodation coefficients is true, then the accommodation coefficient should be somewhat temperature-dependent. As temperature increases and the mean speed of gas phase species increases, larger fractions of the collisions should be too energetic to lead to adsorption. The accommodation coefficient might be expected, then, to decrease with temperature.

A great deal more is known about temperature accommodation. Saxena and Joshi [242] have reviewed the available data. The accommodation of hydrogen on metals is shown in Figure 87. The temperature accommodation coefficient for various gases on glass is shown in Figure 88. The most noticeable feature of these data is that temperature accommodation coefficients are typically smaller than the momentum accommodation coefficients cited by Rader. The temperature accommodation coefficients

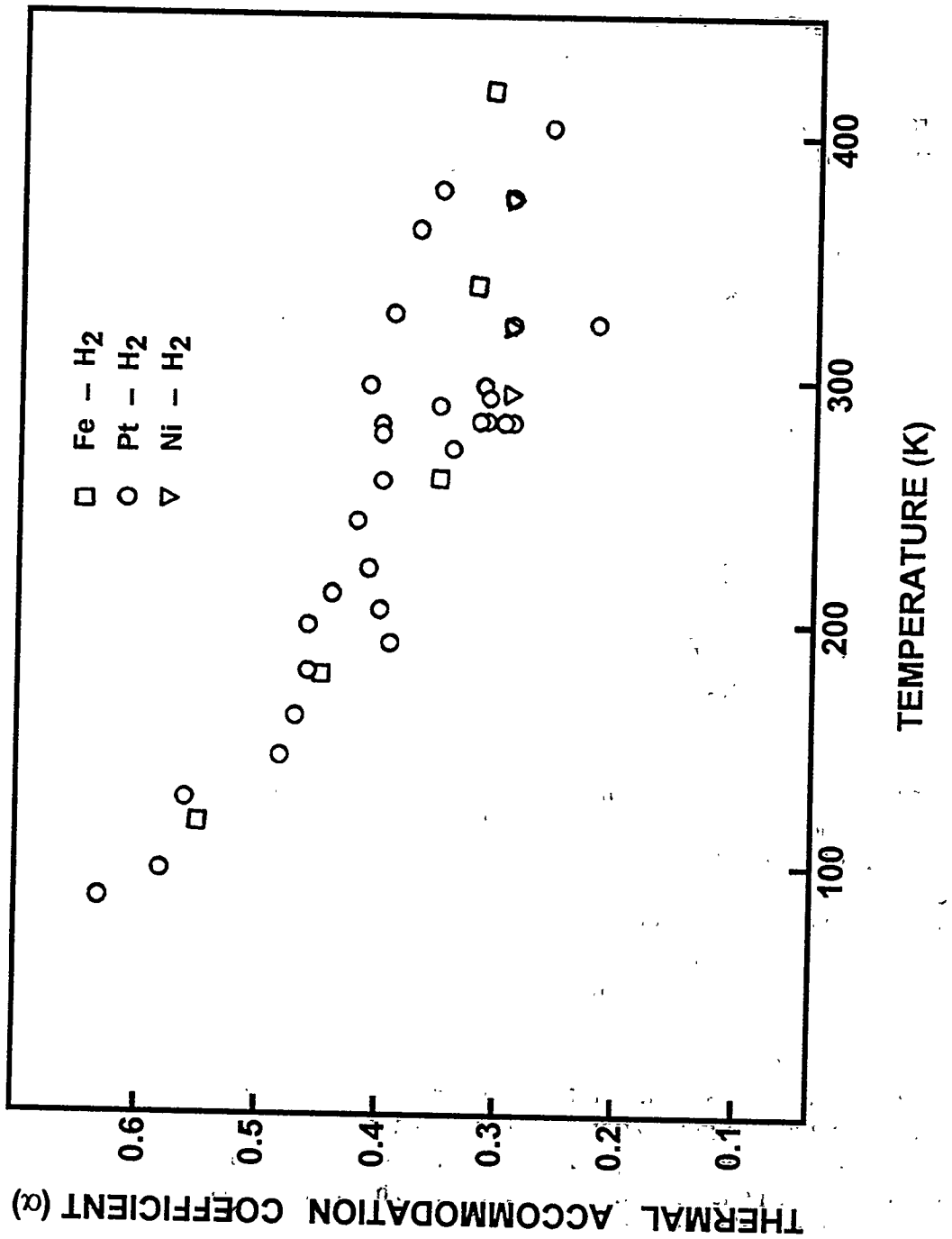

Figure 87. Temperature accommodation coefficient of hydrogen on metal surfaces [237]

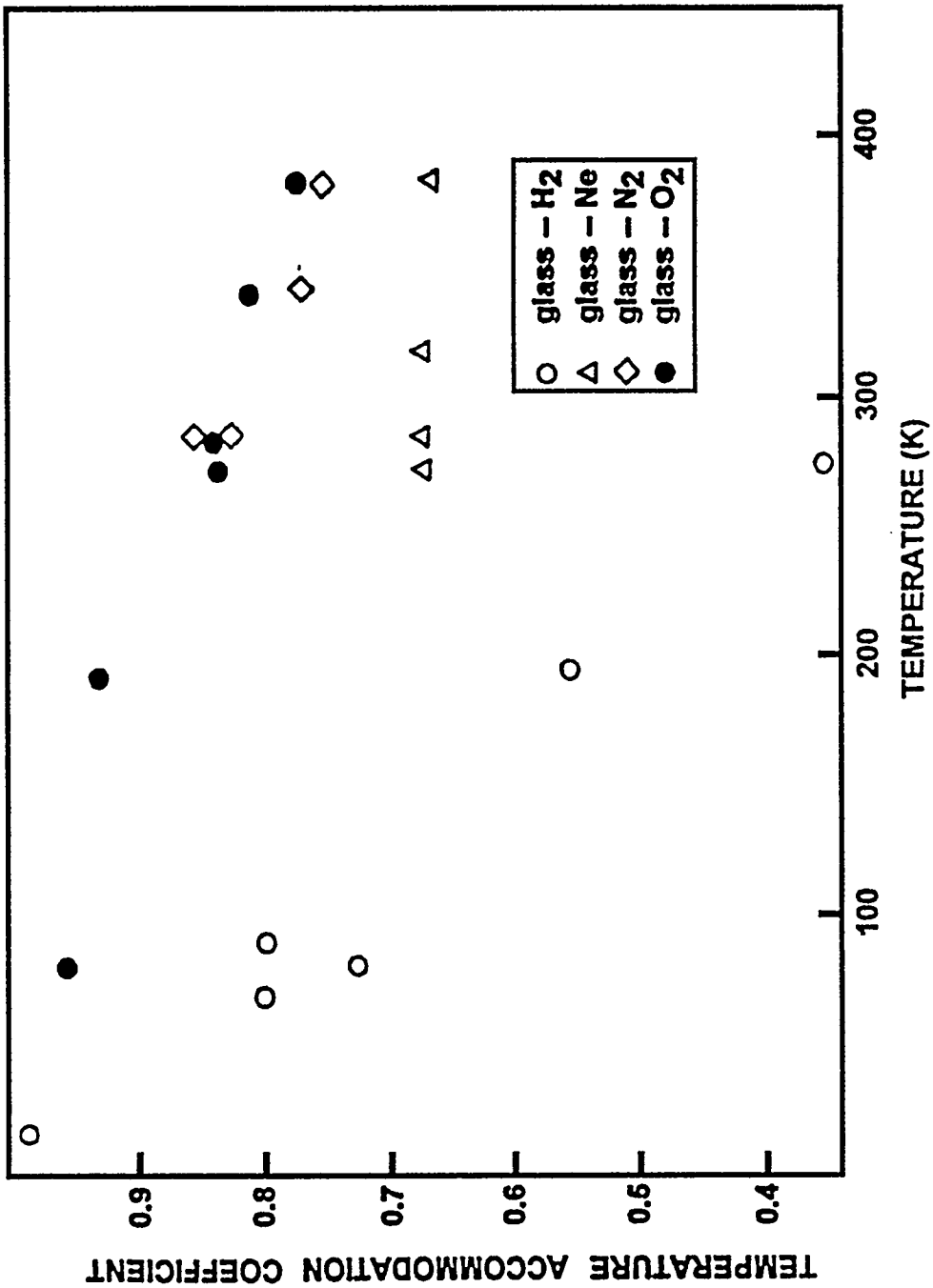

Figure 88. Temperature accommodation coefficients of various gases on glass surfaces [237]

do seem to decrease with temperature. Also, the accommodation coefficient does seem to decrease with the molecular weight of the gas.

There have been numerous theoretical studies of the temperature accommodation coefficient [162,163,237]. Simple expressions for the accommodation coefficient are:

- Baule hard-sphere model

$$\alpha_t = 2\eta/(1 + \eta)^2$$

- Empirical modification of the Baule equation:

$$\alpha_t = 2.4\eta/(1 + \eta)^2$$

- Effective surface mass:

$$\alpha_t = 2\eta'/(1 + \eta)^2$$

where

η = MW(gas) / MW(surface atom)

η' = MW(gas) / MW(effective), and

MW(effective) = effective molecular weight of the surface atom which can be several times the actual molecular weight

As noted by Goodman and Wachman [243], none of the simple formulae "yields extensive agreement with experimental data although each may be valid under particular sets of conditions." As a result, theorectical studies have produced rather complex expressions for the temperature accommodation coefficient that involve properties of the solid and the gas-solid interactions. Such information is unlikely to be available for aerosol materials of interest here.

Estimation of temperature accommodation coefficients for situations of interest here is complicated by the fact that gas mixtures are present. Definition of a single value for the coefficient when it is likely the various gases accommodate differently is a difficulty. Also, it is not obvious what the properties of the surface are. If, in fact, water absorbs on the surfaces of aerosol particles, then the relevant issue is the accommodation of gases by liquid water rather than solid surfaces.

It is clear that accommodation coefficients will not be known accurately for the systems and temperatures of interest here. Simple models of these accommodation coefficients are not available. Consequently, accommodation coefficients will be sources of uncertainty and will have to be treated in a substantially parametric fashion.

The slip correction becomes important only for very small particles. The slip correction factor described above is for perfect spheres. There is, however, no assurance that primary particles will be so geometrically simple. At a minimum, some distortion into oblate or prolate ellipsoids might be expected. Slip corrections are not known for ellipsoids over the entire range of Knudsen numbers. Dahneke has, however, derived expressions for the drag force on oblate and prolate ellipsoids in the free molecular regime [169] and in the continuum regime [170]. He has defined a procedure for estimating the slip correction factor for ellipsoids at arbitrary Knudsen numbers.

Recognize that the slip correction factor is, by definition, given by:

$$F = F(cont) / C$$

where

F = the actual drag force on a particle,

$F(cont)$ = the actual drag force on a particle if the gas could be treated as a continuum, and

C = slip correction factor.

Dahneke proposes to define a spherical particle whose diameter is such that the slip correction factor in the free molecular regime is the same as that for the distorted particle. He finds this diameter from:

$$\frac{F(cont)}{F(fm)} = C = 1 + Kn[\alpha + \beta \exp(-\delta/Kn)]$$

where

$F(fm)$ = drag force on the distorted particle in the free-molecular regime ($Kn >> 1$)

and the formula for the slip correction factor is any one of those described above. Since the slip correction factor for the hypothetical spherical particle is the same as that of the distorted particle in both the free-molecular regime and the continuum regime, he assumes that calculated slip correction factors for the hypothetical sphere will yield good estimates of the slip correction factor for the distorted particle under conditions intermediate between the extremes of the continuum and free-molecular regimes.

Dahneke defines the forces on particles modestly distorted from spherical to be:

$$F(cont) = - C_o \mu_g L_c V$$

$$F(fm) = \frac{-\pi \mu_g L_c V}{Kn(e)} f(E,\alpha_m)$$

where

V = velocity of the particle,

L_c = critical dimension of the particle,

E = aspect ratio of the distorted particle ($E \geq 1$),

α_m = momentum accommodation factor or the fraction of gas atoms scattered diffusely, and

$Kn(e)$ = the Knudsen number for the distorted particle.

The geometry factors C_o and $f(E, \alpha_m)$ are discussed further below. The defining equation, then is:

$$\frac{Kn(e)\ C_o\ \mu_g\ L_c\ V}{\pi\ \mu_g\ L_c\ V f(E,\alpha_m)} = 1 + Kn(s)[\alpha + \beta \exp(-\delta/Kn(s)]$$

or

$$\left[\frac{C_o Kn(e)}{\pi f(E,\alpha_m)} - 1\right] / [\alpha + \beta \exp(-\delta/Kn(s)] = Kn(s)$$

where $Kn(s)$ is the Knudsen number for the adjusted spherical particle. The diameter of the equivalent spherical particle is:

$$d_p(equiv.) = \frac{1}{2} L_c\ Kn(e) / Kn(s)$$

The geometric factors C_o and $f(E, \alpha_m)$ depend on the geometry and the orientation of the particle. For prolate ellipsoids with semi-major axis a and semi-minor axis b:

$$f(E, \alpha_m) = \sin^2\theta \left[X_p \left\{ 4 + \left[\frac{\pi}{2} - 1 \right] \alpha_m \right\} + \frac{Z_p}{Y_p^2} \left\{ 2 + \left[\frac{4Y_p^2 + \pi - 6}{4} \right] \alpha_m \right] + \right.$$

$$\left. + \cos^2\theta \left[2X_p \alpha_m + \frac{Z_p}{Y_p^2} \left\{ Y_p^2(4-2\alpha_m) - 4 + \left[3 - \frac{\pi}{2E^2} \right] \alpha_m \right\} \right] \right.$$

$$C_o = \frac{16\pi(E^2-1)\sin^2\theta}{\left[\frac{2E^2-3}{\sqrt{E^2-1}} \right] E \ln\left(E + \sqrt{E^2-1}\right) + E^2} + \frac{8\pi(E^2-1)\cos^2\theta}{\left[\frac{2E^2-1}{\sqrt{E^2-1}} \right] E \ln\left(E + \sqrt{E^2-1}\right) - E^2}$$

where

$E = a/b > 1,$

$Kn = \lambda/b,$

$X_p = \dfrac{\sin^{-1}(Y_p)}{Y_p}$

$Y_p = (1 - 1/E^2)^{1/2},$

$Z_p = 1/E - X_p,$ and

θ = angle of transport relative to the polar axis of the particle.

For oblate ellipsoids with semi-major axis a and semi-minor axis b, Dahneke finds:

$$f(E,\alpha_m) = \sin^2\theta \left[X_o^2 Y_o \left\{ \frac{(6-\pi)\alpha_m}{4} - 2 \right\} + Z_o \left\{ 4 - \frac{(4-\pi)}{2}\alpha_m \right\} + E\alpha_m \right] +$$

$$+ \cos^2\theta \left[X_o^2 Y_o \left\{ 4 - \frac{(6-\pi)}{2} \alpha_m \right\} E^2 + Z_o\alpha_m + E\alpha_m \right]$$

$$C_o = \frac{16\pi(E^2-1)\sin^2\theta}{\left[\frac{3E^2-2}{\sqrt{E^2-1}}\right]\text{atn}(\sqrt{E^2-1}) - 1} + \frac{8\pi(E^2-1)\cos^2\theta}{\left[\frac{E^2-2}{\sqrt{E^2-1}}\right]\text{atn}(\sqrt{E^2-1}) + 1}$$

where

$$E = a/b > 1,$$

$$Kn = \lambda/a$$

$$X_o = 1 / \sqrt{E^2-1}$$

$$Y_o = E - Z_o$$

$$Z_o = X_o \ln (E + 1/X_o), \text{ and}$$

again θ is the angle from the polar (semi-minor) axis of the particle.

The distorted particles are, presumably, randomly oriented and do not rotate for most situations [165]. The statistical average force is taken by Dahneke to be found from:

$$\frac{1}{f(avg)} = \frac{1}{3}\left[\frac{1}{f(\theta=0°)} + \frac{2}{f(\theta=90°)}\right]$$

and

$$\frac{1}{C_o(avg)} = \frac{1}{3}\left[\frac{1}{C_o(\theta=0°)} + \frac{2}{C_o(\theta=90°)}\right]$$

A plot of the statistically averaged slip correction factor for a prolate distorted particle calculated using Dahneke's method is shown in Figure 89. Also shown in the figure is the slip correction factor calculated using the volume equivalent sphere methods. For small distortions from spherical that are of interest here, the differences between the slip correction factors calculated by the two methods are not especially large. The extent of distortion and whether it is oblate or prolate distortion are uncertainties of equivalent or greater importance.

3. Hygroscopicity of Aerosols Produced in Reactor Accidents

The analyses of water condensation presented above show that if the chemical activity of water condensing on the aerosol surface can be reduced sufficiently, the aerosol particle will grow. Growth

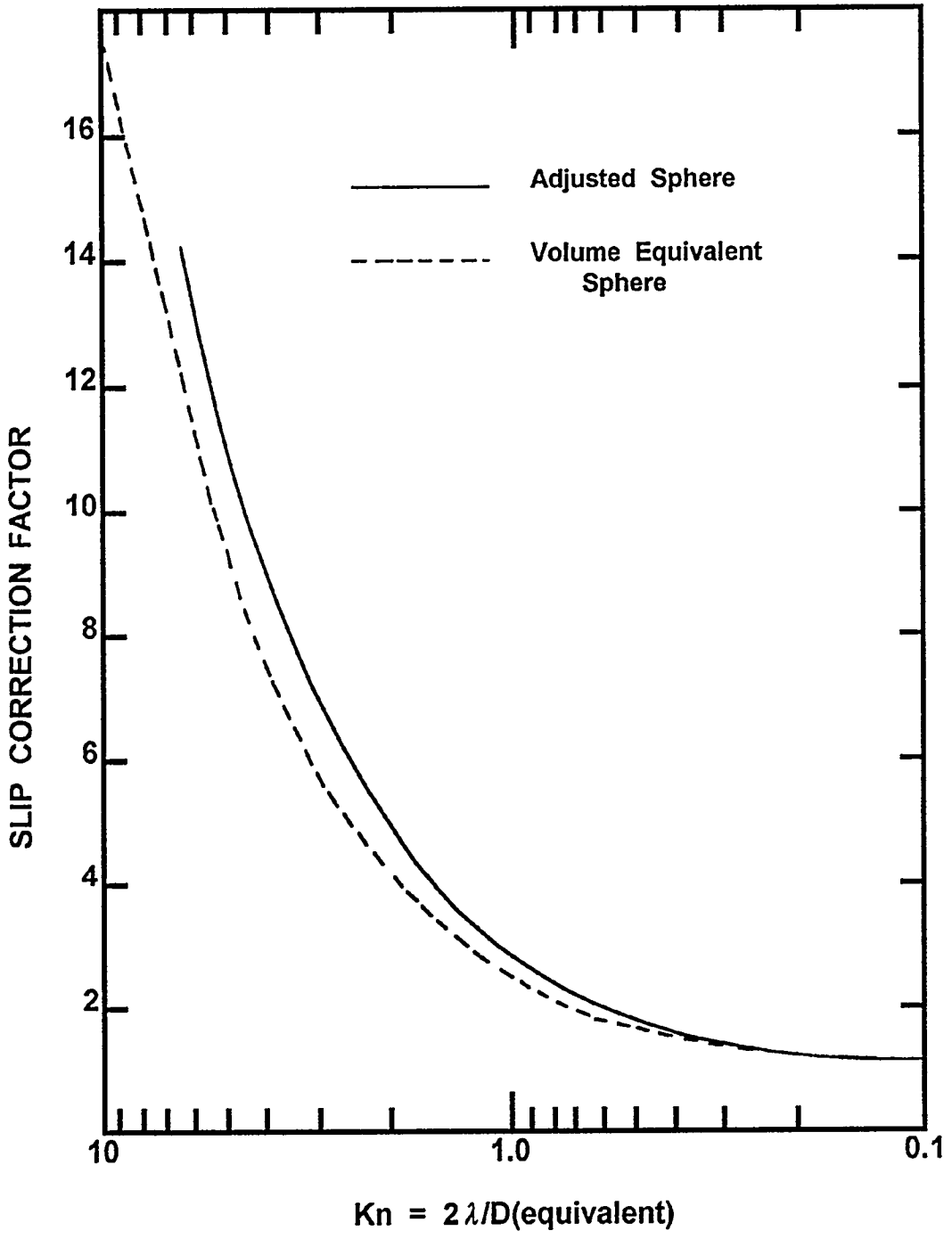

Figure 89. Comparison of slip correction factors for a prolate distorted particle (E = 2.0) calculated using the adjusted sphere and the volume-equivalent sphere method

can be quite rapid. When the growth occurs, even quite small particles can become large enough that one or more of the aerosol trapping mechanisms discussed above will become efficient.

The reduction in the chemical activity of condensed water is the key to the growth of aerosol particles. The reduction must be sufficient to overcome both the Knudsen effect and the slight undersaturation of the bubble atmosphere as it rises through the pool. The only readily apparent mechanism for the reduction in the chemical activity of condensing water is for the water to dissolve some of the aerosol material. The question then becomes how soluble will aerosols produced in reactor accidents be?

Models of radionuclide releases during severe reactor accidents often treat the chemical form of aerosol materials quite crudely. These models often speak of chemical species such as CsOH, CsI, and inert aerosols [14,23,25]. Certainly, CsOH and CsI are quite soluble in water as is shown by the data in Table 17. Were these materials to make up the aerosols entering the suppression pool, there is little doubt that water condensation would lead to particle growth.

It is, however, not evident that CsOH and CsI will be aerosol materials. In the last few years, more attention has been paid to the issue of chemical form of the aerosol produced during severe accidents [268]. Rich opportunities for reaction of chemically reactive species like CsOH have been found. Some important reactions include:

$$CsOH + HBO_2 \rightleftarrows CsBO_2 \cdot H_2O$$

$$2CsOH + ZrO_2 \rightleftarrows Cs_2ZrO_3 + H_2O$$

$$CsI + Ag + H_2O \rightleftarrows CsOH + AgI + 1/2\ H_2$$

$$2CsI + CdO + H_2O \rightleftarrows 2\ CsOH + CdI_2$$

Table 17. Water solubilities of some materials expected to be present in aerosol produced during severe reactor accidents

CsOH		CsI	
T (K)	Solubility (moles/kg H_2O)	T (K)	Solubility (moles/kg H_2O)
288	2.94	273	1.17
344	3.50	293	1.68
374	3.66	313	2.06
402	3.92	333	2.31
		353	2.52
		373	2.64

For exactly the same reasons CsOH absorbs water so extensively, CsOH is also quite reactive towards other oxides to form materials of much lower water solubility. Dissolution of these materials may not produce the reduction in the chemical activity of water needed to promote particle growth.

Another development in the understanding of severe reactor accident phenomena has been the recognition that nonradioactive materials are far more abundant contributors to the aerosols than are radionuclides. The situation is particularly extreme in the case of core debris interactions with concrete. Typically, it is found in analyses of these interactions that radionuclides constitute only 1 percent of the total aerosol mass being evolved. Most of the aerosol mass comes from constituents of concrete such as CaO, SiO_2, FeO, etc. Early in the course of core debris interactions when the molten core debris is quite hot and the most extensive releases of radionuclides take place, the nonradioactive aerosol materials might be expected to form chemical species with very low water solubilities. Adams [248] found that condensing steam did not accentuate the deposition of aerosols produced by feeding concrete into a plasma torch though condensing steam did accelerate deposition of Fe_2O_3 and U_3O_8 aerosols formed in a similar fashion.

Aerosol particles produced during severe reactor accidents are not likely to be composed of a single chemical species. It is, in fact, usually assumed that at least within given a size class aerosol particles will be composed of mixtures of materials with varying water solubilities. The two issues of interest, then, are, (1) can water soluble material making up a few percent of an aerosol particle produce the reduction in chemical activity necessary to promote growth by water condensation and, (2) can the dissolution occur fast enough to affect the particle during its transport through the suppression pool. Dissolution kinetics may be especially troublesome if the water soluble material is encased in materials that are not especially soluble. Particle morphology and structure as well as chemical composition must be understood to resolve the issues of particle growth by water condensation.

L. Aerosol Behavior

The trapping of aerosol is, of course, the process of main interest here. It is convenient to consider aerosol trapping in four regimes of particle transport:

- aerosol trapping during transport to the steam suppression pool,
- aerosol trapping during bubble formation,
- aerosol trapping during collapse or disintegration of bubbles immediately after bubbles detach from orifices or vents in the suppression pool, and
- aerosol trapping during the quasi-steady state rise of bubbles through the pool.

The first of the regimes, aerosol trapping during transport to the pool, is considered outside the scope of this work. Trapping aerosols by diffusiophoresis within downcomers has been mentioned above. Other phenomena that lead to aerosol trapping during transport to the suppression pool are described below (Section IV L-4). These phenomena are not further pursued. They might, however, affect not only the mass of aerosol to be removed by the pool, but also the size distribution of the aerosol particles that enter the suppression pool. The discussion below will show that many of the phenomena that can lead to aerosol trapping in the suppression pool are sensitive to the aerosol particle size.

Attentions here are focused on the trapping of aerosol by the suppression pool itself. The assumption is made here that a particle that contacts the water in the suppression pool is permanently trapped in the pool. Gross re-entrainment of particle-ladden liquid droplets by sparging gases has been neglected here. Models of this entrainment phenomenon are available [200-202]. Typically, such models predict that the mass of liquid entrained by gas sparging is about 10^{-4} of the mass of sparging gas. Until the pool becomes very concentrated in radionuclides, this re-entrainment will not significantly reverse the decontamination produced by the suppression pool. Neglect of this re-entrainment process does, however, mean that some limit ought to be imposed on the decontamination that is predicted by the models of aerosol trapping that are discussed here. In general, the authors feel that predicted decontamination factors* in excess of 10^6 should be viewed with suspicion because entrainment and the possible enrichment of surfaces with particulate relative to the bulk liquid have been neglected.

Rather than discussing aerosol trapping processes in the sequence they would be experienced by the aerosol produced in a reactor accident, the discussions of aerosol trapping are presented in subsections beginning with aerosol trapping during bubble rise through the pool. This is done because the trapping phenomena have been more thoroughly described for rising bubbles. These phenomena will be more familiar to the reader and can be used to obtain an understanding of the more complex phenomena associated with aerosol trapping during bubble collapse and during bubble formation.

1. Aerosol Trapping During Bubble Rise

The removal of aerosol particles from gas bubbles rising through water is a classic problem that has been addressed by a number of authors [148-150,153]. Usually, aerosol removal from the gas is considered to occur as a result of particle sedimentation within the bubble, diffusion of particles to the bubble walls and, in cases where gases circulate within the bubble, as a result of inertial impaction of particles on the bubble walls. For the particular situation of interest here, it is necessary to consider two additional phenomena that lead to aerosol trapping. Both of these additional phenomena arise because of the behavior of water vapor within a rising bubble as was discussed above (see Section IV-D). Analyses of the thermodynamics of bubbles rising through a water pool showed that water vapor will evaporate from the walls and diffuse or convect into the bulk gas of the bubble. The evaporating water imposes a Stefan flow and a diffusiophoretic force on aerosol particles near the bubble surface. The thermodynamic analyses also showed that there could be a thermal gradient near the bubble walls. This thermal gradient will create a thermophoretic force on particles that will oppose particle deposition. In the discussions of the various aerosol trapping mechanisms presented below, the bubbles are assumed to be smooth ellipsoids. This is, of course, an idealization. In reality the surfaces of the bubbles, especially surfaces of bubbles in swarms, will be continuously deformed and reformed. Aerosol trapping by the shape oscillations of bubbles is also discussed in this subsection.

a. Diffusion of Particles to the Bubble Walls

Diffusion of aerosol particles to the walls of bubbles is caused by the Brownian motion of the particles and the stochastic nature of impulses imparted to the particles during collisions with gas molecules. There are a variety of possible treatments of diffusion of aerosol particles. Most frequently adopted is

*The decontamination factor, as used throughout this document, is the dry aerosol mass injected into the suppression pool divided by the dry aerosol mass that emerges from the pool.

an argument developed by Fuchs [148]. This treatment of particle diffusion to the walls of bubbles is somewhat peculiar. The argument is reproduced below for a spherical bubble. The development of the argument for an ellipsoidal bubble has been presented elsewhere [150].

Fuchs assumes that gases within the bubble circulate. Certainly, the discussions above show that this may not be the case. Ideally, when gases do circulate within a spherical bubble, the gas velocity tangential to the walls is:

$$U_{tang} = 1.5\ U_B \sin\theta$$

where

U_{tang} = tangential velocity,

U_B = rise velocity of the bubble, and

θ = angle from the pole of the bubble.

The rate at which particles of size d_p flow through a region between the bubble surface and a stream line (actually a stream surface) displaced a distance δ_o from the surface of the bubble at the equator is:

$$\frac{dN}{dt} = \delta_o\ D_B\ \pi n \sin\theta\ U_{tang} = 1.4\ \delta_o\ D_B\ U_B\ \pi n \sin^2\theta$$

where n is the number concentration of particles of size d_p. Fuchs makes the questionable assumption that diffusion to the bubble surface is negligible except between polar angles of $\pi/4$ and $3\pi/4$. In the above specified region, the time required for particles to traverse this arc is

$$t = \int_{\pi/4}^{3\pi/4} \frac{0.5\ D_B\ d\theta}{U_{tang}} = \int_{\pi/4}^{3\pi/4} \frac{D_B}{3U_B} \frac{d\theta}{\sin\theta} = \frac{-D_B}{6V_B} \ln\left[\frac{1+\cos\theta}{1-\cos\theta}\right]\Bigg|_{\theta=\pi/4}^{\theta=\frac{3\pi}{4}} \cong 0.588\ D_B/U_B$$

During this time period the random walk displacement of particles by Brownian motion, δ, is given by:

$$\delta = 2\sqrt{\frac{Đt}{\pi}} = 0.8650\sqrt{Đ\ D_B/U_B}$$

where

Đ = particle diffusion coefficient,

= $CkT / 3\pi\mu_g d_p \chi$,

C = Cunningham slip correction factor (see Section IV K-2),

χ = dynamic shape factor, and

k = Boltzmann's constant.

Over the interval from $\theta = \pi/4$ to $\theta = \pi/2$, the separation between the reference stream line and the bubble wall varies from $2\delta_0$ to δ_0. Fuchs defines the reference streamline by:

$$\bar{\delta} = 1.5\ \delta_0$$

He then makes the somewhat startling assumption that all of the particles in the region deposit on the wall. That is, he has very roughly divided the zone in half to account for the fact that half the particles will move toward the wall as a result of Brownian motion and half will move away. For calculational purposes, he segments these two classes of particles on either side of the boundary line $\bar{\delta} = 1.5\ \delta_0$. The particle deposition rate is then given by:

$$\frac{dN}{dt} = 1.5\ \delta_0\ \pi D_B\ U_B\ n = \bar{\delta}\ D_B\ U_B \pi n \cong 0.8650\ \pi n\ (Đ\ D_B^3\ U_B)^{1/2} \cong 2.717\ n\ (Đ\ D_B^3\ U_B)^{1/2}$$

An overall deposition velocity, referenced to the entire surface area of the bubble even though the deposition is taking place only over 70.7 percent of the bubble surface, can be defined as:

$$\frac{1}{\pi D_B^2}\ \frac{dN}{dt} = V_D n = 0.8650\ n \left[\frac{Đ\ U_B}{D_B}\right]^{1/2}$$

or

$$V_D = 0.8650 \left[\frac{Đ\ U_B}{D_B}\right]^{1/2}$$

Similarly, the deposition coefficient for the fraction of particles deposited per unit bubble rise, $\alpha(D)$, can be defined as:

$$\frac{6}{\pi D_B^3 n}\ \frac{dN}{dx} = \alpha(D) = 5.190 \left[\frac{U_B\ Đ}{U_{rise}^2\ D_B^3}\right]^{1/2}$$

where x is the distance of bubble rise. Here, it is useful to make distinctions among the rise velocity of an isolated bubble, U_B, the rise velocity of the bubble relative to the water, U_{slip}, and the velocity relative to the fixed coordinate frame of the pool. Then,

$$\alpha(D) = 5.190 \left[\frac{Đ\ U_{slip}}{D_B^3\ U_{rise}^2} \right]^{1/2}$$

For an oblate ellipsoidal bubbles of eccentricity* E, expressions derived from arguments completely parallel to those made by Fuchs for spherical bubbles are [150]:

$$V_D = \frac{\frac{2}{E^{2/3}} \sqrt{\frac{Đ\ U_{slip}}{8\pi D_B}} \left[\frac{(E^2-1)}{1 + (4+2(E^2-1))^{1/2}} \right] \left[\frac{1.76E^2}{(E^2-1)} - \sqrt{2} \right]^{1/2}}{\left\{ 1 + \frac{\ln\left[\frac{E + \sqrt{(E^2-)}}{E - \sqrt{(E^2-1)}} \right]}{2E\sqrt{(E^2-1)}} \right\} \left\{ \frac{E^2 \tan^{-1}\left[(E^2-1)^{1/2}\right]}{\sqrt{(E^2-1)}} - 1 \right\}^{1/2}}$$

and

$$\alpha(D) = \frac{6 \sqrt{\frac{Đ\ U_{slip}}{8\pi D_B^3\ U_{rise}^2}} \left[\frac{(E^2-1)}{1 + (4+2(E^2-1))^{1/2}} \right] \left[\frac{1.76E^2}{(E^2-1)} - \sqrt{2} \right]^{1/2}}{\left\{ \frac{E^2 \tan^{-1}\left[(E^2-1)^{1/2}\right]}{\sqrt{(E^2-1)}} - 1 \right\}^{1/2}}$$

It should be noted, however, that these expressions for an oblate ellipsoidal bubble have been derived assuming that vortex flows in an oblate ellipsoidal bubble are simple geometric distortions of Hill's vortex in spherical bubbles. This is probably not an accurate representation of the vortex flow in an oblate ellipsoid [203]. In fact, oblate distortions of a Hill's vortex asymptotically approach a vortex ring which is a rather different structure than that assumed for the derivations of these expressions.

Certainly, the Fuchs derivation is sufficiently peculiar that it is surprising that it has been so widely used in the absence of any real validation. Mills and Hoseyni [204] have criticized the derivation on the basis of inconsistency. Consider the deposition velocity, V(D), which is a mass transport coefficient. Cast in terms of a Sherwood number, the mass transport coefficient is:

*Eccentricity is defined here as the ratio of the semi-major axis length divided by the length of the semi-minor axis.

$$Sh = \frac{V(D)\ D_B}{Đ} = f(E) \left[\frac{U_{slip}\ D_B}{Đ} \right]^{1/2} = f(E)\ Pe^{1/2}$$

where Pe is the Peclet number. This relationship between the Peclet number and the Sherwood number is the expected result from penetration theory for mass transport. Penetration theory is based on the assumption of a well-mixed bulk fluid and not vortex flow. Mills and Hoseyni correctly note that the Kronig-Brink solution is the proper solution for the case of vortex flows [88]:

$$Sh = \frac{\sum_{i=1}^{\infty} A_n^{\,2}\ \lambda_n \exp[-16\ \lambda_n\ \tau_p]}{\sum_{i=1}^{n} A_n^{\,2} \exp[-16\ \lambda_n\ \tau_p]}$$

where

$$\tau_p = 4\ Đt\ /\ D_B^{\,2}$$

and the values of the parameter λ_n and A_n for the first seven terms are [205]:

n	λ_n	A_n
1	1.656	1.29
2	9.08	0.596
3	22.2	0.386
4	38.5	0.35
5	63.0	0.28
6	89.8	0.22
7	123.8	0.16

In the very long term ($\tau_p \rightarrow \infty$),

$$Sh = 17.66$$

which is independent of the rise velocity. The time averaged mass transport coefficient is given by:

$$Sh = \frac{-2}{3\tau_p} \ln\left\{ \frac{3}{8} \sum_{n=1}^{\infty} A_n^{\,2} \exp[-16\ \lambda_n\ \tau_p] \right\}$$

Mills and Hoseyni suggest, based on work by Calderbank and Korchinski [206]:

$$Sh = \frac{3\pi^2}{4} \frac{\alpha(t)}{\sqrt{1-\alpha(t)}\ (1 - \sqrt{1-\alpha(t)})}$$

where

$$\alpha(t) = \exp\left[\frac{-9\pi^2}{4}\ \tau_p\right]$$

In the long term,

$$Sh = 14.6$$

Circulation of gases within the smaller bubbles is not assured especially in the contaminated water of the suppression pool. If the gas is essentially stagnant, the Sherwood number is given by [148]:

$$Sh = \frac{\frac{2\pi^2}{3}\sum_{n=1}^{\infty} \exp[-n^2\ \pi^2\ \tau_p]}{\sum_{n=1}^{\infty} \frac{1}{n^2} \exp[-n^2\ \pi^2\ \tau_p]}$$

The long-term asymptote of this expression is:

$$Sh = 6.58$$

The time-average Sherwood number in this case is:

$$Sh = \frac{-2}{3\tau_p} \ln\left\{\frac{6}{\pi^2} \sum_{n=1}^{\infty} \frac{1}{n^2} \exp\left(-n^2\ \pi^2\ \tau_p\right)\right\}$$

Deposition velocities for particles of various sizes computed with these alternative models are shown in Figure 90. Time-average values shown in this figure were taken to be for 10 seconds which is about the time required for a bubble to rise through a suppression pool. Deposition velocities calculated using Fuchs' model are very high compared to those calculated with other models. Mills and Hoseyni feel, based on findings by Brunson and Wellek [206], that Fuchs' model might be more appropriate for oscillating bubbles. It is also evident from the results shown in Figure 90 that there are substantial differences between the time-average values of the deposition velocity and the long-term asymptote values. This suggests that the dynamic expressions for the Sherwood number, Sh, or deposition velocity ought to be used for analysis of aerosol decontamination by diffusion.

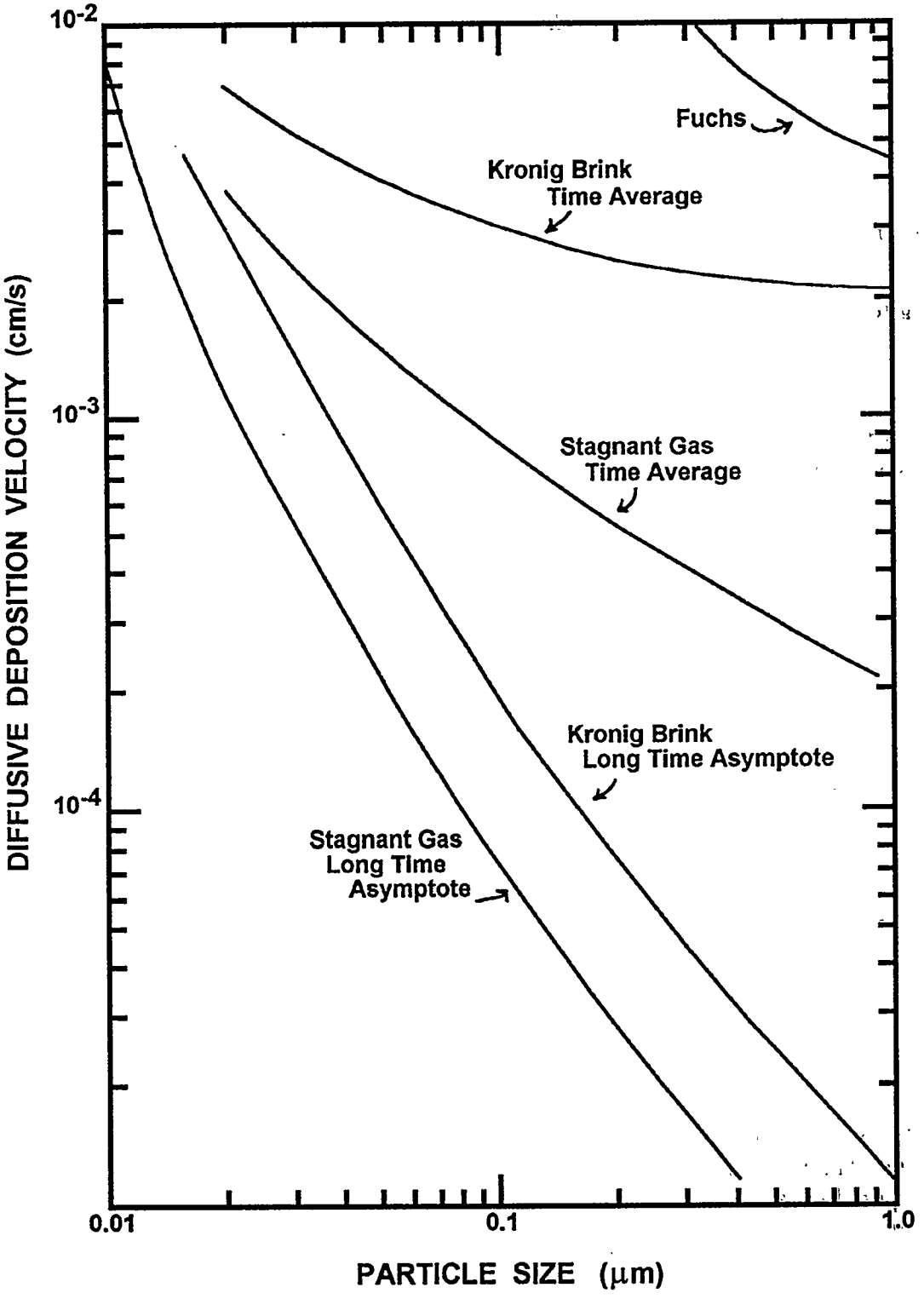

Figure 90. Diffusive deposition velocities according to several models for aerosol particles in a 0.5-cm bubble at 373 K

In summary, it is apparent that there is a significant uncertainty in the diffusive deposition of aerosol particles. As discussed below, diffusive deposition is most important for very small particles (<0.1 μm). Since small particles will contribute so little to the aerosol mass expected in a reactor accident, the uncertainties in diffusive deposition are not likely to create very large uncertainties in the total decontamination factor achieved by suppression pools. But, the relative magnitude of diffusive deposition (which increases in efficiency with decreasing particle size) is important in comparison to other aerosol deposition processes such as inertial impaction and sedimentation (which decrease in efficiency with decreasing particle size). These relative magnitudes will determine the aerosol particle size least efficiently removed by the suppression pool and consequently the particle size of aerosols most likely to penetrate the pool and become available for release from the plant.

b. Sedimentation Within a Bubble

The coefficient for aerosol sedimentation per unit rise of an ellipsoidal bubble is:

$$\alpha(s) = 1.5\ E^{2/3}\ J/D_B\ U_{rise}$$

where

E = eccentricity of the bubble,

$J = \gamma\ g\ \rho_p\ d_p^2\ C\ /\ 18\ \mu_g\ \chi$,

ρ_p = aerosol material density, and

γ = collision shape factor.

The deposition velocity into just the projected area of the lower half of the ellipsoid is:

$$V(D) = J$$

The deposition velocity normal to the surface of the ellipsoid is:

$$V(\text{normal}) = \frac{-JE\ \cos(\eta)}{\left[(E^2-1)\ \cos^2(\eta)\ +\ 1\right]^{1/2}}$$

for $\eta = \pi/2$ to π. The normal deposition velocity is zero for $\eta = 0$ to $\pi/2$. The differential area for deposition is:

$$dA = \frac{\pi D_B^2}{2E^{1/3}} \sqrt{(E^2-1)} \left[\frac{1}{E^2-1} + \cos^2(\eta)\right]^{1/2} \sin(\eta)\ d\eta$$

A plot of $\frac{V(normal)}{\pi D_B^2 J} \frac{dA}{d\eta}$ as a function of η is shown in Figure 91 for values of the eccentricity from 1.1 to 4.

Sedimentation is a strong function of particle size as is shown by the plot of J against particle size in Figure 92. It is likely that most particles large enough to deposit by sedimentation during bubble rise through a suppression pool would have been removed by deposition processes during transport to the pool.

c. Inertial Deposition

Circulation of gases within a bubble can lead to deposition because large particles are unable to follow stream lines in the flow. Deposition from the circulation vortex in a spherical bubble has been derived by Fuchs [148]. Derivation of the deposition from an oblate ellipsoid has been based on the consideration of simple geometric distortion of the Hill's vortex in spherical bubbles [149,150]. As noted above, this is not an accurate portrayal of the circulation in an oblate ellipsoidal bubble [203]. The deposition coefficient for the fraction of particles deposited per unit rise of a bubble of eccentricity E is:

$$\alpha(I) = \frac{6\, U_{slip}^2\, \tau\, E^{4/3}}{D_B^2 U_{rise}} \frac{\left\{(E^2-1)^2 + (E^2-1)^{1/2}\,(E^2-2)\,\tan^{-1}\left[\sqrt{(E^2-1)}\right]\right\}}{\left\{\sqrt{(E^2-1)} - E^2\,\tan^{-1}\left[\sqrt{(E^2-1)}\right]\right\}^2}$$

where

τ = J/g = $\gamma\, \rho_p\, d_p^2\, C / 18\, \mu_g\, \chi$, and

γ = collision shape factor

A deposition velocity over the entire surface area of the bubble is:

$$V(I) = \frac{2U_{slip}^2\, \tau\, E^{2/3} \left\{(E^2-1)^2 + (E^2-1)^{3/2}\,(E^2-2)\,\tan^{-1}\left[\sqrt{(E^2-1)}\right]\right\}}{D_B \left\{1 + \frac{\ln\left[\frac{E + (E^2-1)^{1/2}}{E - (E^2-1)^{1/2}}\right]}{2E\,(E^2-1)^{1/2}}\right\} \left\{\sqrt{(E^2-1)} - E^2\,\tan^{-1}\left[(E^2-1)^{1/2}\right]\right\}^2}$$

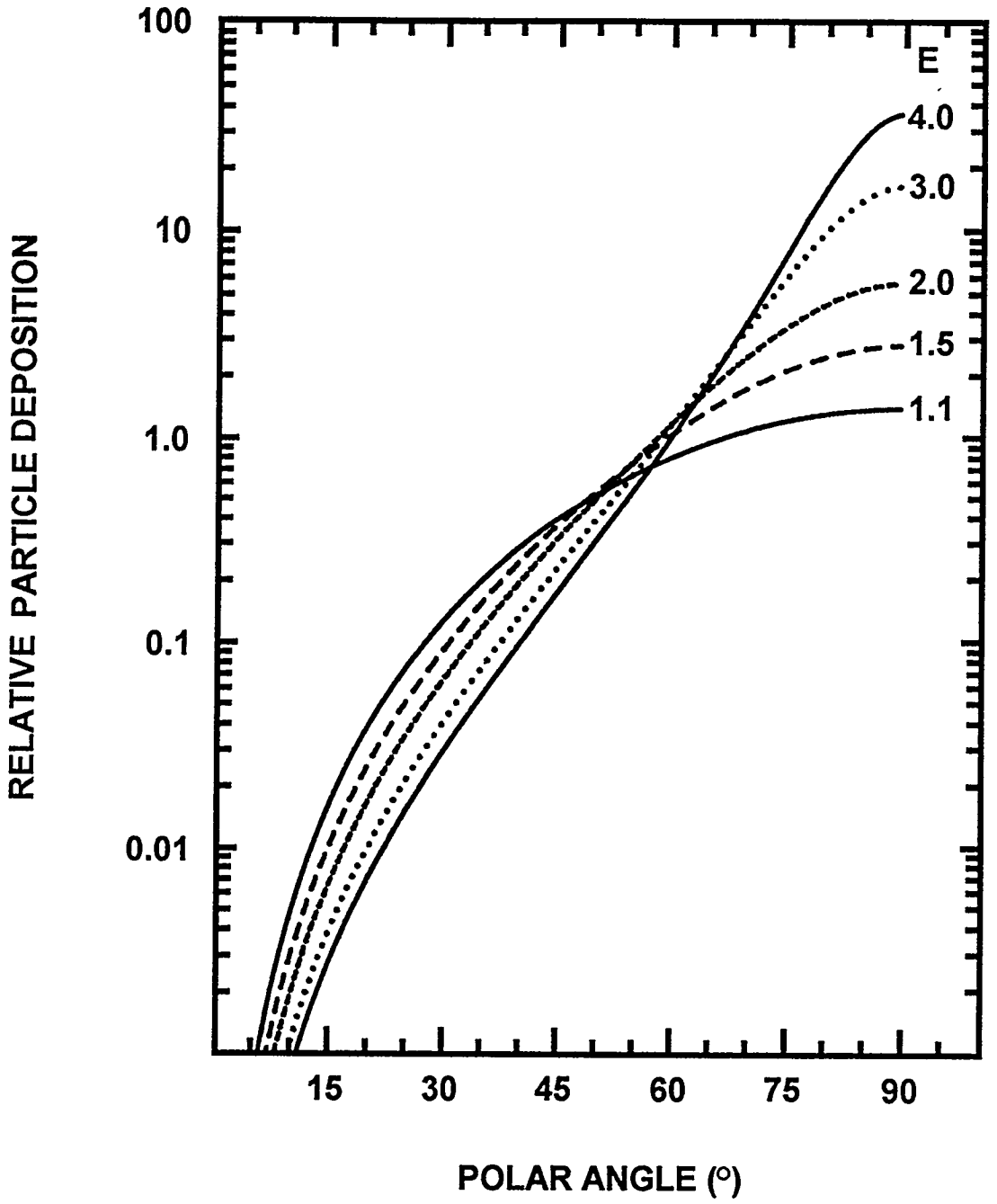

Figure 91. Patterns of particle deposition by sedimentation within ellipsoidal bubbles of various eccentricities

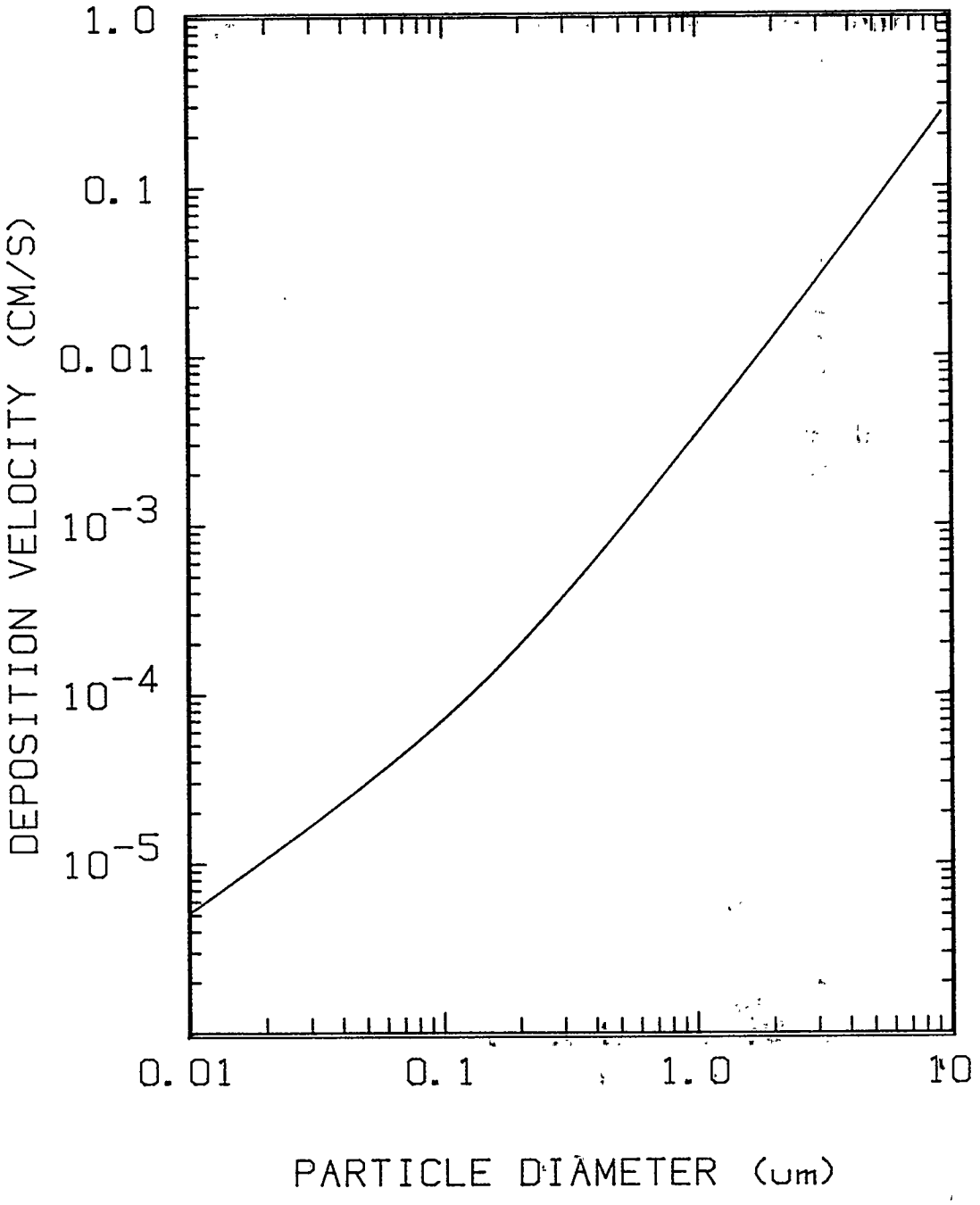

Figure 92. Sedimentation deposition velocity as a function of particle size

The centrifugal acceleration responsible for the deposition is given by:

$$\text{acceleration} = a = \frac{2U_{slip}^2 \sin^2(\eta) \sqrt{E^2-1}\ E^{5/3}}{D_B \left\{ \cos^2(\eta) + \frac{1}{E^2-1} \right\}^{5/2} \left\{ \sqrt{E^2-1} - E^2 \tan^{-1}\left[\sqrt{E^2-1}\right] \right\}^2}$$

where η is the polar angle of a vector from the origin of the ellipsoid to a point on the surface. The local deposition velocity is given by

$$\frac{\gamma\ \rho_p\ d_p^{\ 2}\ C\ a}{18\ \mu_g\ \chi} = V_D(\text{local}) = a\tau$$

The differential area for deposition is:

$$dA = \frac{\pi D_B^{\ 2}}{2E^{1/3}} \sqrt{E^2-1} \left\{ \frac{1}{E^2-1} + \cos^2(\eta) \right\}^{1/2} \sin(\eta) d\eta$$

for $\eta = 0$ to π. Plots of the patterns of deposition of particles by inertial impaction in ellipsoidal bubbles of various eccentricities are shown in Figure 93. It is apparent from results shown in this figure that most of the inertial impaction of particles occurs in a region around the midplane of the bubble. This region becomes narrower as the eccentricity of the bubble increases.

Deposition velocities due to inertial impaction are shown in Figure 94 as functions of particle size for bubbles of various sizes and eccentricities. These results show that inertial impaction can affect particles that are smaller than those affected by gravitational settling but does not affect particles that are efficiently deposited by diffusion. Combining the three classic mechanisms of aerosol deposition—diffusion, sedimentation and inertial impaction—produces an overall deposition velocity that passes through a minimum when plotted against particle size. The exact position of this minimum deposition velocity does depend on bubble size and system properties, but it is typically in the vicinity of 0.1 to 0.3 μm diameter particles.

d. Particle Deposition by Diffusiophoresis

In general, the gas within a bubble will not be in equilibrium with the water pool. As discussed above (see Section IV-D) the partial pressure of water vapor in a bubble will be depressed below the equilibrium partial pressure of water vapor in the suppression pool. There will, then, be a flux of water vapor from the bubble surface directed into the bubble which will oppose particle deposition. In principle, gases such as H_2, CO, and CO_2 will diffuse from the bubble into the water until the water pool becomes saturated. As discussed above, the saturation concentrations of these gases are so low that this flux of gas, which would tend to enhance deposition, is thought to be negligible. Attentions here are, then, fixed upon the inhibition to deposition by the water vapor flux into the bubble—diffusiophoresis. In the analysis of diffusiophoresis, temperature gradients between the bulk

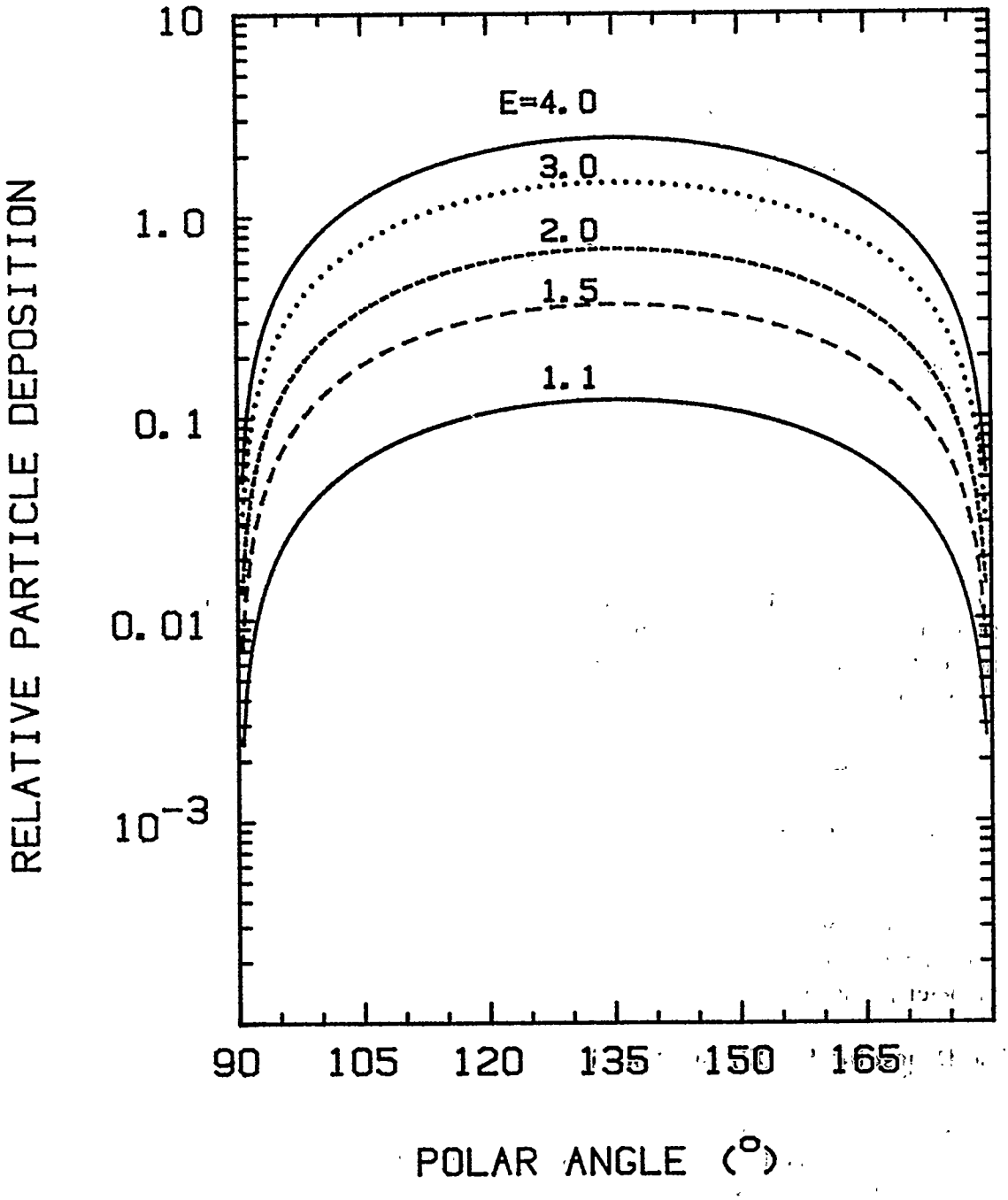

Figure 93. Patterns of particle deposition by inertial impaction in ellipsoidal bubbles of various eccentricities. Note that the deposition pattern is symmetrical about a polar angle of 90°.

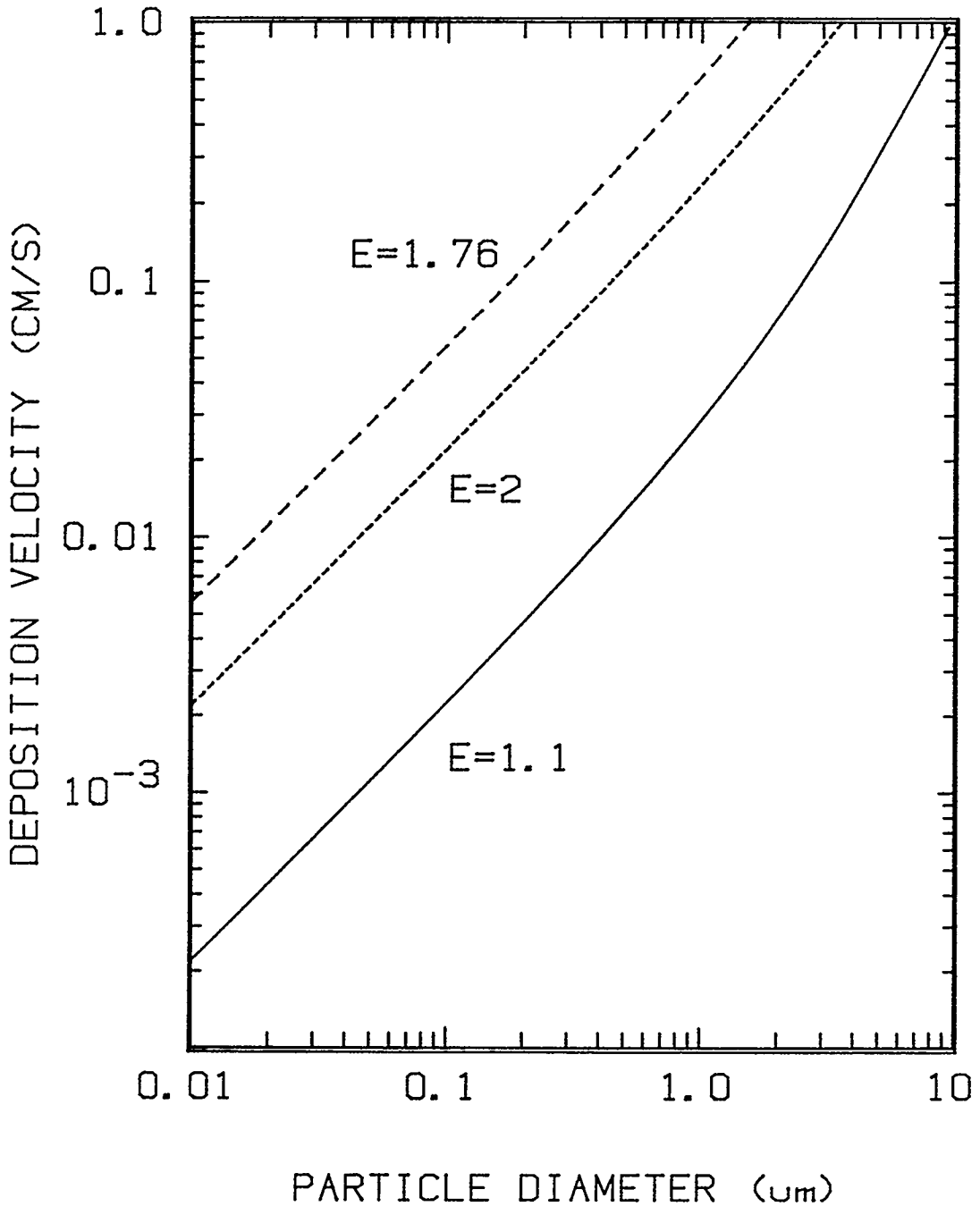

Figure 94. Inertial impaction deposition velocities as functions of particle size

gas and the bubble wall will be neglected. Thermodynamic calculations presented above show these gradients are small. The effect of the temperature gradients is to induce a thermophoretic velocity to the particles. This thermophoretic effect and the combined effects of diffusiophoresis and thermophoresis will be discussed in the next subsection.

Because the rising bubble is slightly unsaturated in water vapor, there will be a water vapor concentration gradient in the bubble near the bubble wall. The flux of water vapor away from the wall will subject aerosol particles to a Stefan flow and a diffusiophoretic force. According to Waldmann and Schmidt [166], the Stefan flow is given by:

$$V(\text{Stefan}) = \frac{Đ\ (H_2O)}{P_T - P(H_2O)}\ \nabla P(H_2O)$$

The diffusiophoretic force is given by:

$$F_D = -\sigma_{12}\ \frac{Đ\ (H_2O)}{P_T}\ 3\pi\mu_g\ d_p\ \nabla P(H_2O)$$

where

$Đ(H_2O)$ = diffusion coefficient of water vapor in a noncondensible gas within a bubble,

P_T = total pressure, and

σ_{12} = collision integral to be discussed below.

The deposition velocity of aerosol particles due to both diffusiophoresis and Stefan flow is:

$$V_D = \frac{C}{\chi}\left[\frac{\chi}{C} + \sigma_{12}\ (1 - P(H_2O)/P_T)\right]\ \frac{Đ(H_2O)}{[P_T - P(H_2O)]}\ \nabla P(H_2O)$$

Waldmann and Schmitt [166] indicate that the quantity σ_{12} is theoretically:

$$\sigma_{12} = \frac{m(H_2O) - m(\text{gas})}{m + (m(H_2O)\ m(\text{gas}))^{1/2}}$$

where $m = m(H_2O) + m(\text{gas})$. But, to match experimental data well, they find

$$\sigma_{12} = \frac{0.95(m(H_2O) - m(\text{gas}))}{m(H_2O) + m(\text{gas})} - 1.05\ \frac{(\sigma(H_2O) - \sigma(\text{gas}))}{\sigma(H_2O) + \sigma(\text{gas})}$$

In the free molecular regime, Waldmann and Schmitt recommend:

$$1 + \sigma_{12}\,(P - P(H_2O)/P =$$

$$= \frac{P\left[1 + \pi\alpha_t\,(H_2O)/8\right]\sqrt{m(H_2O)}}{P(H_2O)\left[1 + \pi\alpha_t(H_2O)/8\right]\sqrt{m(H_2O)} + (P - P(H_2O))\,(1 + \pi\alpha_t\,(gas)/8)\,\sqrt{m(gas)}}$$

where

$m(H_2O)$ = molecular weight of H_2O

$m(gas)$ = molecular weight of the noncondensible gas

$\alpha_t(H_2O)$ = thermal accommodation coefficient of H_2O

$\alpha_t(gas)$ = thermal accommodation coefficient of the noncondensible gas.

The molar flux of water vapor to the bubble surface is given by:

$$j(H_2O) = \frac{-Đ(H_2O)}{RT}\,\frac{\nabla P(H_2O)}{(1 - P(H_2O)/P_T)}$$

It is assumed here that the partial pressure of steam varies only with the normal distance from the bubble walls. Then, in oblate ellipsoidal coordinates*, the gradient is:

$$\nabla P(H_2O) = \frac{\partial P/\partial\xi}{\left[C^2\cos^2(\eta) + C^2\sinh^2(\xi)\right]^{1/2}}$$

and,

$$j(H_2O) = \frac{Đ(H_2O)}{RT}\,P_T\,\frac{\partial\ \ln P(H_2O)/\partial\xi}{\left[C^2\,\cos^2(\eta) + C^2\sinh^2(\xi)\right]^{1/2}}$$

The total rate of mass transfer to the bubble surface is:

*Cartesian coordinates x and y in terms of the oblate ellipsoidal coordinates are:

$x = C\sinh(\xi)\cos(\eta)$ $\quad y = C\cosh(\xi)\sin(\eta)$

$C^2 = a^2 - b^2$

where a and b are the length of the semi-major and semi-minor axes, respectively.

$$\int_A j(H_2O)dA = \int j(H_2O)\, 2\pi y\, ds$$

$$ds = \frac{a(E^2-1)^{1/2}}{E}\left[\frac{1}{E^2-1} + \cos^2(\eta)\right]^{1/2} \sin(\eta)\, d\eta$$

so,

$$\int j(H_2O)dA = \frac{\pi^2 a\, Đ(H_2O)\, P_T}{RT}\left.\frac{\partial \ln P(H_2O)}{\partial \xi}\right|_{\xi = \xi_o}$$

Similarly,

$$\int j(H_2O)\, dA = -k_m A[P(sat) - P(H_2O)]/RT$$

where

$$A = 2\pi a^2\left\{1 + \frac{1}{2E\sqrt{E^2-1}} \ln\left[\frac{E+\sqrt{E^2-1}}{E-\sqrt{E^2-1}}\right]\right\}, \text{ and}$$

$$a = D_B E^{1/3} / 2$$

Then,

$$\left.\frac{d \ln P(H_2O)}{d\xi}\right|_{\xi = \xi_o} = \frac{-A[P(sat)-P(H_2O)]\, k_m}{\pi^2 a\, Đ(H_2O)\, P_T}$$

and

$$\nabla P(H_2O)\,|_{\xi = \xi_o} = \frac{-P(H_2O)\, k_m\, E}{\pi^2 a^2 P_T\, Đ(H_2O)} \frac{\left\{1 + \frac{\ln\left[\frac{E+\sqrt{E^2-1}}{E-\sqrt{E^2-1}}\right]}{2E\sqrt{E^2-1}}\right\}[P(sat)-P(H_2O)]}{\sqrt{E^2-1}\left[\cos^2(\eta) + 1/(E^2-1)\right]^{1/2}}$$

A theoretical expression for the external mass transport in potential flow over an oblate ellipsoid is [267]:

$$Sh = \frac{k_m D_B}{Đ} = \frac{2\pi D_B^{\,2} Pe^{1/2}}{\sqrt{\pi} A} \left\{ \frac{2 (E^2-1)^{3/2}}{3\left[E^2 \tan^{-1}\left(\sqrt{E^2-1}\right) - \sqrt{E^2-1}\right]} \right\}^{1/2}$$

Taking this expression as approximately applicable also for the interior, rotational flow yields:

$$\nabla P(H_2O)\Big|_{\xi=\xi_o} = -\frac{8}{\pi^{3/2}} \frac{Pe^{1/2}}{D_B} \frac{P(H_2O)}{P_T} \frac{E^{1/3}[P(sat)-P(H_2O)]}{\left[\cos^2(\eta)+1/(E^2-1)\right]^{1/2}} \left[\frac{2(E^2-1)}{3\left\{(E^2 \tan^{-1}(\sqrt{E^2-1}) - \sqrt{E^2-1}\right\}} \right]^{1/2}$$

where

Pe = $U_B D_B / Đ(H_2O)$, and

D_B = diameter of the volume equivalent sphere.

A plot of the relative variation of the partial pressure gradient and consequently the diffusiophoretic flux of particles around the surface of the bubble is shown in Figure 95. Since, in general, the saturation partial pressure at the bubble surface will be greater than the partial pressure of water vapor in the bubble, the gradient is negative. That is, the flow of evaporating water will force particles away from the surface.

e. Thermophoresis

A particle in a thermal gradient will migrate toward lower temperature due to the thermophoretic force. This effect, which is so difficult to accurately measure, has prompted a remarkable amount of intemperate language in the specialized literature (see for examples References 225 and 226). Bakanov (225) provides a readable review of the topic. Thermophoresis literature is challenging because nomenclature is not standardized.

By far, the most widely used expressions for predicting the thermophoretic motions of particles is that derived by Talbot et al. [154]:

$$V_D = \frac{\frac{2C_s \mu_g}{\chi \rho_g} \left[\frac{k_g}{k_p} + C_t Kn \right] C \nabla \ln T}{[1 + 3C_m Kn]\,[1 + 2k_g/k_p + 2C_t Kn]}$$

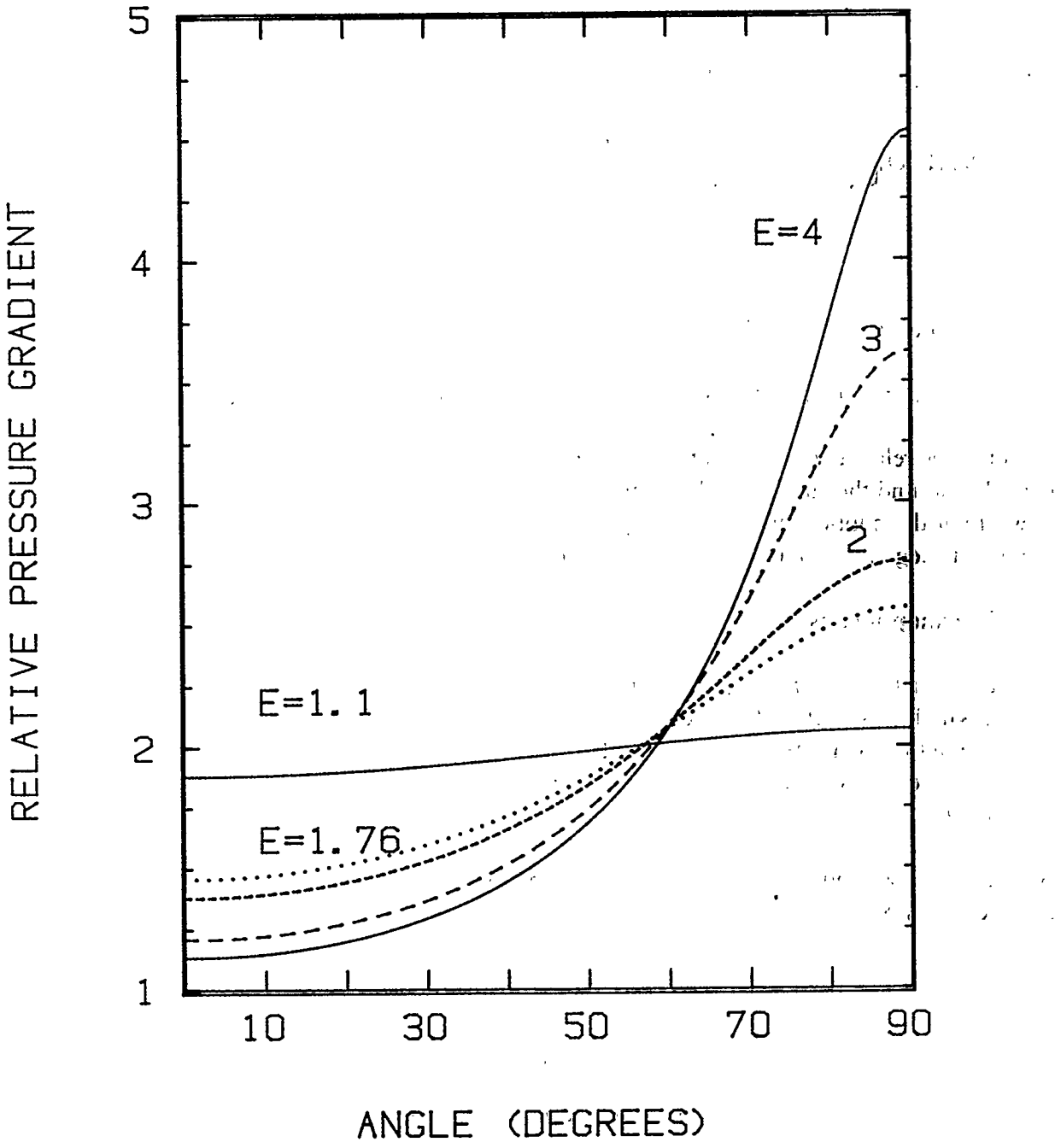

Figure 95. Relative variation in the water vapor pressure gradient at the surfaces of ellipsoidal bubbles of various eccentricities. Note that variations are symmetrical about polar angles of 90 and 180°.

$$F_T = \frac{\dfrac{-6\pi\mu_g d_p C_s}{\rho_g}\left[\dfrac{k_g}{k_p} + C_t\,Kn\right]\nabla \ln T}{[1 + 3C_m Kn]\,[1 + 2k_g/k_p + 2C_t Kn]}$$

where

F_T = thermophoretic force

V_D = thermophoretic deposition velocity

C_s = 1.128

$$C_m = \frac{2-\alpha_m}{\alpha_m}$$

$$C_t = \frac{15}{8}\,\frac{(2-\alpha_t)}{\alpha_t}$$

Loyalka [227] has suggested some alternate expressions for parametric quantities that depend on the intermolecular force law

$$C_s = 0.75\,(1-\alpha_m) + 3\,\alpha_m\,\xi(s)$$

$$C_t = \frac{15}{8}\,\frac{(2-\alpha_t)}{\alpha_t}\left[(1-\alpha_t)\,\frac{5}{8}\,\sqrt{\pi} + \alpha_t\,\xi(t)\right]$$

$$C_m = \left(\frac{2-\alpha_m}{\alpha_m}\right)\left[(1-\alpha_m)\,\frac{\sqrt{\pi}}{2} + \alpha_m\,\xi(m)\right]$$

$\xi(s)$ = 0.35 to 0.383

$\xi(t)$ = 1.263 to 1.296

$\xi(m)$ = 0.996 to 1.02

Derjaquin and Yalamov [161] have used arguments based on irreversible thermodynamics to derive:

$$V_D = \frac{\dfrac{-3.0\,\mu_g}{\rho_g}\left[\dfrac{k_g}{k_p} + C_t\,Kn\right]\nabla \ln T}{[1 + 2C_m Kn]\,[1 + 2k_g/k_p + 2C_t Kn]}$$

which differs from that found by Talbot et al. by a factor of $2C_s/3 \cong 0.75$.

Fulford et al. [159] have correlated experimental data to obtain.

$$\log_{10}\left[\frac{F_T}{\nabla T}\right] = -11.418 - 0.7525\ \log_{10} Kn - 0.2231\ (\log_{10} Kn)^2 - 0.2695\ (\log_{10} Kn)^3$$

and

$$V_D = -F_T\ C/3\pi\ \mu_g\ d_p$$

Phillips [244] has produced what is the most heroic expression for thermophoretic force:

$$F_T = \frac{-27}{2}\ \pi\ \beta_t \left[\frac{k_g}{2k_g + k_p}\right] \frac{\mu_g^2}{\rho_g}\ \nabla \ln T$$

where

$$\beta_t = \frac{1 + N(1)\ Kn + N(2)\ Kn}{1 + D(1)\ Kn + D(2)\ Kn^2 + D(3)\ Kn^3}$$

$$N(1) = \frac{k_p\ C_t}{k_g} - \frac{15}{4}\ \frac{(k_p - k_g)}{k_g}\ C_m$$

$$N(2) = \frac{15}{4}\ \frac{k_p}{k_g}\ C_t\ C_m$$

$$D(1) = \frac{9}{2}\left[\frac{k_g}{2k_g + k_p}\right] + \left[\frac{2k_p}{2k_g + k_p}\right] C_t + 3\ C_m$$

$$D(2) = \frac{9}{2}\left[\frac{k_p}{2k_g + k_p}\right] C_t - \frac{135}{8}\ \frac{(k_p - k_g)}{(2k_g + k_p)}\ C_m + \frac{6k_p}{(2k_g + k_p)}\ C_t + C_m$$

$$D(3) = \frac{135}{8}\left[\frac{k_p}{2k_g + k_p}\right] C_t\ C_m$$

Phillips, however, has argued that the particle moving in a thermal gradient distorts the gradient so that the deposition velocity is

$$V_D = \frac{-9}{4} \beta_t C \left[\frac{k_g}{2k_g + k_p} \right] \frac{\mu_g}{\rho_g} \left[\frac{1 - \sqrt{1-2\gamma}}{\gamma} \right] \nabla \ln T$$

where

$$\gamma = \beta_u \frac{k_g k_p}{(2k_g + k_p)^2} (\beta_t C)^2 Kn$$

$$\beta_u = \frac{N_p/16 + BKn \exp(-C'Kn)}{1 + DKn}$$

$$B = 46900$$

$$C' = 31.8$$

$$D = 18$$

$$N_p = \left[\frac{8 RT}{\pi MW} \right]^{1/2} \frac{d_p^3}{8} \frac{(\nabla \ln T)^2}{\alpha_p}$$

MW = molecular weight of the gas, and

α_p = thermal diffusivity of the particle.

This distortion of the thermal gradient can accentuate the thermophoretic settling of particles by the factor $(1 - \sqrt{1-2\gamma}) / \gamma$.

Phillips' model predicts somewhat lower deposition velocities when the thermal gradient correction is not made than does the model developed by Talbot et al. Parametric variations that are part of this work can cause Phillips' model to predict particle motions up the thermal gradient. Consequently, Phillips' model is not used here.

Some comparisons of the predictions for the dimensionless deposition velocity

$$\frac{V_D \rho_g}{\mu_g \nabla \ln T}$$

to data for oil drops in hydrogen and carbon dioxide are shown in Figures 96 and 97. Thermophoretic deposition velocities seem fairly well predicted for values of the Knudsen numbers greater than about 0.5. Some comparisons for inorganic species are listed in Table 18. The empirical model matches these data closely since the data were used to make the empirical fit.

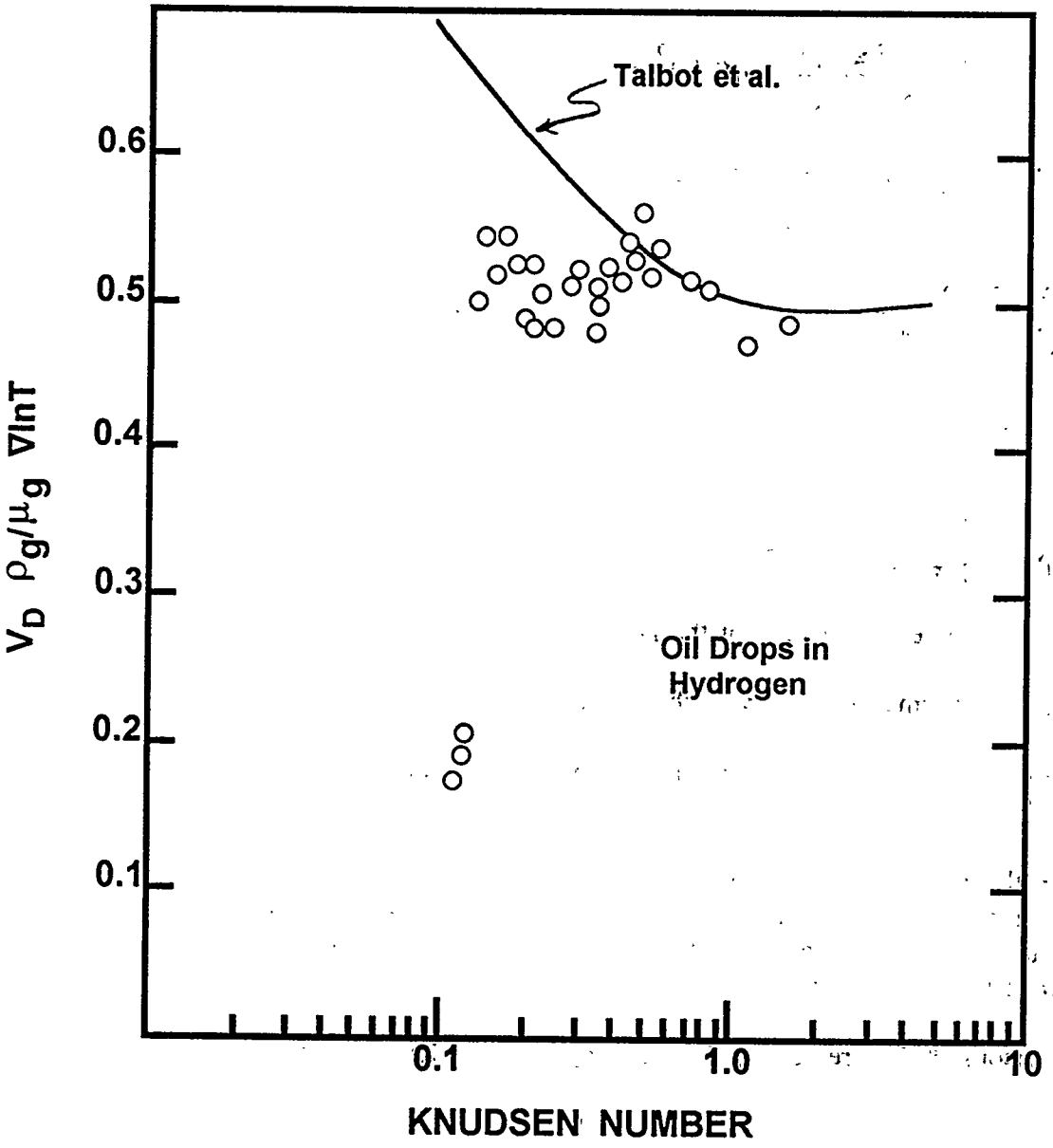

Figure 96. Comparison of dimensionless thermophoretic velocity predicted by the Talbot et al. model to data [229] for oil drops in hydrogen

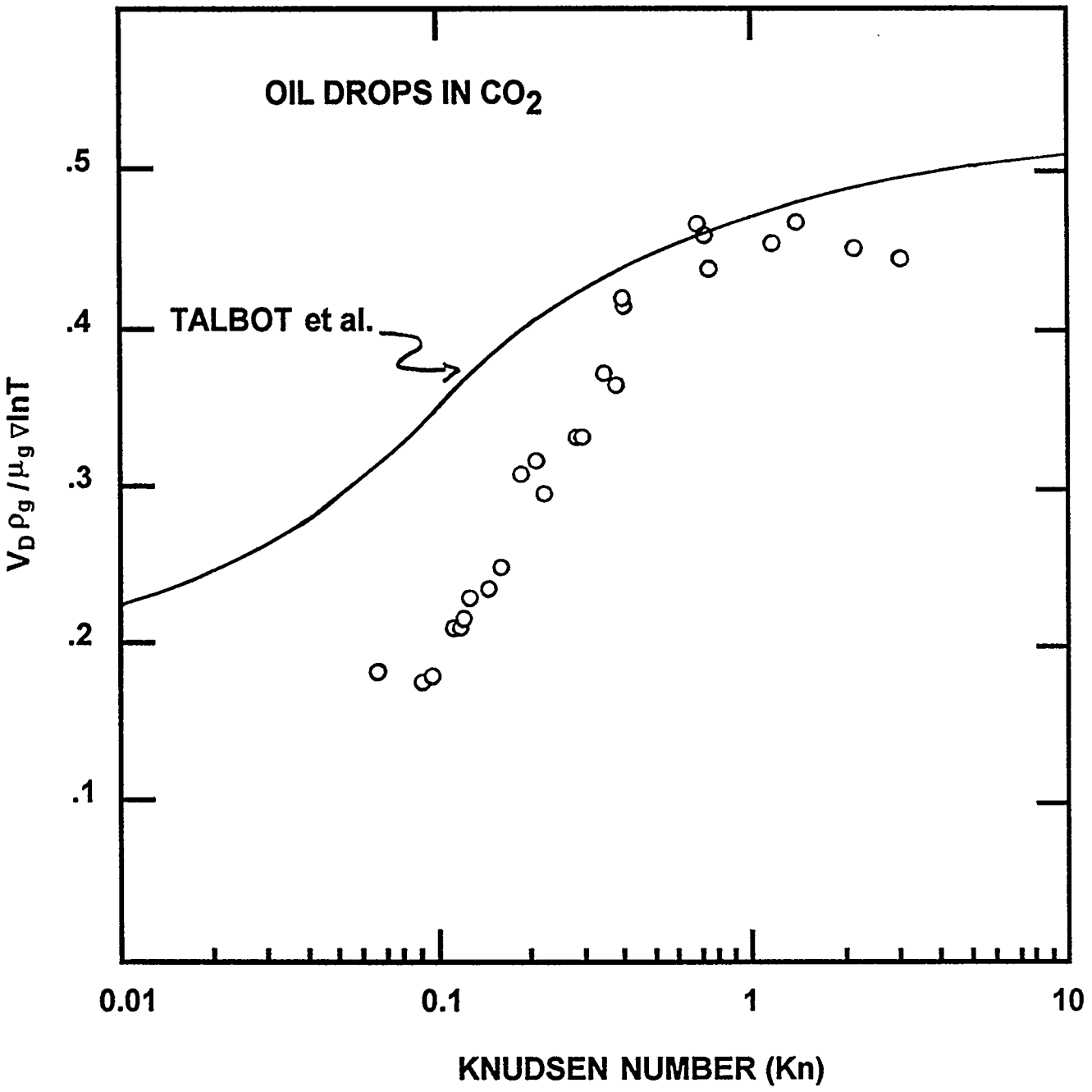

Figure 97. Comparison of dimensionless thermophoretic velocity predicted by the Talbot et al. model to data [229] for oil drops in carbon dioxide

Table 18. Comparison of observed and predicted thermophoretic deposition velocities

Particle material	Gas	Kn	Observed [161,228]	Talbot et al.	Fulton et al.
NaCl	air	0.15	0.57	0.33	0.247
NaCl	He	0.38	0.73	0.42	-
NaCl	air	0.25	0.70	0.38	0.18
NaCl	N_2	0.15	0.37	0.31	0.25
Al_2O_3	N_2	0.15	0.22	0.31	0.25
MgO	N_2	0.15	0.26	0.31	0.25
Fe	N_2	0.15	0.25	0.31	0.25
Zn	N_2	0.15	0.25	0.31	0.25
Al	N_2	0.15	0.25	0.31	0.25
Ag	N_2	0.15	0.33	0.31	0.25
Pt	N_2	0.15	0.39	0.31	0.25

There has been a continued controversy over thermophoresis. Some theoretical models predict thermophoretic flow would be in the direction of increasing temperature [225, 232, 233]. This has not been observed in experiments. Balakov [225] accepts the theoretical prediction and terms the phenomenon "second-order slip." Other authors have not been so generous [226]. We ignore this possibility here in the suspicion that the predicted flow up the temperature gradient may be a deficiency of the models and not a real phenomenon.

Arguments have also been made that particles can rotate in the boundary layers [230]. It appears, however, that this can occur only for particles larger than those of interest here [231].

Following the same procedure used for the analysis of diffusiophoresis, the thermal gradient is:

$$\nabla T = \frac{-h\Delta TE}{a^2\,\pi^2 k_{th}\,\sqrt{E^2-1}} \left[1 + \frac{\ln\left[\dfrac{E+\sqrt{E^2-1}}{E-\sqrt{E^2-1}}\right]}{2E\sqrt{E^2-1}} \right] \Bigg/ \left[\cos^2(\eta) + \frac{1}{E^2-1} \right]^{1/2}$$

where h is the heat transfer coefficient. Then,

$$\nabla T = \frac{-8\Delta T E^{1/3}}{D_B\,\pi^{3/2}} \frac{1}{\sqrt{E^2-1}} \left[\frac{U_{slip}\, D_B\, C_p(g)\, \rho(g)}{k_{th}(g)} \right] \frac{f(E)}{\left[\cos^2(\eta) + \dfrac{1}{E^2-1} \right]^{1/2}}$$

$$f(E) = \left\{ \frac{2(E^2-1)^{3/2}}{3\left[E^2 \tan^{-1}\left(\sqrt{E^2-1}\right) - \sqrt{E^2-1} \right]} \right\}^{1/2}$$

f. Particle Growth by Water Condensation

The discussions in the preceding subsections have shown that the rate at which particles are removed from a bubble rising through a suppression pool is a strong function of the aerosol particle size. In the water-rich environment of a steam suppression pool, the possibility that aerosol particles might grow as a result of water vapor condensation on their surfaces needs to be considered. Such particle growth could significantly affect the decontamination that could be achieved by a suppression pool.

Condensation that affects particle size has to be on the external surfaces of the particles. (Condensation of water in voids within particle agglomerates and the effects this internal condensation can have on particle shape factors has been discussed above in Section IV-K.) The convex external surfaces of individual aerosol particles and particle agglomerates resist condensation because of the Kelvin effect. And, of course, in a rising bubble the partial pressure of steam in the bubble will always be slightly below saturation. Growth of aerosol particles will occur, then, only if there is some process that will

reduce the chemical activity of water on the surfaces of aerosol particles so that the vapor pressure of the deposited water is less than the partial pressure of water vapor in the bubble. The most obvious mechanism for this reduction in the chemical activity of condensed water is the dissolution of some aerosol material into the water. Nearly all of the inorganic materials likely to be present in aerosols produced in nuclear reactor accidents will cause a reduction in water activity when they dissolve. Indeed, some of the chemical species considered to make up aerosols discharged to the suppression pool are quite water soluble. Saturation solubilities of CsOH and CsI at 373 K exceed 3.6 and 2.6 moles/kg-H_2O, respectively. Aerosol particles composed of these materials would surely grow by water condensation during transport in bubbles through the suppression pool. It is not obvious that such highly soluble species will actually be present in the aerosol produced during severe reactor accident. Though all materials exhibit some solubility in water, the solubility may not be enough to cause a sufficient reduction in the chemical activity of water to lead to aerosol growth by water condensation. The magnitude of water solubility that is needed to lead to particle growth is given by:

$$\ln a_w = -4\sigma_l \bar{V}/d_p RT$$

where

a_w = chemical activity of water

$\bar{V}$ = molar volume of water

At 373 K, the chemical activity of water that will just lead to particle growth for aerosol particles of various sizes is:

$d_p(\mu m)$	a_w	molality (moles/kg-H_2O)
1.0	0.9986	0.039
0.1	0.9864	0.38
0.01	0.8722	3.8

The molality of a solution of an electrolyte composed of univalent ions necessary to produce such reductions in water activity can be estimated from:

$$a_w = \exp\left[\frac{-2m\phi}{55.51}\right]$$

where

m = molality, and

ϕ = osmotic coefficient

For the purposes of these estimates, the osmotic coefficient has been taken equal to 1. A more sophisticated estimate of the osmotic coefficient can be made.*

It is apparent from the values listed above that substantial solubilities of aerosol materials in water would be needed to get growth of even 1 μm particles. (Particles larger than 1 μm are so efficiently removed from bubbles by physical processes that their growth by water condensation is not very important.) There are few materials so soluble in water that 0.01 μm particles of these materials will grow by water condensation.

There are kinetic as well as thermodynamic factors that will inhibit aerosol growth by water condensation. Condensation of water on aerosol particles liberates heat which raises the particle temperature and the vapor pressure of condensing water. Unfortunately, there are few mechanisms available to dissipate this heat except conduction into the gas phase. In the subsections below, the heating of aerosol particles by water condensation is examined. The examination is done first for the free molecular regime ($Kn = 2\lambda/d_p << 1$ where λ is the mean free path of the gas phase) and for the continuum regime ($Kn >> 1$). Interpolation formulae and example calculations are then presented.

f-1. Condensation in the Free Molecular Regime

Assume that thermal gradients in the gas phase around a particle are small. The thermal accommodation coefficient of water onto a water surface has been measured to be 0.96 [172]. This is close enough to unity that diffuse reflection of molecules from a surface can be assumed. The molar flux of water vapor deposition on a particle surface in the free molecular regime is then given by:

---

*In Pitzer's formulation of the osmotic coefficient for univalent electrolytes such as CsOH and CsI [186]:

$$\phi - 1 = f^{\phi} + mB^{\phi} + m^2 C^{\phi}$$
$$f^{\phi} = -A_{\phi} [m^{1/2} / (1 + 1.2\, m^{1/2})]$$
$$B^{\phi} = \beta^0 + \beta^1 \exp(-2m^{1/2})$$

Near 373 K, $A_{\phi} = 4.48 \times 10^{-3} + 1.223 \times 10^{-3}$ T(K). For CsI,

$$\beta^0 = 0.0244$$
$$\beta^1 = 0.0262$$
$$C^{\phi} = -0.00365$$

For CsOH,

$$\beta^0 = 0.150$$
$$\beta^1 = 0.30$$
$$C^{\phi} = 0$$

$$\left.\frac{dN(H_2O)}{dt}\right|_{fm} = \frac{S\pi d_p^2}{4}\left\{\frac{P(\infty)}{RT(\infty)}T(\infty)^{1/2} - \frac{P(s)}{RT(s)}T(s)^{1/2}\right\}\left\{\frac{8R}{\pi MW}\right\}^{1/2}$$

$$\cong d_p^2\, 32.81 S\left\{\frac{P(\infty)}{T(\infty)^{1/2}} - \frac{P(s)}{T(s)^{1/2}}\right\} \text{ moles/s}$$

where

$N(H_2O)$ = moles of H_2O deposited on the particle,

S = probability that a water molecule striking the surface will stick to the surface,

$P(\infty)$ = partial pressure (atm) of water vapor in the gas phase,

$P(s)$ = equilibrium partial pressure of water vapor at the particle surface (atms),

$T(\infty)$ = temperature of the bulk gas (K),

$T(s)$ = temperature of the particle surface (K), and

d_p = diameter of the particle (cm).

The so-called sticking coefficient, S, that appears in the kinetic equations is not especially well known. Pruppacher and Klett [176] cite several determinations. Their citations are reproduced in Table 19. They note that the determinations of S can be grouped into two categories. Low values, on the order of S = 0.03, have been determined by static methods. High values, on the order of S = 0.9 to 1.0, have been determined by methods involving rapid renewal of the water surface. This would suggest that surface contamination, which has been found to profoundly affect the behavior of small bubbles (see Section IV-F), may also affect the sticking coefficient. On the other hand, Hsu and Graham [178] argue that the large dipole moment of water is responsible for the low sticking coefficient. Presumably, the orientation of the molecule as it approaches the surface can lead to attractive or repulsive forces. Certainly, other molecules with large dipole moments such as HCl are found to have low sticking coefficients with water even when very dynamic jet methods are used for the determination.

Pruppacher and Klett recommend the use of a low sticking coefficient for work with water drops. Whether this recommendation also applies to the issue here of water condensation on particles is not entirely evident. Wagner [179] found that large values of the sticking coefficient yielded better matches to aerosol growth data. But, a variety of other parametric assumptions were involved in deriving this result. Levine [180] used a Millikan oil drop apparatus to measure the sticking coefficient. He obtained a mean value of 0.95 from 35 measurements, but the variance in his data is enormous. As noted by Barrett and Clement [177], the issue of the sticking coefficient is unresolved.

Table 19. Determinations of the sticking coefficient cited by Pruppacher and Klett [176]

Author	Year	Temperature (K)	S
Alty	1931	291 to 333	0.006 - 0.016
Alty and Nicole	1931	291 to 333	0.01 - 0.02
Alty	1933	265 to 277	0.04
Alty and Mackay	1935	288	0.036
Baramaer	1939	-	0.033
Pruger	1940	373	0.02
Yamamoto & Miura	1949	-	0.023
Hammeke & Kappler	1953	293	0.045
Delaney et al.	1964	273 to 313	0.0415
Kiriukhin & Plaude	1965	280	0.019
Chodes et al.	1974	293	0.033
Rogers & Squires	1974	-	0.065
Narusawa & Springer	1975	291 to 300	0.038
Sinarwalla et al.	1975	295.6 to 298.8	0.026
Hickman	1954	273	0.42
Berman	1961	-	1.0
Nabavian & Bromley	1963	283 to 323	0.35 - 1.0
Jamieson	1965	273 to 343	0.35
Mills & Seban	1967	280 to 283	0.45 - 1.0
Tamir & Hasson	1974	323	0.20
Narusawa & Springer	1975	291 to 300	0.18

To understand the particle surface temperature, the heat imparted to the particle by condensation and the heat losses must be considered. Decay heating is neglected here because of the time scales. Heat losses are considered to be by conduction. The relative movement of particles with respect to the ambient gas is small enough that convection is negligible. Radiant heat losses are also neglected.

In the free molecular regime the rate of heat input to the particle due to water condensation is [177]:

$$L - \frac{RT(s)}{2} \left.\frac{dN(H_2O)}{dt}\right|_{fm}$$

Then,

$$\left.\frac{dQ}{dt}\right|_{fm} = \left.\frac{-dq}{dt}\right|_{fm} + [L - 0.5RT(s)] \left.\frac{dN(H_2O)}{dt}\right|_{fm}$$

where

$\left.\frac{dQ}{dt}\right|_{fm}$ = net heat input in the free molecular regime, and

$\left.\frac{dq}{dt}\right|_{fm}$ = heat loss due to conduction.

If average molecular properties are assumed:

$$\left.\frac{dq}{dt}\right|_{fm} = 553.5\ d_p(cm)\ P_T(atm)\ \frac{T(s) - T(\infty)}{\sqrt{T(\infty)\ MW}}\ cal/s$$

where

P_T = total pressure of the gas, and

MW = average molecular weight of the gas.

A closure equation for the water condensation is:

$$Q = C_p(p)\ \frac{\pi}{6}\ d_p^{\ 3}\ \rho_p\ (T(s)-T(\infty)) + C_p(H_2O)\ N(H_2O)\ (T(s)-T(\infty))$$

where

$C_p(p)$ = heat capacity of the particle material (cal/g-K), and

$C_p(H_2O)$ = heat capacity of water condensed on the external surface of the particle (cal/g-K).

This closure equation has been derived assuming that the thermal conductivity of water and the material making up the aerosol particle are infinite. The entire particle and condensed water system is then at the surface temperature. The assumptions behind this closure equation will lead to lower surface temperatures than would be predicted if thermal conductivities of the condensed materials were taken to be finite.

f-2. Condensation in the Continuum Regime

The possibility of there being a thermodynamic driving force for condensation on particles is higher for particles that are large relative to the mean free path of gas molecules. Still, even for these larger particles, during bubble rise through the suppression pool there must be some reduction in the chemical activity of condensed water for there to be condensation.

Kulmala and Vesala [181] have built upon earlier work by Barrett and Clement [177] to describe particle growth in the continuum regime ($Kn << 1$). Again, convection in the gas phase is neglected (but, see Reference 182). Radiation heat transfer is also neglected (see Reference 183). The pseudobinary diffusion coefficient of steam in the gas phase is taken to have the temperature dependence:

$$Đ(T) = Đ(o) \left[\frac{T}{T(\infty)} \right]^n$$

where

$Đ(o)$ = diffusion coefficient at $T(\infty)$, and

$n \neq 2$.

For a hard sphere gas, $n = 1.5$. The temperature profile in the vicinity of the particle is taken to be linear:

$$T(r) = T(\infty) + [T(s) - T(\infty)]\, d_p/2r$$

where r is the distance from the center of the particle and $r > d_p / 2$. The variation in the partial pressure of steam in the gas phase surrounding the particle is also taken to be linear:

$$P(H_2O,r) = P(H_2O,\infty) + [P(H_2O,s) - P(H_2O,\infty)]\, d_p/2r$$

Composition dependencies of the gas phase thermal conductivity are neglected. Thermal diffusion is included, but the Dufour effect is neglected. Then,

$$\frac{dN(H_2O)}{dt} = \frac{2\pi d_p P_T D(o)}{RT(\infty)} \left\{ C(1) \ln\left[\frac{P_T - P(s)}{P_T - P(\infty)}\right] + \frac{C(2)}{4} \alpha[P(s) + P(\infty)] \right\}$$

where

$$C(1) = \left[\frac{T(s) - T(\infty)}{T_{(\infty)}^{n-1}}\right] \left[\frac{2 - n}{T_{(s)}^{2-n} - T_{(\infty)}^{2-n}}\right],$$

$$C(2) = \left[\frac{T(s) - T(\infty)}{T_{(\infty)}^{n-1}}\right] \left[\frac{3 - n}{T_{(s)}^{3-n} - T_{(\infty)}^{3-n}}\right],$$

$P(\infty)$ = $P(H_2O, \infty)$, and

α = thermal diffusion coefficient.

The heat imparted to the particle is:

$$\left.\frac{dQ}{dt}\right|_{cont} = \left.\frac{-dq}{dt}\right|_{cont} + \left.\frac{L\ dN(H_2O)}{dt}\right|_{cont}$$

where

$$\left.\frac{dq}{dt}\right|_{cont} = 2\pi\, k_{th}\, d_p\, [T(s) - T(\infty)] \quad , \text{and}$$

k_{th} = thermal conductivity of the gas.

The temperature of the particle surface is:

$$T(s) = T(\infty) + \frac{L}{2\ \pi d_p\ k_{th}} \left.\frac{dN(H_2O)}{dt}\right|_{cont}$$

f-3. Condensation in the Transition Regime

There is no solution for the condensation of water vapors in the transition regime where Kn ~ 1. Williams and Loyalka [184] have suggested some interpolation formulae to predict processes in this transition regime from expressions for the limiting cases of the free molecular regime and the continuum regime. These interpolation formulae are modified for use here:

$$\left.\frac{dq}{dt}\right|_{trans} = \left.\frac{dq}{dt}\right|_{cont} f(Kn(h))^{-1}$$

$$\left.\frac{dN(H_2O)}{dt}\right|_{trans} = \left.\frac{dN(H_2O)}{dt}\right|_{cont} h(Kn(c))^{-1}$$

where

$$f(Kn(h)) = 1 + \left[\frac{\Omega\ E(h) + J(h)}{Kn(h)\ E(h) + 1}\right] Kn(h)$$

$$g(Kn(c)) = 1 + \left[\frac{\theta\ E(c) + J(c)}{Kn(c)\ E(c) + 1}\right] Kn(c)$$

$$h(Kn(c)) = g(Kn(c)) \Big/ \left\{1 + \left[\frac{1-s}{s}\right] \frac{\sqrt{\pi}\ Kn(c)}{g(Kn(c))}\right\}$$

$$\Omega = \left.\frac{dq}{dt}\right|_{cont} \Big/ \left.\frac{dq}{dt}\right|_{fm}$$

$$\theta = \left.\frac{dN(H_2O)}{dt}\right|_{cont} \Big/ \left.\frac{dN(H_2O)}{dt}\right|_{fm}$$

$$Kn(h) = 2\,\lambda(h) / d_p$$

$$Kn(c) = 2\,\lambda(c) / d_p$$

$$\lambda(h) = 0.8 k_{th} \frac{T(\infty)}{P_T} \left[\frac{MW}{2RT(\infty)}\right]^{1/2}$$

$$\cong \frac{2.562 \times 10^{-3}\ k_{th}\ (cal/s\text{-}cm\text{-}K)\ T(\infty)^{1/2}\ MW^{1/2}}{P_T(atms)}\ (cm)$$

$$\lambda(c) = 2\, D_{AB}^{(o)} \left[\frac{18.016}{RT(\infty)}\right]^{1/2} \cong \frac{6.58 \times 10^{-4}\, D_{AB}(cm^2/s)}{T(\infty)^{1/2}} \quad (cm)$$

$$E(h) = 1.9234$$

$$E(c) = 4/3$$

$$J(h) = 5/8\sqrt{\pi}\, p$$

Loyalka and Ferziger [290] suggest values of p varying from 1.1136 to 1.1759. Williams and Loyalka [184] suggest J(c) depends on the composition of the gas phase:

$$J(c) = 0.9769 - 0.0518\, z + 0.018\, z^2 + 0.0196\, z^3$$

$$z = \log_{10} \frac{MW(nc)}{MW(H_2O)}$$

where MW(i) is the molecular weight of the i^{th} gas species.

g. Aerosol Capture by Bubble Oscillations

Ellipsoidal bubbles with Reynolds numbers in excess of 200 to 800 (See Section IV-f) can undergo shape oscillations. In principle, it might be possible for the oscillating bubble walls to sweep out any aerosols within the amplitude of the motion. The critical issue is whether the aerosol particles can respond to the motions of the bubble walls.

To estimate the possible magnitude of aerosol sweep out by the shape oscillations of bubbles, the oscillations are approximated as a sinusoidal motion. The velocity of the gas within the bubble is, then, given by:

$$U_g = A\, \omega \cos \omega t$$

where

A = amplitude of the motion,

ω = $2\pi f$, and

f = frequency of the shape oscillation

The motions of aerosol particles will be, in general, out of phase with the gas motion. The amplitude of particle motion may also be different than that of the gas. Following arguments by Clift et al. [82], the velocity of an aerosol particle is taken to be:

$$U_p = A\eta\, \omega \cos (\omega t + \beta)$$

where

β = phase shift, and

η = amplitude magnification factor.

Clift et al. find:

$$\beta = \tan^{-1} [h(2) / (1 + h(1))]$$

$$\eta = \left\{[1 + h(1)]^2 + h(2)^2\right\}^{1/2}$$

where

$$h(1) = H(1) (1 + H(2))$$

$$h(2) = H(1) H(2) (1 + 2 \tau_o)$$

$$\tau_o = 4 \mu_g / \rho_g \omega d_p^2$$

$$H(1) = 2(1 - \gamma)/(2\gamma + 1) \Big/ \left[H(2)^2 (1 + \sqrt{2\tau_o})^2 + (1 + H(2))^2\right]$$

$$H(2) = 9 (\sqrt{\tau_o/2}) / (2\gamma + 1)$$

$$\gamma = \rho_p / \rho_g$$

Plots of β and η for particles of various sizes are shown as functions of frequency in Figures 98 and 99. It is evident from these figures that the motions of the particles are delayed relative to the gas. For very small particles ($d_p < 0.1$ μm) very high frequencies must be reached before the phase shift of particle motion is significant. For particles with diameters on the order of 1.0 μm, the phase shift is large even at frequencies of only 10 Hz. Once the particle is set in motion, it is slow to stop. The amplification factors for the sinusoidal motions of very small particles do not become significant until very high frequencies are reached. Amplitude magnification factors are large for larger particles even at low frequencies.

It is not immediately obvious what oscillation frequencies will occur in bubbles. It seems likely that oscillations would be at harmonic frequencies. For spherical bubbles the harmonic frequencies are given by

$$(2\pi f)^2 = \frac{8n(n-1)\ (n+1)\ (n+2)\ \sigma_l}{D_B^3\ [(n+1)\ \rho_l + n\rho_g]}$$

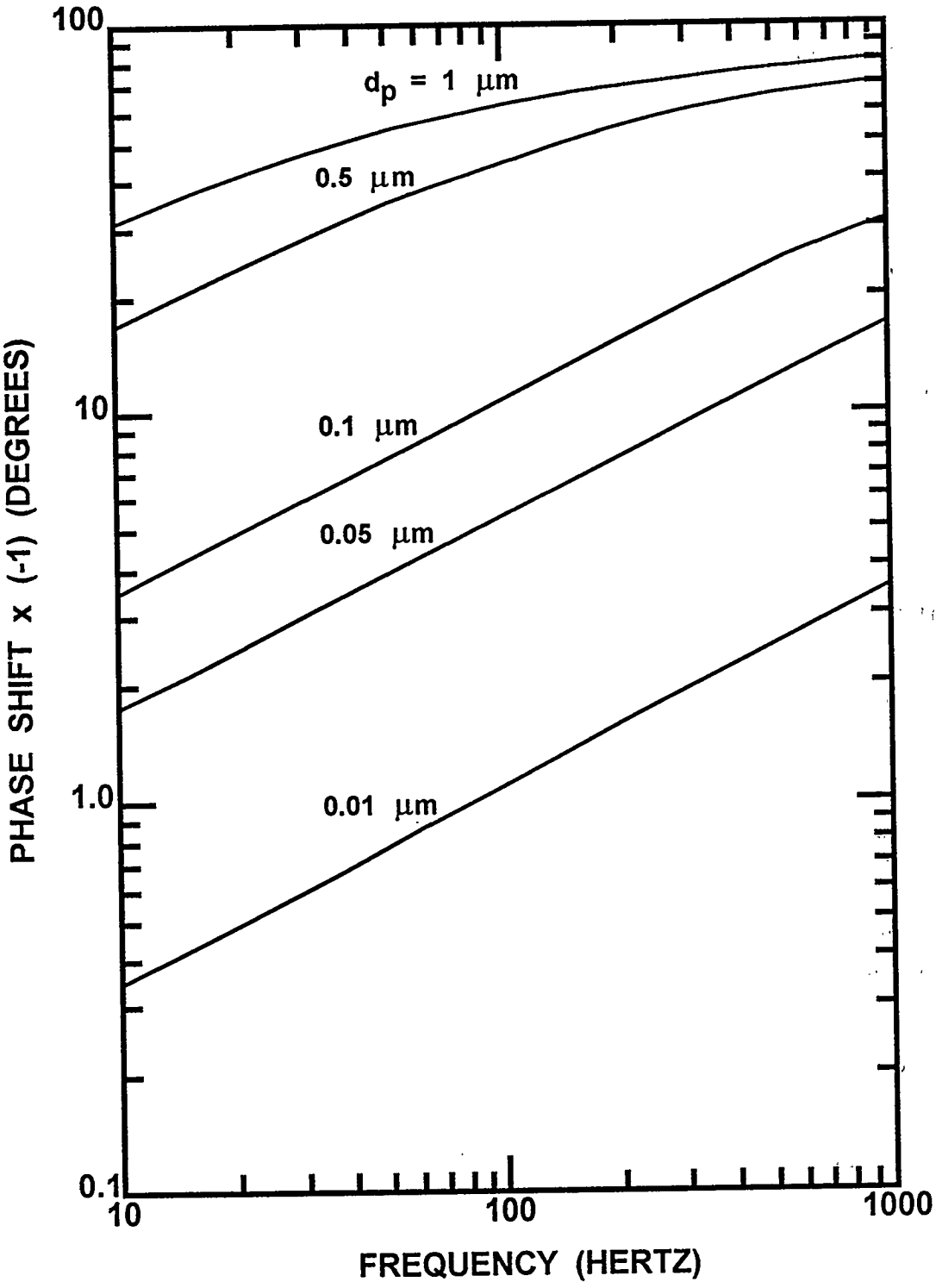

Figure 98. Phase shift for motions of particles (ρ_p = 2 g/cm^3) of various sizes in bubbles undergoing sinusoidal oscillations

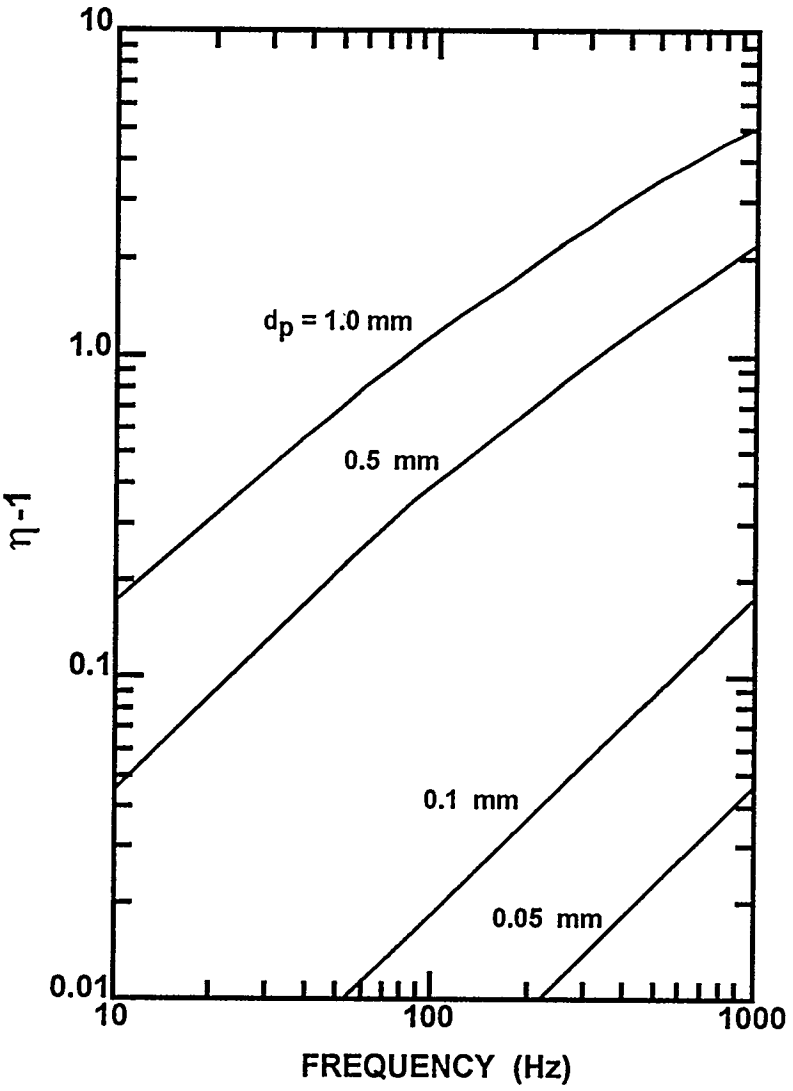

Figure 99. Amplitude magnification factors for motions of particles (ρ_p = 2 g/cm^3) of various sizes in bubbles undergoing sinusoidal oscillations

where n is the mode number. These resonant frequencies are shown in Figure 100 as functions of the bubble diameter in water at 373 K.

It is evident that particle capture by oscillation of the bubbles can occur. The rate of capture depends on particle size, bubble size, and the amplitude of oscillation. The authors are not aware of detailed theory of particle capture by this type of process. On strictly intuitive grounds, the mass transport rate is taken here to be:

$$k_m = -2\,\psi\,\frac{(\eta-1)\,\beta}{\pi}\,\sqrt{f\,Đ_p}$$

where $Đ_p$ is the diffusion coefficient for the particles in the bubble and ψ is an uncertain, dimensionless parameter with a nominal value of 1.2. In principle, all resonant modes of bubble oscillation ought to be considered (n = 2 to ∞). The understanding of oscillations and particle behavior is, however, too crude to justify this level of sophistication, so only the first nonzero vibration mode (n = 2) is considered.

2. Aerosol Trapping During Bubble Collapse

Once bubbles detach from orifices and begin to rise through the suppression pool they can collapse and disintegrate as discussed above (see Section IV B). The collapse process is very rapid. Experimental observations suggest that it is complete after bubble rise of 2 to 10 initial bubble diameters [30]. Behaviors of both the bubbles and the aerosol must be very complex during this period. No attempt is made here to model these complicated behaviors in detail. Instead, it is assumed that:

- simple disintegration of bubbles because they are unstable does not in itself lead to a significant amount of aerosol capture, and

- condensation of steam removes aerosols in proportion to the volume change of the bubble regardless of aerosol size.

As can be seen from the discussions above, the most profound effect on aerosol trapping caused by the collapse and disintegration of bubbles following detachment is the substantial reduction in bubble size. As shown above (Section IV-L-1), aerosol deposition processes become more efficient with decreasing bubble size. Paul et al. [30] speculate that disintegration of the bubbles released to the pool produces very small bubbles that subsequently coalesce to form larger bubbles observed to rise through the pool. During the period that aerosols are present in the very small bubbles, aerosol deposition processes could be very efficient indeed. No attempt is made to model or qualitatively describe this very transient period. Its duration is not long, so the extent of decontamination, despite the efficiency of the deposition processes, may not be great. Some partial remediation for neglect of decontamination during the transient period is realized because particle concentrations in bubbles rising through the pool will be somewhat higher than in reality.

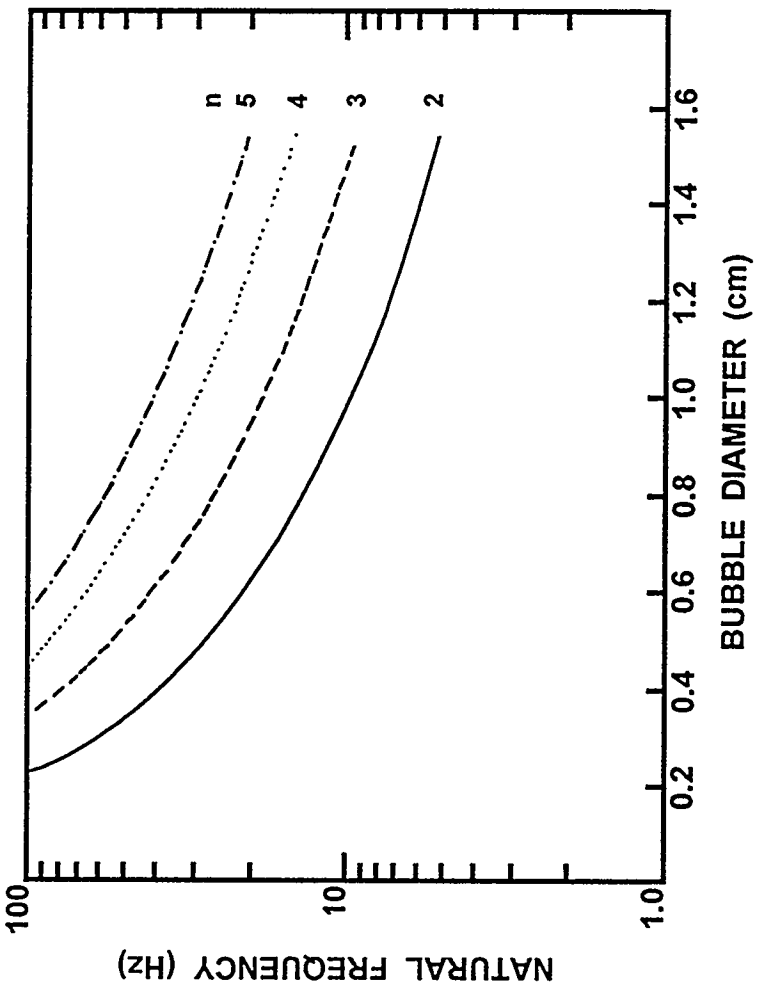

Figure 100. Natural vibration frequencies of bubbles in water at 373 K

3. Aerosol Capture During Bubble Formation

Bubble formation at orifices and vents in the suppression pool has been discussed at length above (see Section IV-A). The process is not entirely simple. There would appear to be opportunities for substantial aerosol capture as the bubbles form and before they detach and rise through the suppression pool. Among the possible mechanisms of aerosol capture during bubble formation are:

- impaction of particles from the jet of gas passing through the orifice stagnating at the bubble wall,
- diffusiophoretic deposition of particles as steam entering the bubble condenses on the bubble walls, and
- inertial deposition of particles from recirculating flows within the bubble.

Of course, diffusion and gravitational sedimentation are omnipresent processes that can contribute to the trapping of aerosols during bubble formation.

Systematic studies of aerosol capture during bubble formation have, apparently, not been undertaken. Approximate descriptions of the aerosol trapping processes are provided in the SUPRA code [7,8] and in the SPARC code [6]. The BUSCA code [9], apparently, is constructed to allow users to select between these two approximate descriptions.

The SUPRA code [7,8] considers aerosol capture during bubble formation to be predominantly the result of:

- impaction of particles from the decelerating jet emerging from the orifice, and
- inertial impaction from gases circulating within a growing bubble.

Documentation available to the authors concerning these models in the SUPRA code does not provide a great deal of detail. Fortunately, Ramsdale [9] provides more information. The impaction model is based on curve fits for particle impaction on a fixed flat plate from a round gas jet. Two parameters are considered. A geometric parameter is defined by:

$$\delta = \frac{\left[\frac{6}{\pi} V_B\right]^{1/3}}{D_{jet}}$$

where D_{jet} is the diameter of the gas jet which, presumably, is the same as the diameter of the orifice. Also, a Stokes number is defined as:

$$Stk(i) = \rho_p \, d_p(i)^2 \, V_{jet} \, C/\mu_g \, D_{jet}$$

$$V_{jet} = 4 \, \dot{m}_g \, / \, \pi \, \rho_g \, D_{jet}^2 \, C_v$$

where

$\dot{m}_g$ = mass flow rate of gas through the orifice

C_v = the velocity coefficient of the orifice

The efficiency with which a particle of size $d_p(i)$ is captured is a function of both Stk(i) and δ:

(1) $\epsilon(i) = 0$ for $Stk(i) \leq 0.090$

(2) for $\delta \leq 0.75$; $Stk(i) \leq 0.3364$

$$\epsilon(i) = \begin{cases} Stk(i)^{1/2} - 0.3 & \text{for } Stk(i) \leq 0.16 \\ 16(Stk(i))^{1/2} - 6.3 & \text{for } 0.16 < Stk(i) \leq 0.2025 \\ 0.7(Stk(i))^{1/2} + 0.59 & \text{for } 0.2025 < Stk(i) \leq 0.3025 \\ 0.98 & \text{for } 0.3025 < Stk(i) \leq 0.3364 \end{cases}$$

$0.75 < \delta \leq 1.5$

$$\epsilon(i) = \begin{cases} 0 & \text{for } Stk(i) \leq 0.1024 \\ 1.25 \, (Stk(i))^{1/2} - 0.4 & \text{for } 0.1024 < Stk(i) \leq 0.16 \\ 8(Stk(i))^{1/2} - 3.1 & \text{for } 0.16 < Stk(i) \leq 0.25 \\ 1.6(Stk(i))^{1/2} + 0.1 & \text{for } 0.25 < Stk(i) \leq 0.3025 \\ 0.98 & \text{for } 0.3025 < Stk(i) \leq 0.3364 \end{cases}$$

$1.5 < \delta \leq 4$

$$\epsilon(i) = \begin{cases} 0 & \text{for Stk(i)} \leq 0.1296 \\ 1.43\ (\text{Stk(i)})^{1/2} - 0.51 & \text{for } 0.1296 < \text{Stk(i)} \leq 0.1849 \\ 11.43(\text{Stk(i)})^{1/2} - 4.81 & \text{for } 0.1849 < \text{Stk(i)} \leq 0.25 \\ 1.6(\text{Stk(i)})^{1/2} + 0.1 & \text{for } 0.25 < \text{Stk(i)} \leq 0.3025 \\ 0.98 & \text{for } 0.3025 < \text{Stk(i)} \leq 0.3364 \end{cases}$$

$\delta > 4$

$$\epsilon(i) = \begin{cases} 0 & \text{for Stk(i)} \leq 0.1296 \\ 1.67(\text{Stk(i)})^{1/2} - 0.6 & \text{for } 0.1296 \leq \text{Stk(i)} \leq 0.2025 \\ 9.38(\text{Stk(i)})^{1/2} - 4.07 & \text{for } 0.2025 < \text{Stk(i)} \leq 0.2809 \\ 1.6(\text{Stk(i)})^{1/2} + 0.05 & \text{for } 0.2809 \leq \text{Stk(i)} \leq 0.3364 \end{cases}$$

(3) $\epsilon(i) = 0.98$ for Stk(i) > 0.3364

The numerous linear expressions are simply the results of attempts to fit the classic "S"-shaped curve of impaction efficiency as a function of the square root of the Stokes number for various orifice-to-plate separation distances. Certainly, there are more succinct expressions available for the impaction efficiency. The real issue is whether impaction on a fixed, infinite wall is an appropriate approximation. A more obvious approximation is to recognize that there is a boundary layer at the bubble wall opposite the orifice. This boundary layer should have a diameter on the order of $D_b/Re^{1/6}$ [195]. Then, deposition of aerosol particles can be treated as impaction on a disk of this diameter. The Stokes number is defined to be [194]:

$$\text{Stk(i)} = Re^{1/6} \rho_p\ V_{jet}\ d_p(i)^2 C/18\ \mu_g\ \chi\ D_b$$

where $Re = D_o\ V_{jet}\ \rho_p/\mu_g$ and D_o is the diameter of the orifice. The particle collection efficiency for this approximation is compared to those for a flat plate in Figure 101. The infinite plate model predicts a transition from nearly complete capture to essentially negligible particle capture over a narrow range of particle sizes. The boundary layer disk model predicts that this transition takes place over a much broader range of particle sizes. Capture efficiencies at given jet velocities and particle sizes are lower for the disk model than the plate model.

Also shown in Figure 101 are predictions from a correlation for scrubbers suggested by Taheri and Calvert [221]:

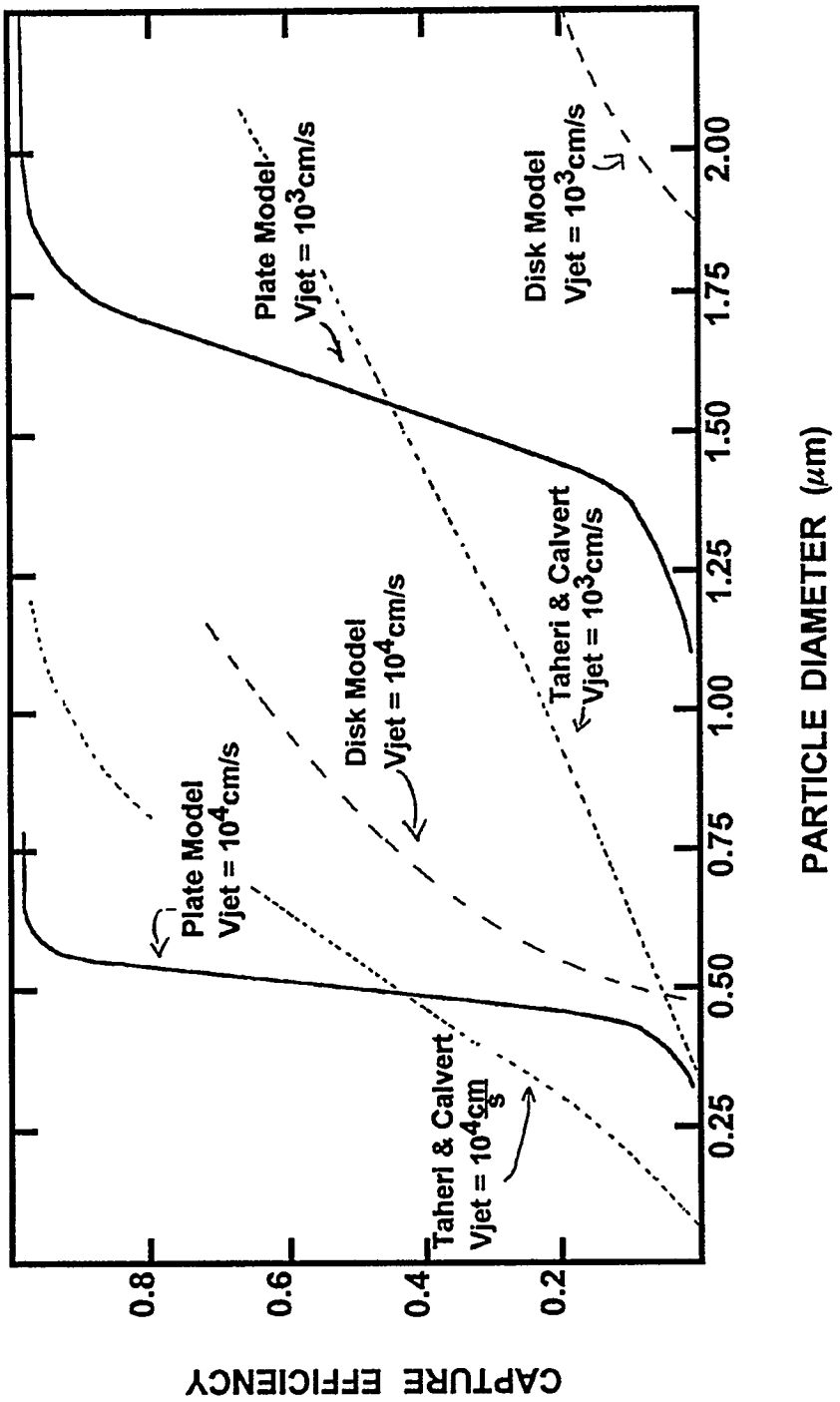

Figure 101. Comparison of various models of aerosol deposition by impaction from the orifice stream

$$\epsilon(i) = 1 - \exp[-40\ Stk(i)]$$

where

$\epsilon(i)$ = efficiency of capture of particles of diameter $d_p(i)$, and

$Stk(i) = d_p(i)^2 \rho_p V_{jet} C / 9 \mu_g D_o$

This correlation indicates an even broader size range of particle capture than the disk model. That is, the transition from very inefficient particle capture to essentially complete particle capture occurs over a larger range of particle sizes than is predicted by the plate model.

The SUPRA model describes particle capture within the forming bubble due to inertial impaction from circulating gases by:

$$DF(i) = \frac{1}{1 - \epsilon(i)} = \exp[\alpha^* t_d]$$

where

$\alpha^* = V_{jet}^2 \tau / D_b(d)$,

$\tau = \rho_p d_p(i)^2 C / 18 \mu_g$,

$D_b(d)$ = spherical equivalent bubble diameter at the time of detachment, and

t_d = time required for a bubble to grow and detach from the orifice.

Less attention has been given to the capture of aerosol particles during the convective mass transfer associated with bubble formation. Skelland and Minhas [222] suggest the mass transport coefficient, averaged over the period of bubble formation, can be obtained from:

$$k_m = \frac{0.0432}{t_f} D_B \left[\frac{V_{jet}^2}{D_B\ g}\right]^{0.089} \left[\frac{D_B^2}{t_f \bar{D}}\right]^{-0.334} \left[\frac{\mu_g}{\sqrt{\rho_g D_B \sigma_l}}\right]^{-0.601}$$

where D_B is the diameter of the bubble at the time it detaches and t_f is the time required for the bubble to grow to this size. Particle capture efficiencies calculated with this model are shown as functions of particle size in Figure 102. Very small particles (<0.1 μm) are predicted to be removed quite efficiently. Efficiency drops quite rapidly with increasing particle size because of the small diffusion coefficients of larger particles. Particle removal efficiency decreases slowly for particles larger than 0.3 μm. This slow decrease reflects particle capture during the period when the bubble was quite small. Capture efficiencies for the larger particles decrease with increasing jet velocity because the bubble grows large.

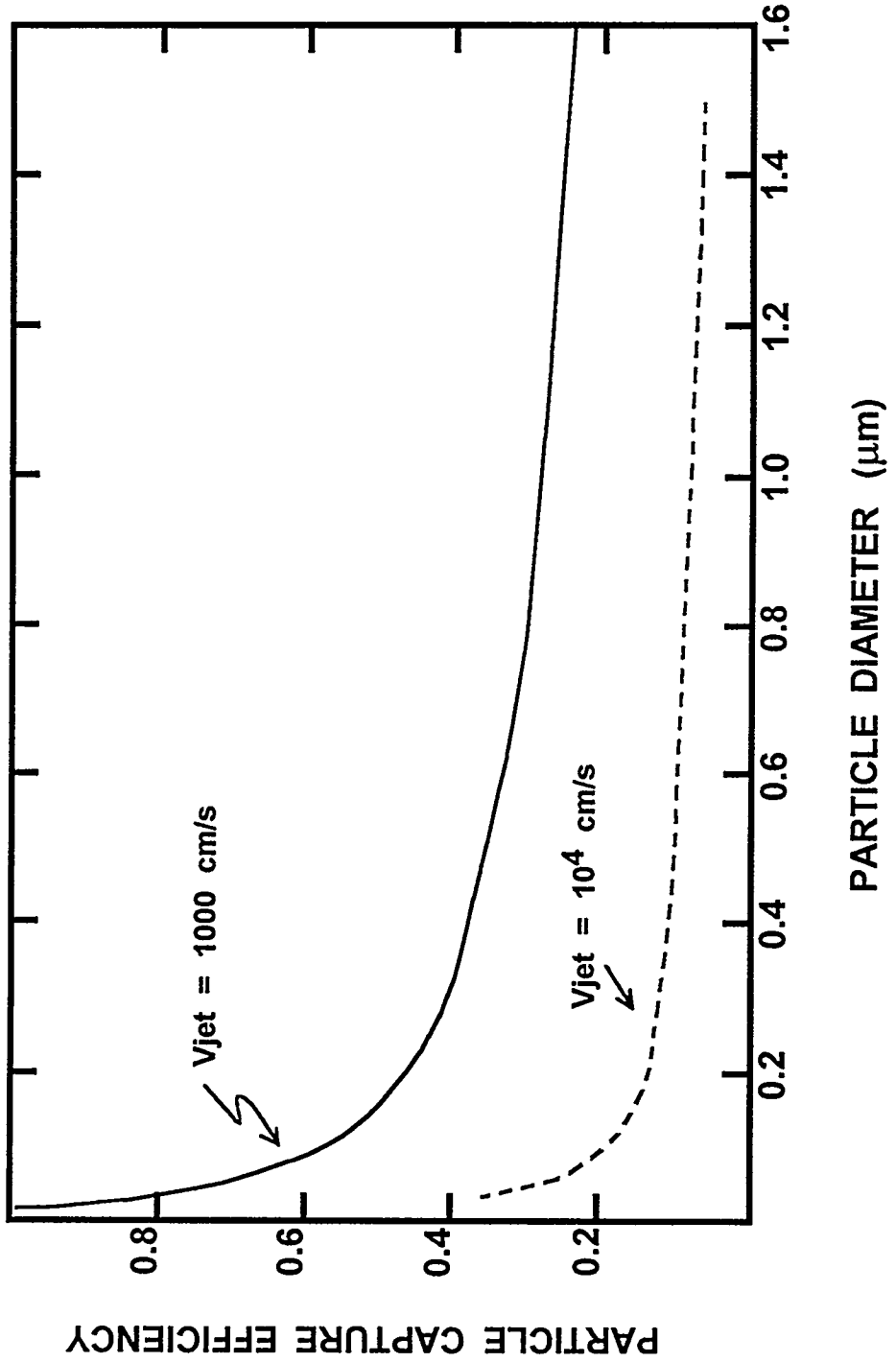

Figure 102. Particle capture by convective mass transport during bubble formation according to the mass transfer correlation developed by Skelland and Minhas. Bubble formation times and final bubble sizes were calculated using the correlation developed by Paul et al.

The SPARC 90 code [6] has a much more involved description of aerosol removal during bubble formation. This code attempts to account for impaction, diffusion, gravitational settling and the circulation of gases within the bubble. Like the SUPRA code, impaction is treated in SPARC 90 in analogy to impaction on fixed plates. The efficiency expressions are similar:

$$\ln \epsilon(i) = \begin{cases} 0.58323 + \left(5.9244 \times 10^{-3}\right)^{\xi} \ln\left(3.3437 \times 10^{-11}\right) & \text{for } 0 \le \text{Stk(i)} \le 0.811595 \\ 0.050532 + \left(4.2597 \times 10^{-3}\right)^{\xi} \ln\left(1.4173 \times 10^{-6}\right) & \text{for } 0.811595 \le \text{Stk(i)} \le 0.3365 \\ -0.01005 & \text{for Stk(i)} > 0.3365 \end{cases}$$

where

$$\xi = [\text{Stk(i)}]^{1/2}$$

Diffusion is treated by:

$$\text{DF(i)} = \exp\left[\frac{16}{3 Đ_o}\left[\frac{Đ(i)\ t_f}{\pi}\right]^{1/2}\right]$$

where

D_o = orifice diameter

$Đ(i)$ = particle diffusion coefficient

t_f = time of bubble formation

Gravitational settling is treated by:

$$\text{DF(i)} = \exp\left[\frac{A_s\ V_g(i)\ t_f}{\text{V(glob)}}\right]$$

where

$A_s = 2\ \text{V(glob)} / \pi D_o + D_o^2\ (\pi/8 - 1/6)$,

V(glob) = gas bubble volume, and

$V_g(i)$ = particle settling velocity.

Aerosol trapping by gases circulating within a bubble is treated by:

$$DF(i) = \exp[V_c(i) / \dot{R}]$$

where

$$V_c(i) = V_s^2 V_g(i) / r_c g$$

r_c = curvature of the surface of the bubble

$\dot{R}$ = growth rate of the bubble

V_s in the above expression is a complicated expression for the gas flows in a prolate ellipsoidal bubble. Bubble rise velocity appears in the expression. It is not immediately obvious how this value of the rise velocity is determined for a bubble attached to the orifice.

It is evident that there is substantial uncertainty about decontamination that occurs during bubble formation. There is no data base to clarify hypotheses about aerosol trapping during bubble formation. Considering the general difficulty that has been encountered in obtaining data on mass transport during bubble formation, it appears unlikely that a data base will soon be available to resolve the several issues that arise concerning bubble formation and the associated aerosol removal. These issues include:

- the appropriate description of the removal of large particles by inertial impaction from the input gas jet, and
- the removal of small particles by diffusion and convective mass transport to the growing bubble surface.

There are also the issues of the thermophysical state of the carrier gas and the importance of condensation or evaporation as an aerosol removal mechanism during bubble formation. If, as discussed above (Section IVA-3), the carrier gas equilibrates during transport to the pool, then condensation and evaporation processes will not be significant during bubble formation. On the other hand, aerosol removal over the period during which equilibrium is achieved may be quite significant.

V. Uncertainty in Predictions of Aerosol Removal by Steam Suppression Pools

In both Chapters III and IV uncertainties that will affect the predictions of aerosol removal by steam suppression pools have been identified and discussed. To determine the cumulative effect of these several uncertainties, a mechanistic model of aerosol removal by steam suppression pools is formulated and used in a Monte Carlo uncertainty analysis. The mechanistic model is described in the subsection immediately below.

The Monte Carlo uncertainty analysis is begun by defining parameters that describe each of the uncertainties identified above. The range of possible values each parameter can assume is defined. These ranges are defined from examination of accident analyses, experimental studies, bounding analyses or, as a last resort, engineering judgement. Subjective probability distributions for values of the parameters within their respective ranges are defined. The Monte Carlo uncertainty analysis is carried out by randomly sampling values of the parameters, according to their respective probability distributions, and using these sampled values in a calculation with the mechanistic model. Results of the calculation are accumulated and the process repeated until a satisfactorily representative sample of the distribution of results obtained with the mechanistic model has been acquired. Sampling and calculations were repeated in this work until there is a 99 percent confidence that 95 percent of the range of predictions by the mechanistic model has been sampled. Results of the many calculations are then ordered and subjected to a nonparametric statistical analysis [see Appendix A of Reference 3] to obtain estimates of the probability distributions for the predictions of aerosol removal by steam suppression pools.

A. Mechanistic Model

The essential elements of the mechanistic model of aerosol removal by steam suppression pools are shown in Figure 103. Most steps in the calculational sequence involve significant phenomenological uncertainty. The phenomenological models are outlined in later sections of this chapter in connection with the discussion of uncertainties. The mechanical features of the model are described in this subsection.

1. Input

Because the model is used in a generic uncertainty analysis that includes uncertainties in the initial and boundary conditions, the fixed input to the model is quite restricted. Only inputs that are likely to be known with some certainty are supplied. These are the depth of the suppression pool and the phase of a severe accident that is of interest. The accident phases are those defined in the revised severe accident source term [3]:

- gap release phase
- in-vessel release phase
- ex-vessel release phase
- late in-vessel release phase

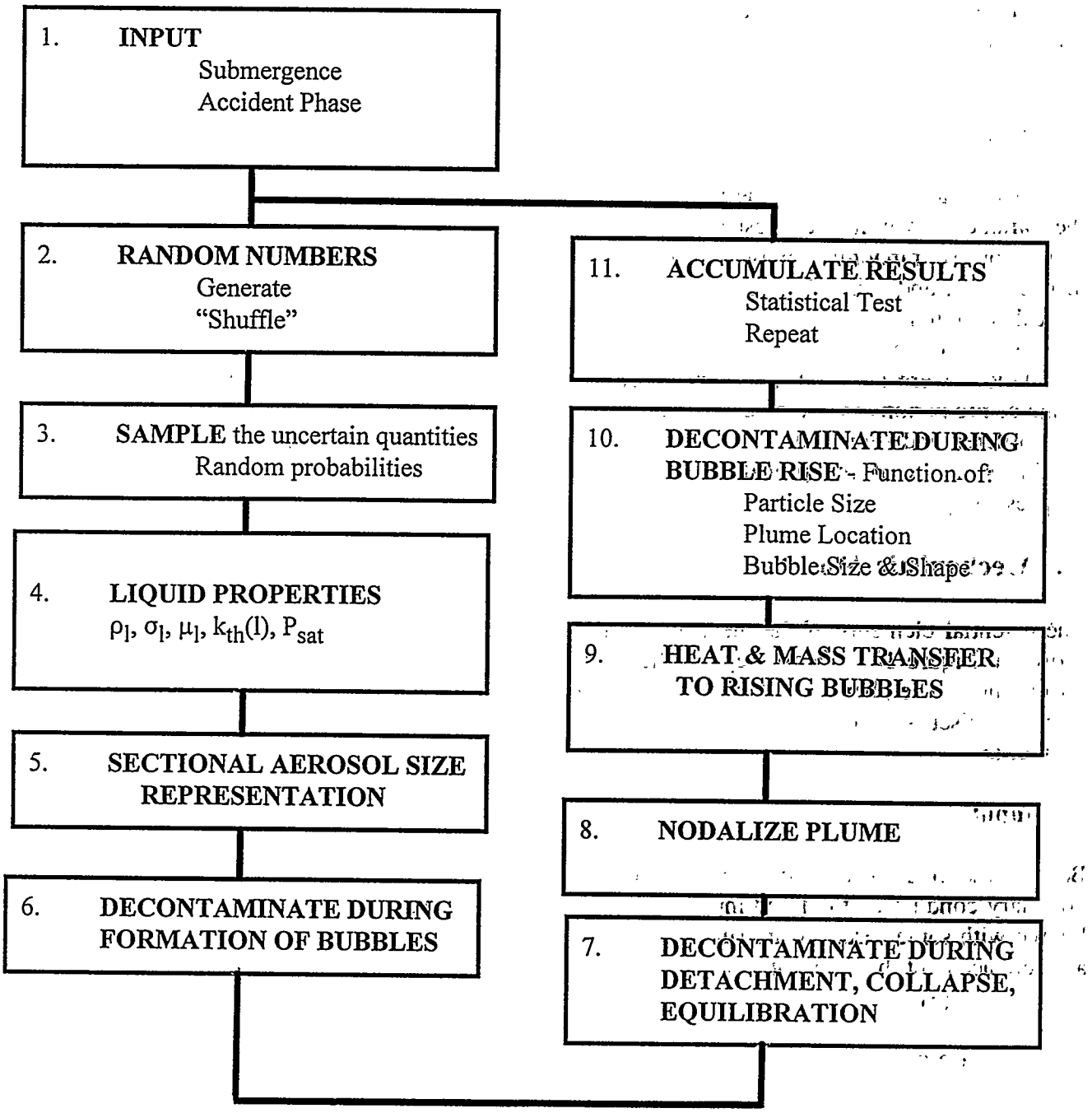

Figure 103. Essential elements of the mechanistic model of aerosol removal by steam suppression pools

Other expected inputs to such a mechanistic model of aerosol removal by suppression pools such as aerosol size distribution, gas flow rate and gas composition are uncertain quantities whose distributed values are sampled by the computer code.

2. Generation of Random Numbers

Random numbers are generated by a linear congruential random number generator. Such generators are known to produce cyclical sequences of pseudorandom numbers. To avoid this problem, the random numbers are "shuffled" using an algorithm suggested by Knuth [269]. A subtle point about linear congruential random number generators is that they can yield zero as a random number, but they can never produce exactly one as a random number. Thus, the random numbers are uniformly distributed over the range [0,1) rather than (0,1) or [0,1].

3. Sampling Uncertain Inputs and Parametric Quantities

The random numbers defined above are used to sample the various uncertain inputs and parametric quantities. As will be discussed further below, there are four types of probability density functions that can be sampled:

- uniform,
- log-uniform,
- lognormal, and
- Student's t.

These density functions are compared in Figure 104.

The random numbers are used as probabilities that the true value of some uncertain quantity is less than some critical value. Inversions of the uniform and log-uniform distributions to obtain the critical values of the uncertain quantity at a randomly selected probability are quite obvious. For uniform and log-uniform distributions over the interval [a,b], the critical value of the uncertain quantity, x, at a probability R is found from:

$$x = a + R(b - a)$$

and

$$\ln x = \ln(a) + R[\ln(b) - \ln(a)]$$

Implicit equations are used to invert the lognormal and the Student's t distributions. The critical value of a quantity with a lognormal distribution is found from:

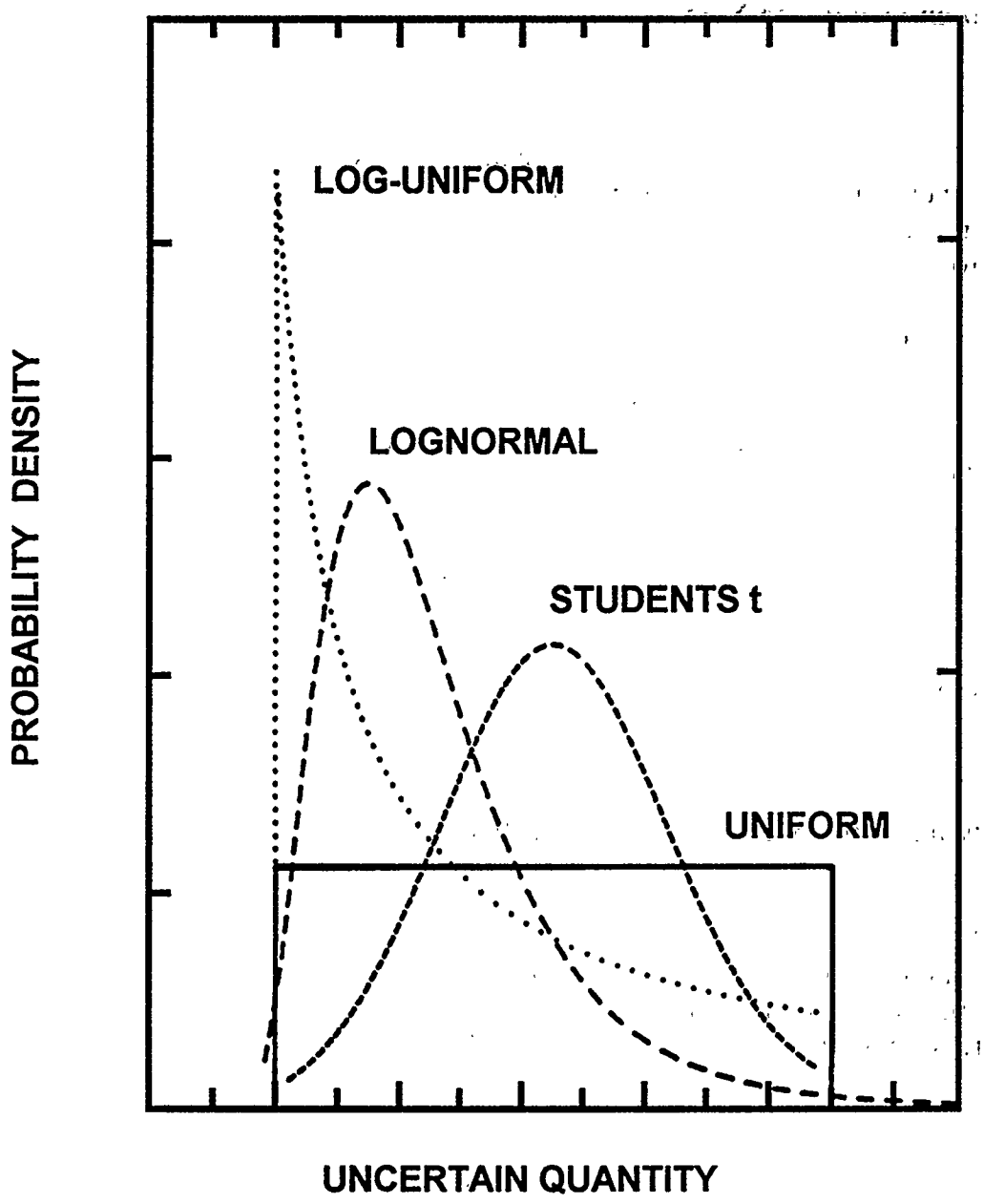

Figure 104. Comparison of uniform, log-uniform, lognormal, and Student's t probability density functions

$$R = 0.5(1 + \mathrm{erf}(z))$$

where

$z = \ln(x/\mu) / \sqrt{(2)} \ln \sigma$,

μ = mean of the distribution,

σ = geometric standard deviation, and

erf(z) is the error function of z defined by:

$$\mathrm{erf}(z) = \frac{2}{\sqrt{\pi}} \int_0^z \exp(-y^2)\, dy$$

The Student's t distribution specifies the cumulative probability that the absolute value of a quantity ξ where

$$\xi = \left| \frac{\chi - \mu}{\sqrt{\chi^2/\nu}} \right|,$$

μ = mean of the distribution,

χ^2 = chi-squared statistic, and

ν = degrees of freedom

is less than some value t. The cumulative probability is given by:

$$\Pr(\xi < t) = 1 - I_Z(A,B)$$

where

$A = \nu/2$

$B = 1/2$

$z = \nu / (\nu + t^2)$

and $I_z(A,B)$ is the incomplete Beta function:

$$I_z(A,B) = \frac{\Gamma(A)\ \Gamma(B)}{\Gamma(A+B)} \int_0^t y^{A-1}\ (1-y)^{B-1}\ dy$$

and $\Gamma(A+B)$ is the gamma function of A+B.

The inversions necessary to find critical values of $(x - \mu / \sqrt{x^2/\nu})$ in both the positive and negative domains are:

- For $R < 0.5$

  $$1 - 2R = 1 - I_z(A,B)$$

- For $R \geq 0.5$

  $$2(R - 0.5) = 1 - I_z(A,B)$$

These implicit equations are readily solved by Newton-Raphson techniques recognizing that the derivative of $1 - I_z(A,B)$ with respect to z is:

$$\frac{\Gamma(A)\ \Gamma(B)}{\Gamma(A+B)}\ z^{A-1}\ (1-z)^{B-1}$$

4. Properties of the Liquid

Thermophysical properties of the liquid are calculated using the equations described in Chapter IV for pure water. Explicit account for the effects of contamination on liquid properties is not taken. Any uncertainty in the liquid properties caused by contamination is thought to be small in comparison to other uncertainties considered here. This contrasts with the treatment of water pools overlying core debris interacting with concrete [3] where the effects of contamination on water properties were taken into account. Much of the contamination of water pools overlying core debris interacting with concrete actually comes from the action of hot water on the concrete. Water pools overlying core debris interacting with concrete become very heavily laden with dissolved and suspended materials [270] —far more so than is expected to occur in steam suppression pools. The effects of these dissolved and suspended materials on the liquid properties are then much greater than the effects of contaminants on properties of water in the suppression pool. The total aerosol mass produced during a severe reactor accident is typically about 4×10^6 grams. Suppression pools, typically, contain at least 2×10^9 grams of water. Thus, mass loadings of the suppression pool by suspended materials will be less than 0.2 percent. Molar concentrations of dissolved species would be expected to be less than 0.05 moles/kg

H_2O. Such concentrations are not expected to affect substantially the physical properties of water that are of interest here.

5. Discretization of the Aerosol Size Distribution

The size distributions of aerosols suspended in the gas flowing to a suppression pool are very uncertain. It is assumed here that the size distributions are adequately approximated by lognormal distributions with uncertain means and geometric standard deviations.

The efficiencies of the various processes that remove aerosols from the gas are quite dependent on the aerosol particle sizes. Consequently, decontamination must be calculated as a function of particle size. To do this, the aerosol particle size distribution is segmented into size classes. The size classes are chosen such that initially each class has the same mass of aerosol particles. Decontamination of the size class is calculated based on the behavior of a particle with a diameter representative of the size class.

Experience in previous studies of source term attenuation [1,2] indicates that lognormal distributions can usually be adequately represented by 20 equal-mass size classes. Thus, the boundaries of the size classes can be found from:

$$0.05 + (i - 1)\ 0.05 = 0.5\ (1 + \mathrm{erf}(z_i))$$

where

$z_i = \ln[d_p(i) / \mu] / \sqrt{(2)}\ \ln \sigma$

$d_p(i)$ = upper size limit of the i^{th} size class

μ = mean of the lognormal size distribution

σ = geometric standard deviation of the lognormal size distribution.

The upper limit of the twentieth size class is, by the definition above, infinity. For practical purposes this upper limit is defined by:

$$0.999 = 0.5\ (1 + \mathrm{erf}(z_{20}))$$

The particle diameter that is taken to be representative of the i^{th} size class is the mass mean particle size in the class given by:

$$0.025 + (i - 1)\ 0.05 = 0.5\ (1 + \mathrm{erf}(z))$$

The nondimensional particle sizes, $\ln(d_p(i) / \mu) / \sqrt{(2)}\ \ln \sigma$, that define and represent the size classes of the aerosol are listed in Table 20. Also shown in this table are dimensional particle sizes that define and represent size classes for some example particle size distributions.

Table 20. Dimensionless and example dimensional discretization of the particle size distributions

	Dimensionless*		Dimensional		
			μ = 0.25 μm, σ = 3.2		μ = 2.5 μm, σ = 3.2	
Bin #	Range (-)	Rep. size	Size range (μm)	Rep. size (μm)	Size range (μm)	Rep. size (μm)
1	-∞ to -1.163087	-1.385904	0 to 0.0369	0.0256	0 to 0.369	0.256
2	-1.163087 to -0.906194	-1.017902	0.0369 to 0.0563	0.0469	0.369 to 0.563	0.468
3	-0.906194 to -0.732869	-0.813420	0.0563 to 0.0749	0.0656	0.563 to 0.749	0.656
4	-0.732869 to -0.595116	-0.660855	0.0749 to 0.0939	0.0843	0.749 to 0.939	0.843
5	-0.595116 to -0.476936	-0.534159	0.0939 to 0.1141	0.1038	0.939 to 1.141	1.038
6	-0.476936 to -0.370807	-0.422680	0.1141 to 0.1358	0.1247	1.141 to 1.358	1.247
7	-0.370807 to -0.272463	-0.320858	0.1358 to 0.1597	0.1475	1.358 to 1.597	1.475
8	-0.272463 to -0.179144	-0.225312	0.1597 to 0.1862	0.1726	1.597 to 1.862	1.726
9	-0.179144 to -0.088856	-0.133727	0.1862 to 0.2160	0.2006	1.862 to 2.160	2.006
10	-0.088856 to 0.0	-0.044341	0.2160 to 0.2500	0.2324	2.160 to 2.500	2.324
11	0.0 to 0.088856	0.044341	0.2500 to 0.2894	0.2689	2.500 to 2.893	2.689
12	0.088856 to 0.179144	0.133727	0.2894 to 0.3357	0.3115	2.893 to 3.357	3.115
13	0.179144 to 0.272463	0.225312	0.3357 to 0.3914	0.3622	3.357 to 3.914	3.622
14	0.272463 to 0.370807	0.320858	0.3914 to 0.4601	0.4238	3.914 to 4.601	4.238
15	0.370807 to 0.476936	0.422680	0.4601 to 0.5478	0.5011	4.601 to 5.478	5.011
16	0.476936 to 0.595116	0.534159	0.5478 to 0.6654	0.6019	5.478 to 6.654	6.019
17	0.595116 to 0.732869	0.660855	0.6654 to 0.8346	0.7414	6.654 to 8.346	7.414
18	0.732869 to 0.906194	0.813420	0.8346 to 1.110	0.9529	8.346 to 11.100	9.529
19	0.906194 to 1.163087	1.017902	1.110 to 1.694	1.334	11.100 to 16.937	13.339
20	1.163087 to 2.185124	1.385904	1.694 to 9.098	2.444	16.937 to 90.985	24.435

*$(\ln d_p/\mu) / \sqrt{(2)} \ln \sigma$

6. Formation of Bubbles and Decontamination During Bubble Formation

The model of bubble formation is selected depending on the accident phase. Aerosol laden gases during the gap release and in-vessel release are assumed to always go through the quenchers. This is not universally true, but seems to be the case for frequency-dominant accidents discussed in Chapter III. Aerosol-laden gases produced in the ex-vessel and the late in-vessel phases of an accident, of course, are discharged to the suppression pool through large diameter vents and downcomers.

Decontamination of the gas by inertial impaction from the gas jet and diffusion are poorly understood. In the authors' opinions, these are very important processes that have received insufficient study. They are treated in the model by uncertain, size-dependent collection efficiencies. There will, of course, be some aerosol removal as a result of steam condensation during bubble formation. This removal is neglected in the model used for uncertainty analysis. All of the effects of steam condensation during bubble formation, detachment from the orifice, collapse and equilibration with the steam suppression pool are calculated in the model of decontamination during the equilibration of the bubble with the pool.

7. Detachment and Equilibration of the Bubble

The events that take place immediately after a bubble detaches from an orifice or vent are very complicated. A mechanistic treatment of these processes is not attempted. Rather, it is assumed that over a distance between 2 and 10 times the initial bubble diameter, the bubble disintegrates to a stable size and that it comes into equilibrium with the pool at the local conditions of pressure and the bulk pool temperature. Collapse and disintegration of the bubble are not thought to cause any significant decontamination. Condensation of some fraction of the gas as the bubbles equilibrate with the pool is assumed to remove a proportionate amount of the aerosol independent of particle size.

8. Plume Formation

The modified Milgram model described in Chapter IV with many of the parameters taken to be uncertain is used to predict the behavior of bubble swarms. Each arm of a quencher is taken as a plume source. Also, each downcomer is treated as a plume source. The plume model indicates that the rise velocities of bubbles, and in some cases the slip velocities, vary both axially and radially. The rise velocities dictate, of course, how long the rising bubbles are exposed to the actions of the suppression pool. The slip velocities enter into the analyses of aerosol capture. Decontamination of bubbles should then depend on radial location within the plume.

The plume geometry and properties are calculated using a fourth order Runge-Kutta differential equation solver with an adaptive step-size controller configured to control errors to 1 part in 10^4. This same differential equation solver is also used to calculate mass transfer to the bubbles.

At each axial location, the plume is nodalized in the radial direction so that there is a constant fraction of the gas flux through each ring node. That is, the total gas flux is given by:

$$Q(z) = \int_0^\infty \left[U_l(r,z) + U_{slip}(r,z)\right] \epsilon(r,z)\, 2\pi r\, dr$$

where

$U_l(r,z)$ = liquid velocity at radial location r and axial location z =

$= U_l(z) \exp [-r^2 / b(z)^2]$

$U_{slip}(r,z) = F(\epsilon)U_B$

U_B = rise velocity of an isolated bubble,

$\epsilon(r,z) = \epsilon(z) \exp [-r^2 / \lambda^2 b(z)^2]$

$$F(\epsilon) = \begin{cases} 1 \\ 1 - \epsilon(r,z) \\ \text{or} \\ [1 - \epsilon(r,z)]^2 \end{cases}$$

Nodes are defined by the bounding radial coordinates R(i-1) and R(i) for i = 1 to N such that:

$$\frac{Q(z)}{N} = \int_{R(i-1)}^{R(i)} [U_l(r,z) + U_{slip}(r,z)]\, \epsilon(r,z)\, 2\pi r dr$$

The N^{th} radial coordinate is, however, taken to be such that:

$$\frac{Q(z)}{N} - 0.001 = \int_{R(N-1)}^{R(N)} [U_l(r,z) + U_{slip}(r,z)]\, \epsilon(r,z)\, 2\pi r dr$$

An example nodalization for $U_{slip} = U_B (1 - \epsilon(r,z))^2$ at three elevations are listed in Table 21. Some numerical tests showed that, for the purposes of the uncertainty analysis, 5 radial nodes at each axial level was sufficient to characterize the plume.

Rise and slip velocities were taken to be the averages of these quantities across the node. These averages are:

Table 21. Example nodalizations of a plume

	for z = 60 cm			for z = 200 cm			for z = 305 cm		
Node #	R(i) (cm)	$<U_{Rise}>$ (cm/s)	$<U_{slip}>$ (cm/s)	R(i) (cm)	$<U_{Rise}>$ (cm/s)	$<U_{slip}>$ (cm/s)	R(i) (cm)	$<U_{Rise}>$ (cm/s)	$<U_{slip}>$ (cm/s)
1	1.706	141.0	7.19	5.721	116.1	22.02	8.405	108.1	23.14
2	2.483	133.2	8.55	8.324	109.9	22.28	12.231	102.4	23.29
3	3.138	125.0	10.02	10.524	103.4	22.56	15.463	96.4	23.44
4	3.756	116.5	11.60	12.594	96.6	22.83	18.505	90.2	23.59
5	4.375	107.5	13.31	14.670	89.3	23.10	21.556	83.6	23.74
6	5.029	97.9	15.14	16.867	81.6	23.38	24.783	76.4	23.89
7	5.765	87.4	17.08	19.334	73.1	23.66	28.408	68.7	24.04
8	6.664	75.6	19.15	22.353	63.6	23.94	32.845	60.0	24.20
9	7.970	61.3	21.38	26.734	52.3	24.23	39.284	49.0	24.35
10	14.967	32.6	24.31	45.959	31.9	24.58	67.725	31.1	24.54

$$\text{Average Rise Velocity} = \langle U_{Rise} \rangle = \frac{1}{\pi[R(i)^2 - R(i-1)^2]} \int_{R(i-1)}^{R(i)} [U_l(r,z) + U_{slip}] 2\pi r \, dr$$

$$\text{Average Slip Velocity} = \langle U_{slip} \rangle = \frac{1}{\pi[R(i)^2 - R(i-1)^2]} \int_{R(i-1)}^{R(i)} U_{slip} 2\pi r \, dr$$

The average liquid rise velocity is

$$\langle U_{liq} \rangle = b^2 U(z) \left\{ \exp\left[\frac{-R(i-1)^2}{b^2}\right] - \exp\left[\frac{-R(i)^2}{b^2}\right] \right\} \Big/ (r(i)^2 - R(i-1)^2)$$

Then, the average bubble rise velocity is:

$$\langle U_{Rise} \rangle = \langle U_{liq} \rangle + \langle U_{slip} \rangle$$

where

$$\langle U_{slip} \rangle = U_B \qquad \text{for } U_{slip}(r,z) = U_B$$

$$\langle U_{slip} \rangle = U_B \left[1 - \frac{\lambda^2 b^2 \epsilon(z)}{R(i)^2 - R(i-1)^2} \left\{ \exp\left[\frac{-R(i-1)^2}{\lambda^2 b^2}\right] - \exp\left[\frac{-R(i)^2}{\lambda^2 b^2}\right] \right\} \right]$$

$$\text{for } U_{slip}(r,z) = U_B(1 - \epsilon(r,z))$$

$$<U_{slip}> = U_B \left[1 - \frac{2\lambda^2 b^2 \epsilon(z)}{R(i)^2 - R(i-1)^2} \left\{ \exp\left[\frac{-R(i-1)^2}{\lambda^2 b^2}\right] - \exp\left[\frac{-R(i)^2}{\lambda^2 b^2}\right] \right\} \right.$$

$$\left. + \frac{\epsilon(z)^2 \lambda^2 b^2}{R(i)^2 - R(i-1)^2} \left\{ \exp\left[\frac{-2R(i-1)^2}{\lambda^2 b^2}\right] - \exp\left[\frac{-2R(i)^2}{\lambda^2 b^2}\right] \right\} \right]$$

$$\text{for } U_{slip}(r,z) = U_B(1 - \epsilon(r,z))^2$$

These average quantities for the example nodalizations are also listed in Table 21.

Note that nodalizations are fixed at the start of each spatial step and not altered in the Runge-Kutta calculations for the step.

9. Mass Transfer to the Bubble

Mass transfer to the bubble were calculated using the thermodynamic model described in Chapter IV (See Section IV-D). Heat transfer to and within the bubble was taken to be rapid. Numerical tests showed that thermal gradients were likely to be small enough that thermophoresis of aerosol particles could be neglected in comparison to diffusiophoresis.

10. Decontamination During Bubble Rise

Decontamination of bubbles in each of the 5 nodes is calculated for each of the 20 size classes. These results are summed to determine on overall decontamination factor. A mass-weighted mean particle size is calculated from:

$$<\ln d_p> = \frac{\sum_{i=1}^{20} \sum_{j=1}^{5} M(i,j) \ln d_p(i)}{\sum_{i=1}^{20} \sum_{j=1}^{5} M(i,j)}$$

where M(i,j) is the aerosol mass of size class i remaining in node j. A standard deviation of the size distribution of aerosol particles emerging from the suppression pool is calculated using the expression:

$$\ln^2 \sigma = \frac{\sum_{i=1}^{20} \sum_{j=1}^{5} M(i,j) \left[\ln(d_p(i)) - \langle \ln d_p \rangle\right]^2}{\sum_{i=1}^{20} \sum_{j=1}^{5} M(i,j)}$$

11. Accumulation of Results

The overall decontamination factor and the characteristics of the particle size distribution were accumulated for subsequent statistical analyses. Results are accumulated until there was at least a 99 percent confidence that 95 percent of the range of these output quantities had been sampled. The accumulated samples were ordered and used to uncertainty distributions at 50 and 90 percent confidence levels as described elsewhere [1].

B. Uncertain Models, Inputs and Parametric Quantities

Uncertainties that affect the predictions of aerosol removal by steam suppression pools include uncertainties in the boundary and initial conditions dictated by accident progression, uncertainties in the aerosol properties, and uncertainties in phenomena and processes. Many of these uncertainties are readily expressed in terms of parameters that can assume ranges of values. Probability distributions can be hypothesized to describe the distributions of the values of these parametric quantities within these ranges.

Especially in connection with the phenomena and processes responsible for the removal of aerosols from gases sparging through a steam suppression pool, there is another type of uncertainty. This is uncertainty in the physical model used to describe the process or phenomenon. It is not obvious how this type of uncertainty can be reduced to a parametric quantity with a range of values and a distribution of values within this range that can be sampled in the Monte Carlo uncertainty analysis. Yet, such model uncertainty is very important to the overall uncertainty in predicting the decontamination that can be achieved by a steam suppression pool. Thus, model uncertainty cannot be neglected in the Monte Carlo uncertainty analysis.

Reduction of model uncertainty to a parametric quantity is done here in two ways. Consider two models that purport to describe the same phenomenon. The prediction of the first model is designated $\pi(A)$. The prediction of the second model is designated $\pi(B)$. If the models are quite distinct, say because they invoke different physics to describe the phenomenon, a parameter, δ, is defined to be uniformly distributed over the range from zero to one. The quantity used in the mechanistic model, π, is then derived from the two models by:

$$\pi = \begin{cases} \pi(A) & \text{if } \delta < 0.5 \\ \pi(B) & \text{if } \delta \geq 0.5 \end{cases}$$

On the other hand, the two models might be quite similar. They may differ only by different parameterization of a correlation for some set of data. Then, a parameter ϵ is defined to be uniformly distributed over the range of 0 to 1. The quantity used in the mechanistic model is then found from the two alternative models from:

$$\pi = \epsilon\pi(A) + (1 - \epsilon)\ \pi(B)$$

These two procedures for reducing model uncertainty to a parametric quantity are easily extended to situations involving more than two alternative models.

In the subsections below, the various parametric quantities sampled in the Monte Carlo uncertainty analysis including parameters used to represent model uncertainty are described. The emphases of the discussions are to justify credible ranges for the values of these parameters and to define subjective probability distributions for values of parameters within their respective ranges.

The authors are unaware of any algorithm for the definition of subjective probability distributions for uncertain quantities within justifiable ranges. The authors are aware that some investigators [271,272] develop fairly elaborate distributions for uncertain quantities. The very limited justifications offered for these complicated distributions do not appear persuasive to the authors. Based on criticisms levelled at these complicated distributions, it appears others in the technical community are also skeptical.

Here, simple, high-entropy probability distributions are ascribed to parametric values according to a set of rules. These rules are:

1. Values predicted by correlations derived from least-squares fits of experimental data are taken to be distributed according to a Student's t distribution.

2. Uncertain quantities whose meaningful range of values spans less than an order of magnitude are assigned a uniform distribution.

3. Uncertain quantities whose meaningful range spans more than one order of magnitude are assigned a log-uniform distribution.

4. If there is a substantial basis to believe values of a parameter are better known than would be reflected by the uniform or log-uniform distributions, this parameter is assigned a lognormal distribution.

High-entropy distributions such as the Student's t distribution, the uniform distribution, and the lognormal distribution have been adopted primarily because the authors believe there is very little

knowledge about the parameter values within their respective ranges. It is more defensible to further decompose an issue into more fundamental parts than to attempt to define some highly structured probability distribution for a parameter. There is, however, another advantage associated with the use of high-entropy distributions. By restricting the distributions that can be assigned to values of a parameter to high-entropy distributions, the results of the uncertainty analyses are not very sensitive to the particular distributions assigned to the parameters. This relieves a question concerning the sensitivity of results to the parameter distributions that nags all probabilistic uncertainty analyses. Relief from this question comes about because of the peculiar similarities of high-entropy distributions in the vicinities of the tails of the distributions. For nearly all of the high entropy distributions:*

$$x(5) = \mu - 1.6(\pm 0.05)\,\sigma$$

$$x(95) = \mu + 1.6(\pm 0.05)\,\sigma$$

where

$x(5)$ = 5th percentile value of the uncertain quantity x,

$x(95)$ = 95th percentile value of the uncertain quantity x,

μ = mean of the distribution, and

σ = standard deviation of the distribution.

Since the ranges assigned to values of a parameter essentially fix both the mean and the standard deviation of the distribution, all of the distributions become rather similar. This is especially true near the "tails" of the distributions. The tails of distributions in the vicinities of the 5 and 95 percentiles are often of great interest in analyses of reactor safety issues because parametric values in these tail regions can produce the hazardous circumstances of accidents. It is usually the sensitivity of results to tails of parameter distributions that cause the greatest controversies when complicated, structured distributions are employed. Though there can still be some legitimate concern about the tails of distributions when high-entropy distributions are employed, this concern is much attenuated relative to the situation when other types of subjective distributions are used.

1. Input and Boundary Condition Uncertainties

The first class of uncertainties to be described are those that arise because of

- the variability in the designs of boiling water reactors, and
- the variability of conditions that prevail during the various types of severe accidents hypothesized to occur at boiling water reactors.

*The authors were made aware of this interesting property of high-entropy distributions by A. N. Roumiantsev of the Kurchatov Institute in Moscow, Russia.

In the subsections below, ranges are defined and probability distributions are assigned to uncertainties of these types.

Discussions in Chapter III show that conditions vary so significantly over the four phases of severe accidents that it is useful to draw distinctions among the uncertainties that prevail during these accident phases. Therefore in the discussions of many of the uncertainties in the subsections below, distinct ranges are identified for the gap release phase, the in-vessel phase, the ex-vessel phase and the late in-vessel phase of an accident.

It is also found that especially for the ex-vessel phase of an accident that it is useful to distinguish between Mark I boiling water reactors and other types of boiling water reactors. Such a distinction is also useful during the gap and in-vessel release phases of an accident because the submergence of quenchers in the suppression pools are so different in Mark I reactors than in other types of boiling water reactors.

The various uncertainties discussed in the subsections below are summarized in Table 22. Also shown in this table are the ranges and the probability distribution functions ascribed to these uncertainties.

a. Pool Depths

The submergence of the orifices and vents in the suppression pools are assumed to be known by the analyst. Calculations are done for submergences of 100 to 700 cm. The submergence depth is used to correlate results of the uncertainty analyses to formulate simplified models are described in Chapter VII.

b. Orifice Sizes

Orifices in quenchers are taken to have diameters uniformly distributed over the range from 0.993 to 1.27 cm. The number of orifices was fixed at 19056 which is characteristic of Mark I suppression pools. Mark II and Mark III suppression pools have between 17952 and 23936 quenchers orifices. This range is small in comparison to the range of volumetric flows to the orifices. Consequently, it was assumed that the uncertainty in the flow through an orifice would be dominated by the uncertainty in the gas source and not very sensitive to the uncertainty concerning the number of orifices.

Downcomers vents were taken to have diameters between 59.7 to 69.8 cm. In Mark I and Mark II suppression pools there are between 82 to 136 downcomers. It was assumed, however, that at the low gas generation rates typical of the ex-vessel phase and late in-vessel phase of reactor accidents, there would not be simultaneous flow through all these downcomers.

c. Wetwell Pressures

Boiling water reactors are susceptible to ATWS type sequences that cause pressurization of the drywells and wetwells even before gap release can begin. They are also subject to station blackout accidents in which pressure builds up, in some cases to failure, over the course of the accident. Consequently, the ranges of gas pressures that can exist over the suppression pools are the same for all phases of the accidents. This range is essentially from 1 atmosphere to the failure pressure.

Table 22. Input uncertainties

Uncertainty		Range	Distribution
a.	**Pool depth**	known quantity	
b-1.	**Orifice diameter (cm)**		
	gap release	0.993 to 1.27	uniform
	in-vessel release	0.993 to 1.27	uniform
	ex-vessel release	59.7 to 69.8	uniform
	late in-vessel release	59.7 to 69.8	uniform
b-2.	**Number of Orifices**		
	gap release	19056	fixed
	in-vessel release	19056	fixed
	ex-vessel release	82 - 136	uniform
	late in-vessel release	82 - 136	uniform
c.	**Wetwell pressure (atms)**		
	gap release	1.1 - 9	uniform
	in-vessel release	1.1 - 9	uniform
	ex-vessel release	1.1 - 9	uniform
	late in-vessel release	1.1 - 9	uniform
	Mark II and III		
	gap release	1 - 5	uniform
	in-vessel release	1 - 5	uniform
	ex-vessel release	1 - 5	uniform
	late in-vessel release	1 - 5	uniform
d-1.	**Mean aerosol particle diameter (μm)**		
	gap	$\mu^{-3} = -366 + 0.958\ Q$	correlated with flow
	in-vessel	0.5 to 5.0	lognormal (μ=1.6, σ=2)
	ex-vessel	1.1 to 7.0	uniform
	late in-vessel	0.19 to 3.0	log uniform
d-2.	**Geometric standard deviation of aerosol size distribution**		
	gap	1.2 to 1.8	uniform
	in-vessel	1.8 to 3.8	uniform
	ex-vessel	1.6 to 3.8	uniform
	late in-vessel	1.6 to 3.8	uniform

Table 22. Input uncertainties (concluded)

Uncertainty	Range	Distribution
e. Aerosol material density		
gap	2.8 to 6.1	uniform
in-vessel	3.25 to 10.96	uniform
ex-vessel	2.9 to 5.65	uniform
late in-vessel	3.15 to 2.65	uniform
f. Shape factors		
• primary particle diameter	0.001 to 0.1	log-uniform
• fractal dimension	1.5 to 2.2	uniform
g. Steam Production Rates (moles/s)		
gap		
in-vessel	2500 to 400	uniform
ex-vessel	500 to 50	uniform
Mark I	1 to 10%	uniform
Mark II/III	of total gas correlated with gas production	-
$\epsilon(x)$	0-1	uniform
late-invessel		
Mark I	10 to 35% of total gas	Uniform
Mark II/III	correlated with gas production	-
$\epsilon(y)$	0-1	uniform
h. Hydrogen Production (moles/s)		
gap	20 to 120	uniform
in-vessel	20 to 120	uniform
i. Total Gas Production (moles/s)		
ex-vessel		
Mark I	100 to 300	uniform
Mark II/III	150 to 1100	uniform
late-invessel		
Mark I	20 to 80	uniform
Mark II/III	160 to 500	uniform

There are radical differences in the failure pressures predicted for the various types of boiling water reactors. The Mark I steel containments have been calculated to rupture at differential pressures up to 8 atmospheres. Mark III containments are not as strong and are thought to rupture at differential pressures of about 4 atmospheres. Consequently, a distinction is drawn here between the range of wetwell pressures in Mark I containments and the range of wetwell pressures in the Mark II and Mark III containments. Wetwell pressures in the Mark I are considered to be uniformly distributed over the range of 1.1 to 9 atmospheres. Wetwell pressures in the Mark II and Mark III reactors are taken to be uniformly distributed over the range of 1 to 5 atmospheres. Again, the ranges of wetwell pressures are taken to be the same for all phases of severe accidents.

d. Aerosol Particle Size

It is assumed for this work that aerosols reaching the steam suppression pool have a lognormal size distribution. Discussions above show that this can only be an approximation. The uncertainty in this approximation is, however, confronted only through the uncertainties in the parameters that characterize a lognormal distribution—the mean particle size and the geometric standard deviation of the distribution. That is, the Monte Carlo uncertainty analyses done here do not consider size distributions that differ from the lognormal distribution. This is probably not a serious omission. It is quite likely that all aerosols that reach the suppression pool have aged sufficiently long that coagulation and deposition processes have eliminated any features of the distribution that deviate much from lognormal such as bimodality in the distribution. The most likely discrepancy from an exactly lognormal distribution is probably a lack of aerosol mass at the larger, low-probability sizes.

The size distributions of aerosol reaching the steam suppression pool are expected to be different in the four phases of the severe reactor accident defined in the U.S. Nuclear Regulatory Commission's revised severe accident source term [1]. The aerosol size distributions are, however, not expected to vary according to the type of boiling water reactor of interest.

d-1. Gap Release Size Distribution

Only small amounts of aerosol mass are introduced into large gas flows during the gap release phase of the accident. There will be little opportunity for such dilute aerosol particles to grow. Any particles that do coagulate or grow to a substantial size are very likely to be removed from the high velocity flow stream by impaction in bends and flow discontinuities in the pathway to the steam suppression pool. For these reasons, aerosol reaching the steam suppression pool is expected to have a size distribution with a small mean particle size and a small geometric standard deviation.

For all of the interest that has been paid to gap release, there is remarkably little experimental data on particle size distributions to validate these theoretical predictions. Further, there has been little published information on particle sizes predicted by analysis. Jordan et al. [273] have argued that aerosol particles nucleate from vapors such as those released from the fuel cladding gap to rapidly form particles 0.05 μm in diameter. If it is further assumed that particle concentrations are quickly reduced to 10^8 particles/cm^3 by coagulation. Then, final, mean particle sizes during gap release would be expected to range from 0.05 to 0.25 μm. These estimates seem consistent with results of calculations with the Source Term Code Package reported by Gieseke et al. [27] for a station blackout accident at a Mark III boiling water reactor.

The analysis presented above suggests that the mean particle size will be correlated closely with the molar flow. Here, this correlation is take to be:

$$\mu^{-3} = -1448 + 3.78\ Q$$

where

μ = mean particle size in μm, and

Q = flow through the reactor coolant system in moles/s.

The material released from the fuel cladding gap may be rich in CsOH and CsI. These are two very hygroscopic materials. Though particles of CsOH and CsI may not grow by water adsorption in the reactor coolant system itself, they will surely grow as the aerosol-laden gas cools within the piping system leading to the suppression pool. Adsorption of water might be expected to continue until the particles become saturated liquids. Then, particle sizes are given by the correlation:

$$\mu^{-3} = -366 + 0.958\ Q\ (\text{moles/s})$$

which is the correlation adopted here.

The geometric standard deviation of the size distribution is much more difficult to predict. It depends, among other things, on the heterogeneity of processes taking place during the release and transport of the aerosol. It is expected here that the size distributions will be narrow. Geometric standard deviations observed in flame vaporization processes are as low as 1.2 [274]. Consequently, the geometric standard deviation for aerosol produced during gap release is taken to be uniformly distributed over the range from 1.2 to 1.8. The upper end of this range has been selected because for larger values of the geometric standard deviation, the aerosol would have a noticeable spread in particle sizes.

d-2. In-Vessel Release Size Distributions

In contrast to the case during the gap release phase of the accident, a very large amount of material is aerosolized during the in-vessel release phase of the accident. Most of this aerosol mass will be non-radioactive. A great amount of aerosol will come from vaporization of steel, tin from the zircaloy cladding, and vaporization of UO_2. Radioactive species will constitute a relatively small portion of the total aerosol release. The aerosol that reaches the suppression pool will have a size distribution dictated by the interplay of particle growth and particle deposition processes.

There has not been much information published on the sizes of particles that are predicted to be released to the suppression pool during the in-vessel phase of an accident. Denning et al. [23] report, for an ATWS accident sequence, mean particle sizes of about 13 μm at the suppression pool. On the other hand, another analysis [296] of the aerosol suddenly released to the drywell of a boiling water reactor at the time of vessel failure indicates a nearly lognormal size distribution with a mean particle diameter of 0.8 μm. Distributions shown in Figure 13 similarly indicate a very broad uncertainty in the size distributions of aerosols produced during the in-vessel release phase. Not all of the analyses that produce the widely ranging size distributions have considered in detail opportunities for particle deposition during transport to the suppression pool. The deposition processes are often quite dependent

on the aerosol particle size and tend to preferentially extract particles larger than 1 to 2 μm. Based on this reasoning, the mean aerosol particle size during the in-vessel phase of an accident is taken to be lognormally distributed around 1.6 μm with a geometric standard deviation for the distribution of the mean taken to be 2. Then, the 5 and 95 percentiles for the mean are at about 0.5 and 5.0 μm, respectively.

The geometric standard deviation of the aerosol size distribution is expected to be large. Here it is assumed to be uniformly distributed over the range of 1.8 to 3.8.

d-3. Ex-Vessel Release Size Distributions

Considerably attention has been paid to the size distribution of aerosols produced during core debris interactions with concrete. During the vigorous phase of interactions when most of the release of radionuclides occurs, predictions derived from correlations of experimental data indicate that mean particle sizes are between 1.1 and 2.2 μm. These predictions apply, however, to the aerosol immediately above the core debris and not to the aerosol that enters the suppression pool. Aerosol that is produced by core debris interactions with concrete mixes with the drywell atmosphere and has an opportunity to age. That is, the aerosol will coagulate to larger particle sizes before it passes to the suppression pool. Again, notice should be taken of the wide range of aerosol particle sizes predicted by the Source Term Code Package to be present in the drywell (See Figure 13).

Because of the aging of aerosol in the drywell, the mean particle size of aerosol produced by core debris concrete interactions is taken to be the lower bound on the mean size of aerosol discharged to the suppression pool during the ex-vessel release phase of a severe accident. The upper limit on this mean size is taken to be 7.0 μm based on accident calculations with the Source Term Code Package [14].

The geometric standard deviation of the aerosol size distribution is, because of the mixing and flow in the drywell, expected to be large. Experimental studies of aerosols produced during core debris interactions with concrete have shown geometric standard deviations that vary from about 1.6 to 3.8. Aerosol discharged to the suppression pool will probably have a similarly large range of geometric standard deviations in its size distributions.

Aerosol produced during intense core debris interactions with concrete is expected to be chemically stable and not very hygroscopic. Certainly this is what Adams [248] found when he produced aerosols from concrete and introduced them into a condensing steam atmosphere. Little particle growth by water condensation on the external surfaces of the particles is to be expected. (Internal voids are expected to be filled with water when the aerosol reaches the suppression pool as discussed above in Section IV-K.1).

d-4. Late In-Vessel Release Size Distributions

Almost nothing is known about the release by revaporization of radioactive materials that had been deposited in the reactor coolant system during earlier phases of the accident. The material released from the reactor coolant system will be relatively volatile. Cesium iodide, cesium hydroxide and tellurium oxides are expected to be important constituents of the released material. The late in-vessel release is expected to be slow so that aerosol concentrations will be correspondingly low. Particle sizes might also, then, be small.

When aerosol (or vapors) produced by the late in-vessel release emerge into the reactor drywell, they will encounter aerosols produced by the long-term core debris interactions with concrete. After the initial, intense aerosol production marking the ex-vessel release phase of the accident, core debris/concrete interactions settle into a quasi-steady state interaction that produces aerosols mostly from constituents of concrete at rates of 1 to 10 grams per second. Though these are small rates of aerosol production in comparison to rates of aerosol production during ex-vessel release, they are significant rates in comparison to the rates of late in-vessel aerosol production. It is likely, then, that aerosol reaching the steam suppression pool during the late in-vessel phase of the accident will have size characteristics determined by aerosols produced by the quasi-steady state core debris/concrete interactions. Model predictions of these aerosols indicate mean particle sizes of 0.19 to 0.30 μm. These predictions are based on an assumption concerning the nature of aerosol growth. This assumption has not been validated by experimental studies. These mean particle sizes do not account for growth of particles during residence in the drywell. Residence periods can be quite long during this late-stage of the accident when gas production rates are low. To account for this growth, the mean aerosol particle size during the late in-vessel phase of the accident is taken to be loguniformly distributed over the range from 0.19 to 3.0 μm.

Size distributions of aerosol produced during the late stage of core debris interactions with concrete are assumed to have geometric standard deviations of 2.3 [19]. This is an average of experimental observations that have varied from 1.6 to 3.8. Consequently, the geometric standard deviation of the size distributions of aerosol produced during the late in-vessel phase of an accident is taken to be uniformly distributed over the range from 1.6 to 3.8.

The aerosol produced in the drywell during the late in-vessel phase of an accident might be quite hygroscopic. Certainly CsOH and CsI vaporized from the reactor coolant system are hygroscopic. Aerosols produced by core debris/concrete interactions at this late stage of the accident are rich in hygroscopic oxides of sodium and potassium. On the other hand, the atmosphere will contain quite a lot of carbon dioxide that will react with oxides and hydroxides to form decidedly less hygroscopic bicarbonates.

e. Aerosol Material Density

Material densities enter into the descriptions of aerosol removal processes. The material densities are expected to vary some among the four phases of the accident.

e-1. Gap Release

Room temperature densities of the materials expected to make up much of the gap release are shown below:

Material	Density (g/cm^3)
CsI	4.510
CsOH	3.675
TeO	5.682
TeO_3	5.075 - 6.1

Cesium hydroxide and cesium iodide are so hygroscopic that they may be present as saturate solutions rather than as solid particles. These densities would be reduced substantially to 2.8 to 3.2 in saturated solutions. Consequently, the aerosol material densities during the gap release are taken to be uniformly distributed over the range 2.8 to 6.1 g/cm^3.

e-2. In-Vessel Release

Aerosol material densities during the in-vessel release will be determined primarily by the massive amounts of nonradioactive materials released during this phase of the accident. Some typical densities of these materials are:

Material	Density (g/cm^3)
UO_2	10.96
U_3O_8	8.30
UO_3	7.29
ZrO_2	5.6 - 5.89
$ZrO_2 \cdot z\,H_2O$	3.25
Sn	5.75 to 7.28
SnO	6.446
SnO_2	6.95
Fe_3O_4	5.18

Material densities during the in-vessel phase of a severe reactor accident are taken to be uniformly distributed over the range of 3.25 to 10.96.

e-3. Ex-Vessel Release

Examination of calculated results for a variety of severe accidents [25] shows that material densities during the period of intense aerosol generation in core debris interaction vary from about 5.65 to 2.9 g/cm^3.

e-4. Late In-vessel Release

Again, the aerosol properties during the late in-vessel release will actually be determined by the aerosol materials generated by the long-term, quasi-steady core debris interactions with concrete. Material densities during this phase of an accident are calculated [25] to be in the range of 3.15 to 2.65 g/cm^3.

f. Uncertainty in Shape Factors

It is assumed here that there is enough water adsorption by aerosol particles that these particles become porous spheres. The collision shape factor, γ, and the dynamic shape factor, $\varkappa$, are equal for all particles:

$$\varkappa = \gamma = 1/\alpha^{1/3}$$

It is also assumed that shape factors are size dependent and this dependency is described by:

$$\alpha = \frac{\epsilon\rho_p + (1-\epsilon)\rho_\omega}{\rho_p}$$

$$\epsilon = \min\left[1, \left[\frac{z}{d_p}\right]^{3-d_f}\right]$$

where z is the diameter of primary particles that make up agglomerated particles and d_f is the fractal dimension of agglomerates. This primary particle size is taken to be uncertain and has a log-uniform distribution over the interval from 0.001 to 0.1 μm. The fractal dimension of the agglomerates was taken to be uniformly distributed over the range from 1.5 to 2.2.

g. Gas Flow Rates

Gas flow rates to the suppression pool are expected to be quite variable over the course of the four phases of severe accidents considered here. An assumption made in the analyses done here is that gases flow to the quenchers during the gap release and the in-vessel release phase of the accident. Gases flow to the suppression pool through downcomers and horizontal vents during the ex-vessel and late in-vessel phases of the accidents. Possible bypass of the suppression pool is neglected throughout the analyses.

g-1. Gap Release Phase

Based on the discussions of accident sequences presented in Chapter III, the gas flows to the quenchers for all types of boiling water reactors are taken to be uniformly distributed over the range of 2500 to 400 moles per second. Hydrogen generation rates are taken to be uniformly distributed over the range of 20 to 120 moles/s.

g-2. In-Vessel Release Phase

Again, from the discussions in Chapter III steam flows to the quenchers during the in-vessel phase of an accident are taken to be uniformly distributed over the range of 50 to 500 moles/s. The hydrogen flows are taken to be uniformly distributed over the range 20 to 120 moles/s. No attempt is made here to account for episodic eruptions of steam that accompany the relocation of core debris to the water-filled lower plenum of the reactor vessel.

g-3. Ex-vessel Release Phase

Gas production during the ex-vessel phase of a severe reactor accident must be treated differently for Mark I reactors than for Mark II and Mark III reactors. The differences arise because in the Mark II and Mark III reactors, degassing of the concrete introduces substantial quantities of water vapor into the gases being discharged to the suppression pools. Consequently, molar flows to the suppression pool in the case of Mark I reactors are taken to be uniformly distributed over the range of 100 to 300 moles/s. Molar flows to the suppression pool in the case of Mark II and Mark III reactors are taken to be uniformly distributed over the range of 150 to 1100 moles/s.

The condensible portion of the gas produced during the ex-vessel phase of an accident in a Mark I boiling water reactor would be calculated to be very small (<1 percent) if only core debris interactions with concrete were considered. There is not much concrete exposed to heating that will degas to add water vapor to the gas discharged to the suppression pool. The reactor pedestal is concrete that can degas and there may be some evaporation from residual water in the reactor coolant system. Consequently, gas discharged to the suppression pool in an accident at a Mark I reactor is taken to have a water vapor content uniformly distributed over the range of 1 to 10 percent.

Much of the gas discharged to the suppression pools during the ex-vessel phases of an accident in Mark II and Mark III reactors can be water vapor. The water vapor content is taken here to be correlated with the gas production rate:

$$\dot{m}(H_2O) = \begin{cases} \dot{m}(\text{total}) - 0.8[100 + \epsilon(x)200] & \text{for } \dot{m}(\text{total}) > 300 \dfrac{\text{moles}}{\text{s}} \\ 0.2\ \dot{m}(\text{total}) & \text{for } \dot{m}(\text{total}) \leq 300 \dfrac{\text{moles}}{\text{s}} \end{cases}$$

where

$\dot{m}\ (H_2O)$ = moles water vapor discharged to the suppression pool per second,

$\dot{m}\ (\text{total})$ = total number of moles of water vapor discharged to the suppression pool per second, and

$\epsilon(x)$ = uncertain number uniformly distributed over the range 0 to 1.

g-4. Late In-vessel Release Phase

Similar reasoning to that discussed above in connection with gas generation during the Ex-Vessel Release phase of an accident is used to draw a distinction between gas generation during the Late In-Vessel Release phases of accidents at Mark I reactors and accidents at Mark II and Mark III reactors. Gas production during the Late In-Vessel Release phase of an accident in a Mark I reactor is taken to be uniformly distributed over the range of 20 to 80 moles/s. As discussed in Chapter III, much more of this gas can be water vapor. Here the water vapor content of the gas is taken to be uniformly distributed over the range of 10 to 35 percent.

On the other hand, during accidents at Mark II and Mark III reactors, the gas production is taken to be uniformly distributed over the range of 160 to 500 moles/s. Water vapor production is taken to be:

$$\dot{m}(H_2O) = \dot{m}(\text{total}) - [20 + 60\ \epsilon(y)]$$

where $\epsilon(y)$ is uniformly distributed over the range of 0 to 1.

2. Phenomenological Uncertainties in Bubble Behavior

In the subsections below, the phenomenological uncertainties in bubble behavior recognized in the Monte Carlo uncertainty analyses are described. The uncertain parameters, the possible ranges of values they can assume, and the distributions of values within these ranges are summarized in Table 23.

a. Uncertainty in Bubble Formation

It is apparent from the discussions above (see Section IVA) that there is no universally applicable model of bubble formation. The two-stage model devised by Kumar and Kaloor [31] has the attractions of validation by comparison to a wide variety of data and because it has explicit dependencies on orifice geometry. The empirical correlation devised by Paul et al. [30] yields predictions that are different than those obtained from the Kumar and Kaloor model. But, the empirical correlation is attractive because it is based on data obtained from a simulated quencher orifice. Neither the Kumar and Kaloor model nor the empirical correlation seems to have been thoroughly validated for steam-rich gases entering steam suppression pools that are significantly sub-cooled.

To treat the uncertainty of bubble formation at quencher orifices, a parameter $\delta(b)$ is defined to be uniformly distributed over the range $0 \leq \delta(b) < 1$. Then, the Kumar and Kaloor model is used when randomly sampled values of $\delta(b)$ are less than 0.5. The empirical correlation developed by Paul et al. is used when $\delta(b) \geq 0.5$.

When the Kumar and Kaloor model is selected, the orifice orientation angle, γ, is randomly selected from the range $0 \leq \gamma < 90°$. When the correlation developed by Paul et al. is selected, the prediction of the model is taken to be uncertain. The uncertainty in the natural logarithm of the normalized volume is given by a Students' t distribution with 15 degrees of freedom and a standard error of:

$$\text{standard error} = 0.225 \left[0.0588 + \frac{(\ln(We) - 7.6562)^2}{145.952} \right]^{1/2}$$

where

$$We = \text{Weber number} = U^2 \rho_l D_o / \sigma_l,$$

Table 23. Uncertainties in the phenomena affecting bubbles

Uncertain quantity	Range of values	Distribution
Bubble Formation		
• gap and invessel release		
δ(b), parameter to select among models	0 to 1	uniform
θ, orientation in Kumar and Kaloor model (degrees)	0 to 90	uniform
e(P), uncertainty in correlation of the natural logarithm of the normalized bubble volume	$se = \left\{0.0588 + \frac{[\ln(we) - 7.6561]^2}{145.952}\right\}^{1/2}$	Students' t v = 15
• ex-vessel and late invessel		
C, coefficient in Davidson Schular model	0.976 to 1.722	uniform
Initial Bubble Size		
e(bs), uncertainty in the correlation of the natural logarithm of the mean bubble size	$se = 0.0634\left[0.0833 + \frac{(y^2 - 0.4434)^2}{1.1847}\right]^{1/2}$	Students' t v = 12
$\sigma(\beta)$, geometric standard deviation of the log-normal bubble size	1.36 to 1.61	uniform
Bubble Shape		
δ(E), parameter to select between models	0 to 1	uniform
Bubble Slip Velocity		
δ(v), parameter to select between models of two phase flow	0 to 1	uniform

Table 23. Uncertainties in the phenomena affecting bubbles (continued)

Uncertain quantity	Range of values	Distribution
Bubble Rise Velocity		
$e(J_1)$, uncertainty in the correlation of $\log_{10}$ J with $\log_{10}$ H for H < 59.3	$se = 0.0915\left[0.01563 + \frac{(\log_{10}H - 1.17945)^2}{10.66}\right]^{1/2}$	Students' t v = 62
$e(J_2)$, uncertainty in the correlation of $\log_{10}$ J with $\log_{10}$ H for 59.3 ≤ H ≤ 1000	$se = 0.02693\left[0.01887 + \frac{(\log_{10}H - 2.1655)^2}{4.3305}\right]^{1/2}$	Students' t v = 51
$e(J_3)$, uncertainty in the correlation of U_T^2 for H > 1000	$se = 527.8\left[0.01429 + \frac{\left[\frac{D_B}{2} - 5.586\right]^2}{97.7}\right]^{1/2}$	Students' t v = 68
Plume Parameters		
$e(\alpha)$, uncertainty in the correlation of the entrainment coefficient with the Froude number, F_B	$se = 4.185\left[0.0145 + \frac{(1/F_B - 0.2145)^2}{1.8474}\right]^{1/2}$	Students' t v = 67
$\gamma = 1 + \zeta$ = momentum amplification factor		
ζ		lognormal $\mu = 0.5$ $\sigma = 3.28$
λ	0.7 to 1.0	uniform

$$V_N = \text{normalized volume} = \frac{4V}{\pi D_o^{\,2}} \left[\frac{(\rho_l - \rho_g)}{\sigma_l} g \right]^{1/2},$$

$$U = 4\dot{m}/\rho_g \pi D_o^{\,2},$$

D_o = orifice diameter,

$\dot{m}$ = mass flow rate,

V = bubble volume,

ρ_g = gas density at the orifice.

Data for bubble formation at large diameter horizontal vents and downcomers are scarce. Though it is not strictly applicable, the Davidson-Schuler model is used to predict the size of bubble formed at these large diameter vents:

$$V_B = \frac{\pi}{6} D_B^{\,3} = C Q^{6/5} g^{-3/5}$$

The leading coefficient in the Davidson-Schuler model, C, is taken to be uncertain and is assumed to be uniformly distributed over the range of 0.976 to 1.722.

b. Uncertainty in the Equilibration Distance

Bubbles that detach from orifices are large and may be steam-rich relative to the partial pressure of water in equilibrium with the suppression pool. It was assumed that over an uncertain distance between 2 and 10 initial bubble diameters, the gas comes into compositional and thermal equilibrium with the suppression pool. The most important effect of this equilibration is, of course, to remove aerosols by the condensation of excess steam in the gas. Removal of aerosols during this equilibration compensates for the neglect of aerosol removal by steam condensation during bubble formation.

The equilibration of steam-rich bubbles is a fairly violent process. Undoubtably, mechanisms other than condensation of steam may well remove aerosols from the gas during this equilibration process. It has not been possible to identify these additional mechanisms quantitatively. It is an area meriting additional experimental attention.

c. Initial Size of Bubbles in the Plume

Experiments by Paul et al. [30] and by Hakaii et al. [69] show that bubbles rising through the pool have a distribution of sizes. The experimental evidence is for bubbles that are formed above quencher orifices. Presumably bubbles with similarly distributed sizes are formed when gas globules detach from

downcomers and horizontal vents and then disintegrate. Experimental studies by Paul et al. [30] and by Hakaii et al. [69] showed that the bubble sizes were lognormally distributed.

The mechanistic model of source term attenuation by steam suppression pools used for the Monte Carlo analyses has been constructed for bubbles of a fixed size. Consequently, bubble size must be treated as an uncertain quantity. The uncertain bubble size is taken to be lognormally distributed. The mean of the bubble size distribution has been taken from a correlation of the experimental results obtained by Paul et al. as described in Section IV-C. The mean size, $\mu(B)$, is found from:

$$\mu(B) = 0.435 \{1 + \exp[-0.08789/Q]\} \exp[-0.5972\ y^2]$$

where

$\mu(B)$ = mean of the bubble size distribution,

Q = volumetric flow rate through the orifice, and

y = mole fraction of steam in the gas flowing through the orifice.

The logarithm of the mean size is taken itself to have a Student's t distribution with 10 degrees of freedom, and a standard error given by:

$$0.0634 \left[0.0833 + (y^2 - 0.4434)^2/1.1847\right]^{1/2}$$

The geometric standard deviation for the bubble size distribution is only modestly uncertain. Based on the experimental data obtained by Paul et al. this geometric standard deviation, $\sigma(B)$, is taken to be uniformly distributed over the range 1.36 to 1.61.

d. Uncertainty in Bubble Shape

The mechanistic model used here for the Monte Carlo uncertainty analyses has been constructed for ellipsoidal bubbles of eccentricity E. This eccentricity is a function of bubble size and behavior. Eccentricities are recalculated at each time step. Models for the dependencies of eccentricity on bubble properties are uncertain. The available data on eccentricities are scattered. There is at least some evidence that bubbles in swarms are less distorted than are isolated bubbles. Proof of this speculation, however, has not been found. Consequently two models for the eccentricities of bubbles are considered. One is a correlation of data for isolated bubbles [82]:

$$1/E(A) = \begin{cases} 1 & \text{for } Ta < 1 \\ [0.81 + 0.206 \tanh\{2(0.8 - \log_{10} Ta)\}]^3 & \text{for } 1 \leq Ta \leq 39.8 \\ 0.24 & \text{for } Ta > 39.8 \end{cases}$$

where

$$Ta = Re\, M^{0.23},$$

$$Re = \rho(l)\, U(slip)\, D_B / \mu(l),$$

$$U(slip) = \text{slip velocity of the bubble, and}$$

$$\rho = \text{Morton number} = g\mu_l^4 (\rho_l - \rho_g) / \rho_l^2 \sigma_l^3.$$

The second model is an empirical correlation of experimental data obtained by Paul et al. [30]:

$$1/E(B) = \begin{cases} 1 & \text{for } D_B \leq 0.15 \text{ cm} \\ 0.68 - 0.57 \exp[-D_B/0.26] & \text{for } D_B > 0.15 \text{ cm} \end{cases}$$

A parameter $\delta(E)$ is defined to be uniformly distributed over the range 0 to 1. The eccentricity model used in a particular calculation, then, is found from:

$$E = \begin{cases} E(A) & \text{for } \delta(E) < 0.5 \\ E(B) & \text{for } \delta(E) \geq 0.5 \end{cases}$$

e. Bubble Slip Velocity

The slip velocities of bubbles in a rising plume depend on the void fraction of the plume. An indepth treatment of this two-phase flow issues has not been attempted. Rather, the uncertainty in the slip velocity dependence on void fraction is reflected by the consideration of various models. A parameter $\delta(\epsilon)$ is defined to be uniformly distributed on the range from 0 to 1. Then, the slip velocity is found to be:

$$U(slip) = \begin{cases} U_B & \text{for } \delta(\epsilon) < 1/3 \\ U_B(1 - \epsilon(r,z)) & \text{for } 1/3 \leq \delta(\epsilon) < 2/3 \\ U_B(1 - \epsilon(r,z))^2 & \text{for } \delta(\epsilon) \geq 2/3 \end{cases}$$

where

U_B = rise velocity of an isolated bubble of the same size, and

$\epsilon(r,z)$ = void fraction at axial location z above the orifice and radial location r away from the orifice.

The rise velocity of an isolated bubble is found from:

$$U_T(cm/s) = \begin{cases} 0.735 \sqrt{g D_B(cm)} & \text{for } H > 1000 \\ \dfrac{\mu_l}{\rho_l D_B} M^{-0.149} (J - 0.857) & \text{for } H \leq 1000 \end{cases}$$

where

M = Morton number

$$J = \begin{cases} 0.94\ H^{0.757} & \text{for } 2 \leq H \leq 59.3 \\ 3.42\ H^{0.441} & \text{for } 59.3 < H \leq 1000 \end{cases}$$

$$H = 4/3\ E_o\ M^{-0.149} (\mu_l\ (poise) / 0.009)^{-0.14}$$

The correlations of J in terms of H were found by linear least-squares fitting of log J as a function of log H. The uncertainty in the predictions of log J derived from the correlations are then given by Students t distributions. For the regime of $2 \leq H \leq 59.3$ the parameters of the distribution are:

degrees of freedom = 62

$$\text{standard error} = 0.0915 \left[0.01563 + \frac{(\log H - 1.17945)^2}{10.66} \right]^{1/2}$$

For the regime $59.3 < H \leq 1000$, the parameters are:

degrees of freedom = 51

$$\text{standard error} = 0.02693 \left[0.01887 + \frac{(\log H - 2.1655)^2}{4.3305} \right]^{1/2}$$

The values of U_T for $H > 1000$ were found from linear least-squares fitting of $U_T{}^2$ values to D_B values. The uncertainty in the predicted values of $U_T{}^2$ follows a Students' t distribution:

degrees of freedom = 68

$$\text{standard error} = 527.8 \left[0.014286 + \frac{\left[\frac{D_B}{2} - 5.586 \right]^2}{97.7} \right]^{1/2}$$

f. Uncertainty in Plume Parameters

Three uncertain parameters are used in the description of the bubble plumes rising through the suppression pool:

- the entrainment coefficient, α
- the momentum amplification factor, γ, and
- λ which is the ratio of the size parameters for the void and liquid velocity distribution parameter.

Milgram [44] provides a correlation for entrainment coefficients, α, derived from experimental values. The correlation was derived by linear least squares fitting of the experimental values. Consequently, the uncertainty in the predictions of the correlation should have a Students' t distribution. Though Tacke et al. [45] argue that the uncertainty is larger than this, this prescription is adopted here.

Milgram's correlation for the momentum amplification factor proves to be computationally difficult to use. Milgram's arguments concerning the correlation of the momentum amplification factor are difficult to follow. Detailed examination of the correlation derived by fitting an expression to data suggests that there may be little correlation. Consequently, the momentum amplification factor is treated as an uncertain parameter. Theoretical arguments suggest its value is always greater than 1.0 and perhaps greater than 1.07. Comparisons to data suggest values in the range of 1.1 to 2.8 characterize properties of bubble plumes reasonably well. Here the momentum amplification factor is taken to be:

$$\gamma = 1 + \xi$$

where ξ is an uncertain parameter with a lognormal distribution of values around a mean of 0.5 with a geometric standard deviation of 3.28. Then, 95 percent of the values of γ are greater than 1.07, and 94 percent of the values of γ are less than about 4.6.

The distribution of liquid velocities with radial distance in the plume is taken to be exponential:

$$U_l(r,z) = U_l(z) \exp(-r^2/b^2(z))$$

Void fraction is also taken to be exponentially distributed with radial distance:

$$\epsilon(r,z) = \epsilon(z) \exp(-r^2/b_\epsilon^2(z))$$

The plume model used in the mechanistic model has been constructed under the assumption that the radial distributions of void fraction and liquid velocities are related by:

$$\lambda = \frac{b_\epsilon(z)}{b(z)}$$

where λ is a constant that is independent of position, flow, etc. Milgram [44] argues that predictions of the plume model are not especially sensitive to the values of λ that is assumed. Values of $\lambda = 0.7$ to 1.0 have been used by various investigators [45]. Here it is assumed that λ is uncertain and that its values are uniformly distributed over the range of 0.7 to 1.0.

g. Uncertainty in Bubble Growth

As bubbles rise through a pool they will grow as a result of both the loss of pressure head and the vaporization of water into the bubble. Paul et al. [30] did not observe a significant amount of bubble growth in their tests. Certainly, the developers of the SPARC code [6] took this as the justification for treating the bubbles as though their sizes were invariant with axial distance. Certainly, the low ionic strength medium used for the tests conducted by Paul et al. would be conducive to the establishment of a dynamic equilibrium between bubble disintegration and coalescence. Dissolution of salts in the pool, which would be expected in a reactor accident, might interrupt this equilibrium. On the other hand, growth of bubbles may not have been detectable except near the very top of the pool.

The growth of bubbles as they rise through a water pool can reduce the efficiencies of processes such as diffusion, inertial impaction, and sedimentation at depositing aerosol particles on the bubble walls. A dynamic equilibrium that keeps bubble size about the same along the axial dimension of the plume would certainly keep the deposition efficiency high. The dynamic equilibrium could have another effect when the variation in the efficiency of aerosol removal with radial distance modeled here is recognized. The dynamic equilibrium of coalescing and disintegrating bubbles would move aerosol-laden gases

between regimes of maximal and minimal attenuation. In the model used here, bubble growth is recognized and calculated following the thermodynamic model described in Chapter IV. Heat transfer to and within the bubble is taken to be instantaneous. There are no thermal gradients near the surface of the bubble that would inhibit aerosol deposition on the surface.

h. Radial Mixing in the Bubble Plume

Bubble within a plume. There can, in fact, be a dynamic equilibrium of bubbles coalescing and disintegrating. This dynamic process has the effect of moving aerosol-laden gases from regions of low aerosol removal rates in the plume into regions where removal is more rapid. Unfortunately, there is not now an indication of how much mixing occurs. Consequently, it is assumed that at the end of each computational step a fraction of the bubbles in a radial node exchanges with bubbles in an adjacent node. This fraction is taken to be uniformly distributed over the range of 0 to 1.

3. Phenomenological Uncertainties in Aerosol Behavior

Uncertainties that arise in the description of processes that remove aerosol from gas bubbles in the suppression pool are described in the subsections below. The discussions address aerosol removal during formation of bubbles at orifices, downcomers and vents as well as aerosol removal as bubbles rise through the suppression pool. Uncertain parameters defined in these discussions are summarized in Table 24. Also shown in this table are the ranges of possible values theses parameters can assume and subjective probability distributions for values within these ranges. Note that no uncertainties are ascribed to the transition period between the time bubbles detach from the orifice and the formation of a bubble plume. Aerosol mass removal during this period is taken to be proportional to the amount of gas removed by condensation and the aerosol removal is taken to be independent of aerosol particle size.

a. Uncertainty in Aerosol Trapping by Inertial Impaction

Inertial impaction of aerosol on the walls of rising bubbles is a very important mechanism for the attenuation of aerosol source terms in suppression pools. This mechanism depends, of course, on the circulation of gases within a rising bubble. The issue of the circulation of gases has been much discussed in the literature. In many of the earlier discussions, it has been assumed that there is some critical dimension at which circulation of gases within a rising bubble begins. Bubbles smaller than this critical dimension were found to rise through liquid as though they were rigid spheres. Larger bubbles rose through the liquid as though they were fluid spheres.

More recently, attentions have been directed toward the accumulation of surface active agents, present as often minute impurities in the liquid, at the gas liquid interface. Immobilization of the gas-liquid interface by these impurities rather than simply the bubble dimension is thought to be responsible for stagnation of gases within a bubble. Bubbles initially released into a pool may have circulating gases. As they rise and accumulate impurities gas circulation is damped.

Arguments concerning the surface activity of liquid phase impurities are quite significant with respect to discussions of steam suppression pools. Though it might be argued waters in these pools are quite pure at the start of an accident, these waters will surely become contaminated as a severe accident progresses. The possibility that the contamination will immobilize the gas-liquid interface of rising bubbles and, consequently, inhibit circulation of gases within the bubble must be recognized.

Table 24. Uncertainties in the phenomena affecting aerosol behavior

Uncertain quantity	Range of values	Distribution
Efficiency of Inertial Impaction		
V_m (cm^3/mole), molar volume of surface-active agents	40 to 1,000	log-uniform
C(surf)(moles per liter), surface-active agent concentration	10^{-10} to 10^{-4}	log-uniform
Diffusive Deposition		
S*, Sherwood number for particle mass transfer from Hill's vortex	14.6 to 17.66	uniform
Momentum Accommodation Coefficient		
$\alpha_m = 1 - A \exp(-300/T)$, A	0 to 0.6	uniform
Temperature Accommodation Coefficient		
$\alpha_t = \alpha_m [1 - A' \exp(-300/T)]$, A′	0 to 1	uniform
Oscillation Capture		
C(o), criterion for the onset of oscillations	2.96 to 4.24	uniform
δ(osc), parameter for evaluation of oscillation frequency	0 to 1	uniform
Capture During Bubble Formation		
ϵ(f), parameter to interpolate between models of inertial impaction	0 to 1	uniform
δ(f), parameter to select model of particle mass transport within the forming bubble	0 to 1	uniform

Uncertainty

It is hypothesized here that bubbles are formed with entirely mobile interfaces. As they rise through the pool, surface active contaminants accumulate at the interface and progressive immobilize this interface beginning at the trailing boundary of the bubble and progressing, perhaps, to eventually immobilize the entire bubble interface. Thus, at an arbitrary position in the pool, a bubble will have its interface immobilized over polar angles from 0 to ϕ. For analysis purposes, the interface over polar angles from ϕ to π radians is assumed to be entirely free of surface active agents. Experimental data suggest that this may be only an approximate description of the actual nature of bubble surfaces [237]. Though accumulations of surface active agents necessary to immobilize the gas bubble interface may first develop at the trailing surface of rising bubbles, all surfaces may quickly be partially contaminated with surface active agents at concentrations that at least affect interface mobility.

Sadhal and Johnson [238] have analyzed the circulation of gases within spherical bubbles with partially immobilized interfaces. It is assumed here that the proportionate reduction in particle deposition calculated from gas flows in spherical bubbles with partially immobilized interfaces will apply as well to ellipsoidal bubbles with partially immobilized interfaces considered in the mechanistic model. The non-dimensional stream function found by Sadhal and Johnson for gas flows in spherical bubbles with partially immobilized interfaces is:*

$$\psi = 1.5(\xi^4 - \xi^2)\int_{\cos\theta}^{1} P_1^{o}(x)\,dx + \sum_{k=1}^{\infty} C_k \left[\xi^{k+3} - \xi^{k+1}\right] \int_{\cos\theta}^{1} P_k^{o}(x)\,dx$$

where

$\xi = 2r / D_B$,

θ = polar angle,

$P_k^{o}(x)$ = $k^{\underline{th}}$ degree Legendre polynomial,

---

*The integral $\int_{\cos\theta}^{1} P_k^{o}(x)\,dx = \sin\theta\, T_k^{-1}(\cos\theta)$ where $T_k^{-1}(\cos\theta)$ is an associate Legendre function. Associated Legendre functions, which are integrals of classic Legendre polynomials, are not discussed as frequently as are the derivatives of Legendre polynomials. The recurrence relationship for the first integrals is:

$$(n+1)\, T_n^{-1}(\cos\theta) = (2n-1)\, T_{n-1}^{-1}(\cos\theta) - (n-2)\, T_{n-2}^{-1}(\cos\theta)\ .$$

Note that $T_1^{-1}(\cos\theta) = 0.5 \sin(\theta)$ and $T_2^{-1}(\cos\theta) = 0.5 \sin(\theta)\cos\theta$.

$$C_1 = -\left\{\frac{1}{4\pi}\,[2\phi + \sin\phi - \sin 2\phi - \frac{1}{3}\,3\phi] + 1\right\}$$

$$C_k = \frac{1}{4\pi}\left\{\sin(k+2)\phi - \sin k\phi + \sin(k+1)\phi - \sin(k-1)\phi - 2\left[\frac{\sin(k+2)\phi}{k+2} + \frac{\sin(k-1)\phi}{k-1}\right]\right\}$$

The velocity of the gas tangential to the gas-liquid interface is found from:

$$V(\text{tangential}) = \frac{-1}{\xi \sin\theta}\,\frac{\partial\psi}{\partial\xi}\bigg|_{\xi=1}$$

Normalized tangential velocities are shown in Figure 105 as functions of polar angle for various values of ϕ. As immobilization of the interface progresses, the circulation of gases within the bubble becomes confined into a smaller region near the leading front of the rising bubble. Particle deposition is proportional to the angular acceleration:

$$a_\theta = K\,\frac{V(\text{tangential})^2}{D_B}$$

where K is the proportionality constant. Total deposition of particles by inertial impaction over the gas-liquid interface is given by:

$$\text{Deposition} \propto \int_0^\pi \frac{\pi D_B}{2}\,\sin\theta\; a_\theta\; d\theta$$

The variation in the deposition with ϕ is shown in Figure 106. There is a sharp reduction in the amount of deposition as ϕ exceeds 30°. As ϕ exceeds 125° particle deposition approaches 0. This variation in particle disposition by inertial impaction is given, approximately, by:

$$[1 - m(\phi)]/[1 + m(\phi)] = z(\phi)$$

where $m(\phi) = (1/2\pi)[2\phi + \sin\phi - \sin 2\phi - 1/3 \sin 3\phi]$.

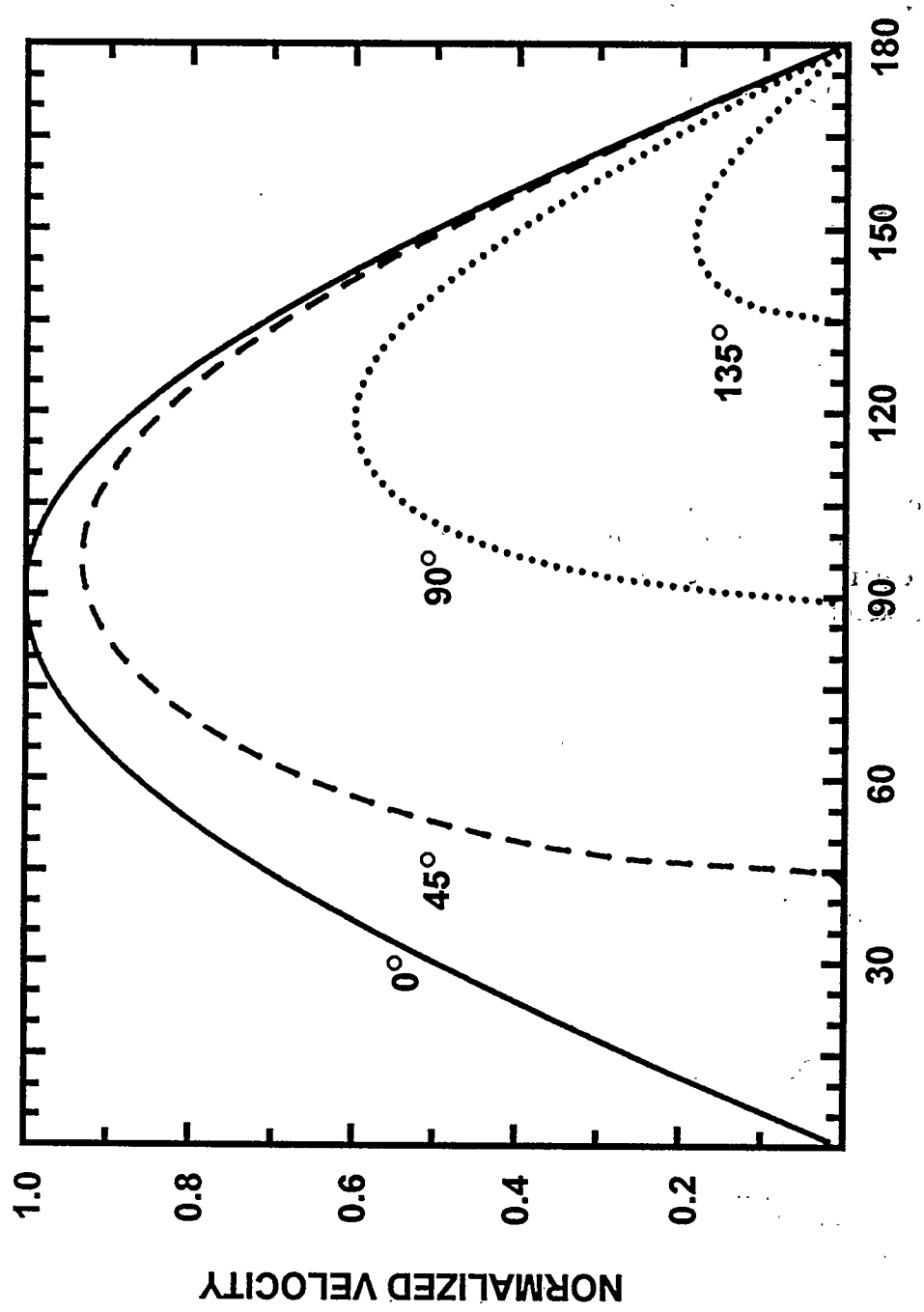

Figure 105. Variation of the normalized tangential velocities about a spherical bubble with various amounts of surface immobilization. Curves are labelled by values of ϕ in degrees.

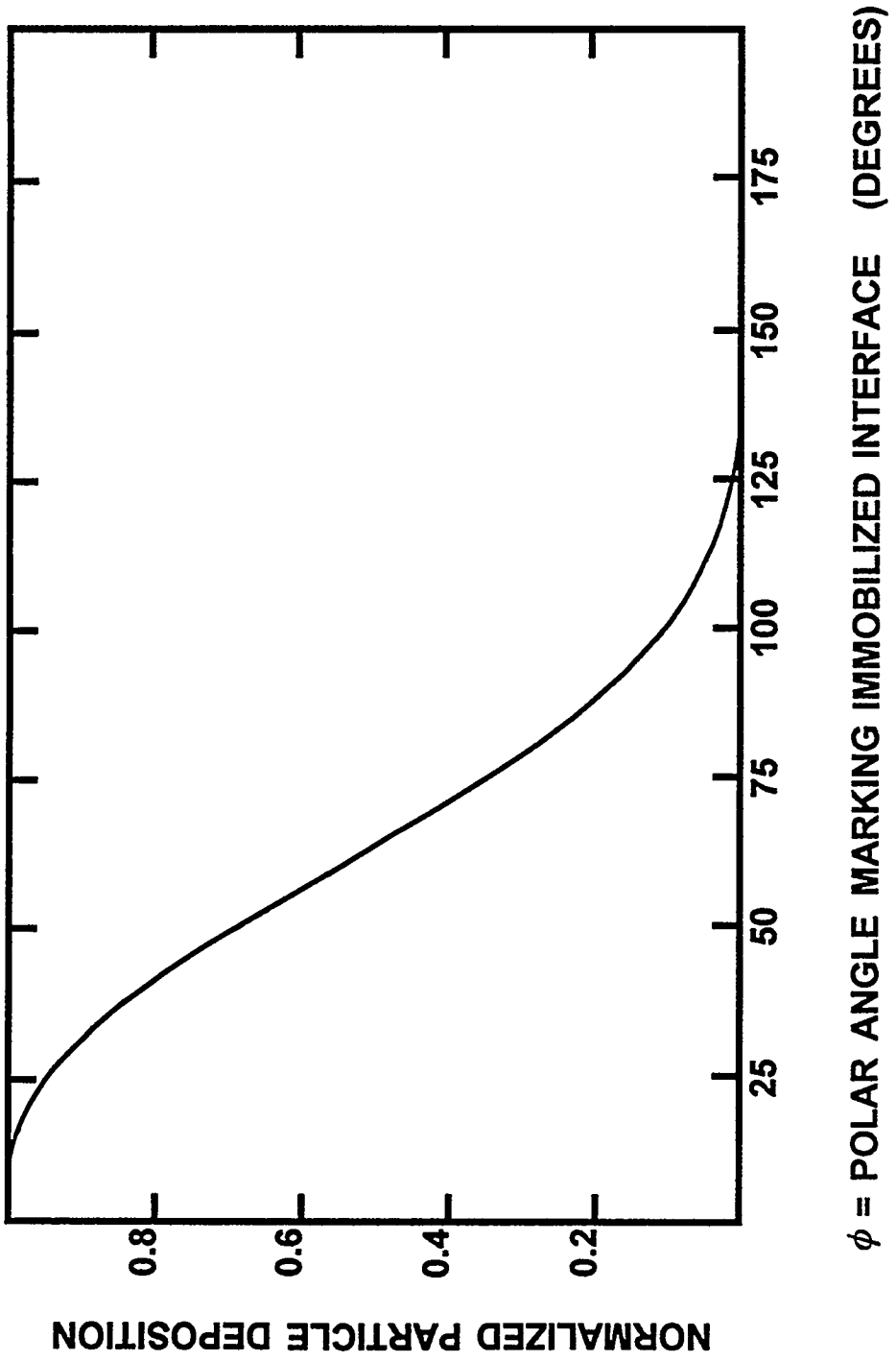

Figure 106. Variation of the normalized, integrated particle deposition by inertial impaction as a function of the extent of surface immobilization

Sadhal and Johnson find the angle of surface immobilization, ϕ, to be related to the molar amount of surface active agent, N(surf), by:

$$N(surf) = U_{slip} \frac{\pi D_B^2}{2RT} \mu(l) [2\phi - 4\phi \cos\phi - \sin 2\phi + 4\sin\phi]$$

Assume the surface active agent is present in the liquid at a molar concentration of C(surf). Then,

$$\frac{dN(surf)}{dx} = \pi D_B \frac{Đ\ Sh\ C(surf)}{1000\ U_{slip}}$$

where

C(surf) = concentration of surface active agent (moles/liter),

Sh = Sherwood number for mass transport to the bubble,

Đ = diffusion coefficient of the surface active agent in water (cm^2/s),

x = distance the bubble has risen in the pool (cm), and

U_{slip} = slip velocity of the bubble in the bubble plume rising through the suppression pool (cm/s).

Then, to a satisfactory level of approximation

$$N(surf) = \chi\ \pi\ D_B\ Đ\ Sh\ C(surf)/U_{slip}\ 1000$$

There is no information on what types of agents might be responsible for immobilization of bubble interfaces in a suppression pool. Trace concentration organic species are, of course, often quite potent surface active agents. The Wilke-Change method for the estimation of diffusion coefficients of such species in water yields:

$$Đ = \frac{5 \times 10^{-9}\ T}{\mu(l)\ V_m^{0.6}}\ cm^2/s$$

where V_m is the molar volume of the surface active agent at its normal boiling point. Such molar volumes might vary from 40 to 1000 cm^3/mole. Similarly, the concentrations of the surface active agents are unknown, but can be imagined to be in the range of 10^{-10} to 10^{-4} moles per liter of water.

Solution of the above equations for ϕ allows $m(\phi)$ to be found. Then, the deposition velocities of aerosol particles by inertial impaction are found from:

$$V_D(\phi) = \frac{2U_B^2 \sin^2(\eta) \sqrt{E^2-1}\ E^{5/3}\ z(\phi)\ \tau}{D_B \left\{ \cos^2(\eta) + \frac{1}{E^2-1} \right\}^{5/2} \left\{ \sqrt{E^2-1} - E^2 \tan^{-1}\left[\sqrt{E^2-1}\right] \right\}^2}$$

b. Uncertainty in Aerosol Trapping by Diffusion

Controversies concerning the proper description of aerosol trapping by diffusion of particles to the bubble walls have been discussed above in Section IV-L.1.a. There are three models available. Fuchs [148] has derived a model that is widely used. The derivation is based on vortex flows within the bubble. But, Mills and Hoseyni [204] point out that the result of the derivation is more appropriate for conditions in which the gas making up the bubble is well-mixed. They correctly note that for vortex flows the Kronig-Brink model [88] of mass transfer is more appropriate. They also point to Calderbank-Korchinski model [206] as being applicable. As noted above, vortex flows may be substantially damped in a bubble due to contamination. As the gas in the bubble becomes stagnant there is no convective enhancement of the diffusion of particles to the bubble walls. A complicated situation can be imagined in which a substantial volume of the bubble is stagnant and the rest is involved in a vortex flow or is well-mixed. But, for bigger bubbles shape oscillations (see below) may produce mixing--even when otherwise the gas would be stagnant within a bubble.

The analyses presented above provide a definition for the region of a bubble that is involved in vortex flows. Diffusive deposition in this region is calculated from:

$$Sh = S^*$$

where S* is uncertain and is taken to be uniformly distributed over the range from 14.6 (the long time limit of the Calderbank-Korchinski model) and 17.66 (the long time limit of the Kronig-Brink model). The diffusive deposition of particles from stagnated gases in small bubbles that do not undergo shape oscillations is found from:

$$Sh = 6.58$$

which is the long time limit of Newman's solution for diffusion in a sphere. When shape oscillations are predicted to occur are assumed here to mix well all regions of the bubble. The diffusive deposition is calculated from Fuchs' model:

$$Sh = f(E)\ Pe^{1/2}$$

c. Uncertainty in Slip Correction Factors

There have been a variety of empirical, slip correction factors used by various authors. Several of these are described in Section IV-K.2. Despite the differences in the parametric values of the different impressions, there are not great differences among the predictions derived from the expressions. With the exception of the expression obtained by Allen and Raabe [143] these various expressions have been obtained by fitting to the same or at least similar database. The functional form of the slip correction factor expression is such that there is a great deal of correlation among the three adjustable parameters. Small differences in the procedure used to obtain parametric values produce fairly significant changes in parametric values. But, because of the correlation the three adjustable parameters do not vary arbitrarily. There is a compensation in the variations so that large variations in the predictions of the expressions within the range of the database are not produced.

The empirical expressions are, however, based on a rather narrow database that does not seem closely related to the conditions of interest here. Most of the data used in the fitting process was obtained for oil droplets at room temperature. The theoretical expression obtained by Phillips [145] is more attractive for the substantial extrapolation to be done in this work:

$$C = \frac{15 + 12C_1\,Kn + 9(C_1^2 + 1)\,Kn^2 + 18C_2(C_1^2 + 2)\,Kn^3}{15 - 3C_1\,Kn + C_2(8 + \pi\alpha_t)\,(C_1^2 + 2)\,Kn^2}$$

where

$C_1 = (2 - \alpha_m) / \alpha_m$,

$C_2 = 1 / (2 - \alpha_m)$,

α_m = momentum accommodation coefficient, and

α_t = thermal accommodation coefficient.

This theoretical expression was derived, of course, based on a variety of questionable assumptions. It does seem to predict well the slip correction factors in the regimes where the many empirical expressions are applicable. Consequently, the Phillips model is taken here to be accurate (no uncertainty). Uncertainty in the slip correction factors arises from uncertainty in the accommodation coefficient to use in the theoretical expression. It is assumed here that this uncertainty is a much bigger effect than uncertainty that can arise because particles are slightly distorted from perfect spheres.

d. Uncertainty in Accommodation Coefficients

All available data seem to suggest that momentum accommodation coefficients vary from perhaps as low as 0.74 to 1.0. Most measured values are around 0.9. But, the available data are quite limited. In particular, few measurements have been made at elevated temperatures in steam-rich atmospheres.

Intuition suggests that the momentum accommodation coefficient should decrease with temperature. Here, the momentum accommodation coefficient is taken to be

$$\alpha_m = 1.0 - A \exp(-300/T)$$

where A is an uncertain parameter uniformly distributed over the range from 0 to 0.6.

What data are available suggest that the temperature accommodation coefficient is no greater than the momentum accommodation coefficient. Consequently, the temperature accommodation coefficient is taken to be:

$$\alpha_t = \alpha_m [1 - A' \exp(-300/T)]$$

where A′ is an uncertain parameter uniformly distributed over the range of 0 to 1.

e. Uncertainty in Aerosol Capture by Bubble Oscillations

Bubbles rising through the pool can be big-enough that they do not rise smoothly. Rather, there are sharp oscillations of the bubbles. These oscillations are assumed to sweep out aerosol particles. The uncertainties that arise concerning this mechanism of aerosol capture deal with the onset of bubble oscillations as well as the effectiveness of oscillations at aerosol capture.

Available information concerning the onset of oscillations of bubbles is really for isolated bubbles. It is not clear such information is actually applicable to bubbles in swarms, but this is assumed to be the case here. Oscillations are then assumed to occur when:

$$\frac{\rho_l}{\sigma_l} U_{slip}^3 D_B > C(o)$$

where C(o) is uniformly distributed over the interval from 2.96 to 4.24 (see Section IV-F).

The removal of particles by oscillations is described by:

$$\frac{1}{A} \frac{dn(d_p)}{dt} = \frac{-k_m(osc)}{V_B} n(d_p)$$

or

$$\frac{1}{A}\frac{dn(d_p)}{dx} = \frac{-k_m(osc)}{U_{slip}\ V_B}\ n(d_p)$$

where

$n(d_p)$ = number of particles of diameter d_p in the bubble,

x = rise distance of the bubble,

$k_m(osc)$ = mass transfer coefficient = $\frac{2\psi\ (\eta-1)\ \beta}{\pi}\sqrt{f\ Đ(d_p)}$, and

ψ = uncertain parameter uniformly distributed over the interval 0 to 2.4.

Other quantities in these equations are defined in Section IV-L.1.g. The frequency of bubble oscillation is calculated from

$$(2\pi f)^2 = \frac{8n(n-1)\ (n+1)\ (n+2)\ \sigma_l}{D_B^3\ [(n+1)\ \rho_l + n\rho_g]}$$

where n = 2.

f. Uncertainty in the Summation of Aerosol Capture Processes

The discussions of mechanisms of aerosol capture processes were presented as though each of the mechanisms was independent of the others. This, of course, is not the case. Treatment of the processes as though they were independent is certainly a common approximation. The next level of approximation is a vector addition of the deposition velocities. That is, the net deposition velocity, V(net), is given in the BUSCA code [9] by:

$$V(net) = V(impaction) + V(thermophoresis) + V(diffusiophoresis)$$
$$- V(settling)\cos\theta + V(impaction) + V(diffusion)$$

and this is integrated over the surface of the bubble. In the SPARC code [6],

$$V(net) = V(impaction) + V(diffusion) - V(settling)\cos\phi - V(vapor)$$

where V(vapor) is the velocity of the vapor evaporating from the bubble surface.

Vector addition, appealing as it is, still does not fully correct for the full effects of coupling among mechanisms. Physically, the additional coupling comes about because the various mechanisms affect the concentration gradients in the boundary layers which has a strong effect on the diffusive mechanisms. Derevich and Zaichik [251] formulate the net flux to the wall using the Fokker-Plank equation to be:

$$J = \left[\left(\frac{Đ}{2\pi\tau} \right)^{1/2} n + \frac{1}{2} \frac{d\, Đn}{dy} - (U_y + \tau a_y) \frac{n}{2} \right] \Bigg|_{y=o}$$

where

J = particle flux to the surface,

y = distance from the wall,

$Đ$ = diffusion coefficient,

$\tau = \rho_p\, d_p^2 / 18\, \mu_g$,

U_y = gas velocity perpendicular to surface,

a_y = accelerations on particle, and

n = particle concentration.

The gradient in the term Đn is the source of complicated coupling. Goldberg [251] has solved the Fokker-Plank equation for simultaneous gravitational settling and diffusive deposition of particles. The fraction of particles that would be deposited by the coupled gravitational settling and diffusive deposition mechanisms are shown in Table 25 for dimensionless times of $\xi = 2V_s t / D_B$ and various values of $2\,Đ / V_s\, D_B$. also shown in the table are the fraction of particles that would deposit by pure diffusive deposition and pure gravitational settling. Simply summing these pure deposition processes does, of course, overpredict deposition (it even yields physically impossible values greater than 1).

Rosner and coworkers [252-5] have discussed the complicated coupling between thermophoresis and other deposition processes. They find a complicated correlation of the deposition flux with thermophoresis, and without thermophoresis that depend in complicated ways on the specifics of the situation.

Here the vector addition procedure is utilized in the form:

$$V = V(\text{impaction}) + V(\text{thermophoresis}) + V(\text{diffusiophoresis}) - V(\text{settling})\cos\phi + V(\text{impaction}) + \alpha_s\, V(\text{diffusion}) - V(\text{vapor})$$

Table 25. Effects of coupling between diffusion and gravitational settling

		Fraction of particles deposited by				
$\alpha = 2Đ / V_S D_B$	$\xi = 2V_S t / D_B$	pure gravitational settling f_S	pure diffusion f_D	sum $f_D + f_S$	coupled calculation f_{DS}	ϵ^* for $f_{DS} = f_S + \epsilon^* f_D$
0.05	0.1	0.075	0.224	0.299	0.223	0.661
0.10		0.075	0.308	0.384	0.310	0.763
0.20		0.075	0.419	0.454	0.645	1.360
0.50		0.075	0.607	0.682	0.705	1.036
1.00		0.075	0.770	0.845	0.744	0.869
0.05	0.2	0.150	0.308	0.458	0.333	0.594
0.10		0.150	0.419	0.568	0.437	0.685
0.20		0.150	0.557	0.706	0.561	0.738
0.50		0.150	0.770	0.920	0.769	0.804
1.00		0.150	0.916	(1.065)	0.906	0.825
0.05	0.4	0.296	0.419	0.715	0.499	0.484
0.10		0.296	0.557	0.853	0.603	0.551
0.20		0.296	0.718	(1.014)	0.740	0.618
0.50		0.296	0.916	(1.212)	0.911	0.671
1.00		0.296	0.988	(1.284)	0.993	0.705
0.05	0.7	0.504	0.528	(1.032)	0.675	0.324
0.10		0.504	0.686	(1.189)	0.774	0.394
0.20		0.504	0.847	(1.350)	0.901	0.469
0.50		0.504	0.981	(1.484)	0.978	0.483
0.05	1.0	0.688	0.607	(1.294)	0.799	0.183
0.10		0.688	0.770	(1.458)	0.903	0.279
0.20		0.688	0.916	(1.603)	0.945	0.280

where α_s is an uncertain parameter uniformly distributed over the range from 0.5 to 1.5. When oscillations of the bubble become important, the mechanisms of aerosol deposition are taken to be diffusion, oscillations, and gravitational settling and they are taken to be independent.

g. Uncertainty in Aerosol Capture During Bubble Formation

Three mechanisms of aerosol capture during bubble formation are consider here:

- inertial impaction from the jet,
- convective deposition from circulating gases, and
- diffusiophoretic deposition due to the condensation of steam.

Uncertainty in the diffusiophoretic deposition of aerosol particles is assumed here to be dominated by the uncertainty in heat transfer from the forming bubble and uncertainty in the gas composition. These uncertainties have been discussed above. Uncertainty in the other two mechanisms are discussed here.

Most computer codes used as a model for inertial impaction from the gas jet a model appropriate for stagnation flow against a fixed plate. This model predicts a rather abrupt variation in the efficiency of particle capture with variations in particle size. Above, an alternative model is described. This model shows much less variation in particle capture efficiency with particle size. Since there are not data to guide selection between these models, a parameter $\epsilon(f)$ is defined to be distributed uniformly over the range from 0 to 1, and the particle capture efficiency as a function of particle size is found from

$$\epsilon(d_p) = \epsilon(f)\ E(\text{plate}) + [1 - E(f)]\ E(\text{disk})$$

where

$\epsilon(d_p)$ = fraction of particles of diameter d_p captured,

E(plate) = fraction of particles of diameter d_p captured according to the fixed plate model, and

E(disk) = fraction of particles of diameter d_p captured according to the alternative (disk) model.

The capture of particles from convective motion of gases within the bubble can be described in terms of inertial impaction or, in terms of convective mass transport. These are qualitatively different hypotheses and it is not clear which best describes what takes place within the bubbles. Consequently, a parameter $\delta(f)$ is defined to be uniformly distributed over the range 0 to 1. The convective deposition efficiency of particles is determined from:

$$\epsilon = \begin{cases} \epsilon(\text{inertial}) & \text{for } \delta(f) < 0.5 \\ \epsilon(\text{convection}) & \text{for } \delta(f) \geq 0.5 \end{cases}$$

4. Summary of Uncertainties

The uncertainty analyses described in Chapter VI consider 38 uncertainty quantities. Nine of these uncertain quantities (described in Table 22) deal with the boundary conditions dictated by plant geometry and accident progress. Nineteen of the uncertain quantities deal with the behaviors of gas bubbles forming and rising in the steam suppression pool (see Table 23). Ten uncertain quantities deal with the behavior of aerosol particles in bubbles in the suppression pool (see Table 24).

VI. Results of the Uncertainty Analyses

Results of the Monte Carlo uncertainty analyses are described in this chapter. Uncertain quantities predicted by the mechanistic model of decontamination by a steam suppression pool and of interest here are:

- the extent of decontamination, and
- the sizes of aerosol particles that emerge from the pool.

The extent of decontamination of gases that sparge through suppression pools is of interest because this represents an attenuation of the severe accident source term. Particle size information for aerosol materials that do emerge from the suppression pool is of interest for prediction of the subsequent behavior of these aerosols.

Decontamination of aerosol-laden gases sparging through suppression pools is characterized here by decontamination factors. These decontamination factors are defined as the aerosol mass input to a process divided by the aerosol mass that emerges from the process.

The calculations done for the Monte Carlo uncertainty analysis were organized so that distinct decontamination factors were accumulated for the processes:

- bubble formation, DF(form)
- bubble detachment, collapse and equilibration with the suppression pool, DF(equil), and
- bubble rise through the pool, DF(rise).

The product of these three decontamination factors in a particular calculation yields the total decontamination factor, DF(total), predicted for the particular set of values of uncertain quantities of the calculation. Some correlation among the three decontamination factors is to be expected. Consequently, accumulated values of DF(form), DF(equil), and DF(rise) ought not be separately analyzed and the results multiplied to form an estimate of DF(total).

Condensation of excess steam is an important decontamination process during both bubble formation and bubble equilibration. The mechanistic calculations treat decontamination by considering it to occur only during equilibration. The product, DF(FE) = DF(form) DF(equil) is more physically meaningful than the component decontamination factors.

In this chapter, uncertainty distributions are discussed for:

- DF(FE)
- DF(rise)
- DF(total)
- the mean size of aerosol particles that emerge from a suppression pool, d_p(mean) and

- the standard deviation of the distribution of particle sizes, σ, of aerosol that emerges from the pool.

Example uncertainty distribution for DF(total), d_p(mean), and σ are shown in Tables 26, 27, and 28, respectively. Other distributions calculated in this work is collected in tabulated form in Appendix A.

Each uncertainty distribution is derived from a finite sample obtained in the Monte Carlo calculations. Consequently, the uncertainty distributions can be determined only to a specified confidence interval. That is, each quantile of the cumulative uncertainty distribution is characterized by a range of values of the uncertain quantity. The uncertainty distributions shown here and in Appendix A provide ranges for quantiles at 5 percent intervals between 5 and 95 percent. The ranges are shown for confidence levels of 50 and 90 percent. At a confidence level of 100(1-α) percent, there is a confidence of 100(1-α) percent that the value of the uncertain quantity corresponding to the specified quantile of the "true" uncertainty distribution lies within the specified range. There is a 100 α percent probability that this true value is actually above of below the specified range. The widths of the ranges increase as higher levels of confidence that the range include the true value are demanded. The widths of the ranges shrink with increasing sample size. Unfortunately, the ranges decrease in size only with the square root of the number of samples taken in the Monte Carlo analyses. There is, then, a rapidly diminishing return obtained by increasing the sample size.

As noted in the introduction to this document, sample sizes were selected so that there was a 99 percent confidence that 95 percent of the ranges of uncertain values were sampled. In general, the ranges of values of the uncertain quantities associated with quantiles of the uncertainty distributions are small compared to the 10 to 90 percent range of uncertain values spanned by the distribution. However, especially for the decontamination coefficients, ranges at the 90 and 95 percent quantiles do become quite large.

In the remainder of the discussion here only selected features of the uncertainty distributions are described in detail. These selected features are:

- the medians or 50 percentiles of the distributions which are considered here to be the best estimates of the uncertain quantities,

- the 90 percentiles of the distributions which are considered here to be reasonable upper bound values of the uncertain quantities,

- the 10 percentiles of the distributions which are considered here to be reasonable lower bound values of the uncertain quantities, and

- the means of the distributions which may be of interest to some but have no particular statistical significance for the uncertainty distributions developed here.

A. Decontamination During Release Through 'T' Quenchers

Uncertainty distributions for the decontamination factors and size characteristics of particles that emerge from a suppression pool were calculated for materials discharged to the pool through 'T' quenchers during the gap release and the invessel release phases of an accident. The quenchers were assumed to

Table 26. Uncertainty distribution for the total decontamination of invessel release material after passing through a 'T' quencher 500 cm deep

Percentile	Values of $\log_{10}$ DF(total) Characteristic of the indicated percentile at a confidence level, C, of	
	C = 90%	C = 50%
5	7.14 to 13.1	8.65 to 11.4
10	13.2 to 26.3	16.6 to 20.4
15	23.0 to 42.5	27.7 to 36.1
20	35.8 to 64.4	42.3 to 53.1
25	49.6 to 90.3	62.1 to 79.6
30	73.1 to 125	87.5 to 101
35	99.3 to 190	111 to 141
40	133 to 287	167 to 218
45	202 to 490	243 to 372
50	328 to 728	440 to 548
55	501 to 1256	608 to 908
60	783 to 1945	998 to 1570
65	1390 to 3090	1690 to 2500
70	1995 to 6456	2860 to 3990
75	3715 to 26100	5600 to 13200
80	12100 to 189000	16750 to 55300
85	52700 to 647000	187000 to 263000
90	395000 to 15.8×10^6	1.68×10^6 to 7.72×10^6
95	16.8×10^6 to 3×10^8	26.6×10^6 to 78.3×10^6
	Mean = 1720	

Table 27. Uncertainty distribution for the mean particle size of invessel release after passing through a 'T' quencher 500 cm deep

Percentile	Values of d_p (μm) Characteristic of the indicated percentile at a confidence level, C, of	
	C = 90%	C = 50%
5	0.114 to 0.138	0.122 to 0.130
10	0.138 to 0.154	0.144 to 0.150
15	0.150 to 0.169	0.155 to 0.159
20	0.159 to 0.185	0.169 to 0.179
25	0.176 to 0.207	0.182 to 0.193
30	0.188 to 0.221	0.198 to 0.212
35	0.210 to 0.231	0.216 to 0.226
40	0.222 to 0.243	0.228 to 0.238
45	0.231 to 0.256	0.242 to 0.248
50	0.244 to 0.276	0.251 to 0.265
55	0.257 to 0.291	0.267 to 0.283
60	0.279 to 0.314	0.287 to 0.302
65	0.293 to 0.339	0.307 to 0.325
70	0.321 to 0.375	0.330 to 0.358
75	0.353 to 0.409	0.366 to 0.394
80	0.393 to 0.452	0.408 to 0.433
85	0.433 to 0.494	0.452 to 0.478
90	0.482 to 0.569	0.500 to 0.539
95	0.571 to 1.293	0.627 to 0.700
	Mean = 0.270 μm	

Table 28. Uncertainty distribution for the standard deviation invessel release after passing through a 'T' quencher 500 cm deep

Percentile	Values of σ Characteristic of the indicated percentile at a confidence level, C, of	
	C = 90%	C = 50%
5	1.0001 to 1.003	1.001 to 1.001
10	1.003 to 1.012	1.006 to 1.007
15	1.008 to 1.036	1.012 to 1.022
20	1.022 to 1.064	1.036 to 1.052
25	1.050 to 1.089	1.063 to 1.074
30	1.069 to 1.141	1.081 to 1.112
35	1.100 to 1.189	1.125 to 1.164
40	1.150 to 1.243	1.172 to 1.207
45	1.190 to 1.293	1.212 to 1.265
50	1.250 to 1.353	1.277 to 1.328
55	1.295 to 1.416	1.341 to 1.372
60	1.357 to 1.457	1.386 to 1.434
65	1.420 to 1.485	1.452 to 1.465
70	1.462 to 1.525	1.474 to 1.501
75	1.489 to 1.577	1.520 to 1.544
80	1.539 to 1.634	1.571 to 1.621
85	1.621 to 1.691	1.632 to 1.665
90	1.676 to 1.760	1.697 to 1.738
95	1.762 to 1.854	1.771 to 1.823
	Mean = 1.302	

be submerged to depths of 100, 200, 300, 500, and 700 cm. Selected features of these uncertainty distributions are summarized in Tables 29 through 33. Note that the uncertainty distributions were developed for logarithms of uncertain quantities. Actual values rather than logarithms are listed here to facilitate discussion.

The median, 10 percentile, and 90 percentile values of the decontamination factor associated with bubble formation at a 'T' quencher during gap release are shown as functions of quencher submergence in Figure 107. A similar plot of these decontamination factors for aerosol-laden gases released through a 'T' quencher during the invessel release phase of an accident is shown in Figure 108. In both of these figures, the bars indicate the limits of the 50 percent confidence level for median values and the 90 percent confidence level for the 10 and 90 percentile values.

Decontamination during formation and equilibration is rather insensitive to the depth of quencher submergence. There is much less than a factor of 10 change in the decontamination by bubble formation and equilibration as the assumed submergence of the 'T' quencher is varied from 100 to 700 cm.

Decontamination during the gap release is consistently, but modestly, less than decontamination during the invessel release phase. Decontamination by bubble formation during the gap release phase is much less than during the invessel release phase because gas flow velocities are so much higher during the gap release phase of a severe reactor accident. On the other hand, gas flowing to the suppression pool during the gap release phase is mostly steam. Consequently, equilibration of the gas with the suppression pool during gap removes a very large amount of aerosol material relative to the amount removed by the equilibration process during invessel release when a significant amount of noncondensible hydrogen is present in the gas.

The predicted decontamination factors during bubble formation and equilibration with the suppression pool can be correlated simply as constants for particular percentiles and phases of an accident. For gap release through a 'T' quencher:

- Median (50 percentile)

  $\log_{10}$ DF(FE) = 1.313
  DF(FE) = 20.6

- Lower Bound (10 percentile)

  $\log_{10}$ DF(FE) = 0.905
  DF(FE) = 8.0

- Upper Bound (90 percentile)

  $\log_{10}$ DF(FE) = 1.786
  DF(FE) = 61.0

Table 29. Summary of the uncertainty distributions for the decontamination factor associated with formation and equilibration of bubbles, DF(FE), during gap release and invessel release through 'T' quenchers

Quencher submergence (cm)	Decontamination factor, DF(FE)			
	Upper bound (90 percentile*)	Median (50 percentile**)	Lower bound (10 percentile*)	Mean
Gap release				
100	57.5 to 83.8	20.2 to 22.0	6.87 to 9.14	22.0
200	48.3 to 78.9	19.5 to 21.3	5.48 to 9.84	21.0
300	49.6 to 68.5	20.2 to 21.6	7.33 to 9.68	21.1
500	43.6 to 60.7	18.7 to 20.9	6.47 to 8.53	19.7
700	55.7 to 77.3	19.9 to 21.5	8.11 to 10.5	22.2
Invessel release				
100	368 to 783	28.9 to 33.5	4.92 to 7.33	47.1
200	406 to 1387	27.3 to 34.5	4.46 to 8.93	54.7
300	570 to 1871	25.9 to 31.3	4.93 to 7.24	51.0
500	197 to 413	24.7 to 29.0	4.08 to 5.16	36.1
700	189 to 333	28.6 to 30.4	5.08 to 7.34	34.0

*90 percent confidence level.
**50 percent confidence level.

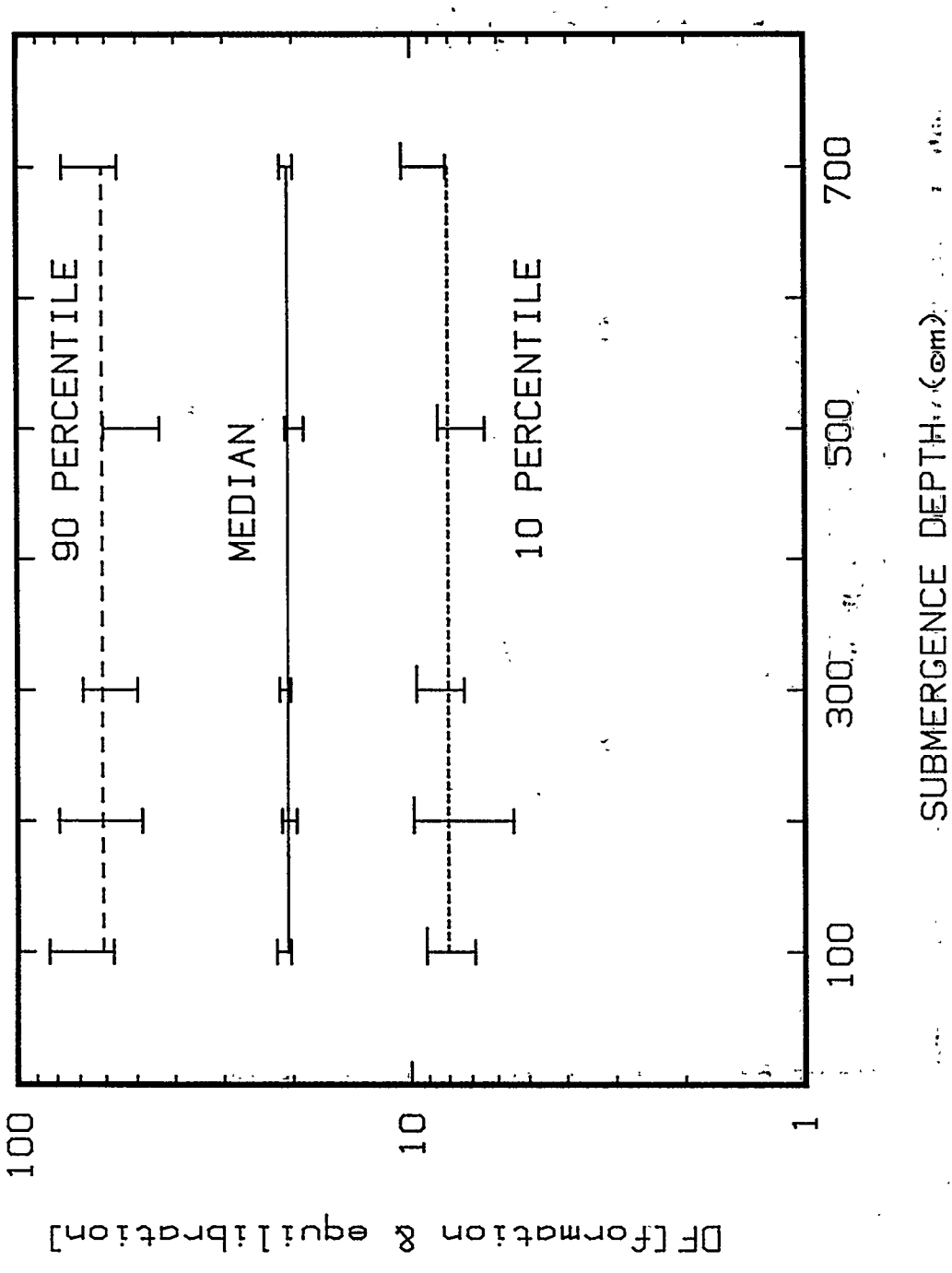

Figure 107. Variation of DF(FE) during gap release through a 'T' quencher with quencher submergence

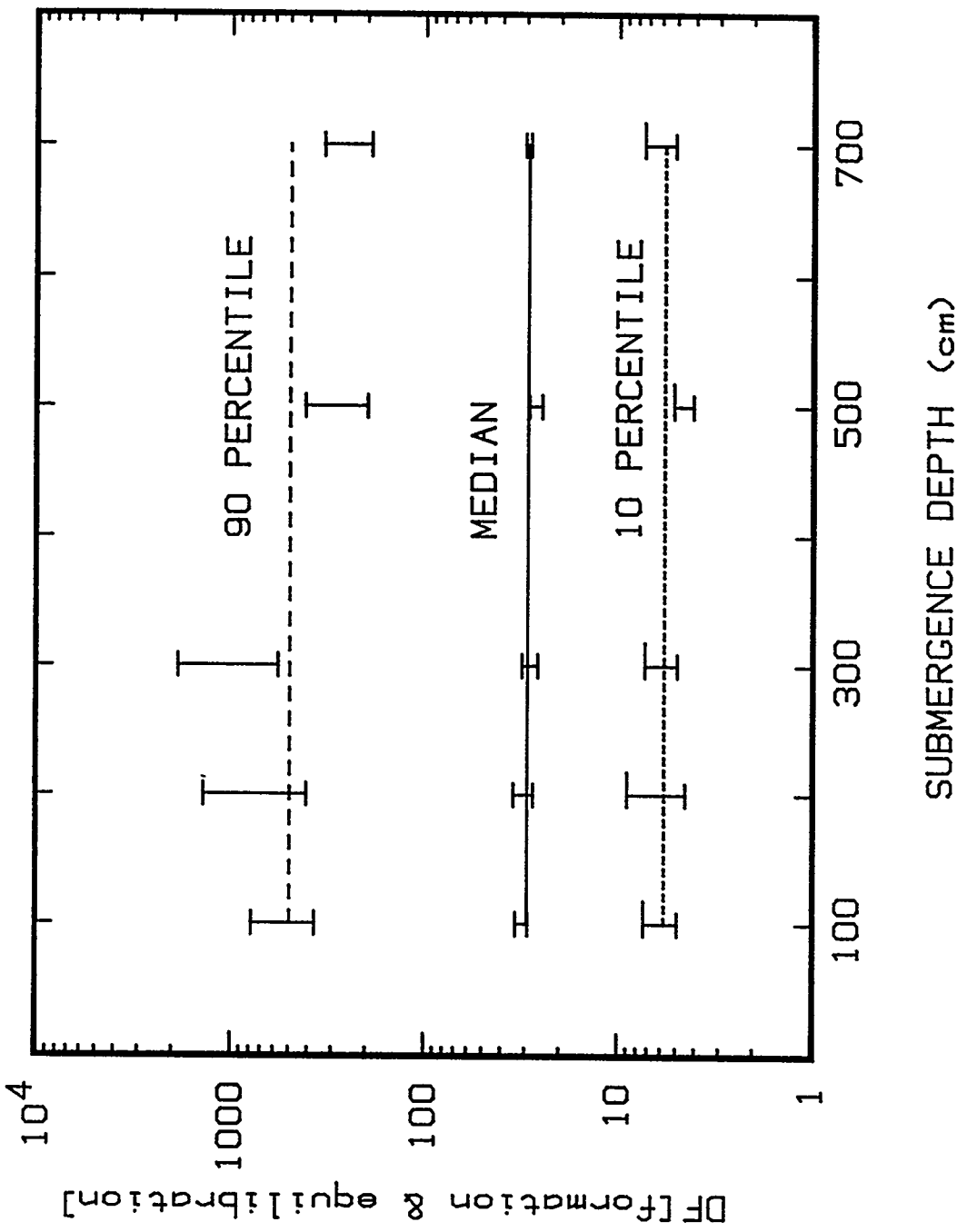

Figure 108. Variation in DF(FE) during invessel release through a 'T' quencher with quencher submergence

- Mean

  $\log_{10}$ DF(FE) = 1.326
  DF(FE) = 21.2

During invessel release through a 'T' quencher:

- Median (50 percentile)

  $\log_{10}$ DF(FE) = 1.466
  DF(FE) = 29.3

- Lower Bound (10 percentile)

  $\log_{10}$ DF(FE) = 0.760
  DF(FE) = 5.8

- Upper Bound (90 percentile)

  $\log_{10}$ DF(FE) = 2.695
  DF(FE) = 495

- Mean

  $\log_{10}$ DF(FE) = 1.642
  DF(FE) = 43.8

Note that no statistical significance is ascribed here to the means of the samples taken to construct the uncertainty distributions for decontamination by bubble formation and equilibration. It is, however, interesting that the mean values are rather similar to the median values. It appears that the uncertainty distributions for the decontamination factors associated with bubble formation and equilibration approximate lognormal distributions.

The decontamination associated with bubble formation and equilibration is most significant since historically this decontamination has not been considered in analyses of bubble rise through water pools [148, 153]. Some modeling of these decontamination processes is included in computer codes used for analyses of reactor accidents [6-9]. Systematic experimental studies of decontamination during the processes of bubble formation and equilibration have not been conducted. Results obtained here, then are strictly the products of modeling described in Chapter IV of this report. It would be useful to have some experimental validation of this modeling. Of particular interest would be studies of the effects of flow within the inflating bubble and the effects of bubble disintegration and coalescence on decontamination.

Much more attention has been devoted to decontamination of aerosol-laden gas bubbles as they rise through water pools. Results obtained here for decontamination as bubbles rise through suppression pools after emerging from 'T' quenchers are summarized in Table 30. Decontamination factors associated with bubble rise, DF(rise), are dependent on the submergences of the quenchers within the pools as is evident

Table 30. Summary of the uncertainty distributions for the decontamination factor associated with bubble rise through a suppression pool during gap release and invessel release through a 'T' quencher

Quencher submergence (cm)	Decontamination Factor, DF (rise) Upper bound (90 percentile*)	Median (50 percentile**)	Lower bound (10 percentile*)	Mean
Gap release				
100	2.56 to 3.93	1.33 to 1.43	1.10 to 1.13	1.66
200	8.01 to 16.6	2.44 to 2.70	1.27 to 1.44	3.24
300	44.8 to 120	3.35 to 3.76	1.54 to 1.66	6.71
500	118 to 762	5.52 to 7.14	1.96 to 2.24	13.6
700	4900 to 37800	19.7 to 26.5	2.88 to 3.65	82.4
Invessel release				
100	5.70 to 11.4	1.72 to 2.12	1.10 to 1.16	2.69
200	78.7 to 447	3.42 to 3.94	1.30 to 1.53	8.55
300	320 to 1570	5.42 to 6.22	1.51 to 1.89	16.0
500	2900 to 3100	12.4 to 17.1	2.08 to 2.54	47.6
700	11900 to 292000	24.4 to 39.9	2.94 to 3.74	153

*90 percent confidence level.
**50 percent confidence level.

from plots of DF(rise) against submergence shown in Figures 109 and 110 for the gap release and invessel release phases of an accident, respectively.

The first notable feature of the uncertainty distributions for decontamination during bubble rise is that these distributions are much wider as measured by the range from the 10 percentile to the 90 percentile. Much of this breadth is actually between the medians and the 90 percentiles. Combinations of small bubble size and large aerosol particles can lead to very extensive decontamination.

The next noticeable feature of results obtained here for DF(rise) is that values of the decontamination factor at the medians and 10 percentiles of the distributions are not large relative to decontamination produced by formation and equilibration of bubbles. Restricting attentions to median values, DF(rise) becomes comparable to DF(FE) only at the deepest submergences considered here.

Decontamination of aerosol-laden bubbles as they rise through the suppression pool is suppressed by the evaporation of water into the bubble as hydrostatic head is lost. (Note that this evaporation flux has been overlooked in many classic treatments of bubble decontamination [148, 153] though it has been included in models used for reactor accident analyses [6-9]). Plume effects shorten the opportunity for decontamination before the bubble reaches the pool surface.

The analyses here have included an effect that does produce decontamination during bubble rise. Bubbles that are large-enough will oscillate and undergo shape deformations as they rise. The movements of the bubble walls will sweep out particles too large to respond to the gas motions within the bubbles induced by bubble deformations. The authors are unaware of experimental studies of decontamination by shape oscillations that would validate the model of this process adopted here.

The results obtained for decontamination during bubble rise can be correlated linearly with quencher submergence, H. During the gap release phase:

- Median (50 percentile)

  $\log_{10} DF(rise) = -0.03007 + 1.892 \times 10^{-3} H(cm)$
  $DF(rise) = 10^{[(H - 15.9)/528]}$

- Lower Bound (10 percentile)

  $\log_{10} DF(rise) = -0.02609 + 0.746 \times 10^{-3} H(cm)$
  $DF(rise) = 10^{[(H-35)/1340]}$

- Upper Bound (90 percentile)

  $\log_{10} DF(rise) = -0.07191 + 5.777 \times 10^{-3} H(cm)$
  $DF(rise) = 10^{[(H-12.4)/173]}$

- Mean

  $\log_{10} DF(rise) = -0.04374 + 2.681 \times 10^{-3} H(cm)$
  $DF(rise) = 10^{[(H-16.3)/373]}$

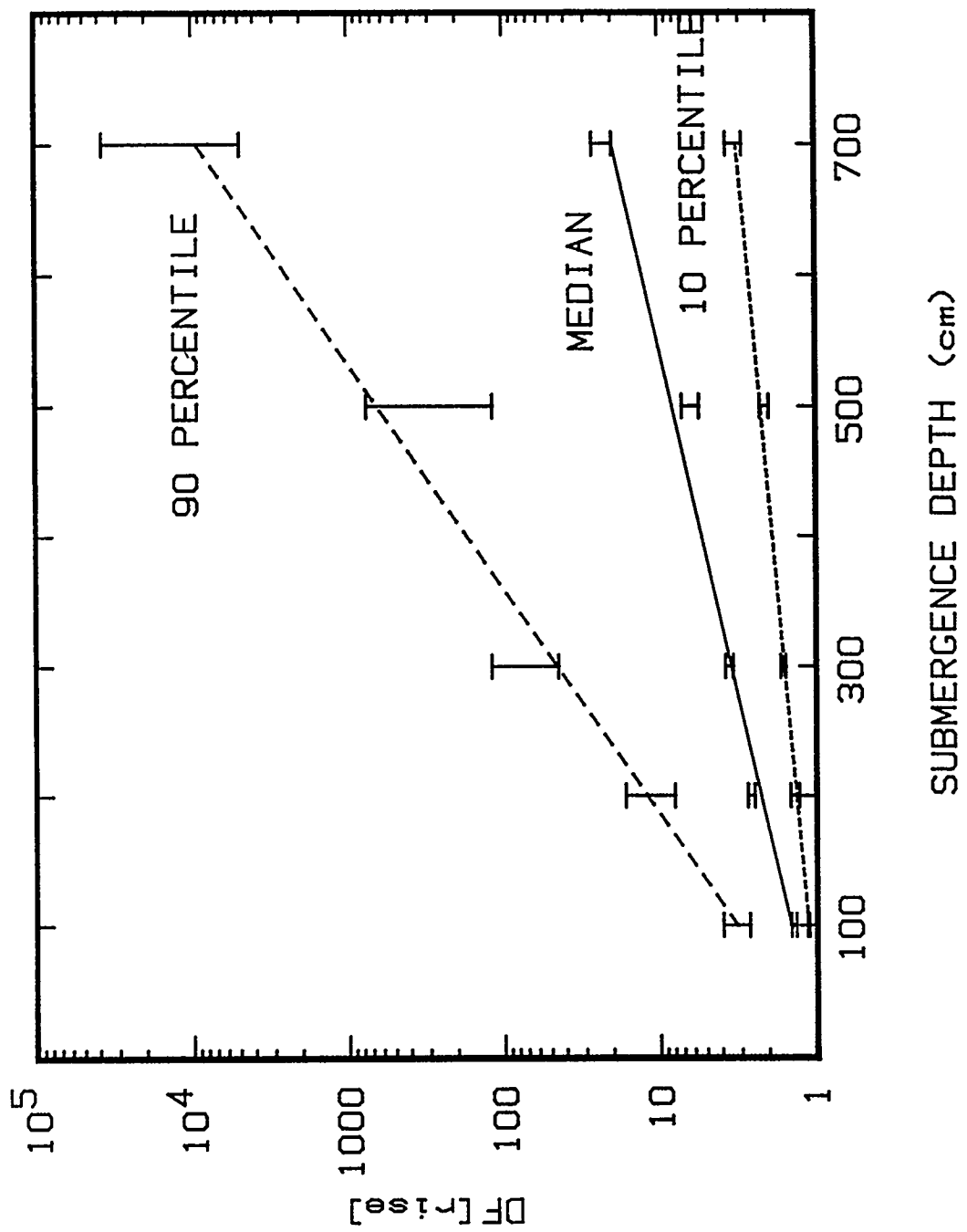

Figure 109. Variation in DF(rise) for gap release through a 'T' quencher with quencher submergence. The solid line are fits to medians of the uncertainty distributions. Dashed lines are fits to the midpoints of ranges for the 10 and 90 percentiles of the distributions.

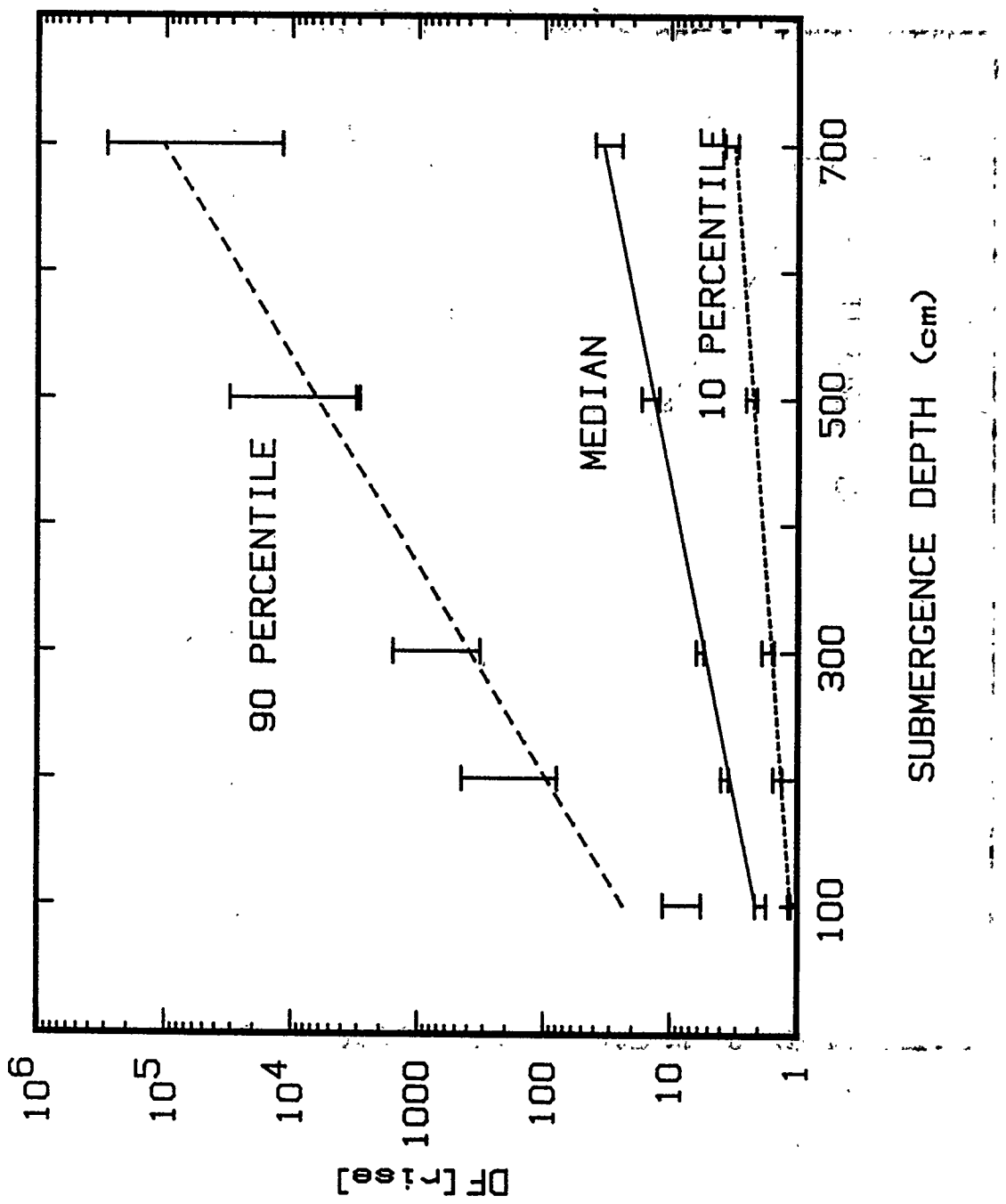

Figure 110. Variation in DF(rise) for invessel release through a 'T' quencher with quencher submergence

The correlations do not extrapolate to DF(rise) = 1 (no decontamination) at zero submergence. This is because the decontamination processes considered in the definition of DF(rise) were assumed inoperative in the injection zone between the quencher orifice and the point at which bubbles had equilibrated with the suppression pool.

Similar correlations of DF(rise) with quencher submergence during the invessel release phase are:

- Median (50 percentile)

  $\log_{10}$ DF(rise) = 0.1204 + 2.021 x 10^{-3} H(cm)
  DF(rise) = $10^{[(H + 59.6)/495]}$

- Lower Bound (10 percentile)

  $\log_{10}$ DF(rise) = -0.0261 + 0.746 x 10^{-3} H(cm)
  DF(rise) = $10^{[(H - 35)/1340]}$

- Upper Bound (90 percentile)

  $\log_{10}$ DF(rise) = 0.770 + 6.07 x 10^{-3} H(cm)
  DF(rise) = $10^{[(H + 127)/165]}$

  - Mean

    $\log_{10}$ DF(rise) = 0.286 + 2.78 x 10^{-3} H(cm)
    DF(rise) = $10^{[(H + 103)/360]}$

Note that at the high levels of decontamination characteristic of deeper submergences, the logarithm of DF(rise) does not vary linearly with depth. This is because of changes in the size distribution caused by decontamination during bubble rise which is discussed further below. More complicated correlations would have to be developed to account for the decreasing efficiency of decontamination with depth and the effects of the injection zone described above. Suffice it to say here that these correlations ought not be extrapolated to deeper or shallower submergences than those considered in developing the correlations.

The total decontamination of aerosol-laden gases is, of course, the product of the effects of bubble formation and equilibration and the effects of bubble rise. Because there is some correlation of these effects in any of the samples used to construct the uncertainty distributions, the distributions for the decontamination by formation and equilibration cannot be simply combined with distributions for decontamination during bubble rise to produce a distribution for the total decontamination, DF(total). Instead, distributions for DF(total) have to be constructed from sampled results. The distributions for DF(total) during the gap release and invessel release phases of the accident are summarized in Table 31. These results are also shown as plots of DF(total) against the assumed submergence of the 'T' quencher in Figures 111and 112.

Note that the upper bound or 90 percentile values of the total decontamination factor exceed 10^6 for the deeper submergences of the quencher. The authors are not persuaded that the models they have

Table 31. Summary of the uncertainty distributions for the total decontamination factor for material released to a suppression pool during gap release and invessel release through a 'T' quencher

Quencher submergence (cm)	Decontamination factor			
	Upper bound (90 percentile*)	Median (50 percentile**)	Lower bound (10 percentile*)	Mean
Gap release				
100	115 to 146	31.8 to 36.2	9.59 to 13.0	36.5
200	257 to 557	58.6 to 64.3	13.7 to 20.5	67.9
300	1190 to 3400	85.5 to 93.8	17.7 to 24.0	142
500	2450 to 15600	142 to 163	18.8 to 36.0	269
700	146000 to 1.3×10^6	497 to 721	42.2 to 63.0	1840
Invessel release				
100	1020 to 7130	64.4 to 71.6	7.11 to 11.4	127
200	11900 to 244000	147 to 200	10.8 to 19.8	468
300	73500 to 1.3×10^6	214 to 275	14.6 to 22.2	820
500	395000 to 15×10^6	440 to 548	13.2 to 26.3	1720
700	2.3×10^6 to 22×10^6	895 to 1580	28.0 to 49.5	52000

*90 percent confidence level.
**50 percent confidence level.

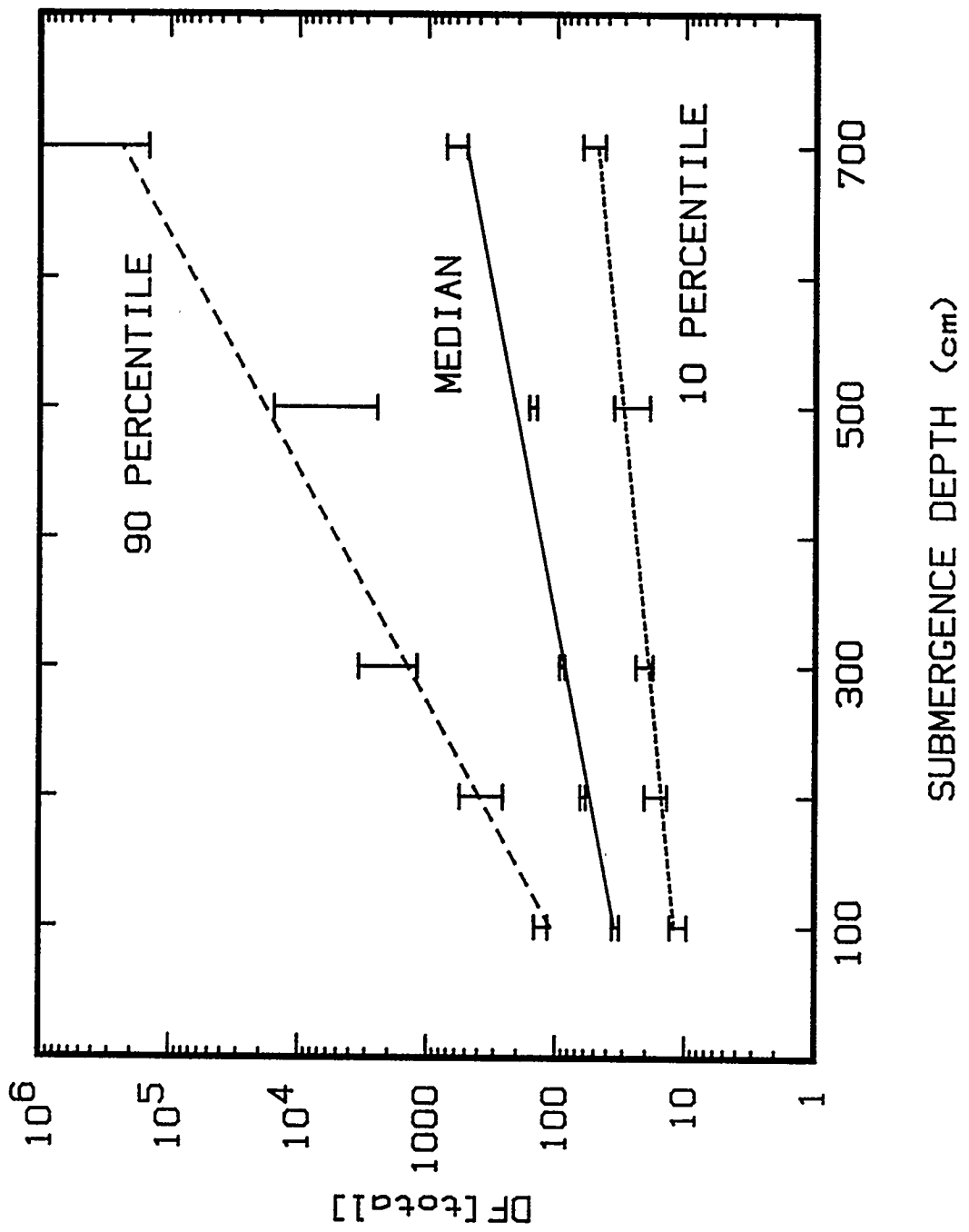

Figure 111. Variation in DF(total) during gap release through a 'T' quencher with quencher submergence

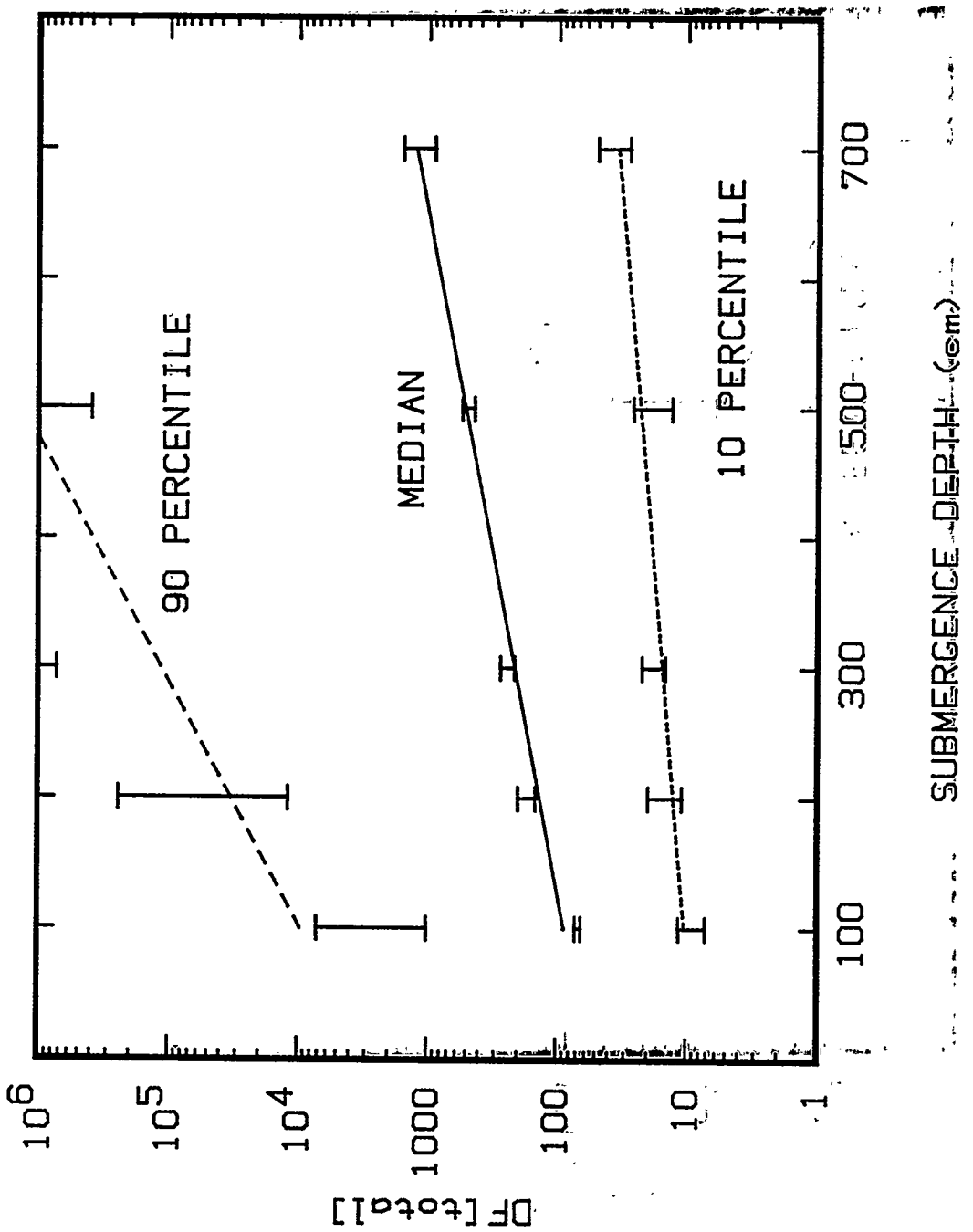

Figure 112. Variation of DF(total) during invessel release through a 'T' quencher with quencher submergence

used are sufficiently accurate to place much faith in such nearly quantitative decontamination. To be sure, the models used here have neglected re-entrainment of contaminated liquids when bubbles break at the pool surface. Such re-entrainment, especially later in an accident, will limit the apparent decontamination based on the radioactivity of gases above a water pool to values of about 10^6. Consequently, the authors recommend that decontamination factors calculated to be greater than 10^6 be interpreted as 10^6.

The efficiencies of many of the processes that lead to decontamination are dependent on the aerosol particle size. Certainly, this is true for decontamination during bubble formation and during bubble rise. Particle-size dependence of decontamination during bubble equilibration is expected to be small and has been neglected here.

Because of the particle-size dependencies of the decontamination processes, the size distribution of aerosols that do emerge from the suppression pool can be quite different than the size distributions of the aerosols that enter the suppression pool. Typically, it is found that the decontamination processes are very efficient for very large and very small aerosol particles, but there is an intermediate particle size for which the combination of all aerosol removal processes has minimal efficiency. As discussed at some length in Chapter IV, the size of minimal removal efficiency is sensitive to details of the modeling. Notably, it is sensitive to removal by inertial impaction modeling both during bubble formation and bubble rise.

Because of the size dependence of aerosol removal processes, the aerosol that emerges from the suppression pool will have a size distribution that is narrower than the size distribution injected into the pool. The mean of the size distribution of aerosol emerging from the pool will be shifted toward the size of minimal aerosol removal efficiency. As decontamination progresses the aerosol size distribution will become very sharply peaked at this size of minimum removal efficiency. The rate of decontamination drops from high values when large or small particles were being rapidly removed to the minimal rate.

These expectations concerning the changes of the aerosol size distribution caused by passage through the suppression pool are reflected in the results obtained here. The size distribution of aerosol emerging from the pool was characterized by a mass weighted mean d_p (μm), and a standard deviation, σ. Uncertainty distributions for d_p (μm) and σ are summarily described in Tables 32 and 33. Values of d_p (μm) and σ are plotted against the assumed submergence of the 'T' quencher in Figures 113 to 116.

The characteristic features of the mean particle size decrease modestly with increasing submergence of the 'T' quencher. Much of the change in the size distribution occurs by very rapid removal of large and small particles during bubble formation and over rise distances of less that one meter. Continued change in the size distribution is not rapid because particles that remain in bubbles are difficult to remove. Some removal does still occur preferentially at the tails of the distributions since the standard deviations decrease with increasing submergence of the 'T' quencher.

Interestingly, the mean size of aerosol emerging from the suppression pool is consistently smaller during the gap release phase of the accident than during the invessel release phase. This is largely due to:

- somewhat smaller bubbles are, on average, expected to be present during the gap release phase, and

Table 32. Summary of the uncertainty distributions for the mean size of aerosol particles emerging from a suppression pool during gap release and invessel release through a 'T' quencher

Quencher submergence (cm)	Mean particle size (μm) Upper bound (90 percentile*)	Median (50 percentile**)	Lower bound (10 percentile*)	Mean
Gap release				
100	0.143 to 0.166	0.094 to 0.097	0.079 to 0.081	0.105
200	0.139 to 0.159	0.097 to 0.101	0.081 to 0.084	0.104
300	0.137 to 0.149	0.100 to 0.103	0.082 to 0.085	0.106
500	0.139 to 0.160	0.102 to 0.105	0.084 to 0.089	0.108
700	0.143 to 0.154	0.109 to 0.111	0.088 to 0.093	0.113
Invessel release				
100	0.508 to 0.573	0.302 to 0.319	0.174 to 0.195	0.331
200	0.634 to 0.771	0.313 to 0.331	0.147 to 0.180	0.330
300	0.517 to 0.655	0.268 to 0.281	0.147 to 0.166	0.289
500	0.482 to 0.569	0.251 to 0.265	0.138 to 0.154	0.270
700	0.464 to 0.617	0.245 to 0.251	0.127 to 0.143	0.258

*90 percent confidence level.
**50 percent confidence level.

Table 33. Summary of the uncertainty distributions for the standard deviation of the size distribution of aerosol particles emerging from a suppression pool during gap release and invessel release through a 'T' quencher

Quencher submergence (cm)	Decontamination factor			
	Upper bound (90 percentile*)	Median (50 percentile**)	Lower bound (10 percentile*)	Mean
Gap release				
100	1.604 to 1.644	1.429 to 1.456	1.221 to 1.261	1.430
200	1.573 to 1.621	1.409 to 1.436	1.224 to 1.265	1.415
300	1.562 to 1.594	1.385 to 1.405	1.211 to 1.241	1.394
500	1.522 to 1.593	1.370 to 1.379	1.240 to 1.272	1.388
700	1.474 to 1.531	1.333 to 1.348	1.203 to 1.222	1.348
Invessel release				
100	1.801 to 1.921	1.446 to 1.470	1.030 to 1.090	1.431
200	1.709 to 1.774	1.311 to 1.370	1.010 to 1.034	1.333
300	1.678 to 1.744	1.322 to 1.348	1.007 to 1.026	1.324
500	1.676 to 1.760	1.277 to 1.328	1.003 to 1.012	1.302
700	1.540 to 1.661	1.204 to 1.245	1.002 to 1.012	1.254

*90 percent confidence level.
**50 percent confidence level.

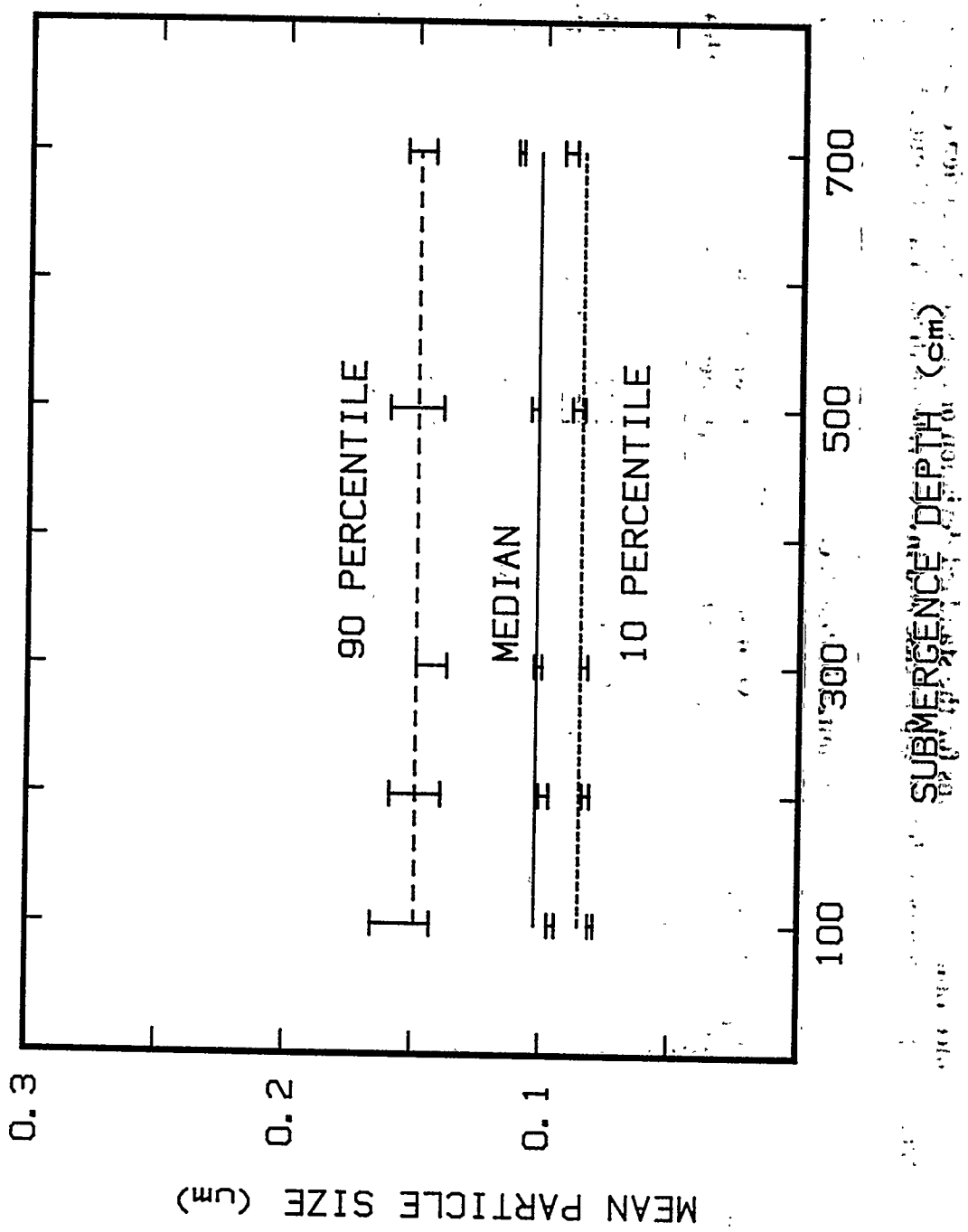

Figure 113. Variation of the mean size of aerosol particles that emerge from a suppression pool during gap release through a 'T' quencher with quencher submergence

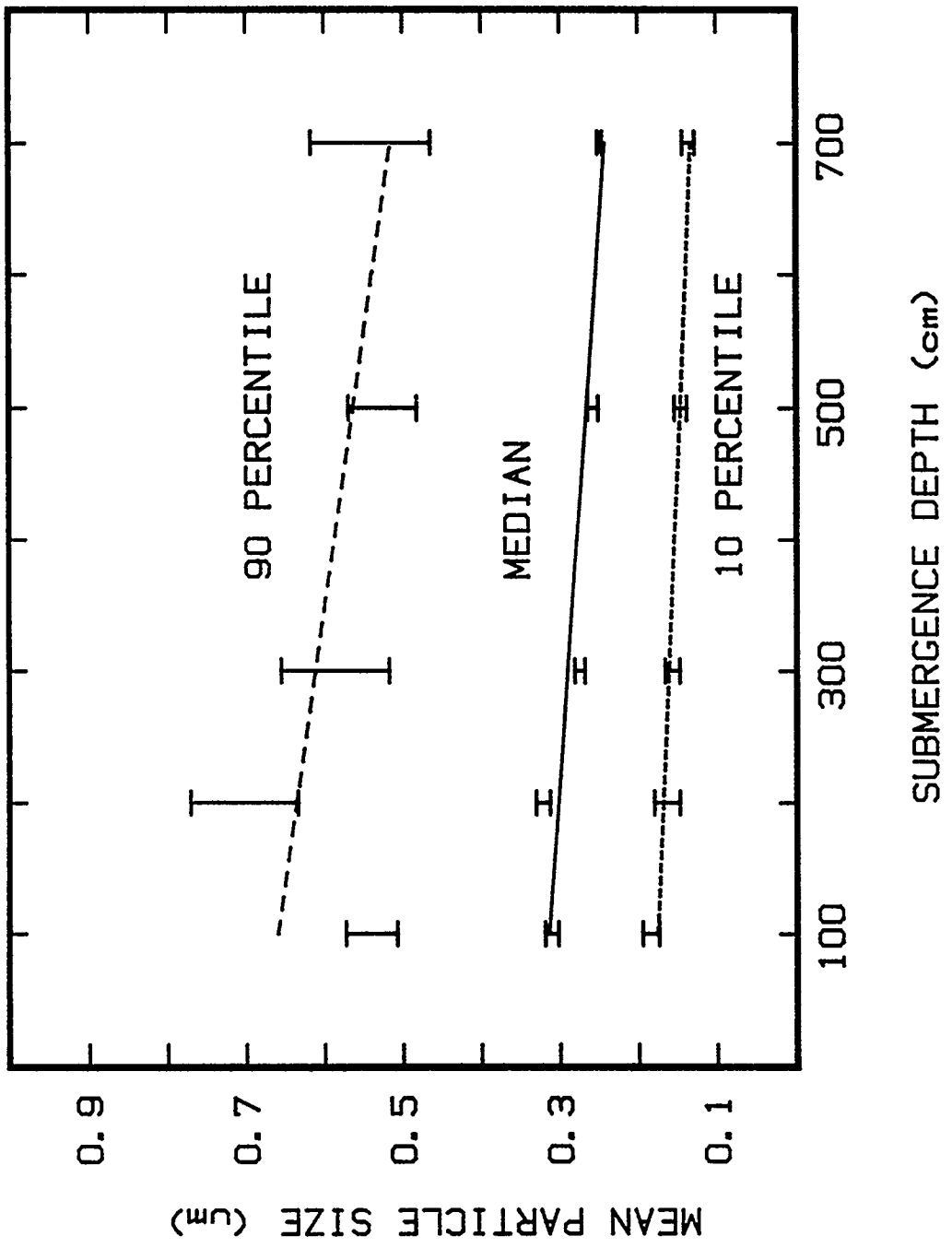

Figure 114. Variation of the mean size of aerosol particles that emerge from a suppression pool during invessel release through a 'T' quencher with quencher submergence

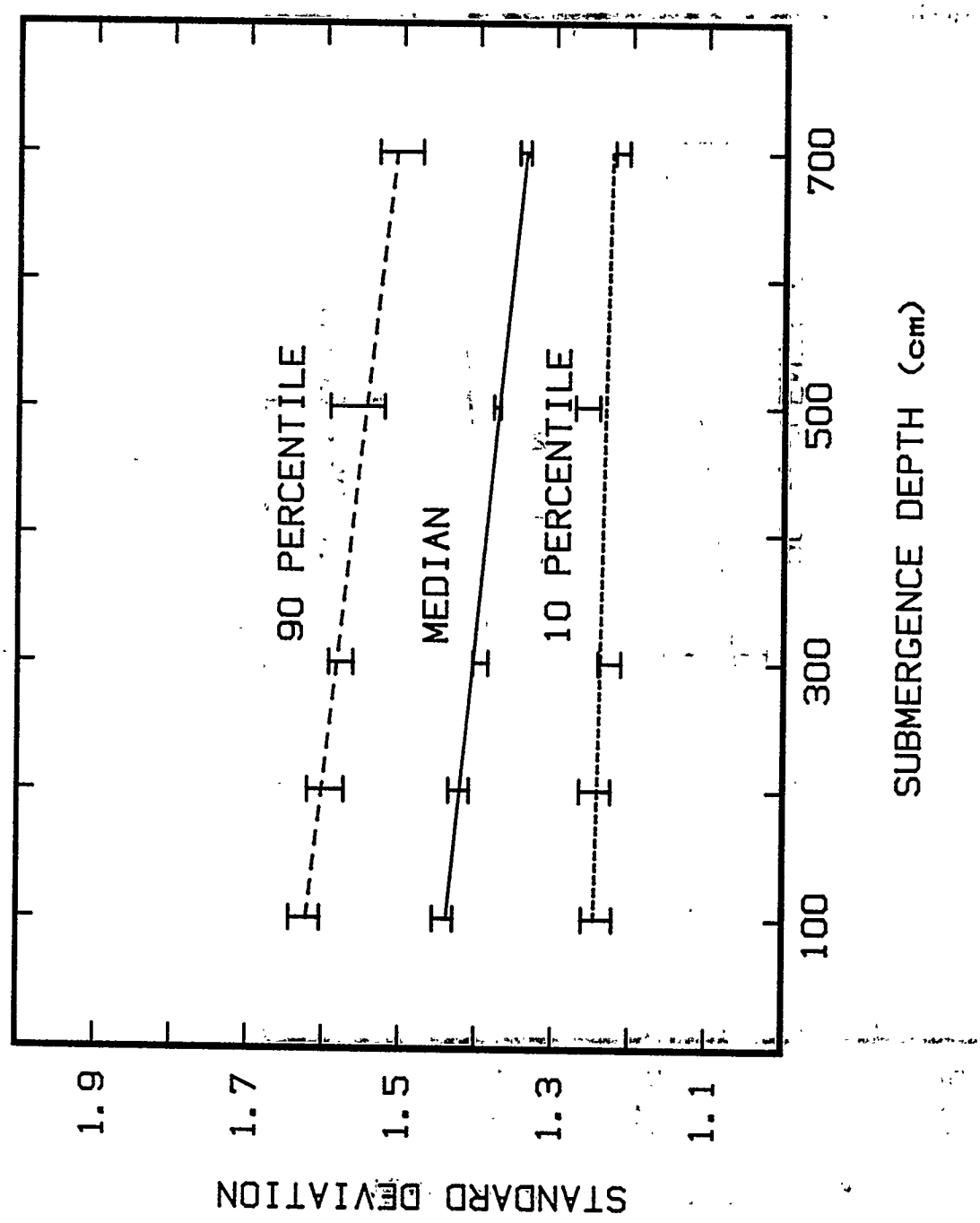

Figure 115. Variation of the standard deviation of the size distribution of aerosol particles that emerge from a suppression pool during gap release through a 'T' quencher with quencher submergence

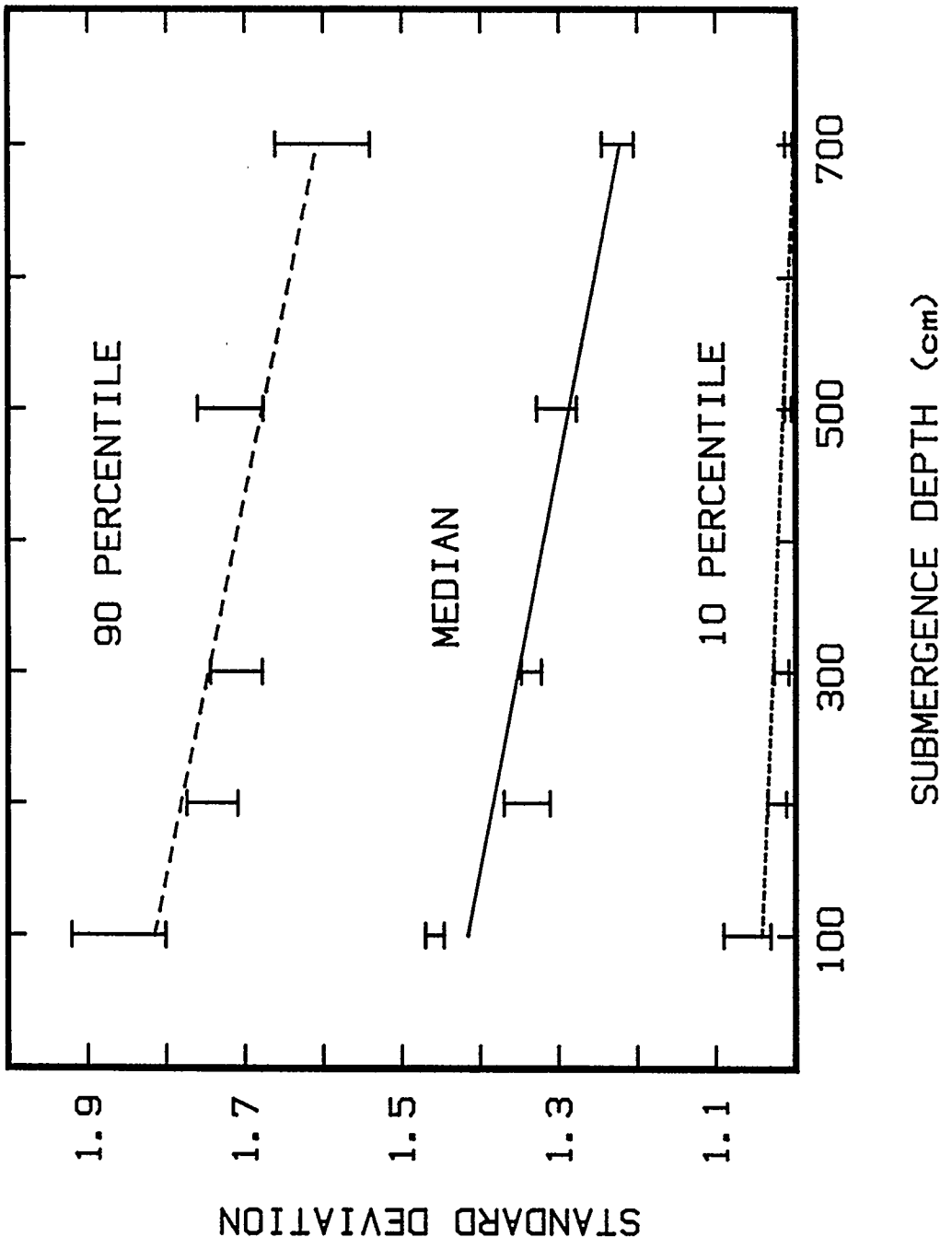

Figure 116. Variation of the standard deviation of the size distribution of aerosol particles that emerge from a suppression pool during invessel release through a 'T' quencher with quencher submergence

- because much of the gas entering the suppression pool during the gap release phase is condensed, plume effects on the rise velocities of gas bubbles are smaller than during the invessel release phase.

It is noteworthy that the uncertainty distributions for the mean particle size of aerosol emerging from the pool are not especially large. Accurate measurements of the mean particle size could be useful for validating the modeling used for this work, but would not be useful for identifying the causes of discrepancies between predictions and observations. Unfortunately, accurately measuring size distributions in the predicted range is challenging.

It should be noted also that the standard deviations of the size distributions found here are small, even at high percentiles of the uncertainty distributions, relative to standard deviations of size distributions measured for aerosols directly from the generation processes. To a defensible level of approximation, certainly at the 50 percentile range, aerosols that emerge from suppression pools are nearly monodisperse. (It was, in fact, for the purposes of generating monodisperse aerosols that decontamination by bubble rises through water pools was first studied [148]). The emerging particles from pools are narrowly distributed around size that are slow to be removed by the pool and often found to be only slowly removed by other processes including filtration and the actions of water sprays.

B. Decontamination During Release Through 'X' Quenchers

Exploratory calculations suggested results obtained for decontamination of gap release material discharged through an 'X' quencher would be little different than results obtained for gap release through a 'T' quencher. Certainly, gap release is only a small fraction of the radioactivity released during a severe accident so whatever small differences arise between discharge to a pool through a 'T' quencher and discharge through an 'X' quencher ought to be negligible.

Calculations were done for invessel release through an 'X' quencher. Qualitatively, results were entirely analogous to results obtained for invessel release through a 'T' quencher. These results for invessel release through 'X' quenchers are summarized in Tables 34 through 38 and are plotted against quencher submergence in Figures 117 through 121.

Correlations of the results obtained for decontamination by bubble formation and equilibration at an 'X' quencher are:

- Median (50 percentile)

  $\log_{10}$ DF(FE) = 1.640
  DF(FE) = 43.6

- Lower Bound (10 percentile)

  $\log_{10}$ DF(FE) = 0.852
  DF(FE) = 7.12

Table 34. Summary of the uncertainty distributions for the decontamination factor associated with formation and equilibration of bubbles, DF(FE), during invessel release through an 'X' quencher

Quencher submergence (cm)	Decontamination factor, DF(FE)			
	Upper bound (90 percentile*)	Median (50 percentile**)	Lower bound (10 percentile*)	Mean
Invessel release				
100	723 to 2930	49.4 to 62.2	7.11 to 8.89	91.4
200	908 to 3910	43.4 to 51.3	6.65 to 8.79	14.8
300	562 to 2170	36.1 to 40.0	6.10 to 7.89	63.8
500	450 to 1770	35.6 to 44.6	6.22 to 8.32	55.1
700	613 to 1900	34.7 to 46.6	4.53 to 7.98	61.9

*90 percent confidence level.
**50 percent confidence level.

Table 35. Summary of the uncertainty distributions for the decontamination factor associated with bubble rise through a suppression pool, DF(rise), during invessel release through an 'X' quencher

Quencher submergence (cm)	Decontamination factor, DF(rise)			
	Upper bound (90 percentile*)	Median (50 percentile**)	Lower bound (10 percentile*)	Mean
Invessel release				
100	10.6 to 18.2	1.86 to 2.01	1.14 to 1.20	2.94
200	56.0 to 180	3.30 to 3.52	1.28 to 1.44	7.59
300	453 to 9910	5.75 to 6.87	1.44 to 1.71	18.0
500	339000 to 6.2×10^6	17.5 to 25.3	1.88 to 3.30	157
700	13000 to 828000	36.1 to 54.0	2.22 to 3.84	162

*90 percent confidence level.
**50 percent confidence level.

Table 36. Summary of the uncertainty distributions for the total decontamination factor, DF(total), for material released to a suppression pool during invessel release through an 'X' quencher

Quencher submergence (cm)	Decontamination factor, DF(total)			
	Upper bound (90 percentile*)	Median (50 percentile**)	Lower bound (10 percentile*)	Mean
Invessel Release				
100	3890 to 27800	57.3 to 123	9.55 to 17.6	268
200	7670 to 98400	179 to 223	13.4 to 21.1	679
300	458000 to 3.3×10^6	232 to 360	13.8 to 27.2	1150
500	3.3×10^6 to 656×10^6	1050 to 1860	19.8 to 45.2	8670
700	2.8×10^6 to 1.5×10^9	2275 to 3860	27.7 to 70.3	9890

*90 percent confidence level.
**50 percent confidence level.

Table 37. Summary of the uncertainty distributions for the mean size of aerosol particles emerging from a suppression pool during invessel release through an 'X' quencher

Quencher submergence (cm)	Mean particle size (μm)			
	Upper bound (90 percentile*)	Median (50 percentile**)	Lower bound (10 percentile*)	Mean
Invessel release				
100	0.534 to 0.633	0.279 to 0.305	0.156 to 0.171	0.302
200	0.564 to 0.691	0.272 to 0.297	0.141 to 0.167	0.293
300	0.487 to 0.594	0.255 to 0.268	0.134 to 0.158	0.269
500	0.501 to 0.625	0.255 to 0.265	0.126 to 0.152	0.272
700	0.499 to 0.616	0.243 to 0.261	0.117 to 0.137	0.260

*90 percent confidence level.
**50 percent confidence level.

Table 38. Summary of the uncertainty distributions for the standard deviation of the size distributions of aerosol particles emerging from a suppression pool during invessel release through an 'X' quencher

Quencher submergence (cm)	Standard deviation, σ			
	Upper bound (90 percentile*)	Median (50 percentile**)	Lower bound (10 percentile*)	Mean
Invessel Release				
100	1.745 to 1.849	1.380 to 1.412	1.007 to 1.055	1.376
200	1.688 to 1.776	1.329 to 1.362	1.002 to 1.019	1.330
300	1.703 to 1.786	1.312 to 1.376	1.007 to 1.013	1.327
500	1.613 to 1.701	1.191 to 1.244	1.0007 to 1.004	1.260
700	1.523 to 1.641	1.127 to 1.175	1.0004 to 1.006	1.216

*90 percent confidence level.
**50 percent confidence level.

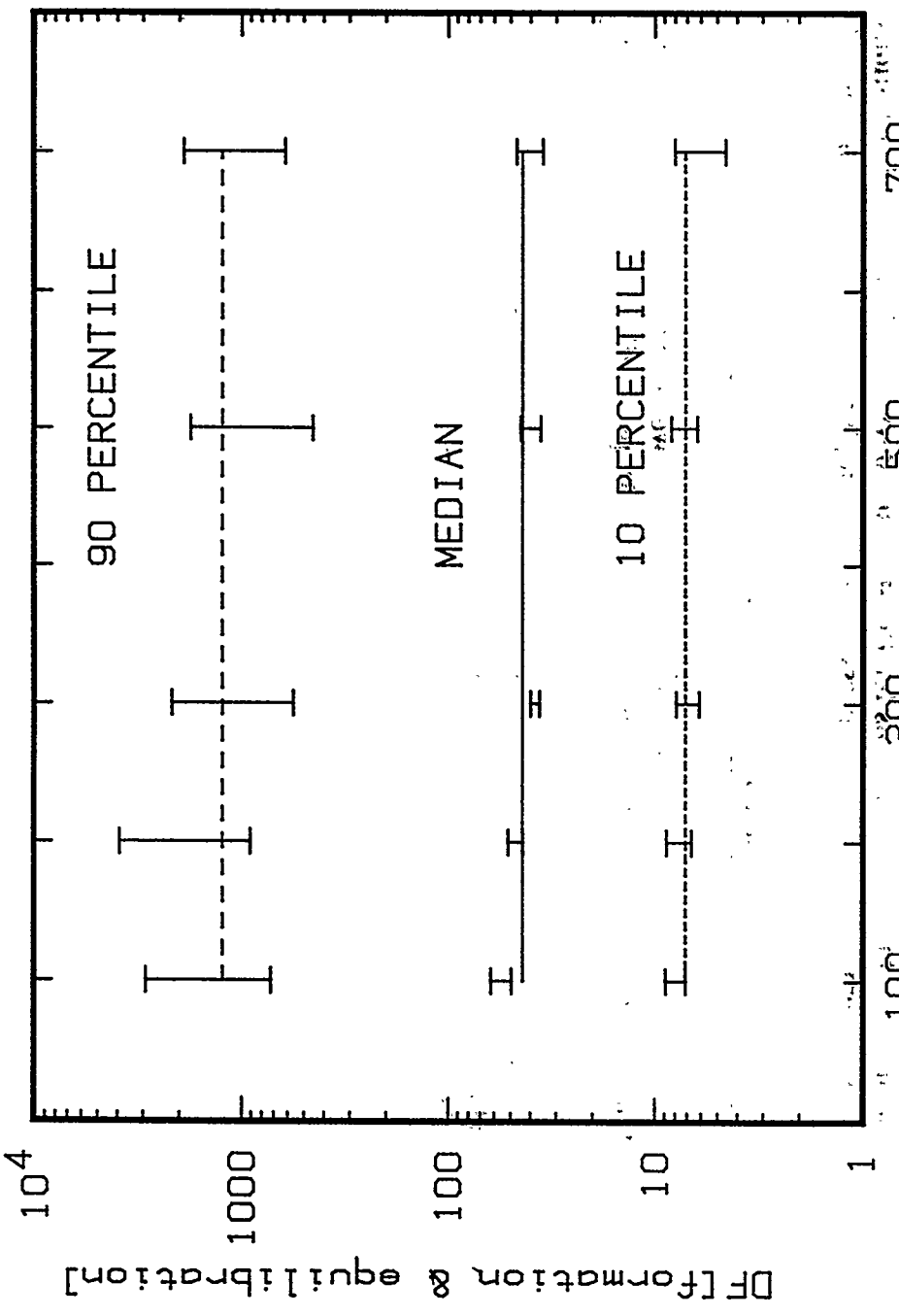

Figure 117. Variation of DF(FE) for invessel release through an 'X' quencher with quencher submergence

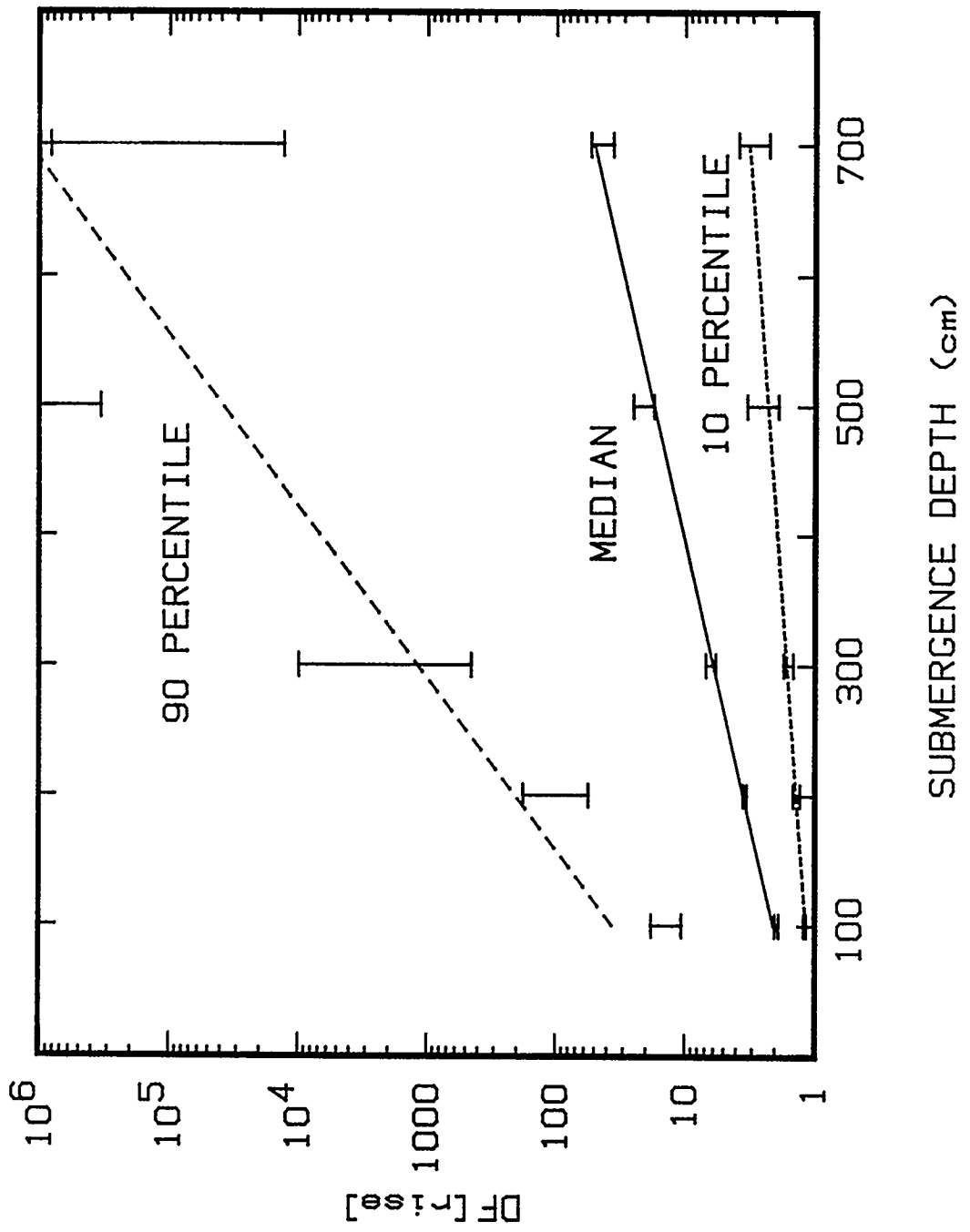

Figure 118. Variation of DF(rise) for invessel release through an 'X' quencher with quencher submergence

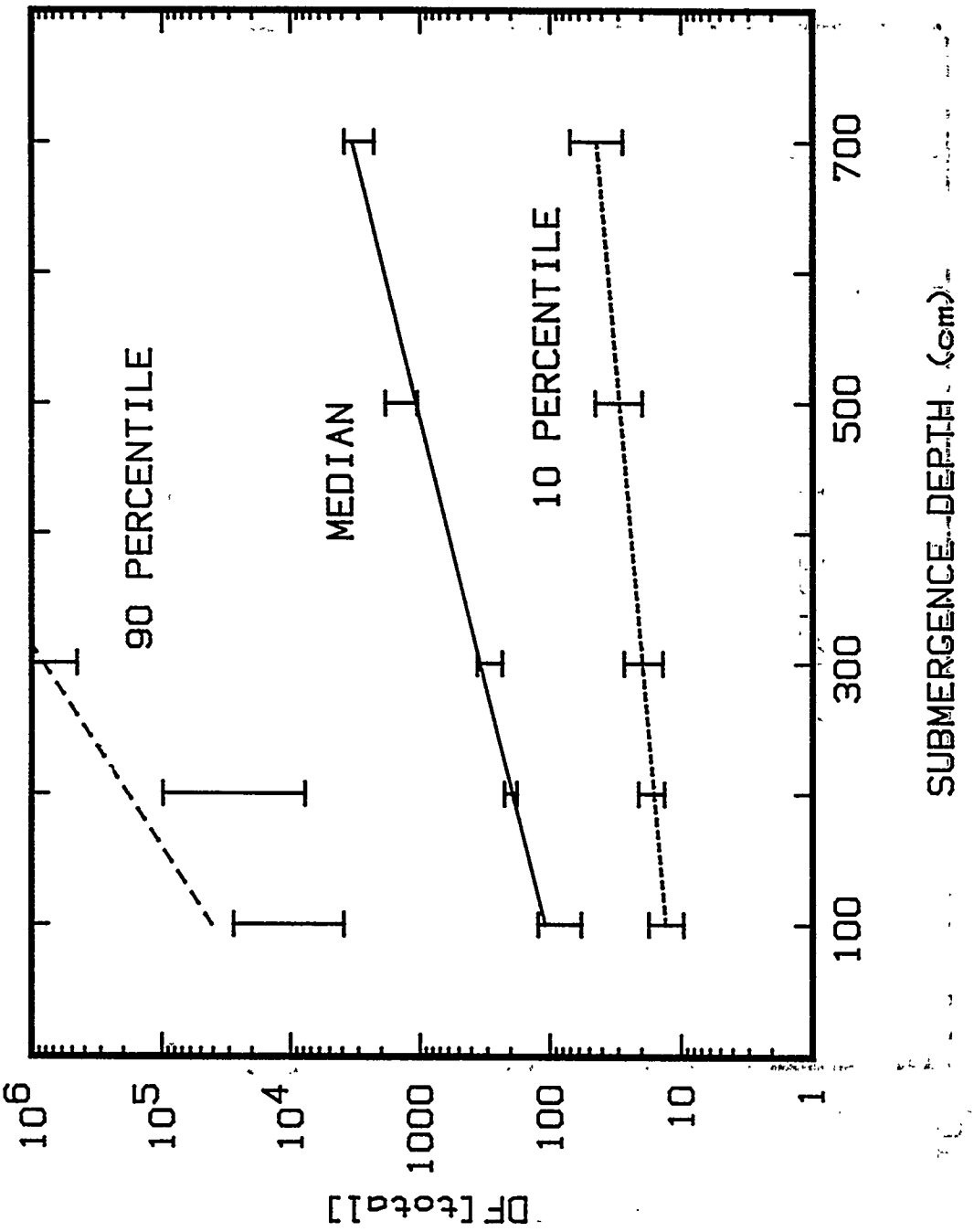

Figure 119. Variation of DF(total) for invessel release through an 'X' quencher with quencher submergence

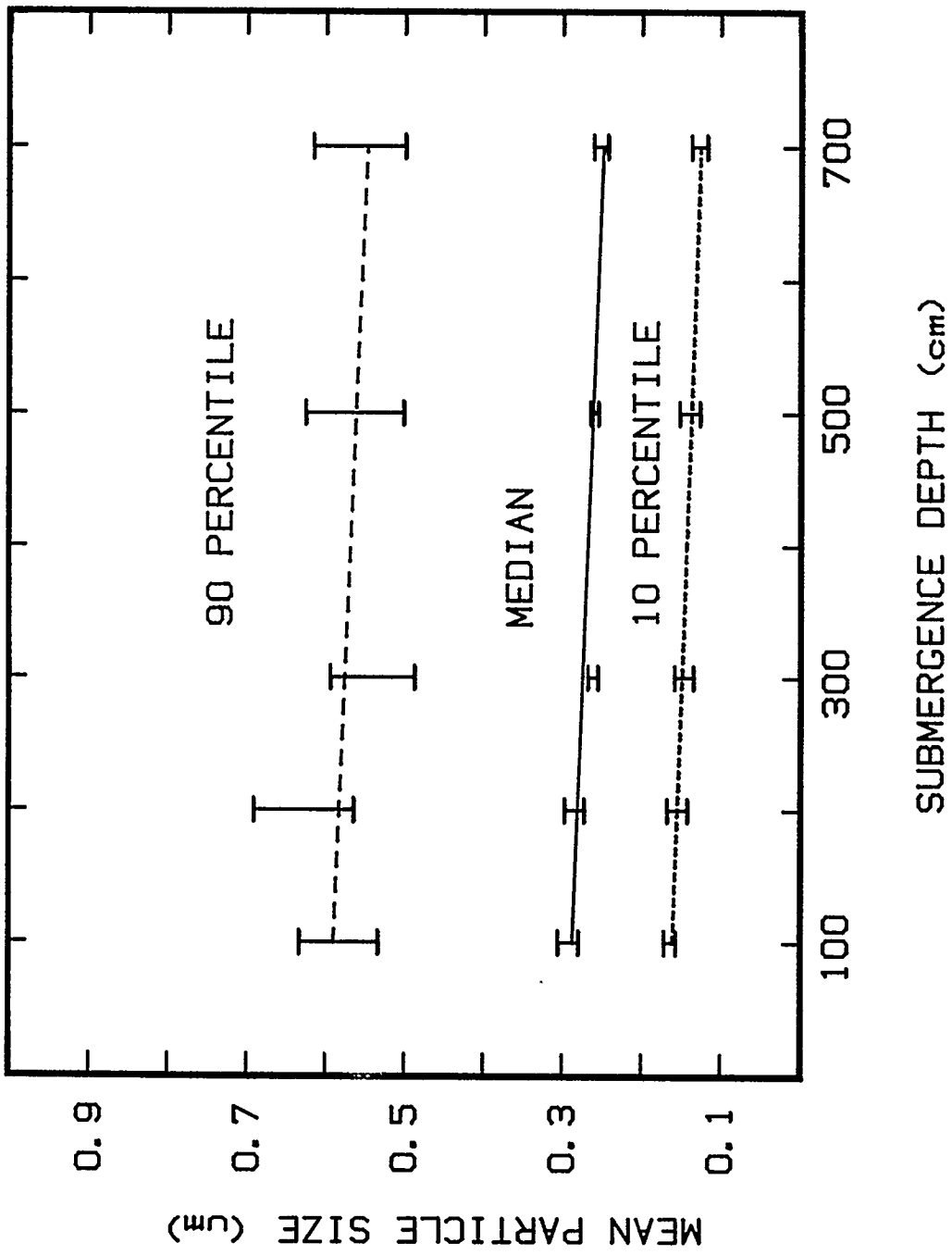

Figure 120. Variation of the mean size of aerosol particles emerging from a suppression pool for invessel release through an 'X' quencher with quencher submergence

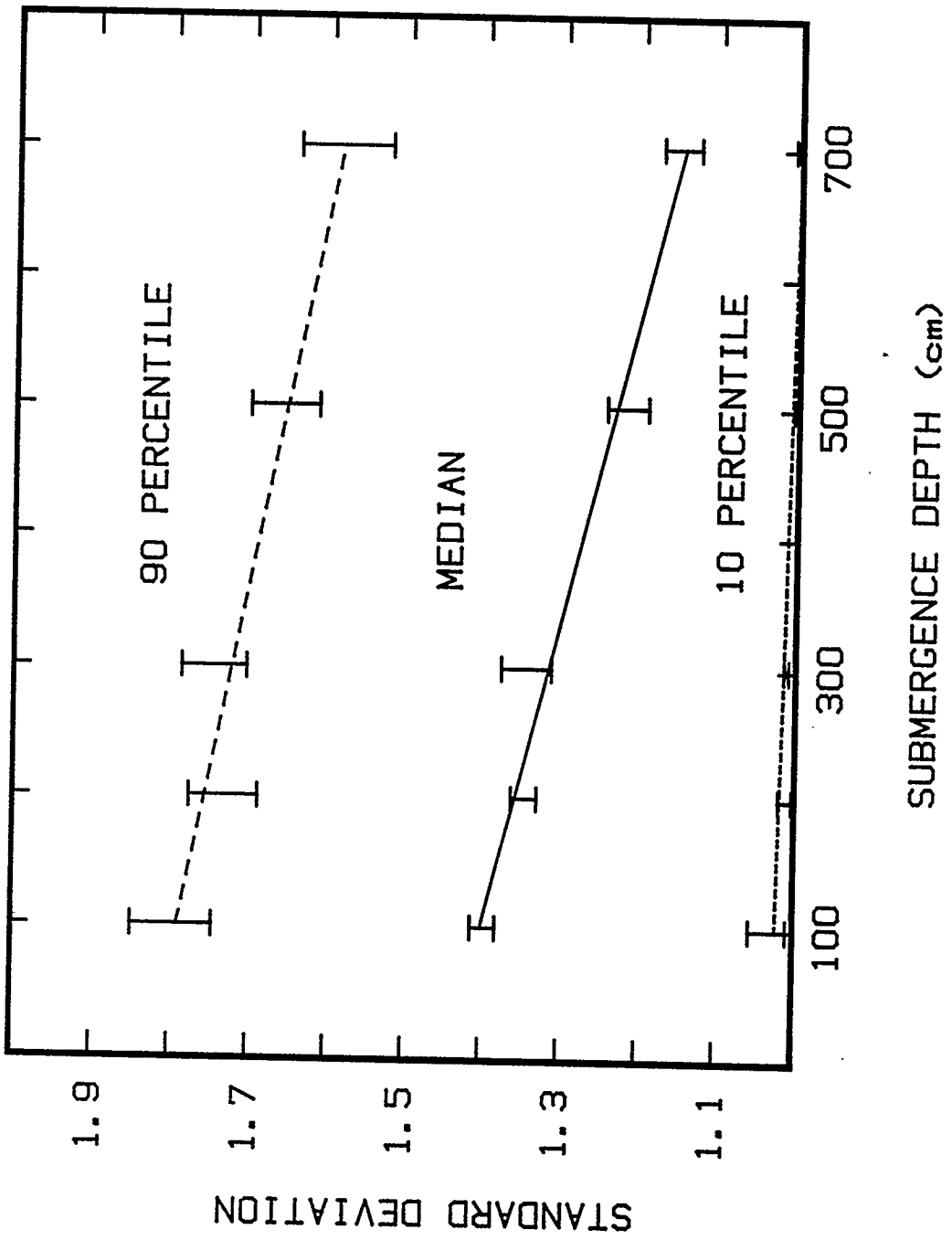

Figure 121. Variation in the standard deviation of the size distribution of aerosols emerging from a suppression pool for invessel release through an 'X' quencher with quencher submergence

- Upper Bound (90 percentile)

  $\log_{10}$ DF(FE) = 3.093
  DF(FE) = 1240

- Mean

  $\log_{10}$ DF(FE) = 1.849
  DF(FE) = 70.6

Correlations of decontamination during bubble rise with the depth of submergence, H(cm), of an 'X' quencher are:

- Median (5 percentile)

  $\log_{10}$ DF(rise) = 0.0836 + 2.315 x 10^{-3} H(cm)

- Lower Bound (10 percentile)

  $\log_{10}$ DF(rise) = -0.0078 + 0.731 x 10^{-3} H(cm)

- Upper Bound (90 percentile)

  $\log_{10}$ DF(rise) = 0.812 + 7.548 x 10^{-3} H(cm)

- Mean

  $\log_{10}$ DF(rise) = 0.283 + 3.107 x 10^{-3} H(cm)

Decontamination by discharge through an 'X' quencher differs by a small amount from decontamination by discharge through a 'T' quencher. Most of the difference is due to differences in the decontamination during bubble formation and equilibration. A detailed examination of the results to identify the exact cause of the difference has not been undertaken. It appears, however, that the narrower range of wetwell pressures considered for the 'X' quencher case in comparison to the range for 'T' quenchers is responsible. Wetwell pressure will affect both the rate of bubble formation and consequently the bubble size at the point bubbles detach from orifices. This, in turn, will affect predictions of particle capture by impaction and by diffusion.

VII. Simplified Model

A simplified model of decontamination by steam suppression pools is constructed by correlation of the results obtained in the Monte Carlo uncertainty analysis. The critical features of decontamination by suppression pools that need to be predicted by a simplified model are:

- total decontamination, and
- size distribution of the emerging aerosol

It is assumed for the development of this model that the decontamination processes are strictly physical so the composition of the aerosol that emerges from a suppression pool is exactly the same as the composition of aerosol discharged to the pool. That is, mechanisms to preferentially deplete or enrich the emerging aerosol in radionuclides are not known.

It is further assumed that the emerging aerosol has a lognormal size distribution so that the fraction of the aerosol mass with particle sizes less than D_p is given by:

$$f(D_p) = \frac{1}{\ln\sigma\sqrt{2\pi}} \int_{-\infty}^{\ln D_p} \exp\left\{-\left(\frac{\ln D_p/d_p}{\sqrt{2}\ln\sigma}\right)^2\right\} d \ln D_p$$

It is assumed that the important parameters DF(total), d_p, and σ will depend on the phase of the accident and the type of quencher used in the suppression pool.

Best estimate values of the important parameters are obtained by correlation of the median values of uncertainty distributions obtained in the Monte Carlo analyses. There is an apparent dichotomy of opinion within the technical community concerning whether medians of uncertainty distributions are best-estimates (as is believed by the authors of this report) or means of the distributions are best-estimates. (Some refer to means by the regrettable term "conservative best-estimate" - whatever that is.) The authors do not propose to resolve this debate, but do provide correlations of the means of the samples used to construct uncertainty distributions from the Monte Carlo uncertainty analyses.

Whatever convention is adopted for the best estimate of uncertainty distributions, it is important to know the width of the distributions. For the simplified model adopted here, the 10 percentile and 90 percentile values are considered reasonable lower bounds and reasonable upper bounds on the distributions. Correlations for these lower and upper bounds are provided.

The important parameters, DF(total), d_p, and σ, in principle, are not entirely independent of one another. results of the Monte Carlo samples were examined for correlations among these quantities. The search for correlations was based on the conventional linear correlation coefficient, r, between sets of values X(i) and Y(i):

$$r = \frac{N \sum_{i=1}^{N} X(i)\,Y(i) - \sum_{i=1}^{N} X(i) \sum_{j=1}^{N} Y(j)}{\left[N \sum_{i=1}^{N} X(i)^2 - \left(\sum_{i=1}^{N} X(i)\right)^2\right]^{\frac{1}{2}} \left[N \sum_{j=1}^{N} Y(j)^2 - \left(\sum_{j=1}^{N} Y(j)\right)^2\right]^{\frac{1}{2}}}$$

where N is the number of samples and X(i), Y(i) were sampled values of $\log_{10}$ DF(total), d_p, or σ.

Significant (99 percent confidence) negative correlation of d_p with $\log_{10}$ DF(total) was found in all cases. Furthermore, significant positive correlation of σ with d_p and negative correlation with $\log_{10}$ DF(total) was found. This, of course, would be expected based on discussions presented in Chapter VI. These indications of correlation among the important predictions of the simplified models means that correlations for the important predictions cannot be selected independently. That is, the best-estimate of the decontamination factor cannot be used in conjunction with the lower bound particle size of aerosol emerging from the suppression pool. Such a combination would be inconsistent with the predictions of detailed mechanistic models.

The acceptable combinations of correlations for important predictions of the simplified model are:

1. Gap release through either 'X' or 'T' quenchers submerged to a depth H(cm):

- Median (Best Estimate)

$$\log_{10} \text{DF(total)} = 1.350 + 1.933 \times 10^{-3}\ \text{H(cm)}$$
$$d_p = 0.102\ \mu\text{m}$$
$$\sigma = 1.454 - 0.166 \times 10^{-3}\ \text{H(cm)}$$

- Mean

$$\log_{10} \text{DF(total)} = 1.283 + 2.68 \times 10^{-3}\ \text{H(cm)}$$
$$d_p = 0.107\ \mu\text{m}$$
$$\sigma = 1.440 - 0.126 \times 10^{-3}\ \text{H(cm)}$$

- Lower Bound (10 percentile)

$$\log_{10} \text{DF(total)} = 0.980 + 1.006 \times 10^{-3}\ \text{H(cm)}$$
$$d_p = 0.149\ \mu\text{m}$$
$$\sigma = 1.640 - 0.189 \times 10^{-3}\ \text{H(cm)}$$

- Upper Bound (90 percentile)

$$\log_{10} \text{DF(total)} = 1.485 + 5.554 \times 10^{-3}\ \text{H(cm)}$$
$$d_p = 0.085\ \mu\text{m}$$
$$\sigma = 1.248 - 0.032 \times 10^{-3}\ \text{H(cm)}$$

2. Invessel release through a 'T' quencher submerged to a depth H(cm) with a wetwell that can sustain pressures in excess of 5 atms:

   - Median (Best Estimate)

$$\log_{10} DF(total) = 1.752 + 1.92 \times 10^{-3} H(cm)$$
$$d_p(\mu m) = 0.326 - 0.121 \times 10^{-3} H(cm)$$
$$\sigma = 1.448 - 0.324 \times 10^{-3} H(cm)$$

   - Mean

$$\log_{10} DF(total) = 2.047 + 2.45 \times 10^{-3} H(cm)$$
$$d_p(\mu m) = 0.343 - 0.132 \times 10^{-3} H(cm)$$
$$\sigma = 1.416 - 0.242 \times 10^{-3} H(cm)$$

   - Lower Bound (10 percentile)

$$\log_{10} DF(total) = 0.930 + 0.870 \times 10^{-3} H(cm)$$
$$d_p(\mu m) = 0.684 - 0.242 \times 10^{-3} H(cm)$$
$$\sigma = 1.850 - 0.346 \times 10^{-3} H(cm)$$

   - Upper Bound (90 percentile)

$$\log_{10} DF(total) = 3.444 + 5.38 \times 10^{-3} H(cm)$$
$$d_p(\mu m) = 0.183 - 0.073 \times 10^{-3} H(cm)$$
$$\sigma = 1.048 - 0.069 \times 10^{-3} H(cm)$$

3. Invessel release through a 'T' or an 'X' quencher at a submergence H(cm) and wetwell that can only sustain pressures less than 5 atms:

   - Median (Best Estimate)

$$\log_{10} DF(total) = 1.791 + 2.477 \times 10^{-3} H(cm)$$
$$d_p(\mu m) = 0.293 - 0.064 \times 10^{-3} H(cm)$$
$$\sigma = 1.441 - 0.420 \times 10^{-3} H(cm)$$

   - Mean

$$\log_{10} DF(total) = 2.256 + 2.764 \times 10^{-3} H(cm)$$
$$d_p(\mu m) = 0.303 - 0.065 \times 10^{-3} H(cm)$$
$$\sigma = 1.395 - 0.260 \times 10^{-3} H(cm)$$

   - Lower Bound (10 percentile)

$$\log_{10} DF(total) = 1.034 + 0.875 \times 10^{-3} H(cm)$$
$$d_p(\mu m) = 0.597 - 0.071 \times 10^{-3} H(cm)$$
$$\sigma = 1.824 - 0.341 \times 10^{-3} H(cm)$$

- Upper Bound (90 percentile)

$$\log_{10} DF(total) = 3.964 + 6.528 \times 10^{-3} H(cm)$$
$$d_p(\mu m) = 0.166 - 0.058 \times 10^{-3} H(cm)$$
$$\sigma = 1.025 - 0.038 \times 10^{-3} H(cm)$$

Two additional points concerning the simplified model are:

- 1 percent of the discharge to suppression pool may leak into the wetwell space and thus bypass the actions of the pool, and

- calculated decontamination factors in excess of 10^6 should be reduced to 10^6.

To illustrate the application of the simplified model consider the concentration of iodine in the wetwell space in the absence of any attenuation mechanisms other than the suppression pool. From NUREG-1465 [3], 5 percent of the initial core inventory is discharged to the suppression pool during the gap release phase of an accident and 35 percent of the initial core inventory is discharged during the invessel release phase. Assume 1 percent of the discharge leaks into the wetwell without passing through the suppression pool. This leakage puts 0.4 percent of the initial core inventory of iodine into the wetwell space.

To calculate the additional iodine passing through the suppression pool assume that the discharge to the pool is through 'T' quenchers submerged to a depth of 150 cm and the wetwell space is always less than 5 atmospheres. The best estimate decontamination factor during gap release is:

DF(total) = 43.6

Then, the amount of iodine entering the wetwell space is 4.95 percent of the initial core inventory (5 percent less the amount leaked) times 1/43.6 or 0.11 percent of the initial core inventory. Lower bound and upper bounds are 0.37 percent and 0.024 percent of the initial core inventory. The best estimate of the mean particle size of the iodine bearing material is 0.102 μm. The reasonable range for this mean size is 0.085 to 0.149 μm.

The best estimate of iodine reaching the wetwell space during invessel release is:

34.65/145.4 = 0.24 percent

The upper and lower bounds on this range are 2.37 percent and 0.0004 percent.

Then, the best estimate of the total iodine released to the wetwell by the discharge that passes through the suppression pool is 0.11 percent + 0.24 percent = 0.35 percent which is slightly less than reaches the wetwell space by leakage. The reasonable range for the concentration of iodine in the wetwell space is:

- Upper Bound = 0.4 + 0.37 + 2.37 percent = 3.14 percent of the initial core inventory

- Lower Bound = 0.4 + 0.024 + 0.0004 percent = 0.42 percent of the initial core inventory.

VIII. Conclusions

Monte Carlo uncertainty analyses of decontamination of aerosol-laden gases sparging through a suppression pool show that decontamination by bubble formation and equilibration with the suppression pool can be significant. For shallow pools, the decontamination by the bubble formation and equilibration processes can be larger than decontamination by bubble rise through the pool. Much less experimental and analytic attention has been given to decontamination during the formation of bubbles and the subsequent processes of disintegration and coalescence than has been given to decontamination during bubble rise through a pool. Decontamination by bubble formation and equilibration found to be relatively insensitive to pool depth but is sensitive to the flow and steam content of gas discharged lot.

Decontamination of aerosol-laden bubbles rising through a water pool is resisted by the evaporation of water from the bubble surface as the hydrostatic head is released. Bubble plumes that entrain water in the upward flow of gases reduce the opportunity for decontamination during bubble rise. On the other hand, bubble oscillations and shape deformations may cause decontamination not considered in some models.

Decontamination is predicted to narrow the size distribution of aerosol discharged to a pool and to shift the mass mean of the size distribution toward values where decontamination processes are minimally effective. This size of minimal effectiveness of removal processes is relatively insensitive to pool depth. It is sensitive to the flow rate of gases to the pool.

Uncertainties in the predicted decontamination that can be achieved by steam suppression pools arise from:

- uncertainties in boundary conditions dictated by the nature of accident progression such as pool temperature and wetwell pressure,
- uncertainties in the sizes of aerosol particles discharged to the suppression pools,
- uncertainties in bubble behavior, is
- uncertainties in aerosol behavior in forming and rising bubbles.

The means, medians, and the 10 percentile and 90 percentile values of uncertainty distributions for total decontamination of gases sparging through suppression pools and the parameters of the size distribution of aerosol emerging from pools can be correlated with pool depth. Parameters of the correlations depend on the phase of the accident and the nature of the discharge to the pool.

IX. References

1. D. A. Powers and J. L. Sprung, A Simplified Model of Aerosol Scrubbing by a Water Pool Overlying Core Debris Interacting with Concrete, NUREG/CR-5901, SAND92-1422, Sandia National Laboratories, Albuquerque, NM, October 1992.

2. D. A. Powers and S. B. Burson, A Simplified Model of Aerosol Removal by Containment Sprays, NUREG/CR-5966, SAND92-2689, Sandia National Laboratories, Albuquerque, NM, June 1993.

3. L. Soffer, S. B. Burson, C. M. Ferrell, R. Y. Lee, and J. N. Ridgely, Accident Source Terms for Light Water Nuclear Power Plants, NUREG/CR-1465, U.S. Nuclear Regulatory Commission, Washington, D.C., February 1995.

4. K. E. Washington, K. K. Murata, R. G. Gido, F. Gelbard, N. A. Rusell, S. C. Billups, D. C. Carroll, R. O. Griffith, and D. L. Y. Louie, Reference Manual for the CONTAIN 1.1 Code for Containment Severe Accident Analysis, NUREG/CR-5715, SAND91-0835, Sandia National Laboratories, Albuquerque, NM, July 1991.

5. R. M. Summers et al., MELCOR 1.8.0: A Computer Code for Nuclear Reactor Severe Accident Source Term and Risk Assessment Analysis, NUREG/CR-5531, SAND90-0364, Sandia National Laboratories, Albuquerque, NM, January 1991.

6. P. C. Owczarski, and K. W. Burk, SPARC-90: A Code for Calculating Fission Product Capture in Suppression Pools, NUREG/CR-5765, PNL-7723, Pacific Northwest Laboratory, Richland, WA, October 1991.

7. A. T. Wassel, A. F. Mills, D. C. Bugby, and R. N. Oehlberg, *Nuclear Engineering and Design 90* (1985) 87.

8. A. T. Wassel, J. L. Farr, Jr., and M. S. Hoseyni, SUPRA: A Code for Simulating Removal of Radionuclides by Water Pools Under Severe Accident Conditions, NP-3886-CCMP, Science Applications, Inc., Hermosa Beach, CA, 1985.

9. S. A. Ramsdale, BUSCA-JUN90 Reference Manual, SRD R542, Safety and Reliability Directorate, United Kingdom, 1991.

10. V. F. Ubanic, and T. R. Heidrich, *J. Nuclear Materials, 75* (1978) 251.

11. M. R. Kuhlman, J. A. Gieseke, M. Merilo, and R. Oehlberg, "Scrubbing of Fission Product Aerosols in LWR Water Pools Under Severe Accident Conditions," p. 633 Paper IAEA-SM-281/47, *Source Term Evaluation for Accident Conditions*, International Atomic Energy Agency, Vienna, Austria, 1986.

12. S. R. Greene, A. E. Levin, C. R. Hyman, A. Sozer, and R. P. Taleyarkhan, BWR Mark II Ex-Vessel Corium Interaction Analyses, NUREG/CR-5623, ORNL/TM-11644, Oak Ridge National Laboratory, Oak Ridge, TN, November 1991.

13. GESAR II BWR/6 Nuclear Island Design, General Electric Co., San Jose, CA, undated.

References

14. J. A. Gieseke, et al., Source Term Code Package: A User's Guide, NUREG/CR-4587, Battelle Columbus Laboratory, Columbus, OH, July 1886.

15. I. K. Madni, Analysis of Long Term Station Blackout Without Automatic Depressurization at Peach Bottom Using MELCOR (Version 1.8), NUREG/CR-5850, BNL-NUREG-52319, Brookhaven National Laboratory, Upton, NY, May 1994.

16. S. A. Hodge and L. J. Ott, Boiling Water Reactor Severe Accident Response (BWRSAR) Code Description and Assessment, Oak Ridge National Laboratory, Oak Ridge, TN, February 1989.

17. Final Safety Analysis Report Peach Bottom Atomic Power Station Units 2 and 3, Volume 2, Philadelphia Electric Co., undated.

18. IDCOR Technical Report 16.2-3, MAAP Modular Accident Analysis Program User's Manual, Atomic Industrial Forum, Bethesda, MD, August 1983.

19. D. A. Powers, J. E. Brockmann, and A. W. Shiver, VANESA: A Mechanistic Model of Radionuclide Release and Aerosol Generation During Core Debris Interactions with Concrete, NUREG/CR-4308, SAND85-1370, Sandia National Laboratories, Albuquerque, NM, July 1986.

20. D. R. Bradley, et al., CORCON-MOD 3: An Integrated Computer Model for Analysis of Molten Core-Concrete Interactions: User's Manual, NUREG/CR-5843, Sandia National Laboratories, Albuquerque, NM, April 1993.

21. Industry Degraded Core Rulemaking Project, Peach Bottom Atomic Power Station, IDCORTask 23.1, Integrated Containment Analysis, Atomic Industrial Forum, Bethesda, MD, 1984.

22. Office of Nuclear Regulatory Research, Severe Accident Risks: An Assessment for Five U.S. Nuclear Power Plants, NUREG-1150 Volumes 1-3, U.S. Nuclear Regulatory Commission, Washington, D.C., June 1989.

23. R. S. Denning et al., Radionuclide Release Calculations for Selected Severe Accident Scenarios, NUREG/CR-4624, BMJ-2139, Volume 1, Battelle Columbus Laboratory, Columbus Ohio, July 1986.

24. D. A. Powers and F. E. Arellano, Large-scale, Transient Tests of the Interaction of Molten Steel with Concrete, NUREG/CR-2282, SAND81-1753, Sandia National Laboratories, Albuquerque, NM, January 1982.

25. P. K. Mast, D. R. Bradley, J. E. Brockmann, R. J. Lipinski, and D. A. Powers, Uncertainty in Radionuclide Release Under Specific LWR Accident Conditions, Volume IV, TC Analysis, Sandia National Laboratories, Albuquerque, NM, December 1985.

26. J. E. Brockmann, *Progress in Nuclear Energy, 19* (1987) 7.

27. J. A. Gieseke, P. Cybulskis, R. S. Denning, M. R. Kuhlman, K. W. Lee, and H. Chen, Radionuclide Release Under Specific LWR Accident Conditions, Volume III, BWR Mark III Design, BMI-2104, Vol. III, Battelle Columbus Laboratory, Columbus, OH, July 1984.

28. N. M. Chown and D. A. Williams, A Limited Investigation of the Sensitivity of the Containment Source Term to Certain Primary Circuit Parameters Under PWR Severe Accident Conditions, AEEW-R2429, Winfrith Technology Centre, Winfrith, UK, 1989.

29. U.S. Nuclear Regulatory Commission, Reactor Safety Study - An Assessment of Accident Risks in U.S. Commercial Nuclear Power Plants, WASH-1400, NUREG-75/04, Washington, D.C., October 1975.

30. D. D. Paul, L. J. Flanigan, R. A. Cudnik, J. C. Cunnane, and R. P. Collier, Radionuclide Scrubbing in Water Pools, Volume 1: Gas-Liquid Hydrodynamics, NP-4154, Volume 1, Battelle Columbus Laboratory, Columbus, OH, August 1985.

31. R. Kumar and N. R. Kuloor, "The Formation of Bubbles and Drops," in *Advances in Chemical Engineering* Volume 8, 1970, pp. 256ff.

32. J. F. Davidson and B. O. G. Schuler, *Trans. Instit. Chem. Engrs.*, (London) *38* (1960) 335.

33. D. W. Van Krevelen and P. J. Hoftijzer, *Chem. Eng. Prog., 46* (1950) 29.

34. J. F. Davidson and H. Harrison, Fluidized Particles, Cambridge University Press, 1963.

35. K. Ruff, *Chemie-Ingenieur Technik, 44* (1972) 1360.

36. D. L. Datta, D. H. Napier, D. M. Newitt, *Trans. Instit. Chem. Engrs.,* (London) *28* (1950) 14.

37. P. D. Coppock and G. T. Meiklejohn, *Trans. Instit. Chem Engrs.*, (London) *29* (1951) 75.

38. L. Davidson and E. H. Amick, Jr., *AIChE J., 2* (1956) 337.

39. W. Siemes, *Chemie Inq. Tech., 26* (1954) 479.

40. C. K. B. Lee and C. K. Chan, Steam Chugging in Pressure Suppression Containment, NUREG/CR-1562, University of California at Los Angeles, Los Angeles, CA, July 1980.

41. W. Kowakchuk and A. A. Sonin, A Model for Condensation Oscillations in a Vertical Pipe Discharging Steam Into a Subcooled Water Pool, NUREG/CR-0221, Massachusetts Institute of Technology, Cambridge, MA, June 1978.

42. D. D. Paul, D. C. Newman, and R. A. Cudnik, Gas-Liquid Hydrodynamics of Large Vent/Suppression Pool Systems of Nuclear Power Plants During Some Accident Conditions,

43. D. A. Sargis, J. H. Stuhmiller, and S. S. Wang, Analysis of Steam Chugging Phenomena Volume 2: User's Manual for the CHUG1 Computer Program, EPRI NP-962, Volume 2, Jaycor, Del Mar, CA, January, 1979.

44. J. H. Milgram, *J. Fluid Mechanics, 133* (1983) 345.

45. K. H. Tacke, H. G. Schubert, D. J. Weber, and K. Schwerdtfeger, *Metallurgical Transactions B, 16B* (1985) 263.

46. T. Y. Sun and G. M. Faeth, *Int. J. Multiphase Flow, 12* (1986) 99.

47. T. Y. Sun and G. M. Faeth, *Int. J. Multiphase Flow, 12* (1986) 115.

48. J. S. Shuen, A. S. P. Solomon, Q. F. Zhang, and G. M. Faeth, *AIAA Journal, 23* (1985) 396.

49. J. S. Shuen, L. D. Chen, and G. M. Faeth, *AIAA Journal, 21* (1983) 1483.

50. J. S. Shuen, L. D. Chen, and G. M. Faeth, *AIChE Journal, 29* (1983) 167.

51. G. B. Wallis, One-Dimensional Two-Phase Flow, McGraw-Hill, 1969.

52. J. F. Davidson and D. Harrison, *Chem. Eng. Sci., 21* (1966) 731.

53. W. K. George, R. L. Alpert, and F. Tamanini, *Intl. J. Heat Mass Transfer, 20* (1977) 1145.

54. T. J. McDougall, *J. Fluid Mechanics, 85* (1978) 655.

55. J. V. Sengers and J. T. R. Watson, *J. Phys. Chem Ref. Data, 15* (1986) 1291.

56. J. Kestin, J.V. Sengers, B. Kamgar-Parsi, and J. M. H. Levelt Sengers, *J. Phys. Chem. Ref. Data, 13* (1984) 175.

57. W. N. Bond and D. A. Newton, *Philosophical Magazine, 5* (1928) 794.

58. F. N. Peebles and H. J. Garber, *Chem. Eng. Progress, 49* (1953) 88.

59. E. Coester, *Z. Angew. Phys., 13* (1961) 254.

60. S. Winnikow, *Chem. Eng. Sci.*, 22 (1967) 477.

61. H. Lamb, Hydrodynamics, Cambridge University Press, 1932.

62. M. E. Weber, *Chem. Eng. Sci., 30* (1975) 1507.

63. J. T. Lindt and R. G. De Groot, *Chem. Eng. Sci., 29* (1974) 957.

64. P. H. Calderbank and M. B. Moo-Young, *Chem. Eng. Sci., 16* (1961) 39.

65. B. F. Le Clair and A. E. Hamielec, *Canadian J. Chem. Eng., 49* (1971) 713.

66. J. R. Grace, T. Wairegi, and T. H. Nguyen, *Trans. Inst. Chem Eng., 54* (1976) 167.

67. A. E. Hamielec, J. H. Storey, and J. H. Whitehead, *Canadian J. Chem. Eng., 41* (1963) 246.

68. R. M. Davies and G. I. Taylor, *Proc. R. Soc, A200* (1950) 375.

69. J. Hakii, H. Kaneko, M. Fikasawa, Y. Masahiro, and M. Matsumoto, "Experimental Study of Aerosol Removal Effect by Pool Scrubbing," 2nd Workshop on LWR Severe Accident Research at JAERI, Tokyo, Japan, 1991.

70. C. N. Amos, "Evaluation of the Contact Time for Pool Scrubbing," Proceedings American Nuclear Society Meeting on Fission Product Behavior and Source Term Research, NP-4113-SR, p. 33-1, M. F. Huebner, editor, Electric Power Research Institute, Palo Alto, CA, July, 1985.

71. C. K. B. Lee, *Int. Comm. Heat Mass Transfer, 10* (1983) 25.

72. T. O. Oolman and H. W. Blanch, *Chem. Eng. Communciations, 43* (1986) 237.

73. A. K. Chesters and G. Hoffman, *Appl. Sci. Res., 38* (1982) 353.

74. P. H. Calderbank, Chemical Engineering (London) 212 (1967) CE209-CE233.

75. G. Marucci and L. Nicodemo, *Chem. Eng. Sci., 22* (1967) 1257.

76. R. L. Lessard and D. A. Zieminski, *Ind. Eng. Chem. Fundamentals, 10* (1971) 260.

77. H. S. Allen, *Philos. Magazine, 54* (1900) 323.

78. A. V. Gorodetskaya, *Russ. J. Phys. Chem., 23* (1949) 71.

79. W. L. Haberman and R. K. Morton, An Experimental Investigation of the Drag and Shape of Air Bubbles Rising in Various Liquids, David W. Taylor Model Basin Report 802, September, 1953.

80. B. Rosenberg, The Drag and Shape of Air Bubbles Moving in Liquids, David W. Taylor Model Basin Report 727, September 1950.

81. C. Bachhuber and C. Sanford, *J. Appl. Phys., 45* (1974) 2567.

82. R. Clift, J. R. Grace, and M. E. Weber, Bubbles, Drops and Particles, Academic Press, 1978.

83. h. c. J. M. H. Levelt Sengers and B. Dooley, *J. Phys. Chem. Ref. Data, 22* (1993) 785.

84. D. Bhaga and M. E. Weber, *J. Fluid Mechanics, 105* (1981) 61.

85. G. B. Wallis, One Dimensional Two Phase Flow, McGraw-Hill, 1969.

86. A. I. Johnson, F. Besik, and A. E. Hamielec, *Canadian J. Chem. Eng., 47* (1969) 559.

87. D. R. Raymond and S. A. Zieminski, *AIChE Journal, 17* (1971) 57.

88. R. Kronig and J. C. Brink, *Appl. Sci. Res., A2* (1950) 142.

89. A. B. Newman, *Am. Inst. Chem. Engrs., 27* (1931) 310.

90. R. Hickling and M. S. Plesset, *Physics of Fluids, 7* (1964) 7.

91. K. Vokurka, *Acustica, 59* (1986) 214.

92. J. W. Rayleigh, *Philos. Magazine, 34* (1917) 94.

93. M. S. Plesset and T. P. Mitchell, *Quarterly Applied Mathematics, 13* (1955) 419.

94. W. Florshuetz and B. T. Chao, *Trans ASME 87C, J. Heat Transfer*, (1965) 209.

95. V. F. Prisnyakov, *Int. J. Heat Mass Transfer, 14* (1971) 353.

96. D. D. Wittke and B. T. Chao, *J. Heat Transfer,* (1967) 17.

97. D. Moalem and S. Sideman, *Int'l. J. Heat Mass Transfer, 16* (1973) 2321.

98. O. Levenspiel, *Ind. Eng. Chem., 51* (1959) 787.

99. V. G. Levich, Physicochemical Hydrodynamics, Prentice-Hall Publ. Co., 1962.

100. J. Loertscher, B. Covelli, and R. Gubler, *Chemi-Ingenieur Technik, 57* (1985) 863.

101. J. R. Grace, T. Wairegi, and B. Brophy, *Canadian J. Chem Eng., 56* (1978) 3.

102. E. R. Elzinga and J. T. Banchero, *Chem. Eng. Progr. Symp. Ser., 55* (1959) 149.

103. N. B. Vargaftik, Tables on the Thermophysical Properties of Liquids and Gases, Second Edition, Hemisphere, 1975.

104. M. W. Chase et al., *J. Phys. Chem. Ref. Data, 11* (1982) 695.

105. D. R. Stull and H. Prophet, JANAF Thermochemical Tables, Second Edition, National Bureau of Standards, June 1971.

106. Y. S. Touloukian, S. C. Saxena, and P. Hestermans, Thermophysical Properties of Matter Volume II Viscosity, IFI Plenum, 1975.

107. F. J. Uribe, E. A. Mason, and J. Kestin, *J. Phys. Chem. Ref. Data, 19* (1990) 1123.

108. J. Millat et al., *Physica, 145A* (1987) 461.

109. A. A. Clifford, J. Kestin, and W. A. Wakenham, *Physica, 97A* (1979) 287.

110. L. B. Thomas and R. C. Golike, *J. Chem. Phys., 22* (1954) 300.

111. A. C. Scott, A. I. Johns, J. T. R. Wats, and A. A. Clifford, *J. Chem. Soc. Faraday Transactions I, 79* (1983) 733.

112. H. L. Johnston and E. R. Grilly, *J. Chem. Phys., 14* (1946) 233.

113. N. Imaishi, J. Kestin, and W.A. Wakeham, *Physica, 123A* (1984) 50.

114. H. M. Roder, *J. Research NBS, 87* (1982) 279.

115. M. J. Assael and W. A. Wakeham, *J. Chem. Soc. Faraday Trans. I, 77* (1981) 697.

116. A. I. Johns et al., *Int'l J. Thermophysics, 9* (1988) 3.

117. A. A. Clifford, J. Kestin, and W. A. Wakeham, *Ber. Bunsenges. Phys. Chem., 84* (1980) 9.

118. J. Kestin, Y. Nagasaka, and W. A. Wakeham *Ber. Bunsenges. Phys. Chem.*,

119. E. N. Haran et al., *Ber. Bunsenges. Phys. Chem., 87* (1983) 657.

120. E. A. Mason and S. C. Saxena, *Physics of Fluids, 1* (1958) 361.

121. P. K. Tondon and S. C. Saxena, *Appl. Sci. Res., 19* (1968) 163.

122. Solubility Data Series, Volume 43, Carbon Monoxide, R. W. Cargill, editor, Pergamon Press.

123. J. J. Carroll, J. D. Slupsky, and A. E. Mather, *J. Phys. Chem. Ref. Data, 20* (1991) 1201.

124. Solubility Data Series, Volume 5/6, Hydrogen and Deuterium, C. L. Young, editor, Pergamon Press.

125. Solubility Data Series, Volume 7, Oxygen and Ozone, R. Battino, editor, Pergamon Press.

126. Solubility Data Series, Volume 10, Nitrogen and Air, R. Battino, editor, Pergamon Press.

127. R. C. Reid, J. M. Prausnitz, and B. E. Poling, The Properties of Gases and Liquids, 4th Edition, McGraw-Hill Book Co., 1987.

128. E. N. Fuller, K. Ensley, and J. C. Giddings, *J. Phys. Chem.*, *75* (1969) 3679.

129. E. N. Fuller, P. D. Schettler, and J. C. Giddings, *Ind. Eng. Chem.*, *58* (1966) 18.

130. C. R. Wilke and C. Y. Lee, *Ind. Eng. Chem.*, *47* (1955) 1253.

131. R. W. Elliott and H. Watts, *Canad. J. Chem.*, *50* (1972) 31.

132. S. Gotoh, M. Manner, J. P. Sorensen, and W. E. Stewart, *Ind. Eng. Chem.*, *12* (1973) 119.

133. S. Gotoh, M. Manner, J. P. Sorensen, and W. E. Stewart, *J. Chem. Eng. Data*, *19* (1974) 169.

134. G. A. Lugg, *Anal. Chem.*, *40* (1968) 1072.

135. B. K. Pathak, V. N. Singh, and P. C. Singh, *Canad. J. Chem. Eng.*, *59* (1981) 362.

136. P. D. Neufeld, A. R. Janzen, and R. A. Aziz, *J. Chem. Phys.*, *57* (1972) 1100.

137. D. M. Himmelblau, *Chem. Rev.*, *64* (1964) 527.

138. C. R. Wilke and P. Chang, *AIChE J.*, *1* (1955) 264.

139. W. Hayduk and B. S. Minhas, *Canad. J. Chem. Eng.*, *60* (1982) 295.

140. E. G. Scheibel, *Ind. Eng. Chem.*, *46* (1954) 2007.

141. D. F. Othmer and M. S. Thakar, *Ind. Eng. Chem.*, *45* (1953) 589.

142. D. G. Leaist, *J. Phys. Chem.*, *91* (1987) 4635.

143. M. D. Allen and O. G. Raabe, *Aerosol Science and Technology*, *4* (1985) 269.

144. C. N. Davies, *Proc. Phys. Soc.*, *57* (1945) 259.

145. W. F. Phillips, *Physics of Fluids*, *18* (1975) 1069.

146. R. A. Millikan, *Phys. Rev.*, *32* (1911) 349.

147. R. A. Millikan, *Phys. Rev.*, *22* (1923) 1.

148. N. A. Fuchs, Mechanics of Aerosols, Pergamon Press, 1964.

149. T. Demitrack and F. J. Moody, *Trans. Amer. Nucl. Soc.*, *45* (1983) 483.

150. D. A. Powers, An Analysis of Radionuclide Behavior in Water Pools During Accidents at the Annular Core Research Reactor, SAND91-1222, Sandia National Laboratories, Albuquerque, NM, May 1992.

151. I. S. Goldberg, *J. Aerosol Sci.*, *12* (1981) 11.

152. I. V. Derevich and L. I. Zaichik, *High Temperature, 26* (1986) 120.

153. J. Pich and W. Schuetz, J. Aerosol Sci., 22 (1991) 27.

154. L. Talbot, R. K. Cheng, R. W. Schefer, and D. R. Willis, *J. Fluid Mech., 101* (1980) 737.

155. S. K. Loyalka and J. H. Ferziger, *Phys. Fluids, 10* (1967) 1833.

156. I. N. Ivchenko and Yu. I. Yalamov, *Russ. J. Phys. Chem., 45* (1971) 317.

157. S. K. Loyalka, *J. Chem. Phys., 48* (1968) 5432.

158. B. K. Annis, *J. Chem. Phys., 57* (1972) 2898.

159. B. V. Derjaquin, Ya. I. Rabinovich, A. I. Storozhilov, and G. I Shcherbina, *J. Coll. Int. Sci., 57* (1976) 451.

160. D. J. Rader, *J. Aerosol Science, 21* (1990) 161.

161. B. V. Derjaquin and Yu. I. Yalamov, "The Theory of Thermophoresis and Diffusiophoresis of Aerosol Particles and Their Experimental Testing," in Topics in Current Aerosol Research, Part 2, G. M. Hidy and J. R. Brook, editors, Pergamon Press, 1972.

162. G. M. Rossenblatt, *Accounts of Chemical Research, 14* (1981) 4.

163. M. E. Riley and D. J. Diestler, *Surface Science, 175* (1986) 579.

164. J. E. Brockmann, "Rage of Possible Dymanic and Collision Shape Factors," Appendix F, R. J. Lipinski et al., Uncertainty in Radionuclide Release Under Specific LWR Accident Conditions, Volume II, TMBL' Analyses, SAND84-0410 Vol. 2, Sandia National Laboratories, Albuquerque, NM, February 1985.

165. M. M. R. Williams and S. K. Loyalka, Aerosol Science Theory and Practice, Pergamon Press, 1991.

166. L. Waldmann and K. H. Schmitt, "Thermophoresis and Diffusiophoresis of Aerosols," Chapter VI in Aerosol Science, C. N. Davies, editor, Academic Press, 1966.

167. P. Goldsmith and F. G. May, "Diffusionphoresis and Thermophoresis in Water Vapour Systems," Chapter VII in Aerosol Science, C. N. Davies, editor, Academic Press, 1966.

168. H-C. Hansson and M. S. Ahlberg, *J. Aerosol Science, 16* (1985) 69.

169. B. E. Dahneke, *Aerosol Science, 4* (1973) 147.

170. B. E. Dahneke, *Aerosol Science, 4* (1973) 139.

171. B. E. Dahneke, *Aerosol Science, 4* (1973) 163.

172. T. Alty and C. A. Mackay, *Proc. Roy. Soc. London, A149* (1935) 104.

173. S. K. Loyalka and J. H. Ferziger, *Phys. of Fluids, 11* (1968) 1668.

174. J. M. Thomas, Introduction to the Principles of Heterogeneous Catalysis, Academic Press, 1967.

175. R. M. Barrer, N. McKenzie, and J. S. S. Reay, *J. Colloid Sci., 11* (1956) 479.

176. H. R. Pruppacher and J. D. Klett, Microphysics of Clouds and Precipitation, D. Reidel Publishing Co.

177. J. C. Barrett and C. F. Clement, *J. Aerosol Science, 19* (1988) 223.

178. Y. Y. Hsu and R. W. Graham, Transport Processes in Boiling and Two-Phase Systems, Hemispher, 1976.

179. P. E. Wagner, "Aerosol Growth by Condensation," Chapter 5 in Aerosol Microphysics II Chemical Physics of Microparticles, W. H. Marlow, editor, Springer Verlag, 1982.

180. N. E. Levine, *J. Geophys. Res., 78* (1973) 6266.

181. M. Kulmala and T. Vesala, *J. Aerosol Sci., 22* (1991) 337.

182. J. Kukkonen, T. Vesala, and M. Kulmala, *J. Aerosol Sci., 20* (1989) 749.

183. J. C. Barrett and C. F. Clement, *J. Aerosol Sci., 21* (1990) 761.

184. S. K. Loyalka and J. W. Park, *J. Colloid and Interfacial Science, 125* (1988) 712.

185. S. G. Jennings, *J. Aerosol Sci., 19* (1988) 159.

186. K. S. Pitzer, "Theory: Ion Interaction Approach," Chapter 7 in Activity Coefficients in Electrolyte Solutions, Volume 1, R. M. Pytkowicz, editor, CRC Press.

187. S. C. Cho and W. K. Lee, *Chem. Eng. Sci., 46* (1991) 789.

188. Chemical Engineer's Handbook, 47th Edition, R. H. Perry, C. H. Chilton, and S. D. Kirkpatrick, editors, McGraw-Hill Book Co., 1963.

189. A. Jeje and B. Ross, *Chem. Eng. Sci., 43* (1988) 2817.

190. F. Mayinger and Y. M. Chen, "Heat Transfer at the Phase Interface of Condensing Bubbles," *Proc. 8th Int'l Heat Transfer Conf.*, Vol. 4, p. 1913, C. L. Tien, V. P. Carey, and J. K. Ferrell, editors, 1986.

191. W. V. Pinczewski, *Chem Eng. Sci., 36* (1981) 405.

192. T. B. Guy and T. J. Ledwidge, *Int'l J. Heat Mass Transf., 16* (1973) 2393.

193. R. B. H. Tan and I. J. Harris, *Chem. Eng. Sci., 41* (1986) 3175.

194. W. E. Ranz, "Principles of Inertial Impaction," Bulletin 66, Department of Engineering Research, Pennsylvania State University, University Park, PA, December 1956.

195. D. W. Moore *J. Fluid Mechanics, 16* (1963) 161.

196. H. Tsuge, Y. Tanaka, and S. Hibino, *Canad. J. Chem. Eng., 59* (1981) 569.

197. W. L. McCabe and J. C. Smith, Unit Operations of Chemical Engineering, McGraw-Hill, 1954.

198. P. A. Kolodzie, Jr. and M. Van Winkle, *AIChE Journal, 3* (1957) 305.

199. P. L. Smith, Jr. and M. Van Winkle, *AIChE Journal, 4* (1958) 266.

200. D. Azbel et al., "Acoustic Resonance Theory for the Rupture of Film Cap of a Gas Bubble at a Horizontal Gas-Liquid Interface," pp. 159-170, Two-Phase Momentum Heat and Mass Transfer in Chemical Process and Energy Engineering Systems, Volume 1, Hemisphere Publishing Company, 1978.

201. I. Kataoka and M. Ishii, *Int. J. Heat Mass Transfer, 27* (1984) 1999.

202. A. M. Rozen, S. I. Golub, and T. I. Votintseva, *Teploenergetika, 23* (1976) 59.

203. C. Pozrikidis, *J. Fluid Mechanics, 168* (1986) 337.

204. A. F. Mills and M. S. Hoseyni, *Aerosol Science and Technology, 8* (1988) 103.

205. P. H. Calderbank and I. J. O. Korchinski, *Chem. Eng. Sci., 6* (1956) 65.

206. R. J. Bunson and R. M. Wellek, *Canad. J. Chem. Eng., 48* (1970) 267.

207. H. Tsuge and S-I. Hibino, *Chem. Eng. Comm., 22* (1983) 63.

208. J. Besset, Contribution to the Thermalhydraulic Study of Vapor Bubble Injection into a Subsaturated Liquid, Doctoral Thesis, The Claude Bernard University, Central School of Lyon, Institute of Applied Science, 1980.

209. M. J. Prince and H. W. Blanch, *AIChE J, 36* (1990) 1425.

210. J. H. Pitts, *Int'l J. Multiphase Flow, 6* (1980) 329.

211. G. G. Brucker and E. M. Sparrow, *Int'l J. Heat and Mass Transfer, 26* (1977) 371.

212. D. Moalem and S. Sideman, *Int'l J. Heat Mass Transfer, 16* (1973) 2321.

213. A. Jeje, B. Asante, and B. Ross, *Chem. Eng. Sci., 45* (1990) 639.

214. A. E. Wraith, *Proc. Int'l Symp. Mining and Metallurgy,* p. 303, 1972.

215. H. Tsuge, P. Rudin, and R. Kannel, *J. Chem. Eng. Japan, 19* (1986) 326.

216. G. K. Batchelor, *J. Fluid Mechanics, 184* (1987) 399.

217. J. Kitscha and G. Kocamustafaogullari, *Int'l J. Multiphase Flow, 15* (1989) 573.

218. P. H. Calderbank, "Mass Transfer," Chapter 6 in Mixing Theory and Practice, Volume II, V. W. Uhl and J. B. Gray, editors, Academic Press, 1967.

219. R. M. Ladyzhensky, *J. Appl. Chem USSR, 27* (1954) 17.

220. C-H. Lee, L. E. Erickson, and L. A. Glasgow, *Chemical Eng. Comm., 59* (1987) 65.

221. M. Taheri and S. Calvert, *J. Air Poll. Control Assoc., 3* (1960) 129.

222. A. H. P. Skelland and S. S. Minhas, *AIChE J., 17* (1971) 1316.

223. N. B. Vargaftik, Tables on the Thermophysical Properties of Liquids and Gases, Second Edition, Hemisphere Publishing Co., 1975.

224. V. B. Okhotskii, *Inzhenerno-Fizicheskoi Zhurnal, 59* (1990) 109.

225. S. P. Bakanov, *Aerosol Science and Technology, 15* (1991) 77.

226. N. A. Fuchs *J. Aerosol Science, 13* (1982) 327.

227. S. K. Loyalka, *Physica A, 163* (1990) 813.

228. E. Y. H. Keng and C. Orr, Jr., *J. Colloid and Interface Science, 22* (1966) 107.

229. K. H. Schmidt, *Z. Natf., 14a* (1959) 870.

230. J. Chomiak and A. K. Gupta, *J. Aerosol Sci., 20* (1989) 1.

231. W. W. Nazaroff, *J. Aerosol Sci., 21* (1990) 827.

232. Y. Sone, *Physics of Fluids, 15* (1972) 1418.

233. H. A. Dwyer, *Physics of Fluids, 10* (1968) 976, *11* (1968) 923.

234. S. R. Greene, S. A. Hodge, C. R. Hyman, B. W. Patton, and M. L. Tobias, The Response of BWR Mark III Containments to Short-Term Station Blackout Severe Accident Sequences, NUREG/CR-5571, ORNL/TM-11549, Oak Ridge National Laboratory, Oak Ridge, TN, June 1991.

235. C. J. Shaffer, L. A. Miller, and A. C. Payne, Jr., Intergrated Risk Assessment for the LaSalle Unit 2 Nuclear Power Plant, Phenomenological and Risk Uncertainty Evaluation Program (PRUEP) MELCOR Code Calculations, NUREG/CR-5305, SAND90-2765, Volume 3, Sandia National Laboratories, Albuquerque, NM, October 1992.

236. S. E. Dingman, C. J. Shaffer, A. C. Payne, and M. K. Carmel, MELCOR Analyses for Accident Progression Issues, NUREG/CR-5331, SAND89-0072, Sandia National Laboratories, Albuquerque, NM, January 1991.

237. F. Durst, B. Schonung, K. Selanger, and M. Winter, *J. Fluid Mechanics, 170* (1986) 53.

238. S. S. Sadhal and Robert E. Johnson, *J. Fluid Mechanics, 126* (1983) 237.

239. A. C. Payne, Jr., Analysis of the LaSalle Unit 2 Nuclear Power Plant: Risk Methods Integration and Evaluation Program (RMIEP), Volume 1, NUREG/CR-4832, SAND90-0537, Sandia National Laboratories, Albuquerque, NM, July 1992.

240. J. A. Gieseke, P. Cybulskis, R. S. Denning, M. R. Kuhlman, K. W. Lee, and H. Chen, Radionuclide Release Under Specific LWR Accident Conditions, Volume II, BWR, MARK I Design, BMI-2104, Volume II, Battelle Columbus Laboratory, Columbus, OH, July 1984.

241. R. A. Lorenz, J. L. Collins, and A. P. Malinauskas, *Nuclear Technology, 46* (1979) 404.

242. S. C. Saxena and R. K. Joshi, Thermal Accommodation and Adsorption Coefficients of Gases, Hemisphere Publishing Company, 1991.

243. F. O. Goodman and H. Y. Wachman, *J. Chem. Phys., 46* (1967) 2376.

244. W. F. Phillips, *The Physics of Fluids, 18* (1975) 144.

245. B. R. Bowsher and S. Dickinson The Interaction of Caesium Iodide with Boric Acid: Vapour Phase and Vapour-Condensed Phase Reactions, AEEW-R 2102, AEE Winfrith, United Kingdom, May 1986.

246. R. M. Elrick, R. A. Sallach, A. L. Ouellette, S. C. Douglas, Boron Carbide-Steam Reactions with Cesium Hydroxide and with Cesium Iodide at 1270 K in an Inconel System, NUREG/CR-4962, SAND87-1491, Sandia National Laboratories, Albuquerque, NM, September 1987.

247. R. G. Bock, J. D. Duncan, and J. E. Leonard, *Nuclear Technology, 11* (1971) 532.

248. R. E. Adams and M. L. Tobias, Uranium Oxide Aerosol Experiments in Steam-Air Atmospheres: NSPP Tests 401-407 Data Record Report, NUREG/CR-4716, ORNL/TM-10165, Oak Ridge National Laboratory, Oak Ridge, TN, September 1986.

249. M. L. Tobias and R. E. Adams, Limestone Concrete Aerosol Experiments in Steam-Air Atmospheres: NSPP Tests 521, 522, and 531, Data Record Report, NUREG/CR-5017, ORNL/TM-10587, Oak Ridge National Laboratory, Oak Ridge, TN, October 1987.

250. D. J. Alpert, D. I. Chanin, and L. T. Ritchie, Relative Importance of Individual Elements to Reactor Accident Consequences Assuming Equal Releases Fractions, NUREG/CR-4467, SAND85-2575, Sandia National Laboratories, Albuquerque, NM, March 1986.

251. I. V. Derevich and L. I. Zaichik, *High Temperature, 26* (1988) 120.

252. I. S. Goldberg, *J. Aerosol Sci., 12* (1981) 11.

253. S. A. Gokaglu and D. E. Rosner, *AIAA Journal, 24* (1986) 172.

254. H. M. Park and D. E. Rosner, *Chem. Eng. Sci., 44* (1989) 2233.
254a. D. E. Rosner and H. M. Park, *Chem. Eng. Sci., 43* (1988) 2689.

255. S. A. Gokoglu and D. E. Rosner, *Chem. Eng. Commun., 44* (1986) 107.

256. D. A. Powers, K. E. Washington, S. B. Burson, and J. L. Sprung, A Simplified Model of Aerosol Removed by Natural Processes in Reactor Containments, NUREG/CR-6189, SAND-9407, Sandia National Laboratories, Albuquerque, NM, July 1996.

257. P. von der Hardt and A. Tattegrain, *J. Nuclear Materials, 188* (1992) 115.

258. A. Kupferberg and G. J. Jameson, *Trans. Instu. Chem. Engrs., 47* (1969) 241.

259. T. B. Guy and T. J. Ledwidge, *Int. J. Heat Mass Transfer, 16* (1973) 2393.

260. W. V. Pinczewski, *Chemical Engineering Science, 36* (1981) 405.

261. R. B. H. Tan and I. J. Harris *Chemical Engineering Science, 41* (1986) 3175.

262. J. Singh and D. K. Gupta *Indian J. Technology, 25* (1987) 457.

263. A. Jeje and B. Ross, *Chemical Engineering Science, 43* (1988) 2817.

264. S. C. Cho and W. K. Lee, *Chemical Engineering Science, 46* (1991) 789.

265. A. K. Chesters, M. van Doorn, and L. H. J. Goosens, *Int'l J. Multiphase Flow, 6* (1980) 499.

266. Y. Sahai and R. I. L. Guthrie, *Metallurgical Transactions B, 13B* (1982) 193.

267. A. C. Lochiel and P. H. Calderbank, *Chemical Engineering Science, 19* (1964) 471.

268. T. J. Heames et al., VICTORIA: A Mechanistic Model of Radionuclide Behavior in the Reactor Coolant System Under Severe Accident Conditions, NUREG/CR-5545, SAND90-0756, Rev. 1, Sandia National Laboratories, Albuquerque, NM, December 1992.

269. D. E. Knuth, Seminumerical Algorithms, second edition, Addison-Wesley Publishing Co., 1981.

270. R. E. Blose et al., SWISS 1 and 2: Sustained Interactions of Molten Steel and Concrete in the Presence of Water, NUREG/CR-4727, SAND85-1546, Sandia National Laboratories, Albuquerque, NM, July 1987.

271. T. G. Theofanous, W. H. Amarasooriya, H. Yan, and U. Ratman, The Probability of Liner Failure in a Mark I Containment, NUREG/CR-5423, University of California, Santa Barbara, CA, July 1989.

272. I. Cook and S. Unwin, *Nuclear Science and Engineering, 94* (1986) 107.

273. H. Jordan and M. R. Kuhlman, Trapmelt 2 User's Manual, NUREG/CR-4205, BMI-2621, Battelle Columbus Laboratory, Columbus, OH, 1985.

274. C. G. Granquist and R. A. Buhrman, *Solid State Communications, 18* (1976) 123.

275. S. R. Forrest and T. A. Witten, *J. Phys. A, 12* (1979) L109.

276. P. Meakin, *J. Chem. Phys., 81* (1984) 4637.

277. R. Richter, L. M. Sanders, and Z. Cheng, *J. Colloid Interface Science, 100* (1984) 203.

278. J. Feder, T. Jossang, and E. Rosenquist, *Phys. Rev. Letters, 53* (1984) 1403.

279. J. E. Martin, D. W. Schaefer, and A. Hurd, *Phys. Rev., A33* (1986) 3540.

280. R. D. Mountain, G. W. Mulholland, and H. Baum, *J. Colloid Interface Science, 114* (1986) 67.

281. R. J. Samson, G. W. Mulholland, and J. W. Gentry, *Langmuir, 3* (1987) 272.

282. A. J. Hurd and W. L. Fowler, *J. Colloid Interface Science, 122* (1988) 178.

283. H. X. Zhang, C. M. Sorensen, E. R. Ramer, B. J. Olivier, and J. F. Merkin, *Langmuir, 4* (1988) 867.

284. G. W. Mulholland, R. J. Samson, R. D. Mountain, and M. H. Ernst, *Energy and Fuels, 2* (1988) 481.

285. F. Lesaffre, *J. Aerosol Science, 20* (1989) 857.

286. P. Meakin, B. Donn, and G. W. Mullholand, *Langmuir, 5* (1989) 510.

287. C. M. Megaridis and R. A. Dobbins, *Combustion Science and Technology, 71* (1990) 95.

288. T. T. Charalampopoulos and H. Chang, *Combustion and Flame, 87* (1991) 89.

289. F. Herning and L. Zipperer, *Gas Wasserfach., 79* (1936) 49.

290. S. K. Loyalka and J. H. Ferziger, *Physics of Fluids, 11* (1968) 1668.

291. P. J. Kerney, G. M. Faeth, and D. R. Olson, *AIChE J., 18* (1972) 548.

292. K. Fischer and W. Häfner, Retention of Aerosols in Water Pools, BF-V38.070-01, Battelle Engineering Corp., Frankfurt am Main, Germany, March 1994 [in German].

293. H. Schmidt, *Int. J. Heat Mass Transport, 20* (177) 635.

294. A. Boushehni, J. Bzowski, J. Kestin, and E. A. Mason, *J. Phys. Chem. Ref. Data, 16* (1987) 445.

295. B. K. Annis, A. P. Malinauskus, and E. A. Mason, *J. Aerosol Science, 3* (1972) 55.

Appendix A
Tabulations of Uncertainty Distributions

Uncertainty distributions calculated in this work for:

- $\log_{10}$ DF (FE): logarithm of the decontamination factor for bubble formation and equilibration,
- $\log_{10}$ DF (rise): logarithm of the decontamination factor associated with the bubble rise through the suppression pool,
- $\log_{10}$ DF (total): logarithm of the total decontamination of aerosol-laden gases passing through the steam suppression pool,
- d_p (μm): mean particle size of aerosol that emerges from the suppression pool, and
- σ_g: standard deviation of the particle size distribution that emerges from the suppression pool

are tabulated in Tables A-1 to A-75. Tabulations show the ranges of values at confidence levels of 90 percent and 50 percent for percentiles of the cumulative distribution from 5 to 95 percentiles at 5 percent intervals. Distributions are shown for pool depths of 100, 200, 300, 500, and 700 cm. The mean of the sample used to construct each uncertainty distribution is also listed, but it should be noted that the mean has no particular statistical significance for the distributions listed here.

Table A-1. Uncertainty distribution for decontamination during bubble formation and equilibration of gap release through a 'T' quencher 100 cm deep

Percentile	Values of $\log_{10}$ DF(FE) characteristic of the indicated percentile at a confidence level, C, of	
	C = 90%	C = 50%
5	0.729 to 0.870	0.748 to 0.840
10	0.837 to 0.961	0.871 to 0.916
15	0.900 to 1.019	0.928 to 0.986
20	0.969 to 1.078	0.991 to 1.034
25	1.014 to 1.168	1.037 to 1.132
30	1.054 to 1.218	1.134 to 1.178
35	1.152 to 1.270	1.177 to 1.234
40	1.183 to 1.305	1.232 to 1.280
45	1.251 to 1.334	1.277 to 1.308
50	1.283 to 1.393	1.306 to 1.343
55	1.312 to 1.443	1.341 to 1.395
60	1.350 to 1.480	1.394 to 1.452
65	1.397 to 1.518	1.452 to 1.488
70	1.454 to 1.579	1.486 to 1.535
75	1.490 to 1.662	1.536 to 1.597
80	1.556 to 1.751	1.608 to 1.680
85	1.656 to 1.837	1.720 to 1.784
90	1.760 to 1.923	1.793 to 1.865
95	1.870 to 2.056	1.922 to 1.992
	Mean = 1.342	

Table A-2. Uncertainty distribution for decontamination of gap release during bubble rise from a 'T' quencher 100 cm deep

Percentile	Values of $\log_{10}$ DF(rise) characteristic of the indicated percentile at a confidence level, C, of	
	C = 90%	C = 50%
5	0.0308 to 0.0450	0.0345 to 0.0400
10	0.0399 to 0.0548	0.0456 to 0.0507
15	0.0478 to 0.0673	0.0544 to 0.0604
20	0.0549 to 0.0798	0.0617 to 0.0701
25	0.0656 to 0.0851	0.0704 to 0.0825
30	0.0733 to 0.106	0.0827 to 0.0914
35	0.0836 to 0.114	0.0902 to 0.108
40	0.0963 to 0.123	0.108 to 0.116
45	0.110 to 0.143	0.116 to 0.125
50	0.118 to 0.172	0.124 to 0.155
55	0.126 to 0.205	0.145 to 0.173
60	0.160 to 0.237	0.173 to 0.218
65	0.177 to 0.263	0.217 to 0.242
70	0.225 to 0.314	0.241 to 0.273
75	0.248 to 0.361	0.273 to 0.332
80	0.291 to 0.406	0.335 to 0.371
85	0.350 to 0.446	0.380 to 0.419
90	0.409 to 0.594	0.425 to 0.577
95	0.579 to 0.860	0.592 to 0.727
	Mean = 0.220	

Table A-3. Uncertainty distribution for the total gap release decontamination after passing through a 'T' quencher 100 cm deep

Percentile	Values of $\log_{10}$ DF(total) characteristic of the indicated percentile at a confidence level, C, of	
	C = 90%	C = 50%
5	0.889 to 1.008	0.920 to 0.982
10	0.982 to 1.113	1.009 to 1.063
15	1.036 to 1.221	1.102 to 1.183
20	1.128 to 1.274	1.194 to 1.226
25	1.208 to 1.348	1.227 to 1.326
30	1.243 to 1.390	1.328 to 1.355
35	1.334 to 1.453	1.354 to 1.404
40	1.359 to 1.493	1.400 to 1.462
45	1.426 to 1.546	1.461 to 1.522
50	1.464 to 1.625	1.503 to 1.559
55	1.580 to 1.640	1.551 to 1.631
60	1.566 to 1.691	1.629 to 1.661
65	1.633 to 1.770	1.656 to 1.698
70	1.671 to 1.834	1.698 to 1.782
75	1.740 to 1.966	1.782 to 1.847
80	1.792 to 2.046	1.865 to 1.996
85	1.946 to 2.110	2.000 to 2.088
90	2.060 to 2.166	2.109 to 2.144
95	2.144 to 2.412	2.166 to 2.261
	Mean = 1.562	

Table A-4. Uncertainty distribution for the mean particle size of gap release after passing through a 'T' quencher 100 cm deep

Percentile	Values of $\log_{10} d_p(\mu m)$ characteristic of the indicated percentile at a confidence level, C, of	
	C = 90%	C = 50%
5	0.077 to 0.080	0.078 to 0.079
10	0.079 to 0.081	0.080 to 0.081
15	0.080 to 0.083	0.081 to 0.082
20	0.082 to 0.083	0.082 to 0.084
25	0.083 to 0.086	0.084 to 0.085
30	0.084 to 0.088	0.085 to 0.086
35	0.085 to 0.090	0.086 to 0.089
40	0.087 to 0.093	0.088 to 0.091
45	0.089 to 0.096	0.091 to 0.094
50	0.091 to 0.101	0.094 to 0.097
55	0.095 to 0.104	0.096 to 0.102
60	0.097 to 0.111	0.101 to 0.105
65	0.102 to 0.121	0.104 to 0.113
70	0.107 to 0.131	0.113 to 0.123
75	0.115 to 0.136	0.123 to 0.133
80	0.127 to 0.142	0.133 to 0.137
85	0.135 to 0.157	0.139 to 0.147
90	0.143 to 0.166	0.152 to 0.162
95	0.163 to 0.204	0.166 to 0.183
	Mean = 0.105 μm	

Table A-5. Uncertainty distribution for the standard deviation of gap release after passing through a 'T' quencher 100 cm deep

Percentile	Values of σ characteristic of the indicated percentile at a confidence level, C, of	
	C = 90%	C = 50%
5	1.199 to 1.233	1.204 to 1.222
10	1.221 to 1.261	1.234 to 1.245
15	1.240 to 1.290	1.247 to 1.277
20	1.265 to 1.312	1.284 to 1.288
25	1.288 to 1.332	1.302 to 1.319
30	1.306 to 1.376	1.319 to 1.348
35	1.321 to 1.410	1.346 to 1.398
40	1.355 to 1.428	1.392 to 1.412
45	1.399 to 1.454	1.412 to 1.431
50	1.414 to 1.472	1.429 to 1.456
55	1.432 to 1.500	1.455 to 1.473
60	1.457 to 1.527	1.473 to 1.505
65	1.479 to 1.546	1.503 to 1.532
70	1.517 to 1.567	1.532 to 1.549
75	1.541 to 1.581	1.549 to 1.569
80	1.554 to 1.602	1.570 to 1.585
85	1.577 to 1.625	1.586 to 1.613
90	1.604 to 1.644	1.617 to 1.633
95	1.634 to 1.657	1.643 to 1.649
	Mean = 1.430	

Table A-6. Uncertainty distribution for decontamination during bubble formation and equilibration of gap release through a 'T' quencher 200 cm deep

Percentile	Values of $\log_{10}$ DF(FE) characteristic of the indicated percentile at a confidence level, C, of	
	C = 90%	C = 50%
5	0.651 to 0.861	0.696 to 0.740
10	0.739 to 0.993	0.862 to 0.924
15	0.903 to 1.037	0.978 to 1.015
20	1.001 to 1.084	1.018 to 1.052
25	1.037 to 1.142	1.056 to 1.114
30	1.077 to 1.185	1.115 to 1.148
35	1.135 to 1.240	1.146 to 1.201
40	1.155 to 1.284	1.198 to 1.262
45	1.204 to 1.319	1.257 to 1.298
50	1.268 to 1.363	1.289 to 1.328
55	1.302 to 1.414	1.321 to 1.369
60	1.333 to 1.478	1.366 to 1.416
65	1.379 to 1.551	1.415 to 1.490
70	1.431 to 1.599	1.488 to 1.571
75	1.534 to 1.645	1.571 to 1.611
80	1.590 to 1.601	1.614 to 1.658
85	1.631 to 1.738	1.669 to 1.692
90	1.684 to 1.897	1.714 to 1.804
95	1.811 to 1.964	1.896 to 1.936
	Mean = 1.322	

Table A-7. Uncertainty distribution for decontamination of gap release during bubble rise from a 'T' quencher 200 cm deep

Percentile	Values of $\log_{10}$ DF(rise) characteristic of the indicated percentile at a confidence level, C, of	
	C = 90%	C = 50%
5	0.0870 to 0.122	0.0911 to 0.105
10	0.105 to 0.157	0.124 to 0.139
15	0.135 to 0.173	0.155 to 0.163
20	0.159 to 0.182	0.166 to 0.176
25	0.172 to 0.220	0.177 to 0.189
30	0.179 to 0.248	0.190 to 0.227
35	0.196 to 0.320	0.227 to 0.265
40	0.235 to 0.378	0.259 to 0.331
45	0.272 to 0.417	0.329 to 0.398
50	0.332 to 0.491	0.388 to 0.431
55	0.399 to 0.520	0.422 to 0.499
60	0.446 to 0.590	0.496 to 0.531
65	0.502 to 0.678	0.530 to 0.603
70	0.550 to 0.716	0.603 to 0.692
75	0.637 to 0.794	0.692 to 0.733
80	0.705 to 0.884	0.741 to 0.820
85	0.785 to 1.010	0.828 to 0.918
90	0.904 to 1.220	0.985 to 1.100
95	1.114 to 1.677	1.021 to 1.423
	Mean = 0.510	

Table A-8. Uncertainty distribution for the total gap release decontamination after passing through a 'T' quencher 200 cm deep

Percentile	Values of $\log_{10}$ DF(total) characteristic of the indicated percentile at a confidence level, C, of	
	C = 90%	C = 50%
5	0.808 to 1.202	0.906 to 1.140
10	1.136 to 1.311	1.205 to 1.263
15	1.229 to 1.373	1.297 to 1.343
20	1.315 to 1.472	1.366 to 1.390
25	1.372 to 1.570	1.398 to 1.520
30	1.421 to 1.634	1.521 to 1.595
35	1.560 to 1.690	1.590 to 1.666
40	1.615 to 1.753	1.653 to 1.708
45	1.673 to 1.800	1.698 to 1.775
50	1.718 to 1.838	1.768 to 1.808
55	1.776 to 1.897	1.801 to 1.849
60	1.814 to 1.967	1.843 to 1.909
65	1.858 to 2.082	1.906 to 1.986
70	1.916 to 2.192	1.982 to 2.095
75	2.008 to 2.222	2.095 to 2.195
80	2.162 to 2.405	2.196 to 2.284
85	2.210 to 2.507	2.297 to 2.426
90	2.410 to 2.746	2.475 to 2.631
95	2.636 to 2.930	2.746 to 2.860
	Mean = 1.832	

Table A-9. Uncertainty distribution for mean particle size of gap release after flow through a 'T' quencher 200 cm deep

Percentile	Values of d_p (μm) characteristic of the indicated percentile at a confidence level, C, of	
	C = 90%	C = 50%
5	0.074 to 0.081	0.079 to 0.081
10	0.081 to 0.084	0.081 to 0.083
15	0.082 to 0.086	0.084 to 0.085
20	0.085 to 0.087	0.085 to 0.086
25	0.086 to 0.089	0.087 to 0.088
30	0.087 to 0.092	0.088 to 0.090
35	0.089 to 0.095	0.090 to 0.093
40	0.091 to 0.097	0.093 to 0.095
45	0.093 to 0.100	0.095 to 0.097
50	0.096 to 0.104	0.097 to 0.101
55	0.098 to 0.107	0.101 to 0.104
60	0.102 to 0.110	0.104 to 0.107
65	0.104 to 0.114	0.107 to 0.110
70	0.108 to 0.119	0.110 to 0.115
75	0.112 to 0.127	0.115 to 0.121
80	0.118 to 0.138	0.122 to 0.133
85	0.125 to 0.147	0.134 to 0.141
90	0.139 to 0.159	0.143 to 0.151
95	0.152 to 0.179	0.159 to 0.170
	Mean = 0.104 μm	

Table A-10. Uncertainty distribution for standard deviation of gap release after passing through a 'T' quencher 200 cm deep

Percentile	Values of σ characteristic of the indicated percentile at a confidence level, C, of	
	C = 90%	C = 50%
5	1.205 to 1.232	1.216 to 1.224
10	1.224 to 1.265	1.233 to 1.251
15	1.245 to 1.286	1.256 to 1.270
20	1.267 to 1.319	1.274 to 1.291
25	1.281 to 1.347	1.294 to 1.326
30	1.304 to 1.366	1.326 to 1.352
35	1.334 to 1.393	1.352 to 1.376
40	1.353 to 1.407	1.374 to 1.397
45	1.377 to 1.427	1.396 to 1.414
50	1.399 to 1.449	1.409 to 1.436
55	1.418 to 1.467	1.433 to 1.451
60	1.438 to 1.494	1.450 to 1.472
65	1.452 to 1.508	1.470 to 1.501
70	1.477 to 1.520	1.500 to 1.512
75	1.502 to 1.543	1.513 to 1.521
80	1.516 to 1.568	1.524 to 1.553
85	1.540 to 1.597	1.558 to 1.588
90	1.573 to 1.621	1.595 to 1.606
95	1.607 to 1.652	1.621 to 1.645
	Mean = 1.415	

Table A-11. Uncertainty distribution for the decontamination of gap release material during bubble formation and equilibration at a 'T' quencher 300 cm deep

Percentile	Values of $\log_{10}$ DF(FE) characteristic of the indicated percentile at a confidence level, C, of	
	C = 90%	C = 50%
5	0.729 to 0.864	0.780 to 0.835
10	0.865 to 0.986	0.916 to 0.950
15	0.962 to 1.060	0.992 to 1.037
20	1.036 to 1.095	1.060 to 1.081
25	1.080 to 1.132	1.091 to 1.112
30	1.105 to 1.173	1.127 to 1.158
35	1.148 to 1.232	1.167 to 1.197
40	1.190 to 1.282	1.215 to 1.254
45	1.234 to 1.318	1.264 to 1.299
50	1.291 to 1.348	1.305 to 1.334
55	1.323 to 1.375	1.337 to 1.363
60	1.352 to 1.424	1.370 to 1.396
65	1.381 to 1.480	1.412 to 1.444
70	1.432 to 1.526	1.457 to 1.502
75	1.484 to 1.586	1.518 to 1.553
80	1.550 to 1.669	1.573 to 1.633
85	1.633 to 1.731	1.665 to 1.692
90	1.696 to 1.836	1.736 to 1.792
95	1.838 to 1.945	1.876 to 1.921
	Mean = 1.324	

Table A-12. Uncertainty distribution for the decontamination of gap release material during bubble rise from a 'T' quencher 300 cm deep

Percentile	Values of $\log_{10}$ DF(rise) characteristic of the indicated percentile at a confidence level, C, of	
	C = 90%	C = 50%
5	0.147 to 0.185	0.168 to 0.179
10	0.186 to 0.219	0.197 to 0.213
15	0.214 to 0.263	0.227 to 0.245
20	0.245 to 0.305	0.262 to 0.283
25	0.278 to 0.352	0.300 to 0.326
30	0.318 to 0.387	0.340 to 0.372
35	0.360 to 0.434	0.383 to 0.411
40	0.398 to 0.491	0.423 to 0.456
45	0.438 to 0.548	0.473 to 0.520
50	0.498 to 0.602	0.525 to 0.575
55	0.552 to 0.674	0.590 to 0.622
60	0.605 to 0.758	0.660 to 0.718
65	0.698 to 0.848	0.740 to 0.798
70	0.780 to 0.984	0.837 to 0.909
75	0.903 to 1.165	0.967 to 1.117
80	1.050 to 1.359	1.156 to 1.248
85	1.247 to 1.750	1.353 to 1.554
90	1.651 to 2.078	1.785 to 1.952
95	2.092 to 2.878	2.185 to 2.538
	Mean = 0.8265	

Table A-13. Uncertainty distribution for the total decontamination of gap release material that has passed through a 'T' quencher 300 cm deep

Percentile	Values of $\log_{10}$ DF(total) characteristic of the indicated percentile at a confidence level, C, of	
	C = 90%	C = 50%
5	1.070 to 1.245	1.106 to 1.233
10	1.248 to 1.381	1.324 to 1.362
15	1.367 to 1.462	1.397 to 1.440
20	1.439 to 1.545	1.461 to 1.518
25	1.492 to 1.628	1.536 to 1.585
30	1.572 to 1.695	1.618 to 1.665
35	1.647 to 1.772	1.677 to 1.739
40	1.714 to 1.879	1.760 to 1.833
45	1.788 to 1.946	1.851 to 1.910
50	1.881 to 2.004	1.932 to 1.972
55	1.950 to 2.058	1.986 to 2.023
60	2.012 to 2.148	2.036 to 2.083
65	2.063 to 2.276	2.120 to 2.223
70	2.180 to 2.422	2.267 to 2.350
75	2.332 to 2.633	2.398 to 2.493
80	2.478 to 2.883	2.597 to 2.813
85	2.810 to 3.147	2.881 to 3.061
90	3.074 to 3.531	3.163 to 3.403
95	3.535 to 4.230	3.705 to 4.032
	Mean = 2.151	

Table A-14. Uncertainty distribution for the mean particle size of gap release material after passing through a 'T' quencher 300 cm deep

Percentile	Values of d_p (μm) characteristic of the indicated percentile at a confidence level, C, of	
	C = 90%	C = 50%
5	0.080 to 0.082	0.081 to 0.082
10	0.082 to 0.085	0.084 to 0.084
15	0.085 to 0.088	0.086 to 0.087
20	0.087 to 0.090	0.088 to 0.089
25	0.088 to 0.091	0.089 to 0.090
30	0.090 to 0.094	0.091 to 0.093
35	0.092 to 0.096	0.093 to 0.095
40	0.094 to 0.098	0.095 to 0.096
45	0.096 to 0.101	0.097 to 0.100
50	0.098 to 0.104	0.100 to 0.103
55	0.102 to 0.107	0.103 to 0.106
60	0.104 to 0.110	0.106 to 0.109
65	0.107 to 0.115	0.109 to 0.112
70	0.111 to 0.119	0.114 to 0.116
75	0.116 to 0.126	0.118 to 0.123
80	0.122 to 0.133	0.126 to 0.130
85	0.130 to 0.140	0.133 to 0.136
90	0.137 to 0.149	0.142 to 0.146
95	0.149 to 0.160	0.152 to 0.157
	Mean = 0.106 μm	

Table A-15. Uncertainty distribution for the standard deviation of gap release material after passing through a 'T' quencher 300 cm deep

Percentile	Values of σ characteristic of the indicated percentile at a confidence level, C, of	
	C = 90%	C = 50%
5	1.201 to 1.210	1.205 to 1.207
10	1.211 to 1.241	1.217 to 1.227
15	1.229 to 1.271	1.241 to 1.259
20	1.258 to 1.303	1.271 to 1.289
25	1.287 to 1.322	1.299 to 1.311
30	1.307 to 1.342	1.320 to 1.337
35	1.329 to 1.363	1.341 to 1.357
40	1.344 to 1.379	1.360 to 1.367
45	1.365 to 1.390	1.374 to 1.384
50	1.381 to 1.415	1.385 to 1.405
55	1.392 to 1.432	1.410 to 1.424
60	1.419 to 1.449	1.427 to 1.443
65	1.435 to 1.467	1.444 to 1.460
70	1.454 to 1.488	1.463 to 1.481
75	1.472 to 1.512	1.484 to 1.493
80	1.492 to 1.530	1.510 to 1.520
85	1.520 to 1.571	1.529 to 1.546
90	1.562 to 1.594	1.577 to 1.590
95	1.594 to 1.626	1.604 to 1.619
	Mean = 1.394	

Table A-16. Uncertainty distribution for decontamination during bubble formation and equilibration for gap release through a 'T' quencher 300 cm deep

Percentile	Values of $\log_{10}$ DF(FE) characteristic of the indicated percentile at a confidence level, C, of	
	C = 90%	C = 50%
5	0.696 to 0.838	0.774 to 0.812
10	0.811 to 0.931	0.839 to 0.904
15	0.861 to 1.004	0.924 to 0.959
20	0.933 to 1.008	0.967 to 1.036
25	0.995 to 1.119	1.043 to 1.097
30	1.064 to 1.193	1.097 to 1.138
35	1.098 to 1.222	1.129 to 1.201
40	1.167 to 1.266	1.199 to 1.228
45	1.207 to 1.311	1.226 to 1.276
50	1.235 to 1.335	1.273 to 1.321
55	1.286 to 1.370	1.319 to 1.343
60	1.323 to 1.420	1.340 to 1.372
65	1.350 to 1.461	1.372 to 1.426
70	1.378 to 1.533	1.425 to 1.474
75	1.443 to 1.571	1.478 to 1.546
80	1.511 to 1.640	1.549 to 1.612
85	1.568 to 1.729	1.619 to 1.653
90	1.640 to 1.783	1.705 to 1.759
95	1.760 to 1.962	1.782 to 1.914
	Mean = 1.295	

Table A-17. Uncertainty distribution for decontamination of gap release during bubble rise from a 'T' quencher 500 cm deep

Percentile	Values of $\log_{10}$ DF(rise) characteristic of the indicated percentile at a confidence level, C, of	
	C = 90%	C = 50%
5	0.196 to 0.300	0.243 to 0.292
10	0.292 to 0.351	0.300 to 0.318
15	0.310 to 0.408	0.338 to 0.360
20	0.353 to 0.463	0.367 to 0.442
25	0.400 to 0.531	0.445 to 0.476
30	0.451 to 0.573	0.477 to 0.546
35	0.481 to 0.638	0.546 to 0.595
40	0.554 to 0.721	0.592 to 0.648
45	0.599 to 0.826	0.641 to 0.755
50	0.667 to 0.942	0.742 to 0.854
55	0.764 to 1.020	0.833 to 0.953
60	0.866 to 1.130	0.948 to 1.040
65	0.972 to 1.130	1.037 to 1.166
70	1.049 to 1.389	1.160 to 1.422
75	1.249 to 1.762	1.427 to 1.652
80	1.464 to 2.061	1.660 to 1.846
85	1.723 to 2.460	1.884 to 2.104
90	2.073 to 2.882	2.315 to 2.570
95	2.589 to 4.053	2.876 to 3.242
	Mean = 1.135	

Table A-18. Uncertainty distribution for total gap release decontamination after passing through a 'T' quencher 500 cm deep

Percentile	Values of $\log_{10}$ DF(total) characteristic of the indicated percentile at a confidence level, C, of	
	C = 90%	C = 50%
5	1.028 to 1.310	1.099 to 1.277
10	1.274 to 1.556	1.311 to 1.525
15	1.420 to 1.625	1.536 to 1.598
20	1.561 to 1.746	1.609 to 1.681
25	1.622 to 1.842	1.692 to 1.789
30	1.727 to 1.922	1.789 to 1.876
35	1.808 to 2.020	1.873 to 1.972
40	1.896 to 2.132	1.952 to 2.058
45	1.980 to 2.208	2.030 to 2.178
50	2.085 to 2.282	2.154 to 2.211
55	2.179 to 2.366	2.210 to 2.299
60	2.212 to 2.543	2.293 to 2.428
65	2.301 to 2.732	2.398 to 2.555
70	2.463 to 2.922	2.553 to 2.775
75	2.604 to 3.018	2.780 to 2.946
80	2.852 to 3.366	2.955 to 3.133
85	3.009 to 3.846	3.223 to 3.455
90	3.390 to 4.192	3.715 to 4.106
95	4.109 to 5.428	4.182 to 4.622
	Mean = 2.430	

Table A-19. Uncertainty distribution for the mean particle size of gap release material after passing through a 'T' quencher 500 cm deep

Percentile	Values of d_p (μm) characteristic of the indicated percentile at a confidence level, C, of	
	C = 90%	C = 50%
5	0.082 to 0.085	0.082 to 0.084
10	0.084 to 0.089	0.085 to 0.087
15	0.086 to 0.092	0.088 to 0.089
20	0.089 to 0.094	0.090 to 0.093
25	0.091 to 0.096	0.093 to 0.095
30	0.093 to 0.099	0.095 to 0.097
35	0.096 to 0.101	0.097 to 0.099
40	0.097 to 0.102	0.099 to 0.101
45	0.100 to 0.104	0.101 to 0.102
50	0.101 to 0.106	0.102 to 0.105
55	0.102 to 0.110	0.105 to 0.107
60	0.105 to 0.114	0.107 to 0.112
65	0.108 to 0.117	0.111 to 0.114
70	0.112 to 0.124	0.114 to 0.118
75	0.115 to 0.131	0.118 to 0.127
80	0.121 to 0.137	0.127 to 0.132
85	0.130 to 0.147	0.133 to 0.144
90	0.139 to 0.160	0.146 to 0.148
95	0.150 to 0.164	0.160 to 0.161
	Mean = 0.108	

Table A-20. Uncertainty distribution for the geometric standard deviation of release material after passing through a 'T' quencher 500 cm deep

Percentile	Values of σ characteristic of the indicated percentile at a confidence level, C, of	
	C = 90%	C = 50%
5	1.198 to 1.248	1.217 to 1.240
10	1.240 to 1.272	1.248 to 1.261
15	1.260 to 1.292	1.271 to 1.283
20	1.273 to 1.304	1.287 to 1.298
25	1.290 to 1.329	1.299 to 1.317
30	1.302 to 1.342	1.317 to 1.335
35	1.323 to 1.355	1.334 to 1.346
40	1.335 to 1.369	1.344 to 1.357
45	1.346 to 1.379	1.357 to 1.370
50	1.359 to 1.391	1.370 to 1.379
55	1.370 to 1.415	1.379 to 1.395
60	1.381 to 1.444	1.393 to 1.420
65	1.397 to 1.455	1.418 to 1.449
70	1.423 to 1.478	1.449 to 1.458
75	1.450 to 1.501	1.458 to 1.483
80	1.477 to 1.521	1.483 to 1.512
85	1.490 to 1.548	1.514 to 1.528
90	1.522 to 1.593	1.532 to 1.557
95	1.557 to 1.637	1.593 to 1.611
	Mean = 1.388	

Table A-21. Uncertainty distribution for decontamination of gap release by bubble formation and equilibration at a 'T' quencher 700 cm deep

Percentile	Values of $\log_{10}$ DF(FE) characteristic of the indicated percentile at a confidence level, C, of	
	C = 90%	C = 50%
5	0.763 to 0.916	0.805 to 0.884
10	0.909 to 1.020	0.943 to 0.982
15	0.980 to 1.071	1.018 to 1.048
20	1.039 to 1.101	1.060 to 1.088
25	1.079 to 1.139	1.093 to 1.116
30	1.103 to 1.178	1.122 to 1.165
35	1.139 to 1.240	1.165 to 1.207
40	1.172 to 1.269	1.212 to 1.249
45	1.225 to 1.310	1.250 to 1.295
50	1.256 to 1.362	1.299 to 1.332
55	1.307 to 1.383	1.333 to 1.367
60	1.360 to 1.448	1.369 to 1.396
65	1.379 to 1.521	1.403 to 1.457
70	1.444 to 1.611	1.476 to 1.546
75	1.520 to 1.675	1.572 to 1.629
80	1.616 to 1.724	1.659 to 1.685
85	1.684 to 1.783	1.707 to 1.746
90	1.746 to 1.888	1.783 to 1.853
95	1.879 to 1.984	1.910 to 1.947
	Mean = 1.347	

Table A-22. Uncertainty distribution for decontamination of gap release during bubble rise from a 'T' quencher 700 cm deep

Percentile	Values of $\log_{10}$ DF(rise) characteristic of the indicated percentile at a confidence level, C, of	
	C = 90%	C = 50%
5	0.318 to 0.471	0.394 to 0.430
10	0.460 to 0.562	0.490 to 0.524
15	0.524 to 0.642	0.561 to 0.593
20	0.580 to 0.718	0.613 to 0.669
25	0.654 to 0.864	0.681 to 0.780
30	0.732 to 1.011	0.787 to 0.923
35	0.863 to 1.143	0.960 to 1.052
40	1.006 to 1.259	1.075 to 1.191
45	1.137 to 1.388	1.192 to 1.293
50	1.220 to 1.573	1.295 to 1.424
55	1.355 to 1.708	1.456 to 1.634
60	1.557 to 1.943	1.658 to 1.769
65	1.684 to 2.157	1.850 to 2.009
70	1.927 to 2.568	2.045 to 2.332
75	2.153 to 2.865	2.369 to 2.715
80	2.592 to 3.298	2.748 to 3.143
85	3.071 to 4.013	3.259 to 3.694
90	3.690 to 4.578	3.968 to 4.390
95	4.527 to 6.577	4.638 to 5.958
	Mean = 1.916	

Table A-23. Uncertainty distribution for total decontamination of gap release after passing through a 'T' quencher 700 cm deep

Percentile	Values of $\log_{10}$ DF(total) characteristic of the indicated percentile at a confidence level, C, of	
	C = 90%	C = 50%
5	1.405 to 1.653	1.500 to 1.606
10	1.625 to 1.799	1.667 to 1.741
15	1.740 to 2.003	1.799 to 1.914
20	1.896 to 2.152	1.955 to 2.061
25	2.034 to 2.254	2.091 to 2.209
30	2.156 to 2.372	2.222 to 2.306
35	2.254 to 2.455	2.319 to 2.397
40	2.361 to 2.637	2.412 to 2.513
45	2.445 to 2.787	2.549 to 2.693
50	2.587 to 2.917	2.696 to 2.858
55	2.740 to 3.097	2.861 to 2.982
60	2.910 to 3.306	2.999 to 3.170
65	3.082 to 3.542	3.179 to 3.422
70	3.298 to 3.849	3.428 to 3.575
75	3.542 to 4.360	3.599 to 3.947
80	3.896 to 4.716	4.171 to 4.532
85	4.529 to 5.493	4.646 to 5.170
90	5.167 to 6.114	5.450 to 5.742
95	5.947 to 8.018	6.384 to 7.506
	Mean = 3.264	

Table A-24. Uncertainty distribution for the mean particle size of gap release after passing through a 'T' quencher 700 cm deep

Percentile	Values of d_p (μm) characteristic of the indicated percentile at a confidence level, C, of	
	C = 90%	C = 50%
5	0.085 to 0.089	0.086 to 0.087
10	0.088 to 0.093	0.090 to 0.091
15	0.091 to 0.095	0.093 to 0.094
20	0.094 to 0.098	0.095 to 0.096
25	0.096 to 0.101	0.097 to 0.099
30	0.098 to 0.103	0.100 to 0.101
35	0.101 to 0.104	0.102 to 0.103
40	0.102 to 0.106	0.104 to 0.105
45	0.104 to 0.110	0.105 to 0.109
50	0.106 to 0.112	0.109 to 0.111
55	0.110 to 0.115	0.111 to 0.113
60	0.112 to 0.117	0.114 to 0.116
65	0.115 to 0.121	0.117 to 0.119
70	0.117 to 0.125	0.119 to 0.123
75	0.121 to 0.132	0.124 to 0.128
80	0.126 to 0.137	0.130 to 0.133
85	0.133 to 0.146	0.135 to 0.143
90	0.143 to 0.154	0.146 to 0.151
95	0.152 to 0.172	0.155 to 0.164
	Mean = 0.113 μm	

Table A-25. Uncertainty distribution for the standard deviation of gap release after passing through a 'T' quencher 700 cm deep

Percentile	Values of σ characteristic of the indicated percentile at a confidence level, C, of	
	C = 90%	C = 50%
5	1.187 to 1.208	1.193 to 1.201
10	1.203 to 1.222	1.211 to 1.216
15	1.216 to 1.246	1.221 to 1.240
20	1.234 to 1.269	1.244 to 1.252
25	1.250 to 1.285	1.258 to 1.279
30	1.272 to 1.297	1.280 to 1.291
35	1.285 to 1.317	1.294 to 1.307
40	1.297 to 1.330	1.309 to 1.322
45	1.314 to 1.340	1.323 to 1.331
50	1.325 to 1.356	1.333 to 1.348
55	1.336 to 1.372	1.348 to 1.358
60	1.354 to 1.394	1.359 to 1.377
65	1.371 to 1.415	1.383 to 1.399
70	1.394 to 1.431	1.401 to 1.424
75	1.414 to 1.447	1.427 to 1.437
80	1.431 to 1.466	1.442 to 1.454
85	1.453 to 1.485	1.462 to 1.474
90	1.474 to 1.531	1.484 to 1.510
95	1.519 to 1.574	1.542 to 1.557
	Mean = 1.348	

Table A-26. Uncertainty distribution for decontamination of invessel release by bubble formation and equilibration at a 'T' quencher 100 cm deep

Percentile	Values of $\log_{10}$ DF(FE) characteristic of the indicated percentile at a confidence level, C, of	
	C = 90%	C = 50%
5	0.545 to 0.693	0.620 to 0.653
10	0.692 to 0.865	0.739 to 0.811
15	0.820 to 1.017	0.878 to 0.969
20	0.933 to 1.075	1.015 to 1.055
25	1.042 to 1.146	1.073 to 1.110
30	1.096 to 1.238	1.125 to 1.173
35	1.155 to 1.353	1.210 to 1.309
40	1.257 to 1.422	1.321 to 1.393
45	1.364 to 1.496	1.400 to 1.459
50	1.425 to 1.596	1.461 to 1.525
55	1.499 to 1.680	1.534 to 1.626
60	1.599 to 1.798	1.648 to 1.723
65	1.686 to 1.920	1.763 to 1.859
70	1.817 to 2.018	1.876 to 1.950
75	1.934 to 2.189	1.993 to 2.112
80	2.066 to 2.339	2.173 to 2.267
85	2.261 to 2.679	2.330 to 2.530
90	2.566 to 2.894	2.698 to 2.837
95	2.891 to 3.944	3.079 to 3.462
	Mean = 1.673	

Table A-27. Uncertainty distribution for decontamination of invessel release during bubble rise from a 'T' quencher 100 cm deep

Percentile	Values of $\log_{10}$ DF(rise) characteristic of the indicated percentile at a confidence level, C, of	
	C = 90%	C = 50%
5	0.0167 to 0.0424	0.0260 to 0.0366
10	0.0412 to 0.0643	0.0513 to 0.0565
15	0.0570 to 0.0889	0.0648 to 0.0796
20	0.0794 to 0.1160	0.0887 to 0.1056
25	0.0974 to 0.1340	0.1140 to 0.1274
30	0.121 to 0.170	0.131 to 0.156
35	0.138 to 0.196	0.164 to 0.179
40	0.174 to 0.223	0.187 to 0.204
45	0.198 to 0.248	0.207 to 0.232
50	0.224 to 0.302	0.236 to 0.270
55	0.249 to 0.345	0.287 to 0.327
60	0.303 to 0.382	0.335 to 0.367
65	0.348 to 0.426	0.377 to 0.394
70	0.387 to 0.499	0.402 to 0.471
75	0.451 to 0.564	0.491 to 0.529
80	0.518 to 0.666	0.550 to 0.625
85	0.618 to 0.830	0.660 to 0.744
90	0.756 to 1.057	0.848 to 0.981
95	1.042 to 1.865	1.188 to 1.480
	Mean = 0.430	

Table A-28. Uncertainty distribution for total decontamination of invessel release after passing through a 'T' quencher 100 cm deep

Percentile	Values of $\log_{10}$ DF(total) characteristic of the indicated percentile at a confidence level, C, of	
	C = 90%	C = 50%
5	0.639 to 0.856	0.758 to 0.804
10	0.852 to 1.058	0.893 to 0.989
15	1.000 to 1.197	1.084 to 1.136
20	1.134 to 1.339	1.195 to 1.280
25	1.265 to 1.415	1.322 to 1.382
30	1.369 to 1.532	1.400 to 1.472
35	1.424 to 1.631	1.500 to 1.580
40	1.557 to 1.741	1.602 to 1.680
45	1.635 to 1.831	1.698 to 1.783
50	1.751 to 1.918	1.809 to 1.855
55	1.834 to 2.033	1.859 to 1.966
60	1.929 to 2.134	1.981 to 2.080
65	2.044 to 2.312	2.092 to 2.217
70	2.144 to 2.428	2.250 to 2.345
75	2.321 to 2.685	2.402 to 2.592
80	2.556 to 2.862	2.652 to 2.757
85	2.753 to 3.171	2.844 to 2.995
90	3.010 to 3.853	3.184 to 3.577
95	3.789 to 5.453	4.150 to 4.941
	Mean = 2.103	

Table A-29. Uncertainty distribution for the mean particle size of invessel release after passing through a 'T' quencher 100 cm deep

Percentile	Values of d_p (μm) characteristic of the indicated percentile at a confidence level, C, of	
	C = 90%	C = 50%
5	0.144 to 0.174	0.156 to 0.167
10	0.174 to 0.195	0.179 to 0.186
15	0.187 to 0.222	0.197 to 0.210
20	0.209 to 0.237	0.220 to 0.233
25	0.230 to 0.251	0.235 to 0.241
30	0.239 to 0.261	0.247 to 0.257
35	0.253 to 0.277	0.259 to 0.270
40	0.263 to 0.293	0.272 to 0.286
45	0.278 to 0.309	0.288 to 0.299
50	0.294 to 0.334	0.302 to 0.319
55	0.309 to 0.356	0.320 to 0.345
60	0.335 to 0.384	0.349 to 0.361
65	0.357 to 0.411	0.364 to 0.394
70	0.385 to 0.449	0.404 to 0.424
75	0.419 to 0.481	0.440 to 0.468
80	0.459 to 0.535	0.478 to 0.516
85	0.508 to 0.573	0.533 to 0.551
90	0.554 to 0.740	0.579 to 0.679
95	0.732 to 0.973	0.770 to 0.901
	Mean = 0.331 μm	

Table A-30. Uncertainty distribution for the geometric standard deviation of invessel release after passing through a 'T' quencher 100 cm deep

Percentile	Values of σ characteristic of the indicated percentile at a confidence level, C, of	
	C = 90%	C = 50%
5	1.004 to 1.030	1.011 to 1.026
10	1.030 to 1.090	1.044 to 1.060
15	1.066 to 1.142	1.096 to 1.128
20	1.125 to 1.186	1.139 to 1.164
25	1.160 to 1.263	1.180 to 1.228
30	1.211 to 1.317	1.242 to 1.288
35	1.276 to 1.379	1.299 to 1.352
40	1.339 to 1.425	1.364 to 1.403
45	1.382 to 1.454	1.411 to 1.436
50	1.427 to 1.485	1.446 to 1.470
55	1.455 to 1.543	1.472 to 1.497
60	1.486 to 1.574	1.504 to 1.558
65	1.544 to 1.616	1.565 to 1.595
70	1.582 to 1.670	1.610 to 1.639
75	1.626 to 1.730	1.649 to 1.711
80	1.703 to 1.773	1.727 to 1.745
85	1.744 to 1.819	1.768 to 1.798
90	1.801 to 1.921	1.835 to 1.879
95	1.914 to 2.052	1.966 to 2.014
	Mean = 1.431	

Table A-31. Uncertainty distribution for decontamination during bubble formation and equilibration for invessel release through a 'T' quencher 200 cm deep

Percentile	Values of $\log_{10}$ DF(FE) characteristic of the indicated percentile at a confidence level, C, of	
	C = 90%	C = 50%
5	0.496 to 0.742	0.584 to 0.648
10	0.649 to 0.951	0.751 to 0.855
15	0.838 to 1.035	0.948 to 1.002
20	0.972 to 1.126	1.022 to 1.081
25	1.037 to 1.232	1.094 to 1.179
30	1.123 to 1.296	1.201 to 1.264
35	1.220 to 1.354	1.276 to 1.310
40	1.289 to 1.415	1.311 to 1.372
45	1.335 to 1.515	1.373 to 1.435
50	1.395 to 1.620	1.436 to 1.538
55	1.448 to 1.731	1.540 to 1.676
60	1.556 to 1.865	1.679 to 1.763
65	1.710 to 2.061	1.765 to 1.927
70	1.813 to 2.155	1.953 to 2.086
75	2.039 to 2.372	2.114 to 2.215
80	2.154 to 2.568	2.227 to 2.420
85	2.388 to 2.708	2.498 to 2.625
90	2.608 to 3.142	2.685 to 2.783
95	2.911 to 4.329	3.422 to 3.651
	Mean = 1.738	

Table A-32. Uncertainty distribution for decontamination for invessel release during bubble rise from a 'T' quencher 200 cm deep

Percentile	Values of $\log_{10}$ DF(rise) characteristic of the indicated percentile at a confidence level, C, of	
	C = 90%	C = 50%
5	0.0528 to 0.115	0.0693 to 0.100
10	0.113 to 0.184	0.119 to 0.163
15	0.153 to 0.225	0.184 to 0.206
20	0.196 to 0.281	0.210 to 0.258
25	0.231 to 0.320	0.272 to 0.300
30	0.280 to 0.390	0.311 to 0.358
35	0.314 to 0.457	0.368 to 0.407
40	0.377 to 0.523	0.410 to 0.474
45	0.423 to 0.575	0.482 to 0.527
50	0.500 to 0.684	0.534 to 0.596
55	0.569 to 0.802	0.596 to 0.713
60	0.640 to 0.930	0.719 to 0.850
65	0.757 to 1.077	0.855 to 0.988
70	0.889 to 1.296	0.999 to 1.140
75	1.052 to 1.414	1.142 to 1.344
80	1.294 to 1.704	1.363 to 1.629
85	1.474 to 2.154	1.640 to 1.955
90	1.896 to 2.650	2.077 to 2.317
95	2.384 to 3.834	2.822 to 3.155
	Mean = 0.932	

Table A-33. Uncertainty distribution for total invessel release decontamination after passing through a 'T' quencher 200 cm deep

Percentile	Values of $\log_{10}$ DF(total) characteristic of the indicated percentile at a confidence level, C, of	
	C = 90%	C = 50%
5	0.707 to 1.055	0.915 to 1.021
10	1.034 to 1.296	1.107 to 1.177
15	1.173 to 1.417	1.279 to 1.384
20	1.346 to 1.536	1.405 to 1.500
25	1.424 to 1.648	1.516 to 1.581
30	1.534 to 1.854	1.595 to 1.766
35	1.624 to 1.972	1.793 to 1.885
40	1.840 to 2.099	1.900 to 1.997
45	1.944 to 2.2528	2.004 to 2.164
50	2.031 to 2.432	2.167 to 2.302
55	2.213 to 2.636	2.302 to 2.587
60	2.371 to 2.846	2.589 to 2.708
65	2.603 to 3.127	2.709 to 2.876
70	2.816 to 3.336	2.878 to 3.181
75	3.116 to 3.510	3.230 to 3.367
80	3.328 to 4.041	3.400 to 3.769
85	3.556 to 4.613	3.964 to 4.122
90	4.077 to 5.388	4.425 to 5.105
95	5.250 to 7.532	5.787 to 6.524
	Mean = 2.670	

Table A-34. Uncertainty distribution for mean particle size of invessel release after flow through a 'T' quencher 200 cm deep

Percentile	Values of d_p (μm) characteristic of the indicated percentile at a confidence level, C, of	
	C = 90%	C = 50%
5	0.124 to 0.153	0.132 to 0.144
10	0.147 to 0.180	0.157 to 0.168
15	0.166 to 0.196	0.180 to 0.185
20	0.183 to 0.220	0.190 to 0.204
25	0.198 to 0.239	0.207 to 0.227
30	0.216 to 0.255	0.230 to 0.243
35	0.237 to 0.276	0.245 to 0.262
40	0.250 to 0.306	0.262 to 0.282
45	0.266 to 0.325	0.285 to 0.313
50	0.291 to 0.363	0.313 to 0.331
55	0.321 to 0.378	0.332 to 0.367
60	0.349 to 0.393	0.367 to 0.382
65	0.372 to 0.437	0.382 to 0.405
70	0.387 to 0.495	0.409 to 0.447
75	0.424 to 0.545	0.454 to 0.507
80	0.489 to 0.617	0.518 to 0.571
85	0.552 to 0.695	0.591 to 0.646
90	0.634 to 0.771	0.689 to 0.734
95	0.740 to 1.100	0.826 to 0.983
	Mean = 0.330 μm	

Table A-35. Uncertainty distribution for the geometric standard deviation of invessel release after passing through a 'T' quencher 200 cm deep

Percentile	Values of σ characteristic of the indicated percentile at a confidence level, C, of	
	C = 90%	C = 50%
5	1.001 to 1.008	1.001 to 1.004
10	1.010 to 1.034	1.014 to 1.026
15	1.025 to 1.070	1.033 to 1.046
20	1.043 to 1.097	1.059 to 1.079
25	1.072 to 1.135	1.084 to 1.107
30	1.092 to 1.178	1.115 to 1.147
35	1.126 to 1.235	1.149 to 1.183
40	1.164 to 1.302	1.186 to 1.256
45	1.215 to 1.346	1.259 to 1.310
50	1.274 to 1.413	1.311 to 1.370
55	1.319 to 1.436	1.374 to 1.417
60	1.391 to 1.514	1.417 to 1.460
65	1.428 to 1.562	1.462 to 1.522
70	1.498 to 1.594	1.533 to 1.572
75	1.543 to 1.632	1.578 to 1.612
80	1.591 to 1.690	1.618 to 1.651
85	1.637 to 1.733	1.658 to 1.715
90	1.709 to 1.774	1.730 to 1.761
95	1.766 to 1.863	1.782 to 1.841
	Mean = 1.333	

Table A-36. Uncertainty distribution for decontamination of invessel release material by bubble formation and equilibration at a 'T' quencher 300 cm deep

Percentile	Values of $\log_{10}$ DF(FE) characteristic of the indicated percentile at a confidence level, C, of	
	C = 90%	C = 50%
5	0.442 to 0.691	0.533 to 0.611
10	0.693 to 0.860	0.779 to 0.831
15	0.847 to 0.982	0.882 to 0.927
20	0.924 to 1.089	0.980 to 1.031
25	1.019 to 1.226	1.082 to 1.158
30	1.133 to 1.254	1.194 to 1.238
35	1.230 to 1.343	1.246 to 1.304
40	1.273 to 1.381	1.312 to 1.351
45	1.345 to 1.472	1.362 to 1.401
50	1.385 to 1.524	1.414 to 1.496
55	1.477 to 1.606	1.509 to 1.548
60	1.528 to 1.714	1.572 to 1.690
65	1.637 to 1.857	1.699 to 1.764
70	1.742 to 1.983	1.807 to 1.915
75	1.906 to 2.183	1.946 to 2.059
80	2.056 to 2.433	2.115 to 2.292
85	2.292 to 2.821	2.406 to 2.692
90	2.756 to 3.272	2.876 to 3.072
95	3.285 to 4.083	3.478 to 3.698
	Mean = 1.708	

Table A-37. Uncertainty distribution for decontamination of invessel release during bubble rise from a 'T' quencher 300 cm deep

Percentile	Values of $\log_{10}$ DF(rise) characteristic of the indicated percentile at a confidence level, C, of	
	C = 90%	C = 50%
5	0.110 to 0.178	0.121 to 0.160
10	0.179 to 0.276	0.225 to 0.257
15	0.269 to 0.330	0.281 to 0.310
20	0.308 to 0.405	0.330 to 0.377
25	0.370 to 0.454	0.396 to 0.432
30	0.419 to 0.487	0.448 to 0.469
35	0.465 to 0.572	0.481 to 0.550
40	0.504 to 0.676	0.554 to 0.620
45	0.582 to 0.759	0.643 to 0.715
50	0.682 to 0.849	0.734 to 0.794
55	0.764 to 0.945	0.821 to 0.885
60	0.860 to 1.046	0.900 to 0.975
65	0.960 to 1.263	0.990 to 1.126
70	1.070 to 1.482	1.240 to 1.328
75	1.294 to 1.794	1.444 to 1.620
80	1.581 to 2.289	1.742 to 2.002
85	1.998 to 2.648	2.256 to 2.469
90	2.505 to 3.197	2.658 to 2.936
95	3.209 to 4.813	3.438 to 4.409
	Mean = 1.205	

Table A-38. Uncertainty distribution for total decontamination of invessel release material after passing through a 'T' quencher 300 cm deep

Percentile	Values of $\log_{10}$ DF(total) characteristic of the indicated percentile at a confidence level, C, of	
	C = 90%	C = 50%
5	0.805 to 1.160	0.892 to 1.097
10	1.163 to 1.346	1.219 to 1.294
15	1.305 to 1.473	1.354 to 1.438
20	1.435 to 1.620	1.473 to 1.544
25	1.524 to 1.809	1.610 to 1.700
30	1.685 to 1.957	1.727 to 1.885
35	1.841 to 2.087	1.894 to 2.021
40	1.988 to 2.216	2.052 to 2.123
45	2.092 to 2.381	2.162 to 2.300
50	2.264 to 2.492	2.331 to 2.440
55	2.395 to 2.692	2.464 to 2.548
60	2.508 to 2.886	2.591 to 2.740
65	2.706 to 3.178	2.782 to 2.966
70	2.922 to 3.416	3.067 to 3.278
75	3.238 to 4.037	3.364 to 3.701
80	3.529 to 4.552	3.898 to 4.250
85	4.247 to 5.187	4.543 to 4.740
90	4.866 to 6.113	5.295 to 5.457
95	6.126 to 8.004	6.348 to 6.754
	Mean = 2.914	

Table A-39. Uncertainty distribution for the mean particle size of invessel release material after passing through a 'T' quencher 300 cm deep

Percentile	Values of d_p (μm) characteristic of the indicated percentile at a confidence level, C, of	
	C = 90%	C = 50%
5	0.100 to 0.147	0.135 to 0.141
10	0.147 to 0.166	0.152 to 0.160
15	0.161 to 0.180	0.169 to 0.175
20	0.175 to 0.196	0.179 to 0.192
25	0.189 to 0.208	0.196 to 0.202
30	0.199 to 0.224	0.205 to 0.216
35	0.211 to 0.236	0.221 to 0.230
40	0.227 to 0.259	0.232 to 0.249
45	0.241 to 0.275	0.255 to 0.264
50	0.260 to 0.299	0.268 to 0.281
55	0.275 to 0.327	0.285 to 0.313
60	0.303 to 0.348	0.321 to 0.336
65	0.329 to 0.369	0.341 to 0.360
70	0.356 to 0.390	0.366 to 0.378
75	0.370 to 0.423	0.383 to 0.409
80	0.397 to 0.459	0.420 to 0.440
85	0.440 to 0.536	0.457 to 0.507
90	0.517 to 0.655	0.544 to 0.603
95	0.656 to 0.873	0.704 to 0.812
	Mean = 0.289 μm	

Table A-40. Uncertainty distribution for the geometric standard deviation of invessel release material after passing through a 'T' quencher 300 cm deep

Percentile	Values of σ characteristic of the indicated percentile at a confidence level, C, of	
	C = 90%	C = 50%
5	1.001 to 1.006	1.002 to 1.003
10	1.007 to 1.026	1.011 to 1.019
15	1.020 to 1.052	1.027 to 1.034
20	1.034 to 1.103	1.051 to 1.079
25	1.077 to 1.141	1.096 to 1.119
30	1.111 to 1.178	1.136 to 1.155
35	1.146 to 1.221	1.169 to 1.199
40	1.181 to 1.292	1.215 to 1.264
45	1.233 to 1.331	1.274 to 1.312
50	1.295 to 1.370	1.322 to 1.348
55	1.336 to 1.427	1.355 to 1.391
60	1.381 to 1.479	1.413 to 1.454
65	1.435 to 1.526	1.463 to 1.496
70	1.489 to 1.553	1.515 to 1.535
75	1.529 to 1.586	1.546 to 1.561
80	1.559 to 1.639	1.580 to 1.617
85	1.616 to 1.707	1.638 to 1.666
90	1.678 to 1.744	1.709 to 1.722
95	1.745 to 1.844	1.773 to 1.821
	Mean = 1.324	

Table A-41. Uncertainty distribution for the decontamination of invessel release material during formation and equilibration of bubbles at a 'T' quencher 500 cm deep

Percentile	Values of $\log_{10}$ DF(FE) characteristic of the indicated percentile at a confidence level, C, of	
	C = 90%	C = 50%
5	0.468 to 0.608	0.518 to 0.560
10	0.611 to 0.713	0.654 to 0.694
15	0.698 to 0.886	0.726 to 0.804
20	0.802 to 1.000	0.884 to 0.969
25	0.955 to 1.119	0.988 to 1.062
30	1.038 to 1.196	1.098 to 1.157
35	1.137 to 1.268	1.180 to 1.246
40	1.215 to 1.351	1.254 to 1.313
45	1.287 to 1.420	1.327 to 1.384
50	1.358 to 1.494	1.393 to 1.462
55	1.436 to 1.611	1.478 to 1.531
60	1.504 to 1.686	1.561 to 1.630
65	1.617 to 1.778	1.653 to 1.724
70	1.706 to 1.686	1.744 to 1.833
75	1.809 to 1.891	1.851 to 1.982
80	1.978 to 2.179	2.013 to 2.118
85	2.117 to 2.332	2.178 to 2.278
90	2.294 to 2.616	2.361 to 2.506
95	2.624 to 3.419	2.820 to 3.092
	Mean = 1.558	

Table A-42. Uncertainty distribution for the decontamination of invessel release during bubble rise from a 'T' quencher 500 cm deep

Percentile	Values of $\log_{10}$ DF(rise) characteristic of the indicated percentile at a confidence level, C, of	
	C = 90%	C = 50%
5	0.205 to 0.316	0.214 to 0.277
10	0.318 to 0.405	0.352 to 0.383
15	0.388 to 0.509	0.416 to 0.453
20	0.444 to 0.571	0.507 to 0.554
25	0.547 to 0.691	0.566 to 0.648
30	0.622 to 0.736	0.674 to 0.711
35	0.701 to 0.903	0.728 to 0.794
40	0.750 to 1.025	0.843 to 0.968
45	0.925 to 1.169	0.979 to 1.081
50	1.040 to 1.288	1.095 to 1.233
55	1.185 to 1.496	1.262 to 1.368
60	1.301 to 1.687	1.412 to 1.585
65	1.512 to 1.838	1.628 to 1.752
70	1.710 to 2.061	1.790 to 1.888
75	1.875 to 2.476	2.008 to 2.291
80	2.269 to 3.121	2.440 to 2.662
85	2.654 to 3.642	3.111 to 3.419
90	3.462 to 4.491	3.677 to 4.169
95	4.522 to 5.621	4.842 to 5.270
	Mean = 1.678	

Table A-43. Uncertainty distribution for the total decontamination of invessel release material after passing through a 'T' quencher 500 cm deep

Percentile	Values of $\log_{10}$ DF(total) characteristic of the indicated percentile at a confidence level, C, of	
	C = 90%	C = 50%
5	0.854 to 1.118	0.937 to 1.055
10	1.119 to 1.420	1.220 to 1.310
15	1.362 to 1.628	1.443 to 1.558
20	1.554 to 1.809	1.626 to 1.725
25	1.696 to 1.956	1.793 to 1.901
30	1.864 to 2.097	1.942 to 2.004
35	1.997 to 2.279	2.046 to 2.148
40	2.125 to 2.458	2.223 to 2.338
45	2.305 to 2.690	2.385 to 2.570
50	2.516 to 2.862	2.643 to 2.739
55	2.700 to 3.099	2.784 to 2.958
60	2.894 to 3.289	2.999 to 3.197
65	3.143 to 3.490	3.229 to 3.400
70	3.300 to 3.810	3.456 to 3.601
75	3.570 to 4.417	3.748 to 4.121
80	4.084 to 5.277	4.224 to 4.743
85	4.722 to 5.811	5.272 to 5.420
90	5.597 to 7.200	6.227 to 6.888
95	7.225 to 8.552	7.425 to 7.894
	Mean = 3.235	

Table A-44. Uncertainty distribution for the mean particle size of invessel release after passing through a 'T' quencher 500 cm deep

Percentile	Values of d_p (μm) characteristic of the indicated percentile at a confidence level, C, of	
	C = 90%	C = 50%
5	0.114 to 0.138	0.122 to 0.130
10	0.138 to 0.154	0.144 to 0.150
15	0.150 to 0.169	0.155 to 0.159
20	0.159 to 0.185	0.169 to 0.179
25	0.176 to 0.207	0.182 to 0.193
30	0.188 to 0.221	0.198 to 0.212
35	0.210 to 0.231	0.216 to 0.226
40	0.222 to 0.243	0.228 to 0.238
45	0.231 to 0.256	0.242 to 0.248
50	0.244 to 0.276	0.251 to 0.265
55	0.257 to 0.291	0.267 to 0.283
60	0.279 to 0.314	0.287 to 0.302
65	0.293 to 0.339	0.307 to 0.325
70	0.321 to 0.375	0.330 to 0.358
75	0.353 to 0.409	0.366 to 0.394
80	0.393 to 0.452	0.408 to 0.433
85	0.433 to 0.494	0.452 to 0.478
90	0.482 to 0.569	0.500 to 0.539
95	0.571 to 1.293	0.621 to 0.700
	Mean = 0.270 μm	

Table A-45. Uncertainty distribution for the geometric standard deviation of invessel release after passing through a 'T' quencher 500 cm deep

Percentile	Values of σ characteristic of the indicated percentile at a confidence level, C, of	
	C = 90%	C = 50%
5	1.0001 to 1.003	1.001 to 1.001
10	1.003 to 1.012	1.006 to 1.007
15	1.008 to 1.036	1.012 to 1.022
20	1.022 to 1.064	1.036 to 1.052
25	1.050 to 1.089	1.063 to 1.074
30	1.069 to 1.141	1.081 to 1.112
35	1.100 to 1.189	1.125 to 1.164
40	1.150 to 1.243	1.172 to 1.207
45	1.190 to 1.293	1.212 to 1.265
50	1.250 to 1.353	1.277 to 1.328
55	1.295 to 1.416	1.341 to 1.372
60	1.357 to 1.457	1.386 to 1.434
65	1.420 to 1.485	1.452 to 1.465
70	1.462 to 1.525	1.474 to 1.501
75	1.489 to 1.577	1.520 to 1.544
80	1.539 to 1.634	1.571 to 1.621
85	1.621 to 1.691	1.632 to 1.665
90	1.676 to 1.760	1.697 to 1.738
95	1.762 to 1.854	1.771 to 1.823
	Mean = 1.302	

Table A-46. Uncertainty distribution for decontamination of invessel release during bubble rise from a 'T' quencher 700 cm deep

Percentile	Values of $\log_{10}$ DF(rise) characteristic of the indicated percentile at a confidence level, C, of	
	C = 90%	C = 50%
5	0.326 to 0.468	0.425 to 0.445
10	0.468 to 0.573	0.505 to 0.514
15	0.530 to 0.671	0.580 to 0.637
20	0.631 to 0.762	0.671 to 0.702
25	0.694 to 0.923	0.738 to 0.866
30	0.831 to 1.057	0.892 to 1.016
35	0.968 to 1.169	1.048 to 1.087
40	1.060 to 1.312	1.090 to 1.241
45	1.187 to 1.457	1.265 to 1.351
50	1.331 to 1.695	1.387 to 1.601
55	1.473 to 2.070	1.634 to 1.852
60	1.775 to 2.286	1.937 to 2.247
65	2.156 to 2.548	2.257 to 2.369
70	2.311 to 2.835	2.438 to 2.708
75	2.573 to 3.399	2.807 to 3.148
80	3.132 to 3.722	3.317 to 3.558
85	3.558 to 4.521	3.715 to 4.072
90	4.076 to 5.466	4.905 to 5.157
95	5.496 to 7.458	5.866 to 6.960
	Mean = 2.185	

Table A-47. Uncertainty distribution for decontamination of invessel release by bubble formation and decontamination at a 'T' quencher 700 cm deep

Percentile	Values of $\log_{10}$ DF(FE) characteristic of the indicated percentile at a confidence level, C, of	
	C = 90%	C = 50%
5	0.498 to 0.698	0.582 to 0.646
10	0.706 to 0.866	0.780 to 0.803
15	0.819 to 0.972	0.870 to 0.928
20	0.926 to 1.057	0.971 to 1.014
25	1.007 to 1.108	1.049 to 1.092
30	1.064 to 1.158	1.103 to 1.130
35	1.115 to 1.306	1.151 to 1.235
40	1.180 to 1.372	1.281 to 1.327
45	1.316 to 1.475	1.346 to 1.427
50	1.389 to 1.546	1.456 to 1.483
55	1.480 to 1.618	1.498 to 1.576
60	1.552 to 1.707	1.588 to 1.639
65	1.622 to 1.792	1.659 to 1.752
70	1.732 to 1.885	1.779 to 1.852
75	1.825 to 1.991	1.872 to 1.937
80	1.898 to 2.096	1.970 to 2.061
85	2.061 to 2.357	2.088 to 2.227
90	2.277 to 2.522	2.366 to 2.399
95	2.524 to 2.764	2.573 to 2.627
	Mean = 1.531	

Table A-48. Uncertainty distribution for total decontamination of invessel release after passing through a 'T' quencher 700 cm deep

Percentile	Values of $\log_{10}$ DF(total) characteristic of the indicated percentile at a confidence level, C, of	
	C = 90%	C = 50%
5	1.298 to 1.444	1.351 to 1.396
10	1.447 to 1.695	1.474 to 1.571
15	1.665 to 1.851	1.717 to 1.808
20	1.799 to 2.047	1.850 to 1.916
25	1.901 to 2.236	2.043 to 2.176
30	2.134 to 2.444	2.235 to 2.388
35	2.345 to 2.599	2.425 to 2.504
40	2.460 to 2.803	2.524 to 2.713
45	2.632 to 3.155	2.778 to 2.917
50	2.886 to 3.353	2.952 to 3.198
55	3.163 to 3.616	3.261 to 3.494
60	3.382 to 3.972	3.576 to 3.715
65	3.642 to 4.317	3.867 to 4.095
70	4.035 to 4.687	4.224 to 4.353
75	4.334 to 5.182	4.611 to 4.931
80	4.905 to 5.535	5.155 to 5.259
85	5.248 to 6.666	5.535 to 6.129
90	6.366 to 7.348	6.777 to 7.239
95	7.360 to 9.838	7.919 to 9.084
	Mean = 3.716	

Table A-49. Uncertainty distribution for the mean particle size of invessel release after passing through a 'T' quencher 700 cm deep

Percentile	Values of d_p (μm) characteristic of the indicated percentile at a confidence level, C, of	
	C = 90%	C = 50%
5	0.111 to 0.127	0.117 to 0.122
10	0.127 to 0.143	0.128 to 0.141
15	0.141 to 0.158	0.146 to 0.151
20	0.150 to 0.167	0.158 to 0.161
25	0.161 to 0.179	0.166 to 0.175
30	0.171 to 0.200	0.179 to 0.187
35	0.183 to 0.214	0.191 to 0.209
40	0.201 to 0.230	0.213 to 0.222
45	0.216 to 0.248	0.225 to 0.240
50	0.233 to 0.260	0.245 to 0.251
55	0.249 to 0.288	0.257 to 0.265
60	0.264 to 0.304	0.267 to 0.295
65	0.292 to 0.326	0.302 to 0.311
70	0.305 to 0.351	0.319 to 0.334
75	0.332 to 0.388	0.342 to 0.369
80	0.368 to 0.431	0.387 to 0.405
85	0.404 to 0.473	0.431 to 0.462
90	0.464 to 0.617	0.476 to 0.537
95	0.618 to 0.879	0.665 to 0.859
	Mean = 0.258 μm	

Table A-50. Uncertainty distribution for the standard deviation of invessel release after passing through a 'T' quencher 700 cm deep

Percentile	Values of σ characteristic of the indicated percentile at a confidence level, C, of	
	C = 90%	C = 50%
5	1.0001 to 1.001	1.0002 to 1.0005
10	1.002 to 1.012	1.002 to 1.005
15	1.010 to 1.029	1.015 to 1.020
20	1.212 to 1.045	1.029 to 1.036
25	1.035 to 1.060	1.043 to 1.053
30	1.052 to 1.094	1.057 to 1.076
35	1.067 to 1.122	1.087 to 1.113
40	1.101 to 1.149	1.118 to 1.138
45	1.125 to 1.231	1.139 to 1.167
50	1.154 to 1.269	1.204 to 1.245
55	1.235 to 1.359	1.247 to 1.335
60	1.275 to 1.400	1.344 to 1.377
65	1.368 to 1.427	1.388 to 1.417
70	1.410 to 1.477	1.425 to 1.442
75	1.440 to 1.495	1.475 to 1.486
80	1.484 to 1.542	1.489 to 1.533
85	1.533 to 1.596	1.542 to 1.576
90	1.540 to 1.661	1.597 to 1.644
95	1.662 to 1.738	1.681 to 1.694
	Mean = 1.254	

Table A-51. Uncertainty distribution for decontamination of invessel release material during bubble formation and equilibration at an 'X' quencher 100 cm deep

Percentile	Values of $\log_{10}$ DF(FE) characteristic of the indicated percentile at a confidence level, C, of	
	C = 90%	C = 50%
5	0.660 to 0.853	0.723 to 0.821
10	0.852 to 0.949	0.872 to 0.898
15	0.904 to 1.159	0.983 to 1.108
20	1.105 to 1.258	1.154 to 1.226
25	1.217 to 1.390	1.240 to 1.324
30	1.297 to 1.474	1.366 to 1.432
35	1.393 to 1.562	1.445 to 1.498
40	1.480 to 1.661	1.538 to 1.589
45	1.567 to 1.761	1.609 to 1.683
50	1.666 to 1.846	1.694 to 1.794
55	1.762 to 1.941	1.822 to 1.866
60	1.847 to 2.050	1.879 to 1.975
65	1.950 to 2.171	2.201 to 2.103
70	2.067 to 2.337	2.132 to 2.228
75	2.195 to 2.492	2.279 to 2.395
80	2.359 to 2.766	2.460 to 2.615
85	2.594 to 3.035	2.763 to 2.854
90	2.859 to 3.467	3.040 to 3.276
95	3.460 to 4.692	3.603 to 4.076
	Mean = 1.961	

Table A-52. Uncertainty distribution for decontamination of invessel release material during bubble rise from an 'X' quencher 100 cm deep

Percentile	Values of $\log_{10}$ DF(rise) characteristic of the indicated percentile at a confidence level, C, of	
	C = 90%	C = 50%
5	0.0299 to 0.0556	0.0343 to 0.0493
10	0.0566 to 0.0813	0.0574 to 0.0705
15	0.0716 to 0.109	0.0821 to 0.0946
20	0.0927 to 0.135	0.107 to 0.122
25	0.120 to 0.154	0.127 to 0.147
30	0.142 to 0.182	0.151 to 0.168
35	0.163 to 0.209	0.174 to 0.195
40	0.189 to 0.240	0.198 to 0.227
45	0.212 to 0.277	0.233 to 0.256
50	0.245 to 0.325	0.269 to 0.303
55	0.277 to 0.358	0.308 to 0.335
60	0.327 to 0.424	0.343 to 0.381
65	0.358 to 0.467	0.400 to 0.440
70	0.429 to 0.523	0.449 to 0.477
75	0.472 to 0.700	0.501 to 0.590
80	0.582 to 0.834	0.654 to 0.756
85	0.752 to 1.086	0.825 to 1.017
90	1.027 to 1.261	1.114 to 1.206
95	1.254 to 1.812	1.455 to 1.760
	Mean = 0.468	

Table A-53. Uncertainty distribution for the total decontamination of invessel release material after passing through an 'X' quencher 100 cm deep

Percentile	Values of $\log_{10}$ DF(total) characteristic of the indicated percentile at a confidence level, C, of	
	C = 90%	C = 50%
5	0.798 to 0.982	0.870 to 0.940
10	0.980 to 1.246	1.072 to 1.156
15	1.172 to 1.416	1.262 to 1.322
20	1.321 to 1.544	1.411 to 1.486
25	1.466 to 1.692	1.522 to 1.580
30	1.576 to 1.773	1.637 to 1.727
35	1.706 to 1.853	1.742 to 1.802
40	1.780 to 1.933	1.816 to 1.881
45	1.858 to 2.035	1.902 to 1.981
50	1.937 to 2.180	1.988 to 2.090
55	2.038 to 2.353	2.141 to 2.259
60	2.180 to 2.493	2.283 to 2.397
65	2.377 to 2.658	2.455 to 2.560
70	2.517 to 2.845	2.583 to 2.719
75	2.675 to 3.060	2.780 to 2.996
80	2.955 to 3.419	3.047 to 3.172
85	3.164 to 3.832	3.383 to 3.577
90	3.590 to 4.441	3.836 to 4.210
95	4.436 to 6.116	4.933 to 5.836
	Mean = 2.429	

Table A-54. Uncertainty distribution for the mean particle size of invessel release material after passing through an 'X' quencher 100 cm deep

Percentile	Values of d_p (μm) characteristic of the indicated percentile at a confidence level, C, of	
	C = 90%	C = 50%
5	0.128 to 0.156	0.138 to 0.147
10	0.156 to 0.171	0.158 to 0.166
15	0.167 to 0.192	0.172 to 0.184
20	0.183 to 0.216	0.192 to 0.201
25	0.197 to 0.226	0.209 to 0.217
30	0.214 to 0.241	0.223 to 0.232
35	0.229 to 0.258	0.234 to 0.248
40	0.242 to 0.269	0.249 to 0.261
45	0.258 to 0.290	0.265 to 0.276
50	0.270 to 0.316	0.279 to 0.305
55	0.291 to 0.337	0.307 to 0.323
60	0.318 to 0.361	0.329 to 0.348
65	0.339 to 0.390	0.352 to 0.369
70	0.365 to 0.418	0.376 to 0.400
75	0.392 to 0.438	0.407 to 0.430
80	0.437 to 0.493	0.437 to 0.467
85	0.464 to 0.552	0.490 to 0.531
90	0.534 to 0.633	0.553 to 0.589
95	0.628 to 0.828	0.694 to 0.769
	Mean = 0.302 μm	

Table A-55. Uncertainty distribution for the geometric standard deviation of invessel release material after passing through an 'X' quencher 100 cm deep

Percentile	Values of σ characteristic of the indicated percentile at a confidence level, C, of	
	C = 90%	C = 50%
5	1.002 to 1.007	1.003 to 1.006
10	1.007 to 1.055	1.023 to 1.043
15	1.044 to 1.091	1.057 to 1.072
20	1.071 to 1.141	1.090 to 1.125
25	1.115 to 1.201	1.133 to 1.163
30	1.151 to 1.255	1.189 to 1.230
35	1.209 to 1.304	1.237 to 1.269
40	1.262 to 1.358	1.281 to 1.325
45	1.310 to 1.390	1.331 to 1.376
50	1.359 to 1.422	1.380 to 1.412
55	1.390 to 1.463	1.415 to 1.437
60	1.423 to 1.526	1.447 to 1.503
65	1.470 to 1.550	1.515 to 1.537
70	1.527 to 1.611	1.543 to 1.572
75	1.558 to 1.653	1.599 to 1.626
80	1.621 to 1.697	1.652 to 1.674
85	1.670 to 1.782	1.696 to 1.734
90	1.745 to 1.849	1.784 to 1.806
95	1.849 to 1.940	1.885 to 1.923
	Mean = 1.376	

Table A-56. Uncertainty distribution for decontamination during bubble formation and equilibration of invessel release through an 'X' quencher 200 cm deep

Percentile	Values of $\log_{10}$ DF(FE) characteristic of the indicated percentile at a confidence level, C, of	
	C = 90%	C = 50%
5	0.630 to 0.822	0.700 to 0.747
10	0.823 to 0.944	0.863 to 0.897
15	0.912 to 1.127	1.009 to 1.095
20	1.094 to 1.242	1.127 to 1.164
25	1.160 to 1.365	1.237 to 1.324
30	1.306 to 1.424	1.343 to 1.399
35	1.387 to 1.487	1.417 to 1.441
40	1.430 to 1.575	1.463 to 1.543
45	1.502 to 1.667	1.558 to 1.610
50	1.587 to 1.759	1.638 to 1.710
55	1.674 to 1.843	1.734 to 1.796
60	1.772 to 1.966	1.816 to 1.900
65	1.867 to 2.096	1.941 to 2.032
70	1.974 to 2.215	2.073 to 2.155
75	2.137 to 2.382	2.188 to 2.308
80	2.279 to 2.687	2.349 to 2.548
85	2.547 to 3.058	2.681 to 2.886
90	2.958 to 3.592	3.085 to 3.277
95	3.630 to 5.406	4.019 to 4.766
	Mean = 1.169	

Table A-57. Uncertainty distribution for decontamination of invessel release during rise from an 'X' quencher 200 cm deep

Percentile	Values of $\log_{10}$ DF(rise) characteristic of the indicated percentile at a confidence level, C, of	
	C = 90%	C = 50%
5	0.0539 to 0.105	0.0832 to 0.0958
10	0.106 to 0.158	0.130 to 0.139
15	0.142 to 0.196	0.162 to 0.184
20	0.184 to 0.234	0.195 to 0.220
25	0.217 to 0.288	0.233 to 0.253
30	0.246 to 0.351	0.275 to 0.314
35	0.302 to 0.422	0.331 to 0.393
40	0.372 to 0.467	0.408 to 0.442
45	0.432 to 0.522	0.454 to 0.503
50	0.481 to 0.582	0.518 to 0.546
55	0.526 to 0.700	0.556 to 0.613
60	0.589 to 0.788	0.664 to 0.726
65	0.709 to 0.943	0.746 to 0.866
70	0.825 to 1.071	0.906 to 1.011
75	0.995 to 1.314	1.041 to 1.152
80	1.149 to 1.476	1.281 to 1.373
85	1.371 to 1.838	1.475 to 1.715
90	1.748 to 2.255	1.916 to 2.113
95	2.265 to 3.523	2.615 to 3.018
	Mean = 0.880	

Table A-58. Uncertainty distribution for the total invessel release decontamination after passing through an 'X' quencher 200 cm deep

Percentile	Values of $\log_{10}$ DF(total) characteristic of the indicated percentile at a confidence level, C, of	
	C = 90%	C = 50%
5	0.835 to 1.122	0.881 to 1.094
10	1.126 to 1.324	1.188 to 1.258
15	1.282 to 1.472	1.370 to 1.426
20	1.425 to 1.646	1.471 to 1.583
25	1.566 to 1.790	1.638 to 1.730
30	1.708 to 1.894	1.777 to 1.844
35	1.813 to 2.037	1.860 to 1.958
40	1.928 to 2.179	1.998 to 2.097
45	2.060 to 2.285	2.118 to 2.241
50	2.217 to 2.487	2.254 to 2.348
55	2.300 to 2.643	2.416 to 2.548
60	2.514 to 2.834	2.577 to 2.751
65	2.674 to 2.956	2.805 to 2.887
70	2.854 to 3.270	2.928 to 3.104
75	3.055 to 3.687	3.194 to 3.465
80	3.414 to 4.115	3.627 to 3.888
85	3.885 to 4.993	4.074 to 4.770
90	4.903 to 6.058	5.041 to 5.359
95	6.078 to 7.777	6.802 to 7.161
	Mean = 2.832	

Table A-59. Uncertainty distribution for the mean particle size after passing through an 'X' quencher 200 cm deep

Percentile	Values of d_p (μm) characteristic of the indicated percentile at a confidence level, C, of	
	C = 90%	C = 50%
5	0.111 to 0.140	0.122 to 0.134
10	0.141 to 0.167	0.151 to 0.162
15	0.163 to 0.183	0.168 to 0.176
20	0.176 to 0.197	0.183 to 0.189
25	0.186 to 0.212	0.195 to 0.204
30	0.202 to 0.228	0.207 to 0.223
35	0.219 to 0.245	0.226 to 0.234
40	0.230 to 0.260	0.239 to 0.252
45	0.245 to 0.281	0.255 to 0.268
50	0.262 to 0.309	0.272 to 0.297
55	0.285 to 0.326	0.304 to 0.319
60	0.311 to 0.347	0.321 to 0.336
65	0.327 to 0.373	0.342 to 0.358
70	0.355 to 0.401	0.370 to 0.381
75	0.377 to 0.442	0.396 to 0.414
80	0.410 to 0.511	0.439 to 0.475
85	0.474 to 0.589	0.510 to 0.556
90	0.564 to 0.691	0.601 to 0.651
95	0.692 to 0.898	0.726 to 0.797
	Mean = 0.293 μm	

Table A-60. Uncertainty distribution for the geometric standard deviation of invessel release after passing through an 'X' quencher 200 cm deep

Percentile	Values of σ characteristic of the indicated percentile at a confidence level, C, of	
	C = 90%	C = 50%
5	1.0005 to 1.002	1.001 to 1.002
10	1.002 to 1.019	1.005 to 1.010
15	1.011 to 1.053	1.022 to 1.041
20	1.040 to 1.101	1.053 to 1.075
25	1.067 to 1.135	1.099 to 1.120
30	1.109 to 1.180	1.133 to 1.166
35	1.151 to 1.228	1.173 to 1.200
40	1.184 to 1.298	1.212 to 1.257
45	1.242 to 1.344	1.278 to 1.322
50	1.301 to 1.388	1.329 to 1.362
55	1.347 to 1.436	1.373 to 1.406
60	1.392 to 1.476	1.419 to 1.446
65	1.441 to 1.508	1.461 to 1.487
70	1.485 to 1.552	1.494 to 1.538
75	1.532 to 1.608	1.546 to 1.575
80	1.571 to 1.644	1.591 to 1.624
85	1.624 to 1.697	1.642 to 1.673
90	1.688 to 1.776	1.698 to 1.745
95	1.778 to 1.872	1.797 to 1.835
	Mean = 1.330	

Table A-61. Uncertainty distribution for the decontamination of invessel release by bubble formation and equilibration at an 'X' quencher 300 cm deep

Percentile	Values of $\log_{10}$ DF(FE) characteristic of the indicated percentile at a confidence level, C, of	
	C = 90%	C = 50%
5	0.591 to 0.796	0.655 to 0.748
10	0.785 to 0.897	0.829 to 0.862
15	0.861 to 1.018	0.896 to 0.971
20	0.928 to 1.134	0.994 to 1.089
25	1.061 to 1.233	1.110 to 1.173
30	1.142 to 1.339	1.184 to 1.263
35	1.232 to 1.458	1.271 to 1.395
40	1.321 to 1.542	1.402 to 1.487
45	1.453 to 1.588	1.500 to 1.555
50	1.530 to 1.674	1.558 to 1.602
55	1.580 to 1.774	1.618 to 1.698
60	1.662 to 1.848	1.716 to 1.792
65	1.766 to 1.992	1.803 to 1.911
70	1.832 to 2.159	1.924 to 2.046
75	1.991 to 2.421	2.129 to 2.257
80	2.169 to 2.660	2.302 to 2.504
85	2.464 to 2.918	2.577 to 2.753
90	2.750 to 3.337	2.912 to 3.192
95	3.311 to 4.108	3.422 to 3.966
	Mean = 1.805	

Table A-62. Uncertainty distribution for decontamination of invessel release material during bubble rise from an 'X' quencher 300 cm deep

Percentile	Values of $\log_{10}$ DF(rise) characteristic of the indicated percentile at a confidence level, C, of	
	C = 90%	C = 50%
5	0.0669 to 0.168	0.0878 to 0.149
10	0.158 to 0.233	0.173 to 0.211
15	0.208 to 0.319	0.232 to 0.278
20	0.269 to 0.381	0.310 to 0.344
25	0.332 to 0.457	0.351 to 0.416
30	0.392 to 0.543	0.432 to 0.512
35	0.457 to 0.646	0.523 to 0.559
40	0.541 to 0.731	0.604 to 0.666
45	0.636 to 0.810	0.670 to 0.751
50	0.703 to 0.881	0.760 to 0.837
55	0.790 to 0.999	0.862 to 0.932
60	0.875 to 1.177	0.941 to 1.062
65	0.988 to 1.311	1.102 to 1.207
70	1.160 to 1.544	1.224 to 1.378
75	1.310 to 1.813	1.474 to 1.623
80	1.568 to 2.274	1.714 to 1.915
85	1.875 to 2.994	2.179 to 2.660
90	2.656 to 3.996	2.860 to 3.466
95	3.754 to 4.804	4.060 to 4.444
	Mean = 1.255	

Table A-63. Uncertainty distribution for total decontamination of invessel release after passing through an 'X' quencher 300 cm deep

Percentile	Values of $\log_{10}$ DF(total) characteristic of the indicated percentile at a confidence level, C, of	
	C = 90%	C = 50%
5	0.845 to 1.185	0.919 to 1.015
10	1.139 to 1.434	1.212 to 1.377
15	1.353 to 1.580	1.433 to 1.497
20	1.470 to 1.754	1.519 to 1.603
25	1.563 to 1.902	1.644 to 1.801
30	1.766 to 2.005	1.827 to 1.963
35	1.900 to 2.136	1.977 to 2.032
40	2.001 to 2.308	2.049 to 2.218
45	2.099 to 2.511	2.234 to 2.357
50	2.275 to 2.634	2.365 to 2.556
55	2.440 to 2.841	2.569 to 2.717
60	2.626 to 3.003	2.759 to 2.940
65	2.832 to 3.308	2.960 to 3.043
70	3.000 to 3.911	3.122 to 3.411
75	3.306 to 4.347	3.422 to 4.043
80	3.979 to 5.144	4.183 to 4.782
85	4.575 to 5.991	5.060 to 5.666
90	5.661 to 6.522	5.973 to 6.256
95	6.419 to 8.005	6.567 to 7.043
	Mean = 3.060	

Table A-64. Uncertainty distribution for the mean particle size of invessel release after Passage through a 'X' quencher 300 cm deep

Percentile	Values of d_p (μm) characteristic of the indicated percentile at a confidence level, C, of	
	C = 90%	C = 50%
5	0.108 to 0.137	0.113 to 0.125
10	0.134 to 0.158	0.142 to 0.154
15	0.152 to 0.167	0.158 to 0.161
20	0.160 to 0.181	0.162 to 0.172
25	0.171 to 0.191	0.178 to 0.184
30	0.182 to 0.211	0.186 to 0.201
35	0.191 to 0.223	0.203 to 0.214
40	0.210 to 0.238	0.214 to 0.226
45	0.222 to 0.264	0.228 to 0.241
50	0.235 to 0.285	0.255 to 0.268
55	0.257 to 0.305	0.269 to 0.289
60	0.284 to 0.328	0.293 to 0.312
65	0.304 to 0.359	0.314 to 0.338
70	0.325 to 0.377	0.341 to 0.366
75	0.358 to 0.410	0.370 to 0.390
80	0.381 to 0.452	0.394 to 0.437
85	0.425 to 0.527	0.451 to 0.488
90	0.487 to 0.594	0.526 to 0.565
95	0.579 to 0.902	0.616 to 0.734
	Mean = 0.269 μm	

Table A-65. Uncertainty distribution for the geometric standard deviation of invessel release after passing through an 'X' quencher 300 cm deep

Percentile	Values of σ characteristic of the indicated percentile at a confidence level, C, of	
	C = 90%	C = 50%
5	1.0009 to 1.007	1.0005 to 1.005
10	1.007 to 1.013	1.009 to 1.012
15	1.011 to 1.029	1.013 to 1.019
20	1.017 to 1.068	1.022 to 1.049
25	1.036 to 1.122	1.060 to 1.099
30	1.073 to 1.187	1.106 to 1.140
35	1.121 to 1.229	1.153 to 1.208
40	1.180 to 1.279	1.210 to 1.244
45	1.224 to 1.352	1.252 to 1.308
50	1.273 to 1.394	1.312 to 1.376
55	1.331 to 1.441	1.377 to 1.403
60	1.388 to 1.498	1.407 to 1.463
65	1.434 to 1.529	1.467 to 1.508
70	1.497 to 1.572	1.515 to 1.543
75	1.529 to 1.630	1.551 to 1.589
80	1.578 to 1.672	1.604 to 1.645
85	1.637 to 1.732	1.653 to 1.704
90	1.703 to 1.786	1.732 to 1.748
95	1.773 to 1.962	1.810 to 1.904
	Mean = 1.327	

Table A-66. Uncertainty distribution for decontamination of invessel release by bubble formation and equilibration at an 'X' quencher 500 cm deep

Percentile	Values of $\log_{10}$ DF(FE) characteristic of the indicated percentile at a confidence level, C, of	
	C = 90%	C = 50%
5	0.559 to 0.840	0.725 to 0.794
10	0.794 to 0.920	0.844 to 0.894
15	0.874 to 1.059	0.909 to 1.004
20	0.928 to 1.148	1.025 to 1.107
25	1.043 to 1.258	1.114 to 1.166
30	1.123 to 1.400	1.167 to 1.307
35	1.198 to 1.512	1.298 to 1.416
40	1.350 to 1.547	1.413 to 1.519
45	1.461 to 1.647	1.517 to 1.558
50	1.523 to 1.706	1.552 to 1.649
55	1.574 to 1.758	1.647 to 1.730
60	1.656 to 1.939	1.719 to 1.790
65	1.732 to 2.096	1.784 to 1.954
70	1.842 to 2.186	1.954 to 2.121
75	1.976 to 2.384	2.121 to 2.220
80	2.145 to 2.638	2.245 to 2.405
85	2.359 to 2.791	2.462 to 2.692
90	2.653 to 3.248	2.746 to 2.922
95	2.930 to 3.803	3.247 to 3.662
	Mean = 1.741	

Table A-67. Uncertainty distribution for decontamination of invessel release during bubble rise from an 'X' quencher 500 cm deep

Percentile	Values of $\log_{10}$ DF(rise) characteristic of the indicated percentile at a confidence level, C, of	
	C = 90%	C = 50%
5	0.0743 to 0.320	0.149 to 0.278
10	0.275 to 0.519	0.328 to 0.437
15	0.419 to 0.598	0.465 to 0.547
20	0.529 to 0.679	0.552 to 0.638
25	0.587 to 0.842	0.644 to 0.732
30	0.670 to 0.960	0.733 to 0.878
35	0.783 to 1.061	0.875 to 0.986
40	0.897 to 1.211	0.981 to 1.076
45	1.025 to 1.355	1.073 to 1.258
50	1.081 to 1.625	1.243 to 1.404
55	1.292 to 1.865	1.397 to 1.779
60	1.418 to 2.126	1.706 to 1.902
65	1.794 to 2.448	1.894 to 2.231
70	1.931 to 2.845	2.210 to 2.526
75	2.253 to 4.014	2.533 to 3.073
80	2.744 to 5.498	3.184 to 4.234
85	3.665 to 5.922	4.438 to 5.634
90	5.530 to 6.794	5.818 to 6.167
95	6.200 to 7.416	6.784 to 7.238
	Mean = 2.197	

Table A-68. Uncertainty distribution for total decontamination of invessel release after passing through an 'X' quencher 500 cm deep

Percentile	Values of $\log_{10}$ DF(total) characteristic of the indicated percentile at a confidence level, C, of	
	C = 90%	C = 50%
5	0.849 to 1.386	1.008 to 1.300
10	1.297 to 1.655	1.390 to 1.465
15	1.441 to 1.943	1.622 to 1.849
20	1.692 to 2.077	1.864 to 2.004
25	1.924 to 2.213	2.024 to 2.150
30	2.049 to 2.522	2.157 to 2.327
35	2.190 to 2.820	2.323 to 2.592
40	2.358 to 3.013	2.581 to 2.853
45	2.621 to 3.214	2.838 to 3.034
50	2.875 to 3.416	3.020 to 3.269
55	3.057 to 3.776	3.260 to 3.430
60	3.290 to 3.906	3.421 to 3.799
65	3.502 to 4.289	3.783 to 3.985
70	3.855 to 5.379	3.972 to 4.388
75	4.151 to 6.613	4.398 to 5.858
80	5.036 to 7.381	5.982 to 7.178
85	6.173 to 8.488	7.213 to 7.988
90	7.524 to 8.817	8.410 to 8.686
95	8.692 to 9.642	8.812 to 9.054
	Mean = 3.938	

Table A-69. Uncertainty distribution for the mean particle size of invessel release material after passing through an 'X' quencher 500 cm deep

Percentile	Values of d_p (μm) characteristic of the indicated percentile at a confidence level, C, of	
	C = 90%	C = 50%
5	0.106 to 0.136	0.112 to 0.126
10	0.126 to 0.152	0.137 to 0.141
15	0.140 to 0.165	0.146 to 0.161
20	0.153 to 0.174	0.162 to 0.168
25	0.164 to 0.191	0.169 to 0.178
30	0.172 to 0.199	0.179 to 0.194
35	0.183 to 0.224	0.194 to 0.205
40	0.196 to 0.252	0.204 to 0.230
45	0.210 to 0.265	0.229 to 0.258
50	0.230 to 0.292	0.255 to 0.265
55	0.259 to 0.324	0.265 to 0.305
60	0.272 to 0.347	0.302 to 0.327
65	0.307 to 0.369	0.327 to 0.357
70	0.329 to 0.407	0.355 to 0.372
75	0.363 to 0.450	0.372 to 0.425
80	0.388 to 0.498	0.427 to 0.467
85	0.440 to 0.564	0.481 to 0.511
90	0.501 to 0.625	0.532 to 0.569
95	0.572 to 0.867	0.622 to 0.789
	Mean = 0.272 μm	

Table A-70. Uncertainty distribution for the geometric standard deviation of invessel release material after passing through an 'X' quencher 500 cm deep

Percentile	Values of σ characteristic of the indicated percentile at a confidence level, C, of	
	C = 90%	C = 50%
5	1.0001 to 1.0013	1.0004 to 1.0009
10	1.0007 to 1.004	1.001 to 1.003
15	1.002 to 1.015	1.004 to 1.005
20	1.004 to 1.027	1.006 to 1.022
25	1.011 to 1.057	1.022 to 1.040
30	1.024 to 1.085	1.041 to 1.062
35	1.046 to 1.132	1.062 to 1.095
40	1.064 to 1.186	1.091 to 1.134
45	1.097 to 1.232	1.132 to 1.191
50	1.140 to 1.313	1.191 to 1.244
55	1.192 to 1.358	1.240 to 1.320
60	1.248 to 1.417	1.316 to 1.378
65	1.326 to 1.476	1.375 to 1.430
70	1.385 to 1.529	1.430 to 1.494
75	1.444 to 1.578	1.494 to 1.535
80	1.502 to 1.612	1.538 to 1.590
85	1.566 to 1.655	1.591 to 1.623
90	1.613 to 1.701	1.639 to 1.668
95	1.670 to 1.952	1.701 to 1.855
	Mean = 1.260	

Table A-71. Uncertainty distribution for decontamination of invessel release by bubble formation and equilibration at an 'X' quencher 700 cm deep

Percentile	Values of $\log_{10}$ DF(FE) characteristic of the indicated percentile at a confidence level, C, of	
	C = 90%	C = 50%
5	0.517 to 0.731	0.553 to 0.653
10	0.656 to 0.902	0.738 to 0.844
15	0.823 to 1.111	0.896 to 1.023
20	0.916 to 1.221	1.066 to 1.134
25	1.089 to 1.298	1.144 to 1.255
30	1.208 to 1.371	1.256 to 1.329
35	1.267 to 1.434	1.329 to 1.393
40	1.350 to 1.513	1.390 to 1.441
45	1.396 to 1.659	1.438 to 1.549
50	1.454 to 1.750	1.540 to 1.668
55	1.556 to 1.847	1.662 to 1.754
60	1.684 to 1.986	1.756 to 1.864
65	1.776 to 2.116	1.862 to 2.020
70	1.899 to 2.206	2.018 to 2.146
75	2.078 to 2.499	2.146 to 2.229
80	2.168 to 2.751	2.273 to 2.539
85	2.467 to 3.008	2.599 to 2.835
90	2.788 to 3.282	2.937 to 3.031
95	3.035 to 4.214	3.282 to 3.375
	Mean = 1.786	

Table A-72. Uncertainty distribution for decontamination of invessel release during bubble rise from an 'X' quencher 700 cm deep

Percentile	Values of $\log_{10}$ DF(rise) characteristic of the indicated percentile at a confidence level, C, of	
	C = 90%	C = 50%
5	0.238 to 0.411	0.291 to 0.383
10	0.384 to 0.584	0.421 to 0.541
15	0.484 to 0.771	0.574 to 0.623
20	0.588 to 0.878	0.651 to 0.827
25	0.760 to 1.015	0.829 to 0.934
30	0.846 to 1.179	0.950 to 1.095
35	1.004 to 1.411	1.091 to 1.217
40	1.114 to 1.536	1.204 to 1.427
45	1.282 to 1.722	1.424 to 1.576
50	1.460 to 1.893	1.558 to 1.732
55	1.591 to 2.047	1.728 to 1.924
60	1.739 to 2.314	1.906 to 2.130
65	1.969 to 2.752	2.080 to 2.340
70	2.223 to 3.169	2.340 to 2.790
75	2.461 to 3.302	2.793 to 3.254
80	2.977 to 4.011	3.262 to 3.464
85	3.295 to 5.298	3.546 to 4.499
90	4.115 to 5.918	4.836 to 5.468
95	5.509 to 7.485	5.934 to 6.737
	Mean = 2.209	

Table A-73. Uncertainty distribution for total decontamination of invessel release after passing through an 'X' quencher 700 cm deep

Percentile	Values of $\log_{10}$ DF(total) characteristic of the indicated percentile at a confidence level, C, of	
	C = 90%	C = 50%
5	1.247 to 1.545	1.383 to 1.441
10	1.442 to 1.847	1.558 to 1.746
15	1.700 to 2.077	1.780 to 1.931
20	1.897 to 2.216	1.976 to 2.122
25	2.063 to 2.728	2.128 to 2.331
30	2.152 to 2.942	2.338 to 2.767
35	2.597 to 3.251	2.757 to 3.061
40	2.856 to 3.352	3.054 to 3.288
45	3.103 to 3.556	3.268 to 3.367
50	3.306 to 3.667	3.357 to 3.587
55	3.394 to 3.947	3.572 to 3.729
60	3.602 to 4.159	3.688 to 4.036
65	3.759 to 4.620	4.028 to 4.481
70	4.049 to 4.870	4.445 to 4.680
75	4.516 to 5.395	4.690 to 4.892
80	4.825 to 6.417	4.906 to 5.676
85	5.243 to 7.337	5.847 to 6.562
90	6.454 to 9.175	6.851 to 8.026
95	8.094 to 10.000	9.181 to 9.808
	Mean = 3.995	

Table A-74. Uncertainty distribution for the mean particle size of invessel release after passing through an 'X' quencher 700 cm deep

Percentile	Values of d_p (μm) characteristic of the indicated percentile at a confidence level, C, of	
	C = 90%	C = 50%
5	0.106 to 0.121	0.114 to 0.117
10	0.117 to 0.137	0.122 to 0.131
15	0.128 to 0.159	0.135 to 0.155
20	0.140 to 0.172	0.158 to 0.169
25	0.159 to 0.187	0.170 to 0.176
30	0.171 to 0.204	0.176 to 0.190
35	0.184 to 0.222	0.189 to 0.204
40	0.196 to 0.241	0.204 to 0.230
45	0.209 to 0.256	0.230 to 0.244
50	0.232 to 0.280	0.243 to 0.261
55	0.246 to 0.304	0.261 to 0.287
60	0.262 to 0.322	0.283 to 0.308
65	0.291 to 0.356	0.307 to 0.339
70	0.311 to 0.369	0.338 to 0.360
75	0.346 to 0.394	0.360 to 0.376
80	0.367 to 0.495	0.377 to 0.422
85	0.386 to 0.515	0.431 to 0.504
90	0.499 to 0.616	0.510 to 0.526
95	0.536 to 0.882	0.617 to 0.790
	Mean = 0.260 μm	

Table A-75. Uncertainty distribution for the standard deviation of invessel release after passing through an 'X' quencher 700 cm deep

Percentile	Values of σ characteristic of the indicated percentile at a confidence level, C, of	
	C = 90%	C = 50%
5	1.00001 to 1.0013	1.00004 to 1.00004
10	1.0004 to 1.006	1.0014 to 1.003
15	1.002 to 1.018	1.005 to 1.011
20	1.006 to 1.027	1.012 to 1.020
25	1.018 to 1.043	1.020 to 1.030
30	1.022 to 1.068	1.030 to 1.049
35	1.035 to 1.100	1.048 to 1.075
40	1.054 to 1.126	1.074 to 1.111
45	1.078 to 1.169	1.109 to 1.127
50	1.115 to 1.240	1.127 to 1.175
55	1.128 to 1.289	1.172 to 1.264
60	1.185 to 1.374	1.258 to 1.298
65	1.271 to 1.403	1.293 to 1.383
70	1.331 to 1.420	1.383 to 1.409
75	1.388 to 1.456	1.410 to 1.424
80	1.414 to 1.522	1.425 to 1.472
85	1.456 to 1.572	1.485 to 1.543
90	1.523 to 1.641	1.557 to 1.614
95	1.618 to 1.671	1.641 to 1.662
	Mean = 1.21	

NRC FORM 335 (2-89) NRCM 1102, 3201, 3202

U.S. NUCLEAR REGULATORY COMMISSION

BIBLIOGRAPHIC DATA SHEET

(See instructions on the reverse)

1. REPORT NUMBER (Assigned by NRC, Add Vol., Supp., Rev., and Addendum Numbers, if any.)

NUREG/CR-6153

2. TITLE AND SUBTITLE

A Simplified Model of Decontamination by BWR Steam Suppression Pools

3. DATE REPORT PUBLISHED

MONTH	YEAR
May	1997

4. FIN OR GRANT NUMBER

L2035

5. AUTHOR(S)

D.A. Powers

6. TYPE OF REPORT

7. PERIOD COVERED *(Inclusive Dates)*

8. PERFORMING ORGANIZATION - NAME AND ADDRESS *(If NRC, provide Division, Office or Region, U.S. Nuclear Regulatory Commission, and mailing address; if contractor, provide name and mailing address.)*

Sandia National Laboratories
Albuquerque, NM 87185

9. SPONSORING ORGANIZATION - NAME AND ADDRESS *(If NRC, type "Same as above"; if contractor, provide NRC Division, Office or Region, U.S. Nuclear Regulatory Commission, and mailing address.)*

Division of Systems Technology
Office of Nuclear Regulatory Research
U.S. Nuclear Regulatory Commission
Washington, DC 20555-0001

10. SUPPLEMENTARY NOTES

J.H. Schaperow, NRC Project manager

11. ABSTRACT *(200 words or less)*

An uncertainty analysis of aerosol removal by nuclear reactor steam suppression pools is described. Uncertainties considered in the analyses include uncertainties in boundary conditions dictated by accident progression, uncertainties in bubble behavior, and uncertainties in aerosol properties. Uncertainty distribution for decontamination factors, aerosol particle sizes, and the geometric standard deviation of the size distributions are developed as functions of suppression pool depth. Results of the uncertainty distribution are used to construct a simplified model of decontamination by steam suppression pools.

12. KEY WORDS/DESCRIPTORS *(List words or phrases that will assist researchers in locating the report.)*

source term, decontamination, suppression pool, aerosol, bubbles, bubble swarms, plumes, shape factors, fractal geometry

13. AVAILABILITY STATEMENT

unlimited

14. SECURITY CLASSIFICATION

(This Page)
unclassified

(This Report)
unclassified

15. NUMBER OF PAGES

16. PRICE